

ornl

ORNL/TM-11719

**OAK RIDGE
NATIONAL
LABORATORY**

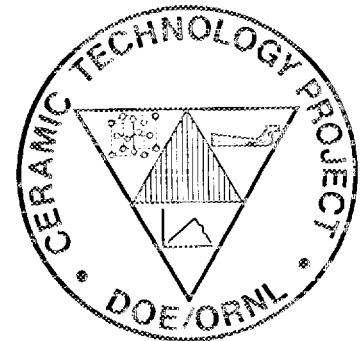
MARTIN MARIETTA

**Ceramic Technology for
Advanced Heat Engines Project
Semiannual Progress Report for
April 1990 Through September 1990**

Prepared for
U.S. Department of Energy
Assistant Secretary for
Conservation and Renewable Energy
Office of Transportation Technologies
Advanced Materials Development Program

**CERAMIC TECHNOLOGY FOR
ADVANCED HEAT ENGINES**

OAK RIDGE NATIONAL LABORATORY
CENTRAL RESEARCH LIBRARY
CIRCULATION SECTION
4809 ROSS AVENUE
LIBRARY LOAN COPY
DO NOT TRANSFER TO ANOTHER PERSON
If you wish someone else to see this
report, send in name with report and
the library will arrange a loan.



MANAGED BY
MARTIN MARIETTA ENERGY SYSTEMS, INC.
FOR THE UNITED STATES
DEPARTMENT OF ENERGY

This report has been reproduced directly from the best available copy.

Available to DOE and DOE contractors from the Office of Scientific and Technical Information, P.O. Box 62, Oak Ridge, TN 37831; prices available from (615) 576-8401, FTS 626-8401.

Available to the public from the National Technical Information Service, U.S. Department of Commerce, 5285 Port Royal Rd., Springfield, VA 22161.

This report was prepared as an account of work sponsored by an agency of the United States Government. Neither the United States Government nor any agency thereof, nor any of their employees, makes any warranty, express or implied, or assumes any legal liability or responsibility for the accuracy, completeness, or usefulness of any information, apparatus, product, or process disclosed, or represents that its use would not infringe privately owned rights. Reference herein to any specific commercial product, process, or service by trade name, trademark, manufacturer, or otherwise, does not necessarily constitute or imply its endorsement, recommendation, or favoring by the United States Government or any agency thereof. The views and opinions of authors expressed herein do not necessarily state or reflect those of the United States Government or any agency thereof.

Metals and Ceramics Division
CERAMIC TECHNOLOGY FOR ADVANCED HEAT ENGINES PROJECT
SEMIANNUAL PROGRESS REPORT FOR
APRIL 1990 THROUGH SEPTEMBER 1990

D. R. Johnson
Project Manager

Date Published: December 1990

NOTICE: This document contains information of a preliminary nature. It is subject to revision or correction and therefore does not represent a final report.

Prepared for
U.S. Department of Energy
Assistant Secretary for Conservation and Renewable Energy
Office of Transportation Technologies
Advanced Materials Development Program
EE 04 00 00 0

Prepared by the
OAK RIDGE NATIONAL LABORATORY
Oak Ridge, Tennessee 37831-6285
managed by
MARTIN MARIETTA ENERGY SYSTEMS, INC.
for the
U.S. DEPARTMENT OF ENERGY
under Contract DE-AC05-84OR21400



REPORTS PREVIOUSLY ISSUED

ORNL/TM-9325	Period March 1983-September 1983
ORNL/TM-9466	Period October 1983-March 1984
ORNL/TM-9497	Period April 1984-September 1984
ORNL/TM-9673	Period October 1984-March 1985
ORNL/TM-9947	Period April 1985-September 1985
ORNL/TM-10079	Period October 1985-March 1986
ORNL/TM-10308	Period April 1986-September 1986
ORNL/TM-10469	Period October 1986-March 1987
ORNL/TM-10705	Period April 1987-September 1987
ORNL/TM-10838	Period October 1987-March 1988
ORNL/TM-11116	Period April 1988-September 1988
ORNL/TM-11239	Period October 1988-March 1989
ORNL/TM-11489	Period April 1989-September 1989
ORNL/TM-11586	Period October 1989-March 1990

Research sponsored by the U.S. Department of Energy, Assistant Secretary for Conservation and Renewable Energy, Office of Transportation Technologies, as part of the Ceramic Technology for Advanced Heat Engines Project of the Advanced Materials Development Program, under contract DE-AC05-84OR21400 with Martin Marietta Energy Systems, Inc.

CONTENTS

SUMMARY	1
0.0 PROJECT MANAGEMENT AND COORDINATION	3
1.0 MATERIALS AND PROCESSING	5
INTRODUCTION	5
1.1 MONOLITHICS	7
1.1.1 Silicon Carbide	7
<i>Turbomilling of SiC Whiskers</i> (Southern Illinois University)	7
1.1.2 Silicon Nitride	21
<i>Sintered Silicon Nitride</i> (AMTL)	21
<i>Microwave Processing of Silicon Nitride</i> (ORNL)	26
<i>Silicon Nitride Milling Characterization</i> (NIST)	34
1.1.4 Processing of Monolithics	39
<i>Improved Processing</i> (Norton)	39
<i>Improved Processing</i> (ORNL)	80
<i>Improved Processing</i> (GTE)	84
<i>Processing Science for Si₃N₄ Ceramics</i> (University of California)	132
1.2 CERAMIC COMPOSITES	140
1.2.2 Silicon Nitride Matrix	140
<i>SiC-Whisker-Toughened Silicon Nitride</i> (Garrett)	140
<i>Fabrication of Si₃N₄/SiC Composites by Transient Liquid Phase Sintering</i> (U. Michigan)	153
1.2.3 Oxide Matrix	168
<i>Dispersion-Toughened Oxide Composites</i> (ORNL)	168

1.2.4	Silicate Matrix	174
	<i>Low Expansion Ceramics for Diesel Engine Applications (VPI)</i>	174
1.3	THERMAL AND WEAR COATINGS	185
	<i>Advanced Coating Technology (ORNL)</i>	185
	<i>Development of Adherent Ceramic Coatings to Reduce Contact Stress Damage of Ceramics (GTE)</i>	187
	<i>Wear-Resistant Coatings (Caterpillar)</i>	194
	<i>Development of Wear Resistant Ceramic Coatings for Diesel Engine Components (Cummins)</i>	200
1.4	JOINING	228
1.4.1	Ceramic-Metal Joints	228
	<i>Joining of Ceramics for Heat Engine Applications (ORNL)</i>	228
	<i>Analytical and Experimental Evaluation of Joining Silicon Nitride to Metal and Silicon Carbide to Metal for Advanced Heat Engine Applications (GTE)</i>	233
1.4.2	Ceramic-Ceramic Joints	241
	<i>Analytical and Experimental Evaluation of Joining Silicon Carbide to Silicon Carbide and Silicon Nitride to Silicon Nitride for Advanced Heat Engine Applications (Norton)</i>	241
2.0	MATERIALS DESIGN METHODOLOGY	265
	INTRODUCTION	265
2.1	MODELING	267
2.1.1	Modeling	267
	<i>Microstructural Modeling of Cracks (University of Tennessee)</i>	267
2.2	CONTACT INTERFACES	269

2.2.2	Dynamic Interfaces	269
	<i>Studies of Dynamic Contact of Ceramics and Alloys for Advanced Heat Engines (Battelle)</i>	269
2.3	NEW CONCEPTS	273
	<i>Advanced Statistical Concepts of Fracture in Brittle Materials (GE)</i>	273
3.0	DATA BASE AND LIFE PREDICTION	287
	INTRODUCTION	287
3.1	STRUCTURAL QUALIFICATION	289
	<i>Microstructural Analysis of Structural Ceramics (NIST)</i>	289
	<i>Microstructural Characterization (ORNL)</i>	297
	<i>Project Database (ORNL)</i>	302
3.2	TIME-DEPENDENT BEHAVIOR	307
	<i>Characterization of Transformation-Toughened Ceramics (AMTL)</i>	307
	<i>Fracture Behavior of Toughened Ceramics (ORNL)</i>	308
	<i>Cyclic Fatigue of Toughened Ceramics (ORNL)</i>	315
	<i>Rotor Data Base Generation (ORNL)</i>	332
	<i>Toughened Ceramics Life Prediction (NASA Lewis Research Center)</i>	341
	<i>Life Prediction Methodology (Allison)</i>	365
	<i>Life Prediction Methodology (GAPD)</i>	373
3.3	ENVIRONMENTAL EFFECTS	382
	<i>Environmental Effects in Toughened Ceramics (U. Dayton)</i>	382
	<i>Low Heat Rejection Diesel Coupon Tests (ORNL)</i>	391

3.4	FRACTURE MECHANICS	396
	<i>Testing and Evaluation of Advanced Ceramics at High Temperature in Uniaxial Tension (North Carolina A&T State University)</i>	396
	<i>Standard Tensile Test Development (NIST)</i>	404
	<i>Development of a Fracture Toughness Microprobe (Rice)</i>	410
3.5	NONDESTRUCTIVE EVALUATION DEVELOPMENT	413
	<i>Nondestructive Characterization (ORNL)</i>	413
	<i>NDE Standards for Advanced Ceramics (ORNL)</i>	420
	<i>X-Ray Computed Tomographic Imaging (ANL)</i>	421
	<i>Nuclear Magnetic Resonance Imaging (ANL)</i>	427
	<i>Physicochemical Characterization and Surface Modification of Silicon Nitride Ceramic Powders (University of Wisconsin-Madison)</i>	429
	<i>Surface Thermodynamics (Rutgers University)</i>	435
4.0	TECHNOLOGY TRANSFER	455
4.1	TECHNOLOGY TRANSFER	455
4.1.1	<i>Technology Transfer (ORNL)</i>	455
	<i>IEA Annex II Management (ORNL)</i>	457
	<i>Characterization of Ceramic Powders (NIST)</i>	460

CERAMIC TECHNOLOGY FOR ADVANCED HEAT ENGINES PROJECT SEMI-ANNUAL
PROGRESS REPORT FOR APRIL 1990 THROUGH SEPTEMBER 1990

SUMMARY

The Ceramic Technology For Advanced Heat Engines Project was developed by the Department of Energy's Office of Transportation Systems (OTS) in Conservation and Renewable Energy. This project, part of the OTS's Advanced Materials Development Program, was developed to meet the ceramic technology requirements of the OTS's automotive technology programs.

Significant accomplishments in fabricating ceramic components for the Department of Energy (DOE), National Aeronautics and Space Administration (NASA), and Department of Defense (DoD) advanced heat engine programs have provided evidence that the operation of ceramic parts in high-temperature engine environments is feasible. However, these programs have also demonstrated that additional research is needed in materials and processing development, design methodology, and data base and life prediction before industry will have a sufficient technology base from which to produce reliable cost-effective ceramic engine components commercially.

An assessment of needs was completed, and a five year project plan was developed with extensive input from private industry. In July 1990 the original plan was updated through the estimated completion of development in 1993. The objective of the project is to develop the industrial technology base required for reliable ceramics for application in advanced automotive heat engines. The project approach includes determining the mechanisms controlling reliability, improving processes for fabricating existing ceramics, developing new materials with increased reliability, and testing these materials in simulated engine environments to confirm reliability. Although this is a generic materials project, the focus is on the structural ceramics for advanced gas turbine and diesel engines, ceramic bearings and attachments, and ceramic coatings for thermal barrier and wear applications in these engines. This advanced materials technology is being developed in parallel and close coordination with the ongoing DOE and industry proof of concept engine development programs. To facilitate the rapid transfer of this technology to U.S. industry, the major portion of the work is being done in the ceramic industry, with technological support from government laboratories, other industrial laboratories, and universities.

This project is managed by ORNL for the Office of Transportation Technologies, Office of Transportation Materials, and is closely coordinated with complementary ceramics tasks funded by other DOE offices, NASA, DoD, and industry. A joint DOE and NASA technical plan has been established, with DOE focus on automotive applications and NASA focus on aerospace applications. A common work breakdown structure (WBS) was developed to facilitate coordination. The work described in this report is organized according to the following WBS project elements:

0.0 Management and Coordination

1.0 Materials and Processing

- 1.1 Monolithics
- 1.2 Ceramic Composites
- 1.3 Thermal and Wear Coatings
- 1.4 Joining

2.0 Materials Design Methodology

- 2.1 Modeling
- 2.2 Contact Interfaces
- 2.3 New Concepts

3.0 Data Base and Life Prediction

- 3.1 Structural Qualification
- 3.2 Time-Dependent Behavior
- 3.3 Environmental Effects
- 3.4 Fracture Mechanics
- 3.5 NDE Development

4.0 Technology Transfer

This report includes contributions from all currently active project participants. The contributions are arranged according to the work breakdown structure outline.

0.0 PROJECT MANAGEMENT AND COORDINATION

D. R. Johnson
Oak Ridge National Laboratory

Objective/scope

This task includes the technical management of the project in accordance with the project plans and management plan approved by the Department of Energy (DOE) Oak Ridge Operations Office (ORO) and the Office of Transportation Technologies. This task includes preparation of annual field task proposals, initiation and management of subcontracts and interagency agreements, and management of ORNL technical tasks. Monthly management reports and bimonthly reports are provided to DOE; highlights and semiannual technical reports are provided to DOE and program participants. In addition, the program is coordinated with interfacing programs sponsored by other DOE offices and federal agencies, including the National Aeronautics and Space Administration (NASA) and the Department of Defense (DoD). This coordination is accomplished by participation in bimonthly DOE and NASA joint management meetings, annual interagency heat engine ceramics coordination meetings, DOE contractor coordination meetings, and DOE Energy Materials Coordinating Committee (EMaCC) meetings, as well as special coordination meetings.

1.0 MATERIALS AND PROCESSING

INTRODUCTION

This portion of the project is identified as project element 1.0 within the work breakdown structure (WBS). It contains four subelements: (1) Monolithics, (2) Ceramic Composites, (3) Thermal and Wear Coatings, and (4) Joining. Ceramic research conducted within the Monolithics subelement currently includes work activities on green state ceramic fabrication, characterization, and densification and on structural, mechanical, and physical properties of these ceramics. Research conducted within the Ceramic Composites subelement currently includes silicon nitride and oxide-based composites, which, in addition to the work activities cited for Monolithics, include fiber synthesis and characterization. Research conducted in the Thermal and Wear Coatings subelement is currently limited to oxide-base coatings and involves coating synthesis, characterization, and determination of the mechanical and physical properties of the coatings. Research conducted in the Joining subelement currently includes studies of processes to produce strong, stable joints between zirconia ceramics and iron-base alloys, as well as Si_3N_4 - and SiC-to-metal joints, and SiC-to-SiC and Si_3N_4 -to- Si_3N_4 joints.

A major objective of the research in the Materials and Processing project element is to systematically advance the understanding of the relationships between ceramic raw materials such as powders and reactant gases, the processing variables involved in producing the ceramic materials, and the resultant microstructures and physical and mechanical properties of the ceramic materials. Success in meeting this objective will provide U.S. companies with new or improved ways for producing economical, highly reliable ceramic components for advanced heat engines.

1.1 MONOLITHICS

1.1.1 Silicon Carbide

Turbomilling of SiC Whiskers

D. E. Wittmer (Southern Illinois University)

Objective/scope

The purpose of this work is to continue the investigation of the turbomilling process as a means of improved processing for SiC whisker-ceramic matrix composites and dispersion of matrix powders prior to composite processing.

Technical progress

Phase II is divided into 4 major tasks:

- Task 1. Beneficiation of SiC whiskers.
- Task 2. Development of aspect ratio reduction parameters.
- Task 3. Improved dispersion of particulate matrices.
- Task 4. Final Report

Task 1. Beneficiation of SiC whiskers

Task 1 was completed ahead of schedule as reported in the previous semi-annual report.

Task 2. Development of aspect ratio reduction parameters.

During this reporting period, the Lasentec 150 Scanning Laser Microscope was standardized, using 1 μm and 10 μm colored latex polymer microspheres, for measuring whisker length and distributions as part of Task 2, and floc size as a function of pH as part of Task 3. Also, a pyrex, vertical flow chamber, designed for measuring whisker lengths utilizing the Lasentec-150 fiber analyzer, was constructed as part of Task 2. It is anticipated that, once consistent measurements are obtained, this instrument will enable the in-situ measurement of whisker aspect ratio or particle size reduction, during turbomilling. To date, the results obtained are not consistent with those obtained on standard slurries, using the standard Lasentec setup. Additional modifications were made to the pyrex vertical flow chamber, designed for in-situ measurements of whisker lengths during turbomilling. An adjustable support device, designed to hold the pyrex flow chamber in the proper position with respect to the laser window, was constructed and installed. Previously, vibrations

present with the earlier setup prohibited stable readings. Due to unforeseen delays in accomplishing this task, a no-cost extension has been granted. This milestone has been rescheduled for completion by 4/30/91.

Task 3. Improved dispersion of particulate matrices.

Task 3 has been altered to focus on the effect of temperature, dispersant and pH on the flocculation/dispersion behavior of the Al_2O_3 and Si_3N_4 matrix materials to determine optimum conditions for turbomilling and pressure filtration of the monolithic matrix, prior to the addition of SiCw¹. In addition, some effort for Task 3 has been redirected to determining the feasibility of producing $\beta\text{-Si}_3\text{N}_4$ "seed" with a controlled morphology for enhancing the formation of toughened microstructures. Once developed, this $\beta\text{-Si}_3\text{N}_4$ seed is to be dispersed in a chosen Si_3N_4 matrix by turbomilling.

For this task the Lasentec 150 is being used to measure the effect of pH on the floc size and settling rate for various Al_2O_3 and Si_3N_4 matrix slurries. The materials presently being studied are:

Al_2O_3 Matrix	Ceralox 0.5 AF (agglomerate free) with and without MgO
	Reynolds RCHP-DBM without MgO
Si_3N_4 Matrix	Starck LC-10N Si_3N_4
	LC-12SX Si_3N_4
	UBE E-10 Si_3N_4
	Starck high-purity Y_2O_3

Flocculation behavior is being analyzed as a function of solids content over the pH range of 2 to 12. Based on preliminary flocculation behavior, the zeta potential, as a function of pH for the same materials, is also being measured for the pH range of 2 to 11. Typical results of floc size (given as number of particle diameters) vs. pH are given in Figures 1 through 5, while results of zeta potential as a function of pH for the Si_3N_4 powders are given in Figures 6 through 8.

¹ For this work Grade 1 silicon carbide whiskers from the former American Matrix Inc. (AMI) were used. The AMI whisker technology and equipment has recently been purchased by Advanced Refractories Technologies, Buffalo, NY.

Based on the observed flocculation behavior as a function of pH, a 1 kg batch of A2Y6 (UBE E-10 Si_3N_4 with 2% Ceralox Al_2O_3 and 6% Starck Y_2O_3 as sintering aids) was processed by turbomilling and pressure filtration at a pH of 4. For comparison, an identical 1 kg batch was processed by turbomilling with 0.25 w/o PVA binder and 5 ml Darvan 821A (J. T. Vanderbilt) dispersant. The green density using pH control only was 60% of theoretical with a casting time of 45 min., compared with a green density of 53% and casting time of 150 min. for the slurry containing binder and dispersant.

From these results, the same A2Y6 composition, using turbomilling and pressure filtration with pH control only, was used in the preparation of the following:

Ball milled A2Y6 matrix only.

Turbomilled A2Y6 matrix only.

25 vol.% SiCw- Si_3N_4 composite containing as-received SiCw.

25 vol.% SiCw- Si_3N_4 composite containing beneficiated coarse SiCw fraction.

25 vol.% SiCw- Si_3N_4 composite containing beneficiated fine SiCw fraction.

25 vol.% SiCw- Si_3N_4 composite containing beneficiated, heat-treated, coarse SiCw fraction.

25 vol.% SiCw- Si_3N_4 composite containing beneficiated, heat-treated, fine SiCw fraction.

Continual problems with the hot-press at the University of Illinois at Urbana, IL delayed hot-pressing of the above compositions. Once the hot-press was repaired, it was determined that the hot-pressing conditions previously used with ORNL equipment were not duplicated, although the runs were made at the same time, temperature and load settings. This resulted in lower hot-pressed density than anticipated and required additional hot-pressing at slightly higher temperatures and additional time. The hot-pressed compositions are presently being machined into MIL Std. 1942 type B test specimens for flexure and fracture toughness measurements. Because of these delays, as with Task 2, a no-cost extension was granted with a change in this milestone to 7/31/91.

Also as part of Task 3, the effect of temperature on turbomilling conditions and viscosity of the resulting slurries was observed for A2Y6-Si₃N₄, and the effect of solids content and aging on the floc size and pH of Starck LC-10N, Si₃N₄ was also measured.

During the summer months, the cooling water for the turbomill is much higher than in the winter months (35°C and 17°C, respectively), so as expected, the viscosities for slurries processing in the turbomill could vary considerably. Characteristically, when turbomilling typical 25-35 vol.% solids slurries at temperatures below about 25°C, the torque and H.P. are observed to decrease during the initial 30 min of turbomilling and then remain relatively constant until the end of the run. This behavior is believed to correspond with the point when all of the powder agglomerates have been completely dispersed. Recently with the higher cooling water temperature (35°C), for the same solids loadings, the torque and H.P. have been observed to initially decrease to a much higher value than observed at the cooler temperatures, and then slightly increased until the end of the run. These results justify the purchase of a captive water cooling system when such resources become available. A more detailed study of this behavior has been initiated.

The effect of aging on the pH and floc size was determined for Starck LC-10N Si₃N₄ powder for turbomilled and ball milled low solids content (5 vol.%) slurries. For the ball milled slurry the pH was 5.1 and the floc size 7.25 μm compared to a pH of 8.3 and floc size of 1.5 μm for the turbomilled slurry. After aging for 48 hours, the ball milled slurry was the about the same, while the turbomilled slurry had a pH of 7.8 and a floc size of 6.9 μm. This would indicate that possibly some silicic acid is forming from a reaction with the water and the higher surface area Si₃N₄ powder produced during the turbomilling process. Currently, turbomilled slurries of Ceralox Al₂O₃, Starck LC-10N Si₃N₄ and LC-12SX Si₃N₄ with higher solids loadings are being investigated for aging effects on pH, floc size and viscosity.

Increasing the solids content for turbomilled slurries of A2Y6-Si₃N₄, using Starck LC-12SX Si₃N₄ powder, from 30 vol.% to 33 vol.% was found to nearly double the slurry viscosity, from 37 to 70 cp, respectively. Aging for 24 hours, turning the slurry slowly on a mill rack, was found to only slightly decrease the viscosity. Entrapped air was found to present a major problem for these higher solids content slurries and deairing techniques were developed. Filter cakes cast from deaired slurries were void of surface pin holes, which were previously observed in high-solids content slurries which were not deaired.

Similar to the previous study using UBE E-10 Si₃N₄, A2Y6 Si₃N₄ slurries, containing Starck LC-12SX Si₃N₄, Ceralox AF Al₂O₃ and Starck HP Y₂O₃, were processed by turbomilling to compare the effect of using dispersants and binders with pH control only. Following turbomilling for

2 h, filter cakes for both cases of about 125 g each were prepared by pressure casting. Green parts containing binder and dispersant were dried very slowly (time to dry was approximately 9 days) by gradually decreasing the relative humidity of the drying environment, before the parts were dried in a vacuum oven to 100°C. Green parts formed from turbomilled slurries using pH control only were placed in a vacuum oven at room temperature and the temperature gradually increased to 100°C (time to dry 1 day). Parts from both processes will be sintered for comparison of shrinkage and density.

Some effort in this sub-contract has been redirected to determine the feasibility of using turbomilling for the dispersion of prepared β - Si_3N_4 seed in a sinterable Si_3N_4 matrix. Conceptually, the β - Si_3N_4 seed would provide nucleation and growth sites for producing a more prominent self-reinforcing Si_3N_4 microstructure. Attempts are being made to prepare small amounts of β - Si_3N_4 seed by high-temperature conversion of high-purity α - Si_3N_4 under an overpressure of 99.99% N_2 .

An initial attempt was made to produce β - Si_3N_4 seed using an as-received commercial Si_3N_4 powder as the source material. About 75 g of UBE E-10 α - Si_3N_4 was heated in a BN crucible at 1850°C for 4 h under an overpressure of 99.99% N_2 . XRD analyses confirmed that only about 10 wt.% of the α - Si_3N_4 was converted to β - Si_3N_4 , while SEM analyses revealed that there was no apparent morphology change. Another attempt using a preoxidation treatment for the produced similar results. Currently, small amounts of rare earth oxides are being evaluated as nucleating agents. The formulation of A2Y6 in dry blended powder form resulted in complete transformation to β - Si_3N_4 at 1750°C for 4 h. This conversion product is presently being analyzed for morphology of the β phase. At this time, problems with the high-temperature furnace used for conversion have delayed additional experimental trials.

Status of milestones

- | | |
|--|---------------------------|
| 1. Run Beneficiation Trials and Report in Bimonthly | Completed |
| 2. Run Aspect Ratio Reduction Trials and Report in Bimonthly | On Schedule
New Target |
| 3. Run Matrix Dispersion Trials and Report in Bimonthly | On Schedule
New Target |
| 4. Rough Draft of Final Report to Contract Monitor | On Schedule
New Target |

Publications

D. E. Wittmer, W. Trimble, and T. Paulson, "Fractography of SiC Whisker Reinforced Ceramic Matrix Composites," Advances in Ceramics 22, Conference on the Fractography of Glasses and Ceramics II, Alfred University, July 15-18, 1990, Alfred, NY, in press.

Presentations

T. Paulson and D. E. Wittmer, "Effect of Beneficiation on Aspect Ratio and Properties of SiCw/Si₃N₄ Composites", 92nd Annual Am. Ceram. Soc. Meeting Abstracts, Dallas, TX, April 22-26, 1990, pp. 74.

D. E. Wittmer, W. Trimble, and T. Paulson, "Fractography of SiC Whisker Reinforced Ceramic Matrix Composites," Conference on the Fractography of Glasses and Ceramics II, Alfred University, July 15-18, 1990, Alfred, NY.

Figure 1. Floc Size vs. pH for Ceralox AF Alumina-0.5 MgO

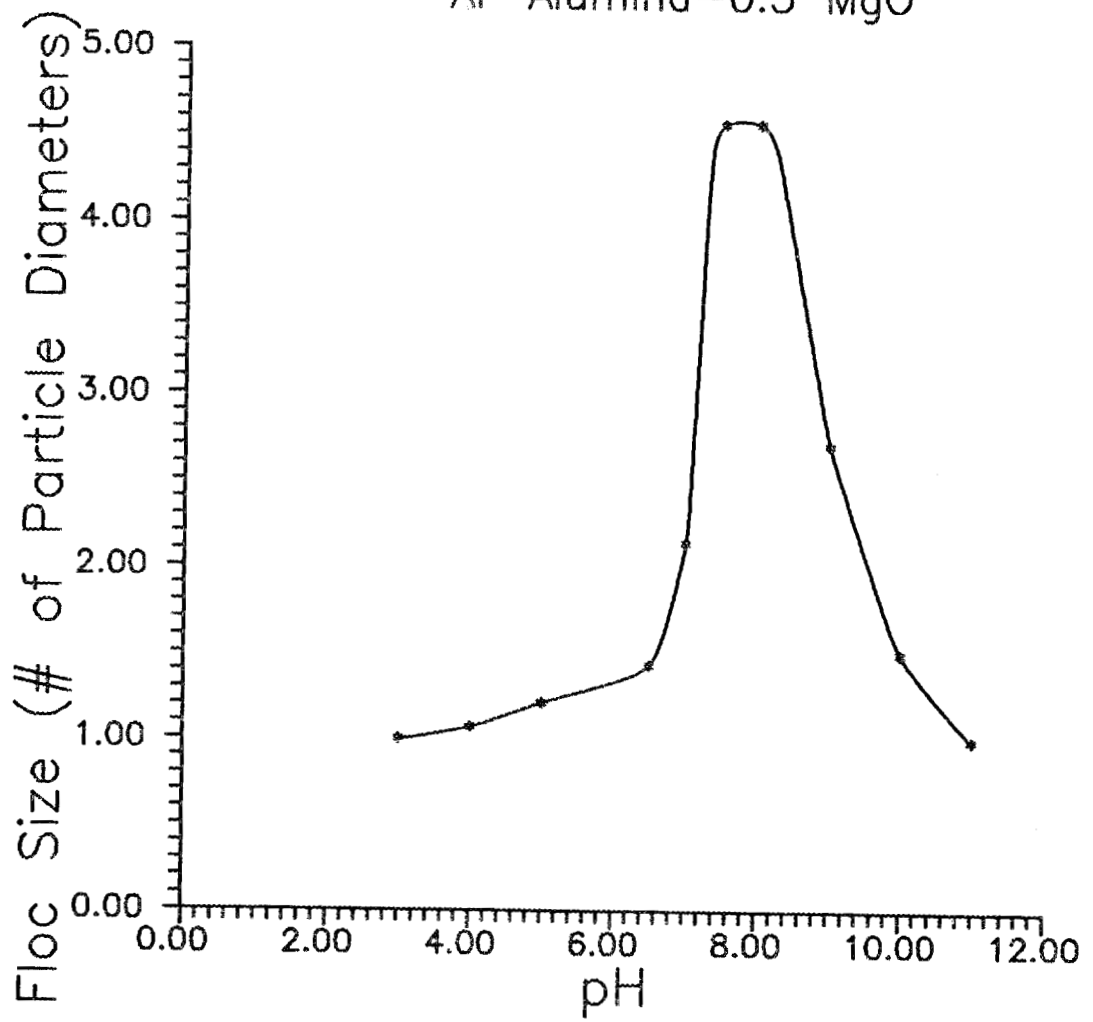


Figure 2. Floc Size vs. pH for Starck LC-10 Silicon Nitride

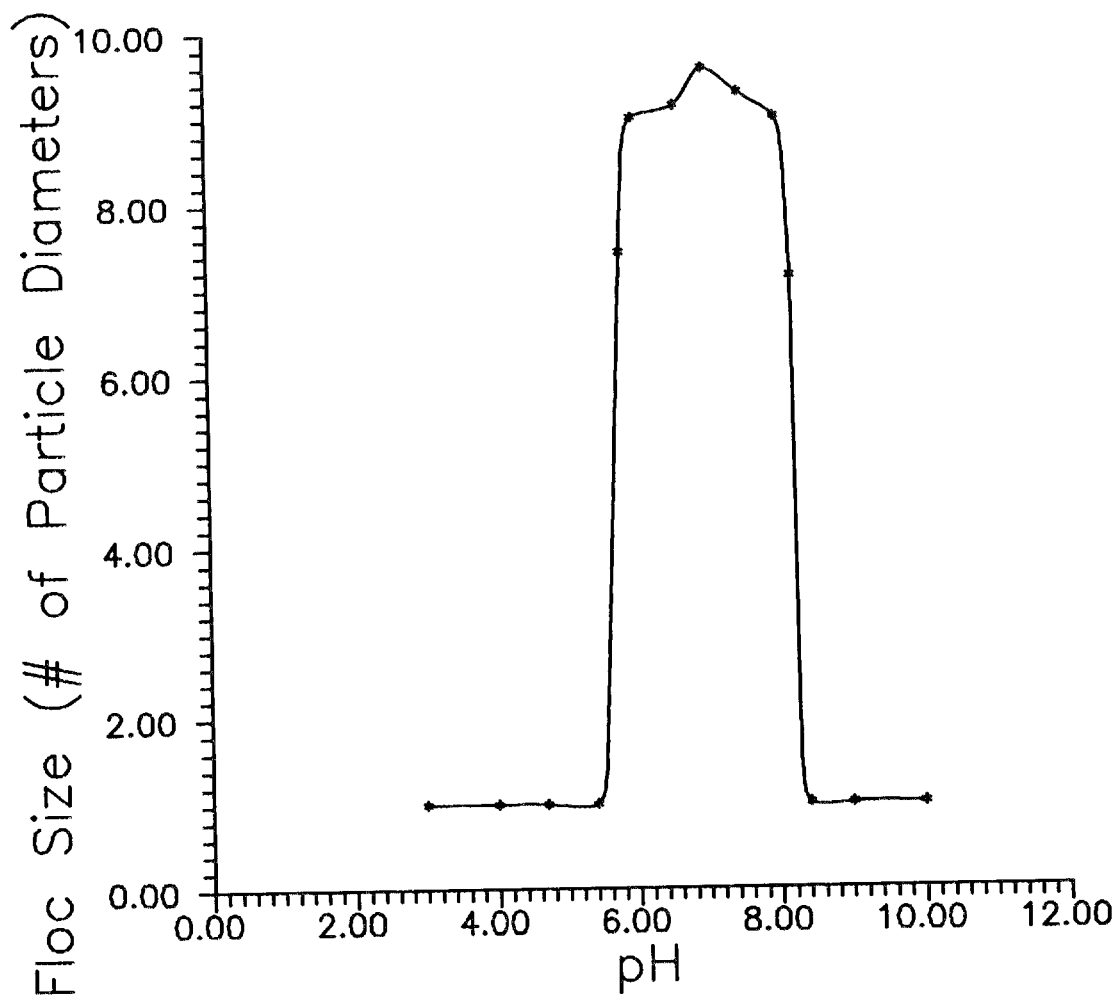


Figure 3. Floc Size vs. pH for Starck LC-12SX Silicon Nitride

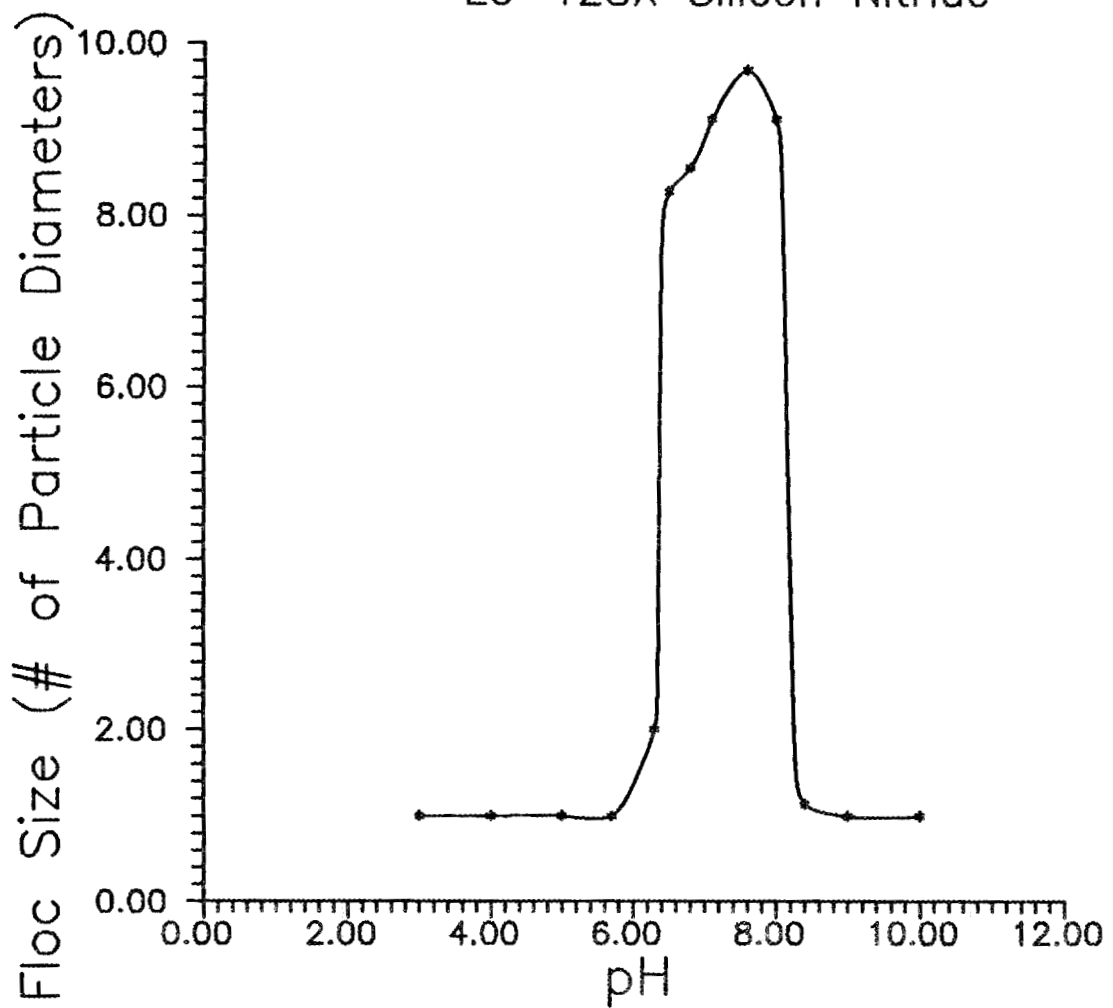
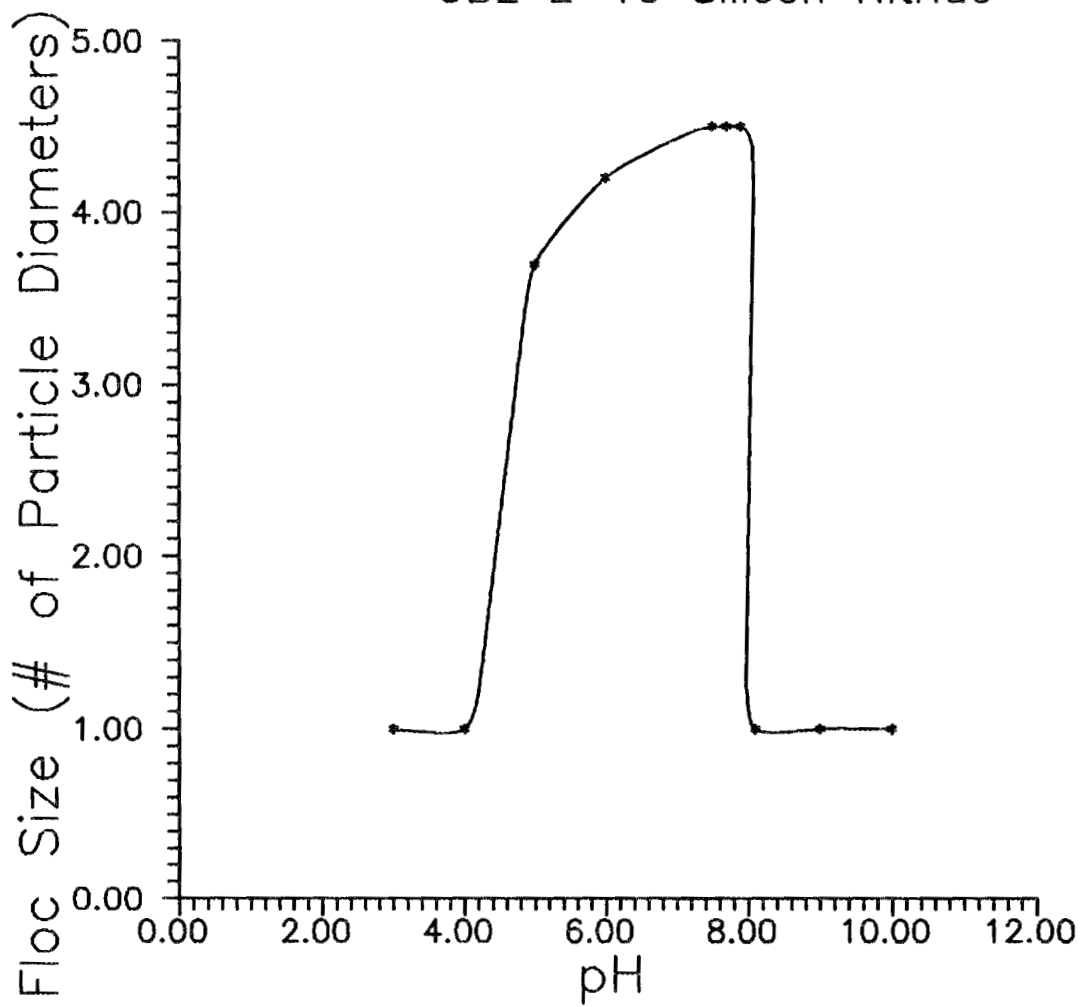


Figure 4. Floc Size vs. pH for
UBE E-10 Silicon Nitride



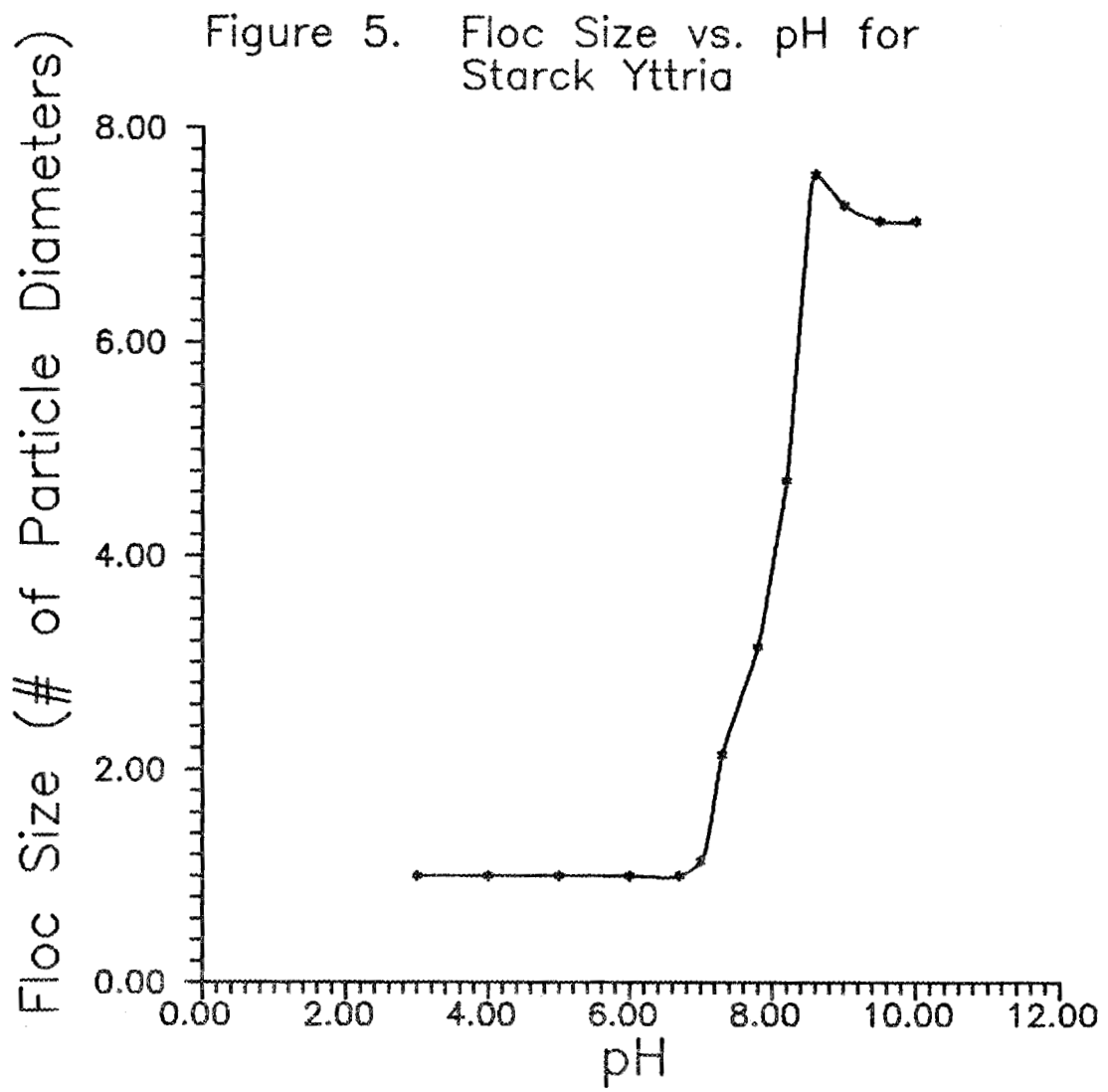


Figure 6. Zeta Potential vs. pH for Starck LC-10 Silicon Nitride

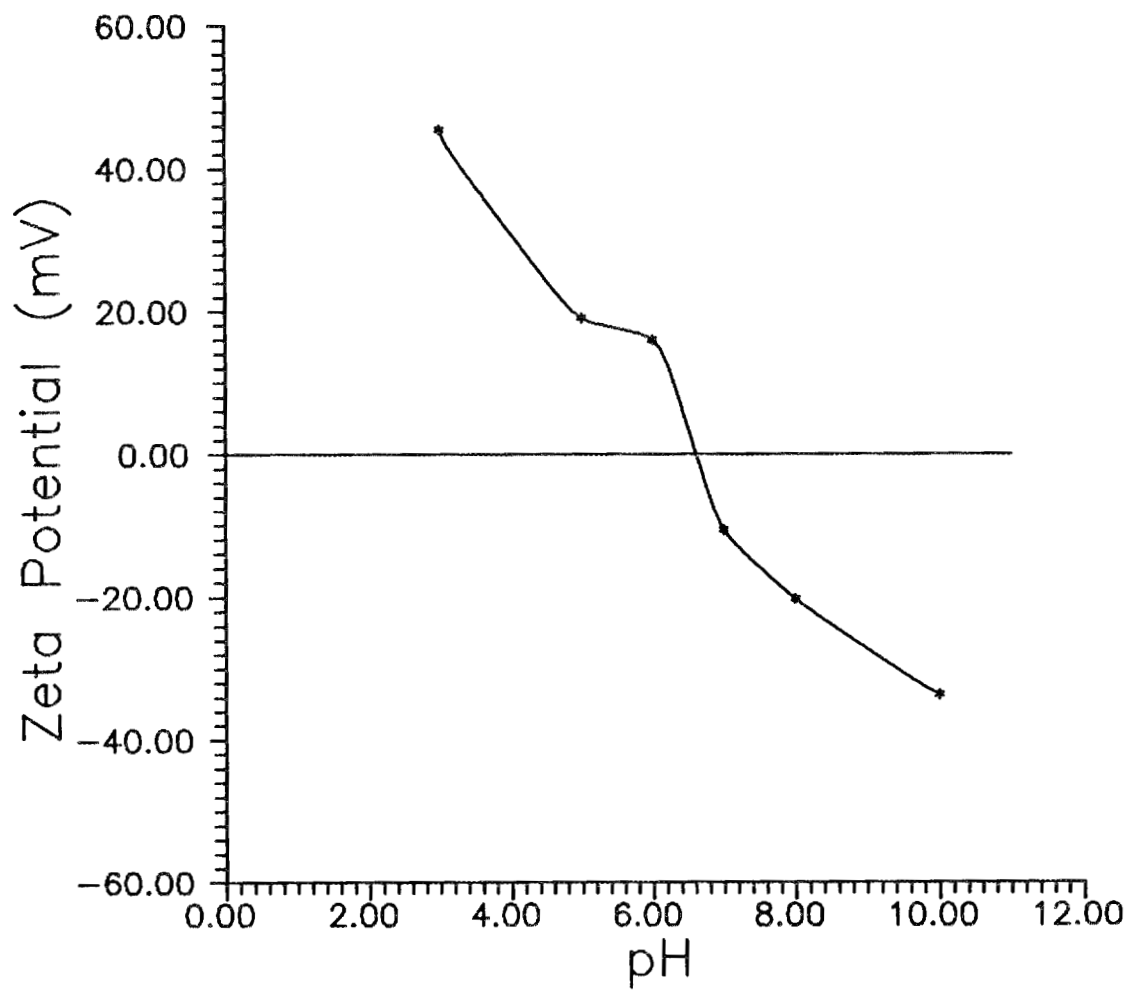


Figure 7. Zeta Potential vs. pH for Starck LC-12SX Silicon Nitride

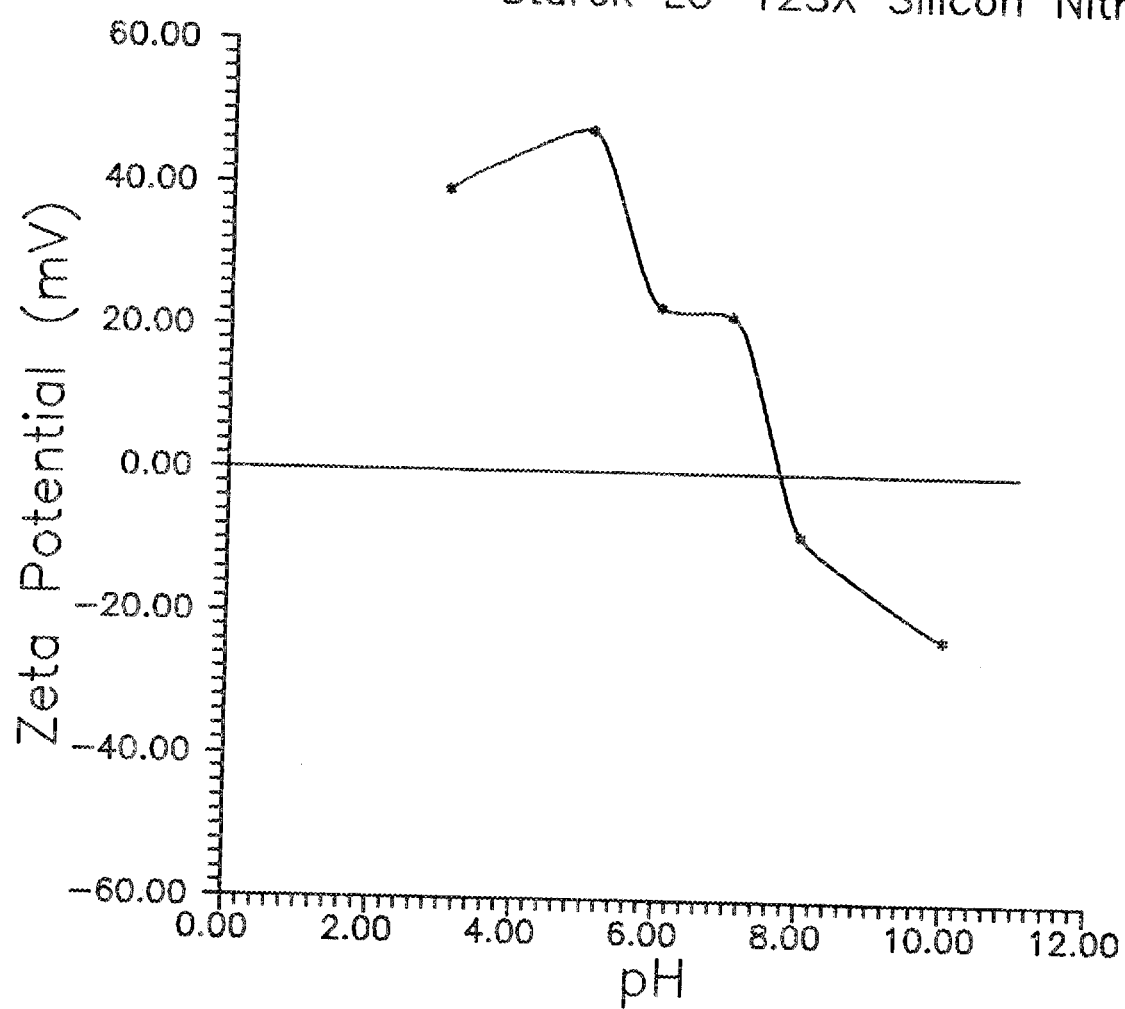
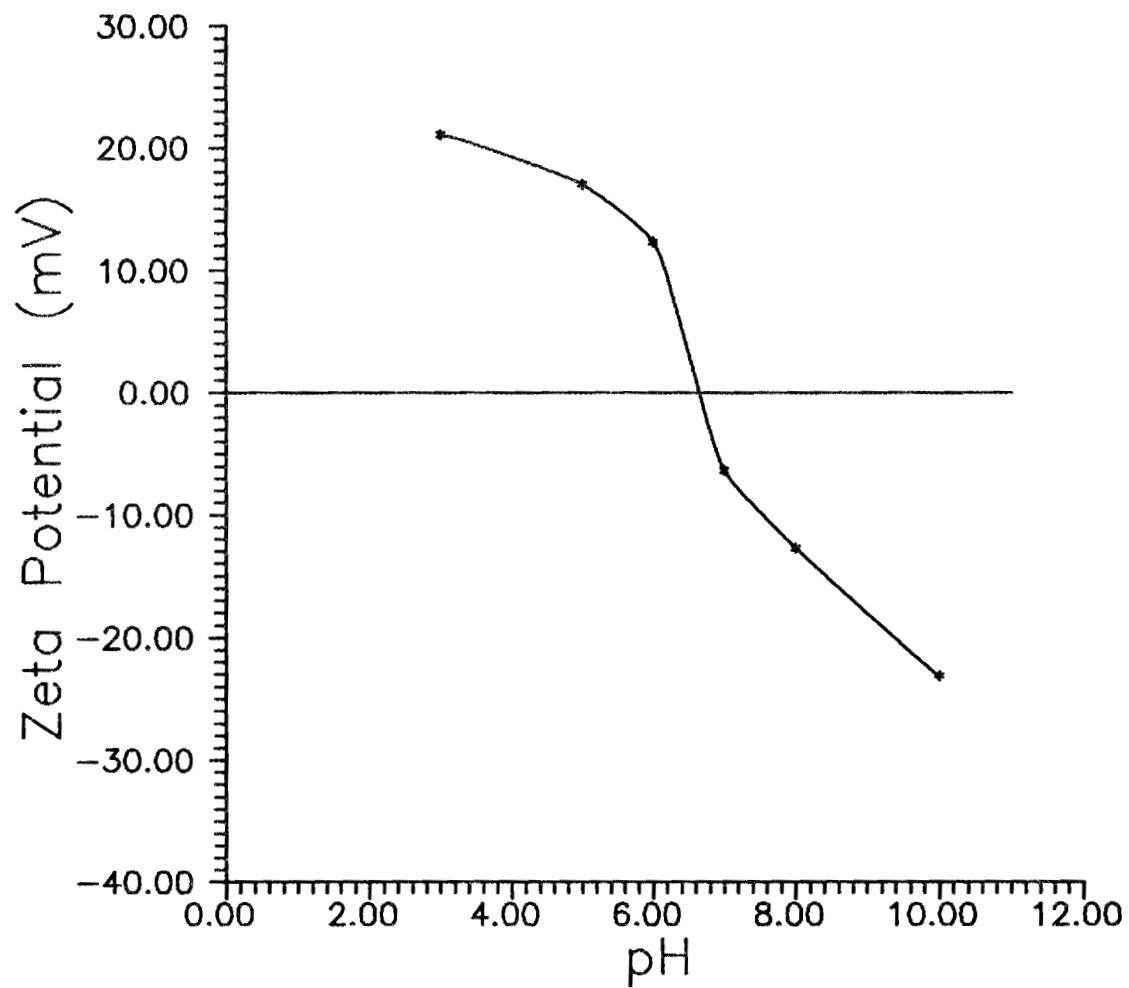


Figure 8. Zeta Potential vs. pH for
UBE E-10 Silicon Nitride



1.1.2 Silicon Nitride

Sintered Silicon Nitride

J. Mangels (Ceradyne Inc.), G. E. Gazza (Army Materials Technology Laboratory)

Objective/Scope

The program is concentrating on sintering compositions in the $\text{Si}_3\text{N}_4\text{-Y}_2\text{O}_3\text{-SiO}_2$ system using a two-step sintering method where the nitrogen gas pressure is raised to 7-8 MPa during the second step of the process. During the sintering, dissociation reactions are suppressed by the use of high nitrogen pressure and cover powder of suitable composition over the specimen. Variables in the program include the sintering process parameters, source of starting powders, milling media and time, and specimen composition. Resultant properties determined are room temperature modulus of rupture, high temperature stress-rupture, oxidation resistance, and fracture toughness. Successful densification of selected compositions with suitable properties will lead to the fabrication of components for engine testing.

Technical Progress

Funding for the in-house program ended in April 1990. Efforts were primarily concentrated on establishing a contract to transition the program to industry for scale-up, data base generation, and fabrication of components for engine testing.

Ceradyne, Inc. was selected to carry out a scale-up and data base generation and evaluation of a silicon nitride-yttria-silica base composition containing molybdenum carbide to be transitioned from MTL to commercial prototype components in a turbine test engine. The contract is a 24 month effort divided into two incrementally funded tasks. Task I will focus on powder processing, densification, mechanical testing, and characterization. If satisfactory results are obtained in Task I, the next step, Task II, involves the processing, evaluation, and fabrication of selected ceramic components for evaluation in a gas turbine development program.

The specific objective of Task I is to scale-up/optimize process procedures and generate a data base for silicon nitride having a general composition of 85.8m/o Si_3N_4 -4.73m/o Y_2O_3 -9.47m/o SiO_2 containing 1.0m/o Mo_2C . The baseline process process, shown in detail in Table I, involves mixing the raw materials in an attritor mill using water as the fluid vehicle. The resulting slurry will be spray dried to form a free flowing powder, agglomerated mixture of the starting ingredients together with a pressing binder. This powder will be isostatically pressed into a compact and then sintered under a combination of temperature and pressure. Components will be machined to near net shape using "green" machining techniques. The final component geometries will be obtained by diamond grinding.

Raw Material Characterization

Silicon Nitride Powder: The baseline Si_3N_4 powder is Ube SN-10. This powder is a high purity, high surface area powder produced from chemical precursors. The powder is composed of a high percentage of alpha Si_3N_4 phase (>95%) and has a relatively low oxygen content (<1.3%). The characterization results are shown in Table II with the actual results being compared to the Ube specifications.

Yttrium Oxide Powder: The baseline powder is Hermann C. Starck Grade Std. TRhis powder has a 99.9% purity level with a surface area of $11 \text{ m}^2/\text{g}$. Table III compares actual results obtained at Ceradyne with Starck specifications.

Silica Powder: The baseline silica powder is Cab-O-Sil produced by Cabot Corp. This powder has a surface area of $197 \text{ m}^2/\text{g}$ and a high purity level. Characterization results are shown in Table IV.

Molybdenum Carbide Powder: The baseline powder is Johnson Matthey's -325 mesh grade. As such, the powder is considered too coarse, as is, for use as a sintering additive in this program. The powder was processed by sedimentation to remove the coarse fraction, resulting in a powder having a maximum particle size of 3 micrometers. The treated powder will be used as the baseline powder in all Matrix I experiments. Characterization results are presented in table V.

Mo₂C Powder Sedimentation Procedure

The as-received, -325 mesh Mo₂C powder was mixed with isopropyl alcohol (IPA) in a ratio of 30g of powder to 500 ml of IPA. This slurry was mixed and allowed to settle for 15 minutes. The supernate was decanted from the sediment. The supernate was filtered through a glass filter to remove the IPA. The resulting powder was characterized to have a median particle size of 1.5um and a maximum particle size of 3 um.

Matrix I Experimental Design

The purpose of Matrix I is to investigate the processing parameters which are thought to control densification. The principal objective of this set of experiments is to define a set of parameters which will result in sintered densities of >99%. Matrix I is an experimental design consisting of a Taguchi L8 orthogonal array in which four processing variables will be investigated at two levels. The experimental design is shown in Table VI. The experimental responses will be: (1) density (2) hardness (3) fracture toughness. Additionally, the phase composition will be determined. Additional experiments are planned during the course of Matrix I. The spray dried powder will be characterized. The pressure-"green" density relationship will be determined for the PVA/PEG binder system. The "green" machining characteristics of the isopressed compacts will be determined both after isopressing and after presintering.

TABLE II

Silicon Nitride Powder Characteristic Results

Ube Grade SN10
Lot No. PO25889

Property	Ube Specification	Ceradyne Values
Purity		
N	>38 %	
O	<1.3 %	1.29 %
Cl	<100 ppm	
Fe	<100 ppm	<10 ppm
Ca	<50 ppm	30 ppm
Al	<50 ppm	23 ppm

Phase Composition: Alpha Si₃N₄--95% Beta Si₃N₄--5%

Surface Area--11.5 sq.m/g

Average Particle Size-- 1.2 microns

TABLE III

Yttrium Oxide Powder Characterization Results
Hermann C. Starck Grade Std.

Property	H.C.Starck Specification	Ceradyne Values
Chem. Comp.		
Y ₂ O ₃	>99.9%	
Purity		
C	0.08%	
Fe	<4 ppm	
Ca	<1 ppm	
Si	<30 ppm	
Surface Area	7-11 sq.m/g	10.6 sq.m/g
Avg. Part.Size	1.5-4 um	1.93 um

TABLE IV

SiO₂ Powder Characterization
Cab-O-Sil (Charact. by vendor)

% SiO ₂	>99.8%
Bulk Density	2.3 lb/cu.ft.
Surface Area	197 sq.m/g
pH in water	4.0
LOI	<2.0%

TABLE V

Mo₂C Powder Characterization Results
Johnson Matthey Grade -325

Condition	Median Part. Size	Max. Part. Size	Percent
As received	10.45 um	50 um	30%
After sediment.	1.5 um	3 um	

TABLE VI

Matrix I Experimental Design

Col. #	Factor	Level-1	Level-2
1	Sintering Temp.	1950C	1875C
2	time @ Temp. & Low Press.	5 hr.	2 hr.
3	Temp. - time Interaction		
4	Mo ₂ C Amount	1m/o	0m/o
5	Mo ₂ C - Temp. Interaction		
6	time - Mo ₂ C Interaction		
7	Pre-sinter Process	Yes	No

Trial No.	Column No.						
	1	2	3	4	5	6	7
1	1	1	1	1	1	1	1
2	1	1	1	2	2	2	2
3	1	2	2	1	1	2	2
4	1	2	2	2	2	1	1
5	2	1	2	1	2	1	2
6	2	1	2	2	1	2	1
7	2	2	1	1	2	2	1
8	2	2	1	2	1	1	2

Experimental Responses:

Density
Hardness
Fracture Toughness

Established Milestones

(A) Establish powder processing approach for preparing selected composition. Determine preferred sintering conditions. Generate data base for room temperature and high temperature properties.

July 1991

(B) Fabricate, inspect, and make components available for engine testing in a gas turbine ceramic component development/evaluation program.

July 1992

Microwave Sintering of Silicon Nitride

T. N. Tiegs, J. O. Kiggans, M. K. Ferber, and H. D. Kimrey
(Oak Ridge National Laboratory)

Objective/scope

The objective of this research element is to identify those aspects of microwave processing of silicon nitride that might (1) accelerate densification, (2) permit sintering to high density with much lower levels of sintering aids, (3) lower the sintering temperature, or (4) produce unique microstructures. The investigation of microstructure development is being done on dense silicon nitride materials annealed in the microwave furnace. The sintering of silicon nitride involves two approaches. The first approach comprises heating of silicon nitride and sialon powder compositions in the 2.45- or 28-GHz units. The second approach deals with using reaction-bonded silicon nitride as the starting material and is done entirely in the 2.45-GHz microwave furnace.

Technical progress

Sintering of silicon nitride

A series of samples were fabricated to investigate the effects of alternative coupling methods to improve sintering of the Si_3N_4 materials in the microwave. Previous sintering results had shown a significant coupling effect at approximately 1300°C , which was attributed to the formation of yttrium-aluminum-silicate glass. To test if the formation of the glass phase would improve the coupling uniformity in the microwave from room temperature, samples were presintered in a conventional furnace to 1350°C prior to microwave sintering. The results are summarized in Table 1.

Table 1. Summary of results on sintering of silicon nitride in the microwave and conventional furnaces

Specimen additives (wt %) ^a	Heating ($^\circ\text{C}/\text{h}$)		Sintered density	
	Conventional	Microwave	(g/cm^3)	(% T.D.P)
9% Y_2O_3 -3% Al_2O_3	1750/1	—	3.082	92.6
9% Y_2O_3 -3% Al_2O_3	—	1725/1	3.197	96.0
9% Y_2O_3 -3% Al_2O_3	1350/1	1725/1	3.134	94.1
11% La_2O_3 -3% Al_2O_3	1750/1	—	3.308	97.3
11% La_2O_3 -3% Al_2O_3	—	1725/1	3.326	97.8
11% La_2O_3 -3% Al_2O_3	1350/1	1725/1	3.313	97.4

^aMatrix is silicon nitride (Grade Ube E10).

As shown, very little difference was observed for the samples that underwent a presintering step. Qualitatively, the presintered materials appeared to have fewer cracks, however, the microwave power required to heat the presintered and the as-fabricated samples was essentially identical at temperatures $<1000^{\circ}\text{C}$. At approximately 1300°C , the presintered specimens experienced a significantly stronger coupling effect than the as-fabricated materials. Additional sintering runs are being performed to test the effect of coatings on improving heating homogeneity.

Microstructure development

As reported previously, an annealing study was performed to investigate microstructural development of silicon nitride in a microwave furnace. Samples of Si_3N_4 -4% Y_2O_3 and Si_3N_4 -6% Y_2O_3 -2% Al_2O_3 were hot-pressed to full density and annealed both by microwave and conventional heating at 1200, 1400, and 1500°C for times of 10 and 20 h.

Initial results showed increased enhanced grain growth for the microwave sintered samples at temperatures significantly lower than observed with conventional heating ($>300^{\circ}\text{C}$). Photomicrographs of fracture surfaces from Si_3N_4 -4% Y_2O_3 annealed at 1400°C for 20 h. and Si_3N_4 -6% Y_2O_3 -2% Al_2O_3 annealed at 1200°C for 20 h are shown in Figs. 1 and 2. Gas pressure was essentially atmospheric - -16 psi. Grain growth for the microwave annealed samples is readily evident. However, it was also noted that the microwave annealed specimens had higher weight losses due to microwave coupling to the grain boundary phases and volatilization of the grain boundary phases. An improvement in the high-temperature creep rate at 250 MPa at 1370°C for the Si_3N_4 -4% Y_2O_3 annealed at 1400°C for 20 h from $\sim 5 \times 10^{-9}/\text{s}$ for the as-fabricated material to $3.3 \times 10^{-9}/\text{s}$ for the microwave annealed material has also been observed. Further creep testing of the Si_3N_4 -6% Y_2O_3 -2% Al_2O_3 annealed at 1200°C for 20 h and other selected samples is currently in progress. The initial analysis indicates that annealing conditions, initial microstructure, sintering aid content, and sintering aid composition are all important for improving properties as they are all interdependent.

Additional annealing experiments have been performed on hot-isostatically-pressed Si_3N_4 -4% Y_2O_3 (Norton NT-154) to determine if microstructural changes and improved creep resistance could be made in this material. Flexural test bars were annealed at 1400°C in the 2.45-GHz microwave furnace for 20 h under 0.1 MPa (15 psi) nitrogen and packed in a Si_3N_4 -BN- Y_2O_3 -SiC powder bed. The temperature was monitored by both a thermocouple and an optical pyrometer. The two measurements were within 20°C of each other during the anneal. Weight losses were <0.01 wt % and the bars showed only a slight change in color.

Initial fatigue testing has given encouraging results for the microwave annealed materials. The results of a test at constant stress showed the microwave annealed specimen to have significantly better fatigue resistance as compared to the unannealed material (Fig. 3). The unannealed specimen failed after about 130 h at 296 MPa, while the microwave annealed specimen survived the 200 h test time. In a stepped-stress test, the microwave annealed sample also had improved fatigue resistance (Fig. 4). After both fatigue tests, the microwave annealed specimens were fast fractured at the end of the test time. Surprisingly, the flexural strength

T015526



T015237

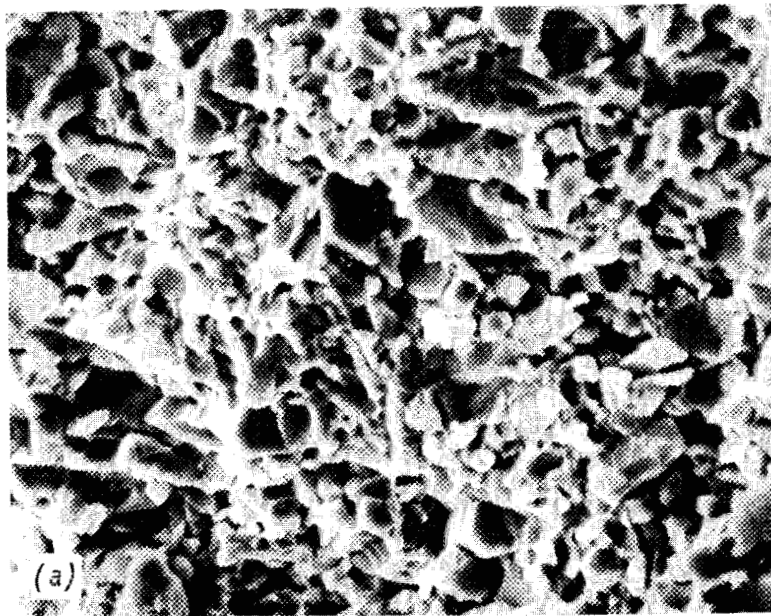
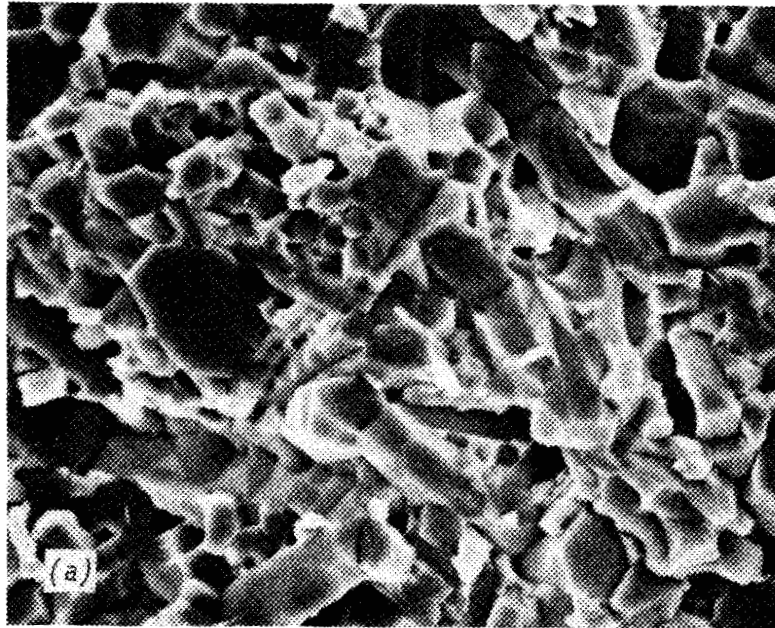


Fig. 1. Photomicrographs of fracture surfaces from Si_3N_4 -4% Y_2O_3 annealed at 1400°C for 20 h. (a) As-fabricated, (b) microwave anneal.

T015227



T015226

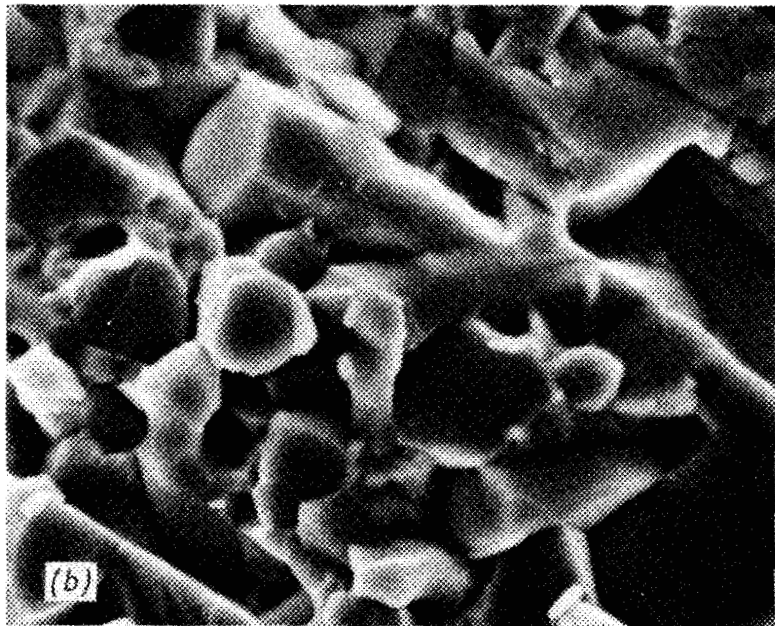


Fig. 2. Photomicrographs of fracture surfaces from Si_3N_4 -6% Y_2O_3 -2% Al_2O_3 annealed at 1200°C for 20 h. (a) As-fabricated, (b) microwave anneal.

ORNL-DWG 90-17115

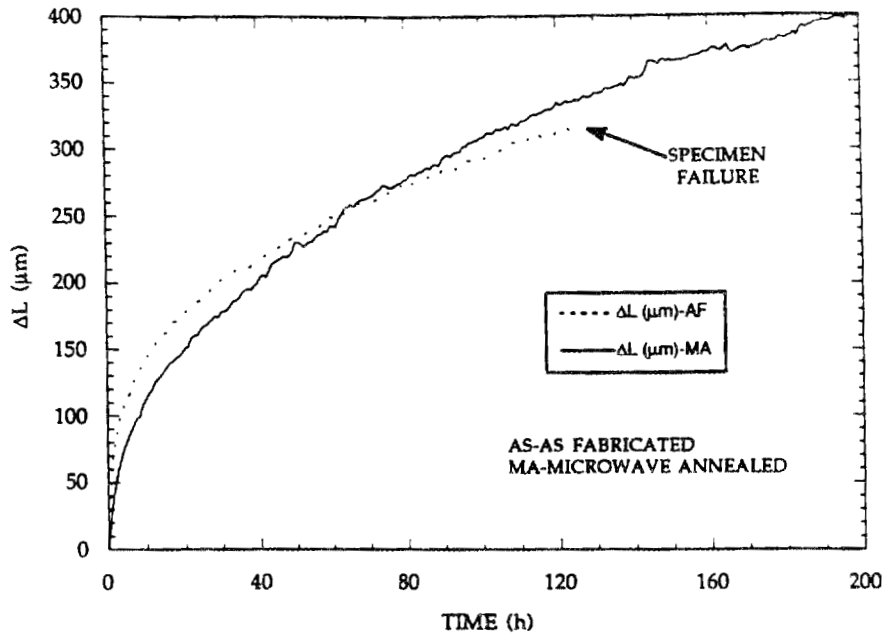


Fig. 3. Interrupted fatigue testing on Si_3N_4 -4% Y_2O_3 (Norton NT-154). Test temperature was 1370°C and the stress was 296MPa. Specimens were microwave annealed at 1400°C for 20h in the 2.45-GHz furnace.

ORNL-DWG 90-17116

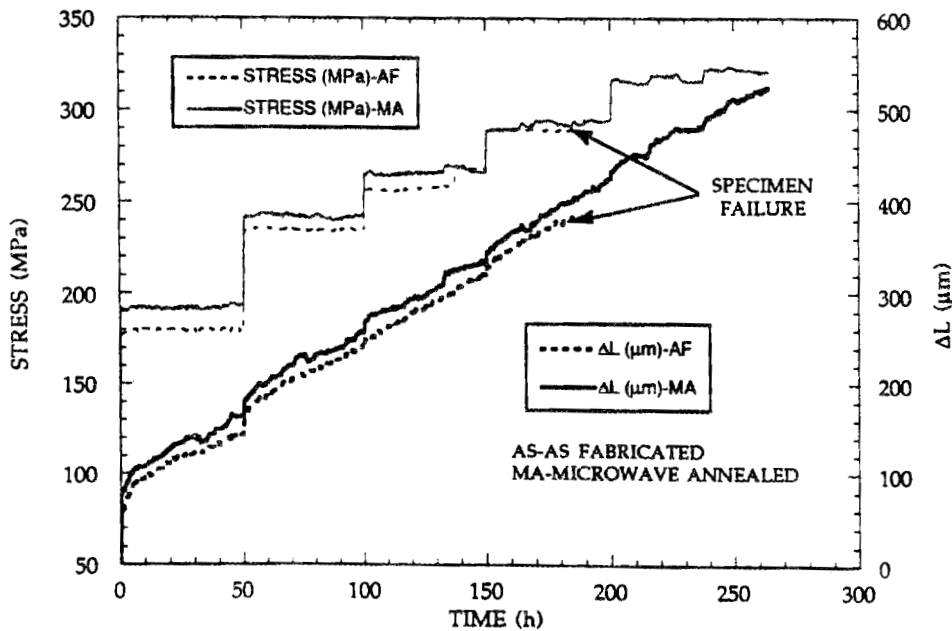


Fig. 4. Stepped stress fatigue testing on Si_3N_4 -4% Y_2O_3 (Norton NT-154). Test temperature was 1370°C . Specimens were microwave annealed at 1400°C for 20h in the 2.45-GHz furnace.

of those specimens was higher than as-fabricated material (Fig. 5). Since the as-fabricated and the microwave annealed samples showed the same creep rates during the testing, the creep damage is probably the same in each type of sample. Therefore, the improvement in fatigue resistance is most

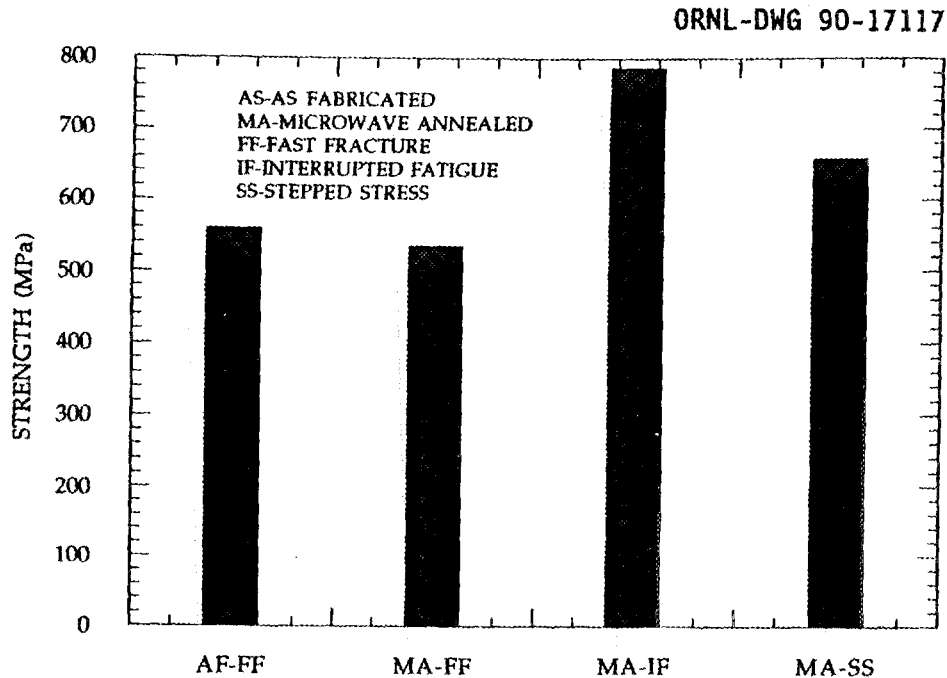


Fig. 5. Fast fracture flexural strength of Si_3N_4 -4% Y_2O_3 (Norton NT-154) at 1370°C. Materials tested included as-fabricated specimens and the microwave test specimens after the fatigue testing shown in Figs.1 and 2.

likely due to microstructural changes in the microwaved materials. SEM and TEM analyses are underway to determine the effect of the microwave anneal on the microstructure of the Si_3N_4 -4% Y_2O_3 . Additional microwave anneals on the Si_3N_4 -4% Y_2O_3 (Norton NT-154) have been performed with the following conditions (temperature/time): 1400°C/10 h, 1200°C/20 h, and 1400°C/10 h-1200°C/10 h. Fatigue testing is in progress.

New microwave furnace

The new microwave furnace has been tested and is now in operation on a daily basis. Results in this report were performed in the new furnace facility.

Reaction-bonded silicon nitride

A series of Si-Si₃N₄ mixtures with additions of Y₂O₃ and Al₂O₃ (to make a final 6 wt%-2 wt% addition, respectively) were nitrided in a 24h cycle to

1340°C and sintered at 1750°C for 30 min in the 2.45-GHz furnace. The results are summarized in Table 2. As shown, significant nitridation occurred for the specimens with $\geq 30\%$ Si_3N_4 . The sintered density of the TM-98 samples is comparable to densities achieved with 100% initial Si_3N_4 , whereas those for the higher Si additions were significantly lower. However, because of the Si additions, the coupling to the materials at low temperatures was much improved and essentially crack-free samples were obtained.

Table 2. Summary of results on sintered reaction-bonded silicon nitride with 6 wt% Y_2O_3 -2 wt% Al_2O_3 additions at 1750°C for 30 min in 2.45-GHz microwave furnace

Specimen number	Si/ Si_3N_4 ratio (wt %)	Si Weight gain (wt%)	Si reacted (%)	Sintered density	
				(g/cm^3)	(% T.D.)
TM-95	90	57.8	87	N.D.	N.D.
TM-96	70	63.4	96	2.60	79.8
TM-97	50	63.1	95	2.50	76.7
TM-98	10	65.0	98	2.91	

To observe the effect of temperature on nitridation kinetics, a series of silicon compacts were heated in conventional and microwave (2.45-GHz) furnaces. The samples differed from previous nitridation experiments in that the sample size was approximately 10-12 grams. The samples were heated at 3°C/min to 800°C and then 1°C/min to the final temperature and held for 1 h. The results are summarized in Fig. 6. As shown, the

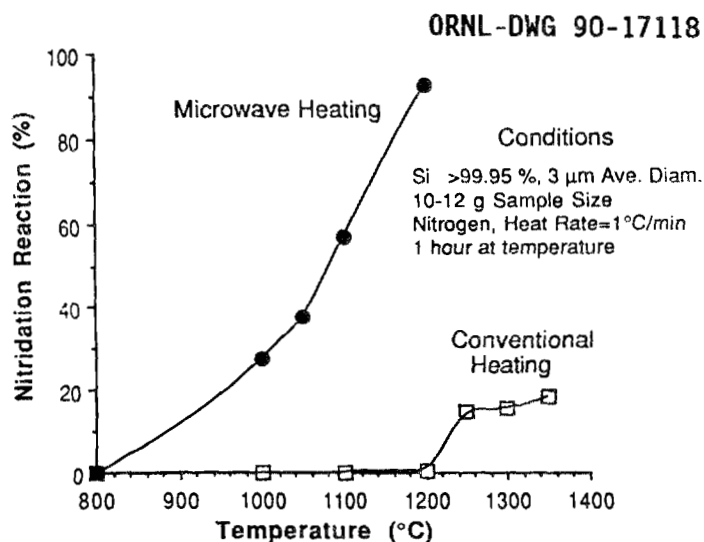


Fig. 6. Summary of results on the effect of temperature on nitridation kinetics of silicon.

microwave-heated samples showed significant nitridation at relatively low temperatures. The temperature of the microwave-heated samples is measured with a thermocouple placed in a hole in the specimen and it may be possible that there is a thermal gradient within the specimen. However, in these small samples the gradient should be small. Additional testing is being performed.

Status of milestones

Milestone 112402 was completed.

Milestone 112403, "Draft open-literature report on feasibility of sintering candidate advanced gas turbine materials," was completed.

Publications

T. N. Tiegs, J. O. Kiggans, and H. D. Kimrey, "Microwave Processing of Si_3N_4 ," to be published in proceedings of Materials Research Society Spring 1990 Meeting, San Francisco, California. This report satisfies the requirements for completion of Milestone 112402.

A draft report entitled, "Microwave Sintering of Silicon Nitride," was written. This report satisfies the requirements for completion of Milestone 112403: Draft open-literature report on feasibility of sintering candidate advanced gas turbine materials. An abstract summarizing the results of this work has been submitted to the American Ceramic Society for presentation at the 15th Annual Meeting on Composites and Advanced Ceramics to be held in Cocoa Beach, Florida, in January, 1991. The paper will appear in the proceedings of that conference.

Silicon Nitride Milling Characterization

S. G. Malghan, L.-S. H. Lum and D. B. Minor
(National Institute of Standards and Technology)

Objective/Scope

Currently, the starting materials in the manufacture of silicon nitride ceramic components are fine powders. These fine sized powders tend to form agglomerates due to van der Waals attractive forces. For improved reliability in the manufacture of ceramic components, the agglomerates in the powders should be eliminated since they form defects. In addition, the powders should have an appropriate range of size distribution and specific surface area for achieving a near-theoretical density of the ceramic after densification. These factors necessitate the use of powder milling as one of the major powder processing unit operations. Therefore, milling of powders is an integral unit operation in the manufacture of silicon nitride components for advanced energy applications. The production and use of these powders require the use of efficient milling techniques and understanding of characteristics of the milled powders in a given environment. High energy attrition milling appears to offer significant advantages over conventional tumbling and attrition mills.

The objectives of this project are to: (1) develop fundamental understanding of surface chemical changes taking place when silicon nitride powder is attrition milled in aqueous environment, and (2) demonstrate the use of high energy attrition milling for silicon nitride powder processing, by developing measurement techniques and data on the effect of milling variables on the resulting powder. This study will provide data and models for effective application of high energy attrition milling to industrial processing of silicon nitride powder. It also will provide recommended procedures for physical and surface chemical characterization of powders and slurries involved in the milling process.

Technical Progress

During the past six months, the primary effort was directed towards experimental research on milling of a closely sized silicon nitride powder. A series of statistically designed experiments was conducted to develop interrelationships between the parameters of high energy agitation milling. A large number of response variables were measured.

Experimental Design. The primary milling parameters included in this design are mill speed (2000 rpm and 2800 rpm), feed rate (240 cc/min and 480 cc/min), volumetric loading of powder in the slurry (34% v/v and 44% v/v). The remaining parameters (surfactant concentration, slurry ultrasonication, media size, and powder feed size) were held constant. In order to develop the interrelationship between the powder feed size and media size, these parameters were fixed at $d_{50} \approx 1.0$ micron (UBE SNE-3 powder) and 2.0mm diameter, respectively.

These experiments are conducted as a 2^3 factorial design with an objective to expand the design as new parameters are identified. The first expansion will be in terms powder feed size distribution and media size.

Effect of Milling Parameters. In the high energy agitation milling of SNE-3 powder in an aqueous environment with 2.0mm diameter media, the milling kinetics are slower than that of milling a 50/50 mixture of SNE-3 and SNE-5. The observed decrease in the milling kinetics with the SNE-3 powder is most likely related to a smaller ratio of media size to mean particle size and a low packing density of the SNE-3 particles. The presence of finer size particles in SNE-5 could have helped in the increased particle loading of the suspension and higher ratio of media to mean particle size. Both factors are expected to enhance the milling kinetics.

Based on the partially completed experimental design it appears that mill speed has a strong effect on the milling kinetics. The powder loading in the slurry appears to decrease the milling rate. The milling rate was evaluated by the measurement of particle size distribution and specific surface area. The particle size distribution of as-milled (not dried) powder was measured using Horiba LA-500 (laser diffraction); while the specific surface area of dry powder samples was measured with a multipoint BET apparatus. In addition, the power (current and total watts) drawn by the mill was measured as a function of milling time. The power data are going to be used to assess the milling rate model.

The data on power drawn by the mill is presented in Fig. 1a (44% v/v loading of powder) and Fig. 1b (34% v/v loading of powder). These data, irrespective of the powder loading, indicate that there is a steady decrease of power drawn as a function of milling time. This type of power decrease is probably related to a decrease in the resistance to flow of slurry. As the slurry undergoes deagglomeration, it attains lower viscosity and hence offers lower resistance to flow.

The increase of specific surface area as a function of milling time is shown in Fig. 2a (44% v/v loading of powder) and Fig. 2b (34% v/v loading of powder). As expected, the specific surface area increases linearly with milling time. At either powder loading, the rate of increase of specific surface area is slightly higher at 2800 rpm than at 2000 rpm mill rotor speed. In general, under the set of variables studied so far, the milling kinetics are fairly slow. The highest rate of milling is expected at a high rotor speed and an optimum ratio of feed particles size to media size.

In the next three months we plan to complete the milling tests and begin testing the milling model. In addition, detailed analysis of the surface chemistry of the milled powders will be conducted.

Status of Milestones

Slightly behind due to expanded experimental design.

Publication

S. G. Malghan, D. B. Minor and L.-S. H. Lum, "Silicon Nitride Powder Milling Kinetics in a High Energy Agitation Ball Mill" Accepted for publication by Powder Technology, October 1990.

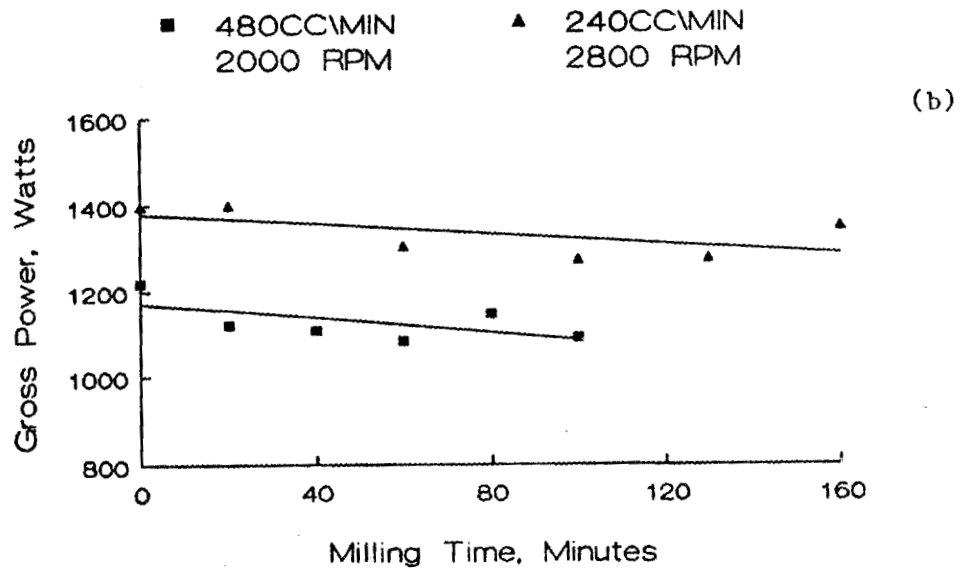
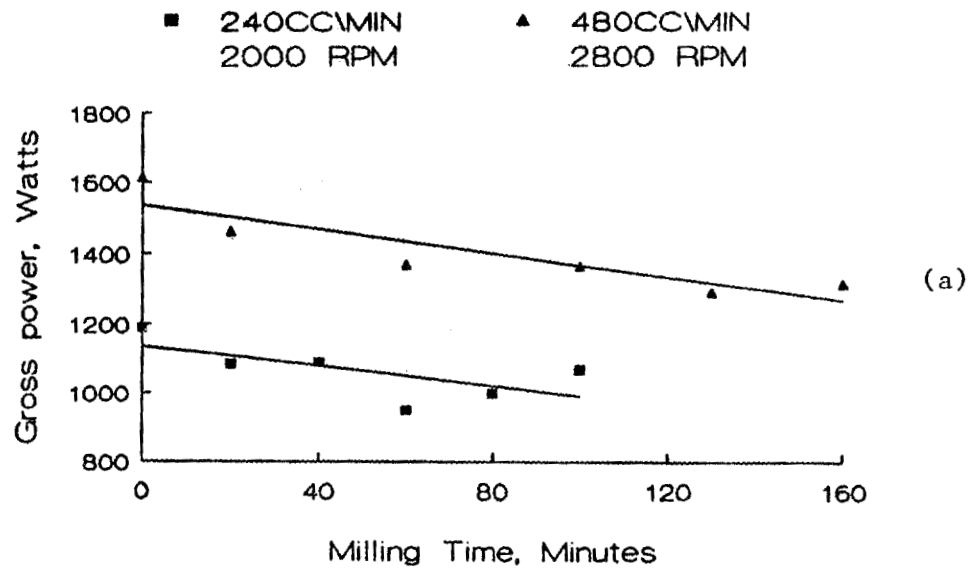


Figure 1. Power drawn by the mill as a function of milling time of SNE-3 powder slurry milled in water at a) 44% v/v and b) 34% v/v.

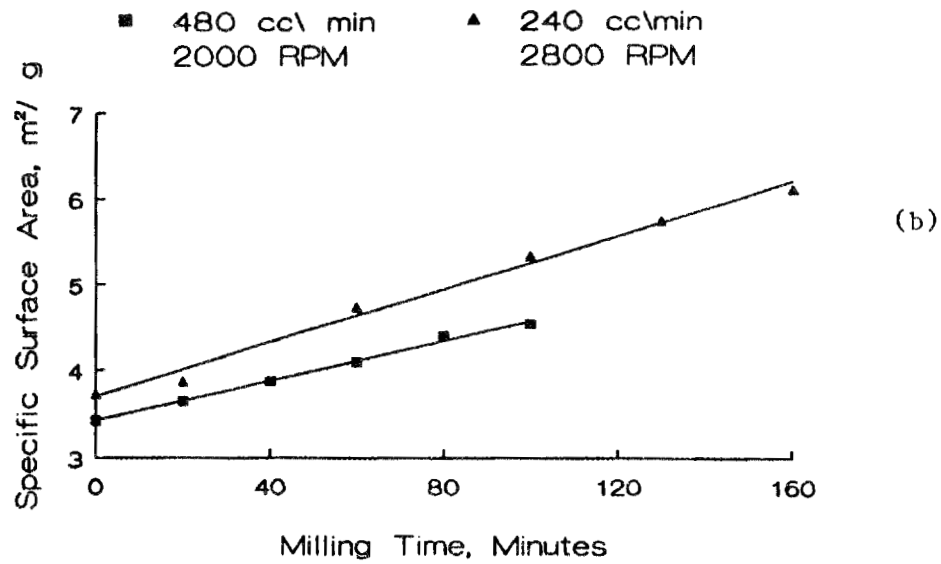
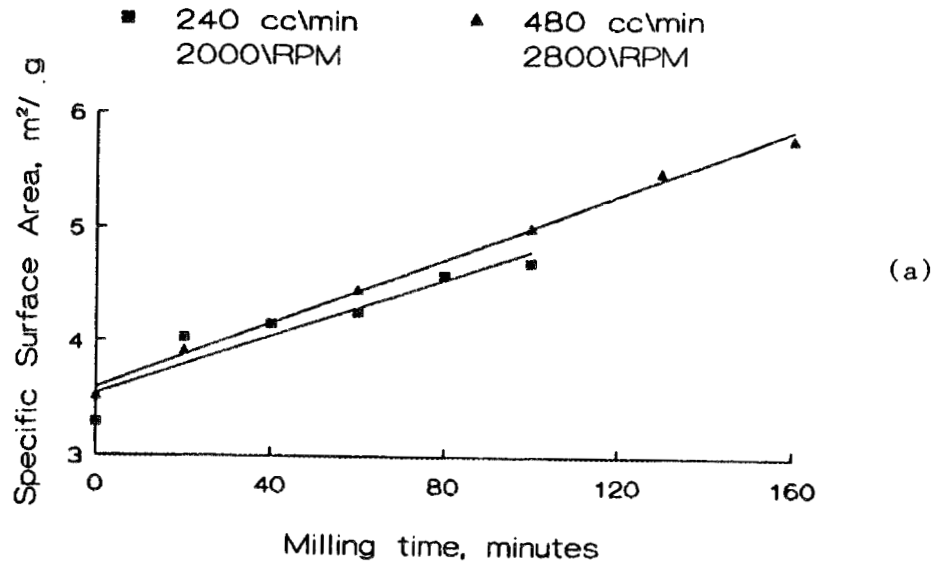


Figure 2. Increase of specific surface area as a function of milling time of SNE-3 powder slurry in water at a) 44% v/v and b) 34% v/v.

1.1.4 Processing of Monolithics

Improved Processing

V. K. Pujari, K. E. Amin, P. H. Tewari, C. A. Willkens, N. I. Paille, G. A. Rossi, R. D. Creehan, M. R. Foley, and L. C. Sales (Norton Company)

OBJECTIVE/SCOPE

The goals of the program are to develop and demonstrate significant improvements in processing methods, process controls, and nondestructive evaluation (NDE) which can be commercially implemented to produce high-reliability silicon nitride components for advanced heat engine applications at temperatures to 1370°C. Achievement of this goal shall be sought by:

- The use of silicon nitride - 4% yttria composition which is consolidated by glass encapsulated HIP'ping.
- The generation of baseline data from an initial process route involving injection molding.
- Fabrication of tensile test bars by colloidal techniques - injection molding and colloidal consolidation.
- Identification of (critical) flaw populations through NDE and fractographic analysis.
- Correlation of measured tensile strength with flaw populations and process parameters.
- Minimization of these flaws through innovative improvements in process methods and controls.

The quantitative program goals are: 1) mean RT tensile strength of 900 MPa and Weibull Modulus of 20, 2) mean 1370°C fast fracture tensile strength of 500 MPa, and 3) mean 1230°C tensile stress rupture life of 100 hours at 350 MPa.

TECHNICAL PROGRESS

The technical progress against the major tasks is described. The major tasks are: 1) Material Selection and Characterization, 2) Material Processing and Process Control, 3) Development and Application of NDE, 4) Property Testing and Microstructural Evaluation, 5) Reporting, and 6) Quality Assurance.

"Research sponsored by the U.S. Department of Energy, Assistant Secretary for Conservation and Renewable Energy, Office of Transportation Systems, as part of the Ceramic Technology for Advanced Heat Engines Project of the Advanced Materials Development Program, under Contract DE-AC05-84OR21400 with Martin Marietta Energy Systems, Inc., Work Breakdown Sub-Element 1.1.4.1."

During this period, major effort was directed towards: 1) the development of baseline data (Milestone #5, Task 1, 2) using the initial process route (IPR) of injection molding which involved microfocus X-ray and dye penetrant examination of all molded tensile bars and room temperature and high temperature tensile testing, 2) mold design and injection molding of MLP (machined from large piece) bars, 3) pressure casting of crack-free tensile bars through binder development and mold design modifications, 4) establishment of detection capabilities of microfocus X-ray, dye penetrant techniques, and film digitization techniques, 5) development of tensile bar NDE and fractography flaw population data correlation methods, and 6) comparison of mechanical properties of co-milled (C-Series) and precipitated (W-Series) powder batches.

TASK 2: MATERIALS PROCESSING AND PROCESS CONTROL

i) Powder Processing

Aqueous milled suspensions were prepared using two different techniques. In the W-Series suspension, after milling the silicon nitride powder, yttria was added by precipitation from a salt solution. In the case of C-Series, both silicon nitride and yttria powder are co-milled.

Four large batches were made to follow-up on the encouraging casting results for small rods from batch W009. Batches W011, W012 and W013 were made in a manner similar to W009, but with improvements made in the mixing conditions during precipitation that lessened the occurrence of yttrium-rich agglomerates. Problems with longitudinal cracking were encountered on drying the larger cast rods as discussed below. Subsequently, it was shown that the yttrium-rich regions were caused by a high concentration of the salt used as the sintering aid. By controlling the salt concentration, the yttrium-rich regions have been eliminated in 5kg batches (W016). A modified process for precipitation is being evaluated for the 28kg batches.

A water co-milled process (C-Series) was developed parallel to the precipitated process (W-Series). Four 28kg batches were prepared (C002-C005) for casting and injection molding studies. The C-Series powder has shown a lower oxygen content than the W-Series, since there is less potential for hydrothermal oxidation. Problems encountered with foaming and partial hydration of the yttria were solved using appropriate surfactants. The slurries were concentrated to >70% solids content.

Properties of CIP'ped/HIP'ped tiles prepared from each batch are discussed under Task 4. Fracture origin analysis indicates that failure is most frequently from very "subtle" low density agglomerates, which may be related to the powder drying step.

ii) Colloidal Consolidation

a. Slip Formulation/Characterization

The objective of this sub-task is to develop an aqueous suspension suitable for pressure casting of crack-free NSF (Net Shape Formed) tensile bars.

Before casting, every slip was characterized for its rheological properties using the Bohlin rheometer to obtain the viscosity versus shear rate curve. A typical curve is shown in Figure 1 for a slurry of the W-Series and in Figure 2 for a slurry of the C-Series.

During this study, it was found that the rheological properties were fairly consistent from batch to batch of the same series. Furthermore, no significant changes in viscosity were found for the same slurry upon aging when the slurry was kept rolling in plastic containers at room temperature.

Measurement and control of pH was done routinely since slight pH changes significantly affect the degree of flocculation and, therefore, viscosity. The optimum pH was found to be about 9.5

The suspensions were also analyzed for the presence of agglomerates. SEM examination of the fracture surfaces of tensile bars which had cracked during drying revealed the presence of agglomerates. In order to detect their presence in the slurry, the Hengman instrument was routinely used. This simple instrument, commonly used in the paint industry, consists of a thick steel plate with two polished rectangular lanes, about 2 cm wide and 16 cm long. Each lane is 100 μm deep at one end and tapers to zero depth at the other. A few drops of the slurry are placed at the 100 μm deep end and the liquid is slowly squeezed towards the other end with a steel blade. In so doing, the thickness of the slurry gradually decreases to zero. If agglomerates are present, they are dragged by the blade and form a visible streak. This instrument was very useful not only for the routine examinations and for the quality control of the slurry, but also for the screening of binders. The relative efficacy of a binder was judged by observing the cracking occurring during drying, i.e. slurries with the best binders did not crack during drying.

Binders were screened for the purpose of solving the cracking problem discussed later. Of all the binders tested, B13 was the best, confirming the results previously obtained.

Binders were added to slurries of both W and C-Series to try to enhance the yield of dry, uncracked tensile bars. It was found that the binder was more useful for lower solids loading and for the bars cast with the C slurries. These bars had a tendency to crack right after removal from the plastic mold when no binder was present.

Using the slurry W-013, a matrix of experiments was designed and conducted with the purpose of finding the best combination of binder, surfactant and pH. Short rods were cast and their density and dry strength were measured. The best combination was the binder B13, pH = 9.5 and no surfactant. This combination was then chosen for subsequent experiments.

b. Pressure Casting of Tensile Bars

Before casting, the suspension was characterized for pH and viscosity, ultrasonicated, de-aired and fed to the split plaster mold. Typically, the slurry was fed to both ends of the mold, corresponding to the buttonheads of the specimen. The typical casting time was 30-40 minutes.

Bars cast from a given slurry had, in general, consistent weight. For example, using the same slurry, 89 bars were cast over a period of six days. The difference between the average weights found during the

first and last days was 1.2%. This result could not have been obtained had the slurry been unstable.

c. Drying Problem and its Solution

Irrespective of the type of slurry used for casting (whether W or C), a longitudinal crack almost always appeared on the bar upon drying. Overall, more cracking occurred in the bars cast from the C slurries. Almost always, the crack followed the parting line. At first it was not clear whether the cracking was due to strain recovery (without water loss) or to drying. It was later found that drying was the main cause, since bars kept in sealed plastic bags in saturated conditions never cracked.

Attempts to solve the cracking problem by drying in controlled humidity conditions using a programmed controlled humidity oven were unsuccessful. This was found to merely delay the cracking event.

Among the possible causes for cracking, agglomerates and density gradients were considered most likely. However, it was found that cracking occurred also when agglomerates were absent and when density differences lower than 1% existed between buttonhead, shank and gauge in cracked bars dried and air-fired at 600°C. It was also found that a higher packing density in the wet bar did not reduce cracking. Bars from the C-Series, with packing densities of about 2 g/cm³ cracked more often than those of the W-Series, with typical packing density of 1.7 g/cm³.

Recently, it was demonstrated at the University of Washington in Professor Aksay's laboratory, that in wet buttonhead region of pressure cast bars, density gradients exist across the diameter (see Figure 3). The technique used for this analysis was gamma ray densitometry. It is, therefore, possible that localized density gradients cause differential stress build-up during the first stage of drying, which, in turn, triggers the crack formation.

In order to solve the cracking problem, freeze-drying was also attempted using two different methods. With the first method, the as-cast bar was frozen and freeze-dried. With the second method, the sonicated, de-aired slurry was poured into a split rubber mold, which was frozen. The frozen bar was extracted from the mold and freeze-dried. Both methods were unsuccessful and virtually all bars were found cracked after freeze-drying.

Finally, the mold design features were examined carefully. The cracking problem was ultimately solved by reducing the porous surface of the plaster mold and, therefore, the casting pattern. The design of the mold was also slightly modified by relocating the gates. After these changes, bars with consistently higher weight were pressure cast using the C003 and C004 slurries. These bars were dried in air with no cracking and close to 100% yield was achieved.

iii. Injection Molding

A. Injection Molding of NSF Bars for Baseline Tensile Data

a. Mold Design

As described in the previous semi-annual report, three distinct gate designs were evaluated ("G1", "G2", and "G3"), with design "G3" (end gate) selected for the baseline NSF specimens. The original die cavity produced an undersize NSF bar (20% in linear dimensions) which was used in the preliminary unit operation developments. The final baseline bars were molded in a double cavity die with cavity volume 1.84 times the undersized bar volume.

b. Molding Process Optimization and Control

Five molding batches were consumed in the iteration, with the last of these (Batch "E" - 32kg) used for the full size bars representing the baseline data. Mold design and molding parameters were optimized relative to bar quality measured in terms of weight, dimensions and roundness. Microfocus X-ray radiography was used to generate preliminary control information for the molding parameters. Using the optimized mold design and molding parameters, all baseline NSF bars were molded.

c. Dewaxing

A dewaxing procedure was developed for the small NSF bars which provided a yield level of 85%. The procedure specified time, temperature, pressure and atmosphere parameters. This procedure was found inappropriate for the full size bars, giving low yields. Parameter experimentation, improvement in temperature control within the furnace using additional thermocouples and proper fixturing procedure using custom designed setter plates resulted in a procedure giving a yield level of 86% for the baseline bars. However, occasional cracking near the buttonhead radius (transition between shank and buttonhead) was observed (by dye penetrant technique on densified bars) as described in Task 3. This is suspected to be caused by molding related residual stresses due to the sharp transition in the cross-section of the bar causing premature buttonhead failures during testing (Task 4). Slight modifications in the mold to incorporate gradual transition in the cross-section near the buttonhead is expected to alleviate this problem.

B. Injection Molding of "MLP" Bars

a. Mold Design

Preliminary testing was done in an MLP shape mold to determine the required molding parameters for this shape. This test pointed out some problems in molding the part, specifically in the transition area between the thick center section and the shank ends. Cracking in this area during molding was evident. The mold has been redesigned and modified with a tapered transition area to replace the earlier sharp transition.

b. Molding

A seven kilogram batch was prepared for the molding of MLP shapes. The technique for preparing this batch was modified from that normally used in an attempt to reduce the occurrence of metallic inclusions. This technique does have a drawback in that the material loaded into the molding machine does not feed as well or as uniformly as the standard

material. This led to some problems during molding caused by a very slow and erratic melting of the material.

A total of eight MLP samples were molded with an average weight of 539.9 g and a standard deviation of 4 g. Figure 4 is a photo of an MLP sample as molded. All samples were submitted for microfocus X-ray and one sample each for NMR and ultrasonic evaluation. Following these tests, samples will be dewaxed and HIP'ped.

IV. Hot Isostatic Pressing

a. HIP Densification Firings

All sample materials were hot isostatically pressed using a proprietary experimental process cycle previously developed by Norton for silicon nitride-4% yttria compositions. During the performance period, a total of twenty-four HIP runs were made. These firings comprised of eighteen tensile rod runs and six test tile runs for powder qualification and testing. Of the eighteen tensile rod runs, twelve of these were used for densifying the Stage I baseline NSF samples from the first process iteration. Of the remaining runs, four tensile rod firings were used for either experimental purposes or for densifying NDE tensile rod standards and two tensile rod firings were made for densifying prototype pressure cast tensile rods.

b. Tensile Rod Yield

Due to several factors, the tensile rod yield from the HIP was reduced from the nearly 100% yields which had been previously achieved. Just prior to the first baseline iteration, the tensile rod design was changed. Increase in tensile rod dimensions required modification of fixturing designs and packing arrangements which had been previously developed for a smaller rod geometry.

This change in NSF specimen dimension also introduced subtle problems in green forming which had a significant, though indirect, influence on HIP yield. Of the total inventory of tensile rods submitted for HIP'ping, approximately 75% were densified intact and nearly 50% achieved theoretical density. It should be noted that the overall HIP yields were heavily biased by the initial development runs where entire runs were lost. Subsequent runs routinely provided between 80 to 100% yields. Based on run-out measurements made initially on all green tensile rods and densified intact tensile rods, no detectable HIP-induced warpage was produced during densification.

c. HIP Process Experiments

During the performance period, a number of experimental modifications in pre- and post-HIP treatments and HIP firing cycle were evaluated. Both alcohol milled and water milled powders were subjected to a standard process cycle, a modified presinter-HIP cycle, a recrystallization treatment, and an oxidation annealing treatment. The results of this study are presented in Table 1 where room temperature fracture toughness, room temperature and high temperature (1370°C) flexure strength, and stress rupture lifetimes are reported for each condition. The results of this study indicate no significant improvement in properties.

d. HIP Reaction Layers

During glass encapsulated HIP'ping of silicon nitride-yttria compositions, a surface reaction layer is typically formed on surfaces of samples. This layer is typically observed optically at low magnification in dark field due to contrast of the lighter surface layer with the darker bulk sample. For standard compositions, the optically detectable reaction layer extends between 5 to 30 mils into the sample.

Typically, these reaction layer compositions are silica rich and yttria deficient with a higher oxygen, boron, sodium and calcium content than the bulk material due to reaction with the glass. X-ray diffraction characterization of surface and bulk samples indicate that the surface reaction layer is typically higher in alpha-Si₃N₄ and the silicon oxynitride (Si₂N₂O) than bulk material with alpha contents typically varying between 1 to 20% and silicon oxynitride generally under 15%. For fixed initial oxygen content in green components, the reaction layer thickness and composition is essentially constant.

While physical and chemical evidence of the surface reaction layer is readily obtained, it is not known to date whether the reaction layer is advantageous, benign or damaging from a mechanical property perspective. There is limited evidence which indicates that the presence of the surface reaction layer is desirable for improved toughness.⁽¹⁾ There is also evidence, as documented in this report (TASK 4), which suggests that high alpha-Si₃N₄ content, as found within the reaction layer, leads to lower room temperature and high temperature strength. Due to the unresolved uncertainty in influence of the reaction layer on mechanical properties, all specimens which have been tested to date have a minimum of 50 mils machined from as-HIP'ped surfaces in order to remove the reaction layer.

V. Machining

Injection molded, HIP'ped NSF bars were final machined by diamond grinding, inspected and delivered to the mechanical test lab for tensile testing. Additionally, 30 tensile bars were finish machined and delivered to ORNL. An SOP for inspecting machined bars was established for the prescribed dimensional tolerances, surface finish (0.4 um Ra.), and concentricity (± 0.00508 mm). The radius at the shank/buttonhead transition is given special attention relative to gripping requirements.

VI. Process Control and Optimization

a. Powder Preparation

Statistical Process Control (SPC) charts which are being maintained on performance variables in the powder preparation unit operations indicate the following:

1. Oxygen content in the co-milled final powders are closer to specified values than in the precipitated powders and appear to have less variability. (See Figures 5 and 6.)

2. Yttria content in the precipitated batches are variable from batch to batch, but have smaller deviations within batches (Figure 7). This dispersion within batches appears to have improved with each successive batch. In the case of co-milled powders, the variability in the latter batches has increased (Figure 8).

3. The surface area of the final powder as in the case of yttria content appears to have large variability from batch to batch, and less variability within a batch for precipitated powders (Figure 9). This is consistent with the variability in yttria content. Similarly, the surface area of the co-milled powders followed the variability of the yttria content (Figure 10).

Procedures are currently underway to determine the cause of the variability in yttria values, and to introduce a homogenizing step in the process.

b. Injection Molding

In the development of SPC charts, "on-line" variables are continually being evaluated, so as to arrive at some easily measured parameter that can be correlated to an actual performance measure. One of these "on-line" variables is the weight of the injection-molded tensile rod. A proposed hypothesis was that the weight of the tensile rod was inversely proportional to the volume of voids (detected using microfocus radiography).

As a by-product of an experiment to reduce voids by varying injection-molding parameters, weights of tensile rods were recorded as molded. An NDE technique was then used to examine the green tensile specimens for voids (and other flaws such as cracks, inclusions). The total volume of voids thus detected was plotted against the weight of the rods. A regression analysis showed no correlation between weights and the volume of voids. Reasons suggested for this (and verified to a certain extent) were that changes in some injection molding control variables affect the density of the material, and thus any relationship between weight and void volume is overshadowed by density variations.

The recording of weights and voids was repeated for the baseline iteration (Initial Process Route) with molding controls kept constant. There appears to be a good correlation between the weights of rods molded and the void volume detected by NDE Figure 11. This could mean that the weights can be used as an on-line control variable to monitor the process.

TASK 3: DEVELOPMENT AND APPLICATIONS OF NDEA. In-House NDEi) Reference Samples

The milestone on preparing appropriate samples of Si_3N_4 with known seeded defects/flaws and computing detection sensitivity of microfocus radiography/dye penetrant was completed.

Inclusions (Fe) were seeded in cylindrical rods (both green, presintered, and HIP'ped) with size range 20 to 200 μm . Samples with simulated voids were made with seeded PMMA in the size range of 20 to 200 μm . Rods with density gradients were prepared with both density variations as high as 16% within individual rods as well as from rod to rod. Agglomerates were seeded in both loose powder pack as well as in Si_3N_4 slips.

Probability of detection (POD) at confidence levels of $G = 95\%$ was determined using the above seeded reference samples. In the green state, the minimum size of Fe particles detected using microfocus film radiography was better than 0.3% of the sample thickness (20 μm in thin sections). A 2% thickness sensitivity was achieved for lower bound probability of detection (>90%). In samples with PMMA simulated voids, minimum size detected was 2% (100 μm) of sample thickness. A thickness sensitivity of 5% was attained at POD >95% at $G = 95\%$. In as HIP'ped samples, probability of detection of Fe is 97% at $G = 95\%$ for thickness sensitivity of >2.4%. No PMMA particles were detected in HIP'ped specimens as all voids were healed during densification.

Experimental design was adopted to optimize the film exposure conditions so maximum contrast can be achieved to help improve detection sensitivity for the above defects. It was found that the use of no screens and medium speed films at particular values of excitation voltage/filament current gave the optimum contrast. The use of mating surfaces to both conform to the cylindrical shape and offset the thickness gradient was found to provide no beneficial effect on contrast and definition. Experimenting with a variety of anodes (Mo, Fe, W, Cu) did not provide practical advantages.

SOP were developed to detect cracks using fluorescent dye penetrant on reference samples with known cracks, introduced using Vicker indentation technique. Using oil base penetrants with different sensitivities, cracks as small as 18 μm (length) were detected. This procedure is being used routinely to monitor the effect of machining on tensile bars.

ii. Process Monitoring

Microfocus radiography was instrumental in monitoring the quality of tensile bars (made by both the injection molding and pressure casting techniques) in as-molded/cast, pre-sintered and HIP'ped states. An example of the defect population measured in such samples is shown in Figure 12. Microfocus technique was also successfully utilized to monitor contaminants in raw powder, compounded material (injection molding) and colloidal slips.

iii. Film Digitization

The milestone on installing and implementing film digitization capability to quantify flaw populations in tensile bars was successfully completed with the help of Argonne National Laboratory.

The film digitization set-up consists essentially of a high resolution CCD camera (1024 x 1624), a frame grabber board (1280 x 1024), high resolution monitor and graphics board, computer hardware and software to provide various contrast enhancements, filtering, size analysis and density analysis (optical).

An example of improved defect detection and the reliability of defect counting is shown in Figure 13.

iv. Flaw Population Data Analysis

The milestone on developing techniques for definition of multiple flaw populations and establishing methods to quantify such population from both NDE and fractography data was accomplished. The effort may be detailed as follows:

A computer program was written by Professor K. Jakus (University of Massachusetts) using BBN & Associates RS1 RPL procedure to do the following:

1. Allow input of fracture strength data from testing of both green and dense specimens.
2. Allow input of optical/SEM fractography data (i.e. location, size, and type of flaw origin).
3. Compute probability of failure for both uncensored and censored data according to flaw type (volume, surface, buttonhead and unknown) using the formulas in Appendix A.
4. Compute Weibull modulus using both least squares fit and maximum likelihood techniques and plot the resulting distributions.
5. Compute flaw density data (number of flaws per unit volume at a given strength) using appropriate fit functions (spline fit and both quadratic and cubic functions).
6. Plot flaw distribution versus strength data at various processing steps.

The above procedure was applied to data from baseline iteration of injection molding. Figure 14 shows the probability of failure versus fracture strength of HIP'ped/machined Si_3N_4 as separated for volume and surface flaws as well as buttonhead failures using censored probability of failure computations (Appendix A). Strength separation here clearly shows the dependence of Weibull Modulus, m , (slope of plot) on the type of flaw population. For volume flaws, $m = 6.85$; for surface flaws, $m = 1.20$, and for buttonhead failures, $m = 5.14$.

B. Subcontractors

i) Precision Acoustic Devices (PAD)

PAD has been engaged in ultrasonic technique development, mainly focusing on developing novel transducers (using air as couplant), PVDF-type transducers with a mating surface and a buffer rod and spherically focused transducers. In addition, scanning techniques (hardware/software) have been developed for inspecting cylindrical samples. The procedure was also developed to image defects in green bars (both pressure cast and injection molded) using both urethane coating and plastic vacuum bagging. An example of C-scan obtained from such techniques is shown in Figure 15. The PVDF transducers were evaluated first on flat samples with around 50 μm seeded WC particles. The data shows very high transducer sensitivity; i.e. ability to detect smaller size inclusions around 10 μm .^[2] Cylindrical samples are presently being evaluated using those PVDF-type transducers.

Surface wave acoustics technique (50 MHz pulse mode with an F0.85 transducer) was successfully tried to evaluate the integrity of the surface of HIP'ped/machined Si_3N_4 tensile rods. Scans provide data on cracks and other surface machining contours as illustrated in Figure 16. Work is continuing to optimize this approach.

ii) Argonne National Laboratories

ANL has been concentrating mainly on technique development in both computed tomography and nuclear magnetic resonance imaging/spectroscopy.

1. Computed Tomography

The 3D image reconstruction code was rewritten to compute 512X512 sections instead of 256X256 and, therefore, achieve higher resolution. Proper system configuration for optimizing density sensitivity was established. Full eight-bit dynamic range of the frame grabber, 256 grey level scale was achieved by electronics modification. It was also found that the presence of a lead mask at the face of the image intensifier, as well as the use of appropriate collimation at the source, gives measurably improved results. Figure 17 shows examples of CT sections collected on both injection molded and pressure cast tensile samples. In the pressure cast sample, a very low density region can be observed in the section which happens to be from the middle of the gauge length.

2. NMR Spectroscopy

Work on quantification of surfactant distribution on powder versus solution (slip) is continuing.

Proton spectra of both compounded, pelletized and injection molded Si_3N_4 samples were obtained, Figure 18. The molded sample shows a downfield shift (increasing ppm) of the observed resonance. Additionally, the full width at half maximum of the resonance increased from approximately 600 Hz in the compounded material to approximately 1300 Hz in the molded specimen. Origin of such changes is being investigated as

related to binder chemical and physical changes (using solid state C-NMR and H relaxation). The changes in binder affects viscosity and moldability of the mix.

3. NMR Imaging

Proton (^1H) studies were conducted on the pure binder in an attempt to define optimum conditions for imaging its distribution in injection molded samples. The binder was identified as consisting primarily of aliphatic carbons (chemical shifts 15-40 ppm) with a small amount of carbons that are either quaternary or bonded to amine functionalities (approximately 48 ppm) and carboxylic acid groups at 181 ppm.

TASK 4: PROPERTY TESTING AND MICROSTRUCTURAL EVALUATION

i) Injection Molded Specimens from Initial Process Route-Baseline Data

a. Room Temperature Fast Fracture

Fast fracture tensile testing was performed on 49 specimens at room temperature, resulting in 26 gauge failures and 23 buttonhead failures. The strength for the specimens which failed at the buttonhead was calculated as the stress in the gauge section at the point of buttonhead failure. The data is summarized in Table 2. Optical and/or electron microscopy was performed on all fracture surfaces. All 23 buttonhead failures were from pre-existing surface cracks due to the forming process. As discussed above, these flaws were detected using the dye penetrant technique.

Table 3 outlines the fractography data for all 26 gauge failures. The same strength limiting flaws if detected by microfocuss X-ray (NDE) are also noted. Inclusions were either Fe, Ti, Al, Cr, Zr, Ni or a combination of these. The size of the flaw was measured from an SEM micrograph as the largest measured dimension. On a few specimens, it was difficult to measure or find the strength limiting flaw. The Weibull Modulus of the strength data was found equal to 3.8 for gauge failures and 4.3 for all data. Also included in Table 2 are data for 35 flexure specimens machined from five tensile rods and tested at room temperature. As expected, the measured flexure strengths are higher than those of tensile specimens.

Fracture toughness measurements performed on four flexure bars machined from tensile rods, by an indentation and fracture technique, resulted in an average value of $5.35 \pm 0.037 \text{ MPa}\cdot\text{m}^{0.5}$.

b. Elevated Temperature Fast Fracture

Fast fracture tensile testing was performed on 15 specimens at 1370°C in air and the data are summarized in Table 4.

There were only two buttonhead failures caused by pre-existing surface cracks introduced probably during forming. Optical and/or electron microscopy was performed on all fracture surfaces and is outlined in Table 5. Seven of the remaining 13 specimens failed due to SCG (Slow Crack Growth) at stresses below 140 MPa, while the remaining

six failed at stress in excess of 250 MPa. Also included in Table 4 is data for 14 flexure specimens machined from five tensile rods and tested at 1370°C. As expected, the strengths are greater in flexure than in tension.

c. Stress Rupture Testing

Tensile stress rupture tests were performed on five specimens at 1230°C in air at an applied stress level of 350 MPa. The times to failure were 0, 2, 5, and 20 minutes, with one specimen failing during loading at a gauge stress of 278 MPa. The fractography results are summarized in Table 6. All specimens failed in a fast fracture mode as opposed to slow crack growth. This may be explained by considering the fact that the average strengths at room temperature and 1370°C are 454 and 204 MPa, respectively. These data suggest that the applied stress of 350 MPa is very close to the fast fracture strength of this material at 1230°C. Flexure stress rupture tests were also performed on four specimens machined from tensile rods with one failing immediately and three surviving 200 hours before test termination.

ii) Comparison of Aqueous Milled Powders

The mechanical properties of eight (8) aqueous milled batches processed by two techniques were evaluated using flexure specimens (machined from CIP'ped and HIP'ped tiles) per MIL STD 1942 (MR) B. As mentioned in TASK 2, powder processed from these two techniques are designated as precipitated (W-Series) and co-milled (C-Series). The mechanical property data from these powder batches are summarized in Table 7. As obvious from Table 7, the strengths of several batches exceed 900 and 500 MPa for room temperature and 1370°C test condition, respectively. The fracture toughness values are similar for all batches, ranging between 5.9 and 6.4 MPa.m^{1/2}. Stress rupture tests at 13730°C/300 MPa were performed on test bars, both from W-Series and C-Series batches. Only 20% of the W-Series specimens survived 200 hours, while 54% of the C-Series specimens survived the 200 hours.

Due to the overall high strength values, the flaw origins in the flexure bars tend to be small and mostly related to large grain, agglomerates or porous regions. A limited number of ferrous inclusions were also observed in the W-Series (11%) and C-Series (7%) test specimens.

As mentioned before, flexure specimens are machined from HIP'ped tiles measuring 63.5mm x 63.5mm x 6.4mm. Using a tracking system, each flexure bar was identified by the tile it was machined from and the position of the tile in the HIP. Within a specific batch and HIP run, a tile-to-tile variation was measured by mechanical testing. Figure 19 is a plot of strength versus tile number for the C-Series batches one through four. Five separate HIP runs were made to produce all 27 tiles. The most pronounced differences are seen in HIP-3 (Batch C002) and HIP-5 (C004). The mean strength differences between these tiles is statistically significant. Thorough chemical analyses are always performed at various stages of the processing as part of the SOP prior to HIP'ping. Subsequent to HIP'ping, properties such as grain size morphology and crystal structure are also measured, but on a

limited basis. Table 8 summarizes the XRD data from four specimens taken from separate batches and the Alpha:Beta ratio indicating that each saw different HIP conditions. It is critical for both reliability and reproducibility reasons that the HIP be monitored more closely. Further post-HIP analyses are being performed to gain insight and to help develop a cause-effect relationship.

REFERENCES

1. B. J. McEntire (et.al.), ATTAP Bi-Monthly Progress Report (March-April 1990), Norton/TRW Ceramics.
2. V. K. Pujari (et.al.), Bi-Monthly Progress Report (August-September 1990), ORNL Processing Subcontract 86X-SB182C.

STATUS OF MILESTONES

All milestones are on schedule.

COMMUNICATIONS/VISITS/TRAVEL

- o K. E. Amin visited Argonne National Laboratory, May 22, 1990 to review progress towards NMRS/NMRI and CT effort.
- o K. E. Amin visited Precision Acoustic Devices Company on May 23, and 24, 1990 to review progress in ultrasonic effort.
- o D. M. Tracey, V. K. Pujari, K. E. Amin, P. H. Tewari and R. H. Licht visited ORNL, Oak Ridge, Tennessee for semi-annual project review, July 20, 1990.
- o K. E. Amin visited Argonne National Laboratory to review progress and to deliver reference samples with density gradients and pressure cast tensile bars made from different mold designs.
- o V. K. Pujari and G. A. Rossi visited Professor I. Aksay at the University of Washington to evaluate density gradients in green pressure cast tensile bars using gamma-ray densitometer.

PROBLEMS ENCOUNTERED

None.

PUBLICATIONS

- o K. E. Amin presented a paper titled, "Characterization of Processing Defects in Ceramics Using Microfocus Radiography", at the 92nd ACS Annual Meeting, Dallas, Texas, April 22, 1990.
- o K. E. Amin presented a paper titled, "The Use of Film Digitization Technology for Improving the Detection and Mapping of Defects in Ceramics", at the ASNT/ACS Conference on NDE of Modern Ceramics, Columbus, Ohio, July 9, 1990.

Appendix A
Failure Probability Computations

I - Uncensored data:

$$\phi(s) = \frac{i-0.5}{J}$$

where i : sample ranking (from lowest strength to highest strength)

J : total # samples in a lot

II - Censored data:

$$\phi(s) = \left(\frac{i + \frac{(J+1-i)}{(J_0+1)} - 0.5}{J} \right)$$

J_0 : # remaining after censoring

Table 1. EXPERIMENTAL PROCESSING STUDY (PRESINTER, HIP & POST TREATMENTS)

POWDER BATCH	PROCESSING ROUTE	R.T. K_{IC} (MPa.m ^{1/2})	1370°C @ 300 MPa		RTFF (MPa)	HTFF (MPa)
			STRESS RUPTURE LIFE (hrs)			
W009	STANDARD CYCLE	6.40	> 200 (2) 53		999	584
W009	MODIFIED PRESINTER/HIP	5.80 (2)	57 127		892	462
W009	MODIFIED PRESINTER/HIP & CRYSTALLIZATION ANNEAL	6.07 (2)	65 69		689	555
W009	MODIFIED PRESINTER/HIP & CRYSTALLIZATION ANNEAL & OXIDATION ANNEAL	6.09	N/A		981	558
C001	STANDARD CYCLE	6.42	138		1027	556
C001	MODIFIED PRESINTER/HIP	6.30 (2)	33 76		819	482
COO1	MODIFIED PRESINTER/HIP & CRYSTALLIZATION ANNEAL	5.95 (2)	26 35		885	551
C001	MODIFIED PRESINTER/HIP & CRYSTALLIZATION ANNEAL & OXIDATION ANNEAL	6.22	N/A		1040	575

TABLE 2: Baseline Tensile Strength Data for the Injection Molded Specimens at Room Temperature

RT FAST FRACTURE

FAILURE LOCATION	AVERAGE STRENGTH (MPa)	STD DEV	RANGE	n
GAGE/VOLUME	506	91	327-663	17
GAGE/SURFACE	356	201	38-629	9
BUTTONHEAD	442	94	276-632	23
ALL	454	121	38-663	49
FLEXURE	760	159	255-965	35

TABLE 3: Room Temperature Fractography Data on Injection Molded Tensile Specimens

SPECIMEN #	FLAW LOCATION VOLUME OR SURFACE	FLAW TYPE*		FLAW SIZE (μ m)		
		SEM	NDE	SEM	NDE	
B-26	V	I	I	80	100	
C-64	V	I/A	-	100	-	
C-65	V	P/I	-	100	-	
B-111	V	I	I	200	400	
T-112	V	A	-	100	-	
T-116	V	I	I	80	100	
B-150	V	A	-	100	-	
B-106	V	P/I	I	500	500	
B-144	V	I	I	100	200	
T-148	V	A/I	-	100	-	
T-135	V	A/I	-	150	-	
B-153	V	I	I	90	130	
T-143	V	I	I	NA	80	
T-149	V	I	I	200	300	
B-130	V	A/P	I	NA	300	
T-132	V	(1)	I	200	300	
B-132	V	I/A	I	NA	300	
C-52	S	C	-	100	-	
B-77	S	C	I	100	200	
B-135	S	C	-	100	-	
T-130	S	L.G.	I	150	175	
T-134	S	C	-	NA	-	
B-23	S	?	I	NA	150	
B-126	S	P	I	NA	300	
B-148	S	C	C	NA	3000	
T-120	S	?	-	NA	-	

* I=INCLUSION; A=AGGLOMERATE; P=PORE OR PORE CLUSTER; C=CRACK;
L.G.=LARGE GRAINS

(1) REGION OF ACICULAR GRAINS VOID OF GRAIN BOUNDARY PHASE

TABLE 4: Baseline Tensile Strength Data for the
Injection Molded Specimens at 1370°C

1370°C FAST FRACTURE

FAILURE LOCATION	AVERAGE STRENGTH (MPa)	STD DEV	RANGE	n
GAGE	199	127	64-370	13
BUTTONHEAD	236	--	230-242	2
ALL	204	118	64-370	15
FLEXURE	456	18	150-607	14

TABLE 5: 1370°C Fractography Data on
Injection Molded Tensile Specimens

SPECIMEN #	FLAW LOCATION VOLUME OR SURFACE	FLAW TYPE		FLAW SIZE (μ m)	
		SEM	NDE	SEM	NDE
B-13	S	SCG	I	-	200
T-99	S	P	-	65	-
B-46	S	SCG	-	-	-
B-52	V	P	I	50	200
T-103	V	C/A	-	65	-
B-133	S	SCG	-	-	-
T-101	V	P/C	-	230	-
B-51	S	SCG/P	I	175	100
T-102	S	SCG	-	-	-
T-147	V	C	-	125	-
B-95	V	P	-	150	-
T-92	S	SCG	I	-	400
T-81	S	SCG/P	-	35	-

* SCG=SLOW CRACK GROWTH; P=PORE; C=CRACK; A=AGGLOMERATE
I=INCLUSION

TABLE 6: Stress Rupture Fractography on
Injection Molded Tensile Specimens

SPECIMEN #	FLAW LOCATION VOLUME OR SURFACE	FLAW TYPE*		FLAW SIZE (μ m)	
		SEM	NDE	SEM	NDE
T-40	V	I	I	125	100
B-41	V	I/P	-	125	-
B-40	S	P	V	75	600
B-43	V	P	I	65	150

* I=INCLUSION; P=PORE; V=VOID

TABLE 7

COMPARISON OF MECHANICAL PROPERTIES RESULTING FROM
AQUEOUS MILLED POWDERS PROCESSED BY TWO DIFFERENT
TECHNIQUES

BATCH	STRENGTH (MPA)				FRACTURE TOUGHNESS* MPA.M ^{1/2}
	M = WEIBULL MODULUS (XX) = STANDARD DEVIATION				
	ROOM TEMPERATURE		1370°C		
	σ_c	M	σ_c	M	
W010	910	14.3	547	16.5	6.1
W011	889	9.4	505	(36)	5.9
W012	930	11.0	550	(40)	6.3
W013	922	21.4	551	(49)	6.2
W014	962	10.5	-	-	6.1
C002	894	9.9	509	(60)	6.4
C003	892	14.8	422	24.7	6.1
C004	905	10.4	482	(88)	-

NOTE: THE WEIBULL MODULUS IS ONLY REPORTED IN SAMPLE SETS OF ≤ 10 SPECIMENS
OTHERWISE THE STANDARD DEVIATION IS REPORTED.

*CONTROLLED FLAW TECHNIQUE

TABLE 8

QUANTITATIVE POWDER XRD DATA FROM FOUR BATCHES OF
HIP'PED SILICON NITRIDE

BATCH	β - Si ₃ N ₄	α - Si ₃ N ₄
W011	89%	11%
W012	73%	27%
C002	69%	31%
C003	95%	5%

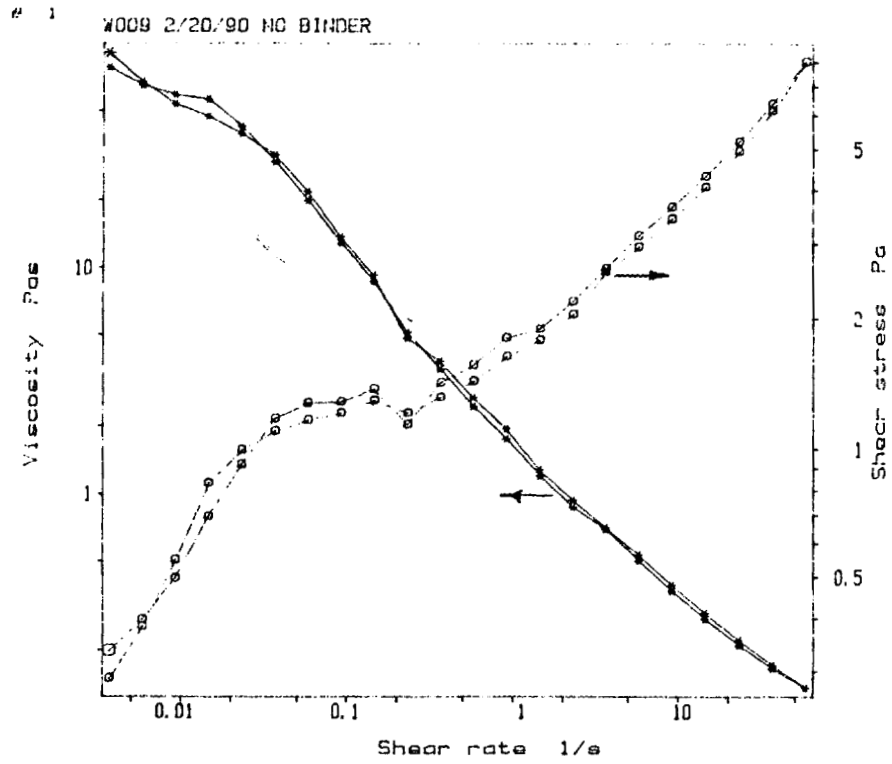


FIGURE 1 Rheology of W-Series Suspension

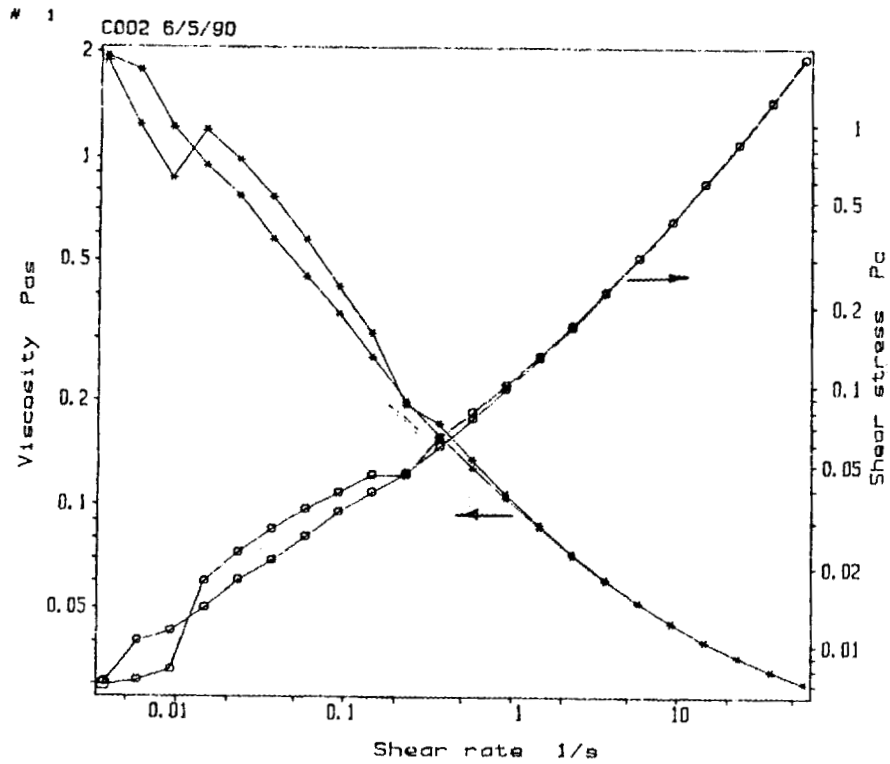


FIGURE 2 Rheology of C-Series Suspension

Saturated Button-Head

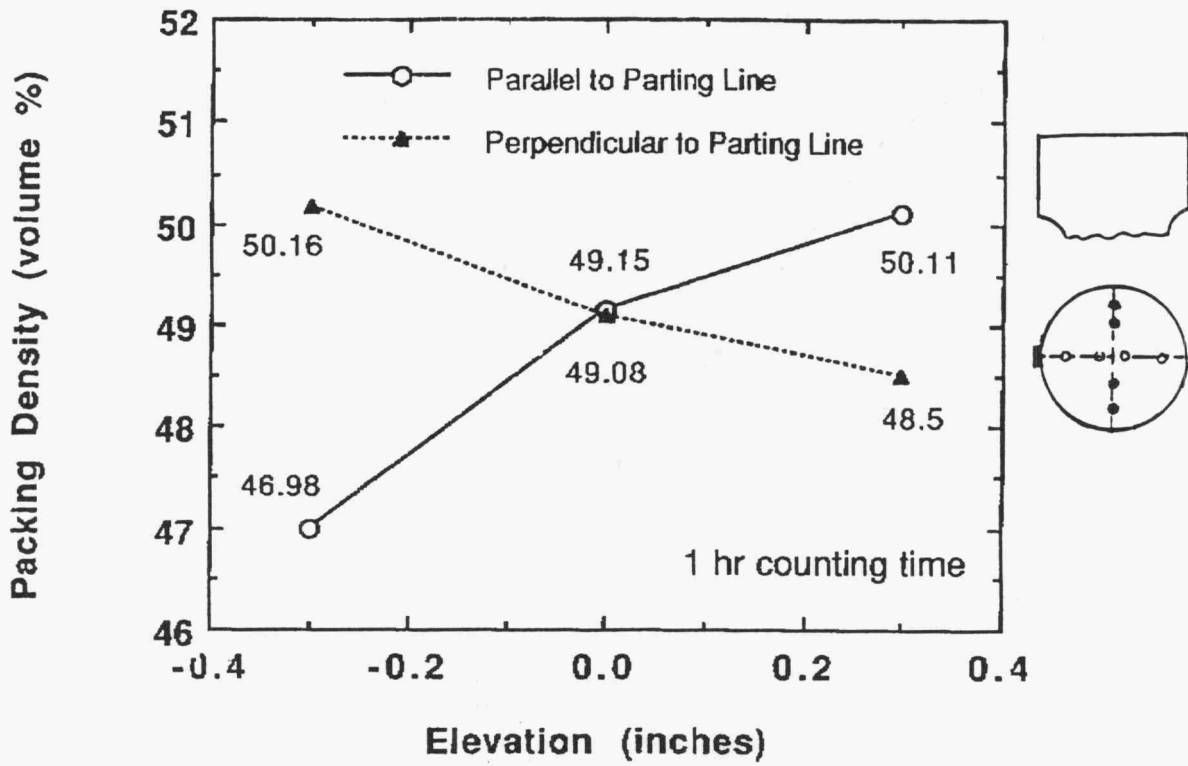


Figure 3 Density gradient in the as-cast tensile bar (buttonhead) measured by gamma-ray densitometer.

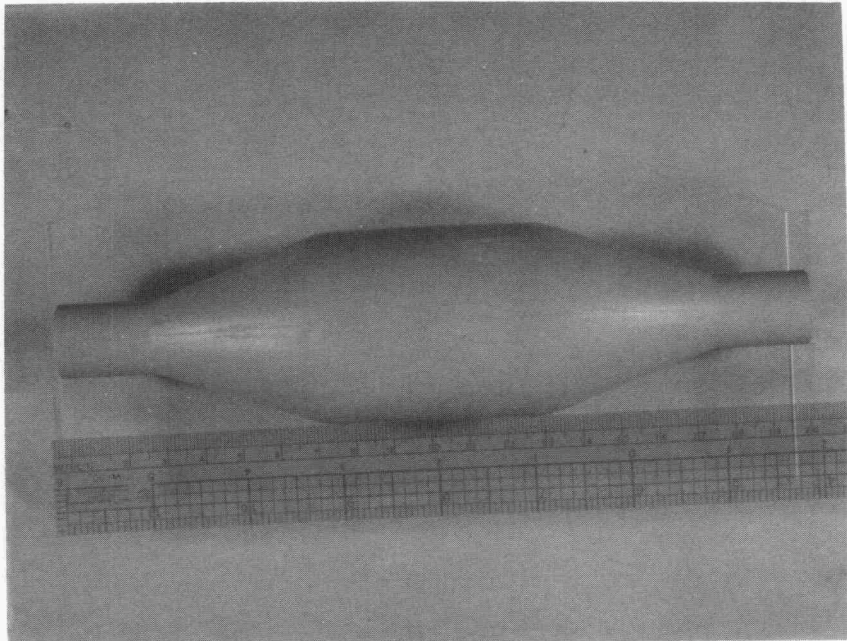


Figure 4 Injection molded "MLP" bar.

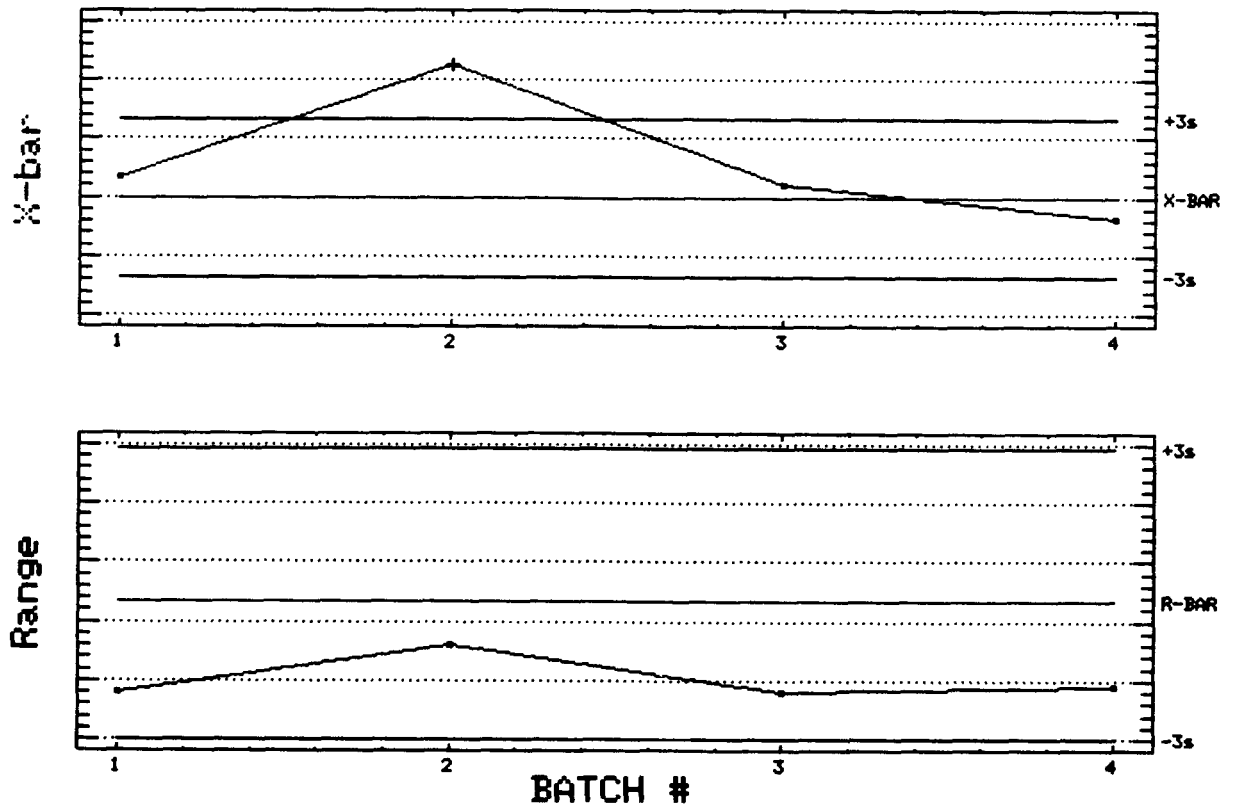


FIGURE 5 Control Chart on % Oxygen W-Series Powder Batches

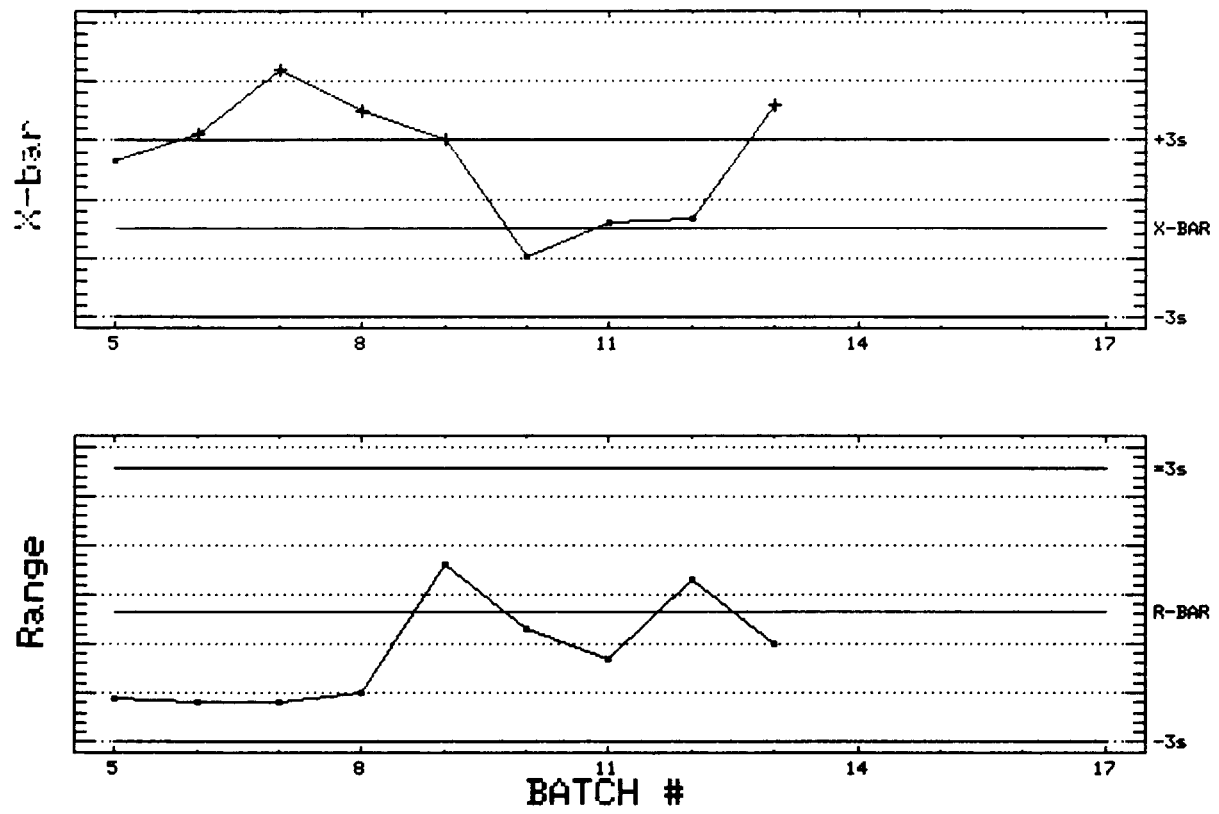


FIGURE 6 Control Chart on % Oxygen W-Series Powder Batches

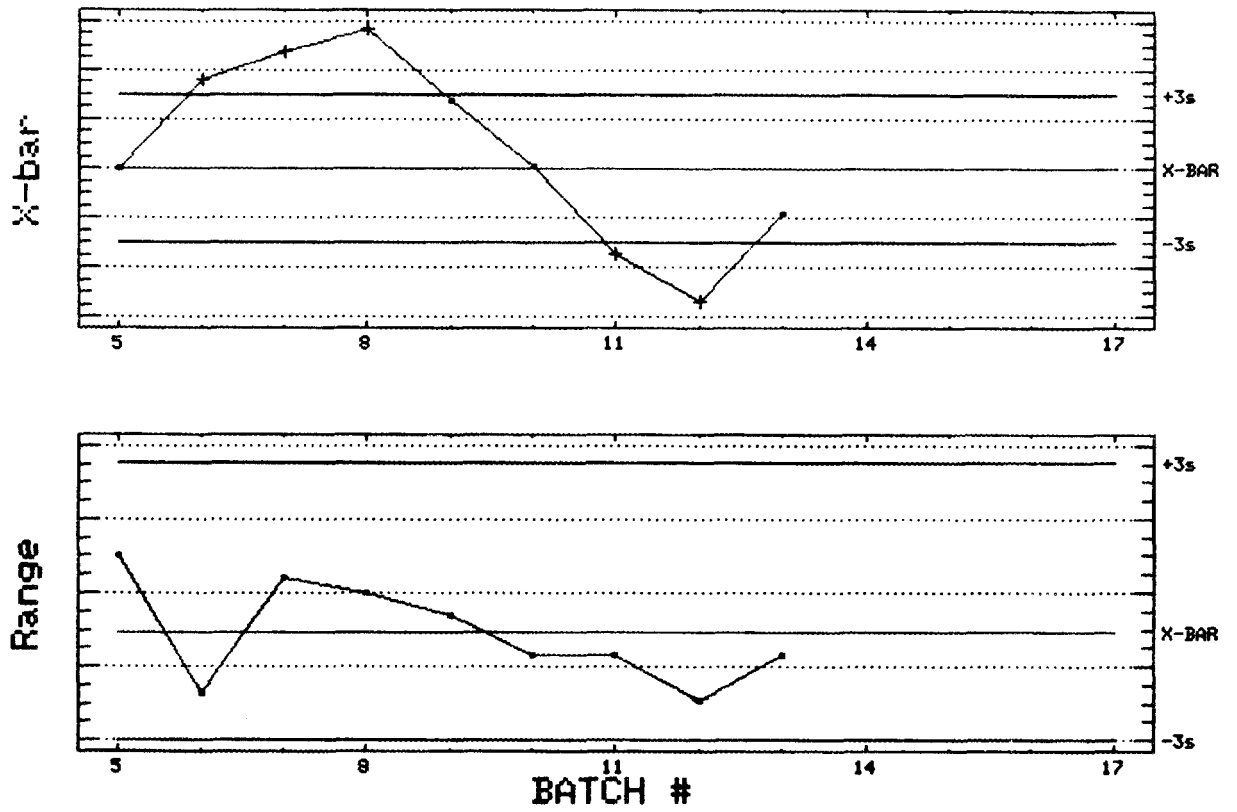


FIGURE 7 Control Chart on % Yttria W-Series Powder Batches

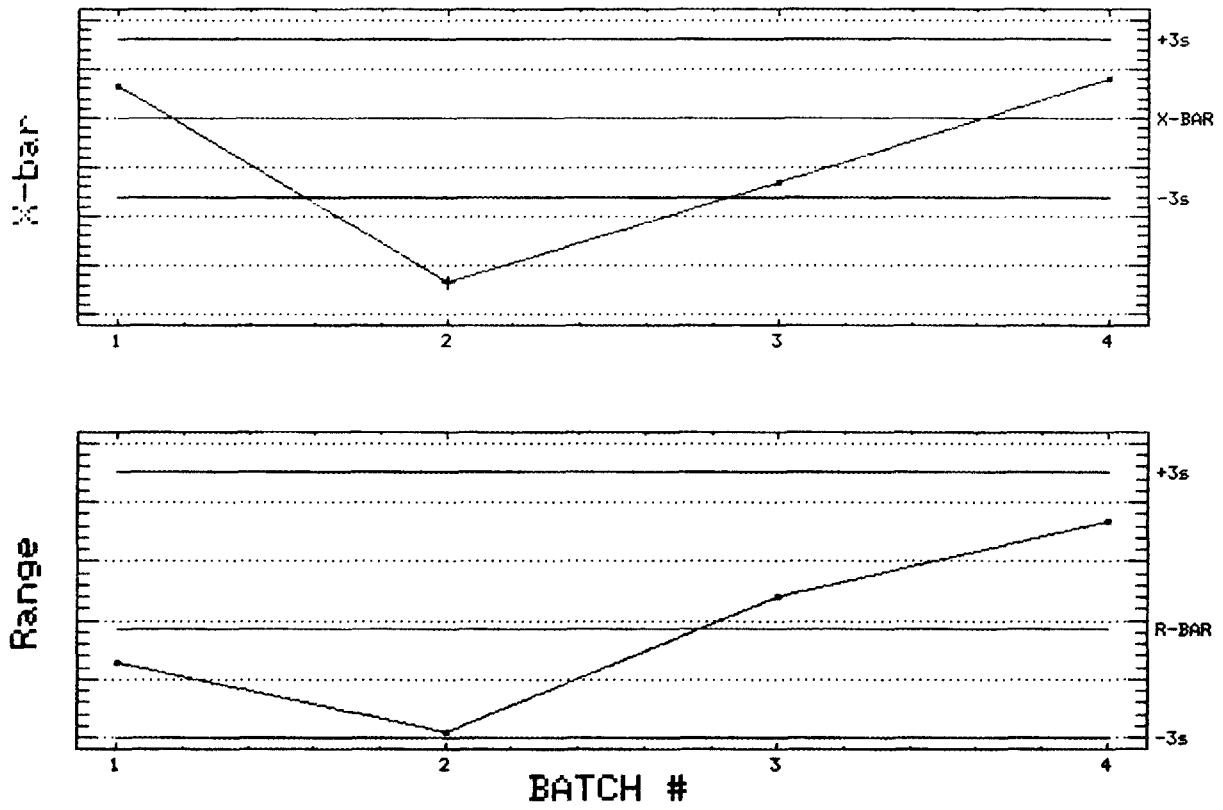


FIGURE 8 Control Chart on % Yttria C-Series Powder Batches

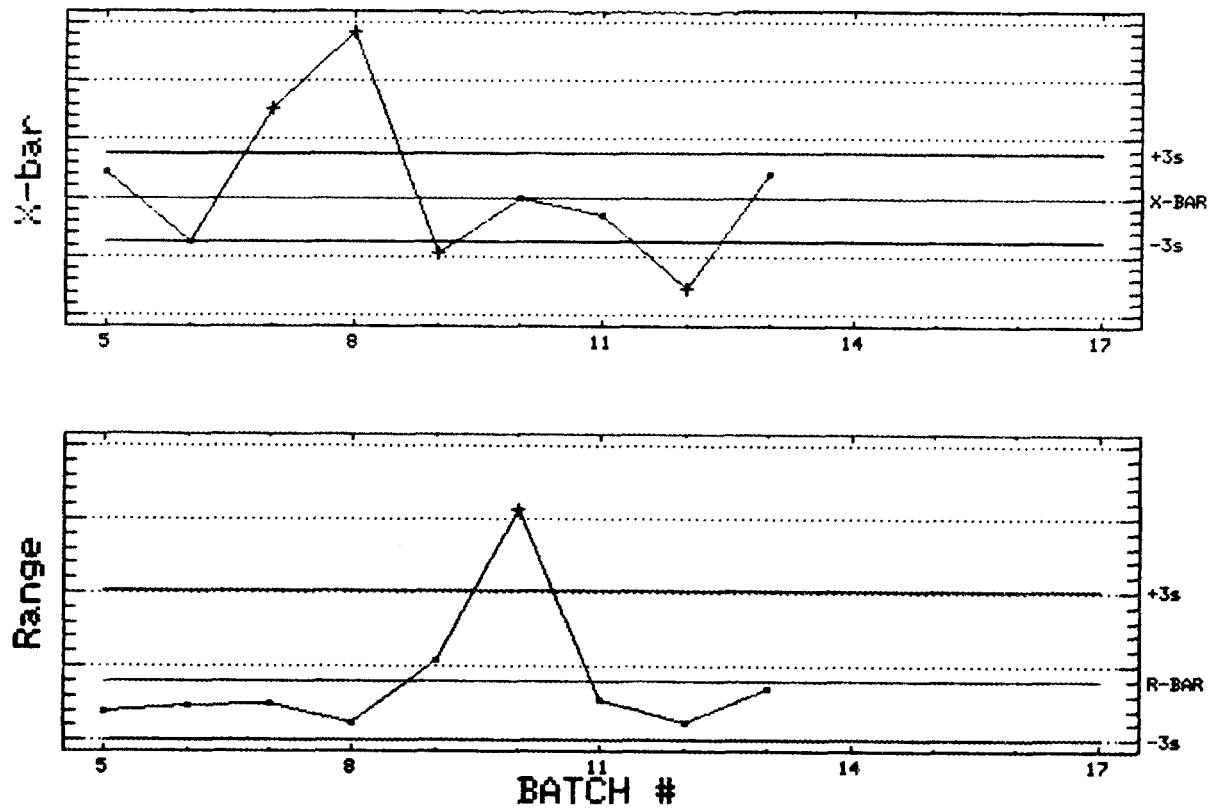


FIGURE 9 Control Chart on Surface Area W-Series Powder Batches

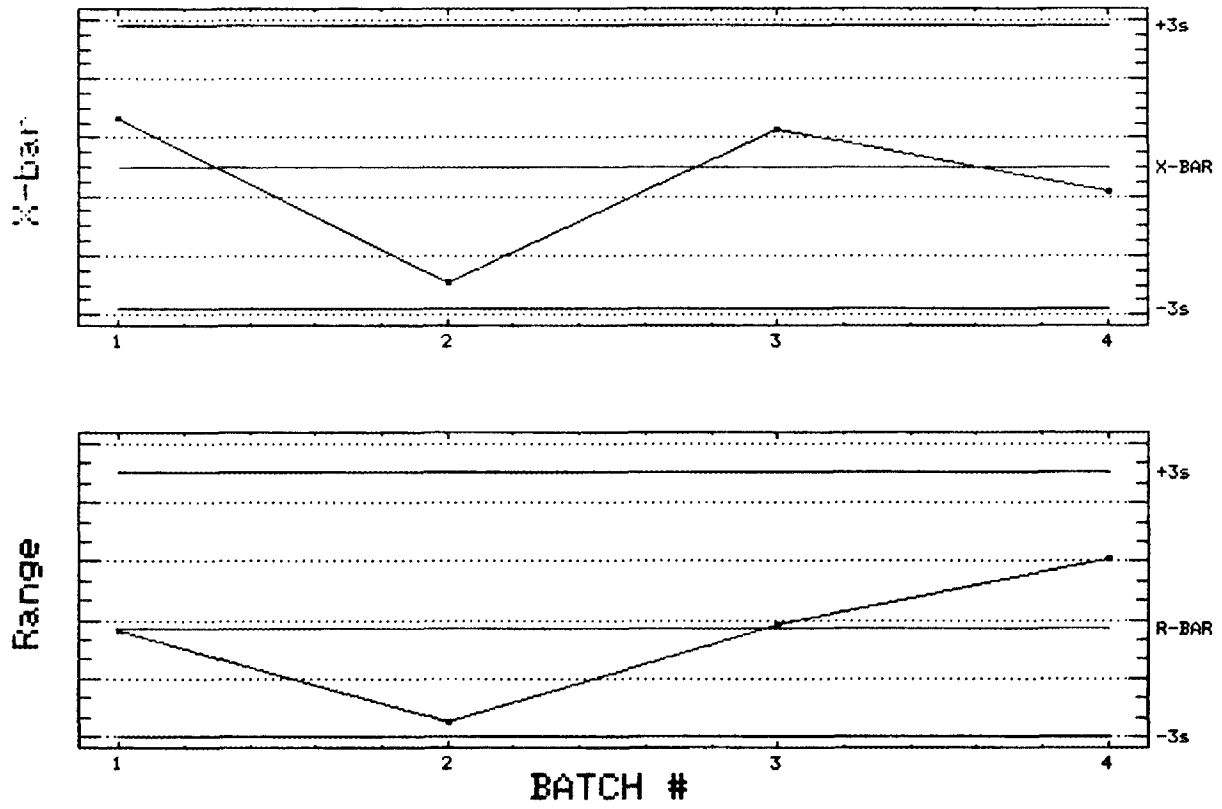
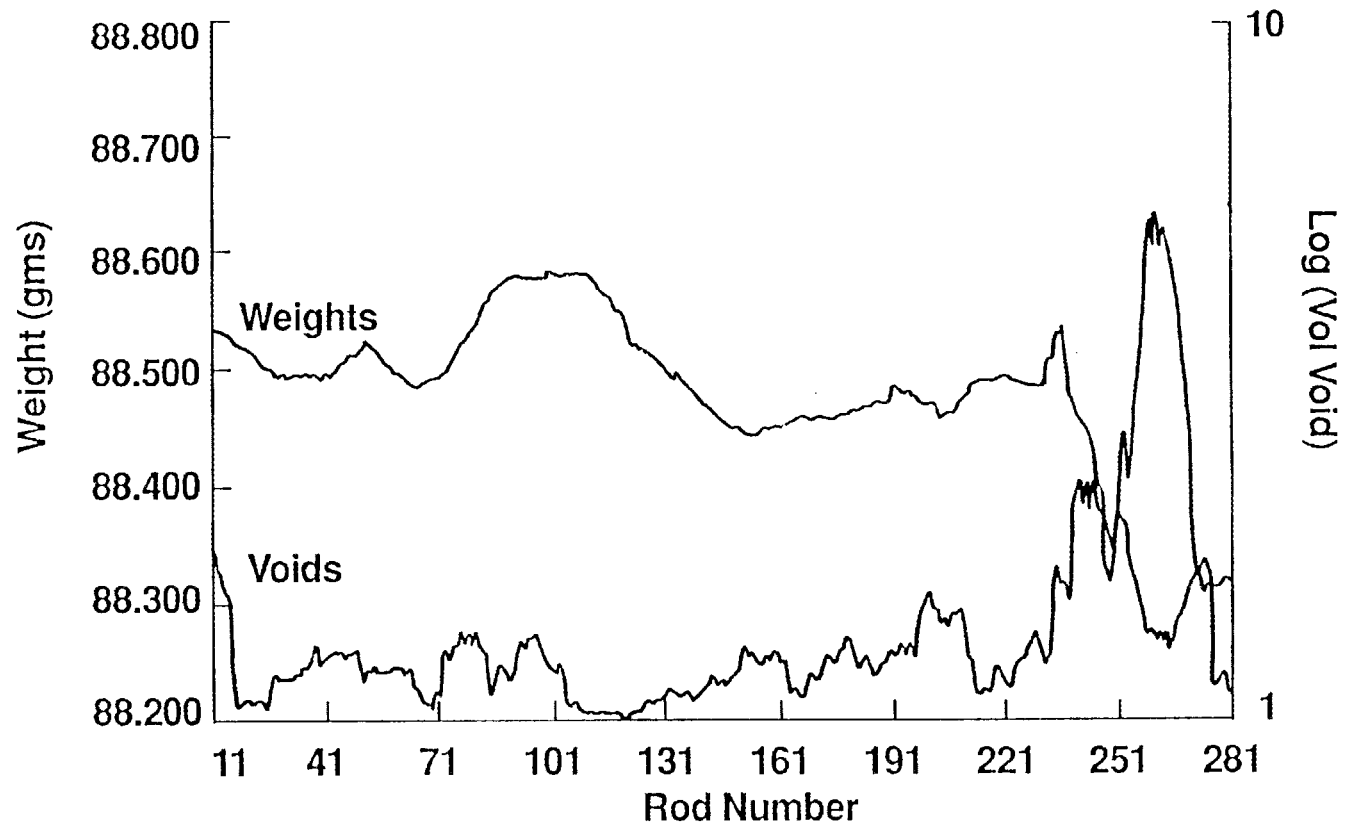


FIGURE 10 Control Chart on Surface Area C-Series Powder Batches

FIGURE 11

PROCESS CONTROL THROUGH PART WEIGHT

Bar Weights vs NDE Voids



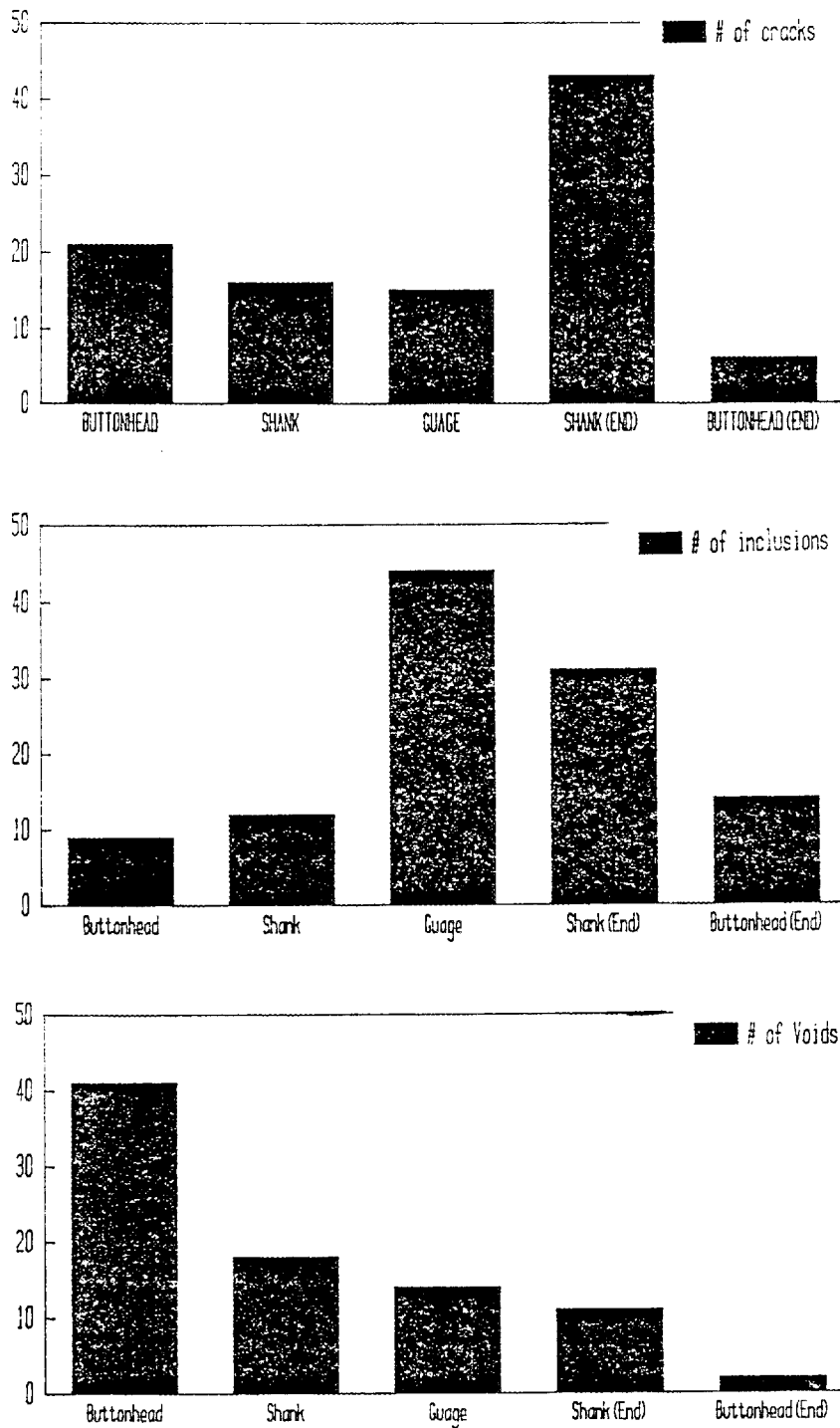
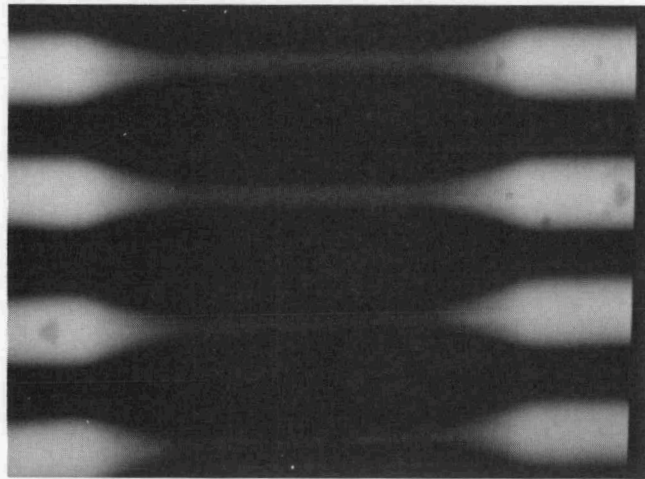
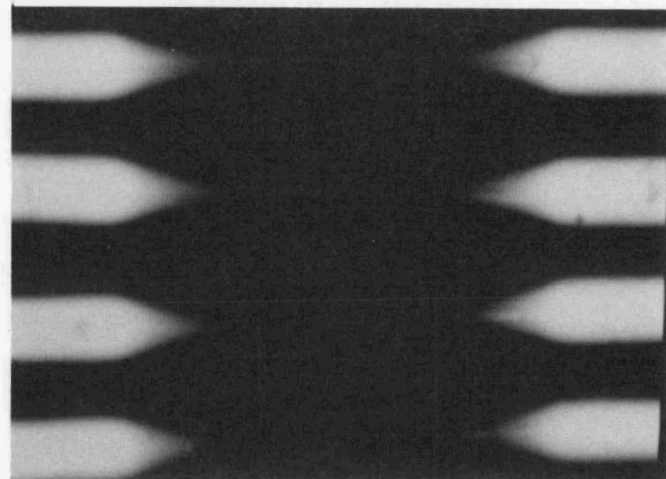


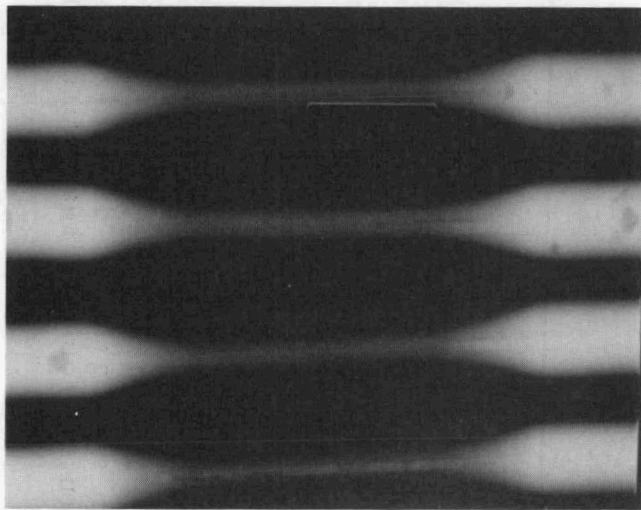
Figure 12. Defect population in Si₃N₄ tensile samples (molded) as measured from microfocuss film radiographs.



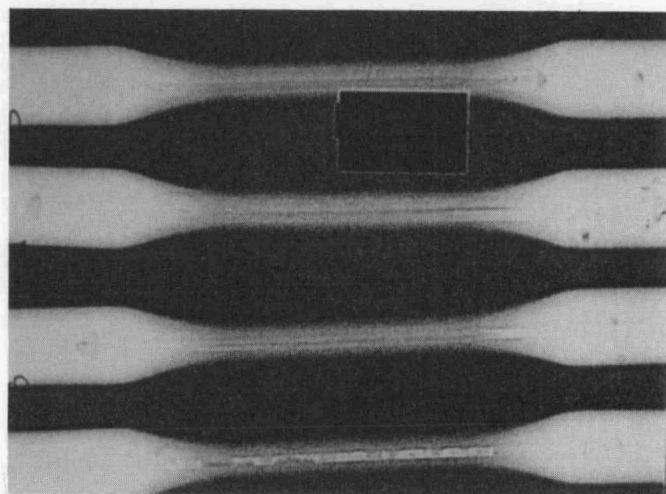
Frame average



Slide / stretch



High pass filter



Transform

The effect of various digital image enhancement routines applied to film radiographs of molded Si_3N_4 tensile samples.

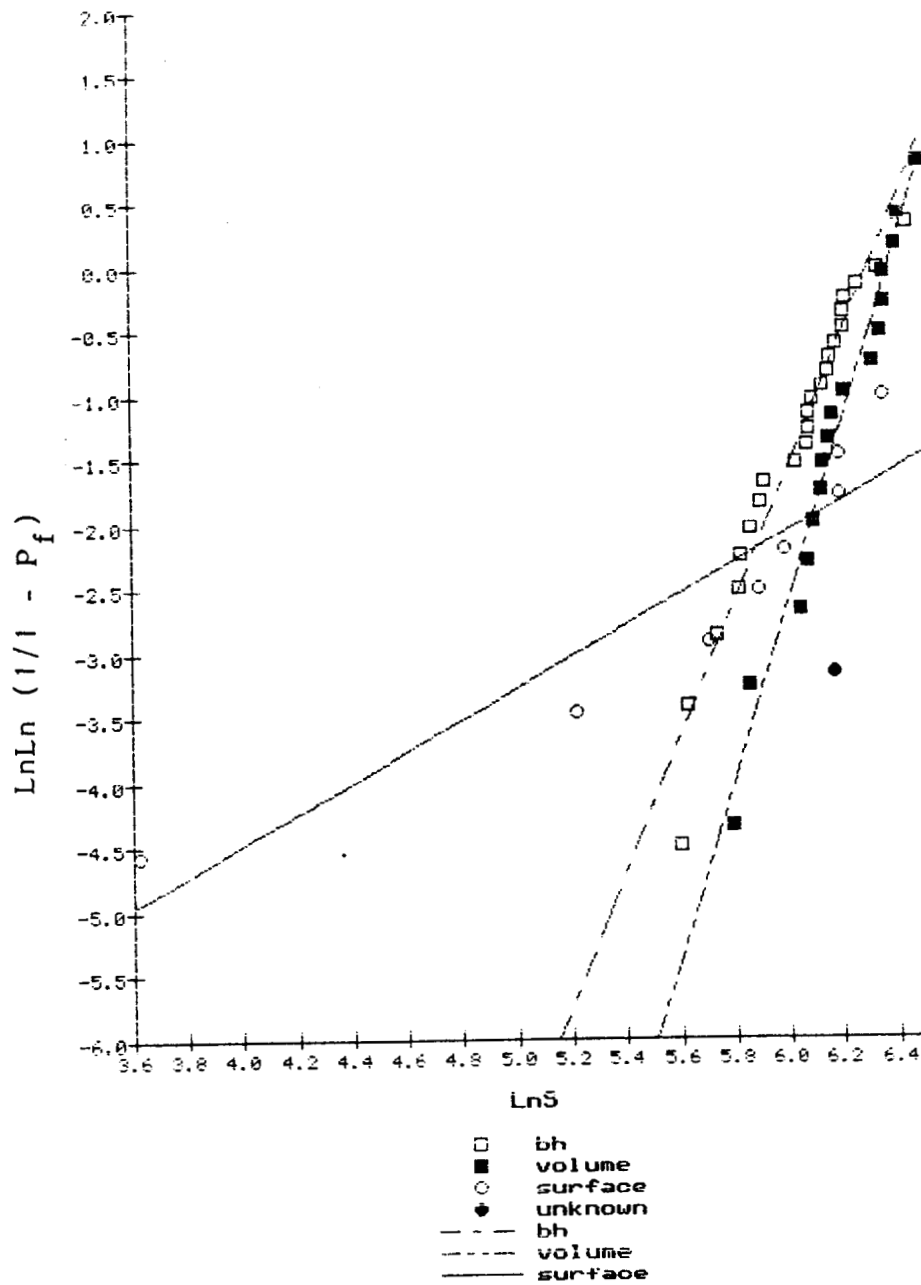
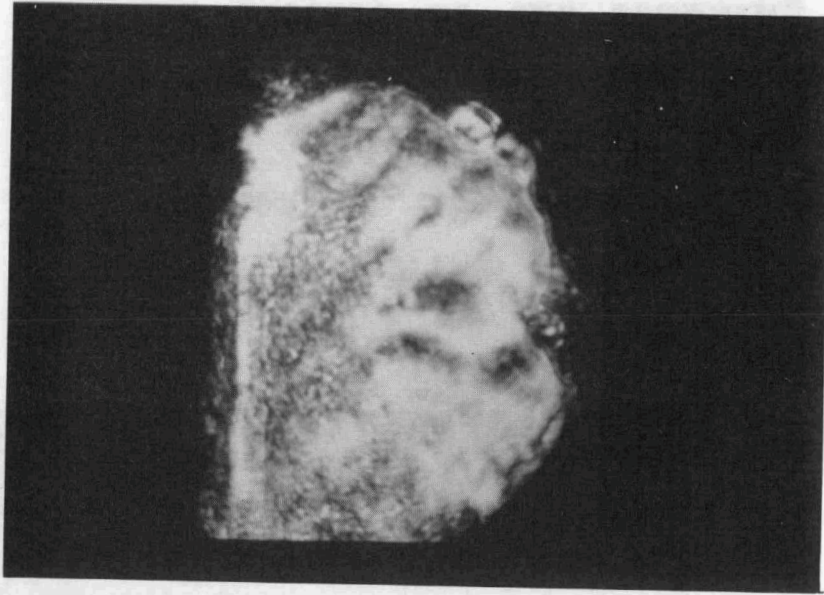
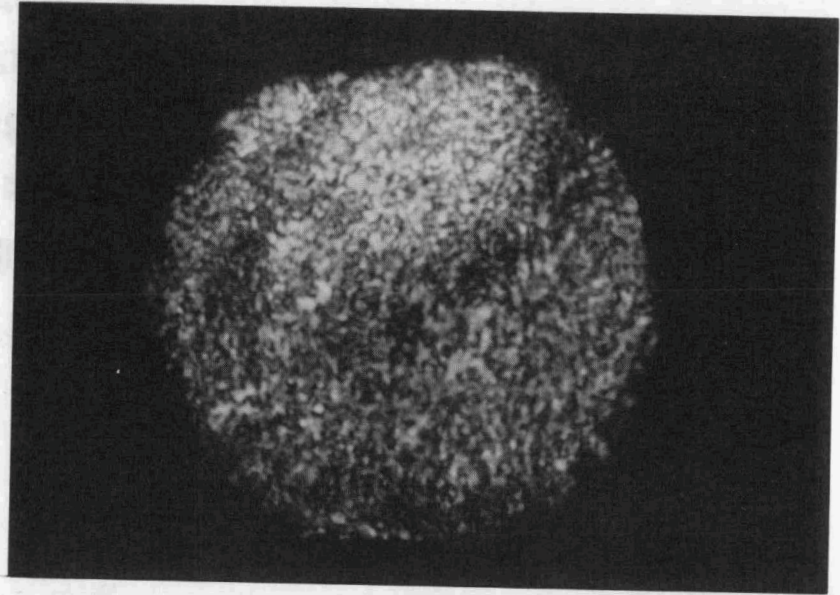


FIGURE 14

Weibull plot of strength, S , data after separation for samples process using injection molding route (Iteration 1).

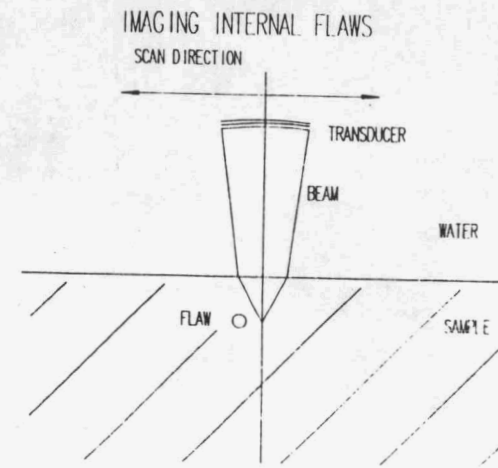


**C-Scan with wax as
couplant**



C-Scan with no wax

**Ultrasonic C-Scans of discs cut from pressure cast
Si3N4 samples taken at 15 MHz / F3 transducer
showing density gradients from surface to center
(voids). Schematics of the setup is shown to the right.**



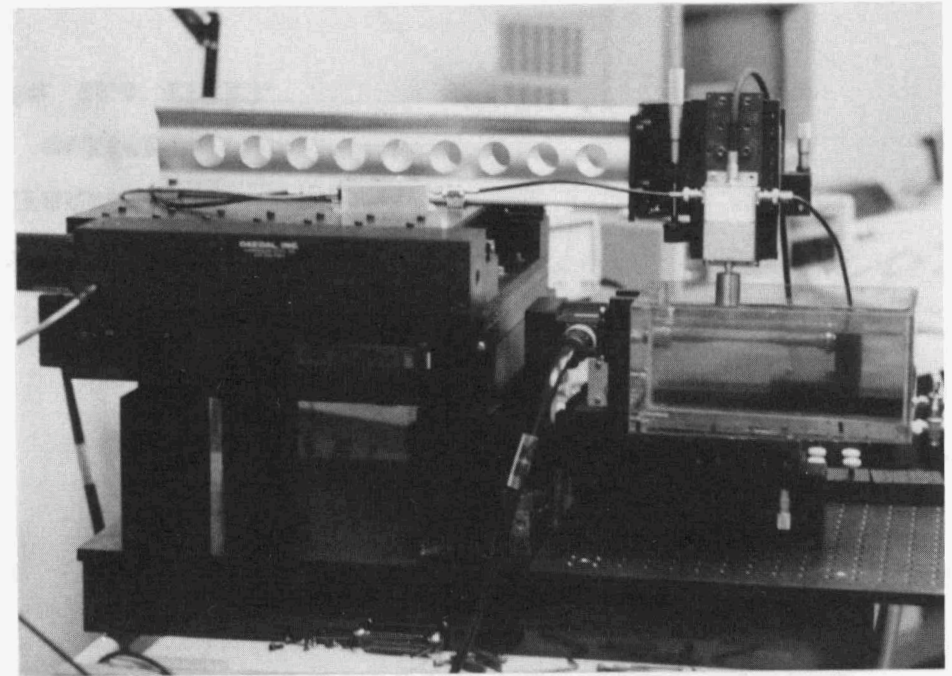
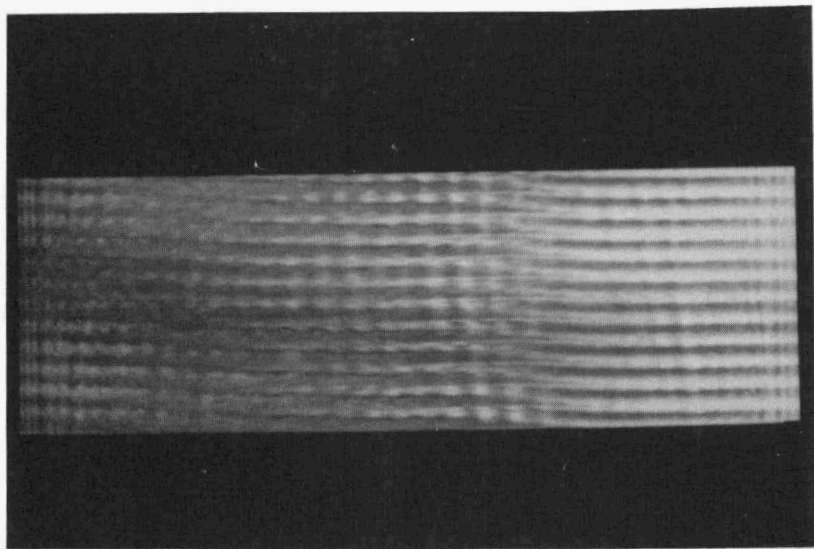
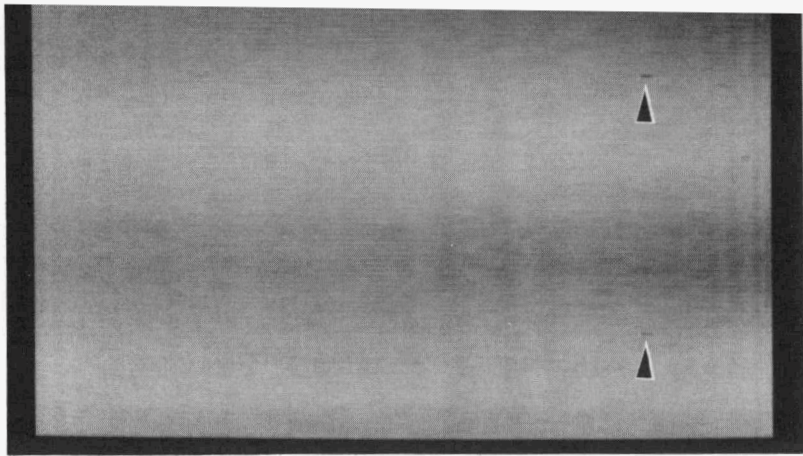
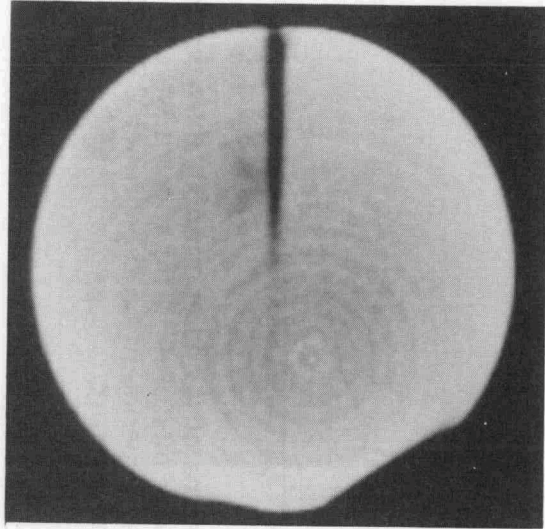


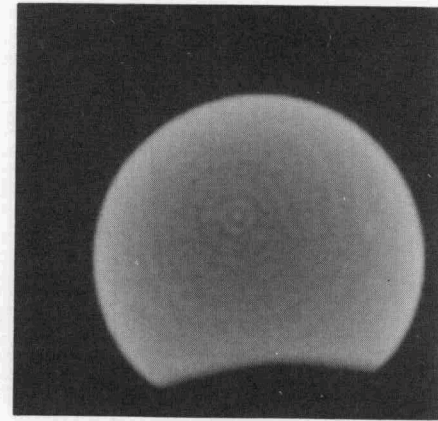
FIGURE 13

Surface Wave Images of machined Si₃N₄ tensile bar, taken at 50 MHz / F0.85, showing both small cracks and grinding marks. Each picture is 650X200 pixels, each pixel resolution is 24 um. To the right is a picture of the scanning hardware.

FIGURE 17



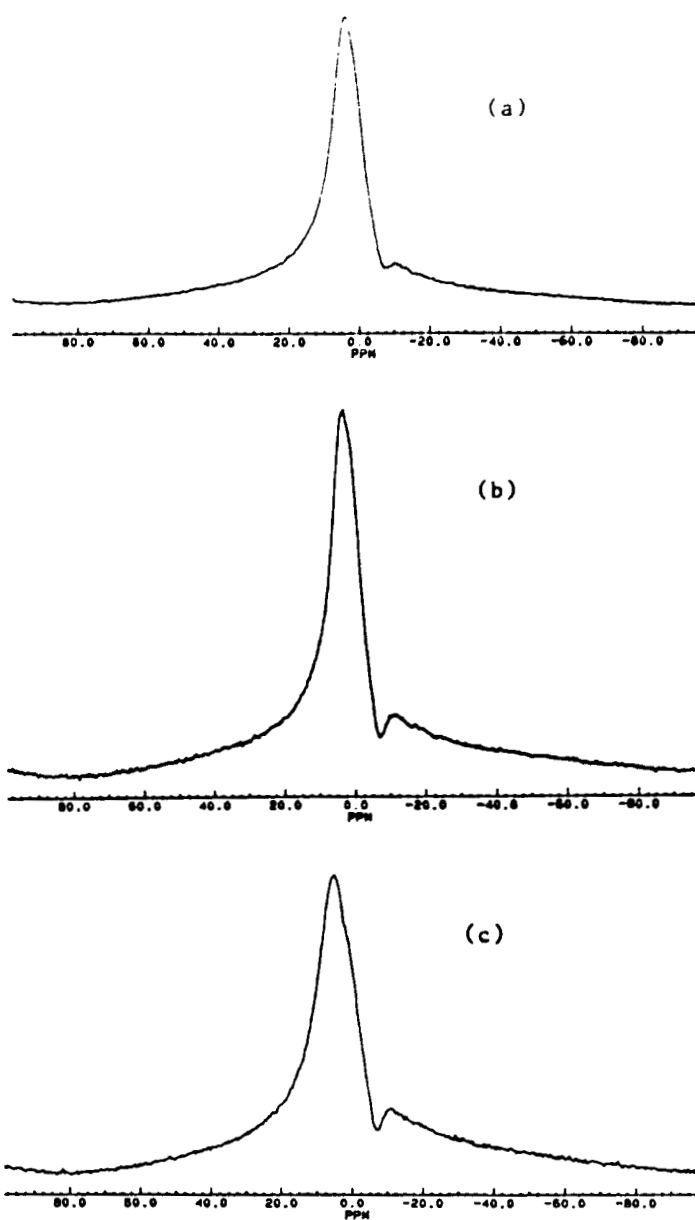
a



b

One millimeter thick X- Ray CT images of both injection molded (b) and pressure cast (a) Si₃N₄ samples. The injection molded tomograph shows the presence of high density inclusions. The pressure cast section reveals the major crack (at the partition line) along with some regions of lower density than the matrix. The sections were taken at different magnifications.

FIGURE 18



Static proton (^1H) NMR spectra of (a) compounded, (b) pelitized, and (c) molded ceramic binder mixtures. The spectra were acquired using a Bloch decay experiment on the Bruker CXP-100 spectrometer at ambient temperature.

95 Percent Confidence INTERVALS
for C-SERIES TILE MEANS (1370)

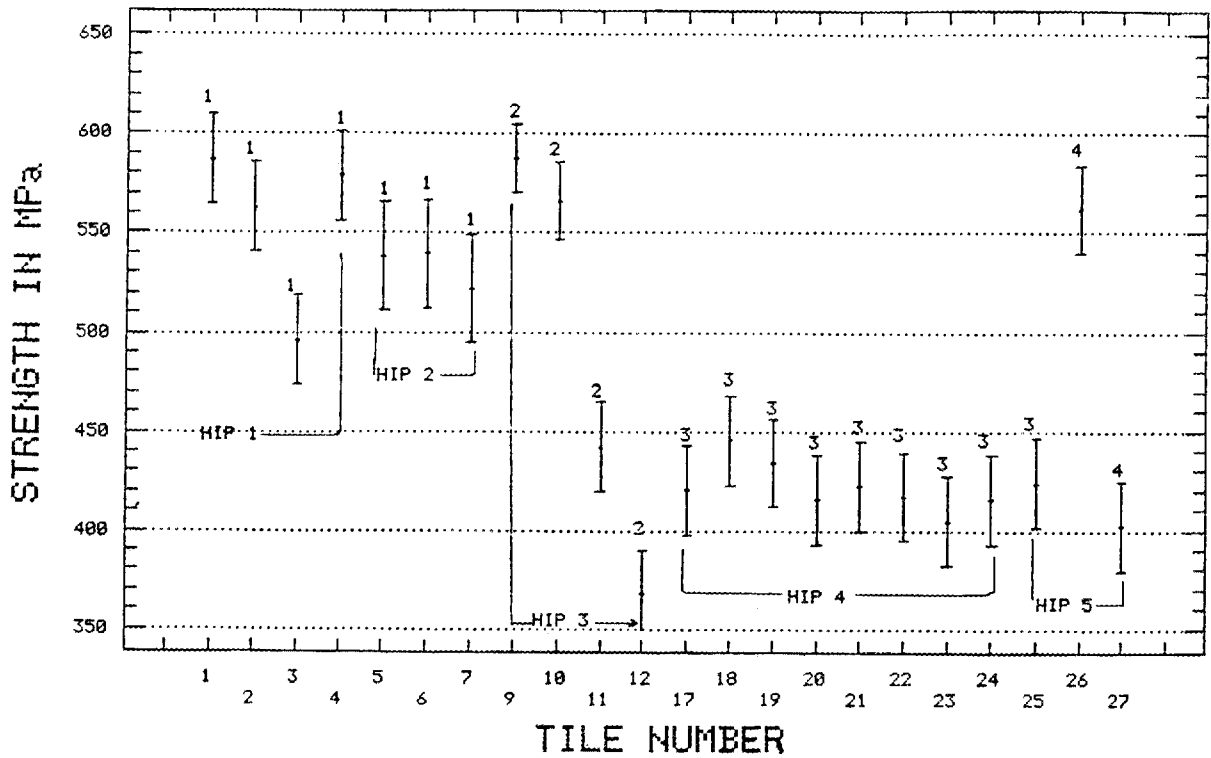


FIGURE 19. Strength versus tile number at 1370°C for C-Series powders HIP'ped from five separate runs.

Improved Processing

R. L. Beatty, R. A. Strehlow, O. O. Omatete (Oak Ridge National Laboratory)

Objective/scope

To determine and develop the reliability of selected advanced ceramic processing methods. This program is to be conducted on a scale that will permit the potential for manufacturing use of candidate processes to be evaluated. The emphasis of this program is on silicon nitride. Issues of practicality; safety, hygiene, and environmental issues; and in-process testing methods are to be addressed in addition to technical feasibility. The methodology includes selection of candidate processes and evaluation of their range of applicability to various kinds of commercially available ceramic powders.

Technical progress

I. Silicon nitride gelcasting and sintering

Installation was completed of a specially designed controlled atmosphere furnace obtained for silicon nitride sintering. The furnace was successfully tested to 2300°C and to 1900°C at the full design nitrogen pressure of 0.2 MPa (2 atm). Graphite crucibles were siliconized in preparation for sintering studies. A second furnace designed for 10 MPa (100 atm) operation was acquired and is being installed. A cooperative research and development agreement was signed with Garrett Ceramic Components Division of Allied Signal Aerospace Co. This work is described below.

II. Drying studies

The purposes of drying studies are to minimize warpage of cast parts and to optimize the drying operation. Gelled parts are not fully consolidated and they shrink during drying as well as during sintering. The extent of shrinkage from cast dimensions during drying decreases as the solids loading of the part increases. Typical values for alumina parts are 3 to 4 lin % at 51 to 55 vol % loadings.

Sialon and alumina specimens are compared in Fig. 1. The castings complete their shrinkage when about half of the moisture has been removed. A green density of about 68 vol % is estimated for the dried bodies at this point which occurs in about a day. Consequently, we believe that accelerated drying can be carried out effectively.

Specimens of silicon nitride were dried at various relative humidities from 75 to 95%. As found earlier for alumina and as shown in Fig. 2, the drying rate decreases linearly with moisture content of the casting for all humidities. The moisture content at the final weight shows the expected residual equilibrium moisture at the specified humidity.

No constant rate drying period was observed for gelcast parts, and the drying behavior appeared to be the same for both silicon nitride and alumina. This gives assurance for the use of alumina data in further studies to refine drying procedures.

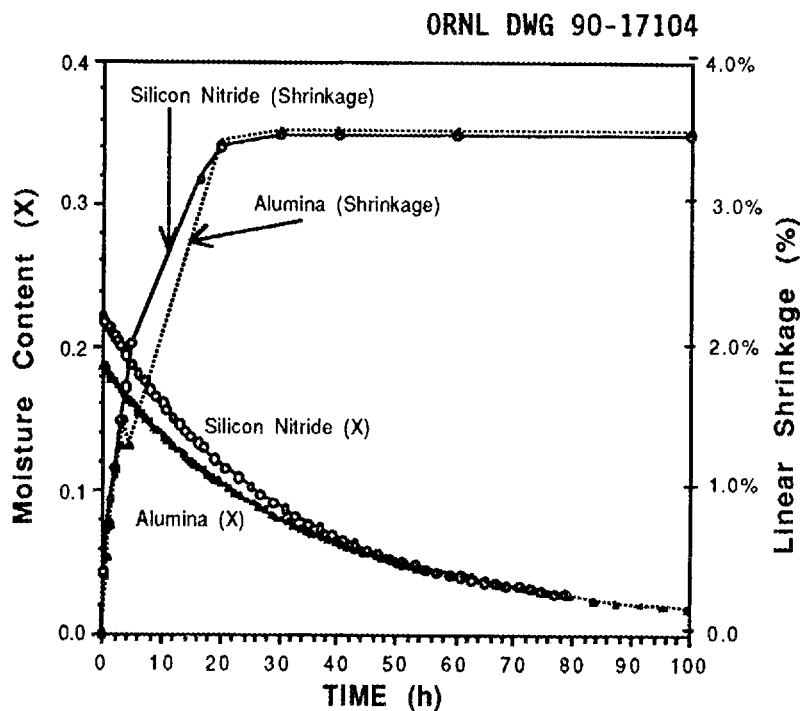


Fig. 1. Shrinkage of sialon and alumina compared.

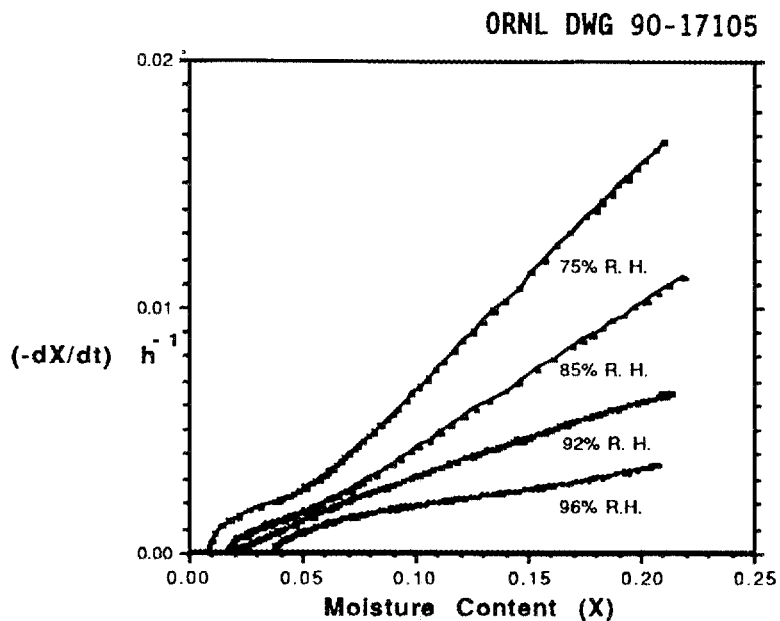
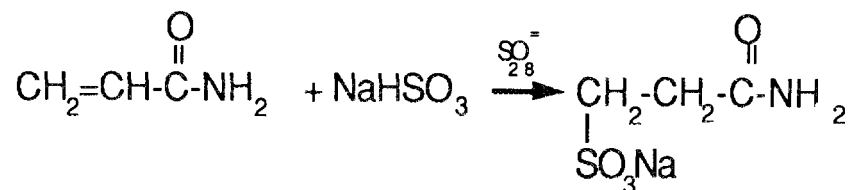


Fig. 2. Drying rate for silicon nitride gelcast plates as a function of moisture content at several relative humidities. Drying begins at the right on this plot, the rate falling linearly.

III. Environmental, Safety, and Health Studies

A series of experiments was conducted to verify the neutralization procedure used for wastes containing monomeric acrylamide. The procedure is based on the addition of sodium bisulfite to the double bond of acrylamide in the presence of peroxide:



The resulting sulfonic acid is not considered hazardous. The rate of the reaction was found to be high, reducing the concentration of test samples from 0.7% to less than 10 ppm in 1 h and to less than 1 ppm (the limit of detection for the method) in 2 h (see Fig. 3). This level is deemed satisfactory for the waste handling procedure being used.

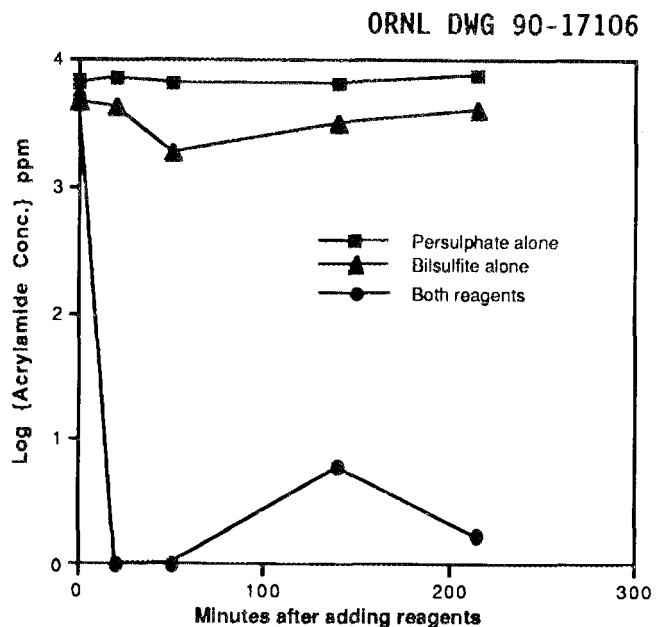


Fig. 3. Neutralization of an aqueous acrylamide solution by ammonium persulfate and by sodium bisulfite separately and mixed.

IV. Cooperative research agreement

A CRADA (Cooperative Research And Development Agreement) was developed with Garrett Ceramic Components Division of Allied-Signal Aerospace Co. It calls for ORNL to gelcast several silicon nitride T-25 turbine rotors along with plates to produce tensile specimens. A proprietary formulation, GN-10, from Garrett is to be used along with molds supplied by that firm. Plates to the ORNL specification will be cast in order to produce tensile specimens.

A subsequent step of the program calls for Garrett to sinter-HIP the castings and send them to ORNL for testing. The objective of the program is to determine whether gelcasting offers significant advantage over other fabrication methods that have been used by Garrett in terms of the resultant materials properties, part quality, and shape forming ability.

Thirteen molds have been received from Garrett along with sufficient materials for the basic GN-10 formulation for these molds. The GN-10 silicon nitride formulation was successfully gelcast. Two T-25 mold rotors were cast along with three plates for tensile test specimens. Surface imperfections were observed that were attributed to inadequate oxygen removal from the mold prior to casting. A valve assembly has been designed and built to permit evacuation and nitrogen flushing of molds in order to remove oxygen.

Improved Processing

A. E. Pasto and S. Natansohn (GTE Laboratories Incorporated)

Objective/Scope

The overall project objective is to develop and demonstrate a process for reproducibly fabricating (by injection molding and HIPing) a series of tensile specimens of PY6 silicon nitride with the following properties:

Average tensile strength of 900 MPa at 25°C

Average tensile strength of 500 MPa at 1370°C

Weibull modulus of 20 in both instances.

This will be accomplished by determining the source(s) of failure-causing defects, and modifying and controlling the manufacturing process to minimize their occurrence. All potential sources of defects will be evaluated, from raw materials through individual powder processing and densification steps and finally through machining and surface finishing of the test specimen.

Technical Highlights

An overall review of the program status is presented. At this point, all of the processing and testing components have been put in place, debugged, and are operating or operable. The silicon nitride and yttria powders have been received, characterized, and blended/milled. Experiments designed to enhance their performance are underway. The new compounder is in-house and undergoing performance testing. Baseline material has been compounded with the currently used equipment, and molded into both ASCERA- and dogbone-shaped rods. A subcontract to design and build a new combination compounder/molder is making excellent progress; construction is underway. The baseline test specimens have been dewaxed and HIPed. Specimen machining parameters which result in minimal surface damage have been determined; a machining contractor has been selected. Baseline HIPed tensile rods have been machined into tensile test specimens, and testing initiated at GTE. Reproducible tensile testing procedures have been developed and validated. Early results show a lower than expected tensile strength, with failure in all cases arising at metallic inclusion defects. It is thought that this high level of metallic defects is due to a recent acceleration of wear in the compounder and/or injection molder, and efforts to minimize the presence of these inclusions have begun. X-ray microfocus examination techniques for defect detection have been quantified, and the subcontract for design, development, and procurement of an ultrasonic examination system is in place and progressing well. A laser surface profilometer has been installed and is operational.

Microfocus x-ray CAT-scanning evaluation of silicon nitride shapes has begun. Program personnel have been trained in the theory and application of Taguchi techniques, and experiments utilizing these methods, related to the improvement of each individual process step, are underway. In short, all of the tasks required to improve the injection-molding process for high quality silicon nitride components are active and on schedule.

Task 1 - Material Selection and Characterization

SOLUBLE SURFACE SPECIES

A brief evaluation was performed of the three additional 180 kg silicon nitride powder lots which were purchased for the program. Specifically, the HF-soluble silicon and ammonia were determined (See previous semiannual report, for Oct. 1989 through March 1990, for procedures). Test specimens were also fabricated to assess the mechanical properties. Results of these tests are compared in Table 1 with the data obtained previously on 20 kg samples of the same lots.

The data show a slight increase in the solubilized silicon but the amount may not be statistically significant. The increase in the dissolved ammonia is more appreciable and results in a Si:N molar ratio which is lower than that measured on the original 20 kg sample of each of the three lots. This implies an increase in the concentration of nitrogenous species on the powder surfaces and it is conceivable that, as the powder was stored for several months tightly sealed under nitrogen, either chemisorption or physical adsorption of the gas occurred.

There is excellent reproducibility in the properties of the hot-pressed PY6 ceramics made from the three different powder lots (3, 4, 5) as well as in those made from a small sample (20 kg) and the remaining 180 kg of each material. Thus, these powders constitute a suitable baseline material for the purposes of this program.

AGEING BEHAVIOR

An ageing study was initiated at the inception of the program to determine the shelf life of silicon nitride powder by monitoring the chemical changes occurring on its surface. Samples of the baseline powder were stored in desiccators in air and argon under "wet" and "dry" conditions. The powder is stored in open trays over water for the "wet" exposure and over anhydrous calcium sulfate for the "dry" one. Results obtained upon subjecting these powders to the standard HF treatment to obtain the soluble silicon and ammonia after 139 and 257 days of such storage are given in Table 2.

The 257-day exposure data show little change in the amount of dissolved Si under the four

storage conditions but the amount of dissolved ammonia has increased by about a factor of two between the measurements. Thus, the molar ratio of Si:N decreased in all cases implying that the surface of the powders contains more soluble nitrogen now than during the intermediate test. The more oxygenated surface, as indicated by a higher Si:N ratio, prevails under wet exposure conditions and more so in wet air than in wet argon, both plausible and anticipated observations. An interesting phenomenon is that the surface solubility of these powder samples, as determined by this experiment, is now quite comparable to that of the initial material, more so than at the earlier stage. This implies that silicon nitride powder is a stable material with a good shelf-life which does not deteriorate gradually. The occasional whiff of ammonia experienced upon opening containers holding powders made by ammonia-related synthesis routes is probably caused by reaction residues rather than by decomposition products.

YTTRIA SOLUBILITY

Characterization of the silicon nitride materials was extended to the determination of the dilute acid solubility of the yttria sintering aid present to the extent of 6 w/o in the PY6 formulation. Yttria solubility was measured in 0.03M HCl, a sufficiently dilute acid concentration to permit easy and accurate determination, both as a function of time at isothermal conditions ($\pm 0.25^\circ\text{C}$) and as a function of temperature. The results obtained in the evaluation of time-dependent solubility of (a) pure yttria, (b) a simple mixture of 6 w/o yttria and 94 w/o silicon nitride and (c) a milled PY6 formulation, are given in Table 3. It is apparent that the dissolution of pure yttria at constant temperature proceeds more rapidly than that of yttria present in PY6 or even in a simple mixture. The data for samples (a) and (b) are plotted in Fig.1. This is a surprising and unexpected finding, particularly in view of the fact that the yttria used in all experiments was the same baseline material. There appears to be no obvious plausible reason why yttria treated by dilute acid in the presence of silicon nitride should dissolve at a measurably slower rate than yttria alone under identical circumstances. The explanation of this puzzling phenomenon is being sought in continued experiments. The greater solubility of yttria in the PY6 material in the later stages of the experiment in comparison with the mixed sample may be a consequence of its increased surface area as a result of milling. This is based on the assumption that the dissolution occurs at the surface of the particles at a rate proportional to the instantaneous surface area¹.

The dissolution kinetics of yttrium oxide follow a cubic rate law which features an initial rapid dissolution rate followed by a gradually decreasing rate as the surface area of the particles decreases. The rate-determining step involves reaction at the particle surface (loc. cit.). This type of behavior is frequently described on the basis of the "shrinking core" model. Its applicability in this case is demonstrated in Fig. 2 in which the experimental

data are compared with the calculated ones; the fit is excellent. The predicted percentage of dissolved yttria was calculated from the actual particle size distribution data obtained for this baseline powder; it did not assume an average value for the initial particle diameter as used by Segal and Sellers. This model is also applicable to the PY6 formulation as shown in Fig. 3 (C_t is the concentration of yttrium in the acid solution at time t while C_∞ is its concentration after all the oxide has been dissolved) but the kinetics of the reaction are slower as discussed above.

The temperature dependence of yttria dissolution from a PY6 powder is given in Fig.4. The samples were held at each temperature for 15 minutes prior to filtration and subsequent Y determination in the filtrate. The data display an unusual trend in that they follow an S-shaped curve. The steepest part of this curve is in the interval of 20-27°C, typical room temperature range, and it is therefore imperative in establishing the time dependence of dissolution data to use isothermal conditions. In order to avoid inaccuracies caused by fluctuating temperatures, the current practice for making single point screening comparisons is to treat the samples for 15 minutes at 35°C, a temperature at which the solubility curve is fairly flat.

HOT PRESSED PY6

The oxidation resistance of hot-pressed PY6 ceramics made from the six different lots of silicon nitride powder which were being evaluated was determined. Sections of polished MOR bars were squared-off so that their surface area could be measured accurately and were heated in static air at 1200°C and 1370°C. The sample weight was monitored at regular time intervals (50 -100 hours) throughout the exposure time of 500 hours. The samples were placed on thin platinum wires to allow air access to the total surface area of the specimens. The results of these oxidation tests are given in Table 4.

The data show no difference in the oxidation resistance for the six materials at either of the two test temperatures. They are comparable to those obtained on the best silicon nitride ceramics designed for high temperature applications and consistent with previous evaluations of the same material grade. The oxidation resistance of this material is appropriate for the temperature range of the program.

POWDER MODIFICATION:

This phase of the program has as its objective the assessment of the effect of modification of the powder surface on the properties of the resulting PY6 ceramics. The baseline silicon nitride powder lot was used in all the experiments described below and all modified materials are compared against this unmodified powder processed in the identical manner.

The sample designations and their treatments are as follows:

Powder O: Baseline unmodified powder.

Powder A: Powder heated to effect thermal oxidation.

Powder B: Powder digested in HNO_3 to effect chemical oxidation.

Powder C: Powder digested in H_2O_2 for identical reasons.

Powder D: Powder slurried in water and stirred continuously for 10 days at room temperature. The pH of this slurry increased from an initial value of 5.8 to an endpoint of 7.8.

Powder E: Powder slurried in HF solution. The purpose of this experiment is to assess the effect of removing an oxygenated layer from the surface of the silicon nitride.

The wet-treated powders were filtered, washed, dried and then evaluated together with the baseline and heat-treated powders by procedures described in the previous report. A summary of the evaluation of these powders is presented in the upper portion of Table 5. The surface area of the heat-treated powder decreased somewhat, which was expected because particle coalescence and necking could occur. The decrease in the surface area of the HF-treated powder could be caused by the dissolution of very fine silicon nitride particles. The increase in the surface area of the C and D powders is difficult to explain; it may be due to either chemical dissolution of fused/hard agglomerates or to increased contouring of the particle surface by etching, neither a very plausible event. The total oxygen content almost doubled in the A powder, but decreased somewhat in the chemically treated powders indicating that the intended chemical oxidation is ineffective, and decreased substantially in powder E because the oxygenated layer was dissolved by the hydrofluoric acid. These trends appear even clearer in the results of the Si solubility determination which are indicative of surface oxygen concentration.

The soluble nitrogen content and the resultant Si:N ratio also attest to the changes on the powder surfaces. The thermally oxidized powder has only a fraction of the soluble nitrogen on its surface as compared to the control sample and therefore the Si:N ratio is very high. Apparently, the silicon oxynitride surface layer was oxidized to silica as indicated by the large amount of dissolved Si. The two chemically treated powders have a higher Si:N ratio than the control due to the lower soluble nitrogen content. It appears as if this treatment reduced the nitrogenated surface layer. Sample D is most comparable to the control and this is to be expected because it did receive the mildest treatment. The amounts of dissolved Si and N as well as the Si:N ratio are lowest in Powder E; this implies that the hydrofluoric acid treatment resulted in the most inert surface.

The iso-electric point values are consistent with the surface analytical results. Generally, the data conform to expectations in that the IEP of the thermally oxidized powder has a low value, similar to that of silica, and reflects the analytical data which indicate that the powder surface consists primarily of silica. The HF-treated powder has a high value indicating very low surface oxygen content while the IEP values of the other samples are in between these two extremes.

Samples of these six powders were processed into the PY6 formulation for ultimate fabrication of ceramic test pieces. The processed powders were also characterized and the results are summarized in the middle portion of Table 5. There is an observed increase in the amounts of both soluble silicon and nitrogen in all samples, probably as a result of the milling process in which powder crystallites were fractured or abraded and fresh untreated surfaces were exposed. The Si:N ratio decreased in all but samples A and E. Utilizing the measured surface areas, one can calculate that the amounts of Si and N dissolved per unit area are very similar to those measured on the unmilled control sample (powder O) lending support to the suggestion that the primary solubility effect is that due to fresh surfaces.

The isoelectric point of all the samples is virtually the same, probably reflecting the presence of the yttria sintering aid on the particle surfaces. The yttria solubility is the same for the control powder and the chemically oxidized powders (B, C and D). However, the solubility of yttria in the PY6 materials made with the thermally-oxidized and HF-treated powders is distinctly greater. These two powders have undergone the most drastic treatment but in opposite directions, one to increase the surface oxygen (powder A) and one to decrease it (powder E), and yet there is an increase in yttria solubility in both these materials. The reasons for the inexplicable manifestations of yttria solubility in these systems are under investigation.

The effect of modification of the silicon nitride powder surfaces on the properties of the resulting ceramics was assessed by evaluating the flexural strength and oxidation resistance of hot-pressed PY6 materials. The results are summarized in the lower portion of Table 5. The data demonstrate an improvement in flexural strength both at room and elevated temperature in the sample made from powder A. The RT strength of ceramics made from powders B through D is virtually equivalent to that of the reference material; the strength at 1370°C is somewhat higher. The strength of the HF-treated sample is poorer.

X-ray diffraction data for these dense materials show virtually complete conversion of the silicon nitride to β -phase, with no other crystalline phases present. Reasons for the observed strengthening require further investigation.

The oxidation resistance of these ceramic samples was evaluated by monitoring their weight gain after prolonged heating in air at 1200°C and 1370°C. The results show that the increase in weight of the thermally oxidized sample is about half that of the control specimen at both of the test temperatures and it is smaller than that of any of the other materials. The oxidation resistance of the HF-treated sample is by far the poorest of the sample set but this may be partially caused by residual fluorine traces. The other samples display equivalent behavior to that of the control material at 1200°C and are somewhat more oxidation-resistant at 1370°C.

In view of these encouraging results a Taguchi L18 matrix study has been designed and is being implemented to define the optimum conditions for the modification of the powder surface. Two different powder lots are being used as a noise factor and the modified powders are being hot-pressed and hot isostatically pressed. The sample attributes to be evaluated will be density, flexural strength and oxidation resistance. Full characterization of the powders will be undertaken to confirm any observed correlation trends.

This study was extended to include three new, recently arrived powder lots. The properties of the PY6 ceramics hot-pressed from these as well as from untreated powders are summarized in Table 6. These results demonstrate clearly the benefits of the treatment of the powders which, in all four powder lots tested, results in an improvement of the flexural strength of the ceramics, particularly at 1370°C where the strength increase exceeds 30% in all cases. Electron as well as x-ray diffraction studies and electron microscopy examinations are now underway to characterize the nature of the intergranular phase in these materials.

CHEMICAL INCORPORATION OF SINTERING ADDITIVES:

A study of the effects of chemical incorporation of the yttrium oxide sintering aid has been initiated. Two approaches were used in the exploratory experiments, one based on yttrium nitrate and the other on yttrium hydroxide additions. In both cases the starting reagent was a solution of the program's baseline yttrium oxide powder in nitric acid which was added to the silicon nitride powder in the amount necessary to effect a PY6 formulation, i.e., 6 w/o yttria. In the hydroxide route, ammonium hydroxide was added dropwise to the stirred slurry to precipitate the yttrium hydroxide. The slurry was filtered, washed, dried, and then heated at 600°C for 6 hours to convert the hydroxide to the oxide. Conversion was complete under these conditions as indicated by TGA data. In the case of nitrate addition, the silicon nitride/yttrium nitrate slurry was evaporated to dryness and then also heated at 600°C for 6 hours to convert the nitrate to the oxide as confirmed by TGA results. The resulting powders were split in half, one of which was sieved and hot-

pressed as is while the other was subjected to the standard processing cycle prior to hot-pressing. A summary of the data for these materials is presented in Table 7.

Results of the flexural strength determination show that incorporation of the sintering aid by a chemical route, as implemented in these experiments, offers no clear advantage. The data indicate that in this set the nitrate route produces stronger ceramics than the hydroxide one and that, as expected, the milled powders result in better materials than the unmilled ones. It is interesting to note that the strength of the billet made from the unmilled nitrate powder is about equivalent to that made from the standard material although the specimen had an inhomogeneous appearance; that made from the processed nitrate powder is somewhat better. This result, if confirmed, would permit reduction in the powder processing time, an advantage anticipated from the chemical binder incorporation. Additional means of chemical binder incorporation are being evaluated.

Task 2 - Material Processing and Process Control

This task has two major thrusts: the first is to develop and apply appropriate techniques for controlling the injection molding/HIPing processes for the chosen silicon nitride composition and shapes through statistical process control (SPC) so as to minimize the occurrence of defects. The second thrust is to improve each individual process step and incorporate these improvements into the overall process.

The task is divided into several subtasks detailed below. The first three subtasks (Design, Fabrication) deal with establishment of a baseline dataset for currently prepared materials. This work entails preparation of three sets of tensile rods, two machined from a near-net-shape preform and one from a large cross-section piece. Following specimens are to be made from a preform which is very close to net shape, minimizing machining and material waste. Another subtask involves development of a database to maintain records of all materials, fabrication data, and characterization data.

Process improvement efforts are then dealt with in following subtask descriptions (Statistical Experimentation, Liquid Processing, Molding Improvements, and Microstructure Control).

BASELINE TENSILE ROD DESIGN: NSF SPECIMENS

Two types of buttonhead specimen are currently being machined from a simple injection-molded "dogbone" shape: long and short, for high temperature and ambient temperature tests, respectively. The gauge sections are geometrically identical with stressed volumes of 1.1 cc, but the shorter overall length of the room temperature specimen allows higher

fabrication rate by enhancing HIP throughput. Short specimens are being tested at GTE and have been sent to ORNL for ambient temperature tensile testing. The longer specimens have been sent to University of Dayton for elevated temperature testing.

All of the above buttonhead specimens were prepared as simple "dogbone" shaped green preforms, shown schematically in Figure 5(a). The majority of future specimens will be prepared in the NSF (Net-Shape-Formed) configuration shown in Figure 5(b), utilizing a molding die expected to be received at GTE in October. This die is designed specifically to prevent as-molded components from becoming stressed or cracking during freezing in the mold. The design principles upon which the die is based are described below.

Injection molding or slip casting of ceramic components occasionally requires the fabrication of components having a shape which restricts the natural tendency for these materials to shrink slightly in the mold following forming. This resistance to shrinkage builds up stresses in the component which can lead to degradation of material quality or complete component failure prior to removal from the mold. A design method has been developed to modify slightly the shape of such components so as to eliminate stresses related to component shrinkage in the mold.

During fabrication in a solid metal mold by injection molding, the hot injected mix solidifies and cools in the mold prior to mold opening and part removal. Studies using simple shapes where shrinkage is unrestricted indicate that injection molded silicon nitride parts have a linear shrinkage on solidification and cooling in the mold of 0.3 to 0.5%.

It can be observed that as the component tries to shrink towards its center of mass, the metal mold in the central portion of the sample will restrict this shrinkage, and a tensile stress will develop which will be highest in the thinnest cross section of the part. In some cases it becomes impossible to fabricate such samples since the tensile stresses developed exceed the strength of the molded material. This difficulty can be overcome by employing a simple design criterion which will insure that no restriction occurs on shrinkage.

After forming, the tensile rod attempts to shrink both radially and in length. The key to the present design concept is to set a specification for the rod based on the ratio of radial and length shrinkage, such that as it shrinks the angles defined by the slope from the gage region to the shank, and from the shank to the outer diameter of the buttonhead, are made sufficient to allow for unrestrained shrinkage.

Tensile specimen preforms such as those in Figure 5(a) were injection molded using a

silicon nitride mix with a wax based binder system. Many of the samples were found to be fractured on mold opening, and other samples indicated internal cracks in the central region when examined by microfocus x-radiography.

A mold was fabricated according to the above design principles (see Figure 5(b)) and the same silicon nitride/wax mix was molded. These samples all survived the molding process and showed no indication of internal cracks of the type seen in the other sample configuration by x-radiography. Overall process yield was dramatically improved.

BASELINE TENSILE ROD DESIGN: MLP SPECIMENS

A second deliverable requirement is for tensile rods which are machined out of thick cross-section components. The design of these MLP(Made from Large Part, Figure 5(c)) rods was finalized after a review meeting at ORNL on July 13, 1990. Design of a molding tool for their fabrication has been completed, and it has been ordered. It is also expected to be at GTE in October.

BASELINE TENSILE ROD FABRICATION PROCESS:

Early in the program, 109 ASCERA-style rods and 62 dogbone-style tensile rods were molded. A total of twenty-four (12 each) of these were examined by NDE, HIPed, and machined into testable specimens. Nine of each were machined into tensile rods, while the other three of each were cut into MOR test bars for generation of preliminary strength data. The data are presented and discussed under Tasks 3 and 4.

The machined tensile test rods received from the grinding service vendors were of the expected (high) quality, indicating that the initial grinding parameters have been successfully established (Milestone 114312). During this period, the tensile and failure analysis data were also collected (see Tasks 3 and 4).

Fabrication of baseline buttonhead and ASCERA-style tensile specimens continues. At the time of this report, tensile rods were in preparation as shown in Table 8. Numerous other rods and shapes are also in various stages of preparation as parts for experimental efforts aimed at characterizing and improving the process.

DATABASE DEVELOPMENT:

The prototype database utilizing Double Helix software has expanded from 26 to 34 files with the addition of a database information file and 6 files dedicated to specific nondestructive testing methods. Figure 6 is a diagram of the database structure which gives file names and shows how the information flow parallels the ceramic processing stream. The file structure is sufficiently flexible to accommodate data from diverse

experiments in addition to data generated during routine processing. Data entry, output and query forms have been designed for each file. The storage of real project data is in progress and has already led to several refinements in file structure and entry methods. A 4-station network for accessing the database using Double Helix Multiuser software has been installed. A Macintosh IIcx having an 80 MB internal hard disk acts as the file server and an Ehman 45 MB removable hard disk drive supplies backup capability.

STATISTICAL EXPERIMENTATION:

During May, personnel from American Supplier Institute spent two weeks at GTE Laboratories, instructing program personnel in the theory and application of Taguchi techniques. In ensuing months, experimental matrices were set up in the areas of powder modification, injection molding, HIPing, and machined component annealing. Experimental efforts are underway on these. An experiment on machining is currently being discussed. Powder processing and compounding are the remaining process steps to be studied, and these experiments will be set up soon.

LIQUID PROCESSING:

Powders prepared during the initial milling study (previous semiannual report) have been densified by hot pressing and hot isostatic pressing.

Hot pressing at 1750°C/3hrs gave high densities for most powders; densities of 3.258 +/- 0.003 were typically achieved. Under these same conditions certain ball-milled powders did not yield good densities. Further attempts to densify these powders by hot pressing at 1775°C/3hrs did not give any improvement. Previous hot pressing at 1750°C of PY6 compositions made by this type of milling has achieved high densities with lower weight losses of 6-9 wt% vs the current 10-12 wt%. One possible explanation for these results is that the sleeves used for the hot pressing process were new, and not the same geometry as those used previously. These possibly gave a looser fit for the ram. More sleeves have been ordered which are identical to the older sleeves, and selected hot pressings will be repeated with these. It should also be noted that of the previously investigated PY6 made from this powder, the particular lot used for these milling investigations is the only one which did not give consistently high densities in repeat hot pressing runs. MOR bars machined from high density hot pressed billets are currently being tested at room temperature and 1370°C.

Hot isostatic pressing gave high densities of 3.252 +/- 0.002 for all powders. Further HIP runs are planned. Selected billets densified by hot isostatic pressing will be machined to give bars for MOR testing.

MOLDING IMPROVEMENTS: BRUNEL UNIVERSITY

The objective of this portion of Task 2 is to develop and construct a combined compounder/molder. The machine is called the Mk.2, and it is based on a currently existing machine called the Mk.1. The Mk. 1 molder was operated extensively during this period. The aim of this work is to formulate a design specification for the Mk. 2.

The ASCERA tensile specimen mold was received and mounted in the Mk. 1 compounder/molder. Installation included modification of the nozzle with an O-ring to provide for cavity evacuation. The mold appeared to be satisfactory with respect to cavity filling and part fabrication. A new sprue bushing was fabricated with a larger taper to facilitate part removal. In addition, the range of the pressure transducer which accompanied the mold limited the injection pressure to 4530 psi. A new higher range pressure transducer was installed. The tool was remounted in the Mk. 1, and test moldings made at maximum injection pressure to test the tool's ability to prevent flashing. This had been an early problem with GTEL's ASCERA mold. No flashing occurred.

The Mk. 1 was then completely disassembled, cleaned, and reassembled in preparation for the molding of the deliverable ASCERA tensile specimens. Very little damage was observed as a result of operation with GTE's silicon nitride material. The only observable wear was on the screw flights of the twin-screw compounder. This is not unexpected as the screw flights of the Mk. 1 are fabricated of relatively soft nitrided steel, and metal to metal contact cannot be completely avoided. The observed wear is minimal and the compounder remains completely operational. Especially encouraging is the condition of the sleeve used on the injection cylinder. It has been used for all Mk. 1 molding for the past six months. There was no observable damage related to the use of GTE silicon nitride material. This system has been able to hold a cushion throughout its use and only a minimal leakage past the sleeve was found on disassembly. Fabrication of three sets of ASCERA tensile specimens will be conducted on the Mk. 1. These will be baseline specimens and cavity evacuation test specimens.

Representatives of Brunel visited GTE Laboratories in March of 1990 and presented a progress report and design review for the proposed GTE Mk. 2 compounder/molder. The basic design was accepted, the purchasing process initiated, and construction begun. Jeff Neil of GTEL visited Brunel in June of 1990 to review progress. A schematic drawing of the machine is presented in Figure 7.

A design for the connecting manifold has been completed. The melt path is contained in three parts which are designed for ease of removal and cleaning. Temperature control is

through water circulation. The ability of this scheme to maintain the melt temperatures required has been tested satisfactorily. Vendors have been identified and orders placed for fabrication of the connecting manifold. Quotes have been obtained and arrangements made for hardfacing of all components comprising the Mk. 2 melt path. The fabrication of the injection unit and the reconditioning of the 200 ton molder and clamp unit are underway. The design of the injection pistons has been finalized. Each will consist of a screw-in end cap which will hold a sleeve in place over the forward portion of the piston shaft. The end cap will not contact the barrel wall. The seal and piston alignment will be maintained by the sleeve. The extruder is in production and scheduled to be sent for hardfacing on August 20, 1990. It is expected that the scheduled delivery of the Mk. 2 to Brunel can still be accomplished in November. At this time, all promised deliveries remain consistent with the original schedule calling for delivery of the Mk. 2 to GTEL by April 1, 1991.

MICROSTRUCTURE CONTROL: HIPing

A study which utilizes Taguchi methods has been designed to examine the HIP process. The goal of the study is to identify the HIP conditions which will lead to improved strength (at both 25°C and 1370°C) and Weibull modulus of the tensile rod material. An L12 X L4 orthogonal array of experiments was laid out to examine ten control factors (two levels each) and four noise factors (two levels each) which are encountered during the HIP procedure. Several factors which involve other processing steps (e.g. powder preparation, injection molding, etc.) will be held constant. The materials produced in each experiment will be evaluated for density and 25°C and 1370°C MOR strength. Based on these quality characteristics, the optimal HIP conditions will be selected and a confirmation run will be performed.

To date, all of the test rods have been injection molded and have gone through the binder removal stage. The HIP experiments laid out in the L12 X L4 array are underway. After each experiment is conducted, the HIPed rods are being machined into MOR bars for ongoing strength measurements. The study is proceeding on schedule.

Task 3 - Development and Application of NDE Methods

OPTIMIZATION OF DEFECT DETECTABILITY:

Milestone 114316 was completed, establishing the detectability limits for microfocus x-radiography of the program test specimens, as will be described below.

Microfocus X-ray imaging parameters have been determined for radiography of tensile specimens. The tensile specimen gage sections are being comprehensively imaged at 5X

magnification in two orientations so that detected flaws can be characterized for type, size, shape, and location. The X-ray accelerating potential employed is a critical factor in optimizing the probability of detection (POD) of defects. Accelerating potential selection curves, shown in Figure 8, have been established for X-ray imaging silicon nitride ceramics². In this case, the optimum accelerating potential for the 6-mm gage section is approximately 60 kilovolts. The POD for laser-machined simulated voids has been determined as a function of thickness sensitivity (relative thickness of defect with respect to part thickness) at the optimum accelerating potential. Results are plotted in Figure 9. At thickness sensitivities of 1.1 percent and greater, the POD was found to exceed 90 percent at a confidence level of 95 percent².

For the tensile specimen gage section geometry, the minimum void size detectable varies as the cross-sectional thickness traversed by the X-ray beam changes, as illustrated in Figure 10. The values of minimum void size detectable are shown at a 1.1 percent and 1.7 percent thickness sensitivity. The extrapolation of the thickness sensitivity data is most valid in the interior of the tensile rod (region A). In the near-surface region, B, the thickness of the cylinder cross-section is minimal; consequently, the voids are not detectable because the film is excessively darkened. Fortunately, this region is interrogated in the orthogonal view when the tensile specimens are rotated.

A multiple film technique was developed to image the tensile specimens' varying cross-sectional thicknesses in one exposure. Two sheets of film having different speeds matched to the cross-sectional thickness range were exposed simultaneously. This technique minimized the size of the near-surface region where detectability was in question. In each exposure, four tensile specimens were imaged side-by-side in a prototype fixture with a thin lead separator between each gage section. The separators reduce X-ray scattering. A permanent fixture has been designed and is being fabricated with tungsten separators. Tungsten is exceptionally effective as an X-ray attenuator and overcomes problems encountered with softer lead materials, where lead contamination of specimens can be mistaken as high density inclusions.

Emphasis has been placed on optimizing and evaluating defect detectability for voids because their detection places the more stringent requirements on the radiographic technique than the detection of high density inclusions (metal contamination) of similar size. The POD of voids has been rigorously studied as a function of thickness sensitivity; however, at the smaller defect sizes (50 micrometers or less) the interaction of thickness sensitivity and resolution controls detectability. This interaction will be investigated as radiography of the baseline tensile specimens progresses.

MODELLING HDI DETECTION SENSITIVITY:

Modelling of the X-ray imaging method was done to study the efficacy of microfocus projection radiography for early-process monitoring of metallic contamination. A comparison of the calculated X-ray linear attenuation coefficients for the pertinent materials is shown in Figure 11 (top). The predominant metallic inclusions are iron based alloys which cause significantly greater attenuation than the PY6 composition. The effective energy level is approximately 30 KeV at the accelerating potential used for radiography of the tensile specimens, providing excellent contrast for X-ray imaging.

The number of HDIs (high density inclusions) detected in the as-molded material exceeded expectations based on NDE results from film radiography of the same components imaged in the dense state. The difference in radiographic density caused by a typical iron inclusion (100 micrometers) in an as-molded and dense specimen was modelled, and the results are shown in Figure 11 (bottom). The change in radiographic density between the iron inclusion in the as-molded and dense specimen is insignificant. Attenuation is linear with density and varies with atomic number, Z , to the fourth or fifth power at the energy level employed for imaging. Therefore, the apparent increase in sensitivity to HDI detection in the as-molded state is not due to the subject contrast alone.

The composite image in Figure 12 shows the results of digital fractography of tested tensile specimens. Fractography was performed with the aid of a machine-vision system capable of 40x optical magnification. Performing low-magnification fractography allows for comparison of fractographs and similarly digitized radiographs with a mutual image processing system. The fracture surfaces of the last 9 tensile specimens tested are shown with dimensions of the defects detected at the failure origin. Without exception, the tensile specimens failed at HDIs. The full size view of one fracture surface is also shown with a corresponding backscatter image obtained with a scanning electron microscope. The fracture surfaces appeared to have a contiguous inclusion (black spot) at each failure origin; however, backscatter images revealed that during densification the inclusions interacted with the surrounding matrix, reducing the resultant radiographic contrast. This effect is consistent with increased HDI detection sensitivity in the as-molded specimens, and will be further investigated as the program continues.

IN-PROCESS NDE: POWDER RADIOGRAPHY

Microfocus film radiography has been employed to nondestructively evaluate milled powders for the baseline process. Three samples of milled PY6 powder were taken from each of the eight baseline batches and radiographed in uniform plastic vials (1.0x1.0x4.0 cm). Additionally, two batches of powder having the same PY6 composition, but milled using an alternative method, were characterized in support of the Task 2 process

improvement effort. Qualitative and quantitative comparison of the processed materials revealed significant differences in the milled powder morphology; in particular, the amount of agglomeration varied.

The images shown in Figure 13 were taken from radiographs of a unit volume of each powder batch. Baseline milled powders for batch 001 through 008 are shown along with a sample of powder milled using an alternative method with and without screening. With the exception of sample 007, the milled baseline powders had a consistent appearance batch-to-batch with agglomeration present. The procedure for densification aid (Y_2O_3) addition was inadvertently changed for batch 007. The radiographic method showed that batch 007 samples had a more homogeneous appearance, relatively free of agglomeration.

The radiographs also showed that the alternative milling method produced a markedly different morphology, appearing homogeneously mixed with no agglomeration compared on the same scale as the baseline milled powders. The composition of the alternatively milled powders was the same as the baseline. One of the three samples of unscreened alternatively milled powders had one large agglomerate. Materials produced using the alternative milling procedure have exhibited superior average strength and Weibull moduli in the past. This process improvement step is being investigated for incorporation into the baseline process.

The radiographic NDE technique for milled powders is being considered as an early-process monitoring method, requiring little sample preparation and taking approximately one-half hour or less for imaging, film developing, and interpretation. The radiographic technique complements traditional particle size analysis, by addressing the extrinsic properties of powder morphology and agglomeration, which are dependent on processing. On the factory floor, radiographs of vials of newly milled powders could simply be compared to a reference standard for acceptance; however, more quantitative analysis methods are being investigated.

Image processing for radiograph enhancement and analysis was employed to quantitatively assess the degree of agglomeration in milled powders. Representative images, displayed in Figure 14, were taken from digitized radiographs of the unit volumes of milled powders. The top image is a three-dimensional grey level map of the powder volume. Peaks in the grey level map correspond to agglomerates, which attenuate the X-rays preferentially, resulting in bright spots on the radiographic image. The input image is shown below. A "blob analysis" routine was employed to discriminate agglomerates based on size (pixel area) and grey level threshold. The agglomerate indications were then

automatically counted. The entire software sequence was performed in a few seconds.

The input parameters of the agglomerate size and grey level threshold were held constant for all the batches of powder analyzed to allow batch-to-batch comparison of the degree of agglomeration. The radiographs, which typically varied in film density, were normalized to approximately the same base brightness by adjusting the intensity of the illuminator backlighting the film while measuring the average radiance over the total powder volume. In this way, an "agglomerate index " (count) could be achieved for each powder batch. The data are displayed in Table 9.

The agglomerate index was calculated by averaging the count of agglomerate indications for three samples of each powder batch. The batches are ranked in Table 9 from lowest to highest in agglomeration. A qualitative visual assessment, based on one observer, is summarized for comparison. Visual ranking was difficult for batches 001 to 006 and 008, because of the subtle difference in their degree of agglomeration. The discrepancy between the agglomerate index and visual assessment for batch 007 was determined to be a result of agglomerates being falsely detected. False detection occurred because of nonuniform packing of the powder in the vial. In future tests, all vials will be tapped for 2000 cycles with a tap density apparatus to attempt to normalize the powder packing.

IN-PROCESS NDE: RADIOGRAPHY OF BINDER CONSTITUENTS

Fractography and failure origin analysis of the baseline tensile specimens have shown that high density inclusions are the prevailing critical defect. Compositional tracing of the constituent elements found at failure origins has implicated the processing machinery (compounder, granulator, and injection molder) as the major contributors to the metallic contamination. Work is in progress to address reduction of metallic contamination from this processing equipment (Task 2). There have been elements located on the fracture surfaces which are not traceable to the processing machinery; for example, titanium has been detected. Titanium has also been found at the failure origins of GTE tensile samples, manufactured similarly, and tested at other laboratories. In an effort to comprehensively trace failure origins to their sources, nondestructive evaluation has been performed on all incoming raw materials.

High density inclusions were detected in the paraffin wax that is used in the baseline material binder system. Microfocus real-time and film radiography were used to image the collected residue of screened wax. The composite image shown in Figure 15 displays a radiograph and optical image of screening residue from a 5-kg batch of wax; the material was screened through a 60-mesh nylon screen. A large amount of organic fibrous residue was observed. The HDIs were clearly imaged as small bright spots on the radiograph.

Fortuitously, the residue and HDIs were encased in a thin coating of wax which facilitated handling.

Microfocus imaging readily detected the high density inclusions which provided exquisite contrast compared to the nylon screen, organic residue, and small amount of solidified wax. The detected defects were mapped by pointers with the aid of real-time radiography. The machine-vision optical image in Figure 16 shows one inclusion, pointed to by the bent paper clip, trapped in the nylon mesh. Several of the HDIs had a milky white appearance, suggestive of titanium oxide, while others appeared metallic. Some of each type were isolated for analysis. Electron probe micro-analysis of the inclusions revealed stainless steel (Fe, Cr, Ni), titanium, and silicon.

Discussions with the manufacturer of the blended wax used in the ceramic binder system revealed that much of the contamination that has been observed may potentially be avoided. The manufacturer will investigate the possibility of contamination from their operations and means to reduce it will be sought. Recently, the processing done at GTE has involved melting, screening, and forming the wax into slabs as feed material for compounding. An alternative is to purchase the wax as-blended in slabs. Lab samples of the slabs and pellets are expected shortly for screening tests and NDE.

The residue of the screened wax also contained a large amount of organic fibrous material. The manufacturer felt this contamination was a result of the paper packaging. In the future, the blended wax will be supplied in plastic bags.

A second screening experiment was conducted with a 400 mesh screen. Additional small fibrous material was trapped in the collected residue; however, no HDIs were detected. Many of the HDIs detected in the original screening were several hundred micrometers in size, and would certainly be strength limiting flaws. The 400 mesh screening operation is now incorporated into the process, during preparation of the binder prior to compounding with the ceramic powders. The NDE method will be employed for process monitoring.

IN-PROCESS NDE: TENSILE RODS

Microfocus radiography has been employed to nondestructively evaluate tensile specimens fabricated from the baseline powder batches. All of the baseline tensile specimens were inspected in the as-molded and finished states. Real-time radiography employing image processing was used to screen the specimens for gross bulk-defects. The tensile specimen gage sections were comprehensively radiographed with a high-contrast film at 5X magnification in two orientations so that detected flaws could be characterized by type,

size, shape, and location. A multiple film technique was developed to image the tensile specimens' varying cross-sectional thickness in one exposure. Two sheets of film having different speeds matched to the cross-sectional thickness range were exposed simultaneously.

Real-time radiography of the initial injection molded specimens revealed apparent longitudinal voids, indicative of mold packing problems. The NDE method provided the characterization necessary to eliminate the packing problem with iterative adjustment of molding parameters and a subsequent mold design modification (changes in the gating).

Microfocus film radiography of as-molded tensile specimens is highly sensitive to the detection of high density inclusions (HDIs) and is providing the data required to benchmark the baseline materials for metallic contamination. Representative results from the as-molded tensile specimen radiography are summarized in the graphs shown in Figure 17. The probability density function plots show the number of HDIs detected in the gage sections of a number of tensile specimens from 3 baseline powder batches. For example, a total of 69 HDIs were detected within the gage sections of the 18 tensile specimens fabricated from the 003 material, with 3 of the specimens having 8 HDIs in their gage volume. The frequency of detectable HDIs per gage volume is a critical feedback characteristic needed to determine the influence of process parameters and modifications on controlling metallic contamination.

Microfocus radiography has now been performed on all of the HIPed tensile rods described in Task 2. Twelve of these have been broken (see Task 4), with all failures occurring at metallic inclusions. These failure locations will be compared to the radiographs to determine whether the failure-causing defects were imaged.

ULTRASONIC TESTING SYSTEM:

The second engineering review of the ultrasonic inspection system specified by GTEL for NDE of ceramics was conducted at Panametrics Inc., Waltham MA on 6/26/90. Ron Roberts, GTEL consultant on ultrasonic testing from the Ames Laboratory NDE Center, attended. The custom designed software for data acquisition and display of surface wave images and user interface was demonstrated. Several options concerning the final mechanical configuration of the system were presented and discussed. A pivoting stage and collet chucking device were incorporated in the final mechanical configuration of the rotational axis to facilitate precise alignment and gripping of the long and short dogbone tensile specimens. A test of two possible hardcopy devices was conducted using

representative images. Progress is ahead of schedule with an early October delivery date anticipated. Comprehensive testing of the completed system, and operational training will be conducted at Panametrics Inc., Systems Division, in Ithaca, NY, prior to shipment.

A discussion with W. A. Simpson, Jr. , of ORNL has yielded a method of ensuring that surface wave images of defects are truly formed from surface waves. The method involves masking the ultrasonic transducer locally to prevent return of the first echo longitudinal wave.

MICROFOCUS CAT-SCANNING DEVELOPMENT:

Computer tomographic examination of ceramic components has been accomplished using the newly developed RTS/Sauerwein microfocus CT system. The microfocus CT system employs a solid state linear array which is optically integrated into the projection radiography Gamma Scope image intensifier, thereby providing conventional projection imaging with tomographic slices on demand. The enabling feature of the system is the precision rotational axis alignment which GTE experience in microfocus CT development has shown to be essential. The reconstruction algorithms also compensate for beam hardening. A complete report on the NDE of baseline material tensile specimens and test phantoms has been received from the vendor.

Task 4 - Property Testing and Microstructural Evaluation

MATERIAL STRENGTH AND FRACTOGRAPHY

Preliminary MOR and tensile strength data were obtained from HIPed materials fabricated early in the program, as described under Task 2. MOR test results are presented in Table 10 and on Figure 18, with corresponding tensile data in Tables 11 and 12. These data are from experiments aimed at setting up appropriate process parameters allowing preparation of the Baseline Materials, and should be considered as such. Baseline data will be reported next period.

The MOR data show the following: 1) at both ambient temperature and 1370°C, bars cut from the thinner ASCERA specimens exhibit higher strength, 2) the Weibull moduli are near the average recently obtained for PY6, and 3) all strengths are lower than expected based on recent results obtained for PY6 prepared for other programs. For instance, in the ATTAP program³, HIPed injection molded MOR specimens of PY6 exhibit strengths of over 900 MPA at ambient and over 400 MPA at 1370°C). Reasons for the low strengths are being investigated. At the present, it is considered likely that these strengths reflect the lack of experience base with this new type of silicon nitride powder. Also, the presence of a significant number of metallic inclusions at the fracture origins implies that a piece of the processing equipment (compounder, injection molder) has recently deteriorated.

Additional specimens have been prepared and testing is continuing.

Tensile strength data are shown in Tables 11 and 12 for the cylindrical (ASCERA) and buttonhead specimens, respectively. All buttonhead specimens tested resulted in failure either within the gage section or at the transition region. Two of the nine cylindrical rods which failed very close to the grips were deemed mistrials and were not included in the final results. The strength data from the cylindrical specimens are very low compared to the buttonhead specimen data, leading to suspicions that the cylindrical test apparatus itself, or the design of the specimen and/or grip, is not providing true values. The effective stressed volume of the two test specimens is nearly identical at about 1.1 cc. Strength data from the buttonhead specimens is also lower than expected, but the tests yield an average strength (455 Mpa) which is consistent with Weibull scaling laws from the MOR data presented in Table 10.

Subsequent to testing, fractography was performed on all tensile specimens (as shown in Task 3). Several techniques were utilized to determine the fracture origin location, geometry, size, and composition (metallic inclusions). The fractures were first inspected with optical microscopy to determine the location of failure. Next, the fracture origin was inspected with SEM using both backscatter and secondary electron imaging techniques. Secondary electron images highlight surface features of the fracture origin as shown in Figure 19. Backscatter electron images help determine the size, shape and distribution of high density inclusions as shown in Figure 20. If the fracture origin was thought to be a metallic inclusion, compositional information was obtained via EDX. Additionally, elemental x-ray dot maps were generated to illustrate the distribution of high density elements within the Si_3N_4 matrix as shown in Figure 21.

Fractography data for cylindrical rods are listed in Table 11. The fracture origins are a mix of porous regions, Fe-based inclusions, and Fe-Cr-Ni based inclusions. Fractography data for the buttonhead rods are shown in Table 12. As indicated, all of these failures have initiated at metallic inclusions, either Fe or Fe-Cr-Ni based. The x-ray dot maps and backscatter images indicate that the metallic contaminants do not exist as discrete flaws. Rather, small pockets of the metallic component are dispersed within the Si_3N_4 matrix in a localized region at the inclusion site, as shown in Figures 20 and 21.

An effort is underway to relate the information obtained from fractographic and non-destructive examinations to identify the likely source of the inclusions in order to guide process improvement and control activities in Task 2.

Test specimens machined from rods listed in Table 8, designated Baseline Material, will be tested and reported on next period.

PHYSICAL PROPERTIES OF BASELINE MATERIAL:

The phase composition, elastic moduli, and fracture toughness of the tensile rod Baseline Material have been characterized. MOR bars are currently being machined from Baseline tensile rods for further strength evaluation. The silicon nitride microstructure has been quantified via digital image analysis. Measurement of the oxidation resistance of the same material is underway.

Phase composition

Based on quantitative X-ray diffraction analyses, the crystalline phase composition of the Baseline injection-molded and HIPed tensile rod material is 100% beta silicon nitride, with possible traces of $\text{Si}_2\text{N}_2\text{O}$ and cubic Y_2O_3 .

Elastic moduli

The elastic moduli were measured using ultrasonic wave velocities through samples which were sliced from tensile rods. The elastic properties and density (measured by Archimedes' method) are listed in Table 13.

Mechanical Properties

The fracture toughness of the Baseline material is $4.2 \pm 0.2 \text{ MPa}\cdot\text{m}^{1/2}$, as measured by the indentation fracture toughness (IFT) method. The Knoop hardness is $13.3 \pm 0.3 \text{ GPa}$. Both the toughness and hardness values are typical of the standard GTE PY6.

The strengths at 25°C and 1370°C will also be evaluated for injection-molded and HIPed tensile rod material. Machining of tensile rod ends into military standard size "A" MOR bars is in progress. The bars will be ready for testing during the next reporting period.

Quantitative microstructural analyses

In order to characterize the Baseline silicon nitride microstructure, polished and etched sections of tensile rods were prepared and examined using a scanning electron microscope (SEM). The SEM micrographs, an example of which is shown in Figure 22, were quantified using digital image processing techniques.

Statistical analyses were performed on the digitized images to determine the grain size distribution, average grain size, aspect ratios, etc., for a total of 447 silicon nitride grains. The microstructure is composed of a fine, relatively narrow grain size distribution. The

average and maximum aspect ratios are similar to the standard GTE PY6. The most relevant data are listed in Table 14.

Oxidation resistance

The oxidation resistance of the Baseline material at elevated temperatures is currently being measured. Test specimens which were machined from tensile rods are being exposed to air at both 1200°C and 1370°C for a total of 500 hours, during which the weight change due to oxidation is measured. The tests are scheduled for completion in November.

Status of Milestones

Successful establishment of a baseline machining technique for the buttonhead tensile test specimens constitutes accomplishment of Milestone #114312. Milestone #114316 was completed, establishing the detectability limits for microfocus x-radiography of the program test specimens. Milestone #114321, submission of the first semiannual report, was also accomplished. Milestone #114305 (Develop design and fabrication technique for NSF specimens), scheduled for August, 1990, is complete. Milestone #114317 (Select surface measurement parameters relating to strength) has been delayed by about a month while specimens being utilized in a Taguchi methods experiment on machined surfaces are being prepared. These machined and/or annealed specimens will serve as the specimens for the required milestone experiment. Overall execution of the remainder of the program is on schedule.

Communications/Visits/Travel

4/3/90 - Representatives of Brunel University visited GTE Laboratories and presented a progress report and design review for the proposed GTE Mk. 2 machine.

4/10 - 11/90, D. Byrne, J. Quinlan, and A. Wu of ASI visited GTE Laboratories and set up a schedule for instruction of GTE personnel in Taguchi techniques.

5/2 - 11/90, A. Wu of ASI instructed GTE personnel in Taguchi techniques.

6/90 - J. Neil visited the Brunel University to review their progress.

6/26/90 - D. Cotter and W. Koenigsberg of GTE and R. Roberts of Iowa State Univ. visited Panametrics Inc., Waltham, MA to review progress on development and construction of the ultrasonic NDE equipment.

7/13/90 - L. Bowen, D. Cotter, S. Natansohn, J. Neil, and A. Pasto visited ORNL for a

6-month program review.

9/28/90 - Dr. R. Grimm, Head of Research and Development, of Sauerwein visited GTEL to discuss microfocus CAT-scanning results.

Problems Encountered

The injection molding dies for the Baseline ASCERA- and dogbone-type tensile test specimens had to be sent back to the manufacturer for rework several times, causing delays in the planned fabrication of baseline specimens.

Publications and Presentations

A. E. Pasto and S. Natansohn, "Advanced Processing of High-Performance Silicon Nitride Ceramics", Pp. 197-206 in Proceedings of the 27th Automotive Technology Development Contractor's Coordination Meeting, SAE P-230, April 1990.

W. D. Koenigsberg and D. J. Cotter, "On the Origin of Anomalous Shadows in Microfocus Projection Radiography", presented at the Conference on NDE of Modern Ceramics, Columbus, OH, July 1990.

W. D. Koenigsberg and D. J. Cotter, "Maximum Contrast X-Ray Imaging of Ceramics", presented at the Sagamore Conference on Heat Engine Conference, Plymouth, MA, October 1990.

References

1. M. G. Segal and R. M. Sellers, "Kinetics of Metal Oxide Dissolution", J. Chem. Soc., Faraday Trans. 1, 1982, **78**, 1149-1164.
2. D.J. Cotter, W.D. Koenigsberg, R.E. Wysnewski, and G. Hamilton, "Improving the Probability of Flaw Detection in Ceramics by X-ray Imaging Energy Level Optimization", to be published in J. Am. Ceram. Soc., **73** (June 1990).
3. J. Neil, G. Bandyopadhyay, D. Sordelet, and M. Mahoney, "Fabrication of Silicon Nitride ATTAP Components at GTE Laboratories", Pp. 303-311 in Proceedings of the Twenty-Seventh Automotive Technology Development Contractors' Coordination Meeting, Dearborn, MI, SAE P-230, 1990.

Table 1. Characteristics of Silicon Nitride Powders

Lot No	Soluble Species(mg/g)		Si:N (molar ratio)	Bend Strength(MPa)	
	(Si)	(NH ₃)		RT	1370°C
3					
(20 kg)	3.53±0.14	0.73±0.01	2.9	905±95	560±6
(180 kg)	3.74±0.06	0.94±0.05	2.4	945±57	549±9
4					
(20 kg)	3.61±0.14	0.73±0.01	3.0	845±160	500±10
(180 kg)	3.72±0.03	1.36±0.12	1.7	909±20	567±14
5					
(20 kg)	3.58±0.09	0.74±0.08	3.0	935±75	540±25
(180 kg)	3.84±0.04	1.25±0.06	1.9	936±51	564±16

Table 2. Characteristics of Aged Silicon Nitride Powders

Conditions	Soluble Si	Soluble NH ₃	Si:N
	(mg/g)	(mg/g)	(molar ratio)
Initial	4.6±0.13	0.65±0.10	4.3
Dry Air-139 Days	4.7±0.19	0.62±0.07	4.6
257 Days	4.9±0.06	1.2 ±0.2	2.5
Wet Air-139 Days	5.0±0.01	0.27±0.07	11
257 Days	4.9±0.2	0.6 ±0.2	4.9
Dry Argon -139 Days	4.6±0.1	0.49±0.04	5.6
257 Days	5.0±0.2	0.85±0.13	3.6
Wet Argon -139 Days	4.4±0.3	0.35±0.04	7.6
257 Days	4.6±0.1	0.7 ±0.2	4.0

Table 3. Solubility of Yttria as a Function of Time

Time (min)	w/o Yttria Dissolved		
	Pure Yttria	Y_2O_3/Si_3N_4	PY6
1	11.4	8.3	
3	23.5	14.6	
5	33.5	19.2	
10	50.8	26.0	
15	62.3	30.1	23.3
20	69.2		
30	82.9	42.0	41.6
45	88.9	51.2	68.4
60	92.9	61.4	74.2
90	100	77.6	89.8
120		84.0	88.7
180		94.2	
210		95.1	
290		100	

Table 4. Oxidation Resistance of Hot-Pressed PY6 Ceramics

Powder Lot No.	<u>Weight Gain After 500 Hours in Air at Temperature</u>					
	<u>0</u>	<u>1</u>	<u>2</u>	<u>3</u>	<u>4</u>	<u>5</u>
1200°C						
(g/m ²)	1.4	1.4	1.6	1.5	1.5	1.5
(w/o)	0.11	0.11	0.13	0.12	0.12	0.12
1370°C						
(g/m ²)	4.0	3.8	3.7	3.6	3.5	3.6
(w/o)	0.32	0.30	0.27	0.29	0.29	0.28

Table 5. Properties of Modified Silicon Nitride Powders.

<u>Powder Code*</u>	<u>Q</u>	<u>A</u>	<u>B</u>	<u>C</u>	<u>D</u>	<u>E</u>
Starting Powders:						
Surface Area (m ² /g)	7.5	7.0	7.7	8.5	8.5	6.6
Total Oxygen (w/o)	1.21	2.33	1.14	1.10	- -	0.58
Soluble Si (mg/g)	4.4	10.8	3.6	3.3	3.7	0.34
Soluble NH ₃ (mg/g)	0.80	0.11	0.30	0.25	0.57	0.090
Molar Ratio Si:N	3.3	6.0	7.4	8.2	3.8	2.2
Isoelectric Point (pH)	6.5	<5	7.0	7	7.3	9.6
Processed PY-6 Powders:						
Surface Area (m ² /g)	11.2	10.4	11.4	11.0	11.6	10.3
Soluble Si** (mg/g)	7.2	11.5	7.4	6.9	8.6	5.3
Soluble NH ₃ ** (mg/g)	1.06	0.76	1.18	1.07	1.42	1.15
Molar ratio Si:N	4.1	9.1	3.8	3.9	3.7	2.8
Isoelectric Point (pH)	7.4	7.0	7.2	7.4	7.4	7.4
Yttria Solubility*** (w/o)	24	66	24	25	29	42
Average Flexural Strength						
Room Temperature (MPa)	960	1080	900	910	970	840
1370°C (MPa)	540	750	590	580	615	340
Oxidation Resistance:						
1200°C - Weight gain after 500 hours						
(g/m ²)	1.4	0.64	1.3	1.5	-	2.7
1370°C - Weight gain after 500 hours:						
(g/m ²)	4.0	2.0	2.7	2.8	-	8.7

* See text for description of code.

** Values corrected for silicon nitride content of the formulation, i.e. 94 w/o.

*** Weight percent yttria dissolved after 15 minutes at 35°C in 0.03 HCl.

Table 6. Properties of PY6 Ceramics Hot-Pressed from Modified Powders

<u>Powder Lot</u>	<u>Treatment</u>	<u>Density</u>		<u>Flexural Strength (MPa)</u>	
		<u>(g/cc)</u>	<u>(%)</u>	<u>RT</u>	<u>1370°C</u>
0	no	3.19	97.9	958±48	537±55
0	yes	3.25	99.6	1082±115	747±86
0	--	3.23	99.1	1149±74	532±20
3	no	3.22	98.8	945±57	549±9
3	yes	3.26	100	993±190	758±22
4	no	3.22	98.8	909±20	567±14
4	yes	3.25	99.7	1070±112	72±55
5	no	3.22	98.8	936±51	564±16
5	yes	3.25	99.7	1016±137	739±50

Table 7. Properties of PY6 Ceramics Hot-Pressed from Powders with Chemically Incorporated Sintering Aids

	<u>Standard</u>	<u>Addition Route</u>			
		<u>Hydroxide</u>		<u>Nitrate</u>	
		<u>(as is)</u>	<u>(processed)</u>	<u>(as is)</u>	<u>(processed)</u>
Density					
(g/cm ³)	3.19	3.19	3.25	3.22	3.24
(% of 3.26)	97.8	97.8	99.6	98.7	99.5
MOR (MPa)					
RT	960±50	840±60	935 ±175	930±120	1020±55
1370°C	540±55	530 ±20	565 ±17	545 ±18	595±28

Table 8. Tensile Specimen Fabrication Summary

Number of Rods	Specimen Type	Stage of Preparation	Intended Use
53	Buttonhead	Machined	Ambient testing at ORNL and GTE
28	Buttonhead	Machined	Elevated temp. testing at UDRI
5	Buttonhead	At machining	Ambient testing
32	Buttonhead	At machining	Elevated temp. testing
57	Buttonhead	HIPed	Ambient testing
31	Buttonhead	Dewaxed	ASCERA-buttonhead comparison
17	ASCERA	Dewaxed	(as above)

Table 9. Agglomeration Index and Ranking for Milled Powders

<u>Batch No.</u>	<u>Ranking*</u>		
	<u>Agglomerate Index</u>	<u>Agglomerate Index</u>	<u>Visual</u>
001	1.7	3	6
002	4.3	4	5
003	8.7	6	8
004	15.3	10	4
005	9.7	7	7
006	12.0	8	9
007	6.0	5	3
008	14.0	9	10
Alt. Milling (screened)	0.0	1	1
Alt. Milling (unscreened)	0.3	2	2

*Ranking based on #1= least agglomerated, #10=most agglomerated.

Table 10. MOR strength results from initial HIPed PY6 tensile specimens

<u>Type</u>	<u># Bars</u>	<u>Average MOR (MPa)</u>	<u>Weibull Modulus</u>
ASCERA (25°C)	15	842	13
ASCERA (1370°C)	6	270	--
Dogbone (25°C)	30	693	12.4
Dogbone (1370°C)	5	246	--

Table 11. Strength and Failure Origin Results for Cylindrical Tensile Specimens

<u>Sample</u>	<u>Tensile Strength (MPa)</u>	<u>Fracture Origin</u>
11A	470.6 *	porous region
11B	215.4	large void
12A	241.9 *	Fe inclusion
31B	301.6 *	porous region
33B	361.2 *	stain. steel inclusion
51A	407.6	Fe inclusion
NN1	271.7 *	Fe inclusion

AVERAGE TENSILE STRENGTH= 324 ±86 MPa

* Denotes fractures occurring outside of acceptable gage region defined by ASCERA.

Table 12. Strength and Failure Origin Results for Buttonhead Tensile Specimens

Specimen Number	Strength (MPa)	Length (μm)	Width (μm)	Avg. Dia. (μm)	Inclusion Chemistry
16	*	180	70	125	Fe
33A	566	65	22	43.5	Fe
13	*	122	43	82.5	Fe
33B	465	137	140	138.5	Fe, Cr, Ni
58	277	200	75	137.5	Fe, Cr, Ni
35	567	35	17.5	26.25	Fe, Cr, Ni
17	350	117	100	108.5	Fe, Cr, Ni
55	492	60	45	52.5	Fe
57	467	100	50	75	Fe

AVERAGE TENSILE STRENGTH = 455 ± 99 MPa

* No value recorded: testing machine malfunction.

Table 13 - Baseline elastic properties of GTE PY6.

Density (g/cc)	3.257
Young's Modulus (GPa)	317
Shear Modulus (GPa)	124
Bulk Modulus (GPa)	240
Poisson's Ratio	0.28

Table 14 - Baseline microstructure characterization results.

<u>PARAMETER</u>	<u>MEAN</u>	<u>STD DEV</u>	<u>MEDIAN</u>	<u>MIN</u>	<u>MAX</u>
Grain Area (sq. μm)	0.5	1	0.2	0.01	9.5
Grain Aspect Ratio	2	1	1.8	1	12.5

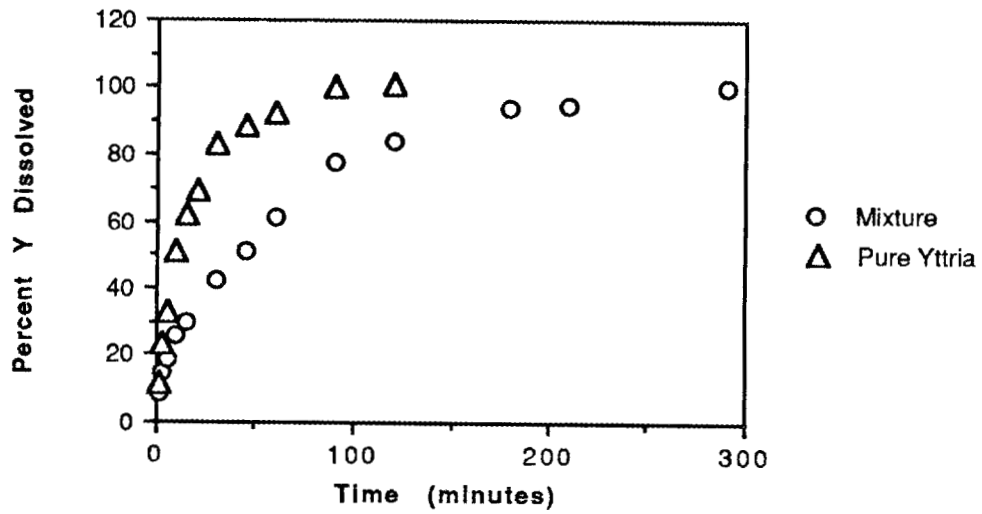


Figure 1. Dissolution of pure yttria and a mixture of yttria and silicon nitride powders.

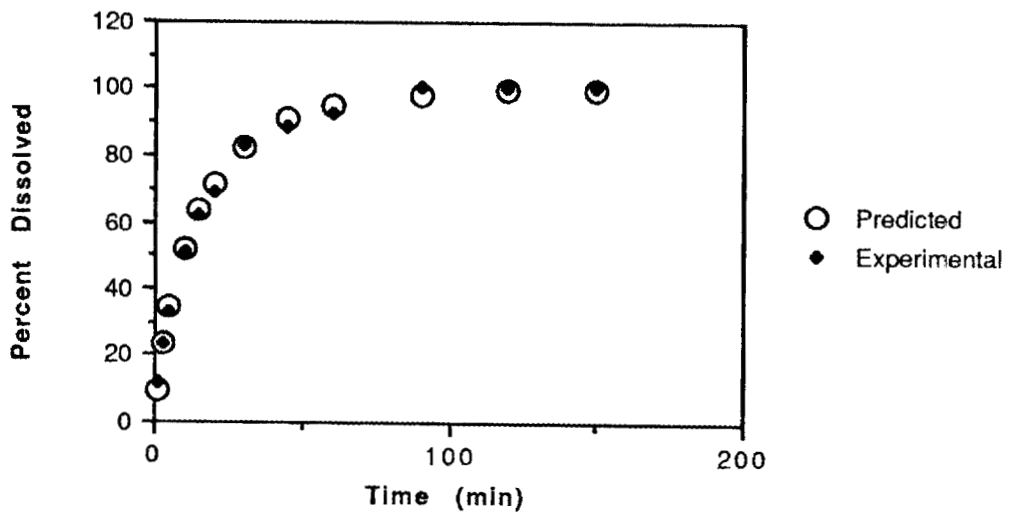


Figure 2. Dissolution of pure yttria.

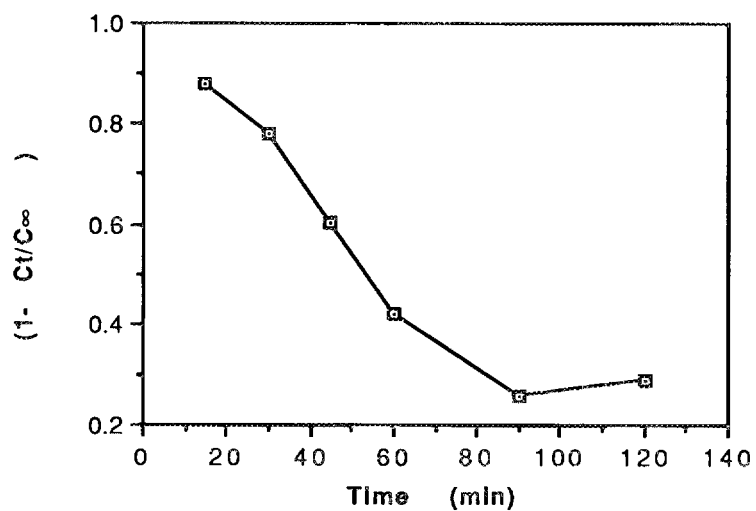


Figure 3. PY6 data fit to a shrinking core model.

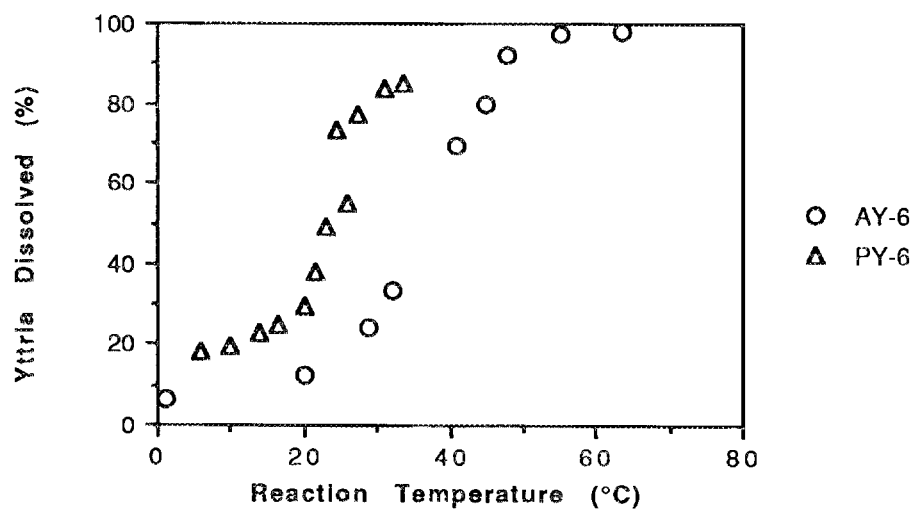
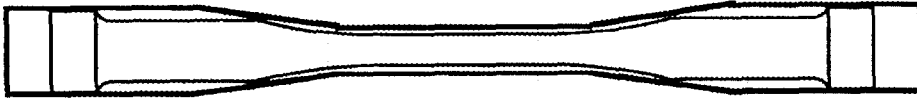


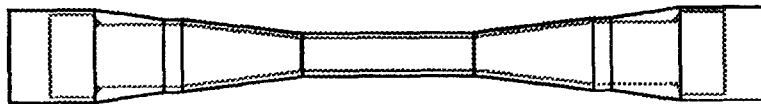
Figure 4. Temperature dependence of yttria dissolution.

Figure 5. Schematic drawings of the long and short varieties of buttonhead tensile rods being fabricated, and the three styles of green preforms from which the dense specimens are made.

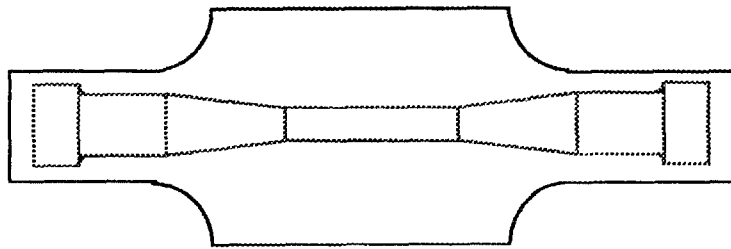
(a) The "Baseline" dogbone preform and the dense long specimen.
(b) The NSF green preform and the dense short specimen.
(c) The MLP green preform and the dense short specimen.



(a)

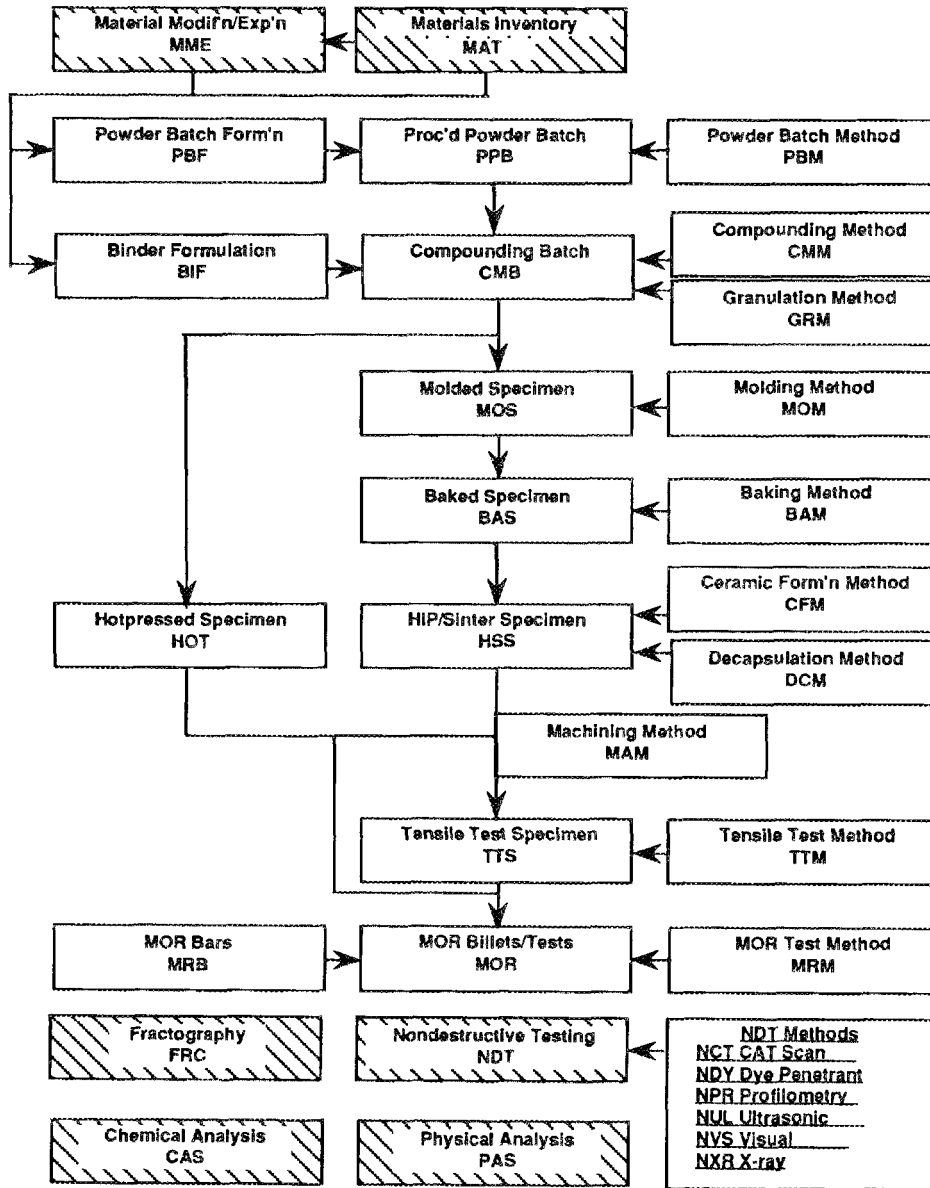


(b)



(c)

Figure 6. Diagram of database.



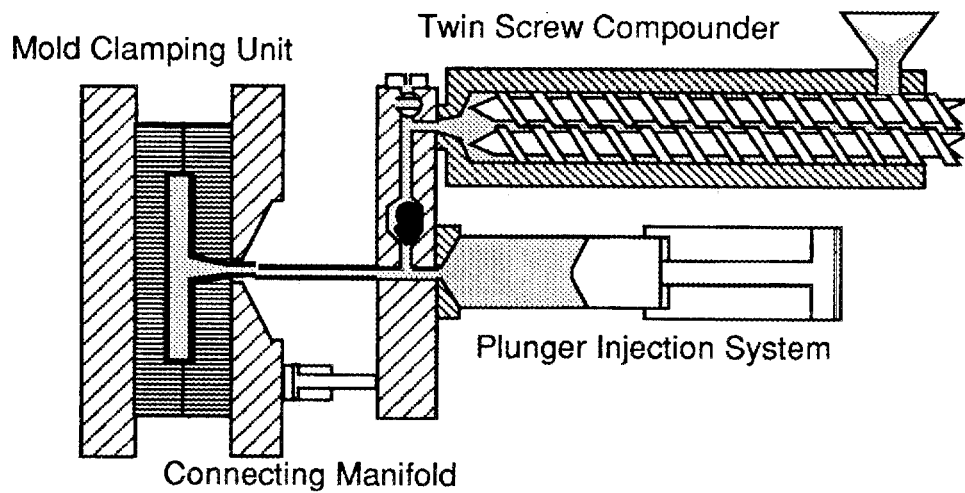


Figure 7. Schematic of the GTE/Brunel Univ. Mk. 2 compounder/molder, currently being constructed.

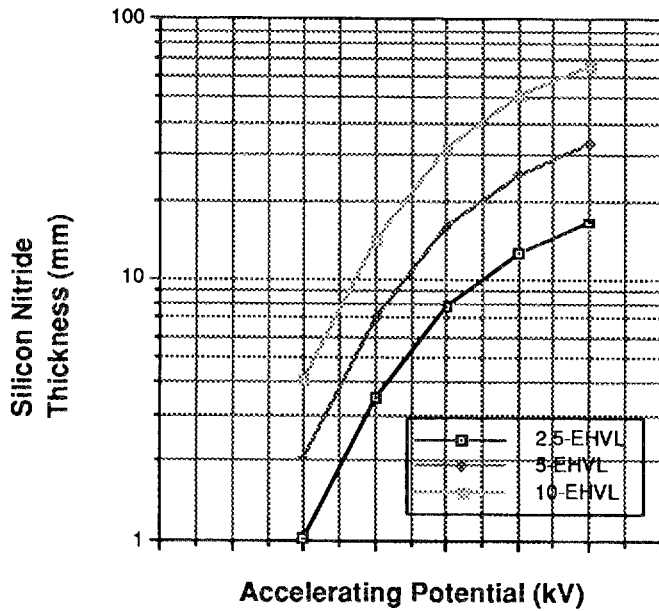


Figure 8. Accelerating potential selection curves have been established for x-ray imaging silicon nitride ceramics. The optimum accelerating potential for the 6-mm gage section is approximately 60 kilovolts.

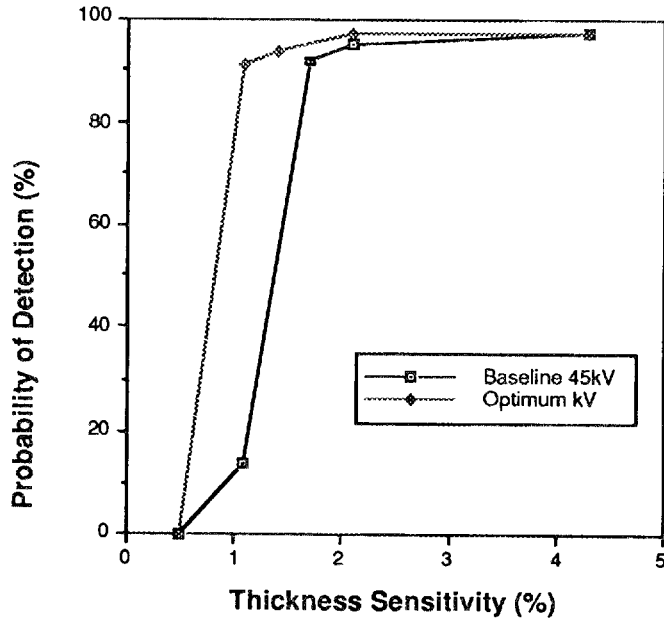


Figure 9. POD was determined as a function of thickness sensitivity for laser-drilled simulated voids at the optimum accelerating potential. At thickness sensitivities of 1.1 percent and greater, the POD was found to exceed 90 % at a confidence level of 95%.

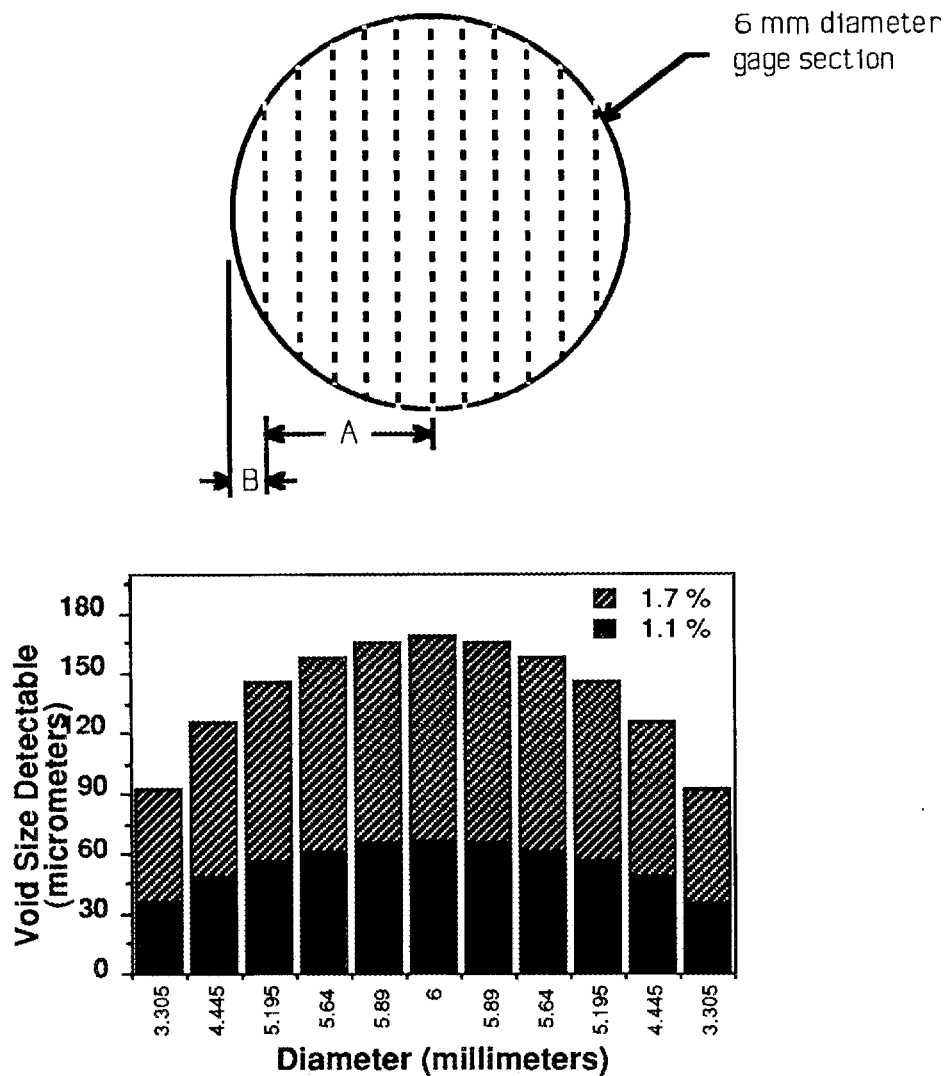


Figure 10. POD for tensile specimens. The minimum void size detectable varies as the cross-sectional thickness traversed by the x-ray beam changes. The divergent beam is shown parallel for simplicity. The values of minimum void size detectable are shown at a 1.1 % and 1.7 % thickness sensitivity. Extrapolation of the thickness sensitivity data is most valid in the interior of the tensile rod (region A). In the near-surface region, B, the voids are not detectable because the film is excessively darkened. This region is interrogated in the orthogonal view when the specimens are rotated.

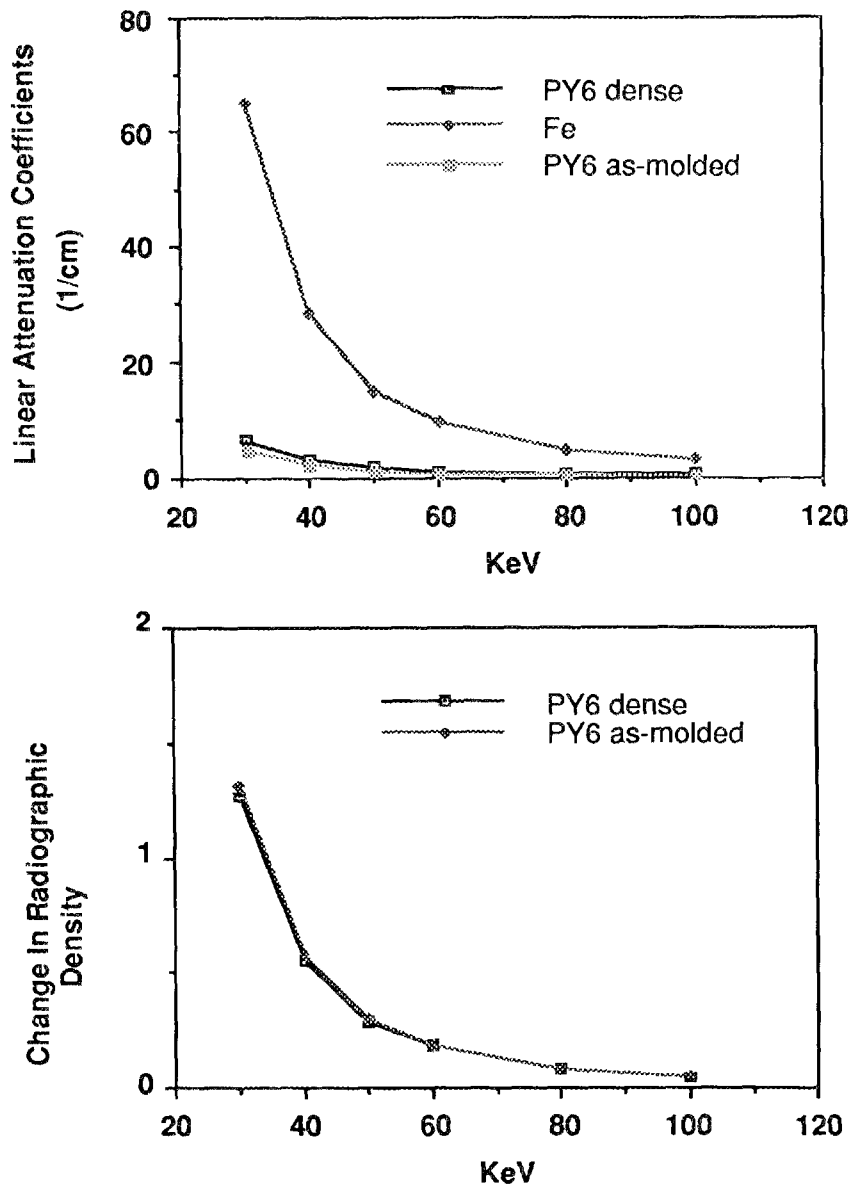


Figure 11. Modelling HDI detection sensitivity. A comparison of the calculated X-ray linear attenuation coefficients is shown (top). The difference in radiographic density caused by a typical iron inclusion ($100\mu\text{m}$) in an as-molded and dense specimen was modelled (bottom). The apparent increase in sensitivity to HDI detection in the as-molded state was not due to the subject contrast alone.

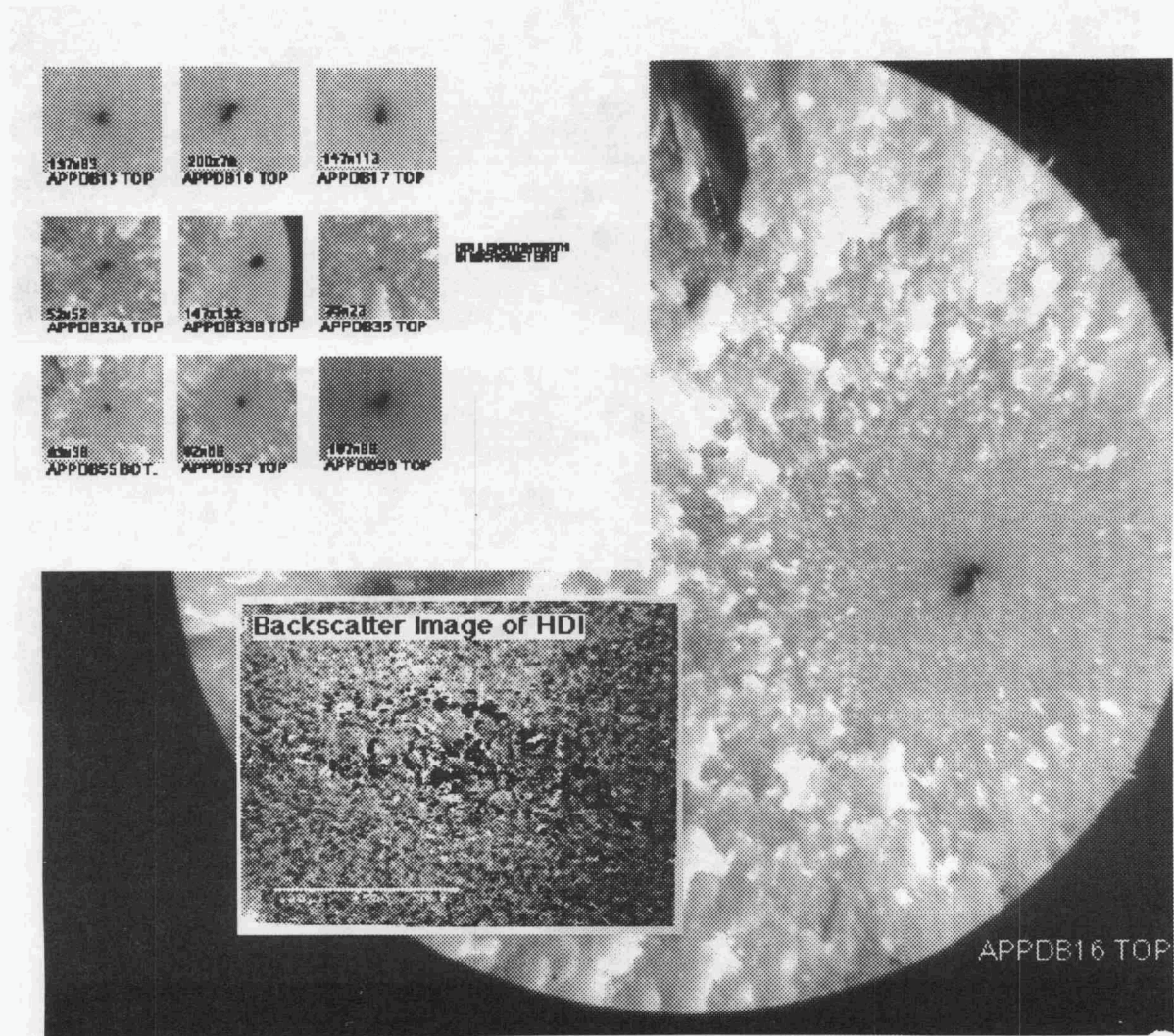


Figure 12. The fracture surfaces of nine tensile specimens are shown with dimensions of the defects detected at the failure origin. The full size view of one fracture surface is also shown with a corresponding backscatter SEM image. The fracture surfaces appeared to have a contiguous inclusion (black spot) at each failure origin; however, backscatter images revealed that during densification the inclusions had interacted with the surrounding matrix, reducing the resultant radiographic contrast.

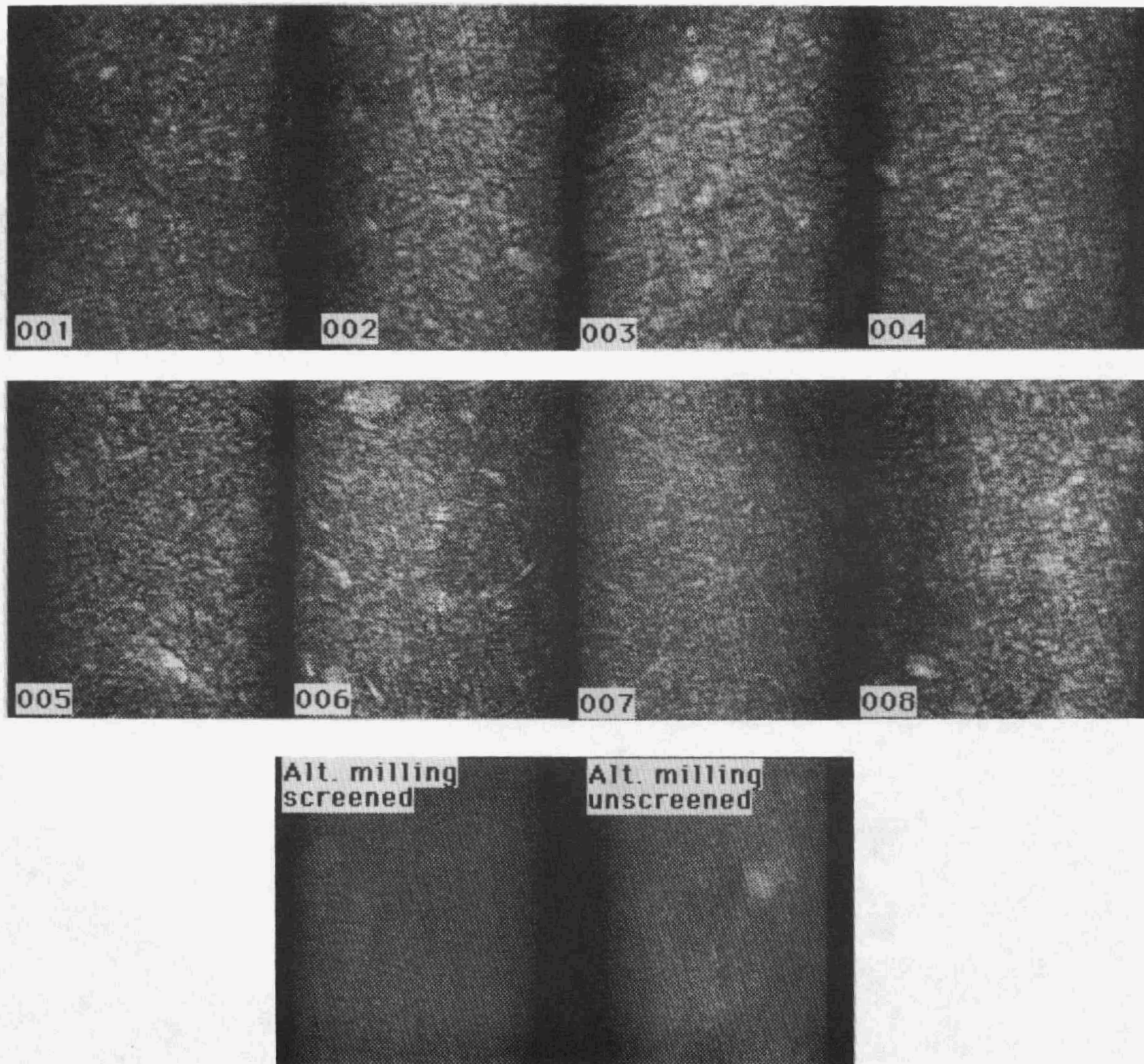
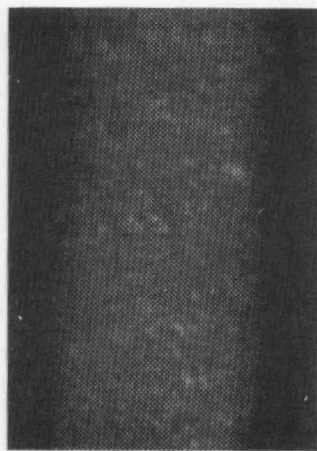
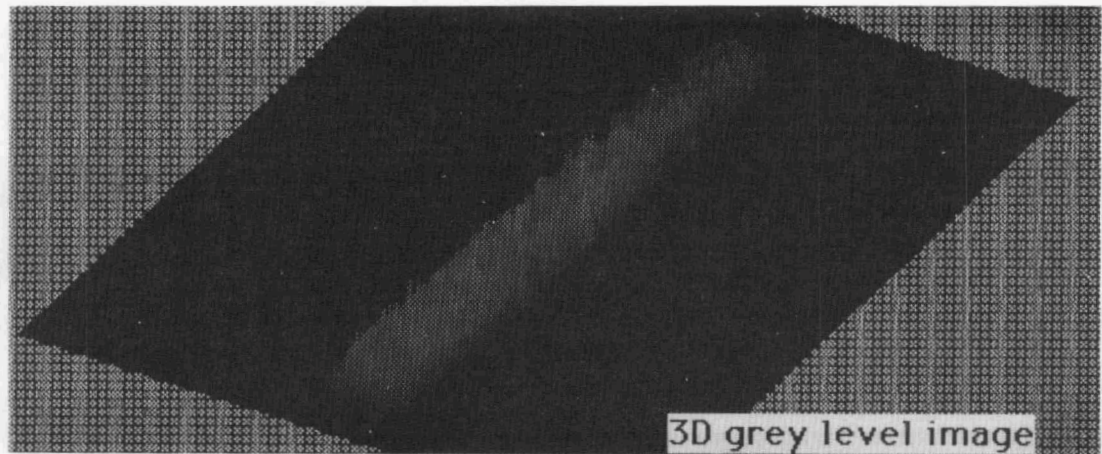


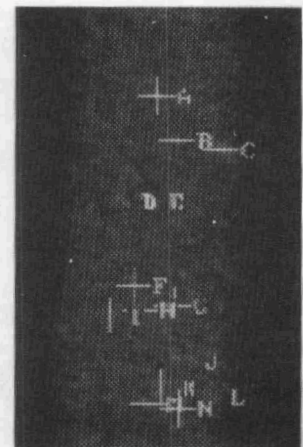
Figure 13. Digitized radiographs of milled powders. The radiographic method revealed that batch 007 samples were relatively free of large agglomerates. The alternative milled powders produced a markedly different morphology, appearing more homogeneous, with no large scale agglomeration.



Input Image



**Thresholded
and
Binarized**



**Agglomerates
Counted**

Figure 14. Quantitative image processing. Image processing was employed to quantitatively assess the degree of agglomeration in milled powders. The top image is a three-dimensional grey level map of the powder volume. The agglomerate indications were automatically counted.

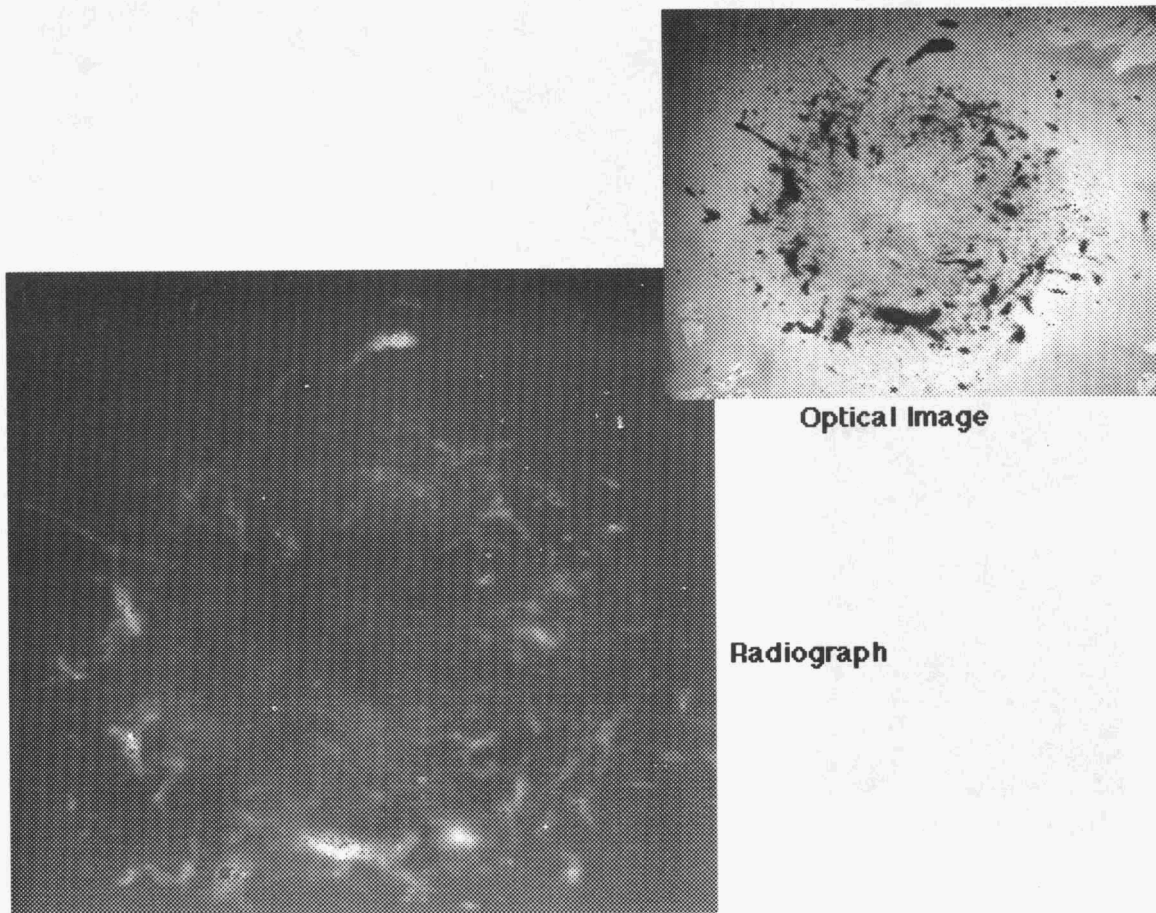


Figure 15. NDE of wax. The composite image shown displays a radiograph and an optical image of screening residue from a 5 kg batch of wax. A large amount of organic fibrous residue is visible. The HDIs were clearly imaged as small bright spots on the radiograph.

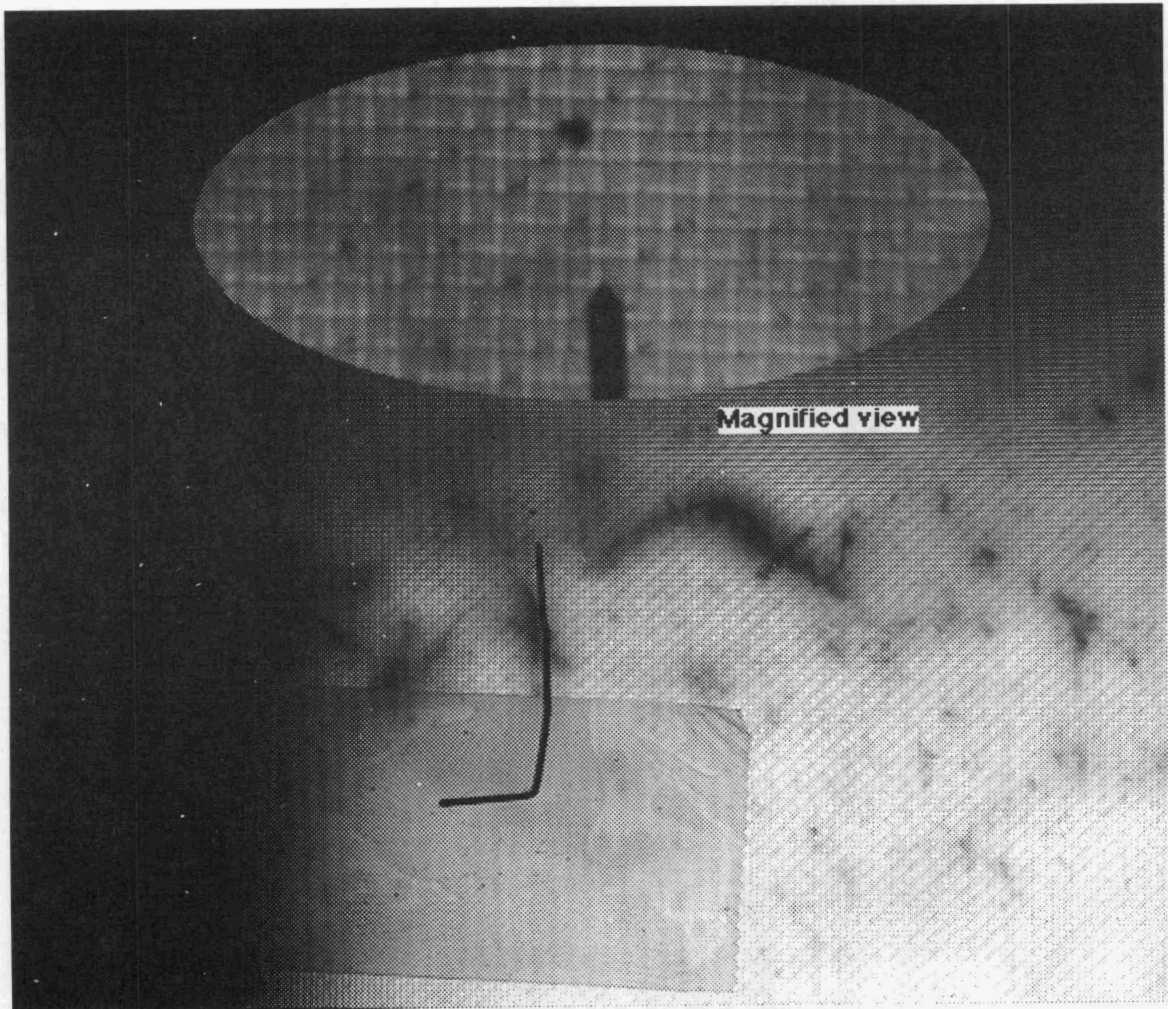


Figure 16. Isolated HDIs. The detected defects were mapped by pointers with the aid of real-time radiography. The machine-vision optical image shows one inclusion trapped in the nylon mesh. Several of the HDIs exhibited a white appearance, suggestive of titanium oxide, while others appeared metallic.

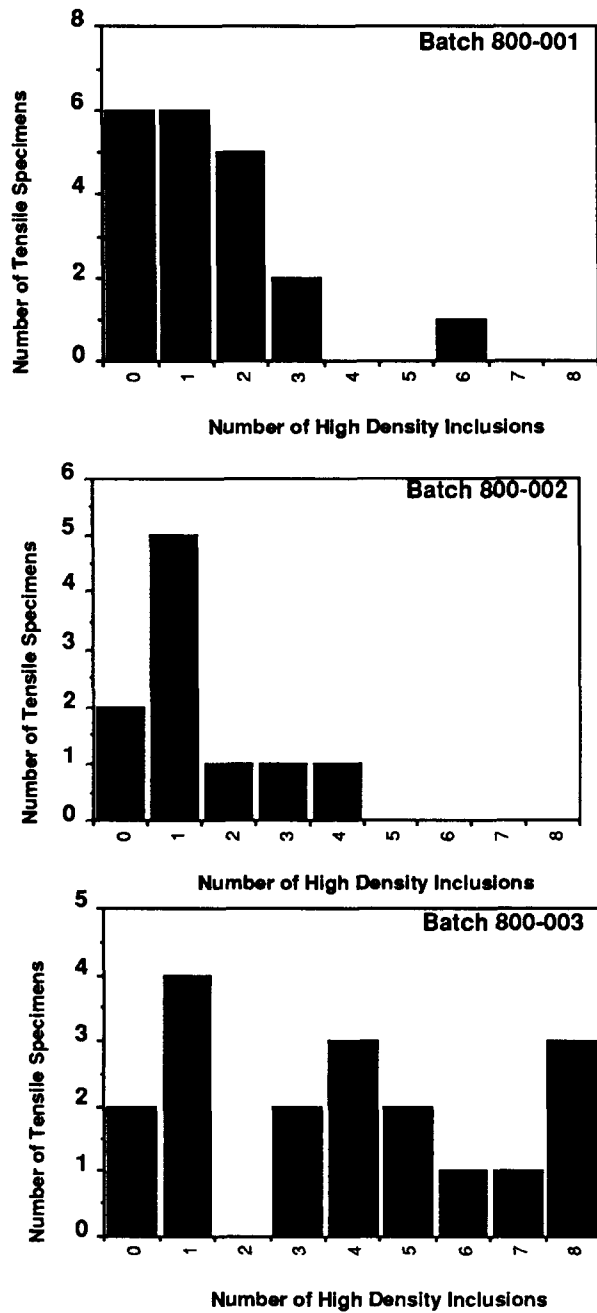


Figure 17. Results from NDE of as-molded tensile specimens. The number of HDIs detected in the gage sections of a number of tensile specimens from three baseline powder batches is shown.

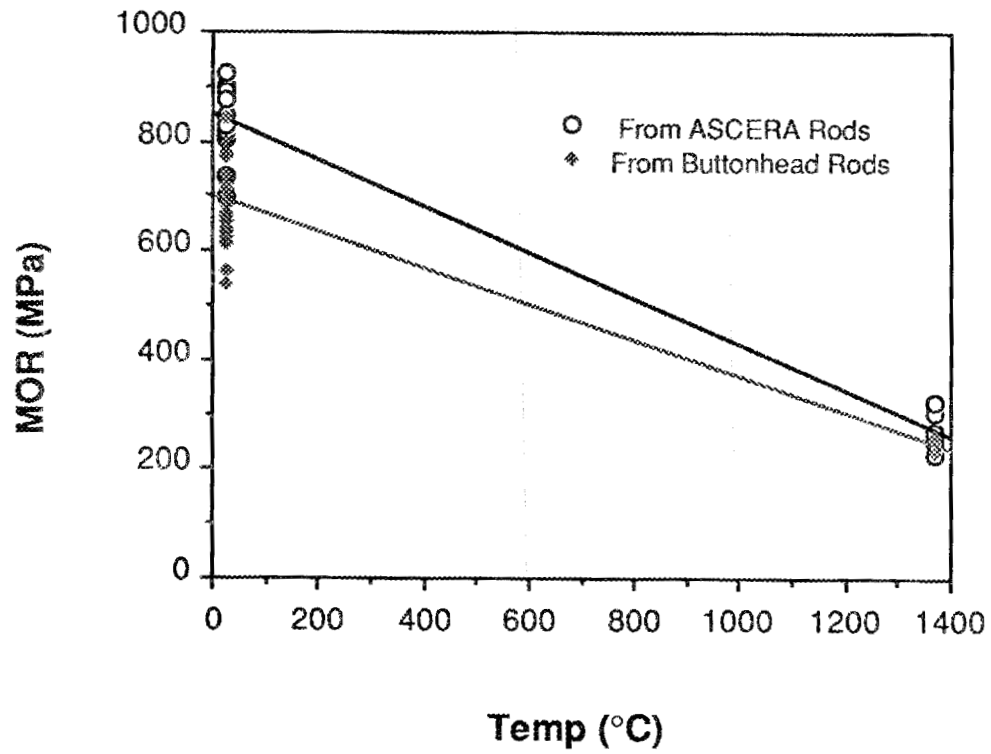


Figure 18. MOR strength results for initial series of silicon nitride rods.

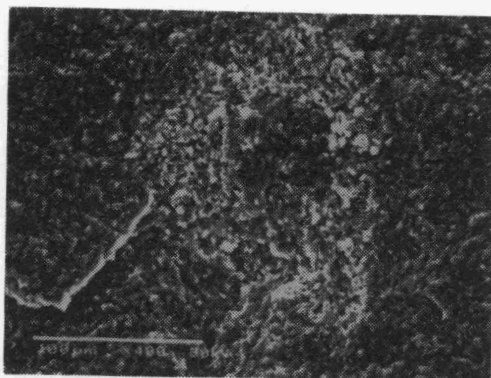


Figure 19. Secondary electron image of a metallic inclusion in specimen #33B.

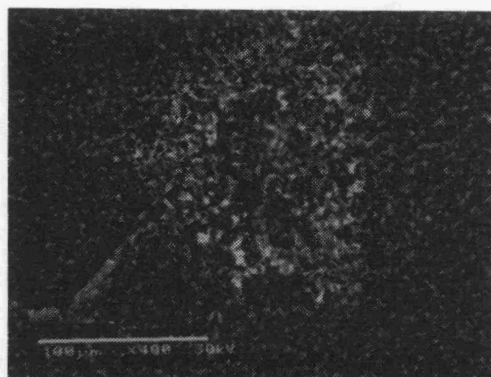


Figure 20. Backscatter electron image of a metallic inclusion in specimen #33B.

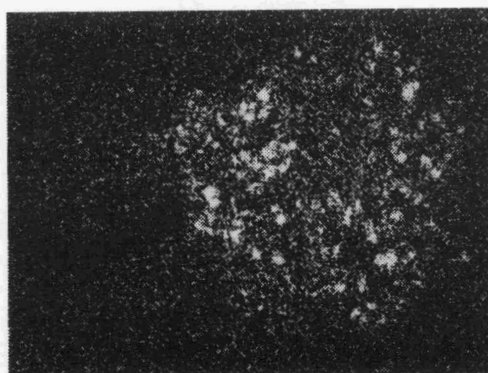


Figure 21. Iron (Fe) x-ray dot-map for specimen #33B (fracture origin).

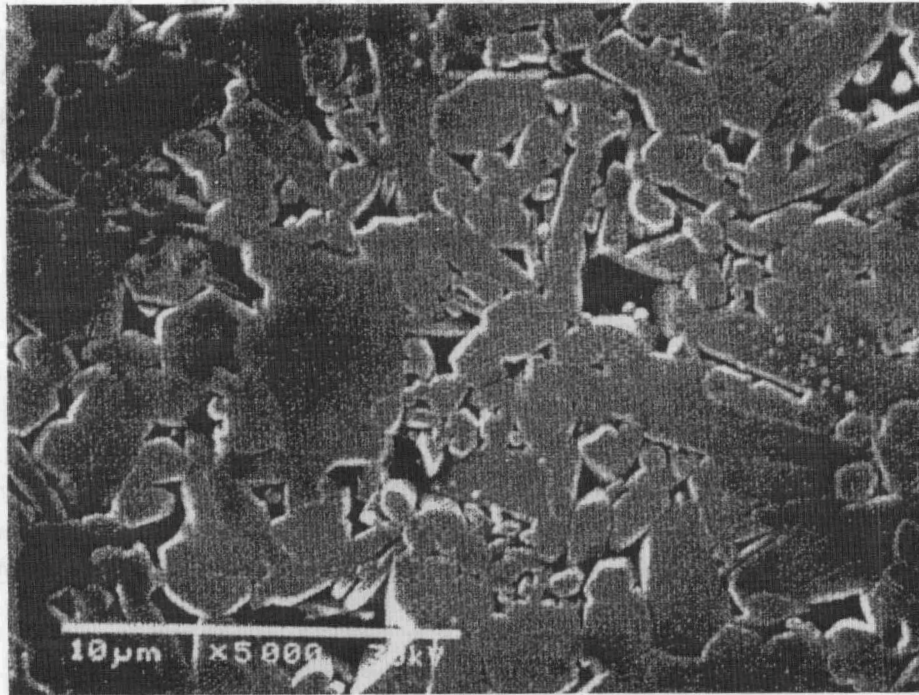


Figure 22. SEM micrograph of polished and etched baseline HIPed PY6. The microstructure was quantified via digital image processing techniques, yielding a silicon nitride grain aspect ratio of 2.

Processing Science for Si₃N₄ Ceramics
(University of California, Santa Barbara)

F.F. Lange, D.S. Pearson

Objective/scope.

We are trying to increase the understanding of the role of interparticle forces in the processing of ceramics. The effects of electrolyte addition and pH changes on the rheological properties of dispersions, the kinetics of pressure filtration, and the mechanical properties and microstructure of the resulting bodies will be compared to each other and to existing models of interparticle forces (*i.e.* DLVO theory).

Technical progress.

This period we have characterized the slurry received from Norton Co. to provide a baseline for our future exploratory work. The rheological properties of the slurry were measured with a stress rheometer. The permeability of compacts were calculated assuming Darcy's Law from data acquired during pressure filtration under a range of pressures in a mechanical test rig and both strain recovery and body rheology were characterized with the same instrument.

Slurry Rheology.

The slurry received from Norton Co. consisted of 45vol% solids dispersed at pH10 (negative surface charge) in water. Exact details of the formulation are unavailable. The particles size measured by sedigraph has $d_{50} = 0.72\mu\text{m}$ and a $d_{90} = 1.14\mu\text{m}$.

The shear stress response of the slurry was measured in a Rheometrics constant stress rheometer using a Couette geometry. A stainless steel fixed cup (46mm ID) held the slurry and a titanium bob (44mm OD, 60mm long) was used to apply the torque. The rate of bob rotation was measured by two different methods: at low stress levels the position of the bob was measured by RVDT and the rate calculated; at high stress levels the rate was measured directly from an optical encoder.

The slurry exhibited shear-thinning behavior as shown in figure 1. If shear-stress is plotted *versus* shear-rate (figure 2), Bingham fluid behavior is observed with an extrapolated yield stress of 4Pa and a plastic viscosity of 0.8Pa s. Data for this slurry was reproducible from sample to sample although they did age in the Couette cell, apparently due to drying since a crust was found around the top of the bob on removal, while the bottom appeared fluid.

Consolidation by Pressure Filtration

The slurry was formed into a compact in a stainless steel die (figure 3) with a membrane filter supported by a sintered stainless steel filter. The die had a diameter of 45mm. Pressure was applied to a stainless steel piston sealed to the outer wall with an rubber o-ring. Pressure was held constant during each of these experiments. A MTS mechanical test system was used to apply the load and the data was recorded using a Data Translation A/D board and a microcomputer. Time resolution was 0.05s, position 0.1 μ m, and pressure 10 Pa.

The kinetics of pressure filtration appeared to follow Darcy's Law. After an initial transient period, the permeability calculated from the collected data was not dependent on piston displacement or applied pressure as shown in figure 4, nor was the relative density (56.5%) of the saturated compact dependent on applied pressure as shown in table 1. This behavior is consistent with what we have seen with well-dispersed alumina slurries.

Strain Recovery.

The response of the saturated compact to the release of pressure was examined in two ways: the pressure was released in steps with the sample allowed to equilibrate and dilation expansion recorded as a function of pressure (figure 5); and the sudden release of pressure with dilational expansion recorded as a function of time (figure 6). The stepped pressure release data shows non-linear recovery behavior of a Hertzian type with more strain observed at small applied stresses and less strain at large stresses. The time-dependent data shows that most of the expansion occurs quickly on pressure release.

Body Rheology.

Stress relaxation experiments were conducted in a MTS mechanical test system. The response of the saturated compact to an applied strain of 1% applied in 0.5s is shown in figure 7. A small amount of stress relaxation occurs, but the bodies support 50% of the load. This behavior differs from what we have seen in alumina samples from stable dispersions where the bodies flow to relieve the applied pressure.

Conclusions.

The silicon nitride dispersion received from Norton Co. gives us a baseline for studying the behavior of slurries which we create. We consider the slurry rheology to be good for processing; as a Bingham-fluid, the low viscosity ($\eta_{pl} = 0.8\text{Pa s}$) at high shear rates permits easy mixing, while the yield stress (4Pa) freezes the dispersion state preventing particle segregation. The relative density (56.5%) of the saturated compacts was constant over a range of experimental pressures. The short relaxation times for strain recovery seen in these samples is similar to what we have seen in well dispersed alumina slurries. The lack of flow in the saturated compact under applied stress is not ideal since flow allows the sample to relieve stress without cracking.

Status of milestones.

114401	Survey rheological characteristics of slurries produced under a variety of pH / electrolyte conditions. Develop methodologies for characterization of slurry rheological properties and green body mechanical properties.	Complete
114402	Status report on testing procedures and preliminary results.	<u>Complete</u>
114403	Determine effect of pH / electrolyte conditions on green body properties including processing rates, mechanical properties, and density.	1 Oct 91
114404	Status report on green body properties and processing relationships.	1 Nov 91

114405	Explore other means to modify interparticle interactions (polymers such as PVA).	1 Apr 92
114406	Status report on polymer effects	1 May 92
114407	Examine flaw populations in sintered bodies.	1 Oct 92
114408	Final report on colloidal processing	1 Nov 92

Publications.

None.

Table 1.

Pressure (GPa)	Density (% theoretical)	slurry volume (ml)
0.2	57.0	20
0.6	57.3	20
1.8	57.0	20
1.9	56.9	30
2.2	56.5	30
2.5	56.5	30
2.5	56.6	30
2.8	56.6	30

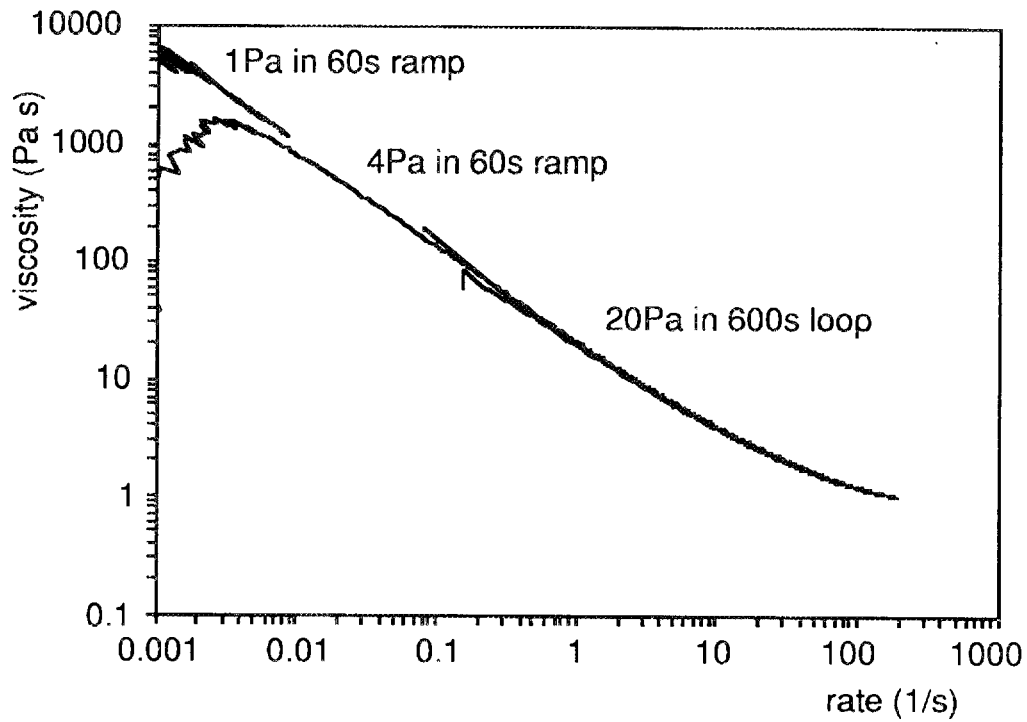


Figure 1, viscosity of the slurry as a function of shear-rate showing shear-thinning.

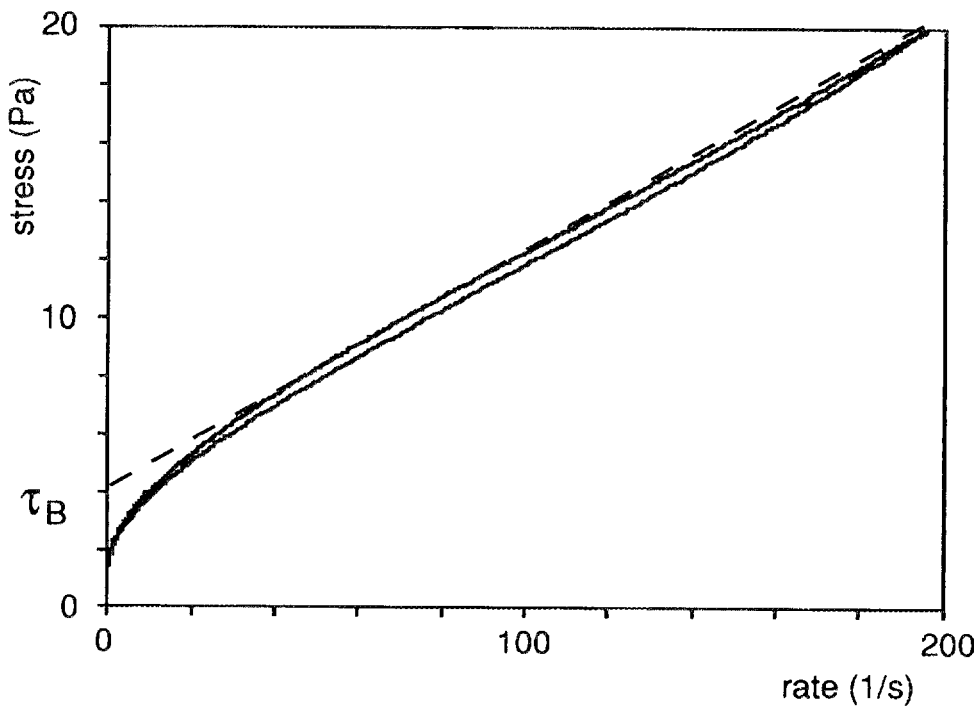


Figure 2, stress as a function of shear-rate showing Bingham-yield behavior.

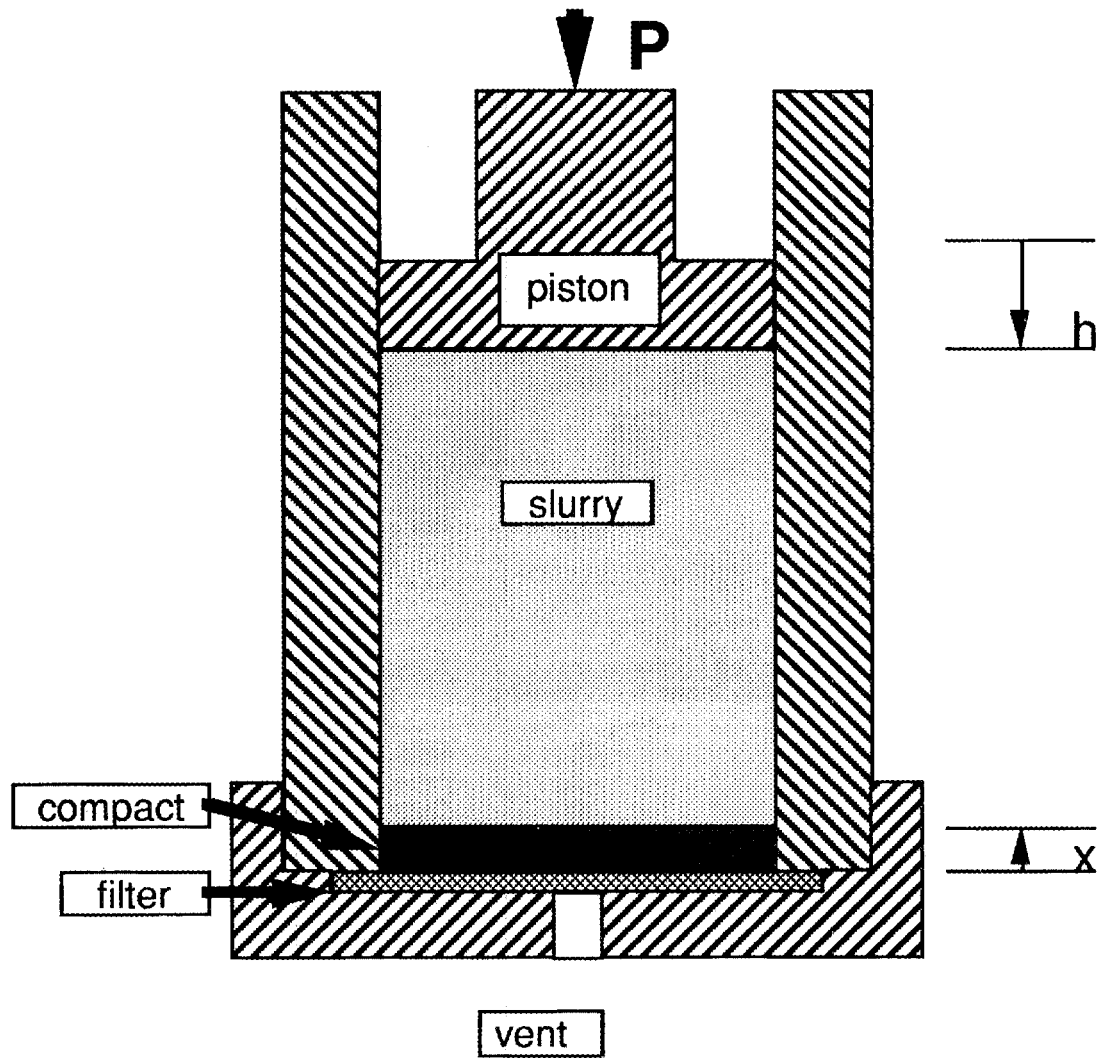


Figure 3, diagram of pressure filtration die.

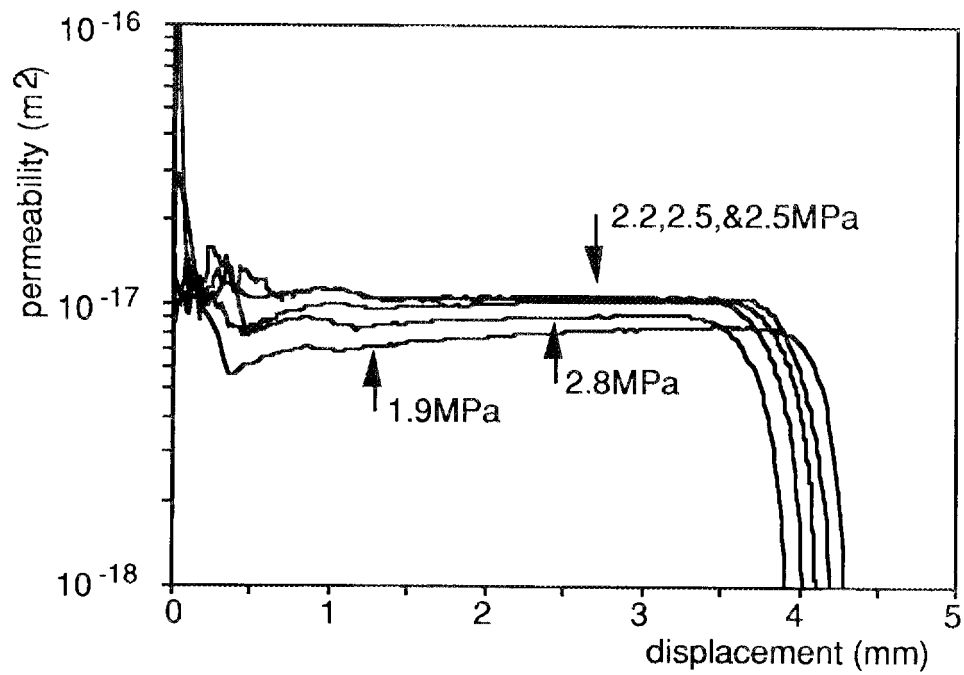


Figure 4, permeability of compacts during filtration at several pressures as a function of position.

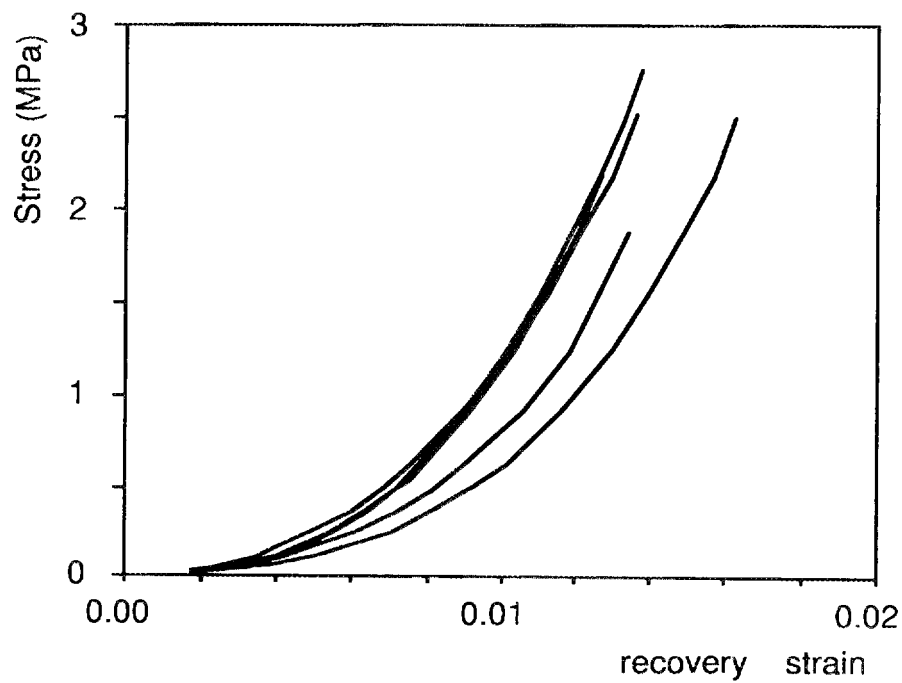


Figure 5, stress plotted versus recovery strain during pressure unloading.

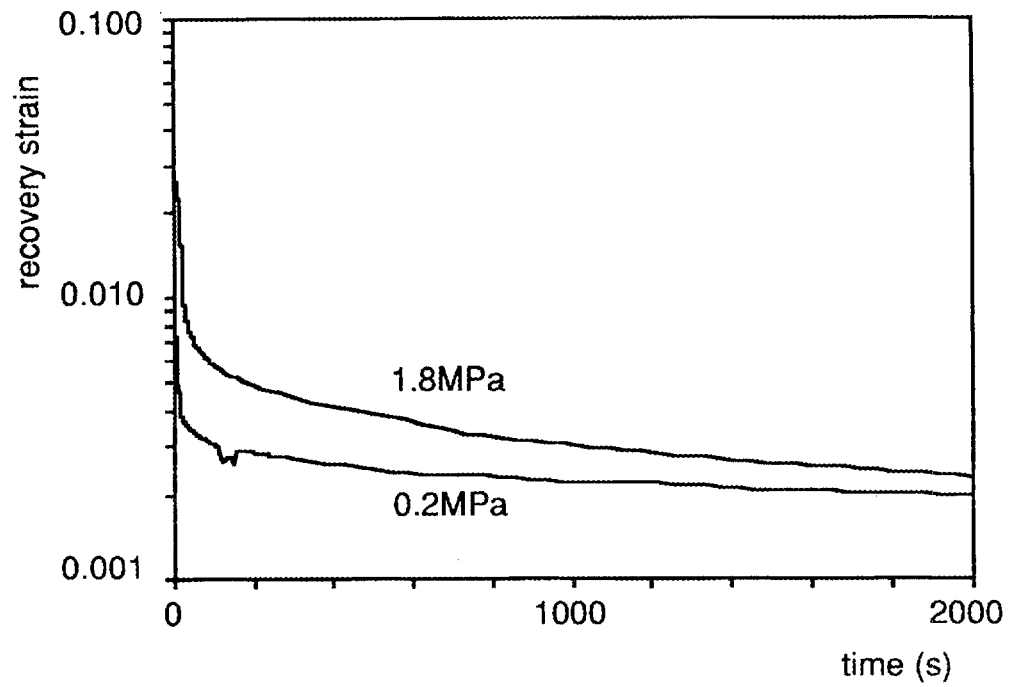


Figure 6, engineering strain as a function of time after pressure release.

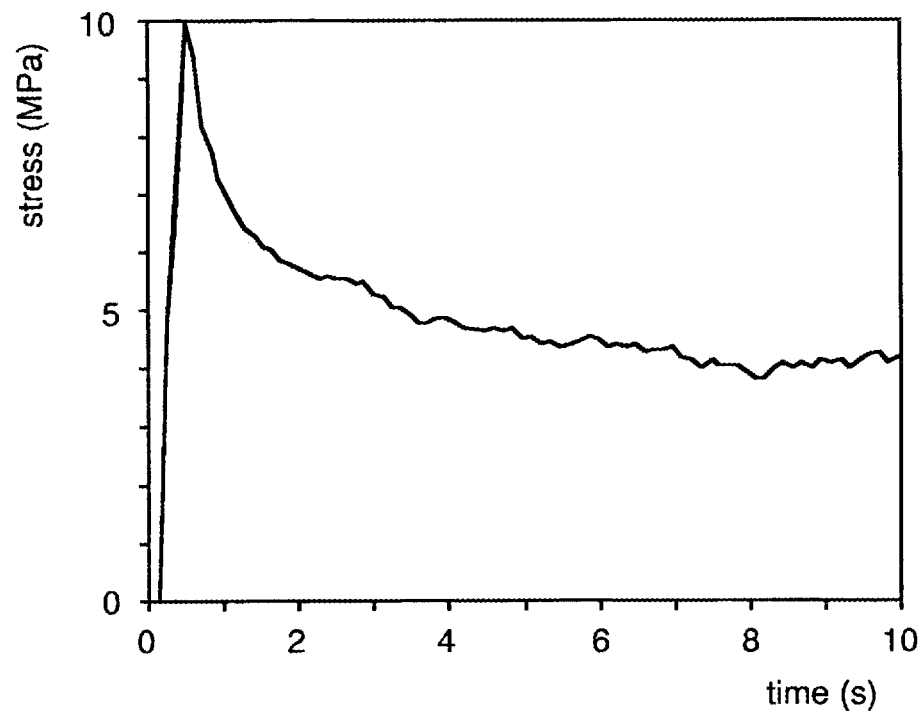


Figure 7, stress shown as a function of time for the applied strain.

1.2 CERAMIC COMPOSITES

1.2.2 Silicon Nitride Matrix

SiC-Whisker-Toughened Silicon Nitride

H. Yeh, E. Solidum (Garrett Ceramic Components),
K. Karasek, G. Stranford and D. Yuhas (Allied-Signal Research
Technology),
S. Bradley (UOP Research Center), and
J. Schienle (Garrett Auxiliary Power Division)

OBJECTIVE/SCOPE

The objective of this program (Phase II) is to maximize the toughness in a high strength, high temperature SiC whisker/Si₃N₄ matrix material system that can be formed to shape by slip casting and densified by a method amenable to complex shape mass production. The ASEA glass encapsulation hot isostatic pressing (HIP) technique shall be used for densification throughout the program.

The program is divided into seven technical tasks with multiple iterations of process development and evaluation. Parametric studies shall be conducted to optimize processing steps developed in the Phase I effort, guided by established analytical and NDE techniques. The seven technical tasks are: Task 1 - Selection of SiC whiskers, Task 2 - Baseline Casting Process, Task 3 - Parametric Densification Study, Task 4 - Effect of Specimen Size and Shape, Task 5 - On-Going Evaluation of Alternate Whisker, Task 6 - Nanometer Deposition of Sintering Aids, and Task 7 - In Process Characterization and Process Control During Drying of Cast Ceramic Parts.

The technical effort was initiated in June 1988. Task 1 was completed in January 1989. Based on the results, HF-etched American Matrix Inc. SiC whisker was selected for use for Tasks 2 -4. Task 2 was initiated in February 1989 and was completed in June 1989. Task 3 effort was initiated in July 1989, and is still in progress. Pending upcoming contract modification, the last part of Task 3 (Subtask 3.C) and the entire Task 4 efforts will be deleted.

Tasks 5, 6 and 7 tasks were added onto this contract in August 1989 to supplement the mainline activities. Task 5 was completed in this reporting period; Tasks 6 and 7 are still in progress.

Research sponsored by the U.S. Department of Energy, Assistant Secretary for Conservation and Renewable Energy, Office of Transportation Technologies, as part of the Ceramic Technology for Advanced Heat Engines Project of the Advanced Materials Development Program under contract DE-AC05-84OR2140 with Martin Marietta Energy Systems, Inc., Work Breakdown Structure Subelement 1.2.2.1.

TECHNICAL HIGHLIGHTS

TASK 1 - Selection of Whisker

All technical efforts had been completed and the results were in Semi-Annual Report October 1988 - March 1989.

In summary, Tateho, as received American Matrix, HF-etched American Matrix, and Advanced Composite Material Corporation (ACMC, formerly ARCO) were evaluated by fabricating 20 wt% SiCw/GN-10 Si_3N_4 composites with the baseline process established under Phase I. Based on the mechanical properties and availability, HF-etched American Matrix SiCw was selected for use under Tasks 2 and 3.

TASK 2- Baseline Casting Process

All technical efforts had been completed and the results were summarized in the April-September 1989 Semi-Annual Report.

In summary, four iterations were conducted to optimize the green forming process for composites containing 10, 20, 30 and 40 wt% SiC whiskers, respectively. In these, the Si_3N_4 powder, prior to blending with SiC whiskers, contained the standard GN-10 sintering aids concentration. The optimized process, was used to fabricate another set of four composites (10, 20, 30 and 40 wt% SiC whiskers), in which the sintering aids concentrations in the Si_3N_4 powder were increased with SiC whisker loading to maintain a constant ratio between sintering aids and the sum of Si_3N_4 and SiC whisker. These series of composites are referred as 10%SiCw/GN-10A, 20%SiCw/GN-10A, 30%SiCw/GN-10A, and 40%SiCw/GN-10A. The purpose of these was to determine the effect of sintering aids concentration on the structure/properties of densified composites. The green composites, a total of eight varieties, plus a monolithic GN-10 were to be densified under Task 3.A -statistical matrix to determine the effect of HIP parameters.

TASK 3 - Parametric Densification Study

Two subtasks (A and B) shall be conducted to evaluate the effects of key densification parameters on microstructures/ properties of $\text{Si}_3\text{N}_4/\text{SiC}(w)$ composites. The samples containing 10 to 40 wt% whiskers and two levels of sintering aids fabricated under Task 2 iterations 4 and 5 shall be densified by a HIP matrix (five runs), resulting in forty (40) different composites. A baseline monolithic GN-10 green sample shall also be included in each HIP run as a reference. Based on these results, the more promising composites shall be selected and refabricated for a more detailed characterization under Subtask B.

A) Statistical Matrix

Work was completed in this reporting period. In summary a HIP matrix consisting of Garrett Ceramic Component's baseline HIP cycle

($T_2^{\circ}\text{C}/t_2$ hr) and three less severe conditions ($T_2^{\circ}\text{C}/t_1$ hr, $T_1^{\circ}\text{C}/t_2$ hr and $T_1^{\circ}\text{C}/t_1$ hr) were conducted during the last semi-annual reporting period, where T_1 is less than T_2 , t_1 less than t_2 . In each HIP run, a baseline monolithic GN-10, four GN-10 matrix and four GN-10A matrix green composite samples were included according to plan. Based on the results a fifth HIP run cycle ($T_3^{\circ}\text{C}/t_2$ hr) was selected, in which T_3 is higher than T_2 . Only 20 and 30 wt% SiCw composites were fabricated for the 5th HIP run ($T_3^{\circ}\text{C}/t_2$ hr). Composites with 10 wt% SiCw were eliminated because they consistently exhibited slightly lower toughness in the previous experiments. Forty wt% SiCw composites were also eliminated, because they always exhibited lower HIP'ed density and severe warpage during HIP'ing due to lower green density.

Fracture toughness was measured by indentation for the samples HIP'ed at $T_3^{\circ}\text{C}/t_2$ hr. Table I lists these results and the earlier toughness results of the counterparts HIP'ed at $T_2^{\circ}\text{C}/t_2$ hr. Contrary to what was anticipated, the toughness values of the $T_3^{\circ}\text{C}/t_2$ hr composites were lower than those of the $T_2^{\circ}\text{C}/t_2$ hr samples. The lower toughness values could be a result of a stronger interfacial bond between the whisker and the matrix and the difference in matrix microstructure. Consequently $T_2^{\circ}\text{C}/t_2$ hr is considered the optimum HIP cycle, for achieving high toughness.

Table I
Indentation Fracture Toughness

Composites	HIP Cycle	
	$T_2^{\circ}\text{C}/t_2$ hr	$T_3^{\circ}\text{C}/t_2$ hr
20% SiCw/GN-10A	6.9+/-0.22	5.98+/-0.22
30% SiCw/GN-10A	6.3+/-0.2	5.74+/-0.21
20% SiCw/GN-10	6.3+/-0.2	5.79+/-0.44
30% SiCw/GN-10	6.5+/-0.7	5.60+/-0.25

B) Property Study

According to plan, the selected optimum HIP cycle ($T_2^{\circ}\text{C}/t_2$ hr) was used to fabricate large composite billets to enable flexural strength and chevron toughness characterizations of the selected compositions (20 and 30% SiCw). (Only small button shape samples were fabricated under Subtask 3.A) These billets have been machined into test bars and are to be tested in the next bi-monthly reporting period.

Before the determination that $T_2^{\circ}\text{C}/t_2$ hr was the optimum HIP cycle, control GN-10 and composite billets were fabricated using $T_3^{\circ}\text{C}/t_2$ hr and $T_4^{\circ}\text{C}/t_2$ hr (HIP cycles, and achieved full densities (Table II). Although these two HIP cycles are not considered optimum, mechanical property results of these materials, when combined with

those from the $T_2^{\circ}\text{C}/t_2$ hr composites, will provide a more comprehensive understanding of the relationship between HIP cycle and mechanical properties.

TABLE II
Average HIP'ed Densities
(g/cc)

Composition	HIP $T^{\circ}\text{C}/t$ hr	
	T_3/t_2	T_4/t_2
20 wt% SiCw/GN-10	3.28	3.27
30 wt% SiCw/GN-10	3.26	3.25
20 wt% SiCw/GN-10A	3.30	3.29
30 wt% SiCw/GN-10A	3.29	3.28

The room temperature 4-pt bend strength (3mm x 4mm x 50mm bar dimension) of these materials HIP'ed at $T_3^{\circ}\text{C}/t_2$ hr and $T_4^{\circ}\text{C}/t_2$ hr were completed. Table III summarizes the strength and fractography results.

TABLE III
Room Temperature MOR and Fractography Results¹

I.D. Material	SiCw Wt%	Matrix	Temp HIP	AVE MOR (ksi)	Failure Origin(%) ²		
					Surface	Internal	Incls
A ₁	0	GN-10	T ₃	109.2	100	0	0
B ₂	0	GN-10	T ₄	85.8	50	0	0
C ₁	20	GN-10	T ₃	93.3	100	0	0
D ₃	20	GN-10	T ₄	64.6	60	40	20
E	20	GN-10A	T ₃	102.5	60	40	20
F ₃	20	GN-10A	T ₄	99.0	80	20	20
G ₂	30	GN-10	T ₃	74.7	40	40	40
H	30	GN-10	T ₄	90.5	50	50	50
J ₃	30	GN-10A	T ₃	98.5	20	60	80
K ₃	30	GN-10A	T ₄	85.7	40	60	20

¹ Based on five (5) tests per material

² The surface and internal failure origins do not always add to 100% since the origins are missing from some bars. The percent of inclusion failures consists of both surface and internal.

The MOR results of the composites, excluding the two monolithic GN-10, were analyzed using Taguchi statistics, and the following are the conclusions:

(a) Strength trends

- 20 wt% whisker loading produces higher strength
- GN-10A matrix yields higher strength
- HIP Temperature has no effect on the strength of the composites.

(b) The failure origin trends:

- 30% SiCw composites have more internal and inclusion failures
- Matrix type and HIP temperature have little influence on failure origin location or type.

TASK 5 - On-Going Evaluation of Alternate Whiskers

This task was concluded (Milestone #122113). In summary, the whiskers examined were obtained from Kobe Steel (AT received 3/89 and A'T received 4/89), Tokai Carbon (TWS-400 received 2/89 and TWS-100 received 5/89), Advanced Ceramic Technologies of Somerset, NJ (Grade L7V5 received 11/89), and Keramont Corporation of Tucson, AZ (Grade 91#49-51 received 9/89). Although two of the whisker versions were more attractive than the others (Tokai TWS-400 and Kobe Steel A'T), there is no reason to expect these whiskers to offer significantly better properties than the American Matrix whiskers when incorporated into a silicon nitride matrix.

Earlier work has shown that whisker chemistry and morphology can impact both processing and properties of the composites. The preferred whiskers should have a low surface oxygen content (<20 at.%) where the oxide resembles a Si-O-C glass rather than SiO₂. Surface impurities-particularly metals such as Fe and Co - are undesirable, as they may catalyze whisker degradation during processing. The preferred whisker should have a straight morphology to avoid breakage during processing. Particulate debris should be minimized as it can limit strength. A large whisker diameter is desired for safety reasons, and the potential for enhancing mechanical properties.

All of these whiskers except the Keramont exhibited desirable surface chemistries. The Keramont whisker sample also contained a large amount of debris and displayed a wide range of diameters. The Advanced Ceramic Technologies whiskers were very straight, but had one of the smallest average diameters. The Tokai TWS-100 had a morphology that was similar to earlier versions, while the Kobe Steel AT had improved morphology. Although the Tokai TWS-400 and Kobe Steel A'T whiskers were most desirable among those evaluated in term of whisker diameter and morphology, they were judged not having the potential to produce composites with properties significantly better than those made with American Matrix whiskers.

Task 6 - Nanometer Deposition of Sintering Aids

During the previous semi-annual reporting period, silicon nitride powders coated with GN-10 sintering aids were prepared using the following methods: precipitation (two approaches), spray drying, polymerization (two approaches), and evaporation of a solution containing carboxylates. Samples were calcined in air to form the desired phases. Sintering aid content was confirmed by inductively coupled plasma atomic emission spectroscopy and sintering aid distribution in the powders was evaluated by SEM and x-ray photoelectron spectroscopy.

Gas pressure sintering was used to evaluate the effect of sintering aid dispersion on the densification of Si_3N_4 powders with GN-10 sintering aids, which were incorporated by different routes, during the present reporting period. Larger batches of two selected deposition routes (polymerization 1 and spray drying) were prepared for fabrication by slip casting and evaluation of sintering aid level on densification and mechanical properties.

Experimental and control samples of GN-10 were gas pressure sintered in nitrogen at 1900°C for six hours. Gas pressure was maintained between 200 and 300 psig during the hold at 1900°C . Samples, which were uniaxially pressed at 10,000 psi followed by isostatic pressing at 30,000 psi, were packed in a powder bed of GN-10 powder mixed with BN. Densities of these samples are listed in Table IV. Isostatically pressing the samples minimized differences in green densities. However, powders prepared by the evaporation and spray drying deposition routes formed compacts with green densities somewhat lower than the others.

Table IV.
Green and Sintered Densities of
Experimental Si_3N_4 Samples.

Sample	Green Density g/cc	Sintered Density g/cc	% Density
Control*	1.92	2.86	87%
Polym. 1	1.89	2.91	88%
Precip. 1	1.88	2.86	87%
Precip. 2	1.89	2.79	85%
Polym. 2	1.89	2.83	86%
Evaporation	1.84	2.81	85%
Spray Dried	1.80	2.78	84%

* Control = GN-10 formed by dry ball milling

Sintered densities fell in a narrow range between 84 and 88% of theoretical which is 3.30 g/cc based on rule of mixtures. Thus,

sintering aid deposition route has little effect on densification under the conditions investigated.

As discussed in the previous semi-annual report, 500 g batches of Si_3N_4 with sintering aids deposited by spray drying, polymerization 1, and ball milling (control) were prepared. All three deposition routes were used to prepare batches with three different sintering aid levels: 6, 8, and 10 wt%. The ratio of the two sintering aid components in each batch was the same as the ratio in GN-10. Green densities for slip cast plates formed from these powders are listed in Table V.

Table V.
Green Densities for Slip Cast Si_3N_4 .

Sintering Aid Deposition Route	% Sintering Aids	Green Density g/cc
Spray Dried	10%	1.81
Spray Dried	8%	1.68
Spray Dried	6%	1.79
Polym. 1	10%	1.54
Polym. 1	8%	1.64
Polym. 1	6%	1.70
Control	10%	2.11
Control	8%	2.12
Control	6%	2.07

Slip cast green plates of the control and spray dried powders were similar in quality. However, the ones with the sintering aids deposited by polymerization 1 were extremely fragile and exhibited a high tendency to crack during drying. Green densities of slip cast parts are generally related to the degree of dispersion. The lower green densities of the experimental materials compared with control were probably a result of a higher degree of powder agglomeration. Drying the solutions after depositing the sintering aids probably causes the powders to agglomerate.

Slip cast samples, which are listed in Table V, were densified by gas pressure sintering. Since our primary objective was to determine if the degree of dispersion of sintering aids had an effect on gas pressure sintering, the slip cast samples were isostatically pressed at 30,000 psi to minimize differences in green densities. After cold isostatic pressing, these materials were sintered at 1900°C for six hours. Pressure was maintained around 250 psig. A reference material with 10% sintering aids added by dry ball milling was also included in the run. This reference sample was prepared by uniaxial pressing at 10,000 psi followed by isostatic pressing at

uniaxial pressing at 10,000 psi followed by isostatic pressing at 30,000 psi. Table VI lists the green and sintered densities.

Table VI.
Green and Sintered Densities for
Slip Cast Si_3N_4 .

Deposition Route & Sintering Aid Content	Green Density (g/cc)		Sintered Density* (g/cc)	% Theoretical Density
	Slip Cast	After Isostatic Pressing (% increase)		
Control 10%	2.11	2.19	2.49	75.5
Control 8%	2.12	2.18		73.7
Control 6%	2.07	2.14	2.25	69.2
Spray Dried 10%	1.81	1.93	2.40	72.7
Spray Dried 8%	1.68	1.91	2.18	66.7
Spray Dried 6%	1.79	--	2.03	62.5
Polym. 1 10%	1.54	1.97	2.40	72.7
Polym. 1 8%	1.64	1.97	2.32	70.9
Polym. 1 6%	1.70	1.95	2.18	67.1
Reference		2.05	2.28	69.1

*Gas Pressure Sintered: 1900°C/6 h/250 psig

Isostatically pressing the slip cast samples with sintering aids deposited by spray drying and polymerization 1 significantly increased the green density. Densification decreased with decreasing sintering aid content for all three deposition routes. This trend was reasonable since the amount of liquid phase decreased with lower sintering aid content. Determination of the effect of deposition route on densification is difficult because of the differences in green densities.

Silicon nitride powders with 10, 8, and 6 wt% sintering aids deposited by spray drying and ball milling (control) were glass encapsulation HIP'ed at various temperatures. The green and HIP'ed densities are listed in Table VII where $T_2 < T_3 < T_4$.

Table VII.
Densities of Glass
Encapsulation HIP'ed Si_3N_4 .

Deposition Route & Sintering Aid Content	HIP'ed Density g/cc			Theoret- ical Density g/cc	
	Green Density g/cc	$T_2^{\circ}\text{C}$ t_1 hr 30 ksi	$T_3^{\circ}\text{C}$ t_2 hr 30 ksi		$T_4^{\circ}\text{C}$ t_2 hr 30 ksi
Spray Dried 10%	1.81	3.28		3.27	3.30
Spray Dried 8%	1.68	3.08		3.26	3.27
Spray Dried 6%	1.79	3.19			3.25
Control 10%	2.11	3.29	3.31	3.29	3.30
Control 8%	2.12		3.29	3.29	3.27
Control 6%	2.07		3.26	3.25	3.25

Full or near full density was achieved for all samples. STEM will be used to characterize microstructures and grain boundary chemistries; and modulus of rupture at room temperature and 1300°C will also be conducted.

To date test bars cut from control and spray dried billets that were glass encapsulation HIP'ed at $T_2^{\circ}\text{C}/t_1$ hr (Table VII) were tested in four-point bend at room and two elevated temperatures. Results are summarized in Table VIII.

Table VIII.
Four Point Flexural Strengths* of
Encapsulation HIP'ed Si_3N_4

Deposition Route & Sintering Aid Content	Strength (ksi)		
	23°C	1100°C	1370°C
Spray Dried 10%	118.1	62.1	50.8
Spray Dried 8%	83.7	46.6	26.8
Spray Dried 6%	108.7	45.7	--
Control 10%	102.5	66.7	43.9

* HIP'ed at $T_2^{\circ}\text{C}/t_1$ hr

Incomplete densification accounts for the lower strengths of the spray dried samples with 8 wt% sintering aids. These initial results suggest that, at 10% sintering level, the spray dried samples have higher strengths at 23 and 1370°C than the control, which were lower than expected.

Two of the samples (control and spray dried) that were glass encapsulation HIP'ed at T_1 have been examined by STEM. Grain boundary pockets, which are similar for the two samples, contained two crystalline phases. Some of the pockets in the control sample also contained a non-crystalline phase. The grain boundaries in the spray dried samples were higher in sintering aid.

In summary:

- 1) The gas pressure sintering results presented in the Feb/March 1990 Bi-monthly and this report indicated that the experimental powders prepared under this task could not achieve full density under the experimental conditions investigated. In addition, the sinterability was not influenced by the various sintering aid deposition routes.
- 2) The surface chemistry results based on XPS and SEM backscattered electron images, Feb/Mar 1990 Bi-monthly, indicated that the powder prepared by spray drying, polymerization I and evaporation techniques have better sintering aids dispersion than those by the other techniques. The evaporation technique is not desirable due to the undesired high carbon content in the powder prepared by the technique. Consequently only powders prepared by spray drying and polymerization I were selected for slip casting evaluation.
- 3) Slip casting evaluations of larger batches of powders prepared by spray drying and polymerization I indicated that the polymerization I powder was highly agglomerated and has a high tendency to cracking during drying.
- 4) The glass encapsulation HIP experiments indicated that the spray dried powder can be HIP'ed to near full density in the temperature range of $T_2 - T_4$ °C. Therefore, spray drying was selected as the sintering aids deposition route and glass encapsulation HIP was selected as the densification technique for preparing an additional large batch of powder for more detailed characterization (Milestone #122114).

The final stage of this Task involves scale-up of the spray drying deposition method and in-depth characterization of materials prepared from the scale-up larger batches. A 3000 g batch of Si_3N_4 with 10 wt% sintering aids deposited by spray drying has been prepared. A control batch has also been prepared by wet ball milling Si_3N_4 with the particulate sintering aids followed by spray drying. The control batch was spray dried in order to minimize differences between the powders due to agglomerate formation by spray drying. These powders will be slip cast and densified by glass encapsulation HIP'ing.

Task 7 - In Process Characterization/Control During Drying of Cast Ceramic Parts

Initial work, discussed in the previous Semi-Annual Report, was focussed in four areas 1) baseline properties of green ceramics, 2) ultrasonic coupling method investigations, 3) facilities development, and 4) automated measurement methods. In summary, compressional wave velocities fell between 1.50 and 1.56 km/sec in dried Si_3N_4 pieces with densities of 1.97 g/cc. Attenuation at 10 megahertz was low suggesting that penetration of several inches is possible. Shear wave velocities for similar pieces fell between 0.99 and 1.02 km/sec. After saturating the piece with water, compressional wave velocity attenuation at 10 megahertz increased more than 40 dB. Shear wave velocity decreased from 1.018 km/sec for the dry sample to 0.913 km/sec for the saturated sample while attenuation increased 30 dB. This change is large in light of the expectation of measuring velocity to a precision of a few tenths of a percent.

A high viscosity organic based couplant provided sufficient stability for measurements of several days. Other methods for coupling the transducer to porous green pieces caused the signals to become unstable after a few hours. Polyvinylidene fluoride transducers, which are sufficiently sensitive to act as ultrasound receivers in the megahertz range, have the ability to conform to curved surfaces. Thus, they have the potential for monitoring complex shapes.

The Matec MBS 8000 was modified for continuous automated measurement over extended time periods. A humidity chamber was assembled that maintains constant humidity while sound velocity, attenuation, and weight loss are measured.

Ultrasonic velocity measurements of a series of dry, green castings ranging in density from 1.73 gm/cc to 2.15 gm/cc were completed. Ultrasonic velocities correlate well with the density and vary from 1.36 km/sec to 1.81 km/sec over this range. Over this density range four 2"x3"x.5" plates were examined to determine the spatial uniformity of sonic velocity. In all cases the spatial variations were less than 1.5% with the average deviation from the mean of 1%.

Drying experiments were performed in a controlled humidity/drying chamber. Sound velocity and attenuation were measured as a function of time after saturated specimens were placed in the drying chamber. Drying time at constant humidity was related to moisture content by monitoring weight loss as a function of time.

To relate sound velocity to moisture content, early experiments were conducted on plates that were initially dried then rewetted to produce samples with known moisture content. The sonic velocity, both shear and longitudinal, increased with decreasing moisture

content. Specifically, in previously dried and rewet samples, the first 6 percent weight gain is accompanied by a 7 to 8 percent decrease in both shear and compressional velocity. Little change was observed in the sonic velocity for weight gains above 6%. These results suggest sonic methods are capable of measuring moisture content in 0 to 6% range. A one percent moisture gain yields a 1.1% decrease in sonic velocity. For moisture contents greater than six percent the sensitivity is poor. These experiments on rewetted samples were used to establish baseline material properties and operating parameters. The next step was to continuously monitor the drying of freshly cast specimens.

Sound velocity as a function of moisture content for freshly cast specimens is shown in Figure 1. The sonic velocity variations in slip cast components appears to be much more complicated than originally thought. Initial results obtained by rewetting of "dry" samples showed a monotonic increase in sonic velocity with moisture loss. In contrast, the variation observed in freshly cast ceramics is complex. Sonic velocity initially drops with moisture loss, reaches a minimum, and then increases as the sample dries. The "double valued" relationship between sonic velocity and the moisture content makes this method unsuitable as a moisture sensor.

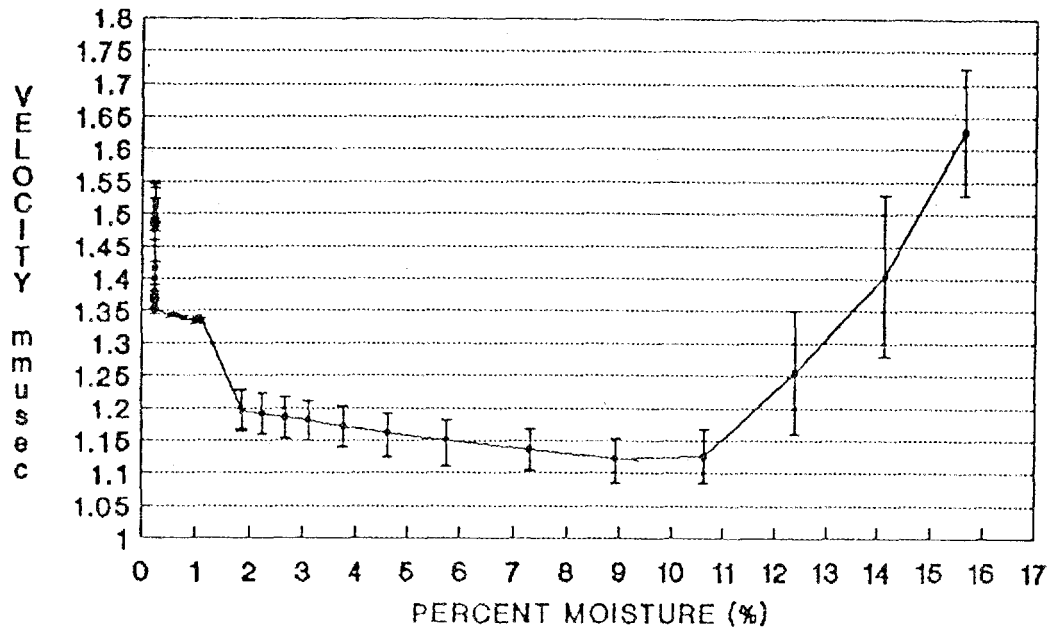


Figure 1 Sound Velocity as a Function of Moisture Content for Freshly Cast Specimen.

The attenuation of these freshly cast specimens was initially quite high. As the sample dried, it decreased more than 30 dB and then appeared to stabilize. This characteristic drying curve (sound

velocity and attenuation vs. moisture content) has been reproduced in several additional experiments. The velocity variation with moisture content change is much larger than that found with the rewetted samples (25% vs. 8%).

The final conclusion on the Matec MBS 8000's ability to automatically measure the changing velocity as a function of moisture content, is that it will not work with our application. The change of velocity in the sample is too great for the MBS 8000 to follow. Also the echo trains through the silicon nitride sample are too distorted for the MBS 8000 to accurately measure the transit time with any reliability.

Finite Element Analysis of ceramic bars during drying will be performed to determine the stresses during drying. Moisture content, bend strength, and shrinkage coefficients are being measured for the model. Previous results on rewetting of dried ceramic castings showed no measurable expansion. Work has begun on measuring shrinkage of fresh castings as they dry. To determine strength of green ceramics as a function of moisture content we will cast flexure bars and conduct 3-point bend tests. Work continues on extracting diffusion coefficients from weight loss data.

STATUS OF MILESTONES

Milestones No. 122113 (Completion of Alternate whisker evaluation) and No. 122114 (Determination of densification process and cycle for powders with nanometer deposited sintering aids) have been completed as scheduled in this reporting period.

Milestone 122115, (complete feasibility of in-process characterization and process control of casting ceramic parts) will be delayed to Dec. 10, 1990. New schedule is being prepared to be incorporated into the new contract modification deleting Task 3.C and Task 4.

PROBLEMS ENCOUNTERED

The delay in milestone 122115 was mainly caused by shortage of manpower due to the change of responsibility of the principal investigator for this milestone.

PUBLICATIONS

K. R. Karasek, S. A. Bradley, J. T. Donner, H. C. Yeh, "SiC-Whisker Characterization: An Update," Paper 20-SIV-90 presented at the 92nd Annual Meeting of The American Ceramic Society, Dallas, Texas. April 24, 1990.

Fabrication of Si₃N₄/SiC Composites by Transient Liquid Phase Sintering
S. D. Nunn and T. Y. Tien (The University of Michigan)

Objective/Scope

The goal of this project is to obtain dense silicon nitride composites containing silicon carbide whiskers by transient liquid phase sintering. The systems SiAlON, SiAlON-Garnet (Y₃Al₅O₁₂) and SiAlON-Cordierite (Mg₂Al₄Si₅O₁₈) were selected for this study. An additional system, SiAlON-N-phase (MgAl₂Si₄O₆N₄), was later added to the study. Mixtures of the starting materials form a sufficient amount of liquid to aid densification at the sintering temperatures. After sintering, the amorphous intergranular phase can be crystallized by heat treatment.

Technical Progress

1.0 INTRODUCTION

The physical properties of 20 vol.% SiC whisker reinforced Si₃N₄ composites prepared using two different liquid phase sintering aids were described in the last report¹. The composites were hot pressed at 1700°C for either 0.5 or 3 hours and a portion of the samples were subsequently heat treated at 1350°C for 20-22 hours to crystallize the grain boundary phase. The two sintering aids used were N-phase (MgAl₂Si₄O₆N₄) and YAG (Y₃Al₅O₁₂). Both have been found to be effective sintering aids for pressureless sintering of SiC whisker reinforced Si₃N₄ and both phases have been crystallized by heat treatment after sintering.² Test samples were prepared to compare the effects on mechanical properties of variations in the thermal expansion coefficient mismatch between the intergranular phase and the matrix grains and reinforcing whiskers.

The fracture strength values for these composites were quite uniform for all of the as-fired composites at about 800 MPa and always decreased after heat treatment. The decrease varied from 11 to 35% and showed a clear dependence on the amount of sintering aid in the composition, the greater the sintering aid content the greater the loss. The β₁₃-SiAlON-N-phase compositions showed the greatest percent change in strength after heat treatment with losses of 30 - 35%.

The fracture toughness values ranged from 3.11 to 5.44 MPa√m. For the as-fired samples, the toughness was significantly higher (15 - 25%) for the composites containing YAG as the sintering aid. After annealing, all of the samples showed a decrease in the measured fracture toughness. The loss in toughness was greater for the samples sintered with YAG (up to 33%) and also depended on the amount of sintering aid in the composition. The higher the amount of sintering aid, the greater the loss in toughness.

During this reporting period the microstructures of the test samples having a β₁₃-SiAlON matrix and different levels of sintering aid additive were evaluated to establish the relationships between the observed microstructures and the measured mechanical properties.

2.0 EXPERIMENTAL

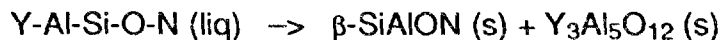
The microstructural characteristics of the SiC whisker reinforced Si₃N₄ composites were evaluated using a scanning electron microscope (SEM). Fracture surfaces of test bars and polished sections were examined. In the samples containing YAG as the sintering aid, the yttrium-containing phase was easily distinguished in the polished sections because of the high mass number of yttrium compared to the other elements present in the samples. The intergranular phase in the samples containing N-phase had a lower hardness than the SiC and Si₃N₄ phases and was readily distinguishable in the SEM due to topographical relief after polishing. The amount of the intergranular phase was measured by quantitative stereology using the point count method.

3.0 RESULTS AND DISCUSSION

Examination of the fracture surfaces indicated that samples with the higher fracture toughness values showed a predominantly intergranular fracture mode with evidence of crack deflection and whisker bridging. The low toughness samples showed an increased level of transgranular fracture with little crack deflection. Additionally, some shrinkage pores were observed in the heat treated samples. Glass compositions in the Y-SiAlON and the Mg-SiAlON systems have been shown to have a density which is less than that of YAG and N-phase, respectively.³⁻⁵ Volume changes during crystallization may account for the presence of shrinkage pores.

SEM examination of polished sections of samples of the β₁₃-SiAlON (Si₅AlON₇)-YAG composites in the as-fired and annealed condition showed substantial changes in the microstructure after heat treatment. The as-fired samples showed a continuous intergranular phase isolating individual Si₃N₄ grains and SiC whiskers. After heat treatment, the amount of the intergranular phase was reduced and no longer formed a continuous "matrix." The differences between the nominal sintering aid additions and the measured values before and after heat treatment are summarized in Table 1, along with the corresponding fracture strength and fracture toughness values.

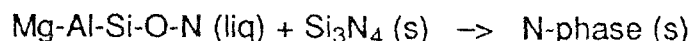
The change in the amount of the intergranular phase can be understood by referring to the β-SiAlON-YAG phase diagram shown in Fig. 1. The compositions which were studied are indicated by the points Y12 and Y6 in the figure. A simple lever rule calculation shows that the amount of liquid phase which is in equilibrium with β₁₃-SiAlON at the hot pressing temperature is substantially greater than the amount of the sintering aid (YAG) addition. Heat treatment results in the formation of additional β-SiAlON plus crystalline YAG according to the following reaction:



thus reducing the amount of the intergranular phase. The difference between the nominal sintering aid addition and the amount measured after heat treatment indicates incomplete crystallization of the liquid phase. Cracks produced by Vickers indentations tended to propagate along the intergranular

phase in the as-fired sample, but showed more transgranular fracture in the heat treated sample.

SEM examination of the samples sintered with N-phase showed that the amount of the intergranular phase in the as-fired samples was less than the nominal sintering aid addition and that there was a small increase in the amount of the intergranular phase after heat treatment. These results, which are also summarized in Table 1, are consistent with the fact that the N-phase compound melts incongruently to form β - Si_3N_4 plus a liquid phase. This is shown in the schematic pseudo-binary phase diagram of a system containing Si_3N_4 and N-phase in Fig. 2. The compositions studied are indicated by the lines marked N6 and N12 in the diagram. At the hot pressing temperature, these compositions are in the Si_3N_4 plus liquid two-phase field. Rapid cooling prevents the crystallization of N-phase in the as-fired samples. During heat treatment at 1350°C the liquid phase plus a portion of the Si_3N_4 form crystalline N-phase according to the following reaction:



reducing the total amount of the Si_3N_4 phase and increasing the amount of the intergranular phase. The amount of intergranular phase present after heat treatment is considerably less than the nominal sintering aid addition and indicates incomplete crystallization.

4.0 CONCLUSIONS

The mechanical properties of 20 vol.% SiC whisker reinforced Si_3N_4 composites which were prepared using two different sintering aid additives show variations which can be correlated with microstructural characteristics. The samples show a reduction in fracture strength after heat treatment to crystallize the grain boundary phase. This strength loss can be accounted for by the formation of shrinkage pores which form due to volume reduction when the glassy intergranular phase transforms to a crystalline phase. The fracture toughness appears to be controlled by the ability of cracks to propagate along the intergranular phase. Samples containing a high volume fraction of continuously interconnected intergranular phase showed the highest fracture toughness values.

Status of Milestones

On schedule.

Publications

None.

References

1. S. D. Nunn and T. Y. Tien, "Pressureless Sintering of $\text{Si}_3\text{N}_4/\text{SiC}$ Whisker Composites," Semi-annual report submitted to ORNL under Contract No. SC-19X-SA125C, April, 1990.

2. S. D. Nunn and T. Y. Tien, "Fabrication of $\text{Si}_3\text{N}_4/\text{SiC}$ Composites by Transient Liquid Phase Sintering," Semi-annual report submitted to ORNL under Contract No. SC-19X-SA125C, October, 1989.

3. R. E. Loehman, "Preparation and Properties of Yttrium-Silicon-Aluminum Oxynitride Glasses," *J. Am. Ceram. Soc.*, **62** [9-10] 491-94 (1979).

4. J. Homeny and D. L. McGarry, "Preparation and Mechanical Properties of Mg-Al-Si-O-N Glasses," *J. Am. Ceram. Soc.*, **67** [11] C225-27 (1984).

5. T. Hayashi and T. Y. Tien, "Formation and Crystallization of Oxynitride Glasses in the System Si, Al, Mg/O, N," *Yogyo-Kyokai-Shi*, **94** [1] 54-62 (1986).

6. H. Honke and T. Y. Tien, "Solid-Liquid Reactions in Part of the System Si,Al,Y/N,O," *Progress in Nitrogen Ceramics*, F. L. Riley, ed., pp. 101-110, Martinus Nijhoff, The Hague, 1983.

Table 1. Sintering aid content of 20 vol.% SiC whisker reinforced β - Si_3N_4 .

Sample	Heat Treatment	Sintering Aid Content		Fracture Toughness (MPa√m)	Fracture Strength (MPa)
		Nominal (Vol.%)	Measured (Vol.%)		
B13-12YAG	As-Fired 1700 C	12.0	19.1	4.92	832
	Annealed 1350 C	12.0	15.0	3.32	631
B13- 6YAG	As-Fired 1700 C	6.0	12.7	4.75	832
	Annealed 1350 C	6.0	7.4	3.81	715
B13-12N	As-Fired 1700 C	24.8	8.0	3.82	777
	Annealed 1350 C	24.8	11.0	3.11	503
B13- 6N	As-Fired 1700 C	12.6	3.0	3.56	837
	Annealed 1350 C	12.6	3.5	3.33	589

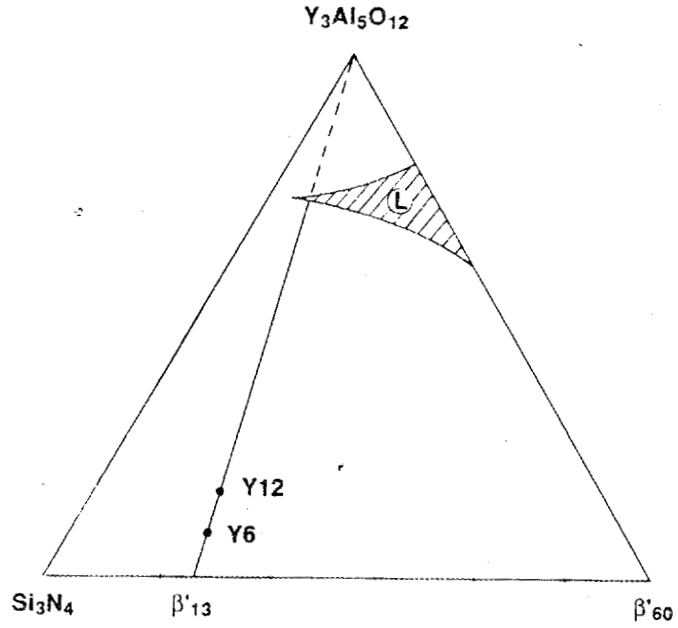


Figure 1. Weight percent representation of the phase diagram of the β - Si_3N_4 -YAG system showing the approximate location of the liquid field at 1700°C. (Adapted from Honke and Tien.⁶)

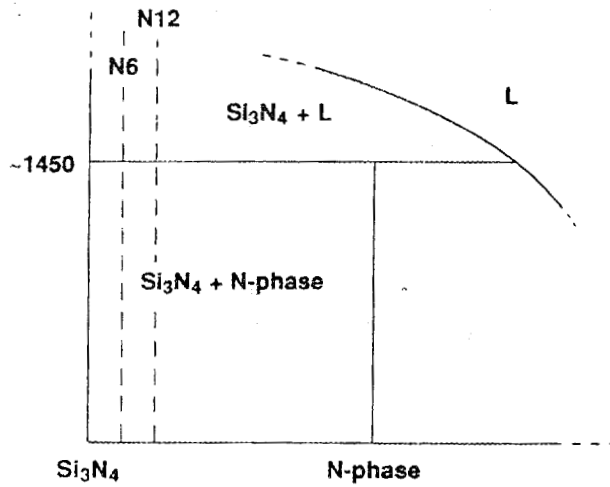


Figure 2. Schematic pseudo-binary phase diagram containing the join between β - Si_3N_4 and N-phase ($\text{MgAl}_2\text{Si}_4\text{O}_6\text{N}_4$) illustrating incongruent melting of the N-phase compound.

FABRICATION OF SiC-ALN COMPOSITES

G. E. Hilmas and T. Y. Tien
(The University of Michigan)

Objective/Scope

The goal of this project is to obtain dense SiC-ALN composites containing ALN-polytypoid phases(s) as a dispersed second phase. ALN-polytypoids (8H, 15R, 12H, 21R and 27R) form as elongated rod-like or platelet-like grains and are stable at high temperatures potentially producing an in-situ reinforcement phase in advanced composites. Hot-pressing was selected for this study to optimize densification at high temperatures.

Technical Progress

1.0 INTRODUCTION

The crystal structures and compositions of ALN-polytypoids have been identified in detail [1,2]. ALN-polytypoids (8H,15R, 12H, 21R and 27R) have been shown to form as elongated rods or platelets with oxide additions to ALN. ALN-ceramic with a fibrous microstructure of 27R polytypoid has been fabricated using $\text{SiO}_2/\text{Y}_2\text{O}_3$ additives [3,4].

From the behavior diagram of the SiAlON system (Figure 1), it can be seen that the compositions of the ALN-polytypoids are restricted to the ALN-rich area. The compositions for these polytypoids and their respective constant cation/anion ratio are represented in Table 1 from Gauckler et al. [2]. The polytypoids prepared in this study have been from two of the SiAlON subsystems, either ALN- Al_2O_3 - SiO_2 or ALN- Al_2O_3 which requires higher temperatures to form the polytypoids [5]. The subsystem ALN- Si_3N_4 - Al_2O_3 has been ignored due to difficulties in sintering.

SiC was chosen as the matrix phase for this composite. The transformation of β -SiC (3C) at high temperature to one or more of the α -SiC polytypes (2H, 6H, 15R, 21R, etc.) has been investigated extensively with the results showing that the transformation and the resulting α -polytype formed is strongly affected by the sintering agents and chemical environment [6]. β -SiC (3C) has also been shown to preferentially transform to α -SiC (2H) in the presence of ALN (2H). These phases then react above 2050 °C to form an extensive solid-solution with the wurtzite structure in the range of 35 to 100 weight percent ALN [7,8]. The formation of this solid-solution by reaction of α -SiC (2H) matrix and ALN-polytypoids have been evaluated in this study.

2.0 EXPERIMENTAL

2.1 Powder Preparation

The ceramic raw materials used in this study are SiC, AlN, Al₂O₃ and SiO₂. The starting SiC powder was either β -SiC (3C) (Hermann C. Starck, >95% β -SiC) or α -SiC (6H) (Hermann C. Starck, >97.5% α -SiC). The AlN-polytypoids studied (15R, 12H and 21R) were either formed from SiO₂, Al₂O₃ and AlN (labeled as type "I") or from Al₂O₃ and AlN (labeled as type "II").

During processing, the raw powders used to form the matrix and polytypoid dispersed second phase were attrition milled for 3 hours using isopropyl alcohol and porcelain milling media. The powders were then oven dried at 85 °C and stored in polyethylene bottles.

2.2 Hot-Pressing

In preparation for hot-pressing, the milled and dried powder was placed in a graphite die that was lightly coated with boron nitride powder (to reduce bonding of the SiC to the die during hot-pressing at high temperatures). The powder was cold-pressed isostatically in the die under a 150 kg/cm² load and then placed in a graphite resistance furnace, heated under "static" nitrogen to 2050 - 2150 °C and held for 1 hour. A 240 kg/cm² load was applied during the heating cycle above 1000 °C and released upon cooling below 1000 °C.

2.3 Electron Microscopy (TEM and SEM)

TEM was performed on a JEOL 2000 FX microscope at 200 kV. The TEM specimens were prepared using standard ceramographic techniques. First, 3 mm diameter disks were ultrasonically cut from 1 mm thick slices of the specimen and ground and polished to 100 μ m before dimpling to 20 μ m center thickness. Final polishing and dimpling was done with 2-4 μ m diamond paste. Ion milling to perforation was performed using 6 kV Ar⁺ ions. SEM was performed on a Hitachi S-800 operating at 5 kV.

2.4 Mechanical Properties

Sections of the hot-pressed samples were machined and then ground and polished down to a 1 μ m diamond paste finish in order to measure microhardness and fracture toughness. A standard Vickers diamond indenter was placed in a Wilson Tukon microhardness testing machine for all measurements. Indentation loads varied from 5 to 25 kg depending upon the sample and to fulfill the requirement that the radial/medial

cracks (2c) be equal to or greater than twice the Vickers indentation diagonal (2a). After measurements of (2c) and (2a) for a minimum of five indentations per sample, the following equations were used to calculate microhardness and fracture toughness [9]:

$$H = [2P(\sin 68^\circ)]/(2a)^2 \quad (\text{in GPa})$$

$$K_{IC} = 0.016(E/H)^{0.5}(P/c^{1.5}) \quad (\text{in MPa}\sqrt{\text{m}})$$

where P=load (N) and E=Young's Modulus (GPa). Poisson's ratio and Young's modulus were measured separately for each sample by non-destructive acoustic pulse-echo methods.

3.0 RESULTS AND DISCUSSION

3.1 Formation of AlN Polytypoids

Using the same powder preparation techniques, two samples of "pure" polytypoid (21R-I and 12H-I, respectively) were hot-pressed to theoretical density at 1800 °C for 1 hour. They were subsequently examined by transmission electron microscopy to observe the morphology of the polytypoid grains.

Figure 2 shows a bright-field TEM image of the general microstructure of dense 21R-I polytypoid. The microstructure contains elongated (rod-like or platelet-like) polytypoid grains that have preferentially grown perpendicular to the hot-pressing direction. The grains are heavily faulted, and more detailed bright-field examination of a $[2\bar{1}\bar{1}0]$ plane reveals the layered atomic stacking structure that makes up the polytypoid grains (Figure 3). The 32.8 Å spacing gives the c-axis repeat distance for this 12H-polytypoid grain.

3.2 Initial Study of SiC-AlN Polytypoid Composites

Initial compositions were either 80 vol% SiC : 20 vol% AlN-polytypoid or 50 vol% SiC : 50 vol% AlN-polytypoid while varying both the starting matrix powder (β -SiC (3C) or α -SiC (6H)) and the AlN-polytypoids being formed (15R, 12H and 21R). These samples were prepared in order to evaluate the feasibility of improving the mechanical properties of a SiC matrix with dispersed AlN-polytypoid additions. Mechanical properties results for a set of these samples showed mild increases in fracture toughness in the range of 4 to 5 MPa $\sqrt{\text{m}}$ in comparison to \sim 2.7 MPa $\sqrt{\text{m}}$ for a β -SiC standard sample.

X-ray diffraction results on these samples also yielded some valuable information. Using β -SiC as the matrix phase: From 2050 °C to 2150 °C the β -SiC (3C) matrix gradually transformed; (1) to α -SiC (2H) for compositions of 50 vol% SiC : 50 vol%

AlN-polytypoid, and (2) to both α -SiC (2H) and α -SiC (6H) for compositions of 80 vol% SiC : 20 vol% AlN-polytypoid. Shifts in the (100) and (002) peaks of the α -SiC (2H) phase suggest that it is reacting with AlN (2H) to form a SiC-AlN (2H) solid-solution (wurtzite structure) above 2050 °C. Using α -SiC (6H) as the matrix phase: α -SiC (6H) remained up to 2150 °C along with formation of the respective polytypoids. There is no evidence for the transformation of α -SiC (6H) to α -SiC (2H) and therefore no SiC-AlN solid-solution in these samples.

Several notes should be made concerning the x-ray results. Temperatures near 2150 °C have resulted in an increase in the formation of free Si, a decomposition product, suggesting the need for higher nitrogen overpressures to suppress decomposition reactions. The formation of the solid-solution by reaction of α -SiC (2H) and AlN-polytypoids at these high temperatures will be continuously evaluated in this study particularly in regard to optimization of the microstructure in the composites. Also, more than one polytypoid was usually formed in each of the compositions evaluated. This is again due to the close proximity of the polytypoid compositions to each other (Figure 1).

3.3 β -SiC:21R(II) Polytypoid Series

In this second step a series of β -SiC samples were prepared with a decreasing percentage of AlN-polytypoid in order to characterize changes in the microstructure. The AlN-polytypoid chosen was 21R-II. Table 2 lists the starting compositions for these samples which were hot-pressed for 1 hour at 2100 °C under “static” nitrogen and 240 kg/cm² of applied pressure.

The microstructure of these samples was observed using the scanning electron microscope. Since SiC is already a good conductor, it was believed that contrast could be obtained between SiC and any AlN-polytypoid grains by taking advantage of the insulating properties of AlN phases which will “charge” under the electron beam. It was determined for samples BS50:21R(II), BS60:21R(II) and BS70:21R(II) that the general microstructure was very fine-grained and equiaxed with no elongated AlN-polytypoid formation. X-ray diffraction revealed that the β -SiC (3C) had transformed to α -SiC (2H) and subsequently formed a 2H solid-solution with AlN (2H), thus leaving no AlN to form the AlN-polytypoid. Sample BS80:21R(II) contained a majority of elongated grains that exhibited “no charging”. X-ray diffraction showed the matrix phase to contain both β -SiC (3C) and α -SiC (6H) along with a small amount of 21R-polytypoid second phase that was not observed in the SEM. Sample BS90:21R(II) showed the most drastic change in microstructure, containing both an elongated α -SiC (6H) matrix and an

elongated 21R-polytypoid dispersed second phase that did indeed exhibit “charging” under the electron beam (Figure 4).

The results of mechanical properties measurements for these samples are summarized in Table 3. The most interesting results from this data are the fracture toughness values, especially for sample BS90-21R(II). The β -SiC standard is typical of a hot-pressed SiC material producing a fine-grained equiaxed microstructure with an indentation fracture toughness in the range of 2.5-3.0 MPa- \sqrt{m} . The samples BS50-21R(II), BS60-21R(II) and BS70-21R(II) had similar fracture toughness values that were indicative of their fine-grained equiaxed microstructures. Sample BS80-21R(II) had a higher fracture toughness of 5.3 MPa- \sqrt{m} . This can be attributed to the partial β -SiC (3C) to α -SiC (6H) transformation resulting in an elongated SiC microstructure causing cracks to take a more tortuous path through the matrix. The BS90-21R(II) sample had a fracture toughness of 8.5 MPa- \sqrt{m} . Upon observation of indentation produced radial cracks in the SEM, it was apparent for this sample that the elongated 6H-SiC matrix may have caused some crack deflection and crack bridging. Nevertheless, the cracks still passed through many of these SiC grains but would not pass through the 21R-polytypoid grains (Figure 5). The two arrows in the figure show where a radial crack has run straight into two different 21R-polytypoid grains but was deflected along the long axis of their interface before continuing on.

4.0 SUMMARY

Formation of AlN-polytypoids by solid-state reaction of AlN-SiO₂-Al₂O₃ and/or AlN-Al₂O₃ has been achieved. SiC-AlN polytypoid composites have been prepared, by hot-pressing at 2050-2150 °C, from direct SiC, AlN, SiO₂ and Al₂O₃ powder mixtures. TEM results emphasized that the AlN-polytypoids grow as elongated “rod-like” or “platelet-like” grains. Mechanical property data has shown improvements in fracture toughness over pure hot-pressed β -SiC(standard) materials. A fracture toughness of 8.5 MPa- \sqrt{m} has been achieved for a sample that is 90 volume% SiC with 10 volume% AlN-polytypoid as a dispersed second phase.

Status of Milestones

On Schedule.

Publications

None.

References

- [1] D. P. Thompson, P. Korgul and A. Hendry, "The Structural Characterization of SiAlON Polytypoids" in "Progress in Nitrogen Ceramics" (Edited by F. L. Riley), NATO ASI Series. Series E: Applied Sciences-No. 65, pp. 61-74, 1983.
- [2] L. J. Gauckler, H. L. Lukas and G. Petzow, "Contribution to the Phase Diagram $\text{Si}_3\text{N}_4\text{-AlN-Al}_2\text{O}_3\text{-SiO}_2$," *J. Am. Ceram. Soc.*, **58** [7] 346-347 (1975).
- [3] K. Komeya, H. Inoue and A. Tsuge, "Role of Al_2O_3 and SiO_2 Additions in Sintering of AlN," *J. Am. Ceram. Soc.*, **57** [9] 411-412 (1974).
- [4] K. A. Schwetz, H. Knoch and A. Lipp, "Sintering of Aluminum Nitride with Low Oxide Addition" in "Progress in Nitrogen Ceramics" (Edited by F. L. Riley), NATO ASI Series. Series E: Applied Sciences-No. 65, pp. 245-252, 1983.
- [5] J. W. McCauley and N. D. Corbin, "High Temperature Reactions and Microstructures in the $\text{Al}_2\text{O}_3\text{-AlN}$ System," *ibid.*, pp. 111-118, 1983.
- [6] S. Shinozaki and K. R. Kinsman, "Evolution of Microstructure in Polycrystalline Silicon Carbide," Proceedings of Crystalline Ceramics; Edited by Hayne Palmer III, R. F. Davis, and T. M. Hare, pp. 641, 1978.
- [7] R. Ruh and A. Zangvil, "Composition and Properties of Hot-Pressed SiC-AlN Solid Solutions," *J. Am. Ceram. Soc.*, **65** [5] 260-265 (1982).
- [8] W. Rafaniello, "Fabrication and Characterization of Silicon Carbide Alloys: The Silicon Carbide-Aluminum Nitride System"; A PhD dissertation, The University of Utah, June, 1984.
- [9] G. R. Anstis, P. Chantikul, B. R. Lawn and D. B. Marshall, "A Critical Evaluation of Indentation Techniques for Measuring Fracture Toughness: I. Direct Crack Measurements," *J. Am. Ceram. Soc.*, **64** [9] 533-543 (1981).

Table 1. Compositions of AlN-Polytypoids

Phases	x	c+/a-	Formula
8H	5	3/4	SiAl ₅ O ₅ N ₃
15R	4 . . . 5	4/5	Si _{6-x} Al _{2+x} O _x N _{10-x}
12H	4.5 . . . 6	5/6	Si _{6-x} Al _{4+x} O _x N _{12-x}
21R	4.5 . . . 6	6/7	Si _{6-x} Al _{6+x} O _x N _{14-x}
27R	0 . . . 6	8/9	Si _{6-x} Al _{10+x} O _x N _{18-x}

Table 2. Compositions of β -SiC : 21R-II Polytypoid Series

Sample	volume % β -SiC	volume % 21R-II
BS50:21R(II)	50	50
BS60:21R(II)	60	40
BS70:21R(II)	70	30
BS80:21R(II)	80	20
BS90:21R(II)	90	10

Table 3. Mechanical Properties of β -SiC-21R(II) Polytypoid Composites

Sample [†]	ν	E (GPa)	H (GPa)	K _{IC} (MPa \sqrt{m})
β -SiC(Standard)*	0.18	437	22.8 \pm 0.7	2.7 \pm 0.2
BS90:21R(II)	0.18	428	14.8 \pm 1.0	8.5 \pm 0.6
BS80:21R(II)	0.19	403	18.6 \pm 0.5	5.3 \pm 0.3
BS70:21R(II)	0.18	406	20.7 \pm 0.6	2.8 \pm 0.1
BS60:21R(II)	0.19	394	21.6 \pm 0.6	2.9 \pm 0.2
BS50:21R(II)	0.19	368	20.3 \pm 0.8	2.7 \pm 0.2

* Hot-pressed at 2000 °C with 1 wt.% B and 1 wt.% C added as sintering aids.

† All samples contain 0.5 wt.% B added as a sintering aid.

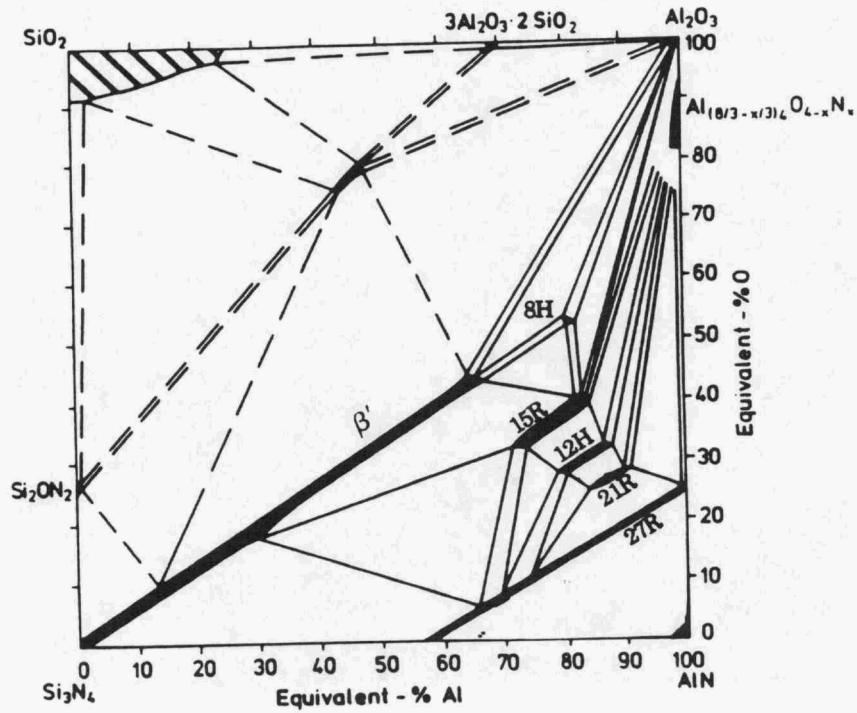


Figure 1. Isothermal section $\text{Si}_3\text{N}_4\text{-AlN-Al}_2\text{O}_3\text{-SiO}_2$ of the system Si-Al-O-N at 1760 °C.

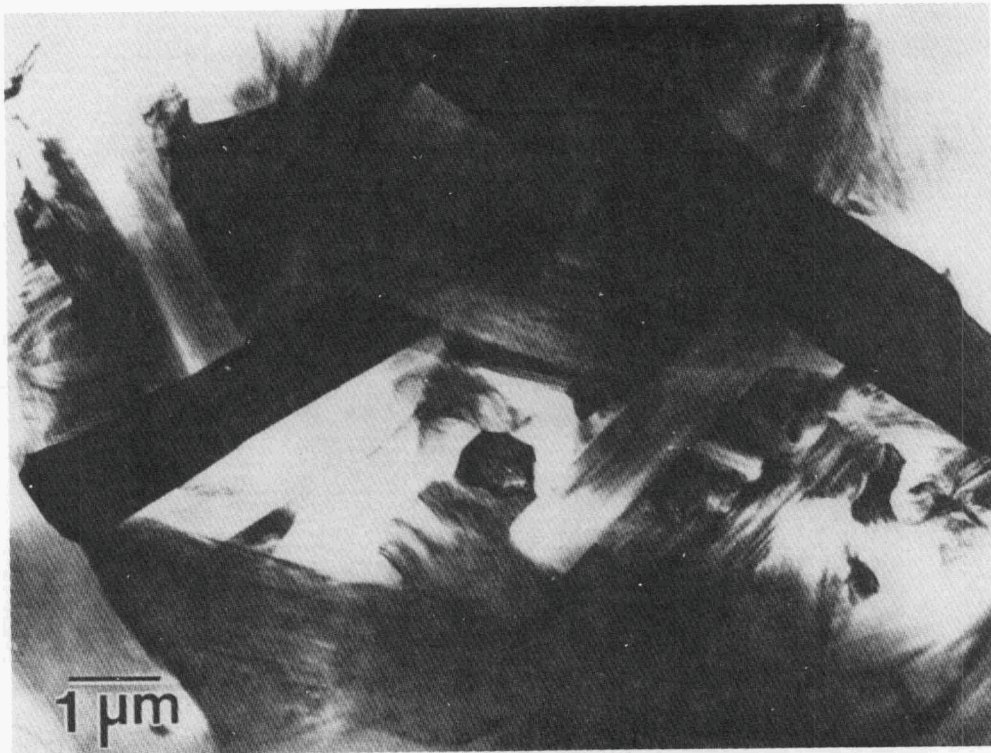


Figure 2. Bright-field TEM image showing the general microstructure of dense 21R-I polytypoid.



Figure 3. Bright-field TEM image showing the layered stacking sequence in the [2110] plane of a 21R-polytypoid grain. Spacing between arrows represents 32.8 Å.

90 vol% β -SiC : 10 vol% 21R-Polytypoid

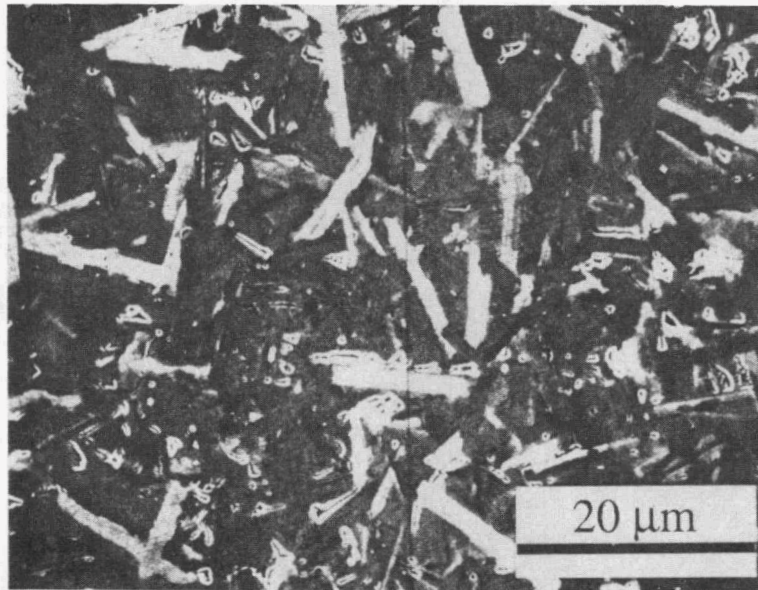
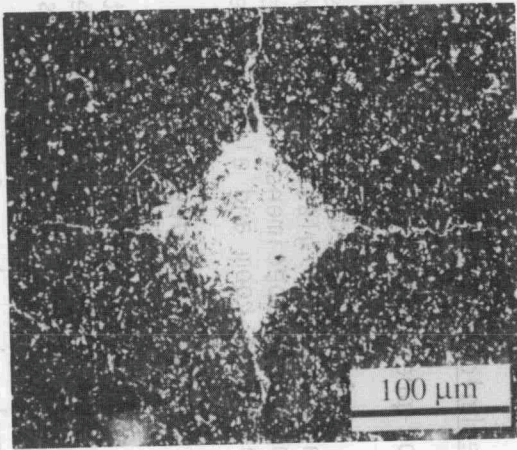


Figure 4. SEM micrograph of the microstructure of BS90:21R-II. AlN-polytypoid grains are "charged" by the electron beam providing bright contrast.

VICKERS INDENT - 20kg LOAD



Figure 5. Radial crack produced by a 20 kg indentation (below) in BS90-21R(II)



1.2.3. Oxide Matrix

Dispersion-Toughened Oxide Composites

T. N. Tiegs, P. F. Becher, W. H. Elliott, D. J. Kim, and D. W. Coffey
(Oak Ridge National Laboratory)

Objective/scope

This work involves development and characterization of SiC whisker-reinforced ceramic composites for improved mechanical performance. To date, most of the work has dealt with alumina as the matrix because it was deemed a promising material for initial study. However, an effort in SiC whisker-reinforced silicon nitride and sialon is in progress. In addition, studies of whisker growth processes were initiated to improve the mechanical properties of SiC whiskers by reducing their flaw sizes. In-situ acicular grain growth is also being investigated to improve fracture toughness of silicon nitride materials.

Technical highlights

Hot-pressed silicon nitride and sialon-SiC whisker composites

As reported previously, samples of various compositions, where the intergranular-glass phases were modified, have been fabricated and machined into test specimens. At the present time they are being flexural-strength tested at room and elevated temperature.

Microstructure development

The series of silicon nitride materials to assess the role of elongated-grain microstructure on fracture toughness has been fabricated and is being machined into test specimens. The compositions and hot-pressing conditions are given in Table 1. In addition, supplemental samples have been fabricated where the hot-pressing has been stopped at intermediate densities. From these specimens we will determine the microstructure development by x-ray diffraction and electron microscopy. The effect of additive composition on the hot-pressing behavior is shown in Fig. 1. The densification rates are dependent on the viscosities of the glass phases that are formed during the reaction of the sintering aids with the silicon nitride. As shown and expected, the least refractory is 8% La₂O₃-2% Al₂O₃ and the most refractory is 8% Y₂O₃. The differences in densification and subsequent grain growth is also reflected in the resulting microstructures. Hot-pressing of the initial samples at 1725°C for 60 min was held minimal to obtain high-density materials for the less refractory compositions. Densities achieved were > 98% T.D. for these samples and SEM examination of fracture surfaces showed relatively small grain sizes less than 0.4 μm for all samples. Only minor differences in the fracture surface microstructures were observed between samples fabricated with these conditions. The two additional series fabricated by hot-pressing at 1800°C for times of 90 and 180 min had fracture surfaces that revealed extensive grain growth with the higher hot-pressing temperatures and longer hold times (Figs. 2 and 3). At the present time, we are

Table 1. Test matrix of silicon nitride materials to determine microstructure development

Composition	Hot-Pressing Conditions (°C/min)				
	1725/60	1800/90	1800/180	1650/60 1800/90	1900/90
6% Y ₂ O ₃ -2% Al ₂ O ₃	Yes	Yes	Yes	Yes	Yes
6% Y ₂ O ₃ -2% Al ₂ O ₃	Yes	Yes	Yes		Yes
GN-10 Additives	Yes	Yes	Yes		
8% La ₂ O ₃ -2% Al ₂ O ₃	Yes	Yes	Yes		Yes
3% Y ₂ O ₃ -4% La ₂ O ₃ -2% Al ₂ O ₃	Yes	Yes	Yes		
2% Y ₂ O ₃ -4% AlN	Yes	Yes	Yes		
4% Y ₂ O ₃ -6% AlN	Yes	Yes	Yes		
6% Y ₂ O ₃ -10% AlN	Yes	Yes	Yes		
4% Y ₂ O ₃	Yes	Yes			
8% Y ₂ O ₃	Yes	Yes	Yes		
11% La ₂ O ₃	Yes	Yes	Yes		

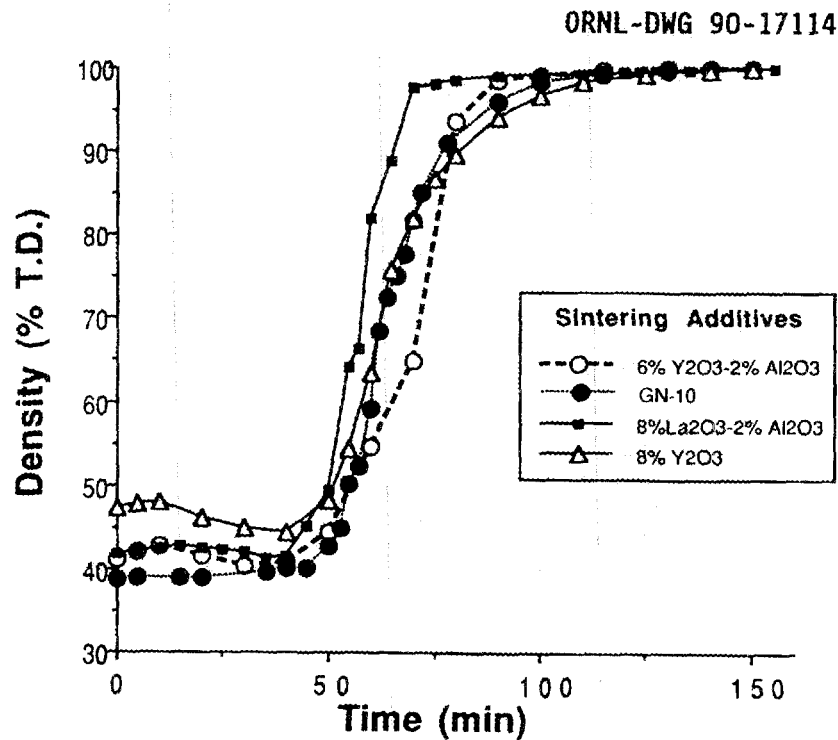
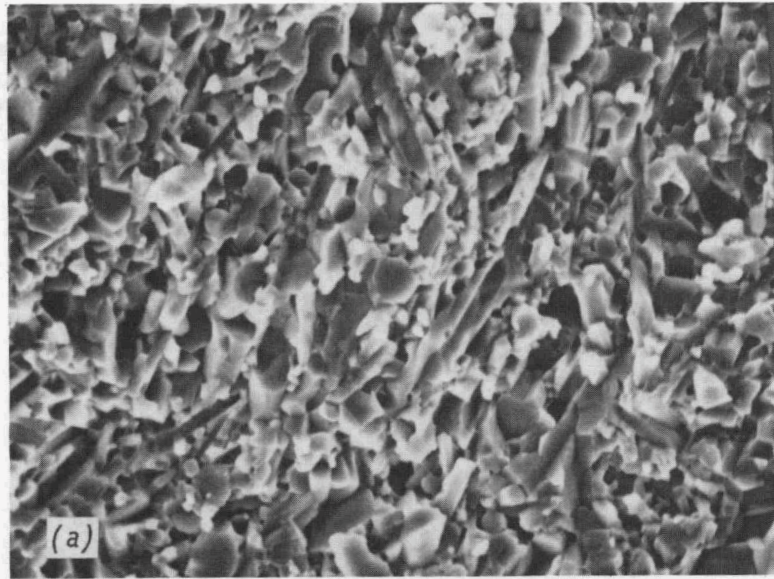


Fig. 1. Densification of various silicon nitride compositions in the hot-press. Compositions include Si₃N₄ with (1) 6% Y₂O₃-2% Al₂O₃, (2) a GN-10 composition, (3) 8% La₂O₃-2% Al₂O₃, and (4) 8% Y₂O₃. Hot-press conditions were room-temperature to 1800°C in 60 min and a 90 min hold.

T014399



T015970

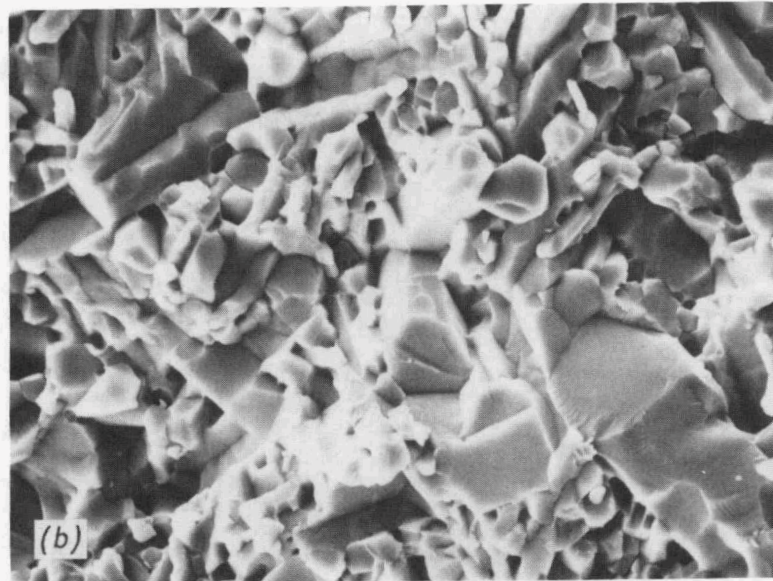


Fig. 2. Fracture surfaces of Si_3N_4 -6% Y_2O_3 -2% Al_2O_3 hot-pressed at (a) 1725°C for 60 min, and (b) 1800°C for 90 min.

T014476



T015883

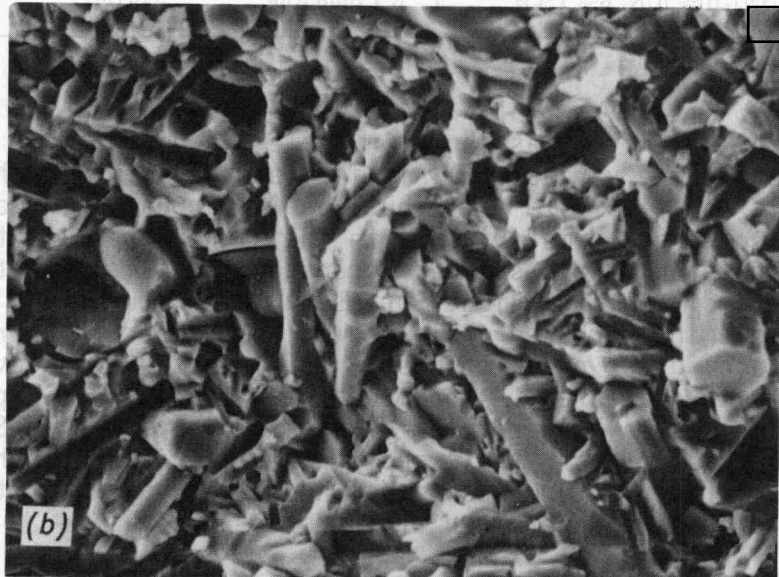


Fig. 3. Fracture surfaces of Si₃N₄-GN-10 additives hot-pressed at (a) 1725°C for 60min, and (b) 1800°C for 90 min.

attempting to quantify the grain growth and relate it to the sintering additive chemistry and densification parameters. The initial fracture toughness and flexural strength measurements are summarized in Table 2.

Table 2. Summary of flexural strength and fracture toughness of silicon nitride materials for microstructural development, hot-pressed at 1725°C for 60 min. Fabrication conditions were minimum to achieve high densities (>98 %).

Composition	Comments	Flexural Strength (MPa)	Fracture Toughness (MPa√m)
Si ₃ N ₄ -6%Y ₂ O ₃ -2%Al ₂ O ₃	Baseline material	916±20	6.6±0.7
Si ₃ N ₄ -6%Y ₂ O ₃ -2%Al ₂ O ₃	40% β-Si ₃ N ₄	777±123	7.6±1.1
Si ₃ N ₄ -GN-10 Additives	Alternate Glass Phase	937±33	6.2±0.4
Si ₃ N ₄ -8%La ₂ O ₃ -2%Al ₂ O ₃	Alternate Glass Phase	1089±302	5.9±0.6
Si ₃ N ₄ -3%Y ₂ O ₃ - 4% La ₂ O ₃ -2%Al ₂ O ₃	Alternate Glass Phase	883±109	6.7±1.3
Si ₃ N ₄ -3% AlN- 2% Y ₂ O ₃	a' - β' Composite	708±185	6.1±0.2
Si ₃ N ₄ -6% AlN- 4% Y ₂ O ₃	a' - β' Composite	556±96	5.1±0.3
Si ₃ N ₄ -10% AlN- 6% Y ₂ O ₃	a' - β' Composite	489±40	4.0±0.2

The flexural strengths, as shown in Table 2, while rather high for some samples were quite variable. This indicates that while the grain sizes were small, the flaw size distributions were broad. The additional two series of hot-pressed materials with the higher pressing temperatures and longer times should have similar strengths, but smaller standard deviations. In addition, the higher pressing temperatures and longer times should result in increased grain growth and higher fracture toughnesses. The effects of glass phase chemistry on microstructure development should also become more apparent. The mechanical testing is in progress at the present time. X-ray diffraction of the samples showed β-Si₃N₄ as the major phase present with the exception of materials with high AlN contents (Table 3). Fracture toughness and flexural strength for the remaining specimens are being determined at the present time.

Status of milestones

Milestone 123110, "Determine effects of process parameters on flaw generation in SiC whiskers" was not completed.

Publications

T. N. Tiegs, P. F. Becher, M. K. Ferber, and P. A. Menchhofer, "High Temperature Strength of SiC Whisker-Reinforced Silicon Nitride Composites," to be published in proceedings of 7th CIMTEC World Ceramics Congress, June 24-30, 1990, in Montecatini Terme, Italy.

Table 3. Summary of initial results showing phases present in silicon nitride materials fabricated to assess role of grain microstructure on fracture toughness

Composition	Comments	Phases Present ^a
Si ₃ N ₄ -6% Y ₂ O ₃ -2% Al ₂ O ₃	Baseline Material	Major β-Si ₃ N ₄
Si ₃ N ₄ -6% Y ₂ O ₃ -2% Al ₂ O ₃	40% β-Si ₃ N ₄	Major β-Si ₃ N ₄
Si ₃ N ₄ -GN-10 Additives	Alternate Glass Phase	Major β-Si ₃ N ₄
Si ₃ N ₄ -8% La ₂ O ₃ -2% Al ₂ O ₃	Alternate Glass Phase	Major β-Si ₃ N ₄
Si ₃ N ₄ -3% Y ₂ O ₃ - 4% La ₂ O ₃ - 2% Al ₂ O ₃	Alternate Glass Phase	Major β-Si ₃ N ₄
Si ₃ N ₄ -3% AlN- 2% Y ₂ O ₃	a' - β' Composite	Major α-Si ₃ N ₄ (~20%) Major β-Si ₃ N ₄ (~80%)
Si ₃ N ₄ -6% AlN- 4% Y ₂ O ₃	a' - β' Composite	Major α-Si ₃ N ₄ (~50%) Major β-Si ₃ N ₄ (~50%)
Si ₃ N ₄ -10% AlN- 6% Y ₂ O ₃	a' - β' Composite	Major α-Si ₃ N ₄ (~80%) Major β-Si ₃ N ₄ (~20%)

^aDetermined by x-ray diffraction.

1.2.4 Silicate Matrix

Low Expansion Ceramics for Diesel Engine Applications (VPI)

D. A. Hirschfeld and J. J. Brown

Objective/scope

Optimize the chemistry, properties, and processing of selected low thermal expansion compositions based on the zircon (NZZP) and the β -eucryptite- AlPO_4 systems. The major long-term goal is to develop an economical, isotropic, ultra-low thermal expansion ceramic material capable of having stable properties above 1200°C .

Technical progress

Zircon (NZZP) System

The axial thermal expansion characteristics of $(\text{Ca}_{1-x}\text{Mg}_x)\text{Zr}_4(\text{PO}_4)_6$ (CMZZP) ceramics were further investigated. The anisotropic expansion of $(\text{Ca}_{0.6}\text{Mg}_{0.4})\text{Zr}_4(\text{PO}_4)_6$ was examined by X-ray diffraction (XRD) from room temperature to 750°C at the ORNL HTML. The resulting data are presented in Figure 1 along with axial expansion of other CMZZP compositions where $x = 0.0, 0.2, \text{ and } 0.3$.

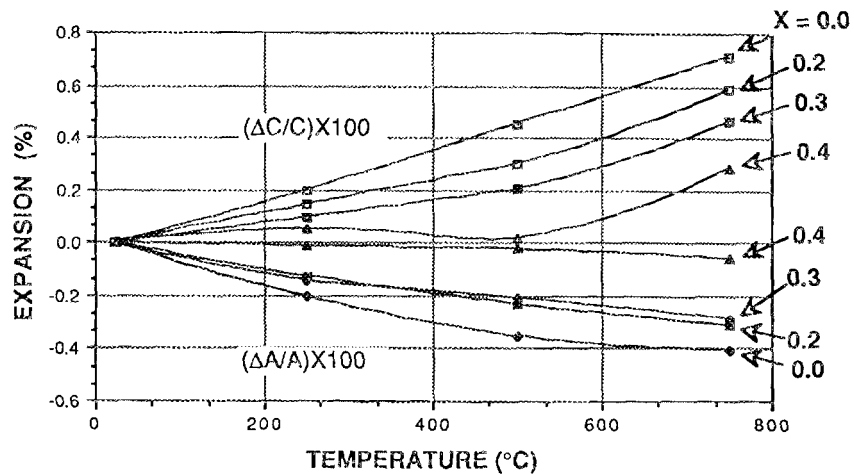


Fig. 1. Axial expansions of $(\text{Ca}_{1-x}\text{Mg}_x)\text{Zr}_4(\text{PO}_4)_6$ compositions.

As reported previously, the anisotropic expansions of the **a** and **c** lattice parameters decrease with increasing Mg concentration. For the composition where $x = 0.4$, the thermal expansion anisotropy is significantly reduced. Expansion along the **a** axis for this composition is almost zero and the **c**-axis expansion is less than that of compositions containing less Mg. A reduction in the anisotropic expansion should contribute to a reduction of temperature-produced stress and possible microcrack formation, and hence, improve the thermal shock resistance of the material.

The overall bulk thermal expansion coefficients for the above mentioned compositions computed from the lattice parameters are as follows:

$\text{MgZr}_4(\text{PO}_4)_6$ Content (mole %)	Bulk CTE ($\times 10^{-7}/^\circ\text{C}$)
0.0	-4.40
0.2	-0.74
0.3	-4.46
0.4	+4.76

Thermal stabilities of the CMZP materials were determined using weight loss analyses. Powder samples of compositions where $x = 0.0, 0.2, 0.3,$ and 0.4 were heated in platinum crucibles in air at 1200°C for 120 h. Weight losses were minimal in all specimens (less than 1%), and may be due to a reaction with the platinum crucibles.

Thermal conductivities of the compositions $(\text{Ca}_{1-x}\text{Mg}_x)\text{Zr}_4(\text{PO}_4)_6$ where $x = 0.0, 0.2, 0.3,$ and 0.5 were obtained using a laser flash thermal diffusivity apparatus and a differential scanning calorimeter (DSC) at the ORNL HTML. The thermal conductivity values were calculated by the product of the thermal diffusivity, specific heat, and bulk density of each sample. Acceptable values of thermal diffusivity at temperatures below 600°C were difficult to obtain, likely owing to the very low thermal diffusivity of the samples and resultant nonlinear heat flow. Densities of the CMZP ceramics ranged between 80% and 90% of theoretical.

Thermal conductivities of the CMZP compositions as a function of temperature are shown in Figure 2. It should be noted that these values are exceptionally low, and that thermal conductivity appears to decrease with increasing Mg content. Also shown in Figure 2 are the corresponding thermal conductivities of a partially stabilized (Y_2O_3) zirconia, a leading thermal barrier material for combustion and turbine engine applications. It is apparent

that compared to the zirconia material, the CMZP composition display substantially lower thermal conductivities at each respective temperature.

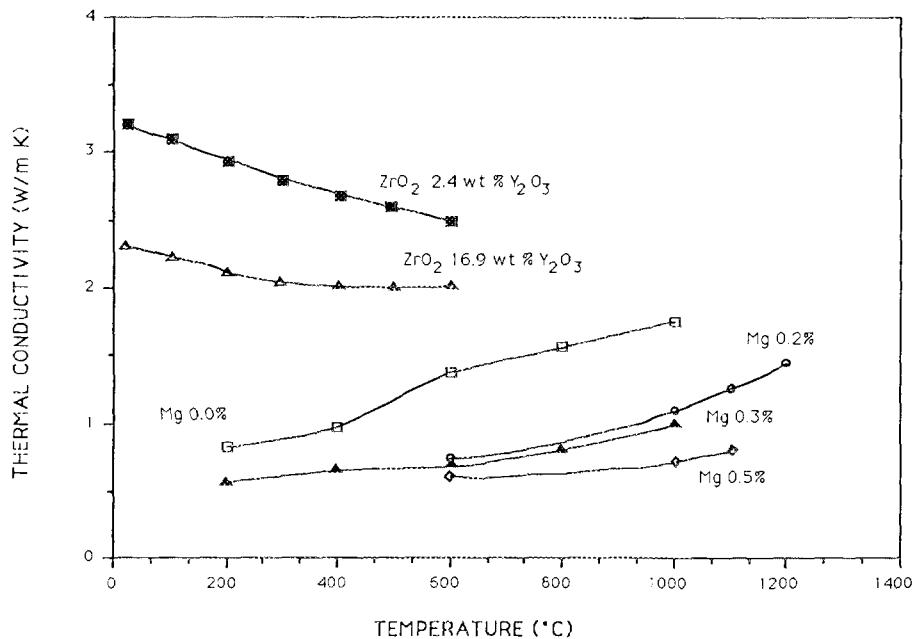


Figure 2. Thermal conductivities of CMZP compositions and stabilized zirconia.

In addition to CMZP compositions, $(Rb_{1-x}Cs_x)Zr_2(PO_4)_3$ (RCZP) compositions were evaluated as candidate low expansion ceramics for use in advanced heat engines. RCZP powders were synthesized using a sol-gel technique similar to one previously used for preparing CMZP powders. Gels were prepared using both basic (pH 9) and acidic (pH 2) conditions. By calcining the sol-gel products at about 950°C, single phase crystalline RCZP powders could be formed regardless of the process pH conditions. Densities greater than 98% of theoretical were achieved by hot pressing the sol-gel synthesized powders at 1200°C and 14 MPa for 5 h. The bulk expansion coefficients of the hot pressed samples varied from 0.0 to 0.8 x 10⁻⁷/°C (30 to 1000°C).

The thermal stabilities of RCZP ceramics were examined after long-term heat treatments in air at temperatures up to 1300°C. The compositions exhibited decomposition, evidenced by the formation of ZrP₂O₇, Zr₂P₂O₉, and ZrO₂ after treatments above 1000°C for 8-40 h. Thus, due to their instability, investigations of the RCZP materials were discontinued. A manuscript describing the results has been prepared for publication.

Ceramic Composites

To produce high density composites, powders of composition $(\text{Ca}_{0.6}\text{Mg}_{0.4})\text{Zr}_4(\text{PO}_4)_6$ were made using a variety of sol-gel techniques. Powders derived by one of the sol-gel methods studied were successfully transformed into single-phase crystalline CMZP by firing at 1250°C for 24 h. The technique used involves a colloidal suspension made by adding NH_4OH to a mixture of solutions of $\text{ZrO}(\text{NO}_3)_2$, $\text{Mg}(\text{NO}_3)_2$, $\text{Ca}(\text{NO}_3)_2$, and $\text{NH}_4\text{H}_2\text{PO}_4$ until a pH of 8-9 is reached. The suspension is dried at $40\text{-}60^\circ\text{C}$ while being stirred, dried at 110°C , and then calcined at 350°C for 10 h.

Composites made of 5 and 10 vol% chopped NICALON-SiC fibers in $(\text{Ca}_{0.6}\text{Mg}_{0.4})\text{Zr}_4(\text{PO}_4)_6$ powders derived by sol-gel techniques were hot pressed either in air, nitrogen, or argon. Initial studies indicated that hot pressing in air at 1200°C for 8 h at 18.4 MPa followed by annealing at 1200°C for 24 h yielded densities greater than 97% of theoretical for disks 50 mm in diameter by 3 mm thick. By increasing the pressure to 27 MPa and using an inert atmosphere, composites having densities greater than 98% of theoretical were formed by hot pressing at 1200°C for 6 h.

Examination of the microstructures of these composites using scanning electron microscopy showed a mean grain size of approximately $10\ \mu\text{m}$. Composites that were hot pressed in air exhibited some bonding between the fiber and the matrix and the fiber surfaces appeared to be rough. The composites pressed in an inert atmosphere exhibited fiber/matrix debonding and smooth fiber surfaces.

The bulk thermal expansion coefficients of the composites containing 5 and 10 vol% fibers ($-6.0 \times 10^{-7}/^\circ\text{C}$ and $-1.8 \times 10^{-7}/^\circ\text{C}$, respectively) are slightly negative compared to that of $(\text{Ca}_{0.6}\text{Mg}_{0.4})\text{Zr}_4(\text{PO}_4)_6$ ($1.0 \times 10^{-7}/^\circ\text{C}$).

Lightweight Ceramics

Two techniques for making lightweight CMZP ceramics have been developed. In one technique, a polymer foam is either coated or saturated with a slurry of CMZP powder, then sintered to yield a structure with pore sizes of 150 to $230\ \mu\text{m}$. In the second technique, a polymer powder is blended with CMZP powders and binders, pressed, then sintered to form a lightweight ceramic with pore sizes of $30\text{-}50\ \mu\text{m}$ (approximately the polymer powder particle size).

The mechanical properties of the lightweight ceramics and the effects of processing parameters on these properties are being studied. Samples of lightweight ceramics were tested in uniaxial tension using an Instron Model 4202 universal test machine with a 4 kN capacity to determine the strengths and elastic moduli. The specimens were epoxied to aluminum stubs which were then attached to the testing machine. The tensile strength of the lightweight ceramics was found to increase with density and to be independent of composition as shown in Figure 3. Lightweight ceramics made by the polymer powder method appear to have higher tensile strength than those made by the polymer foam method.

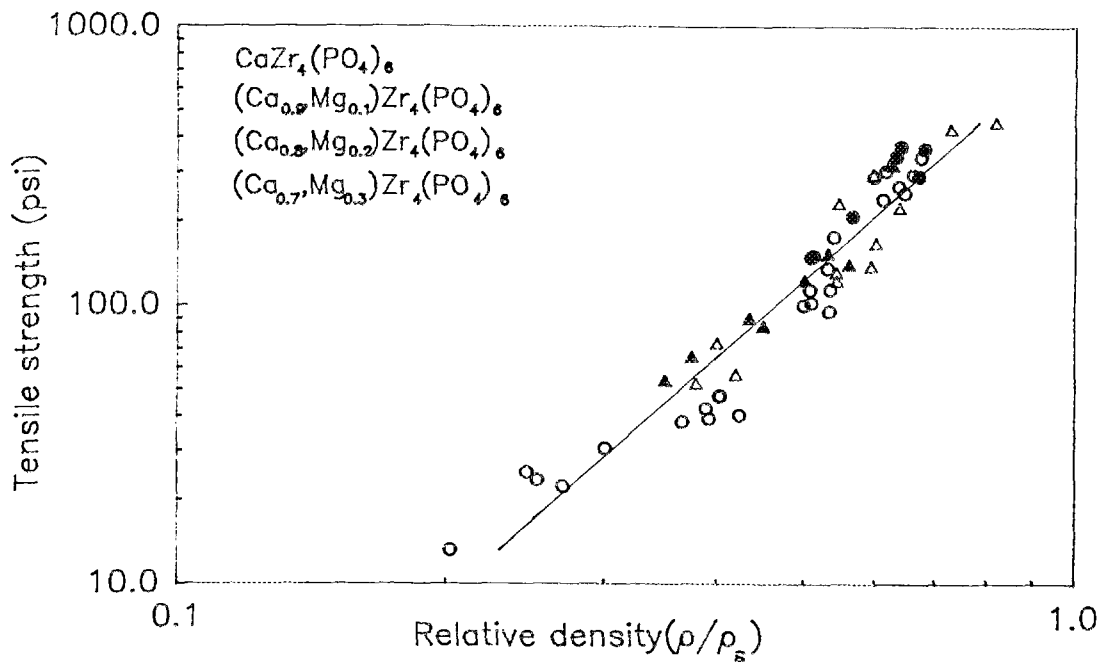


Figure 3. Tensile strength of lightweight ceramics as a function of density.

Because an extensometer could not be attached to specimens without inducing damage, the modulus was determined by subtracting the stiffness of the grips epoxied together from the stiffness of the sample determined from the stress vs cross head displacement of each test. There appeared to be no significant difference in the elastic modulus due to processing technique. The elastic modulus, however, tends to increase with Mg content. The modulus also

increases with density as shown in Figure 4. The amount of sintering aid (ZnO) appears to have an insignificant effect on the thermal expansion and mechanical properties.

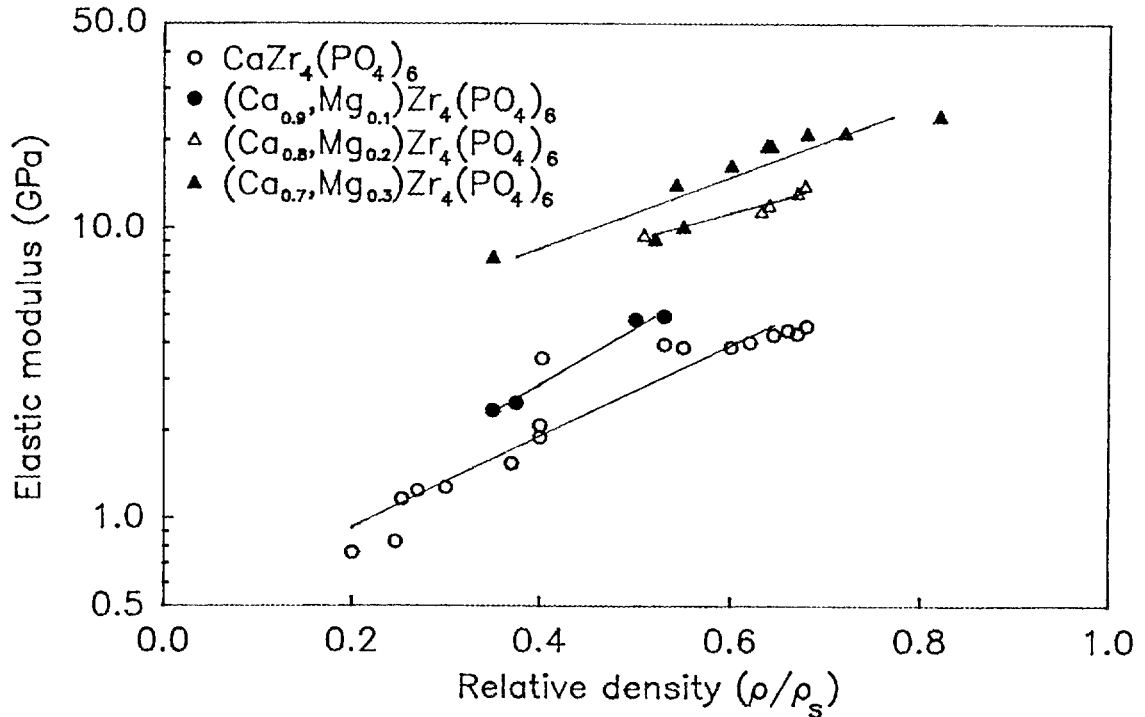


Figure 4. Elastic modulus of lightweight ceramics as a function of density and composition.

Corrosion of lightweight $(\text{Ca}_{1-x}, \text{Mg}_x)\text{Zr}_4(\text{PO}_4)_6$ ($x = 0.1-0.5$) immersed in aqueous HCl ($N = 12.1$) and HNO_3 ($N = 15.8$) was examined. After exposure at room temperature for over 1000 h, weight losses of 1-3% were observed. Results of XRD analyses revealed no evidence of decomposition indicating that the lightweight ceramics have excellent acid-corrosion resistance.

An analysis of the permeability of the lightweight ceramics indicates that material made by the polymer foam method has primarily an open cell structure while the ceramic made by the powder method has a closed cell structure. The relationship between permeability and both processing and relative density is shown in Figure 5.

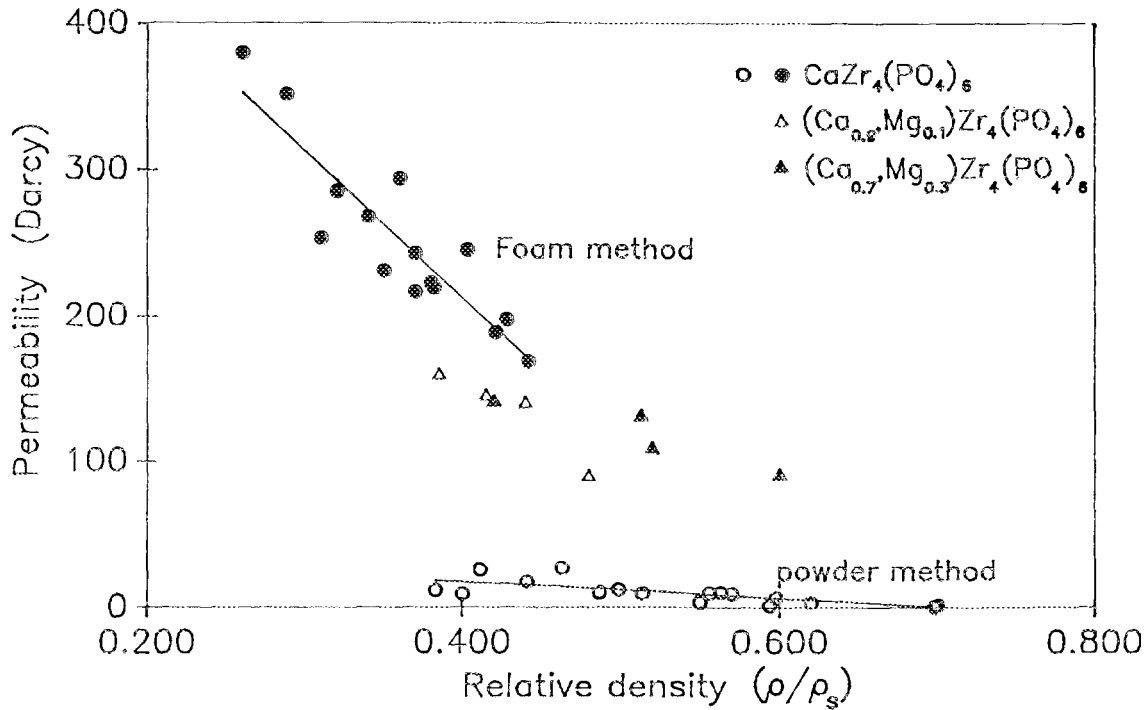


Figure 5. Effect of processing method on the permeability of lightweight ceramics

Densification

To improve the density of the low expansion ceramic materials to the point where they are ready for mechanical testing and application, hot pressing has been investigated. Due to the large differences in thermal expansion of the Al_2O_3 dies and the CMZP compositions, hot pressed samples usually become clinched in the dies after cooling from the fabrication temperature. To avoid cracking/breaking the sample, disposable dies are used that permit easy removal of the sample.

Techniques for hot pressing CMZP and composites of chopped NICALON-SiC fiber/CMZP have been developed to the point where disks 50 mm in diameter by 3 mm thick are routinely produced with densities greater than 97% of theoretical.

β -Eucryptite- AlPO_4 System

The corrosion resistance of recrystallized β -eucryptite was investigated because it is a candidate material for the heat engine regenerator and will be exposed to exhaust gases. Previous studies involved the corrosion behavior in concentrated aqueous HCl solutions on severely microcracked samples. Recently, the effects of exposure to more dilute HCl solutions on thermal expansion and weight loss have been determined for the microcracked material. For comparison, a commercial lithium aluminosilicate (LAS) material obtained from Allied Signal-Garrett Auxiliary Engine Division was exposed to aqueous HCl solutions.

The thermal expansion of modified β -eucryptite was not affected by exposure to an aqueous HCl solution with pH 1 at 100°C for up to 180 minutes. After exposure for longer times, however, the specimen totally disintegrated.

Weight losses of modified β -eucryptite specimens exposed to different concentrations of HCl at room temperature were determined. Weight loss at pH -1.1 (N=12.1) was 0.51 mg/cm²/h and the sample disintegrated after 120 h of exposure. When the solution was at pH 1, the weight loss was 0.15 mg/cm²/h with sample disintegration at 216 h. At pH 2, the weight loss was 0.072 mg/cm²/h. There was no significant weight loss with exposure to a solution with pH 4.

The commercial LAS material was exposed to HCl solutions of pH -1.1 (N = 12.1) and pH 1 for up to 5 h at 100°C. No changes in the thermal expansion were observed in any of the specimens. Energy dispersive X-ray analysis revealed no variations in composition. The introduction of AlPO_4 into β -eucryptite appears to not only decrease its thermal expansion coefficient, but also to decrease its corrosion resistance.

Techniques have been developed to produce modified β -eucryptite using glass-ceramic techniques; however, severe microcracking occurs through the bulk due to thermal expansion mismatches between the parent glass and the recrystallized phase. The microcracks prohibit further study of the mechanical properties of the modified β -eucryptite glass-ceramic.

A new technique for the processing of modified β -eucryptite has been developed. Information on this technique is being withheld until its patentability has been determined.

Status of Milestones

The densification and characterization studies performed by subcontract have been redefined; however, preliminary densification studies performed at Virginia Tech have met the milestones. The milestones have been changed to reflect the changes in the subcontract. Table 1 contains the key to major milestones and Figure 6 the milestones status chart.

The densification and characterization studies were reviewed at a DOE Project Review on June 4, 1990. A Request for Proposal (RFP) was prepared for the commercialization of CMZP. The RFP will be funded by the Virginia Tech Center for Advanced Ceramic Materials. It was issued in September and the proposals received will be reviewed in the near future.

At the DOE Project Review in June, it was decided to redirect the Recrystallized β -Eucryptite Glass study because modified β -eucryptite is severely microcracked due to the thermal expansion mismatch between the parent glass and the recrystallized phase. Other methods of producing dense modified β -eucryptite are being investigated.

Publications

U.S. Patent Application June 7, 1990: "Ceramic Materials with Low Thermal Conductivity and Low Coefficients of Thermal Expansion" by J.J.Brown, S.VanAken, R.E.Swanson, J.Kim, D.M.Liu, T.K.Li, Y.Yang, and D.A.Hirschfeld

References

1. D.P.H. Hasselman, et al., "Thermal Diffusivity and Conductivity of Dense Polycrystalline ZrO_2 Ceramics: A Survey," J. Am. Ceram Soc., 66 (5), 799-806 (1987).

Table I. KEY TO MAJOR MILESTONES (WBS ELEMENTS)*

		<u>Completion Date</u>
VPI 2.4.1	Property Optimization by Hot Isostatic Pressing	July 31, 1992
VPI 2.4.2	Optimization of Compositions	March 31, 1991
VPI 2.4.3	Fiber Reinforced Composites	
	a. Synthesis	July 31, 1991
	b. Characterization of High Temperature Mechanical Properties - β -Eucryptite	July 31, 1992
	c. Characterization of High Temperature Mechanical Properties - NZP Ceramics	July 31, 1992
VPI 2.4.4	Lightweight Insulation	Sept. 30, 1991
VPI 2.4.5	Recrystallized β -Eucryptite Glasses	March 31, 1991
VPI 2.4.6	Submit Technical Paper on Research Results for Publication	July 31, 1991
VPI 2.4.7	Final Report	Sept. 30, 1992

*These milestones are subject to the approval of the Project Manager.

Milestone	1989					1990							*	
	N	D	J	F	M	A	M	J	J	A	S	O		
2.4.1												▶		O
2.4.2												▶		O
2.4.3												▶		O
2.4.4												▶		O
2.4.5												▶		O

* On, Ahead of, or Behind Schedule

Figure 6 Status of milestones

1.3 THERMAL AND WEAR COATINGS

Advanced Coating Technology

B.W. Sheldon, J.C. McLaughlin, and D.P. Stinton (Oak Ridge National Laboratory)

Objective/scope

Sodium corrosion of silicon carbide and silicon nitride components in gas turbine engines is a potentially serious problem. The outer surfaces of SiC and Si₃N₄ parts oxidize at high temperatures to form an SiO₂ layer which inhibits further oxidation. However, sodium which is present in high temperature combustion atmospheres reacts with the SiO₂ layer, such that it is no longer protective. Previous studies performed by J.I. Federer of ORNL indicate that Al₂O₃ is much more resistant to sodium corrosion than this native SiO₂. This suggests the use of an alumina (α -Al₂O₃, etc.) coating to provide both oxidation and sodium resistance; however, sodium is likely to undergo some reaction with a pure alumina coating, such that the α or other alumina phases are converted to a sodium aluminate phase such as β -alumina (Na₂O·11 Al₂O₃). This type of transformation may lead to cause a pure alumina coating to fail. The objective of this program is to develop a coating that will protect the underlying SiC or Si₃N₄ from sodium corrosion and provide simultaneous oxidation protection. To evaluate the behavior of both α and β -aluminas in sodium containing atmospheres, the corrosion resistance of hot pressed samples of both materials will first be evaluated. A chemical vapor deposition (CVD) process will be developed for the application of the appropriate alumina coatings. The effect of the combustion environment upon coating characteristics such as microstructure, strength, adherence, and other properties will then be evaluated.

Technical highlights

Amorphous alumina coatings were deposited from trimethylaluminum and oxygen (see previous reports). These coatings were then heated in sodium-containing combustion atmospheres to produce crystalline sodium-aluminate coatings. The combustion atmospheres were produced by burning methane in air, and introducing sodium by vaporizing sodium carbonate (see previous reports). Powder x-ray diffraction of the coatings indicated the presence of multiple phases, including β/β' aluminas.

Corrosion tests on hot-pressed α - and β -alumina samples have been completed. The details of this work are presented in a recent report. The results provide important information on the corrosion of these materials, and indicate that α -alumina reacts with sodium-containing combustion atmospheres to form β -aluminas. This demonstrates that an α -alumina coating may become a β -alumina coating in a high-temperature sodium containing environment. Under some conditions, the transformed material spalled off of the α -alumina substrate, which suggests that α -alumina coatings are likely to fail. The hot-pressed β -aluminas did not undergo a phase transition, however, the rapid formation of β -aluminas on the α -alumina indicates that the rapid diffusion of sodium through the β -aluminas is likely to create problems for β -alumina coatings unless they are very thick.

The results with the hot-pressed samples demonstrate that both α - and β -aluminas are much more resistant to sodium corrosion in combustion atmospheres, compared to silicon carbide and silicon nitride. However, because of the potential problems that are likely to occur because of rapid sodium diffusion in β -aluminas, further work on developing alumina coatings has been delayed, pending the results of our current investigations into other candidate materials for corrosion resistant coating materials.

One material that has exhibited better resistance to sodium corrosion than SiC is zirconia. Pure ZrO_2 is a complex material that exists in several different crystal structures. The low temperature form undergoes a phase transformation from monoclinic to tetragonal at $1000^\circ C$ which involves a large volume contraction that makes the use of pure zirconia impractical as a bulk material or a coating. Addition of Ca, Mg, Y, or Ce to form a solid solution that has no phase transformation (stabilized zirconia) results in a valuable structural material. Unfortunately, coatings will not normally adhere to a substrate if the thermal expansion mismatch is greater than about 25%. In this case, the coefficient of thermal expansion (CTE) of stabilized zirconia is about 13×10^{-6} which is considerably higher than that of SiC (5.5×10^{-6}). Zirconium carbide, however, has a CTE very similar to that of SiC (about $7.0 \times 10^{-6}/K$) and should adhere quite well to a SiC substrate. Conversion of several microns of the ZrC to ZrO_2 to form a protective oxide layer will be attempted as one method to reduce the effects of sodium corrosion on SiC. Following a review of the literature, zirconium carbide was successfully deposited onto SiC by chlorinating zirconium metal at $450^\circ C$ and reacting those vapors with methane and hydrogen at $1200^\circ C$. Controlled oxidation of the ZrC layer at about $800^\circ C$ produced a thin layer identified by x-ray diffraction as monoclinic ZrO_2 that did spall away from the underlying ZrC. Modifications to the deposition process will be required to incorporate Ca, Mg, Y, or Ce into the ZrC so that controlled oxidation will produce stabilized zirconia. If the thermal expansion of the stabilized zirconia is too great to adhere to ZrC, attempts will be made to deposit partially stabilized zirconia (CTE = 10×10^{-6}) that should adhere to ZrC.

Status of milestones

The June 1990 milestone to produce β/β'' alumina coatings was satisfied.

Publications

None

Development of Adherent Ceramic Coatings to Reduce Contact Stress Damage of Ceramics
- H. E. Rebenne and J. H. Selverian (GTE Laboratories Incorporated)

Objective/scope

The objective of this program is to develop oxidation-resistant, high toughness, adherent coatings for silicon based ceramics. These coatings will be deposited on reaction bonded Si_3N_4 (RBSN), sintered SiC (SSC), and HIP'ed Si_3N_4 (HSN) and used in an advanced gas turbine engine. A chemical vapor deposition (CVD) process will be used to deposit the coatings. These coatings will be designed to provide the best mix of mechanical, thermal, and chemical properties.

Technical progress

High Temperature Coating Deposition Reactor

A new CVD reactor was built to enable coatings to be deposited at temperatures equal to or above those at which the coating will be used in order to minimize residual stresses in the coating/substrate system. This reactor is a hot-wall, crucible type reactor that is heated resistively with graphite heating elements. Source gases enter at the bottom, flow upward past the parts to be coated, and exit through exhaust tubes terminating above the deposition zone. This is illustrated in Fig. 1. A perforated plate defines the upper limit of the deposition zone. Graphite rods are hung from this plate to form a fixture for supporting the substrates. The substrates are placed on a grid of thin alumina rods that pass through holes in the graphite rods. The volume of the deposition zone is ≈ 5 liters. An internal reactor is used for generating volatile AlCl_3 and ZrCl_4 , which are the aluminum and zirconium source materials being used for the AlN and $\text{Al}_2\text{O}_3+\text{ZrO}_2$ coatings, respectively.

Process development for deposition of the coating at temperatures above 1000°C was started in the new high temperature CVD reactor. Initially, attempts were made to deposit a pure Al_2O_3 coating. The first experiment was done at 1000°C to establish reproducibility of coatings obtained in the low temperature CVD reactor. The coating produced was not analyzed, although it appeared to be similar to those obtained in the other reactor. Based on weight gain, the deposition rate was approximately $0.5 \mu\text{m}/\text{hour}$, which was typical of the deposition rate obtained in the other reactor. The deposition temperature was then raised to 1200°C . This gave a $1.5 \mu\text{m}$ thick coating in one hour. However, Al_2O_3 powder also formed due to gas phase nucleation. Most of this powder was easily removed from the samples, and the remaining coating appeared to be nonporous and smooth on the surface. In order to determine if there was a relationship between deposition temperature and gas phase nucleation, an experiment was done at 1120°C . This run produced extensive amounts of powder, causing the reactor exhaust line to plug. In addition, melting of the Al metal in the AlCl_3 generator occurred, so samples from this run were not analyzed. The remainder of the experiments done were deposition of $\text{Al}_2\text{O}_3+\text{ZrO}_2$ or AlN.

Since some success was achieved with deposition of pure Al_2O_3 at 1200°C , the first $\text{Al}_2\text{O}_3+\text{ZrO}_2$ experiment was done at 1200°C . This resulted in extensive gas phase nucleation. The deposit that collected on the substrates was so loosely adherent that it rubbed off, leaving no weight gain of the substrate, which suggested that no coating had formed. Another experiment was done at this temperature, but with the relative amounts of AlCl_3 and ZrCl_4 source varied; i.e., a higher ratio of Zr/Al. This resulted in

a moderate amount of powder formation due to gas phase nucleation. In addition, a very thick, very loosely adherent coating resembling an eggshell formed. This coating was easily peeled off, leaving no adherent coating underneath. A third experiment was done at 1200°C with the same ratio of source materials but with a different temperature profile. Specifically, the temperature profile was made steeper so that the source gases did not get preheated to as high a temperature. It was hypothesized that this would reduce the amount of gas phase nucleation. This succeeded in producing less powder. The coating from this experiment has not yet been analyzed. Additional experiments were done with the original Zr/Al ratio in the source gases and with deposition temperatures of 1300°C and 1375°C. The experiment at 1300°C produced a thick, nonporous, well-adherent coating and a small amount of powder. The coating thickness indicated a deposition rate of 11 $\mu\text{m}/\text{hour}$. This coating is shown in Figure 2. The experiment at 1375°C gave a moderate amount of powder and an eggshell coating similar to the one described above.

Analysis of all of the high temperature Al_2O_3 and $\text{Al}_2\text{O}_3+\text{ZrO}_2$ experiments done so far suggests that there is a transition temperature below which gas phase nucleation dominates and above which surface nucleation dominates. At the lowest deposition temperature used in this program (975°C used throughout Phase I and early Phase II), gas phase nucleation was not measurable, but the deposition rate was very low (<1 $\mu\text{m}/\text{hour}$ for either Al_2O_3 or $\text{Al}_2\text{O}_3+\text{ZrO}_2$). At 1200°C for pure Al_2O_3 and 1300°C for $\text{Al}_2\text{O}_3+\text{ZrO}_2$, the deposition rate was much higher and an adherent coating was formed with only moderate amounts of powder from gas phase nucleation. At intermediate temperatures, extensive powder formation took place, and little or no adherent coating was formed. The only experiment that did not fit this trend was the one in which $\text{Al}_2\text{O}_3+\text{ZrO}_2$ was deposited at 1375°C. It should be emphasized that these results are specific to our deposition system and should therefore not be generalized to predict the behavior of other systems. This is especially important since the temperature profile in the gas phase upstream of the deposition zone appears to strongly influence the results.

The remainder of the experiments were deposition of AlN. Initially, an experiment was done at 1000°C to establish reproducibility of coatings obtained in the low temperature CVD reactor. This resulted in quite different behavior than typically occurred in the low temperature reactor. Specifically, an adherent, thick coating formed along with an extensive amount of powder. The coating thickness varied substantially on a given sample, corresponding to a deposition rate of 6-9 $\mu\text{m}/\text{hour}$. The difference in behavior can only be attributed to the different temperature profile in the gas phase, suggesting that the AlN system is very sensitive to this parameter. A second experiment was done at 1200°C. This also gave extensive powder formation, but a lower and more variable deposition rate (1-5 $\mu\text{m}/\text{hour}$). The coating produced in this experiment is shown in Figure 3. It should be emphasized that the reported deposition rates are only apparent rates since they are determined by measuring coating thickness at several locations and dividing by the total deposition time. Loss of loosely adherent coating or flaking or chipping of strongly adherent coating during fracture of the sample could skew the measurement.

In summary, an acceptable set of deposition parameters for the entire coating configuration at a temperature above 1000°C has not yet been identified. Our current efforts are focused on achieving deposition of AlN/ Al_2O_3 / $\text{Al}_2\text{O}_3+\text{ZrO}_2$ at 1200°C and then carrying out oxidation tests at this temperature. The pure Al_2O_3 intermediate layer is to enhance oxidation resistance and is in accordance with the milestones (see below). Based on results obtained so far, it appears likely that we will succeed in

achieving a total coating thickness in excess of 10 μm at 1200°C. However, a 10 μm thick $\text{Al}_2\text{O}_3+\text{ZrO}_2$ layer may not be achieved.

Meanwhile, the CVD reactor which was previously being used for this program was being modified to incorporate two internal reactors for simultaneously generating two different source materials. Previously, all source materials were generated in one internal reactor. This resulted in poor control over the relative amounts of and distribution of ZrO_2 and Al_2O_3 in the $\text{Al}_2\text{O}_3+\text{ZrO}_2$ composite layer. Details of the composite layer composition were discussed in the October, 1989 Bimonthly Progress Report. The new design will allow better control of the relative rates of generation of AlCl_3 and ZrCl_4 for deposition of the $\text{Al}_2\text{O}_3+\text{ZrO}_2$ composite layer. The modifications are completed and the reactor will be used to develop CVD operating conditions that will result in a uniform distribution of ZrO_2 in the Al_2O_3 matrix and ultimately a transformation-toughened coating. The heating elements have been replaced to provide more uniform temperature within the deposition zone of the reactor. The deposition parameters for the AlN and $\text{Al}_2\text{O}_3+\text{ZrO}_2$ layers are being reestablished and coating should resume the week of October 29.

Contact Stress/Friction Coefficient Tests

Self-mated sliding wear tests have been carried out at room temperature with uncoated samples. These samples included RBSN, SSC, and hot-pressed silicon nitride with the same composition as HSN (referred to as HPSN). Hot-pressed material is being used in place of hot isostatically pressed material for this study due to the availability of hot-pressed plates with the proper dimensions for fabricating into pins and disks. (Any differences between HSN and HPSN are only in contamination of the surface of HSN material with components of the glass encapsulating vessel used in hot isostatically pressing. Since the surface of the plate is removed for fabricating into pins and disks, this difference is essentially removed for purposes of this study.) The wear tests were done using a pin-on-disk configuration in accordance with the procedure established for the VAMAS round robin wear tests [1]. The tests were performed at a velocity of 0.1 m/s with a 1 kg static load in air at a total sliding distance of 1000 meters. Table I summarizes the friction results obtained. The breakaway friction coefficients were measured prior to wear testing on surfaces polished to a 1 μm finish. The values reported for the kinetic friction coefficients are the steady state values obtained after 500 meters of sliding. The microstructure, fracture surface, and reactions at the wear interface are currently being studied to provide more insight into the wear behavior of these ceramics.

Table I. Breakaway and kinetic friction coefficients for uncoated RBSN, HPSN, and SSC.

Pin	Disk	Breakaway Friction Coeff.	Kinetic Friction Coeff.
RBSN	RBSN	0.1	0.5 - 0.8
HPSN	HSN	0.3	0.8
SSC	SSC	0.1	0.3

Self-mated sliding wear tests at 800°C are still underway on uncoated samples. Results will be reported in the December, 1990 Bimonthly Progress Report. Coating of pins and disks for room temperature tests on coated samples will begin the week of October 15. These coatings will be deposited at 1000°C using the CVD operating conditions used throughout Phase I. This is being done to expedite the contact stress/friction coefficient measurement feasibility study. Since coating oxidation resistance above 1000°C is not required for this test, demonstration of feasibility of the technique can be done with the Phase I coating configuration.

Coating Residual Stress Measurement

In an attempt to better understand the failure of the coating during oxidation testing, a series of residual stress measurements of the coating is being done. The technique being used is measurement of the change in the radius of curvature (ROC) of the substrate due to the coating, from which the residual stress in the coating can be calculated. Substrates of HSN were polished to a thickness of 0.012 inch. The ROC was measured in the as-polished condition and after a 1 hour vacuum anneal at 1400°C. A small amount of relaxation was seen after the anneal, with the ROC increasing from 3.6 m to 4.8 m based on Rodenstock optical profilometer measurements. These measurements were in excellent agreement with additional ones taken with a Dektak profilometer. It is felt that the curvature measured for the annealed sample was not due to residual stress but is due to the geometry of the sample. The next set of experiments will involve coating one side of the HSN substrates with the AlN coating, measuring the change in ROC, then coating with the Al₂O₃+ZrO₂ coating and measuring the change in ROC. In this way, the separate effects of each coating layer can be determined. Coating of substrates with AlN is underway.

Status of Milestones

<u>Milestone</u>	<u>Due</u>	<u>Status</u>
Microstructural evaluation of the Al ₂ O ₃ +ZrO ₂ composite layer.	12/89	Completed
Studies of first generation coating configuration to determine cause of failure during oxidation tests at 1200°C and 1375°C.	03/90	Completed
Modification of coating configuration to improve oxidation resistance at ≥1200°C. Develop CVD process and coat samples for testing the following modifications: a) add Al ₂ O ₃ layer between AlN and Al ₂ O ₃ +ZrO ₂ composite layer; b) increase thickness of Al ₂ O ₃ +ZrO ₂ composite layer to 10µm.	09/90	Delayed to 12/90 due to equipment problems.
Feasibility study of measuring friction coefficient and contact stress damage using conventional pin-on-disk or ball-on-disk	12/90	On schedule

wear tests.

Performance tests of modified coating configuration including: i) 500 hour oxidation ii) thermal shock, and iii) flexure strength. Each test will be done on coated and uncoated samples. All tests will be conducted at room temperature, 1000°C, 1200°C, and 1375°C.	03/91	On schedule
Test feasibility of coating a commercial part or equivalent.	06/91	On schedule
Submit draft of final report covering Phase II results.	09/91	On schedule

Publications

None.

References

1. A. W. Ruff and S. Jahanmir, "Measurements of Tribological Behavior of Advanced Materials: Summary of U.S. Results on VAMAS Round-Robin No. 2," NISTIR 89-4170, U.S. Dept. of Commerce, Gaithersburg, MD, 1989.

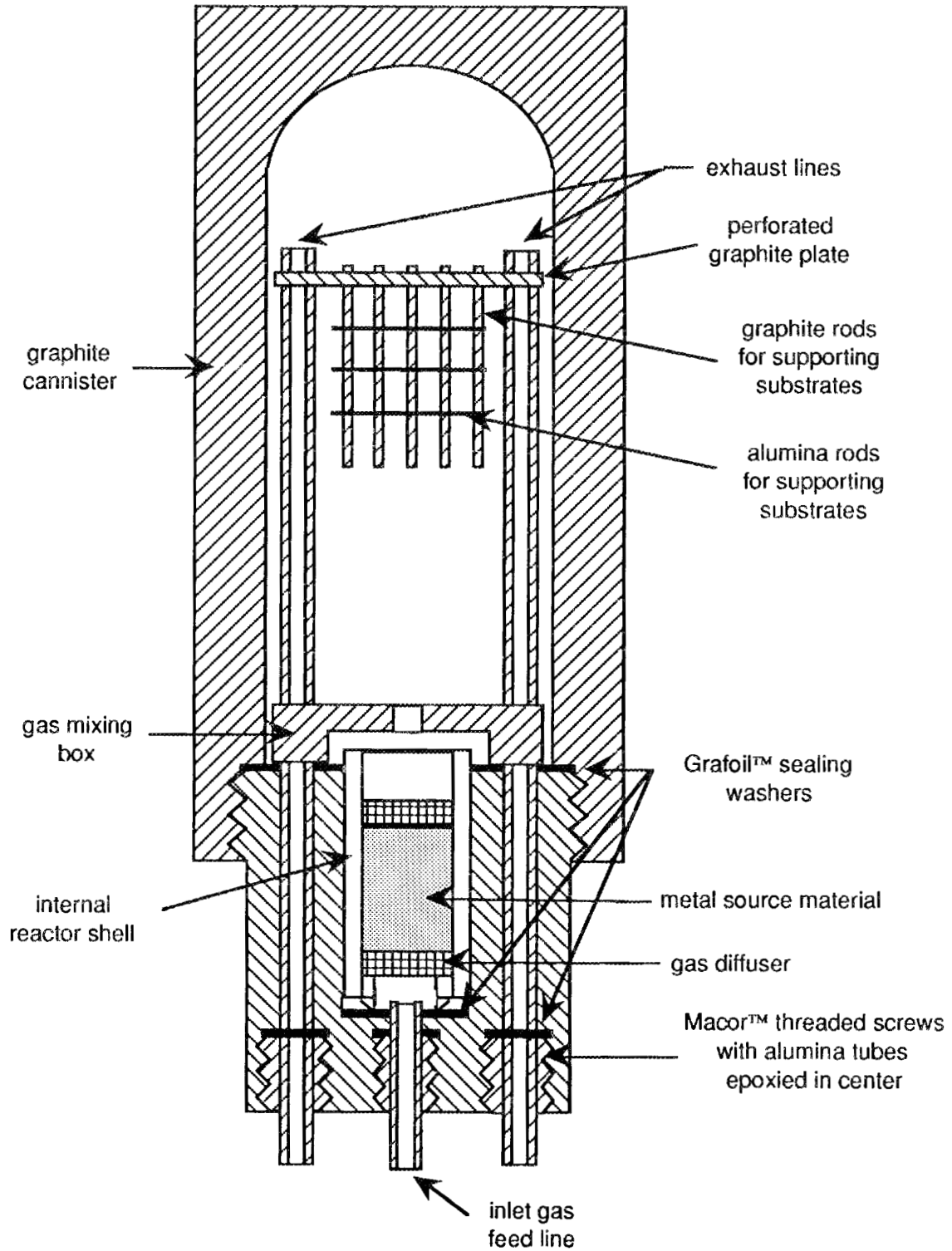


Figure 1. CVD reactor used for high temperature coating deposition.

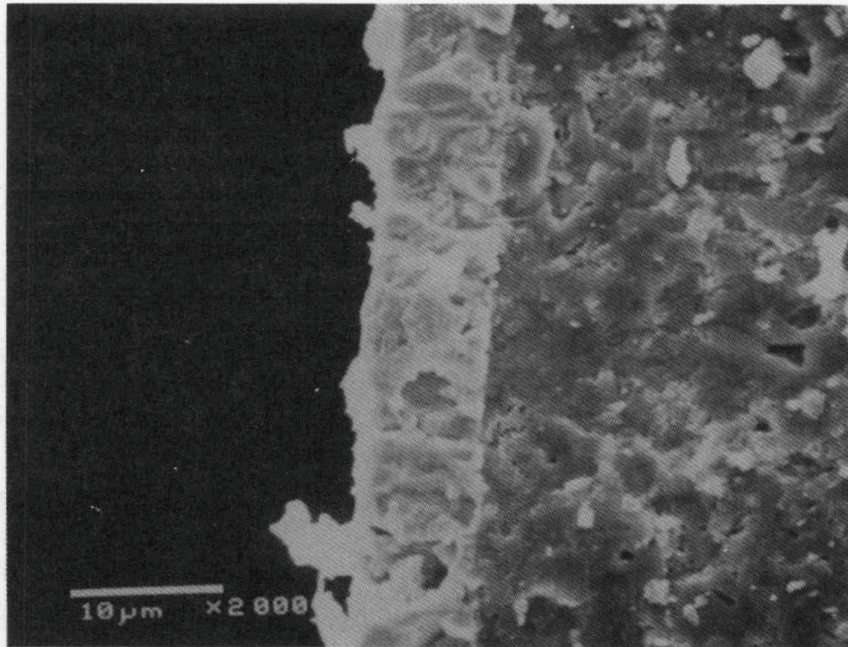


Figure 2. SEM photomicrograph of an $\text{Al}_2\text{O}_3+\text{ZrO}_2$ coating on RBSN. The coating was deposited at 1300°C .

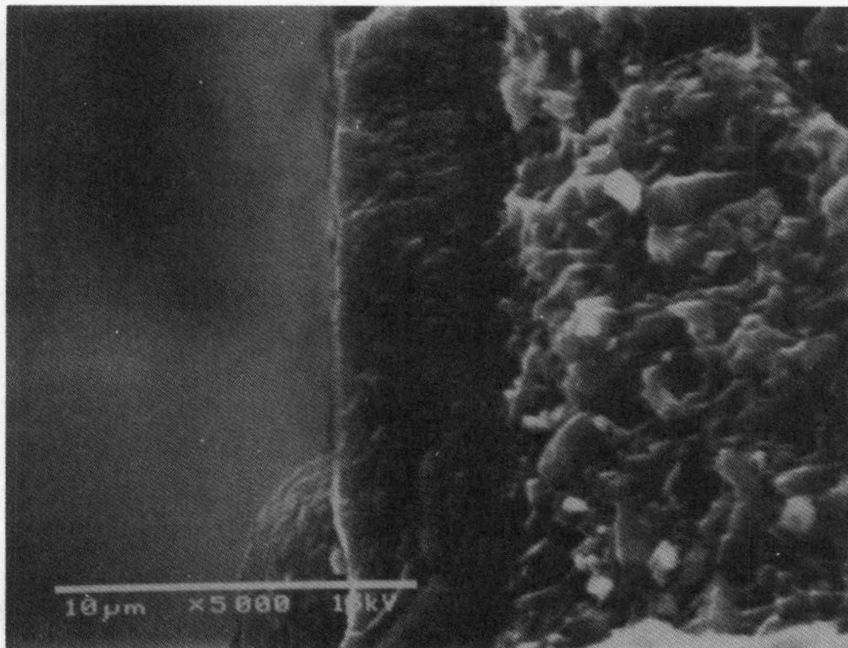


Figure 3. SEM photomicrograph of an AlN coating on HSN. The coating was deposited at 1200°C .

Wear-Resistant Coatings

C. D. Weiss (Caterpillar, Inc.)

Objective/scope

The goal of this technical program is to develop wear-resistant coatings for piston ring and cylinder liner components for low heat-loss diesel engines.

Wear resistant coatings will be applied to metallic substrates utilizing plasma spraying, vapor deposition (CVD/PVD), and enameling coating processes. First, the adherence of each coating for each coating process to the metallic substrate will be optimized. Methods which can be utilized for improving the adherence of these coatings include development of unique substrate preparation methods before application of the coating, grading coating compositions to match thermal expansion, compositional changes, laser or electron beam fusing and/or optimizing coating thickness. Once the adherence of each coating system is optimized, each coating will be screened for friction and wear at 350°C under lubricated conditions. Coatings which show promise after this initial screening will be further optimized to meet the friction and wear requirements. Then, the optimized coating systems will be fully characterized for oxidation resistance, adherence, uniformity, and thermal shock resistance, as well as friction and wear.

Selection of the most promising coatings and coating processes will be made after the characterization task. Criteria for selection will include not only performance (i.e., wear, adhesion, friction coefficient, thermal shock resistance and thermal stability) but also manufacturability/cost factors, as well. Utilizing both criteria a coating system having acceptable cost/benefit relationships will be selected.

Technical progress

The pin-on-disk friction and wear testing against both a ceramic and metallic counterface identified the following coatings as piston ring candidates:

1. Plasma sprayed chromia-silica composite,
2. Plasma sprayed high carbon iron-molybdenum,
3. Plasma sprayed, self-lubricating, PS212, and,
4. Mid-temperature chemical vapor deposited Ti(C,N).

Also identified with this pin-on-disk testing as potential cylinder liner coating candidates were:

1. Plasma sprayed high carbon iron-molybdenum,
2. Plasma sprayed chromia-silica composite, and,
3. Low temperature arc vapor deposited (LTAVD) chrome nitride.

Candidate piston ring/cylinder liner coating pairs were further characterized for friction and wear at 350°C, lubricated, using a Hohman A-6 friction and wear machine. Table 1 contains the results of the various piston ring coatings running against the LTAVD chrome nitride coated cylinder liner. The results of running the candidate piston ring coatings against the chromia-silica composite cylinder liner coating are contained in Table 2. Note that one of the overall goals of this program is to obtain an average wear coefficient for both the piston ring and cylinder liner coating of at least 1.0×10^{-8} .

Table 1 shows that running the high carbon iron-molybdenum piston ring coating against a LTAVD chrome nitride cylinder liner coating met the friction and wear goals of this program.

Running the plasma sprayed chromia-silica, plasma sprayed PS212 or mid-temperature chemical vapor deposited Ti(C,N) against the LTAVD chrome nitride resulted in very low shoe wear (average wear coefficients of 7.32×10^{-10} to 5.69×10^{-9}). However, the average wear coefficient for the chrome nitride disk ranged from greater than 10^{-3} to 7.72×10^{-6} . These wear coefficients were above the goals of the contract. For this reason, the only piston ring/ cylinder liner coating pair selected for further characterization was the high carbon iron-molybdenum running against the chrome nitride.

Although the high carbon iron-molybdenum /LTAVD chrome nitride coating system met the program goals with respect to both friction and wear, the 2 to 3 micron thick chrome nitride coating was completely worn through after 680 minutes of testing. Thus, to meet the commercial durability goals, the chrome nitride coating needs to be applied to a thickness greater than 2-3 microns. Additional specimens, coated using a modified process to produce a denser, thicker, chrome nitride coating were produced and tested.

Initially, the thicker chrome nitride coated disks produced both low friction and wear running against the high carbon iron shoes. However, during the heat-up portion of the second friction and wear test cycle, the chrome nitride coating spalled. A thermal expansion mismatch between the chrome nitride coating and the cast iron substrate was the probable reason for the spallation of the thicker chrome nitride coating.

Table 2 shows that running plasma sprayed high carbon iron-molybdenum shoes against the plasma sprayed chromia-silica coated disk resulted in average wear coefficients of 5.98×10^{-10} for the shoes and 3.34×10^{-8} for the disk. These average wear coefficients met the goals of the contract. A complete wear curve for this coating pair was obtained.

Running plasma sprayed chromia silica shoes against the chromia-silica disk resulted in an average wear coefficient of 3.34×10^{-6} for the disk. An average wear coefficient of 1.52×10^{-5} was recorded for the chromia-silica disk when run against the CVD Ti(C,N). Finally, the plasma sprayed PS 212 coated shoes recorded an average wear coefficient of 7.64×10^{-7} , when run against the plasma sprayed chromia-silica coated disk. These material pairs did not meet the average wear coefficient goals of this contract.

Plasma sprayed high carbon iron-molybdenum and plasma sprayed chromia-silica specimens have completed oxidation resistance and thermal shock testing. The oxidation resistance testing consisted of exposing plasma sprayed specimens to a simulated diesel exhaust atmosphere for 500 hours at 400°C. After 500 hours of oxidation testing the plasma sprayed chromia-silica specimens did not exhibit any change in physical appearance. A small amount of oxidation was observed on the high carbon iron-molybdenum specimens after 500 hours. No spalling and or cracking was observed on any of these plasma sprayed specimens after oxidation testing.

The thermal shock testing consisted of quenching the specimens from 650°C into boiling water 50 times. Although both coatings began to exhibit cracks after the first thermal shock cycle, no coating spallation or disbonding was observed on any of the specimens tested.

The base cast iron porcelain enamel (CIPE) being evaluated as a potential wear resistant cylinder liner coating contains BaO, B₂O₃, and SiO₂ as the main chemical constituents. This composition was selected because it was formulated especially for application and bonding to cast iron.

The base CIPE composition was applied to Falex disks and characterized for friction and wear running against a zirconia counterface in a pin-on-disk friction and wear test. The base CIPE composition ran less than 5 minutes before the test had to be terminated because a 2.5 mm wide wear track developed on the CIPE disk. Examination of the CIPE coating after the test illustrated that the pin had worn through coating to the base metal. The mechanism of failure was coating spallation.

Initially, hard particles, such as chrome oxide and aluminum oxide were added to the CIPE in an attempt to improve its wear resistance. This approach was unsuccessful because the coefficient of friction of the base enamel composition was greater than 0.3 and the addition of the hard particles increased the coefficient of friction of the CIPE to above 0.4. As a result, the addition of the hard particles had the opposite effect and instead of reducing the wear rate of the CIPE, these additions significantly increased the wear rate.

After reviewing these results, the direction of the program was changed. It was decided to first reduce the coefficient of friction of the CIPE composition by the addition of solid lubricants. Once the coefficient of friction of the CIPE composition is reduced to below 0.1, then hard particles can be added to the CIPE composition, if needed, to improve the wear resistance of the CIPE composition.

The chemical and physical stabilities of CIPE slurries containing silver flake, BN, CaF₂, BaF₂, and CeMoO₃S solid lubricant additions was determined first. No adverse chemical reactions were encountered between the solid lubricants and the CIPE. Next, the CIPE compositions containing the solid lubricants were slurry sprayed onto cast iron substrates and fired. Chemical interactions between the CIPE composition and the solid lubricants during the firing cycle required that different firing temperatures and times be determined for each CIPE plus solid lubricant composition. Next, the firing cycle for each CIPE composition was optimized to obtain the proper microstructure. Once the proper microstructure was obtained, the friction and wear properties of these coatings were characterized by running against a zirconia counterface in a pin-on-disk friction and wear test at 350°C, lubricated.

Addition of the 2.5 weight percent silver flake to the CIPE did not reduce the coefficient of friction of the CIPE. Increasing the silver additions to 5 and 10 weight percent did reduce the coefficient of friction of the CIPE from above 0.35 to .31 and .26, respectively. Also, reducing the coefficient of friction of the CIPE did reduce the amount of CIPE wear observed during the pin-on-disk testing. However, the amount of CIPE wear was still above the goals of the contract.

Increasing the amount of BaF₂ solid lubricant to the CIPE from 2.5 to 5 weight percent reduced the coefficient of the CIPE from above 0.3 to 0.26. Again, reducing the coefficient of friction of the CIPE reduced the amount of wear exhibited by the coating during the pin-on-disk friction and wear testing. However, the coefficient of friction was not reduced to a level which enabled the CIPE to have a wear rate which meets the goal of the contract. Increasing the BaF₂ content to 10 weight percent produced a CIPE with a 0.36 friction coefficient. As a result, this composition had significantly poorer wear properties than the compositions containing either the 2.5 or 5 weight percent BaF₂ additions.

BN additions at either a 2.5 or 5 weight percent level did not reduce the coefficient of friction of the CIPE. For this reason, these coatings had very poor wear properties.

The cesium oxythiomolybdate solid lubricant addition produced CIPE coatings initially with coefficient of friction values of 0.09. However, these coefficients of friction values increased to 0.36 after approximately 30 minutes of testing. Thus, while these compositions initially have acceptable wear rates the wear rates increased as the coefficient of friction values increased.

Work is continuing to develop a cast iron porcelain enamel plus solid lubricant combination which will produce both acceptable friction coefficients and average wear coefficients.

TABLE 1.

Average Wear Coefficients of Various Piston Ring Coatings Running Against a Chrome Nitride Cylinder Liner Coating, 350°C, Lubricated

Ring Coating	Coef. of Friction		Avg. Wear Coef.	
	Min-Max.	Average	Shoe	CrN Disk
Plasma sprayed hi-carbon iron-Mo	0.04-0.33	0.10	2.08×10^{-8}	4.90×10^{-8}
Plasma sprayed $\text{Cr}_2\text{O}_3\text{-SiO}_2$	0.04-0.21	0.17	5.69×10^{-9}	$< 10^{-3}$
Plasma sprayed PS212	0.04-0.22	0.21	7.8×10^{-9}	1.04×10^{-4}
CVD Ti(C,N)**	0.08-0.10	0.08	7.32×10^{-10}	7.72×10^{-6}

** Did not obtain 350°C temperature during testing because the CrN coating was completely worn through in 9 minutes.

TABLE 2.

Average Wear Coefficient of Various Piston Ring Coatings Running Against a Chromia-Silica cylinder Liner Coating, 350°C, Lubricated

Ring Coating	Coef. of Friction		Avg. Wear Coefficient mm ³ /N-m	
	Min-Max.	Average	Shoe	Cr ₂ O ₃ -SiO ₂ Disk
Plasma sprayed hi-carbon iron-Mo	0.04-0.21	0.14	5.98x10 ⁻¹⁰	3.36x10 ⁻⁸
Plasma sprayed Cr ₂ O ₃ -SiO ₂	0.09-0.18	0.17	1.69x10 ⁻⁹	3.34x10 ⁻⁶
Plasma sprayed PS 212	0.06-0.22	0.13	7.63x10 ⁻⁷	9.11x10 ⁻⁹
CVD Ti(C,N)	0.08-0.23	0.19	3.50x10 ⁻⁹	1.52x10 ⁻⁵

Status of milestones

All milestones on schedule.

Publications/presentations

M.H. Haselkorn, "Wear Coatings for Advanced Diesel Engine Components", oral presentation at the 92nd American Ceramic Society Meeting in Dallas, TX, April 24, 1990

F.A. Kelley, "Advanced Wear Coatings for Diesel Engine Components", oral presentation at the 1990 Coatings for Advanced Heat Engines Workshop held in Castine, ME, August 6-9, 1990

Development of Wear Resistant Ceramic Coatings for Diesel Engine Components

M.G.S. Naylor
Cummins Engine Company, Inc.

Objective/Scope

The objective of this program is to develop advanced wear resistant coatings for in-cylinder components for future, low heat rejection diesel engines. Coatings and substrates (for piston rings and cylinder liners) are to be developed to meet the following requirements:

1. low wear (as measured in laboratory rig tests at 200 and 350°C), with target wear coefficients (for 350°C tests) of 10^{-12} mm³/mm/N for piston ring coatings and 10^{-10} mm³/mm/N for cylinder liner materials.
2. low friction coefficients when tested under boundary lubricated conditions (target 0.1) and unlubricated conditions (target 0.2) at ambient temperature and 350°C.
3. good thermal shock resistance.
4. high adherence and compatibility with substrate materials up to 650°C.
5. high uniformity and reproducibility.

Technical Progress

Overview of Coating Development

Wear-resistant coatings under evaluation are listed in Table 1 (metallic coatings), Table 2 (ceramic coatings) and Table 3 (cermet materials). All coating development activity has been completed by the subcontractors, and wear testing/microstructural characterization is nearing completion at Cummins. Coating substrates are being machined for the final program task: fabrication of test samples for ORNL.

Coating Development at Northwestern University Basic Industrial Research Laboratory (BIRL)

Northwestern University Basic Industrial Research Laboratory (BIRL) have completed all coating development and characterization activities, and a final report is in preparation. All powders used during the program have been characterized, and coatings have been examined by X-ray diffraction to complement Cummins' evaluation of microstructures and hardness.

Coating	Substrate	Supplier	Knoop Hardness at 100gf (kgfmm ⁻²)
Electroplated Chromium	Ductile Iron	Cummins	820
APS Chromium	422 Stainless	APS Materials	
HVOF NiCrBSi	422 Stainless	UTRC	900
APS and HVOF Mo-Ni	422 Stainless	BIRL	510, 540
APS Mo-MoO ₂	422 Stainless	BIRL	770
APS Armacor M, Armacor T	HK40 Stainless	APS Materials	760, -
APS Tribolite	422 Stainless	APS Materials	

Table 1. *Metallic ring coating materials under evaluation.*
 APS = Air Plasma Sprayed
 HVOF = High Velocity Oxy-Fuel

Coating	Substrate	Supplier	KHN ₁₀₀ (kgfmm ⁻²)
APS and HVOF Cr ₂ O ₃	422 Stainless	BIRL	1440, 1320
APS Cr ₂ O ₃	HK40 Stainless	APS Materials	770
APS Metco 106FP Cr ₂ O ₃ - 2% SiO ₂ - 2% other ox.	422 Stainless	UTRC	850
APS Metco 136 Cr ₂ O ₃ - 5% SiO ₂ - 3% TiO ₂	HK40 Stainless	APS Materials	960
APS Metco 136 Cr ₂ O ₃ + 3% SiO ₂ (mixture)	HK40 Stainless	APS Materials	1020
APS Metco 136 Cr ₂ O ₃ + 15% Al ₂ O ₃ (mixture)	HK40 Stainless	APS Materials	1260
APS Cr ₂ O ₃ - 50% Al ₂ O ₃ (pre-alloyed)	422 Stainless	BIRL	650
APS Metco 143 ZrO ₂ - 18% TiO ₂ - 10% Y ₂ O ₃	422 Stainless	UTRC	450
APS Al ₂ O ₃ - 26% ZrO ₂	422 Stainless	BIRL	1050
APS Al ₂ O ₃ - 41% ZrO ₂	422 Stainless	BIRL	840
Inert Gas Shrouded APS Boron Carbide	422 Stainless	APS Materials	
PVD CrN and TaN	H13 Tool Steel	Vapor Tech.	
Ion-assisted CVD Diamond-like	H13 Tool Steel	Implant Sciences	

Table 2. *Metallic ring coating materials under evaluation.*
 PVD = Physical Vapor Deposition
 CVD = Chemical Vapor Deposition

During the current reporting period, the following materials were sprayed:

Air Plasma Sprayed (APS) and High Velocity Oxy-Fuel (HVOF) Mo - Ni

APS Mo - MoO₂

APS and HVOF Cr₂O₃

APS Cr₂O₃ - 50% Al₂O₃

APS Al₂O₃ - 26% ZrO₂

APS Al₂O₃ - 41% ZrO₂

HVOF WC - Co (sprayed with Turbine Metal Technology Inc. (Tujunga CA) proprietary HVOF gun)

Borided HVOF WC - Co (Turbine Metal Technology Inc. process)

Coating	Substrate	Supplier	KHN_{100} ($kgfmm^{-2}$)
APS WC - 12% Co	HK40 Stainless	APS Materials	1240
LPPS WC - 12% Co	HK40 Stainless	APS Materials	1130
HVOF WC - 12% Co	HK40 Stainless	APS Materials	880
HVOF WC - 12% Co	HK40 Stainless	Boyd Machine	1120
HVOF WC - 12% Co	422 Stainless	BIRL - TMT	960
Borided HVOF WC - 12% Co	422 Stainless	BIRL - TMT	1490 (25gf)
HVOF Cr_3C_2 -NiCr	422 Stainless	UTRC	990
LPPS Ferrotic CM TiC + Tool Steel	422 Stainless	APS Materials	990
LPPS Ferrotic CS40 TiC + Martensitic Stainless	422 Stainless	APS Materials	940
LPPS Ferrotic HT6A TiC + Nickel Base Alloy	422 Stainless	APS Materials	620
APS Metco 136 Cr_2O_3 + 33% Stellite 6 (mixture)	HK40 Stainless	APS Materials	Cr_2O_3 1250 Stellite 440 (10gf)

Table 3. *Cermet ring coating materials under evaluation.*
LPPS = Low Pressure Plasma Sprayed

Coating microstructures are shown in Figures 1 - 6, and are described briefly below. In all cases, bond-line integrity with the substrate and bond coats (where used) was excellent.

The Mo - Ni coatings showed two-phase microstructures, with some unmelted particles (Figure 1). The HVOF spray process resulted in a finer dispersion of the two phases. Both coatings contained unmelted particles and low levels of porosity. Microhardness values for the two coatings were similar (Table 1).

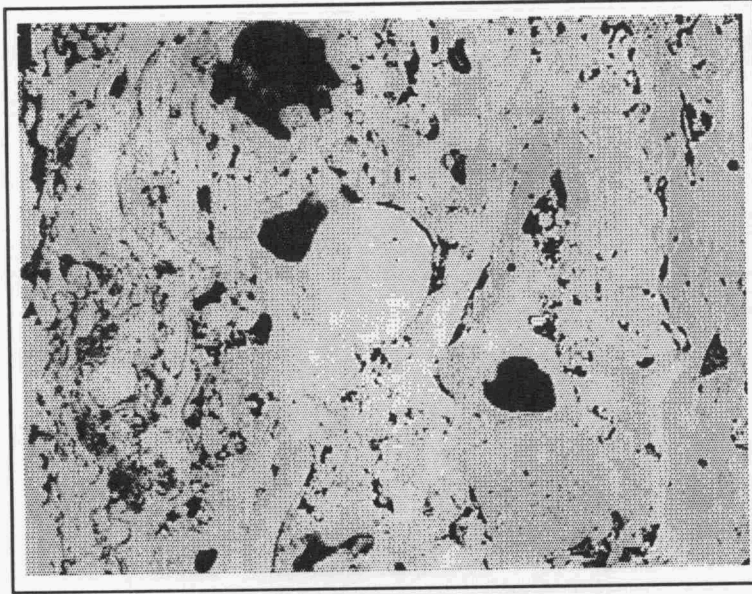
The Mo - MoO_2 coating exhibited a fine, uniform dispersion of oxide in a metallic matrix, with some large pores (Figure 2). This coating was harder than the Mo - Ni materials (Table 1).

The pre-alloyed Cr_2O_3 - 50% Al_2O_3 coating showed a large amount of porosity and inter-splat voids/microcracks (Figure 3). This material proved impossible to spray by HVOF processes. Variations in grey scale observable in the light micrographs suggest that the powder particles were not of uniform composition, as was hoped for. The low microhardness value for this material (Table 2) probably reflects the high level of porosity in the coating, rather than inherent softness of the material.

APS and HVOF chromium oxide coatings are shown in Figure 4. Both coatings exhibited very low porosity compared to other chromium oxide coatings examined during this program, probably due to the fineness of the starting powder. Pores were rounded and evenly distributed, with little inter-splat microcracking. Hardness levels were high compared to other chromium oxides examined previously (Table 2).

The two Al_2O_3 - ZrO_2 coatings are shown in Figure 5. Both materials contained even distributions of equiaxed porosity, with very little inter-splat microcracking. The Al_2O_3 - 26% ZrO_2 material showed light-imaging lamellar features, suggesting some degree of inhomogeneity in the starting powder. The Al_2O_3 - 41% ZrO_2 (eutectic composition) material exhibited some fine-scale microstructure, but was more uniform than the above material. Hardness levels were higher for the Al_2O_3 - 26% ZrO_2 material than for the eutectic composition (Table 2).

(a)



(b)

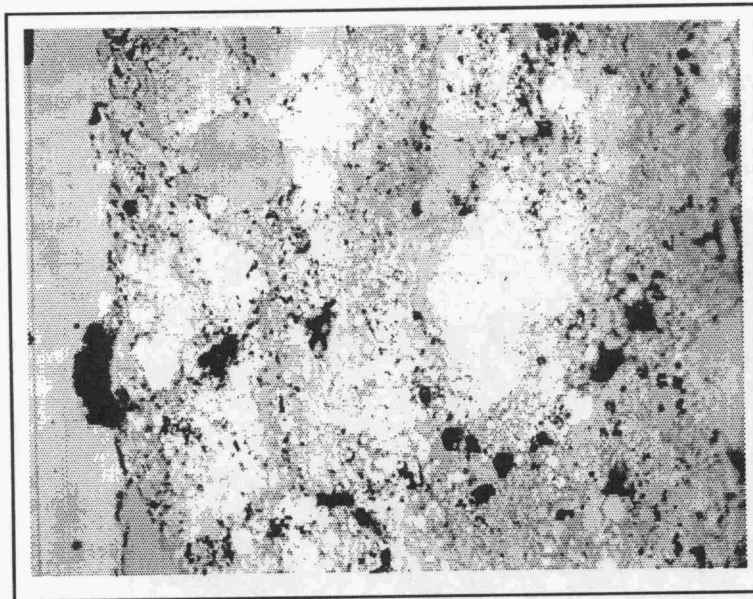
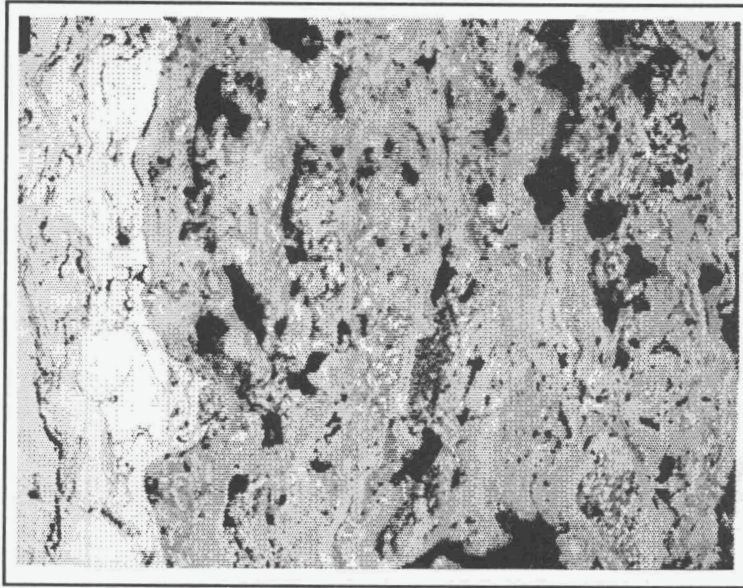
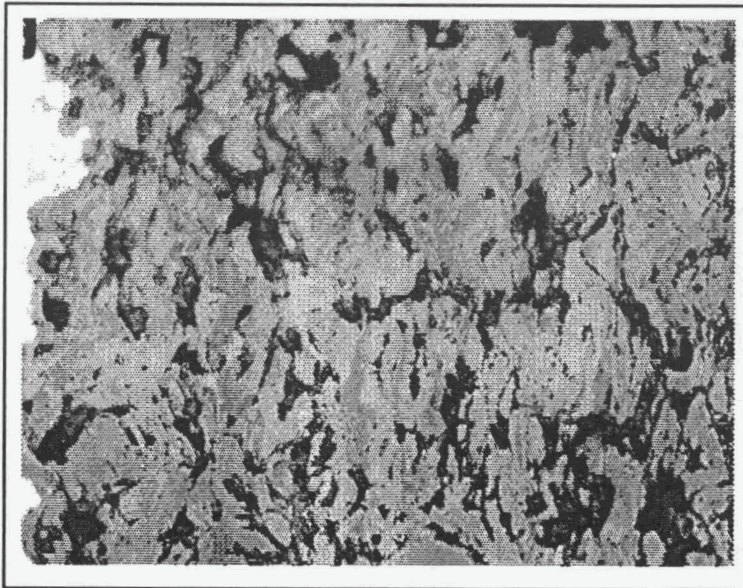
50 μm

Figure 1. Light micrographs of Mo - Ni coatings.
(a) Air Plasma Spray
(b) High Velocity Oxy-Fuel



50 μ m

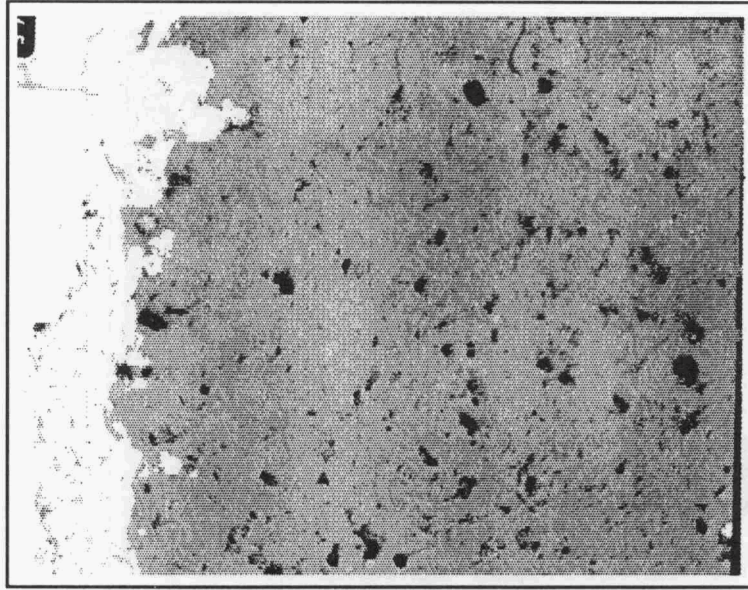
Figure 2. Light micrograph of APS Mo - MoO₂ coating.



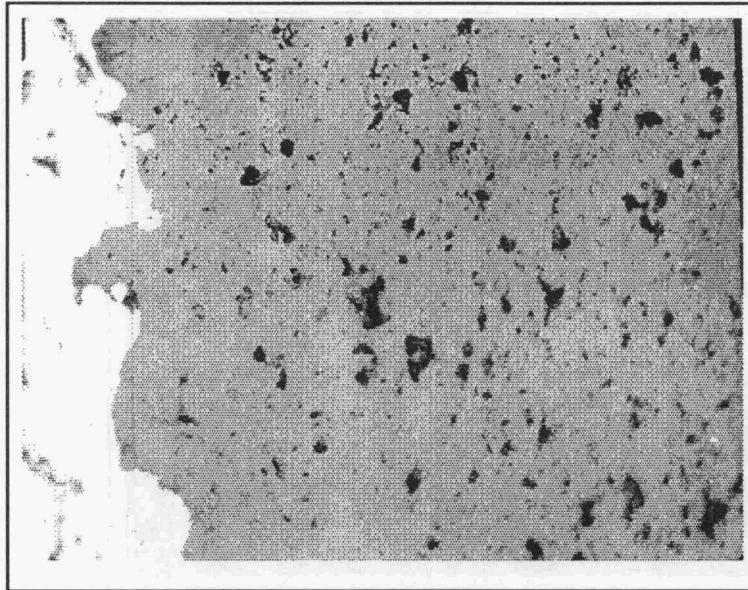
50 μ m

Figure 3. Light micrograph of APS Cr₂O₃ - 50% Al₂O₃ (pre-alloyed) coating.

(a)



(b)



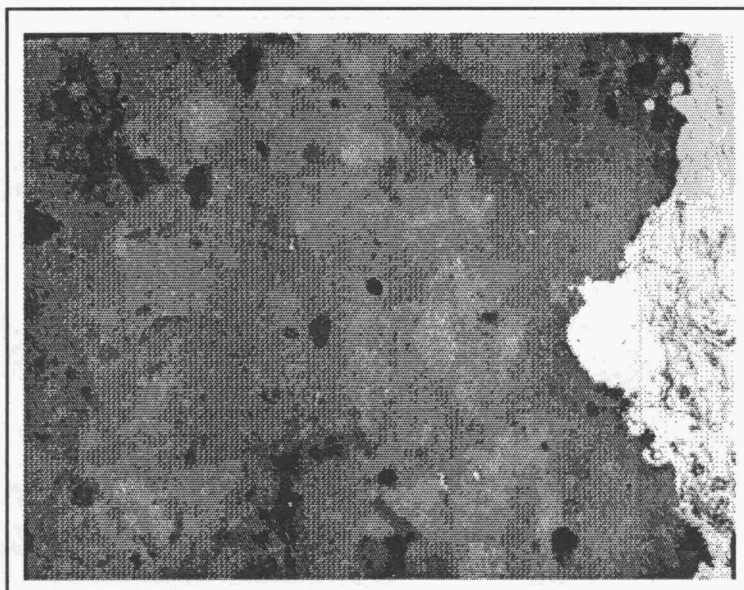
50 μm

Figure 4. Light micrographs of chromium oxide coatings.
(a) Air Plasma Spray
(b) High Velocity Oxy-Fuel

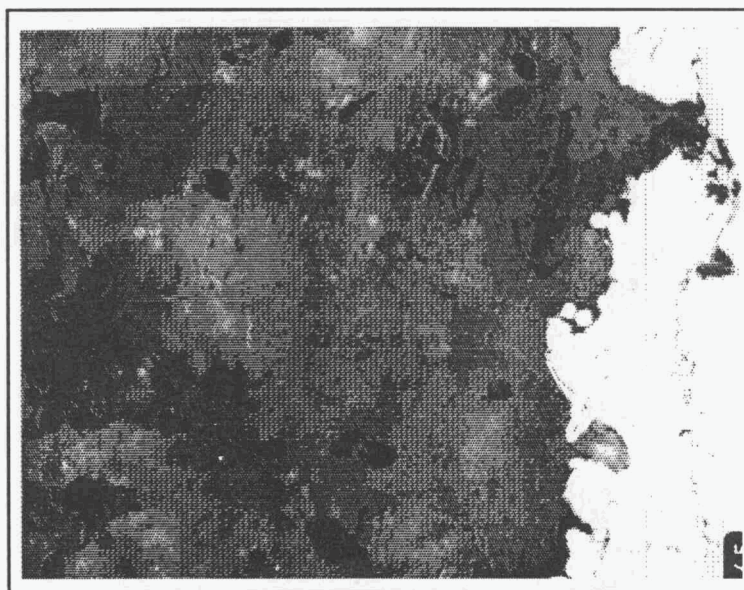
Figure 5.

(a) Al_2O_3 - 26% ZrO_2
(b) Al_2O_3 - 41% ZrO_2 (eutectic composition)

50 μm



(b)



(a)

The Turbine Metal Technology (TMT) HVOF WC - Co material, shown in Figure 6a, exhibited a very fine-scale microstructure compared to other WC - Co materials examined, with extremely low porosity and excellent uniformity. Boride diffusion-alloying this coating resulted in an interesting microstructure, which has not been characterized fully at this point. At the surface, a 10 μm thick darker imaging phase is observable, with a line of fine porosity beneath it (Figure 6b). Below this is a 20 μm thick lighter-imaging layer, with another layer of coarser porosity below it. Beneath this are (presumably) the remnants of the original WC - Co microstructure. The original WC particles are not visible in either of the top two surface layers. The hardness of the coating, measured with 25gf Knoop indentations in the lighter-imaging layer, was approximately 1490 kgfmm⁻².

Coating Development at APS Materials, Dayton OH

APS Materials have produced WC - 12% Co coatings by three different spray methods (APS, Low Pressure Plasma Spray (LPPS) and HVOF) using the same powder (Miller Thermal 1172). Microstructures are shown in Figure 7. The APS and LPPS materials showed similar microstructures, although the LPPS coating was considerably thinner (Figures 7a and 7b). With the LPPS process, problems were encountered with the coating shattering on cool-down after spraying. The carbide particles in both coatings were equiaxed and showed a bimodal size distribution, with a slightly inhomogeneous dispersion through the matrix phase. Both coatings contained some coarse porosity. The HVOF material, sprayed with a "Jetkote" gun, shows some subtle differences in carbide morphology compared to the above materials, with a higher percentage of non-equiaxed particles (Figure 7c). Microhardness values for the APS, LPPS and HVOF coatings were, respectively, 1240, 1130 and 880 kgfmm⁻² (KHN₁₀₀), although there was considerable scatter from one location to another for each coating. The differences are probably caused by different amounts of decarburization and carbide solutionizing during the spray processes, and this is under further investigation by means of X-ray diffraction of the various WC - Co coatings tested in this program.

Three grades of Ferrotic powder have been sprayed using a LPPS system. The materials investigated were:

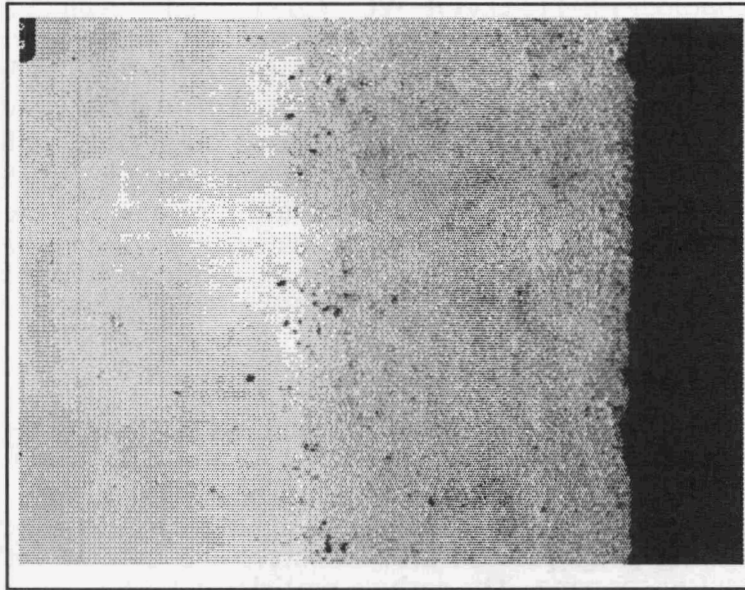
Ferrotic CM	45% TiC in a high chrome tool steel matrix
Ferrotic CS-40	45% TiC in a martensitic stainless steel matrix
Ferrotic HT-6A	35% TiC in an age hardenable nickel base matrix.

Microstructures of the three materials are shown in Figure 8. The CM and CS-40 grades both showed similar microstructures to the APS and LPPS WC - Co materials described above, with a somewhat coarser carbide size distribution, slightly lower carbide content and lower microhardness (Table 3). The HT-6A microstructure (Figure 8c) showed a slightly lower volume fraction of carbide particles than the above grades, and correspondingly lower hardness (Table 3). Porosity levels were lower for the HT-6A material than for the other Ferrotic grades (Figure 8).

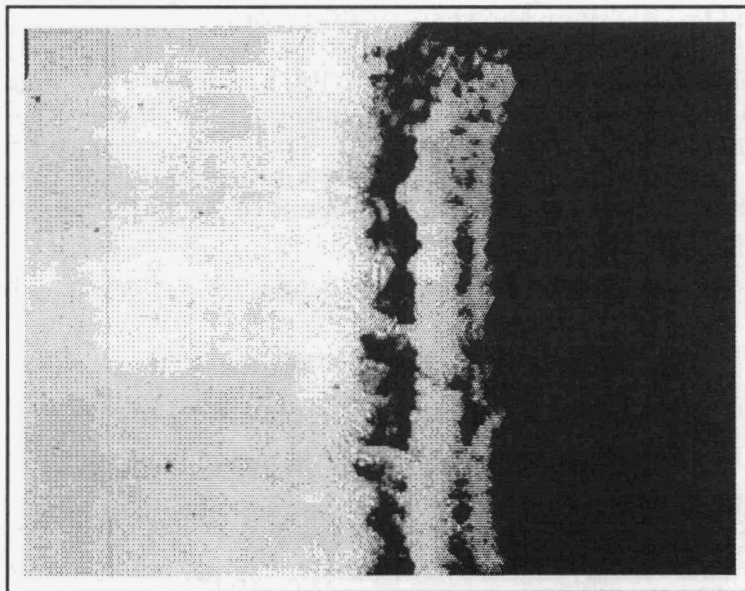
A boron carbide coating has been sprayed using a fine-grained Stark powder (selected by BIRL), using nitrogen shrouded air plasma spray techniques developed at APS Materials. Previous attempts to spray a coarser powder in air and in vacuum proved unsuccessful (see previous semiannual report). Characterization of this material is in progress.

Coatings were sprayed with a "Tribolite" powder, which is a proprietary material of Wear Management Services, Inc. Characterization of this material is in progress. Wear Management Services technical literature describes the material as a very fine boron carbide dispersion in a metallic matrix.

(a)



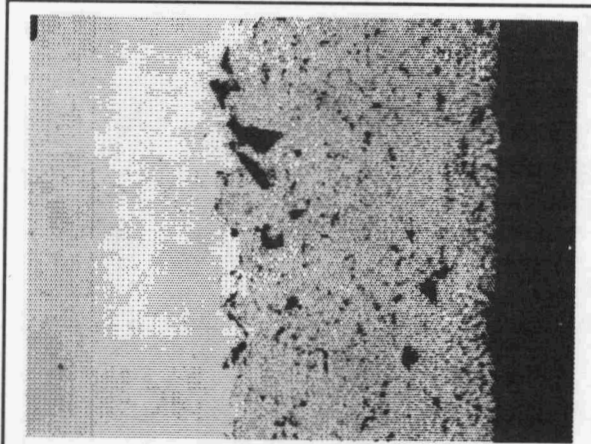
(b)



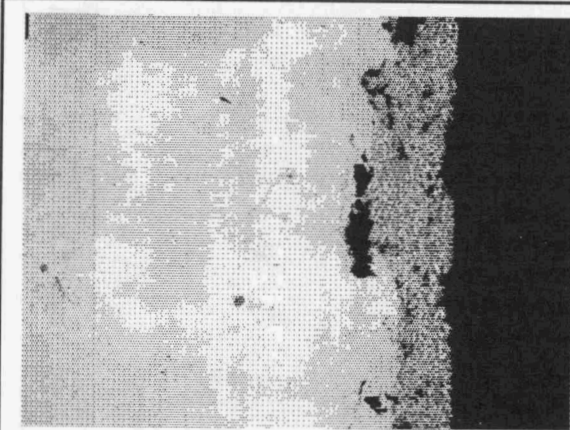
50 μm

Figure 6. *Light micrographs of Turbine Metal Technology HVOF WC - Co coatings.*
(a) *As-sprayed*
(b) *With subsequent boride diffusion alloying process*

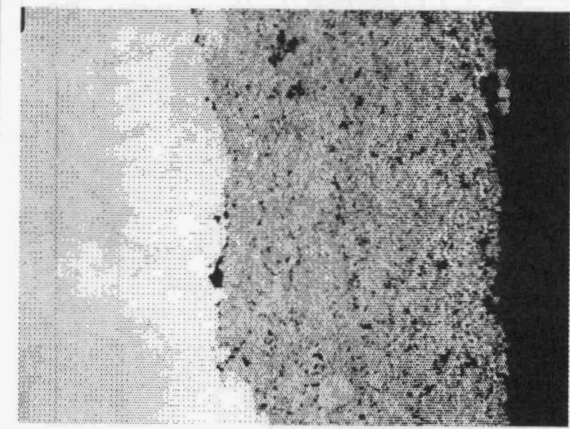
(a)



(b)



(c)



100 μm

Figure 7. *Light micrographs of WC - 12% Co coatings.*
(a) *Air Plasma Spray*
(b) *Low Pressure Plasma Spray*
(c) *High Velocity Oxy-Fuel*

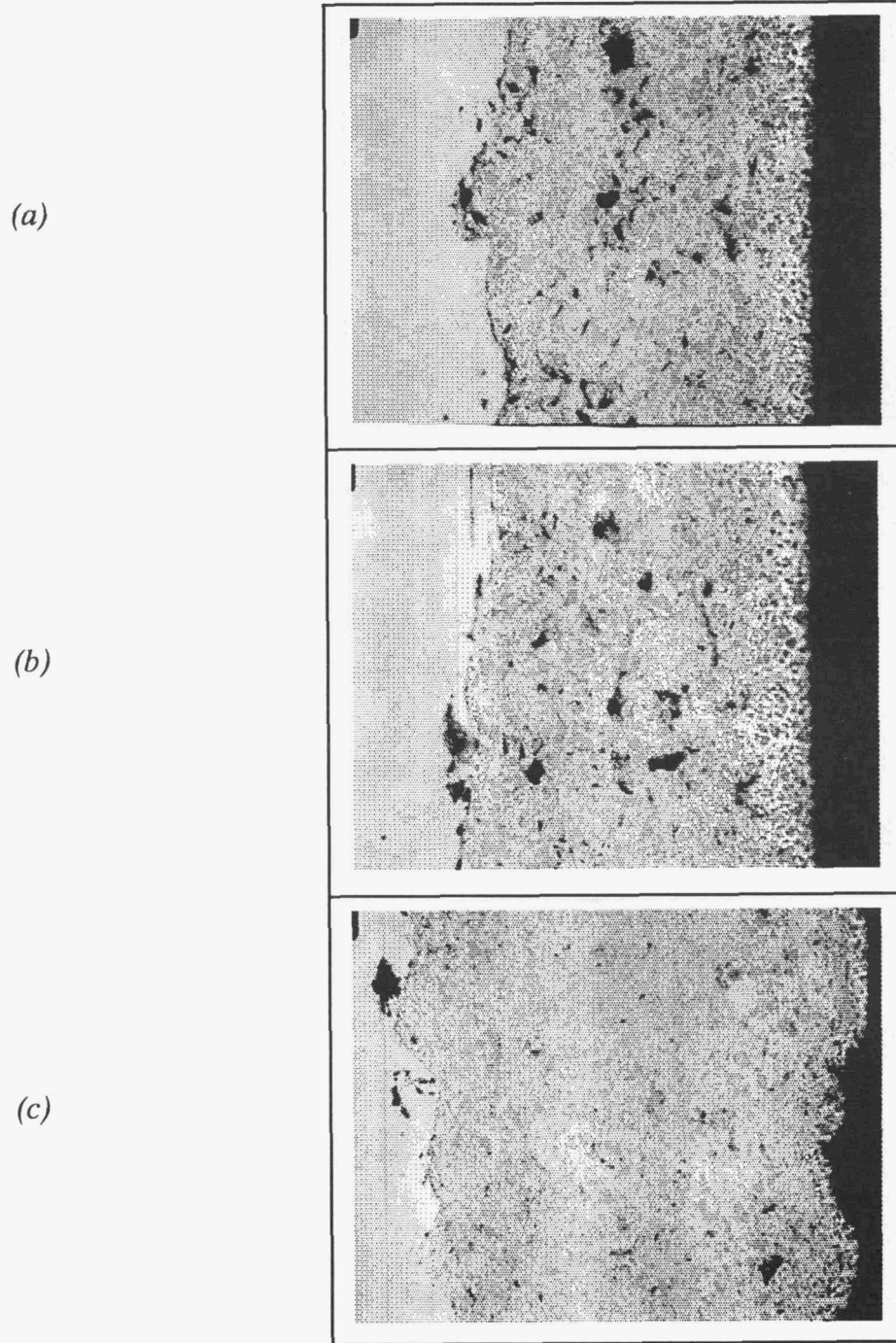


Figure 8. *Light micrographs of LPPS Ferrotic coatings.*
(a) Ferrotic CM
(b) Ferrotic CS-40
(c) Ferrotic HT-6A

A series of test coupons have been sprayed with a Metco 350 Fe-Mo-C powder blended with various metallic and ceramic additions, in an attempt to create a cermet microstructure with a hard matrix phase. The powders were sprayed with a LPPS system in order to retain the highest carbon content possible. The coating mixtures sprayed were:

Metco 350 with titanium	Reactive system
Metco 350 with boron	Reactive system
Metco 350 with 50% TiB ₂	Non-reactive system
Metco 350 with 25% B ₄ C	Non-reactive system

The first two materials formed essentially two-phase metallic coatings with no carbide formation. It is concluded that pre-alloyed powders would be required to achieve sufficient reaction of the carbon with the reactive metal phase. The boride/carbide additions resulted in typical cermet microstructures. On the basis of the microstructural evaluation, it was decided not to undertake further development of this system.

Plasma sprayed chromium samples were obtained for comparison with the baseline electroplated hard chromium piston ring material. Characterization of this material is in progress.

Coating Development at UTRC, East Hartford CT

All coating development and testing phases have been completed. Results have been described in previous bimonthly and semiannual reports.

Coating Development at Vapor Technologies, Inc., Boulder CO

CrN and TaN coatings are to be prepared using a low temperature cathodic arc PVD process. Unfortunately, this project has been delayed due to relocation of manufacturing equipment.

Coating Development at Implant Sciences Corporation, Danvers MA

Diamond-like coatings have been prepared using an ion-assisted CVD process. Substrate materials were H13 tool steel (cylindrical "ring" and flat "liner" samples) and pearlitic grey cast iron (flat "liner" samples). Substrate materials were lapped prior to coating, since the surface finish of a thin coating of this type is controlled by the finish of the substrate. The coatings have been received and final machining of the "ring" samples is in progress.

Wear Testing

Wear tests were performed using test conditions chosen to represent the ring-liner engine environment close to the top ring reversal position, and are detailed in Table 4. Tests were performed using a Cameron Plint TE77 reciprocating wear tester.

Lubricated tests were run with a fresh commercial CE/SF quality 15W40 mineral oil based lubricant and a lubricant obtained from an experimental engine test, in order to assess the effects of oil contamination and degradation from a realistic diesel engine environment on wear of ring and liner materials. The starting lubricant used for this engine test was a CE/SF 15W40 mineral oil based lubricant with identical wear properties to the fresh oil used for this program, but with a slightly different formulation. Characterization of the

<i>Test Schedule for Each Coating:</i>
Fresh CE/SF 15W40 mineral oil based lubricant at 200°C Fresh CE/SF 15W40 mineral oil based lubricant at 350°C 3% Soot Engine-tested CE/SF 15W40 mineral oil based lubricant at 200°C Unlubricated, 200°C
<i>Test Conditions:</i>
225 N on a 7.5 mm wide sample (30 N/mm) "Ring" sample has cylindrical radius of curvature of 50 mm "Liner" sample is flat 20 Hz frequency 5 mm stroke Lubricated tests: 6 hrs with 1 drop of oil every 10 seconds Unlubricated tests: 5 minutes.

Table 4. Wear test conditions.

fresh and engine-tested oils is summarized in Table 5. The engine-tested oil was highly soot-loaded, with moderate levels of oxidation and little additive package depletion. Soot levels were higher than would normally be produced in a commercial engine.

In addition to the lubricated tests, materials were evaluated with no lubrication, in order to rank the sliding wear properties of different materials under "scuffing" conditions. A material with good scuff resistance is desirable in case of temporary loss of oil film in the engine (on start-up or under short duration conditions of extreme hot running, for example). Due to the high loads experienced at top ring reversal, it is generally accepted that dry wear coefficients are too high to permit extended engine operation without lubrication (e.g. reference 1).

Due to the large number of coatings evaluated and the multiplicity of test conditions, screening of ring coating materials was performed using conventional pearlitic grey cast iron cylinder liner counterfaces only, except for the optimization work described below. This approach was taken primarily because of the relative costs involved in manufacturing coated rings versus coated liners, and because it is likely that any new ring coating would have to be compatible with existing cylinder liner materials. Additional wear tests were performed with the UTRC HVOF Cr₃C₂-NiCr material sliding against various liner materials, in order to optimize the system for lowest total wear (ring plus liner).

Wear results have been expressed as *wear coefficients*, which were calculated by dividing the total volume of wear (mm³) by the product of sliding distance (mm) and applied normal load (N). Wear volumes were determined by measurement of wear scar widths (for the rings) and by stylus profilometry (liners).

Results Using Fresh Lubricant

A summary of wear results for all the coatings studied to date is shown in Figures 9 (200°C tests) and 10 (350°C tests). Ring and liner wear coefficients are shown for each material couple on a logarithmic scale. For these plots, wear coefficients for Cr₂O₃ materials were averaged for several coatings of different compositions, since the variations in wear coefficients were relatively small for these materials (see below).

Property	Fresh Oil	Engine-Tested Oil
Viscosity, 40°C (cSt)	95.2	161.0
Viscosity, 100°C (cSt)	14.1	18.6
Viscosity Index	152	130
TBN (mg KOH/g)	6.8	4.2
TAN (mg KOH/g)	2.9	8.3
Zinc Content (ppm)	1800	1750
Phosphorus Content (ppm)	1480	1380
Calcium + Magnesium Content (ppm)	1500	2240
Fe Wear Metal (ppm)	0	285
Cr Wear Metal (ppm)	0	10
TGA Soot (%)	0.5	3.3

Table 5. Properties of fresh and engine-tested lubricants used for wear tests. (Experimental engine test selected for high soot loading.)

Under the test conditions imposed, all materials systems operated in the boundary lubrication regime at both test temperatures, with friction coefficients in the range 0.1 to 0.3. For the lubricant and oil supply rate used in these tests, the "scuffing" temperature (the temperature above which an oil film could not be maintained and friction coefficients in excess of 0.5 were measured) was approximately 360°C. Thus, the 350°C tests are very close to the scuffing limit of the mineral oil based lubricant.

Wear coefficients for the coatings investigated ranged over two orders of magnitude in the 200°C tests (Figure 9a) and over three orders in the 350°C tests (Figure 10a). Broadly, the ranking of materials was similar for both tests, with minor variations. Several of the materials evaluated showed lower wear coefficients than the "baseline" electroplated hard chromium ring material. In particular, the chromium oxide, tungsten carbide - cobalt and chromium carbide - nichrome materials showed great promise. In general, the lowest wear rates were obtained with the cermet materials and the highest wear rates with the metallic thermal spray coatings, even though some of the metallic coatings showed very high hardness levels (Table 1). Ceramic coatings gave mixed results in these tests, with the zirconia - titania - yttria material showing very disappointing performance.

Several WC - 12% Co materials have been evaluated, giving consistently low wear values. Detailed comparisons are difficult, since different powders and processes were used for each coating. The APS and LPPS materials were sprayed using the same powder, and showed no consistent differences in wear rates or microstructure (see above). The HVOF coating sprayed from the same powder is currently under evaluation. Other HVOF WC - Co materials gave the lowest wear coefficients of all the materials tested, the fine-grained TMT material showing particularly low wear.

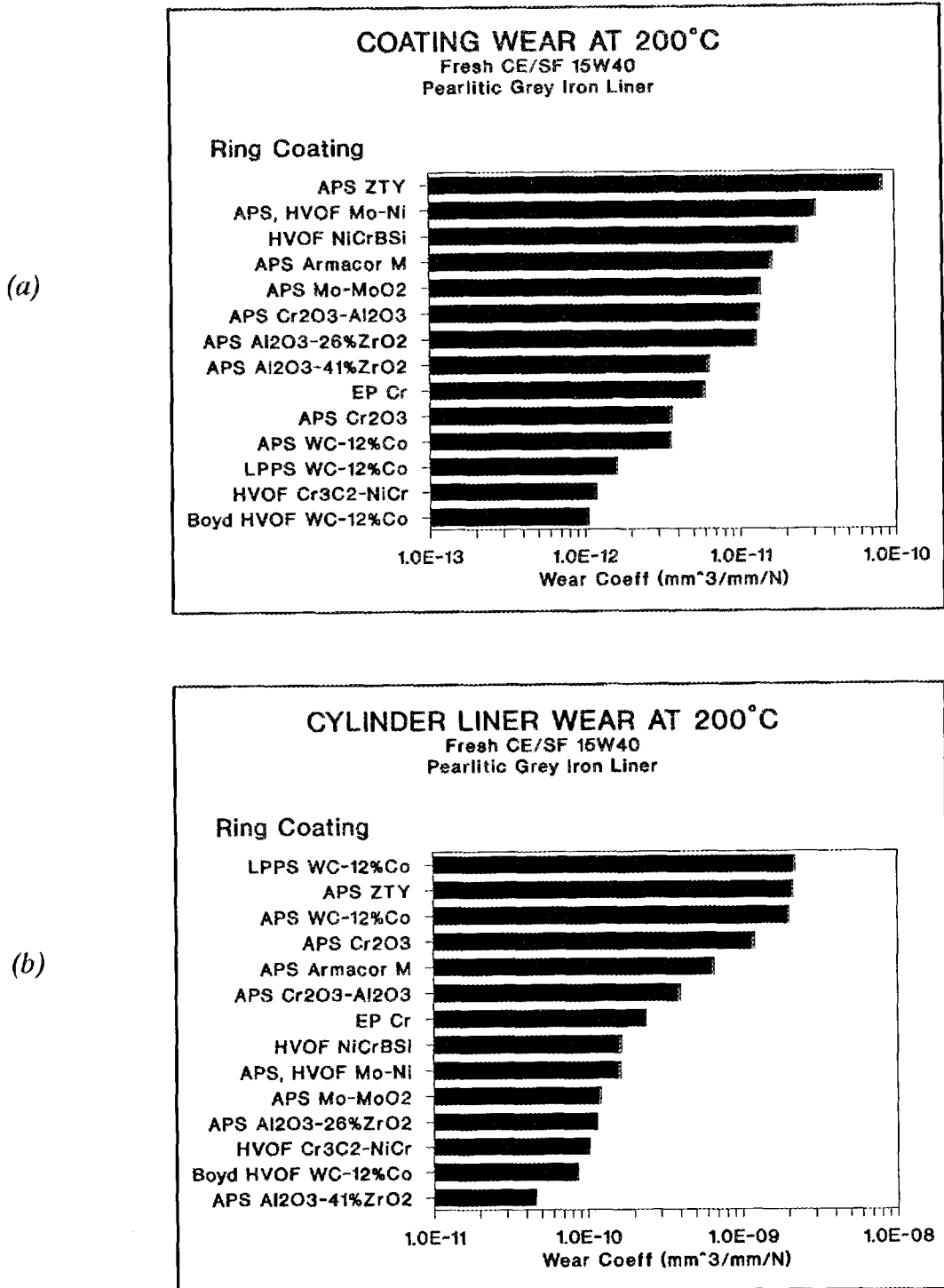


Figure 9. Wear coefficients for various coatings sliding against pearlitic grey iron liners. Tests were run with fresh CE/SF 15W40 mineral oil based lubricant at 200°C. (a) coating wear, (b) liner wear

EP = Electroplated, APS = Air Plasma Spray, LPPS = Low Pressure Plasma Spray, HVOF = High Velocity Oxy-Fuel

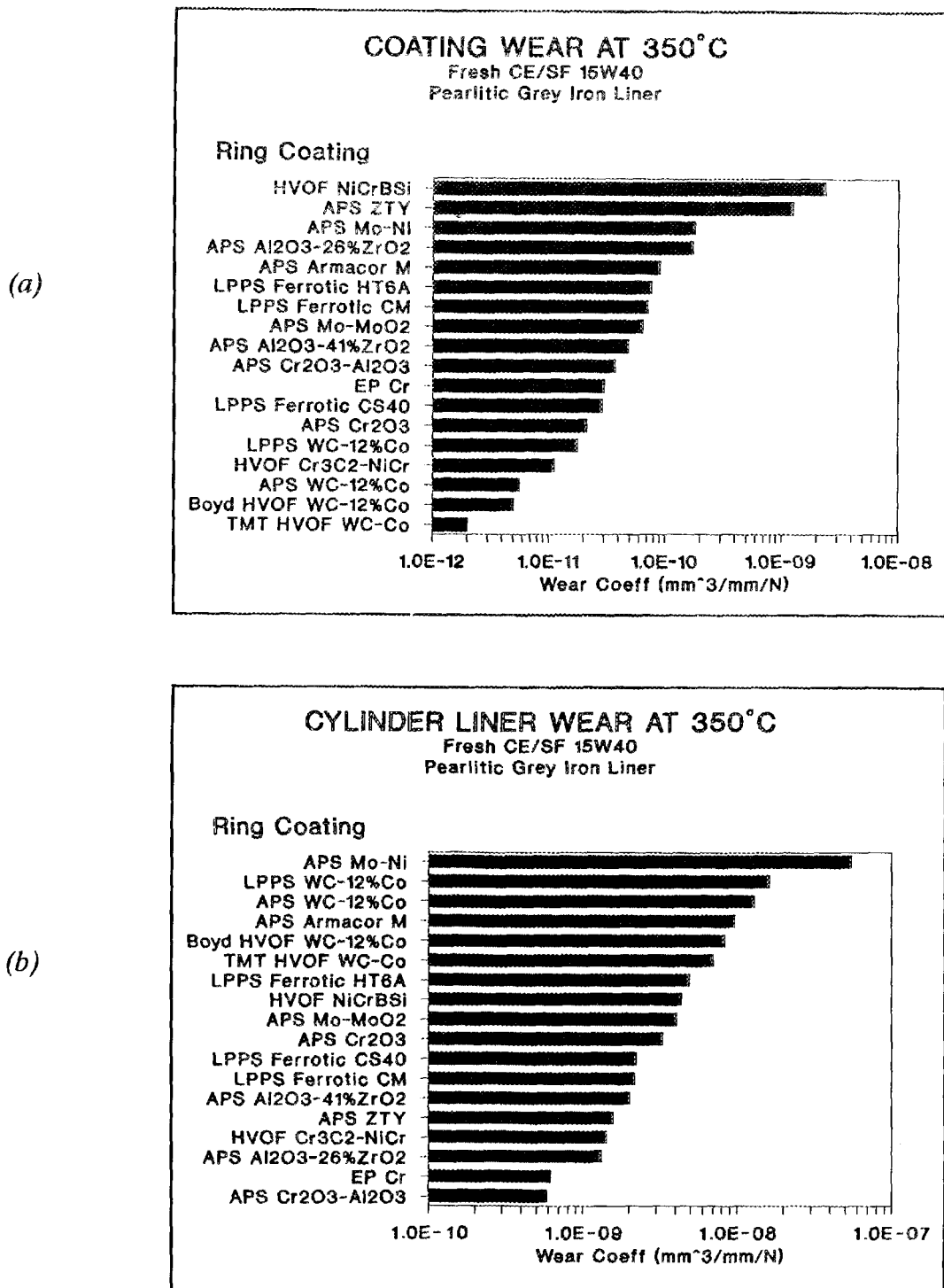


Figure 10. Wear coefficients for various coatings sliding against pearlitic grey iron liners. Tests were run with fresh CE/SF 15W40 mineral oil based lubricant at 350°C. (a) coating wear, (b) liner wear

EP = Electroplated, APS = Air Plasma Spray, LPPS = Low Pressure Plasma Spray, HVOF = High Velocity Oxy-Fuel

The LPPS Ferrotic materials showed generally "average" (compared to EP chromium) wear properties at 350°C. This is surprising, since the hardness values, carbide contents and microstructures of the CM and CS-40 grades were similar to those of many of the WC - Co materials.

The Al₂O₃ - ZrO₂ coatings also showed "average" properties, the eutectic composition (Al₂O₃ - 41% ZrO₂) giving wear coefficients two to three times lower than the Al₂O₃ - 26% ZrO₂ material, despite lower hardness.

Of the Mo - based coatings, the Mo - MoO₂ showed lower wear rates than the Mo - Ni materials. APS and HVOF Mo - Ni coatings gave very similar wear coefficients. Figure 11 shows the wear surface of an APS Mo - Ni coating tested at 350°C, revealing evidence of abrasive (ploughing) wear and extensive spallation by inter-splat fracture.

An important factor to be considered in evaluating the tribological properties of a piston ring coating material is the amount of wear occurring on the cylinder liner counterface. For optimum engine durability, low wear rates are required of both rings and liners, therefore a systems approach is necessary in materials selection. Wear coefficients for pearlitic grey cast iron counterface materials are shown in Figures 9b (200°C) and 10b (350°C). At 200°C, many of the coatings evaluated produced lower liner wear than electroplated chromium, but at 350°C only the Cr₂O₃ - 50% Al₂O₃ material showed lower liner wear. WC - Co materials gave very mixed results: at 350°C, all WC - Co materials produced high liner wear, regardless of surface finish. At 200°C, the materials with as-ground surfaces (approximately 0.65 μm RA) gave high liner wear, but the lapped material (approximately 0.04 μm RA) produced low liner wear. In contrast, the as-ground (0.4 μm RA) HVOF Cr₃C₂-NiCr coating (one of the best for ring wear) gave consistently low values for liner wear in both tests. Chromium oxide coatings generally produced high liner wear, especially at the lower temperature. Surprisingly, the softer coating materials did not necessarily produce low liner wear in these tests (e.g. APS Mo - Ni at 200°C).

A breakdown of the wear coefficients for various chromium oxide materials is shown in Figure 12. Comparing the 200 and 350°C tests, it is difficult to resolve consistent trends from these tests. Differences in wear coefficients were generally related to the amount of porosity and inter-splat microcracking in the coatings, and may also have been related to the coating composition.

Wear As A Function Of Temperature

Figure 13 shows the variation of wear coefficients with temperature for electroplated chromium piston rings sliding against pearlitic grey cast iron cylinder liners, lubricated with fresh CE/SF 15W40 oil. An Arrhenius function, of the form

$$W = W_0 \exp\left(-\frac{Q}{RT}\right)$$

(where W is a wear coefficient, W₀ is a constant and Q is an "activation energy"), was found to fit the data reasonably well (Figure 13). "Activation energies" were determined to be 26.5 kJ mol⁻¹ for the chromium plated rings and 15.6 kJ mol⁻¹ for the pearlitic iron liners. The above analysis is empirical only, since wear coefficients are not true rate constants (dimensions s⁻¹) and wear processes are probably stress-activated as well as thermally activated (perhaps more analogous to "power-law creep", if the rate of material loss is related to plastic deformation, for example). More detailed analysis would require a much greater understanding of the wear mechanisms operating for the tribological systems investigated, and is beyond the scope of this study.

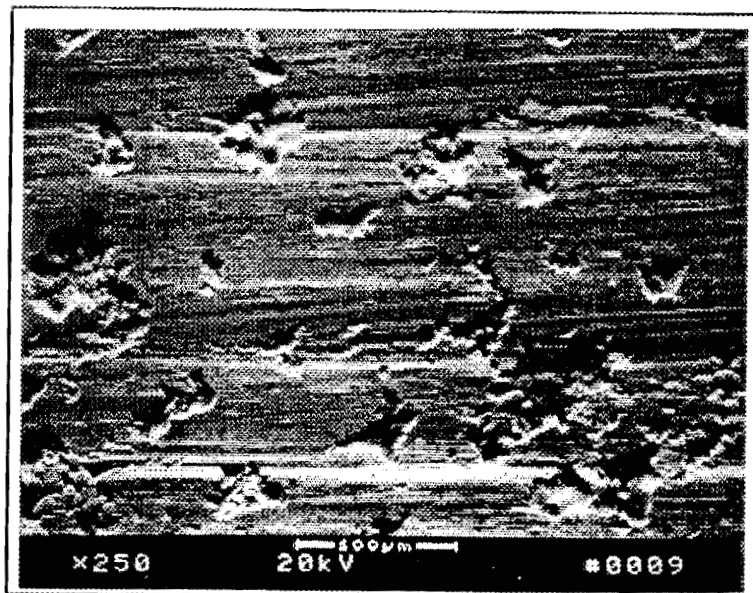


Figure 11. Wear surface of APS Mo - Ni coating after sliding against pearlitic grey iron for 6 hours at 350°C with fresh CE/SF 15W40 mineral oil based lubricant.

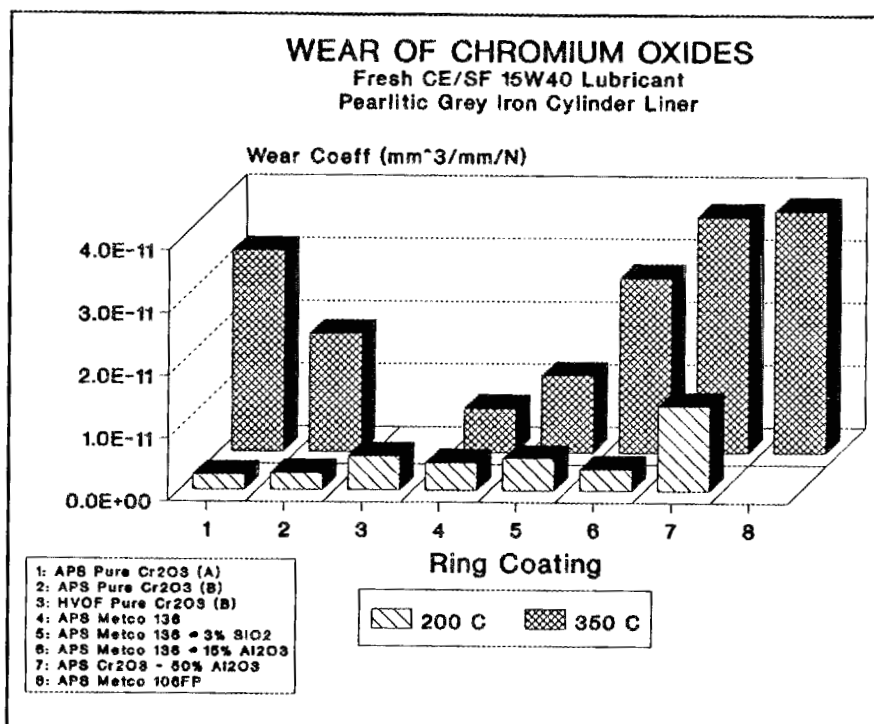


Figure 12. Wear coefficients for various chromium oxide based coatings sliding against pearlitic grey iron liners. Tests were run with fresh CE/SF 15W40 mineral oil based lubricant at 200 and 350°C.

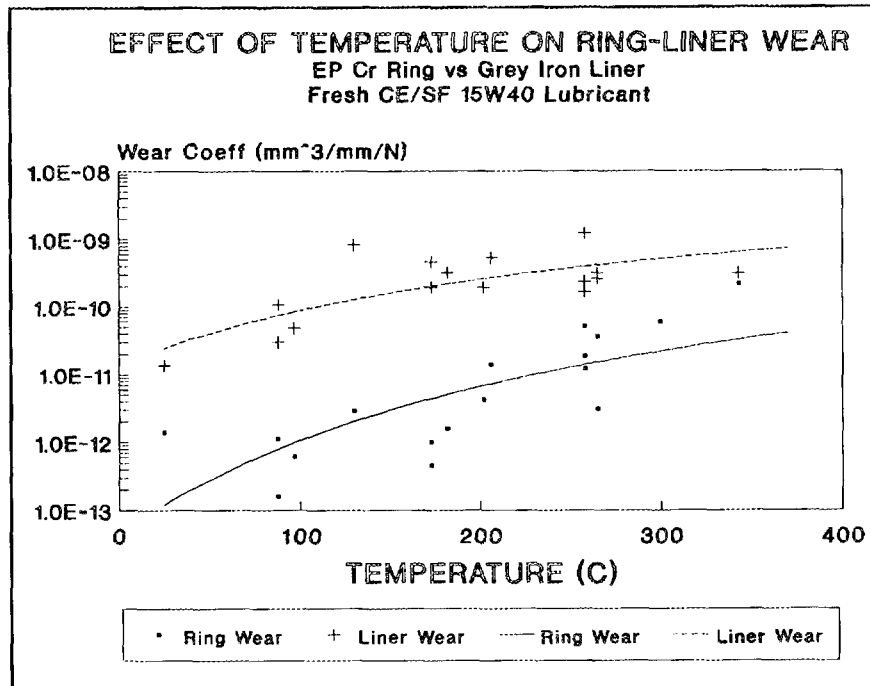


Figure 13. Variation of wear coefficients with temperature for the baseline ring - liner system: electroplated chromium rings and pearlitic grey iron liners. Tests were run with fresh CE/SF 15W40 mineral oil based lubricant.

Figures 9 and 10 clearly show that wear coefficients also increased markedly with increasing temperature for all of the coating materials tested (with grey iron counterfaces). For the purpose of comparing the temperature sensitivities of wear coefficients, Arrhenius equations were fitted to wear data obtained for each material (Figure 14). This is an extrapolation through only two temperature points for most materials, so the analysis should be viewed with caution. For the coatings shown in Figure 14, the extrapolated fitting curves were surprisingly parallel, with "activation energies" all falling in the range 25 - 45 kJ mol⁻¹. Thus, ranking the materials in order of increasing wear coefficients produced broadly similar results at 200 and 350°C (Figures 9 and 10).

An interesting observation is that plasma sprayed Cr₂O₃ sliding against slurry-sprayed silica-chromia-alumina (fresh oil lubricated) has been found previously to show no variation of wear coefficients with temperature for either material (reference 2 and previous reports). A possible explanation of this behaviour is that, for pearlitic grey cast iron liner materials, ring wear may be controlled by oxidation of the liner material rather than (or, perhaps, in addition to) abrasion by the hard phases present in the iron (e.g. Fe₃C or other alloy carbides).

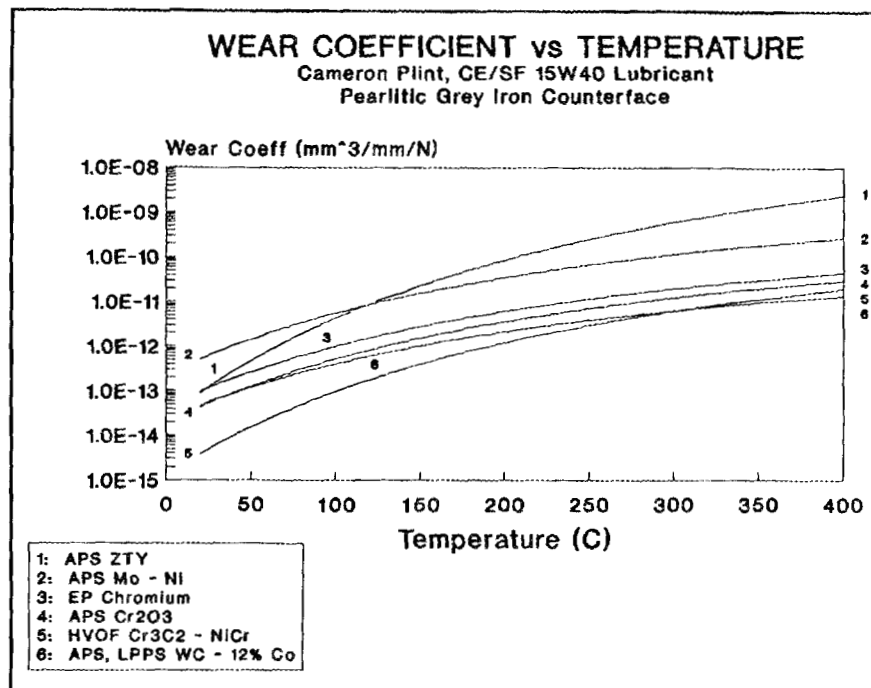


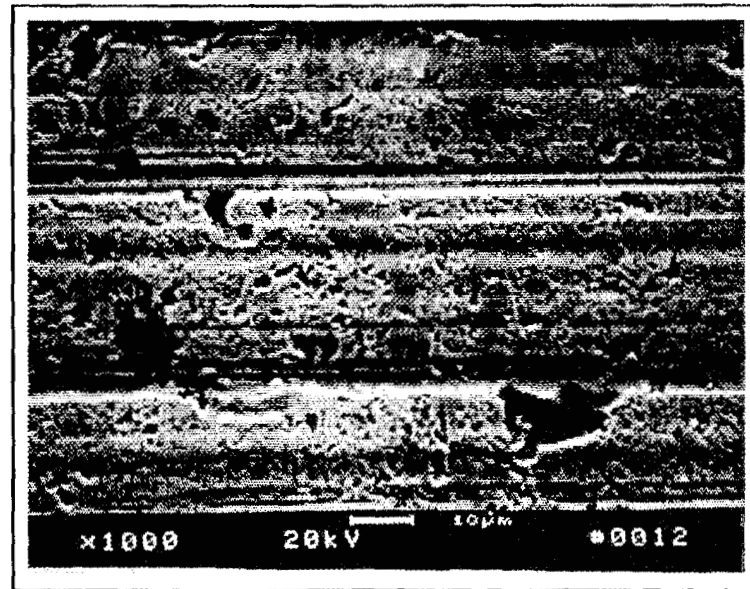
Figure 14. Variation of wear coefficients with temperature for various coatings sliding against pearlitic grey iron liners. Tests were run with fresh CE/SF 15W40 mineral oil based lubricant. Curves show Arrhenius functions fitted to 200 and 350°C data points for each material.

Figure 15 shows wear surfaces of the HVOF Cr₃C₂ - NiCr material after tests at 200 and 450°C. At the lower temperature, wear rates were low enough that the original grinding marks were still discernable, and wear occurred by a polishing type of mechanism, with some pull-out (pitting) and spallation. At 450°C, deep wear grooves were formed across the whole wear scar, possibly due to increased plasticity at the higher temperature or increased abrasive (ploughing) wear from oxide debris. Figure 15b also shows that wear grooves pass from the NiCr matrix phase into the carbides with little or no apparent change in width. The carbides do not stand proud of the wear surface, as has been observed previously for other materials (e.g. HVOF WC - Co at lower test temperatures, see reference 2).

Results Using High-Soot, Engine-Tested Lubricant

Bench wear tests conducted with engine-tested lubricants have established that wear rates may be significantly increased compared to tests with fresh oil. The reasons for this behaviour have not been fully determined, however an important factor for diesel engines is the accumulation of combustion-derived soot (typically 50 - 500 nm sized particles of microcrystalline carbon) in the oil. Many hypotheses have been proposed to explain the "pro-wear" characteristics of soot, including mechanical abrasion, removal of lubricant anti-wear films and chemical attack by species adsorbed on the soot particles.

(a)



(b)

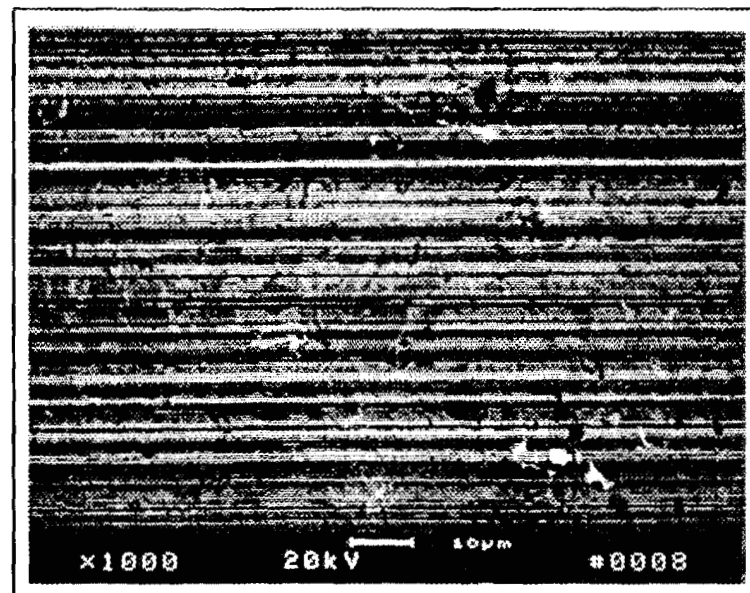


Figure 15. Wear surfaces of HVOF Cr_3C_2 - NiCr coating after sliding against hardened H13 tool steel for 6 hours:
(a) 200°C, fresh CE/SF 15W40 mineral oil based lubricant
(b) 450°C, unformulated Poly-Alpha-Olefin lubricant

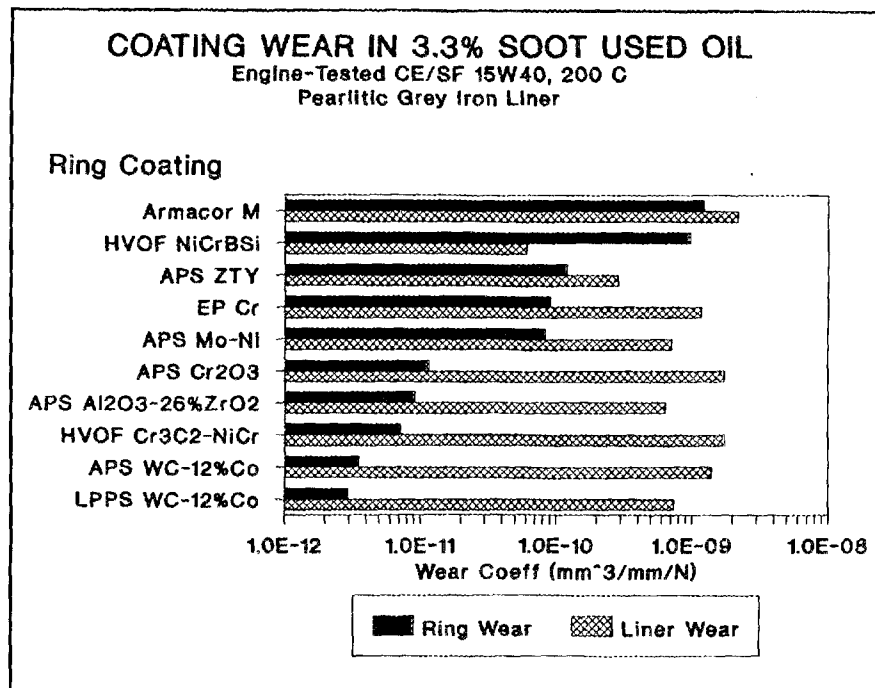


Figure 16. Wear coefficients for various coatings sliding against pearlitic grey iron liners. Tests were run with 3.3% soot, engine-tested CE/SF 15W40 mineral oil based lubricant at 200°C.

Wear coefficients measured for 200°C tests with the high-soot, engine-tested CE/SF 15W40 lubricant are shown in Figure 16. Comparing Figures 16 and 9a, it is apparent that metallic coatings are generally more prone to accelerated wear in used oil than ceramic or cermet coatings. For example, wear rates for electroplated chromium were approximately 15 times higher in used oil than in fresh, whereas chromium oxide coatings were subject to only a threefold increase and WC - Co materials showed less than a factor of two increase. Also, the Al₂O₃ - 26% ZrO₂ material showed lower wear rates than electroplated chromium in tests with the high-soot, engine-tested lubricant, despite showing higher wear in fresh oil. Thus, it is important to take into account the effects of oil degradation in the engine when comparing the wear properties of different coatings.

Unlubricated Wear Test Results

Wear data for unlubricated tests at 200°C are shown in Figure 17. All tests were conducted with a pearlitic grey iron "liner" counterface and were of five minute duration.

Unlubricated wear coefficients were typically three orders of magnitude higher than for lubricated tests for the coatings, and two orders of magnitude higher for the liner material. Differences observed between coatings in the lubricated tests were not necessarily reflected in the unlubricated tests. For example, the Armacor M coating showed low wear rates compared to other materials in dry tests, but comparatively high wear in lubricated tests.

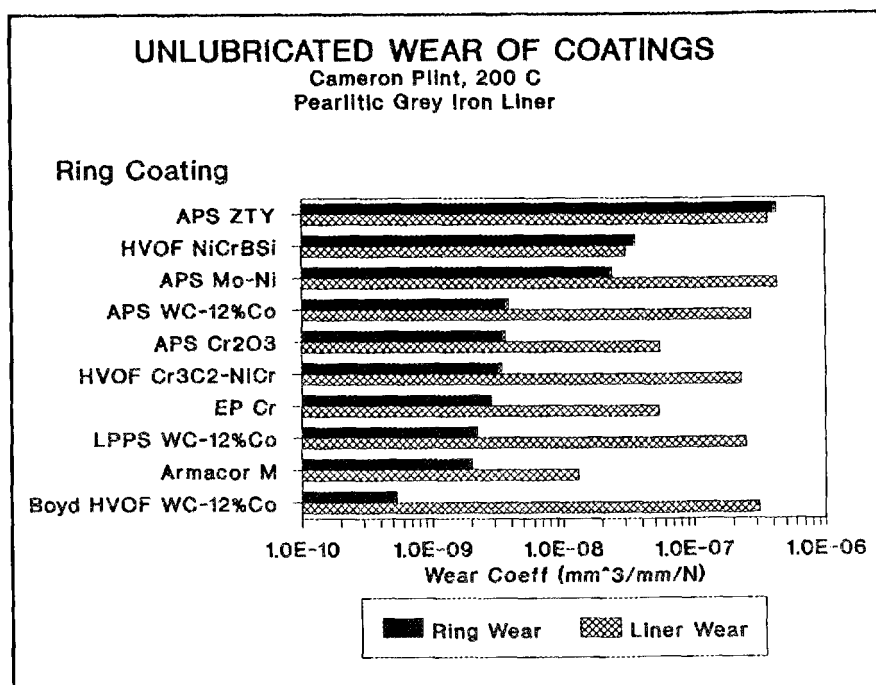


Figure 17. Wear coefficients for various coatings sliding against pearlitic grey iron liners. Tests were run with no lubrication at 200°C.

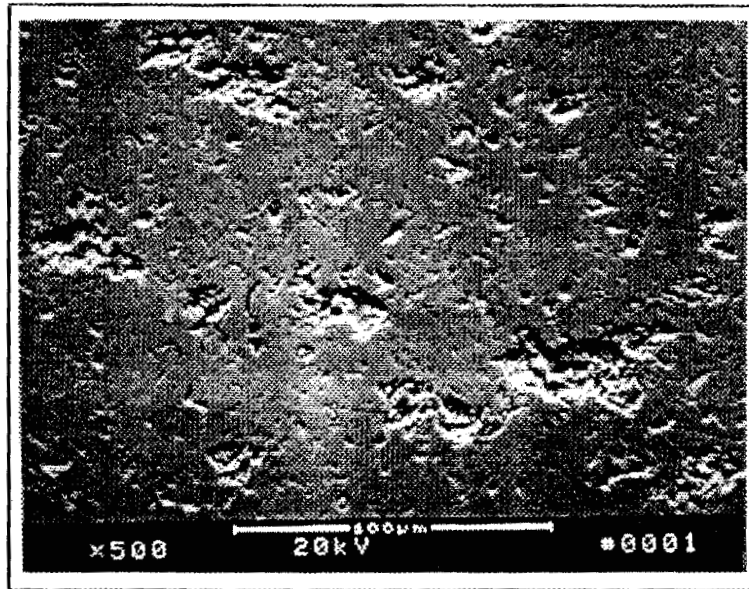
Figure 18 shows the wear surface of a plasma sprayed chromium oxide coating tested unlubricated against pearlitic grey cast iron for 30 minutes. Prior to examining the surface, thick layers of (presumably) iron oxide transferred from the liner material were removed with hydrochloric acid. The center of the wear scar exhibited some spallation, but the material between the shallow pits was highly polished (Figure 18a). The wear surface became progressively rougher near the edge of the scar, showing evidence of fine-scale fracture (Figure 18b). The reasons for the different wear morphologies are unclear.

Optimization of Ring - Liner Tribological System

Figures 9 and 10 show that the HVOF Cr₃C₂ - NiCr material gave the best combination of ring and liner wear coefficients overall. It was decided to test this material with various alternative cylinder liner counterface materials in order to optimize the system for lowest total wear (ring plus liner). The following liner materials were evaluated in these tests (see Table 6 for compositions):

1. pearlitic grey iron (70 - 90 HRG)
2. hardened grey cast iron (42 HRC)
3. high-phosphorus grey iron (79 - 83 HRG)
4. bainitic grey iron (88 - 90 HRG)
5. centrifugally cast H13 tool steel hardened to 50 HRC
6. a slurry sprayed silica-chromia-alumina coating (960 kgfmm⁻², KHN₁₀₀)

(a)



(b)

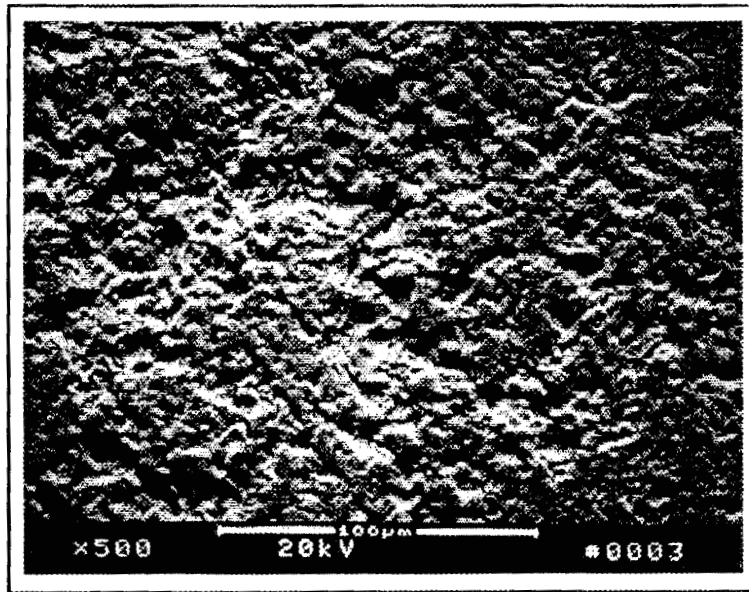


Figure 18. Wear surface of APS Cr_2O_3 coating after sliding against pearlitic grey iron for 30 minutes at 200°C with no lubricant:
(a) center of wear scar
(b) edge of wear scar

Material	C	Si	Mn	P	S	Mo	Ni	Cr	V
Pearlitic, Hardened Irons	3.15 - 3.5	1.8 - 2.6	0.5 - 0.8	0.15 max	0.1 max	0 - 0.5	0 - 0.5	0.2 - 0.8	
High Phosphorus Grey Iron	3.2 - 3.5	1.8 - 2.3	0.5 - 0.8	0.6 - 0.9	0.1 max			0.15 - 0.4	
Bainitic Iron	2.6 - 2.8	1.1 - 1.6	0.8 max	0.08 max	0.08 max	1.0 - 1.5	1.0 - 1.5		
H13 Tool Steel	0.35	1.00	0.35			1.50		5.00	1.00

Table 6. Chemical composition of cylinder liner materials evaluated.

Tests were conducted with an as-ground coating surface finish of 0.42 μm RA. Lapping the coating would result in a significantly better surface finish and potentially lower liner wear.

Coating and liner wear rates are shown in Figure 19. Of the cast iron liners, the pearlitic iron and high-phosphorus materials gave approximately the same ring and liner wear coefficients, but the bainitic material showed significantly (up to ten times) lower liner wear rates in lubricated tests, with only slightly higher ring wear (Figure 19). The excellent wear properties of the bainitic iron may have been partly due to the alloy content, which results in a fine dispersion of molybdenum carbides through the microstructure, in addition to the effect of the slightly higher matrix hardness. Hardening the pearlitic grey iron material resulted in three times lower liner wear in the 200°C tests but very little effect at 350°C, even though the tempering effect during the wear test was small at 350°C (38 HRC at end of test compared to an initial value of 42 HRC). It is speculated that this result may be due to an increase in oxidative wear at the higher test temperature.

The H13 tool steel showed lower wear rates than all the cast iron materials, and even produced lower wear of the ring coating (Figure 19). The SCA liner coating provided the lowest liner wear rates of all, but at the expense of significantly higher ring wear (Figure 19).

High Temperature Wear Tests

Tests were performed with various coatings sliding against hardened H13 tool steel at 450°C with a poly-alpha-olefin base stock as the lubricant. Three coatings have been tested: HVOF $\text{Cr}_3\text{C}_2\text{-NiCr}$, APS Cr_2O_3 and APS $\text{Al}_2\text{O}_3 - 41\% \text{ZrO}_2$. During several of these tests, the oil film periodically underwent spontaneous combustion due to the high test temperature. Despite this, low friction coefficients were maintained throughout the tests (Table 7). Wear coefficients were much higher than for 200 and 350°C tests, but low compared to unlubricated values. The ceramic coatings were slightly more wear resistant than the cermet material at this temperature, the Cr_2O_3 material showing the lowest wear coefficient (Table 7 and Figure 20). At lower temperatures, with a fully formulated mineral oil lubricant, the HVOF $\text{Cr}_3\text{C}_2\text{-NiCr}$ coating showed greater wear resistance than either ceramic material (Figures 9 and 10).

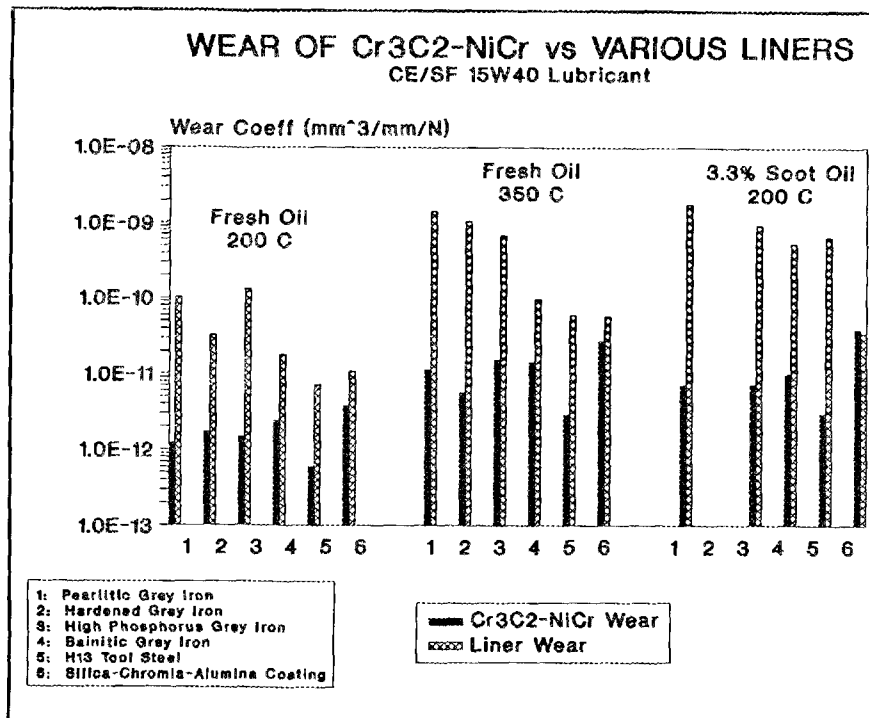


Figure 19. Wear coefficients for HVOF Cr₃C₂-NiCr coating sliding against various cylinder liner materials.

Conclusions

Bench wear tests have been used to rank the wear properties of coating materials for diesel engine piston ring and cylinder liner applications. The characteristics evaluated were:

1. boundary lubricated wear at 200 and 350°C
2. wear rates of a pearlitic grey iron cylinder liner counterface
3. resistance to increased wear with heavily soot-loaded, engine-tested oil
4. unlubricated (scuffing) wear rates.

Metallic coatings generally gave high wear rates and were susceptible to soot-induced wear. Some ceramic coatings were found to give comparatively low wear coefficients, particularly with the high-soot, engine-tested lubricant. Cermet coatings were found to have generally low wear rates in fresh and soot-loaded oil. HVOF WC - Co and Cr₃C₂ - NiCr materials giving extremely low wear coefficients have been identified. Lubricated tests at extremely high temperatures (450°C) showed that ceramic coatings such as Cr₂O₃ may offer advantages over the HVOF cermets under these extreme conditions.

Traditional pearlitic grey cast iron cylinder liners were found not to be the best counterfaces for lowest system wear. SiO₂ - Cr₂O₃ - Al₂O₃ liner coatings gave much lower liner wear, but at the expense of higher ring wear. Of the liner materials tested (versus the HVOF Cr₃C₂ - NiCr ring coating), hardened H13 tool steel was found to give the best combination of ring and liner wear.

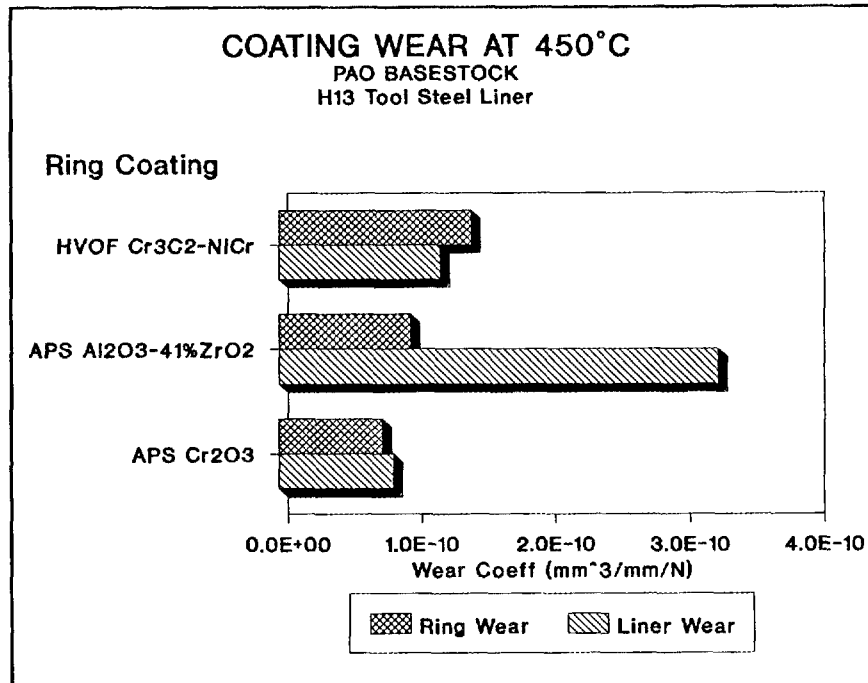


Figure 20. Wear coefficients for various coatings sliding against hardened H13 tool steel liners. Tests were run with poly-alpha-olefin basestock at 450°C.

Ring Material	Liner Material	Lubricant	Temperature (°C)	Ring Wear (mm ³ /mm/N)	Liner Wear (mm ³ /mm/N)	Friction Coeff
UTRC HVOF Cr ₃ C ₂ - NiCr	H13 Tool Steel	PAO Base Stock	448	1.44x10 ⁻¹⁰	1.21x10 ⁻¹⁰	0.17
BIRL APS Al ₂ O ₃ - 41% ZrO ₂	H13 Tool Steel	PAO Base Stock	461	9.83x10 ⁻¹¹	3.28x10 ⁻¹⁰	0.12
BIRL APS Cr ₂ O ₃	H13 Tool Steel	PAO Base Stock	449	7.73x10 ⁻¹¹	8.56x10 ⁻¹¹	0.10

Table 7. Wear rates and friction coefficients for various piston ring coatings sliding against hardened H13 tool steel at 450°C. Cameron Plint tests: load = 225 N, frequency = 20 Hz, stroke = 5 mm. Lubricant = unformulated poly-alpha-olefin.

Status of Milestones

1.	Develop plans for coating deposition	Oct-31-87
2.	Determine wear test conditions	Nov-30-87
3.	Procure substrate materials	Feb-28-87
4.	Develop spray parameters for Cr ₂ O ₃ coatings	Aug-31-89
5.	Tribological evaluation of Cr ₂ O ₃ coatings	Dec-31-89
6.	Develop spray parameters for HVOF coatings	Dec-31-89
7.	Conduct properties evaluation/wear testing of HVOF coatings	Feb-28-90
8.	Develop and test additional plasma sprayed materials	Apr-30-90
9.	Develop and test laser processed coatings	May-31-90
10.	Thermal shock and oxidation testing of coatings	Jun-30-90
11.	Develop liner counterface materials	Jul-31-90
12.	Selection of optimum ring-liner system	Jul-31-90
13.	Fabrication of test samples for ORNL	Aug-31-90

All coating development activity has been completed, with the exception of the Vapor Technologies effort, which has been delayed due to the company re-locating production equipment. Wear testing is nearing completion and substrate materials for the final task are being machined.

Publications

A paper entitled "Development of Wear-Resistant Ceramic Coatings for In-Cylinder Diesel Engine Components" was presented at the DOE-sponsored "Coatings for Advanced Heat Engines" Workshop, Castine, Maine, August 6-9, 1990.

A paper entitled "Wear Properties of High Velocity Oxy-Fuel (HVOF) Thermal Spray Coatings for Diesel Engine Applications", by M.G.S. Naylor, T.M. Yonushonis, T.P. Slavin and A.P. Matarese was presented at the ASM Materials Week '90 conference, Detroit, MI, October 8 - 11, 1990. This paper included results obtained in the current program.

References

1. K.F. Dufrane and P.A. Gaydos, "Dynamic Contact of Ceramics in Ring-Cylinder Applications", Proceedings of the U.S. Department of Energy 26th Annual Automotive Technology Development Contractor's Coordination Meeting, Dearborn, MI, October 24-27, 1988. Publ. SAE P-219, pp. 145-148.
2. M.G.S. Naylor and M.P. Fear, "Development of Wear-Resistant Ceramic Coatings for Diesel Engine Components", proceedings of the U.S. Department of Energy 27th Annual Automotive Technology Development Contractor's Coordination Meeting, Dearborn, MI, October 23-26, 1989. Publ. SAE P-230, pp. 131-141.

1.4 JOINING

1.4.1 Ceramic-Metal Joints

Joining of Ceramics for Heat Engine Applications

M. L. Santella (Oak Ridge National Laboratory)

Objective/scope

The objective of this task is to develop strong reliable joints containing ceramic components for applications in advanced heat engines. The present focus of this work is on the joining of silicon nitride by brazing. The technique of vapor coating ceramics to circumvent wetting problems that was developed for brazing zirconia at low temperatures is being applied to brazing silicon nitride. The emphasis of this activity during FY 1990 was on: (1) high temperature brazing of titanium-vapor-coated silicon nitride, (2) correlating braze joint microstructures with strength data to identify factors controlling joint strength, and (3) developing a method of calibrating the indentation fracture technique to determine the accuracy of residual stresses measurements in ceramic-to-metal joints.

Technical progress

Si_3N_4 joints: Joints of Kyocera SN220 Si_3N_4 were made by vacuum brazing at 1130°C with Au-25Ni-25Pd wt% filler metal. These joints were cut in to flexure bars and tested in 4-point bending at 600°C. The mating Si_3N_4 joint surfaces were either surface ground or were lapped to a 1- μm -diamond finish. The bend test results are shown in Figs. 1 and 2 assuming Weibull statistics apply. The data for specimens with ground joint surfaces, Fig. 1, showed that testing at 600°C produced lower average strength and slightly more scatter ($\sigma_f = 376$ MPa, $m = 6.8$) when compared to room temperature test results ($\sigma_f = 405$ MPa, $m = 7.6$). Examination of the test bars also indicated that the higher test temperature resulted in a greater tendency for fracture to occur in the Si_3N_4 near the joint surfaces.

In the cases where the joint surfaces were lapped prior to Ti vapor coating and brazing, the higher test temperature resulted in slightly lower average joint strength but more scatter ($\sigma_f = 405$ MPa, $m = 6.7$) compared to room temperature data ($\sigma_f = 418$ MPa, $m = 11.2$). For these joints, testing at the higher temperature did not significantly affect the failure location tendency of the joints. At 600°C, over half of the test bars fractured in the Si_3N_4 away from the joint surfaces.

To learn more about the influence of surface condition on braze joint strength, the joint surfaces of Si_3N_4 specimens in two conditions, ground and lapped, were examined by an acoustic surface wave technique. The results of this technique, shown in Fig. 3, verified that lapping greatly reduced the population of near-surface flaws in Si_3N_4 . The 50 MHz acoustic surface waves were sensitive to defects within about the top 100 μm of material. The left image in Fig. 3 shows a ground surface where near-surface defects produced by the grinding are clearly visible. The lapping process used for these specimens removed about 50 μm of material from the

ORNL DWG 90-13114

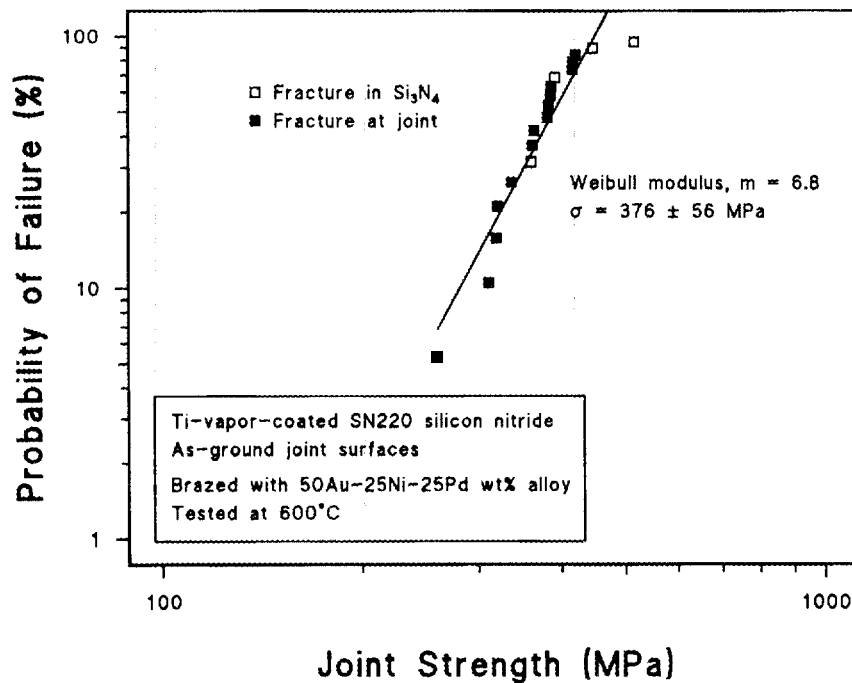


Fig. 1. Four-point bend strength of Si_3N_4 braze joint specimens tested at 600°C. Joint surfaces were finished by surface grinding.

ORNL DWG 90-13113

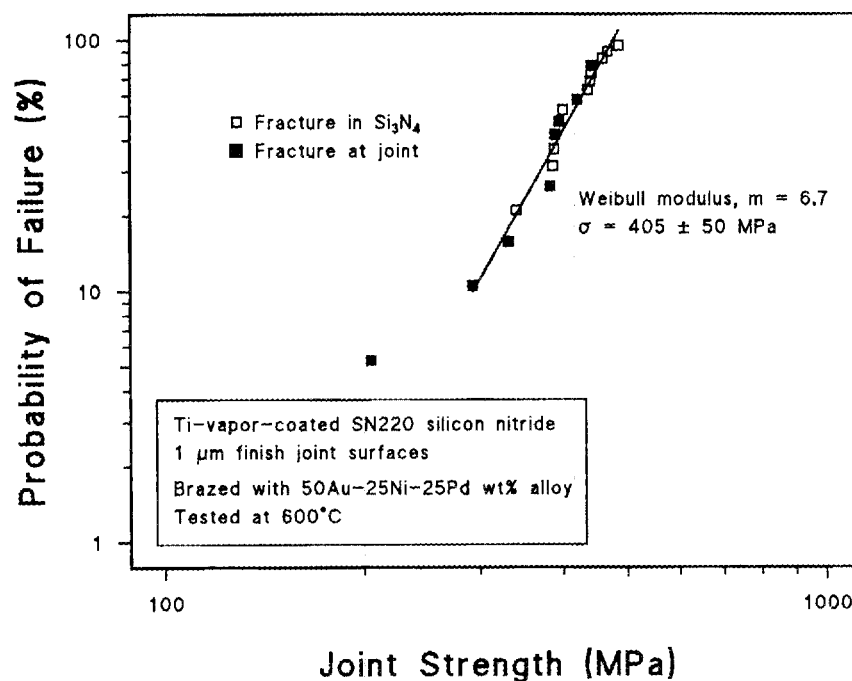


Fig. 2. Four-point bend strength of Si_3N_4 braze joint specimens tested at 600°C. Joint surfaces were finished by lapping.

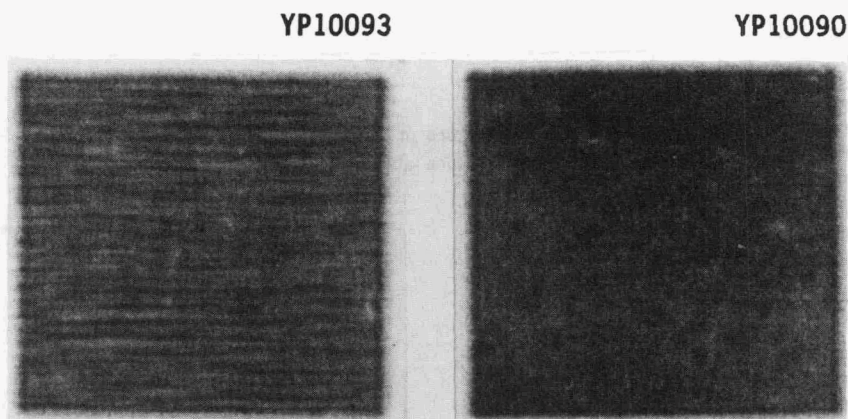


Fig. 3. Images of near-surface flaws produced by examining Si_3N_4 specimens with an acoustic surface wave technique. A surface ground specimen is shown on the left, and a lapped specimen is shown on the right.

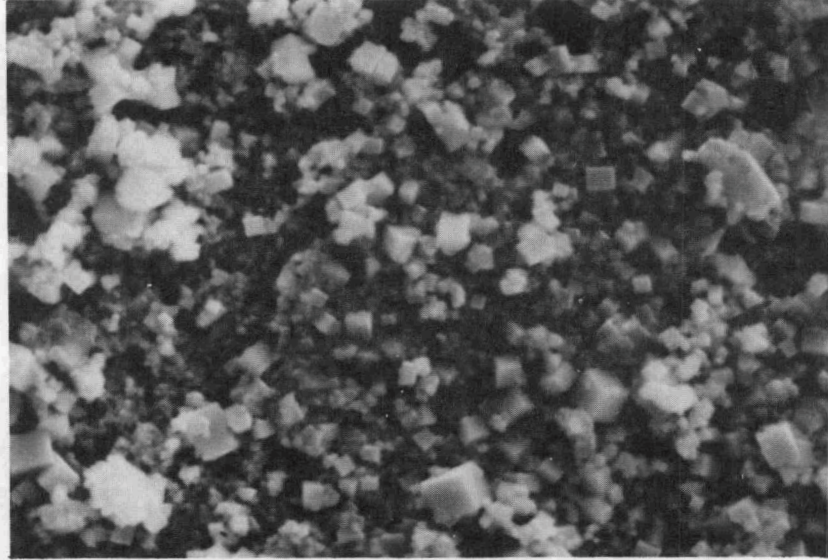
Si_3N_4 surface, and the effect of this treatment on the population of near-surface flaws is shown in the right image in Fig. 3. Lapping has clearly resulted in a significant decrease of near-surface flaws in the Si_3N_4 .

Joint surfaces of both finishes also were examined in an SEM after brazing by dissolving the braze filler metal to reveal the reaction layers between the Ti vapor coatings and the Si_3N_4 . X-ray diffraction was used to show that the reaction layers were mainly TiN. The overall appearance of the TiN reaction layers, shown in Fig. 4, largely mirrored the initial roughness of the Si_3N_4 substrates. Nothing in the appearance of the layers suggested that surface finish affected either the extent or morphology of the reaction of the Ti and Si_3N_4 .

The testing completed so far allows several important conclusions to be made. Braze joints of Si_3N_4 having strength in excess of the monolithic Si_3N_4 strength can be made using the vapor coating approach to circumvent wetting problems. Braze joint strength can exceed filler metal strength at test temperatures up to 600°C , presumably because of triaxial loading in the filler metal layer when subjected to tensile stress. Lapping joint surfaces improved Si_3N_4 joint strength characteristics by reducing the number of near-surface flaws produced by surface grinding.

In addition to the flexure testing, several joints of the Kyocera SN220 Si_3N_4 were annealed for 100 h at temperatures of 600, 700, 800 and 900°C in vacuum. After metallographic preparation, samples were examined in an SEM to determine the effect of annealing on the braze joint microstructures. Initial examination indicated that the appearance of the joint microstructures was not affected appreciably by annealing in this temperature range. The microstructure of the specimen which was annealed at 900°C is shown in Fig. 5. Microanalysis indicated that the composition of the braze layers was also reasonably constant with annealing temperature. The fine scale of the microstructures made accurate chemical analysis of the constituent phases impossible in the SEM, but microanalysis

M30701



M30697

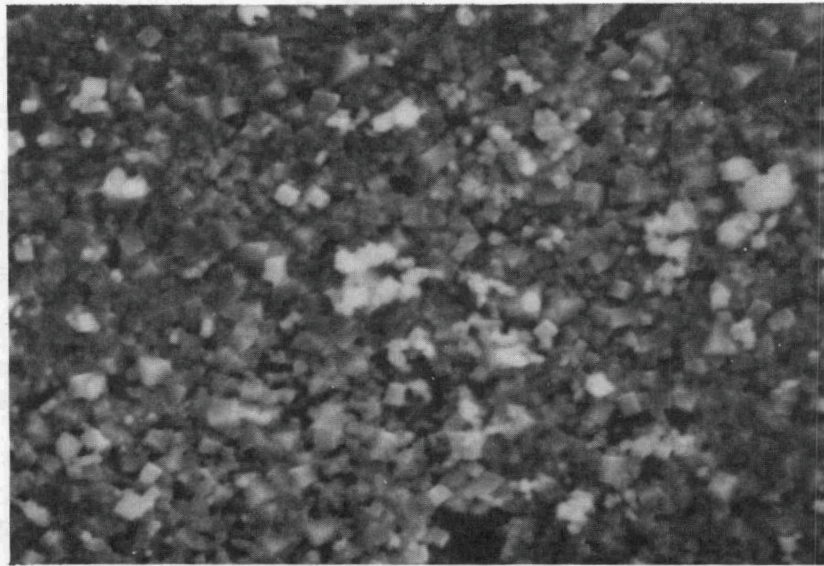


Fig. 4. SEM micrographs of the joint surfaces of ground (top) and lapped (bottom) Si_3N_4 specimens after brazing. The braze layer was dissolved to reveal the reaction layer between the Ti vapor-coating and the Si_3N_4 .

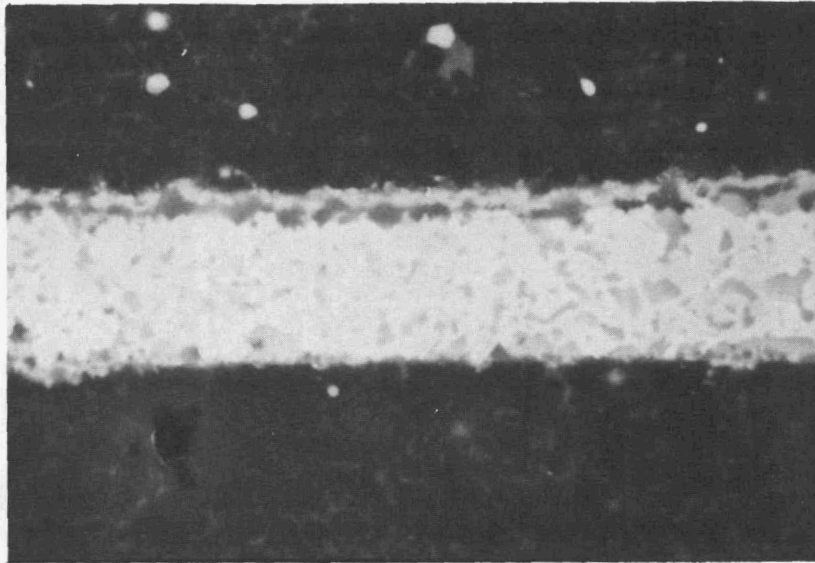


Fig. 5. SEM micrograph of the microstructure of a Si_3N_4 braze joint after annealing at 900°C for 100 h.

did reveal reaction of the Ti vapor-coating and the Si_3N_4 , as well as solution of Ti in the braze layers occurred. Also, the Si content of the braze layers in the annealed specimens was in the range of 2.5-3 wt%. From a microstructural viewpoint the braze layers appeared to be as stable at 900°C as they are at 600°C .

Further analysis of these joint microstructures and comparison with the unannealed microstructure is continuing. Also, additional braze joints are being prepared to provide specimens for flexure testing at temperatures above 600°C .

Brazing furnace: The furnace used for the bulk of our brazing work was retired, and replaced with a new furnace, vacuum system and control system. The major components of this new brazing system were assembled and tested, and this system is now operational.

Status of milestones

141109

Complete initial evaluation of the use of indentation fracture testing for studying residual stresses in ceramic joints.

December 31, 1990 - on schedule

Publications

None

Analytical and Experimental Evaluation of Joining Silicon Nitride to Metal and Silicon Carbide to Metal for Advanced Heat Engine Applications - S. Kang (GTE)

Objective/Scope

The goal of Phase I is to demonstrate analytical tools for use in designing ceramic-to-metal joints, including the strain response of joints as a function of the mechanical and physical properties of the ceramic and metal, the materials used in producing the joint, the geometry of the joint, externally imposed stresses both of a mechanical and thermal nature, temperature, and the effects of joints exposed for long times at high temperatures in an oxidizing (heat engine) atmosphere. The maximum temperature of interest for application of silicon carbide to metal and silicon nitride to metal-containing joints is 950 °C. The initial joint-fabrication work shall include "experimental" joints whose interfacial area is not less than 2 cm². The work shall also include demonstration of the potential for scale-up of the joint size to interfacial areas of commercial significance, applicability of the analytical joint modeling tools, and the ability to use these tools to design and predict the mechanical and thermal behavior of larger joints. These joints, referred to as "scale-up" joints, shall have an interfacial area of at least 20 cm².

The goal of Phase II is to optimize materials systems and joint designs, building on the results of Phase I. The anticipated environment will be oxidizing and will have joint temperatures of up to 950°C. Improved joint materials systems shall be developed to optimize the combination of competing properties which include ductility, yield strength, and creep resistance. The effect of each of these properties on joint performance shall be examined using the FEM model. Finally, a mechanical testing program shall be carried out to confirm the effectiveness of the modeling program. This shall include torsion tests, thermal and mechanical fatigue, and creep testing.

Technical Progress

Design Criteria/Stress Analysis

Probabilistic failure analysis was done with the butt, conical, and taper cylindrical geometries of ceramic-metal joints using the NASA CARES program. Due to the availability of the strength data, only volume analysis was performed to determine the probability of the failure.

The finite element analysis (FEA) in Phase I of the program provided the residual stress states and unit volumes of the elements within the ceramic-metal joint. Using the Weibull parameters for the ceramic component, the CARES program subdivided each finite element volume into smaller regions based on the integration scheme used to provide the stress output. Integrations were performed on each element volume and the probabilities of failure for each sub-element were determined.

In this study, the PY6 silicon nitride-Au5Pd2Ni-Incoloy 909 system was used for these joints, all without an interlayer, and the materials properties are listed in the final report of the Phase I. For the analysis, a normalized Weibull scale parameter of 41.5 ksi was used which was calculated given the specimen geometry and Weibull modulus. Also, a crack density coefficient of 21 was used. This coefficient was obtained based on the normal stress criterion of Batdorf [1,2]. The joint was cooled from 950°C and the residual stress state was used as a basis for the failure analysis.

Table 1 shows the probability of survival for the three joints. Only the taper cylindrical joint was predicted to survive. Figure 1 shows the geometry of the butt joint with the probability of survival (1 - probability of failure) plotted as contour fringes. Note that the structure was axisymmetric. A value of one indicated no chance of failure while a value of zero meant failure by cracking. There are no results for the metal and braze components of the joint since the probabilistic failure analysis does not generally apply to these materials. Figure 1 showed that the region of the ceramic at the braze interface at the outer surface is most likely to initiate a crack. This has been demonstrated in the prototype butt joints. Figure 2 zooms in on this region of interest and shows more accurately the region of crack initiation. Once a crack initiates, some failure criterion (such as the maximum principal stress criterion) can be used to predict the crack propagation path.

Effort was continued on probabilistic failure analysis of the ceramic to metal joints. After analyzing 3 prototypical joint designs (butt, conical and cylindrical with tapered edge) similar probabilistic failure analyses of various joint geometries were completed with the final joint dimensions used for Phase I of the program. Results indicated that all three geometries would initiate cracks in the ceramic component at the top of the metal sleeve. The discrepancy between FEA predictions (cracking) and experimentally produced joints (no cracking) could be attributed to a singularity point in the stress field near the top of the metal interlayer. A finer mesh has been prepared in the region to investigate the problem.

A finite element analysis (FEA) post-processing code is being developed to investigate the crack growth behavior in the vicinity of the braze joint. The code can provide mixed mode stress intensity factors at the tip of a crack in the ceramic. This code will be used to model crack growth behavior with crack-face contact which is known to be an important factor in crack propagation near the joint between dissimilar materials. The crack-face contact mobilizes the crack tip with "apparent-crack-closing-stress" loading, that is, a crack parallel to the interface can grow by large far-field compressive loading which is normal to the interface. This mechanism will be used in predicting the strength of ceramic-metal joints.

Analysis of Shrink Fit

The amount of shrink fit in the final joint geometry, due to the Inconel 909 structural alloy around the silicon nitride ceramic, was calculated by finite element analysis. The stresses acting at the centroid of the 12 ceramic finite elements that are in contact with the interlayer were plotted as a function of temperature. Figure 3 shows that the stresses in the ceramic changed from compressive to tensile in the temperature range of 20°C to 100°C. At elevated temperatures the shrink fit stress was tensile. This tensile stress acted to pull the joint apart, and the entire joint strength was derived from the strength of the chemical bonding at the braze/Ti-coating/silicon nitride interface.

Brazing Alloy Development

Ni-based Brazing Alloys

Ni-Cr and Ni-Cr-Mo alloys were chosen as master alloys for the high temperature brazing alloys because of their excellent high temperature strength and ductility. Some of the important requirements for the design of high temperature brazing alloys are (1) brazability, (2) good ductility and low yield strength, (3) high temperature creep strength and (4) melting point in the vicinity of 1200°C. Design strategies are to find alloy compositions which satisfy the requirements above and to regain the strength properties of the master alloys as much as possible by controlling brazing process.

Two classes of alloying elements were considered in order to lower the melting points of the master alloys with minimum loss of mechanical properties; brittle metalloids such as B, Si and Ge in the range of 1-10% and ductile elements such as Au, Ag, Cu and Pd in the range of 1-30%. In this reporting period, 70 new high temperature brazing alloys were produced and evaluated with Differential Thermal Analysis (DTA), Rockwell hardness and tensile testing. Differential Thermal Analysis (DTA) revealed that the additions of 5-7% B or 6-9% to the Ni-Cr alloys resulted in the melting points of 1060-1120°C and 1110-1140°C, respectively while the additions of 5-7%B or Si to the Ni-Cr-Mo reduced the melting points to 1040-1080°C and 1130-1170°C, respectively. Both elements were found to be effective in reducing the melting points of the alloys, maintaining the liquidus/solidus gap below 50°C.

In order to select the alloys with adequate mechanical properties for high temperature brazing applications, the Rockwell hardness tests were performed. In general, the additions of 1-10% B or Si increased the hardness values (Rockwell B) by 10-50% compared to the master alloys, making the systems hard and brittle. In contrary, additions of IB alloying elements like Au or Cu (<10%) did not change the hardness values of the alloys noticeably. The changes in hardness due to the elements were in the range of -10% to 10% of the master alloys'.

Based on the DTA and hardness data, Ni-Cr-Mo-Au and Ni-Cr-Mo-Cu alloys were chosen for the tensile testing. Alloys were prepared by remelting 4 times, using an arc melting device, for the homogeneity of the alloys in compositions. Small-size specimens which are proportional to standard size with circular cross sections of 0.16" in diameter were made according to ASTM Standard E8. Results of tensile testing at room temperature are shown in Table 2. The effects of two alloying elements (Au and Cu) on the tensile properties of the master alloy were similar, however, addition of Au resulted in a higher ultimate tensile strength (UTS) than that of the Ni-Cr-Mo-Cu alloy. As compared to arc melted master alloy, the change in UTS was almost negligible while significant reductions in yield strength (about 60%) were noted from both alloys. The elongation values were maintained high at 50% even though those were lower than that of the Ni-Cr-Mo master alloy(70%).

Low yield strength alloys with high ultimate tensile strength are desirable for high temperature brazing alloys since the braze alloys can accommodate the deformation associated with thermal mismatch between ceramic and metal. Additional new braze alloys with higher percentages of Au, Cu, and Pd (10-20%) were produced to find optimum compositions in terms of melting points and tensile properties. DTA, metallography, and mechanical testing are in progress with some of these alloys.

Coating Materials Development

For phase I of the program, Ti has been used as a coating material for PY6 silicon nitride. The thickness of the coatings was about 3.0 μm . From the previous study, the adhesion strength of the Ti-coating was found to be degraded significantly as the brazing temperature increased to 1200°C. Therefore, coating optimization was performed with double-layer coatings, varying the thicknesses of the Ti-coatings. The double-layer coatings composed of a reactive metal and a nonreactive metal was intended to keep the Ti-coating from extensive oxidation during the brazing process. Ag-coating of 0.2 μm in thickness was placed on the top of the Ti-coating, using an electron beam deposition technique. The thickness of Ti was in the range of 0.5-6.0 μm . High temperature performance tests were done at 1300°C for 2 hours with or without a braze alloy. Scratch-test results showed that 0.5-1.5 μm thick Ti coating provided better adhesion strength than 5.75 μm thick coating. Unreacted Ti in the 5.75 μm thick coating caused spalling of the coating layers. The experiments with braze alloys (Ni-Cr-Mo-Cu) showed that the wetting of high temperature braze alloys improved as the coating thickness increased. However, unreacted Ti separated the braze alloy completely from the ceramic substrate. Based on the wetting and strength results, about 1.5-2.0 μm thick Ti was determined to be an optimum.

Additional tests were done to evaluate the materials for the second layer coatings. Ag, Cu, Ni, and Al were selected on the basis of their melting points and materials characteristics. The thickness used for the Ti-coatings and the second-layer coatings were 1.5 μm and 0.2 μm thick, respectively. Wetting experiments were done with a Ni-Cr-Mo-Cu alloy. Little difference was found among these materials as second coating layers in terms of adhesion strength and wetting. All exhibited excellent wetting and adhesion strength after being heat-treated at 1300°C for 2 hours in vacuum. However, it seems from the appearance that Ag or Cu performed slightly better than others.

Reactions between Ti- and Zr-coated Si₃N₄ with Pd-Containing Brazes

The results of the wetting tests on Ti-coated Si₃N₄ have been reported in the Phase I final report. The Si₃N₄ used in the present study contained 13 wt % Y₂O₃ and 2 wt % Al₂O₃ as sintering aids. All of the Pd-containing braze alloys studied wet the Ti-coated Si₃N₄ well, reaching a contact angle of approximately 10° after 2 minutes. In general, the reactions between the braze alloys and Ti-coated Si₃N₄ were moderate. The Ti-coating was observed to react with Si₃N₄ to form TiN [3-5]. Wetting tests were also performed on Zr-coated Si₃N₄ substrates. Severe gas evolution was seen for the Pd-containing brazes on Zr-coated Si₃N₄ and the wetting tests were not completed.

A series of experiments designed to study the interaction between braze alloys and the coated Si₃N₄ were run in a furnace/mass spectrometer unit. More N₂ gas was evolved when the brazes were melted on Zr-coated Si₃N₄ as compared to Ti-coated Si₃N₄. The difference in behavior between Ti- and Zr-coated Si₃N₄ was unexpected since Ti and Zr are both Group IVB elements and have many similar chemical characteristics. The gas evolution was not caused by a direct reaction between Pd and Si₃N₄ since Pd does not reduce Si₃N₄ to form a palladium silicide and N₂ [6,7]. The large amount of gas evolved during the wetting tests could not be explained by the comparatively small amount of residual gas initially present in the braze foils.

There was an important difference in the behavior of the Ti-coating and Zr-coating on Si₃N₄. Ti reacted with the Si₃N₄ to form a 2.5- μ m thick titanium nitride layer, possibly composed of 2 forms of titanium nitride. However, the reaction between Zr and Si₃N₄ was a dissolution of N into the Zr without compound formation [8]. The Zr-rich region was 1.8- μ m wide in this joint.

The difference in outgassing behavior between the Ti- and Zr-coated Si₃N₄ can be explained by the microstructures described above. When Ti reacted with Si₃N₄ one or two layers of a titanium nitride compound were formed and the N was tied-up by the Ti. The titanium nitride layer acted as a diffusion barrier and slowed further reaction between the Ti and braze with the Si₃N₄. However, when Zr reacted with Si₃N₄, no zirconium nitride layer was formed.

Status of Milestones

On schedule.

Publications

None.

References

- 1) S. B. Batdorf and J. G. Crose, "A Statistical Theory for the Fracture of Brittle Structures Subjected to Nonuniform Polyaxial Stresses," *J. Appl. Mech.*, **41**, p459-64 (1974).
- 2) S. B. Batdorf and H. L. Heinisch, Jr., "Weakest Link Theory Reformulated for Arbitrary Fracture Criterion," *J. Am. Ceram. Soc.*, **61**, p355-58, (1978).
- 3) S. Kang, E.M. Dunn, J.H. Selverian, H.J. and Kim, "Issues in Ceramic-to-Metal Joining: An Investigation of Brazing a Silicon Nitride-Based Ceramic to a Low-Expansion Superalloy," *American Ceramic Society Bulletin*, **68** (9), p. 1608-1617, (1989).
- 4) J.C. Barbour, A.E.T. Kuiper, M.F.C. Willemsen, and A.H. Reader, "Thin-film reaction between Ti and Si₃N₄," *Applied Physics Letters*, **50** (15), p. 953-955, (1987).
- 5) A.E. Morgan, E.K. Broadbent, and D.K. Sadana, D.K., "Reaction of titanium with silicon nitride under rapid thermal annealing," *Applied Physics Letters*, **49** (19), p. 1236-1238, (1986).
- 6) T.G. Chart, "Thermochemical data for transition metal-silicon systems," *High Temperatures - High Pressures*, **5**, p. 241-252, (1973).
- 7) O. Kubaschewski and C.B. Alcock, "Metallurgical Thermochemistry," p. 310, Pergamon Press, New York, (1979).
- 8) A.P. Tomsia and R.E. Loehman, "Reaction Mechanisms in Active Metal Brazing," presented at American Ceramics Society Annual Meeting in Dallas Texas, (1990).

Table 1. Probability of failure for the ceramic component for each joint geometry.

Joint Geometry	Probability of Survival, P_s
Butt	0
Conical	0
Tapered cylindrical	0.999901*

* (1 failure out of 10,000)

Table 2. Tensile properties of new high temperature braze alloys.

System	Sample #	σ_{UTS} MPa (ksi)	σ_{ys} MPa (ksi)	Elongation (%)
Ni-Cr-Mo-Au	1	724.5 (105.0)	134.5 (19.5)	43.6
	2	721.0 (104.5)	135.9 (19.7)	57.0
	3	728.0 (105.5)	135.2 (19.6)	58.1
	4	736.2 (106.7)	135.2 (19.6)	55.2
Ni-Cr-Mo-Cu	1	661.7 (95.9)	136.6 (19.8)	56.8
	2	675.5 (97.7)	149.0 (21.6)	52.7
Ni-Cr-Mo (as arc melted) (average of 3)	1-3	702.4 (101.8)	331.2 (48.0)	77.3

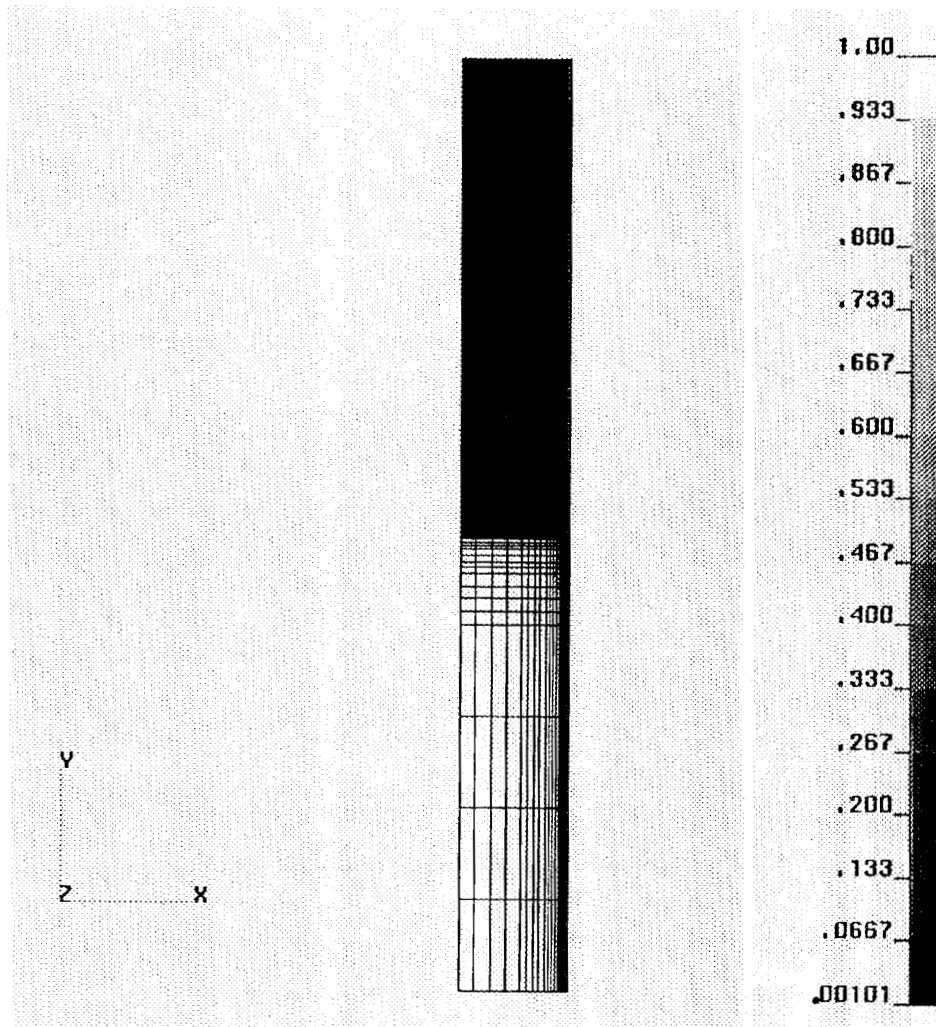


Figure 1. Probability of failure distribution in ceramic-metal butt joint. A value of zero means failure by cracking. Metal (upper half of the structure) was not analyzed for probabilistic failure.

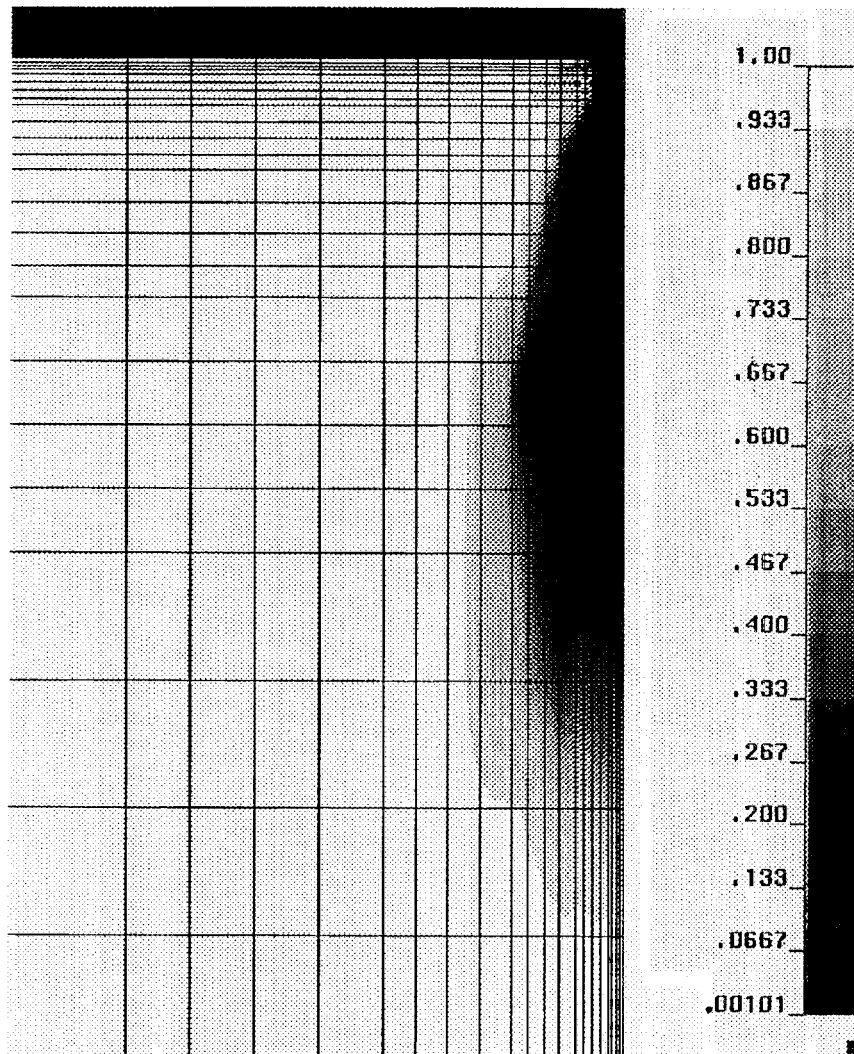


Figure 2. Close-up of region of interest for the probability of failure. Note that the highest likelihood of failure occurs in the ceramic component at the outer surface of the joint near the ceramic-metal interface.

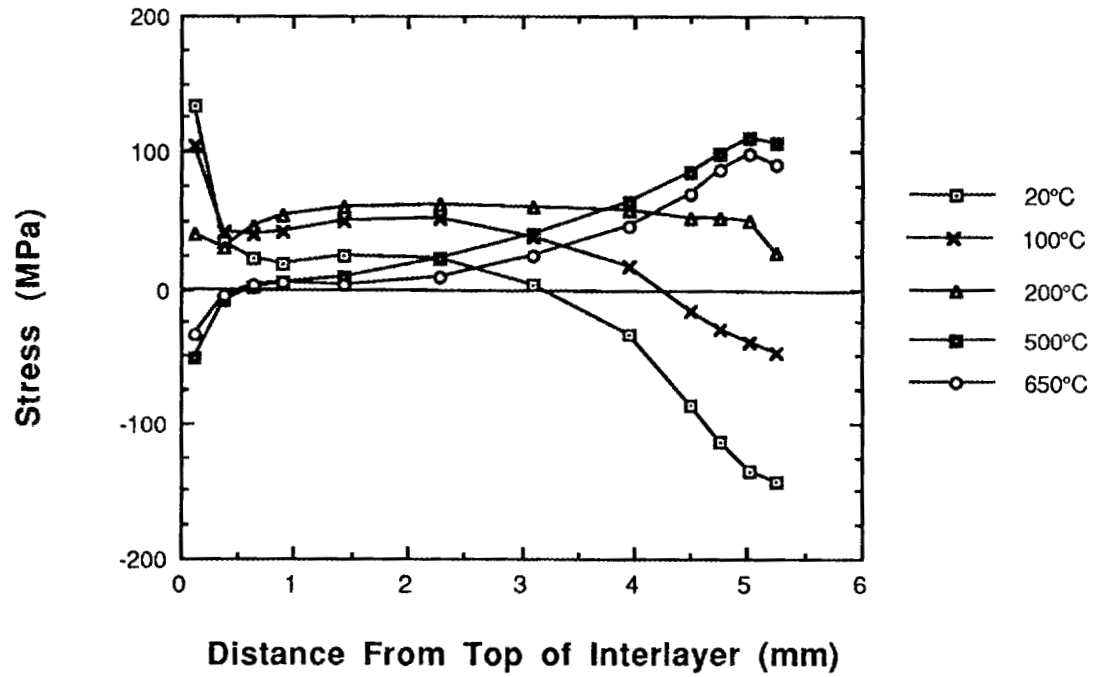


Figure 3. Centroid stresses in the ceramic at the ceramic/interlayer interface as a function of temperature. The joint was initially cooled down to 20°C from the brazing temperature then reheated to the different temperatures.

1.4.2 Ceramic-Ceramic Joints

Analytical and Experimental Evaluation of Joining Silicon Carbide to Silicon Carbide and Silicon Nitride to Silicon Nitride for Advanced Heat Engine Applications

G. A. Rossi, M. R. Foley, G. L. Sundberg, F. J. Wu, J. A. Wade
(Norton Company)

OBJECTIVE/SCOPE

The purpose of this program is to develop techniques for producing reliable ceramic-ceramic joints and analytical modeling to predict the performance of the joints under a variety of environmental and mechanical loading conditions including high temperature, oxidizing atmospheres. The ceramic materials under consideration are silicon nitride and silicon carbide. The joining approach for silicon nitride is based on the ASEA hot isostatic pressing process while the plan is to co-sinter silicon carbide green forms together. These joining methods were selected to produce joints which exhibit the minimum possible deviation in properties from those of the parent ceramic materials. Analytical models will be experimentally verified by measurements on experimental size and scale-up joints produced as part of this work.

Background

Because of their strength, oxidation resistance, and other desirable high temperature properties, silicon nitride and silicon carbide are under extensive study for use in advanced gas turbine and internal combustion engines. In both engine types there are requirements for joining the ceramics to themselves, other ceramics, and various engineering alloys. Existing bonding methods lack the high temperature capabilities required for use in advanced heat engines. Further, analytical modeling techniques to predict joint reliability and performance have not been developed. These technical needs have prevented consideration of economically fabricating large, complex ceramic engine components from smaller, less complicated segments. The current program will address these issues for silicon nitride to silicon nitride and silicon carbide to silicon carbide joints.

TECHNICAL PROGRESS1. Mechanical Testing for Task 1 (Characterization)1.1 Tensile Test on Joined Cylindrical Specimens

Tensile testing on joined cylindrical specimens of NCX-5100 (HIP'ed 4 w/o $Y_2O_3-Si_3N_4$) and NCX-4500 (pressureless sintered beta-SiC) for Task 1 was conducted. For NCX-5100 the tests were performed at 25°C, 500°C and 1370°C. For NCX-4500 tests were done at 25°C, 500°C and 1530°C. The tensile specimen is the ORNL cylindrical buttonhead design with a 6.35 mm gage diameter. The results are shown in Tables 1 and 2 for Si_3N_4 and SiC respectively.

Table 1

Tensile Strength of NCX-5100 Joined Specimens vs. Temperature

T (°C)	Sample No.	Strength	Failure Origin
25	1	904	Volume
25	2	469	Volume
25	3	898	Surface
25	4	588	Surface
25	5	894	Volume
(Avg. = 751 MPa)			
500	1	641	Volume
500	2	611	Volume
500	3	524	Surface
(Avg. = 592 MPa)			
1370	1	285	Volume
1370	2	292	Volume
1370	3	392	Volume
(Avg. = 323 MPa)			

Table 2

Tensile Strength of NCX-4500 Joined Specimens vs. Temperature

T (°C)	Sample No.	Strength	Failure Origin
25	1	220	Surface
25	2	230	Volume
25	3	246	Volume
25	4	279	Volume
25	5	230	Volume
(Avg. = 241 MPa)			
500	1	242	Volume
500	2	230	Volume
500	3	200	Near Surface (within 10 μ)
(Avg. = 224 MPa)			
1530	1	214	Surface
1530	2	202	Surface
1530	3	176	Surface
(Avg. = 198 MPa)			

It is important to point out that none of the specimens failed at the join, in either material.

Extensive fractography, both optical and by SEM, was performed on the broken tensile specimens to identify the fracture origins in each sample.

The conclusion was that, for NCX-5100, most of the failures were caused by iron-rich inclusions. Figure 1a shows an example of such a defect, detected in a rod tested at 1370°C. At higher magnification, using backscattered electron image, (Figure 1b) an area contains small iron rich inclusion can be observed. An EDS spectrum from this area (Figure 2) showed the presence of Fe. In NCX-4500, on the other hand, fractographic analysis showed that the majority of the fracture origins were pores or agglomerates. For example, Figure 3 shows one of these pores in the interior of the bar. Occasionally, metallic inclusions were found also in NCX-4500. Figure 4 shows a spheroidal nodule, about 200 μ in size, embedded in the dense ceramic volume bulk. The SEM/EDS spectrum, presented in Figure 5, confirmed that the inclusion contained mostly Fe, Cr and Al. It can be therefore concluded

that post-sintering HIP'ing should be beneficial in NCX-4500, since it would bring about partial or complete healing of the pores and enhance the strength.

1.2 Creep Testing for Task 1 (Characterization)

A total of sixteen joined NCX-5100 samples and fourteen joined NCX-4500 samples ("flat dog-bone" type) were machined for high temperature creep testing. Several samples of NCX-5100 were successfully tested for creep resistance, four at 1300°C, five at 1370°C and two at 1250°C. Primary and secondary creep only was observed under the experimental conditions used in the tests. Creep results for NCX-5100 are shown in the analytical modeling section of this report. For NCX-4500 creep tests were done at 1530°C. Most of the "flat dog bones" broke either during loading or shortly after the commencement of the test. This was due to the low toughness and presence of pores and agglomerates in the gauge section. Only two samples lasted for more than 200 hours, but no significant creep was observed.

2. Mechanical Testing for Task 2 (Verification)

2.1 Fast fracture (MOR) testing

Fast fracture on MIL STD 1942 B joined MOR bars (3x4x50 mm spans 5 and 40 mm), machined out of joined billets with a bond area of at least 2 cm², was performed at 1100°C for NCX-5100 and at 1250°C for NCX-4500. This was done as verification of the fast fracture data generated in Task 1 and already reported in the previous semi-annual report. Thirty MOR bars were broken for each material. The average strengths were 400 MPa for NCX-4500 and 648 MPa for NCX-5100. Optical fractography and selected SEM examination was carried out on several broken bars. The conclusions were similar to those drawn from the tensile results, i.e. pores and agglomerates were the typical flaws for SiC, whereas iron-rich inclusions frequently caused fracture in Si₃N₄. Fracture caused by surface flaws in the tensile face of the bar was also observed. It is interesting to note that about 80% of the failures were outside the joined region, located at the center of the bar. This has confirmed the results found in Task 1.

2.2 Tensile testing

Tensile testing for Task 2 was performed at 900°C for both NCX-5100 and NCX-4500. Three joined cylindrical specimens for each material were tested, with the join plane at the center of the gauge and perpendicular to the tensile axis. The tensile rods had the same shape and size as in Task 1. Table 3 below shows the results.

Table 3Tensile Strength of Cylindrical Joined Bars at 900oC

Sample	Tensile Strength (MPa)	Average (MPa)	Fracture Origin
SNJ-16	662		Surface
SNJ-18	628	593	Volume
SNJ-20	490		Surface
SCJ-28-2	247		Volume
SCJ-33-6	193	238	Surface
SCJ-29-4	274		Surface
NOTE: SNJ = Joined Silicon Nitride SCJ = Joined Silicon Carbide			

Fractographic analysis was performed on all these samples. It was found, as in Task 1, that primarily metallic inclusions of Fe, Ni and Cr were present at the fracture origins in the Si₃N₄ specimens. Other origins were pores and surface defects. In the case of SiC, the fracture origins were agglomerates and pores. Figures 6a, and 6b, show an agglomerate at two different magnifications.

3. Mechanical Testing for Task 3 (Scale-up)

3.1 Fast Fracture of Joined MOR Bars

Large joined billets with a bond surface area in excess of 20 cm², as requested by the Statement of Work, were fabricated in order to determine the influence of the joined area on the quality of the join. At least sixty joined MOR bars had to be machined for the fast fracture test. Of these bars, thirty had to be tested at room temperature and the other thirty at high temperature. In the case of NCX-5100, one joined billet was sufficient to produce sixty joined MOR bars (MIL STD 1942 B), but for NCX-4500 two billets had to be fabricated, due to machining problems. Therefore thirty MOR bars were obtained from each billet. The sixty bars from the two billets were then mixed and two groups of thirty bars each were formed, for the low and high temperature tests, by choosing the samples at random. The size of the densified joined NCX-5100 billet was 10 x 9.8 x 2.9 cm, and that of the joined NCX-4500 billet was 12.7 x 7.6 x 3.2 cm. The join surface areas were 28.4 cm² for Si₃N₄ and 24.2 cm² for SiC. The Archimedes density was measured on five MOR bars taken at random from each large billet. It was found that, while the density of NCX-5100 was

100% of theoretical (3.24 g/cm^3), that of NCX-4500 was lower than the density measured in smaller joined billets fabricated for Tasks 1 and 2, which had densities of 96-98% of theoretical. Table 4 shows the result of the density measurement.

Table 4

Archimedes Density of MOR Bars from Large Billets with Bond Area > 20 cm²

Material	Billet No.	Bar No.	Density (g/cm ³)	Std.Dev. (%)
NCX-5100	1	1	3.232	
		2	3.241	
		3	3.243	
		4	3.241	
		5	3.240	
(Avg. = 3.239 or 100% of TD)				0.1
NCX-4500	1	1	2.900	
		2	2.966	
		3	2.936	
		4	3.035	
		5	3.134	
(Avg. = 2.994 or 93% of TD)				3.0
NCX-4500	2	1	2.926	
		2	2.904	
		3	3.049	
		4	2.997	
		5	2.921	
(Avg. = 2.959 or 92% of TD)				2.0

The results of the fast fracture tests are shown in Table 5.

Table 5

Flexural Strengths of Joined MOR Bars Machined from Large Billets with Bond Area > 20cm²

Material	Billet No.	T (°C)	Avg. Strength (MPa)	Std. Dev. (%)
NCX-5100	30	25	854	7
NCX-5100	30	1370	517	3
NCX-4500	30	25	324	13
NCX-4500	30	1570	269	11

Tables 6 and 7 summarize the results of flexural and tensile strength as a function of temperature, measured in Tasks 1, 2 and 3.

Table 6

Temperature Dependence of Mechanical Properties
for Joined and Control NCX-5100

T (°C)	Joined/ Control	Tensile Strength (MPa)	Flexural Strength (MPa)
25	Joined	751 (5) T1	940 (45) T1
25	Control	--	967 (30) T1
25	Joined	--	854 (30) T3
500	Joined	592 (3) T1	--
750	Joined	--	677 (30) T1
900	Joined	593 (3) T2	--
1100	Joined	--	648 (30) T2
1370	Joined	323 (3) T1	526 (45) T1
1370	Control	--	570 (30) T1
1370	Joined	--	517 (30) T3
<p>NOTE: T1, T2 and T3 are Task 1, 2 and 3, respectively. Number of samples tested in parenthesis.</p>			

Table 7

Temperature Dependence of Mechanical Properties
for Joined and Control NCX-4500

T (°C)	Joined/ Control	Tensile Strength (MPa)	Flexural Strength (MPa)
25	Joined	241 (5) T1	351 (45) T1
25	Control	--	397 (30) T1
25	Joined	--	324 (30) T3
500	Joined	224 (3) T1	--
750	Joined	--	338 (30) T1
900	Joined	238 (3) T2	--
1250	Joined	--	400 (30) T2
1530	Joined	198 (3) T1	338 (45) T1
1530	Control	--	347 (30) T1
1530	Joined	--	269 (30) T3
NOTE: T1, T2 and T3 are Task 1, 2 and 3, respectively. Number of samples tested in parenthesis.			

The tables show that the average strengths measured in Task 3 are slightly lower than those measured in Task 1 on joined MOR bars. The difference is larger in SiC than in Si₃N₄. The fraction of bars that failed in the join region is an indication of the join strength. Assuming that this region is located at the center of the bar and is 1 mm wide*, the fraction of MOR bars broken in this region was found to be 22% at 25°C and 26% at 1370°C for NCX-5100. For NCX-4500, on the other hand, 37% of the bars broke in the join region at 25°C and 30% at 1530°C. Since the percentage of failures at the join is higher in Task 3 (larger bond area) compared to Task 1 (smaller bond area), where less than 20% of the bars failed in the join, it appears that the larger joints of Task 3 are weaker than the smaller ones of Task 1. This result is expected, since the probability of finding a flaw in the join increases with the join area.

* Note: Since the interlayer thickness, from SEM micrographs, appears to be not larger than 700μ for NCX-4500, it is assumed that this is also the case for NCX-5100, where the interlayer is not visible. Therefore an arbitrarily chosen "join thickness" of 1mm appears reasonable.

The reason why the join in NCX-4500 is relatively weaker than in NCX-5100 in the Task 3 samples is not understood. A possibility is that the interlayer is thicker in SiC than in Si_3N_4 joined billets and therefore there is a higher probability of finding a defect in the larger interlayer volume.

4. Microprobe Analysis of Join in NCX-5100 and NCX-4500

In the previous semi-annual report it was mentioned that microprobe analysis on a joined polished NCX-5100 MOR bar, along the bar axis, had not shown significant variations in composition. A similar analysis was recently conducted on a control (no join) NCX-5100 polished bar and on joined and control NCX-4500 polished bars. The results are shown in Figures 7 and 8, for NCX-5100 and NCX-4500, respectively. The area analyzed at each point was about $1300 \mu^2$. The join is located at the center of each figure. From this study it can be concluded that: 1) there is more variability in chemistry in SiC than in Si_3N_4 ; 2) the join could not be identified in Si_3N_4 ; 3) there is more fluctuation in chemistry in the joined samples and 4) lower Al_2O_3 was found in the SiC joined samples along a line about 380μ long, which is probably the location of the interlayer, as shown by Figure 8b. The interpretation of these results is difficult and more experimental results are needed to draw conclusions.

5. Analytical Modeling of Fast Fracture and Creep

5.1 Fast Fracture Modeling

CARES2 postprocessor has been completely converted to the Silicon Graphics machines with capabilities of processing up to 10,000 elements. NCX-5100 data was used to model the MOR geometry. The database used for the predictions consists of room temperature, 750°C and 1370°C NCX-5100 joined MOR data. As described in the previous reports, the verification runs which calculate the reliability at the above temperatures are within 2% of the experimental data (Figures 9 and 10). Shear sensitive options include Normal Tensile Stress Criteria (NTS), and Principle of Independent Action (PIA). Shear insensitive options include Maximum Tensile Stress Criteria (MTS), Strain Energy Release Rate (SER), and Shetty's Mixed mode sensitivity (SH). Shear sensitivity models can be applied to either Griffith cracks (G) or Penny Shaped cracks (P). A complete description of these options has been referred in previous reports. The two Shetty's mixed mode equation models used have the mode II sensitivity constant $C=0.8$ and $C=1$. The reliability evaluation of MOR geometry has been calculated. Prediction were evaluated at 1100°C and then compared with experimental results (Figure 11). The major difference in the MOR prediction is the Weibull modulus, represented in the figure as the slope of the curve, which was

experimentally lower than predicted. This discrepancy is due to the strength data used in the database. Figure 12 shows the behavior of NCX-5100 MOR data tested during this contract. The calculated average strength and Weibull modulus are plotted as a function of temperature. The non-linear behavior in the Weibull modulus indicates that there is a need for additional MOR data in order to map the entire temperature distribution of the fast fracture strength. Evidence of this non-linearity is further emphasized by the results shown on Figure 13 by comparing the slopes of all NCX-5100 MOR experiments tested during the contract. The amount of variability seems more significant and therefore must be characterized in more detail. Nevertheless, this result will be studied further and additional predictions are being evaluated. Results will be available in the final report. Modeling of NCX-4500 is currently underway. The results will be shown in the final report.

5.2 Creep Modeling

Creep verification and predictions have been calculated for two different models. Each model consists of different equations that govern the behavior of the theta constants as defined in previous reports. Creep curves from four test conditions are used as the database for the predictions. Verification runs consist of modeling the creep behavior under conditions as used in the database. These runs should be consistently in agreement with the experimental database before any prediction can be made. Results, as shown in Figure 14, are within 5% of the experimental data for the verification sample (34B) and within 14% of the experimental data for the prediction sample (22B). Additional results will be available in the final report.

STATUS OF MILESTONES

All milestones are on schedule. The final report is being written and scheduled to be delivered on or before the October 31, 1990 deadline.

PUBLICATIONS

None

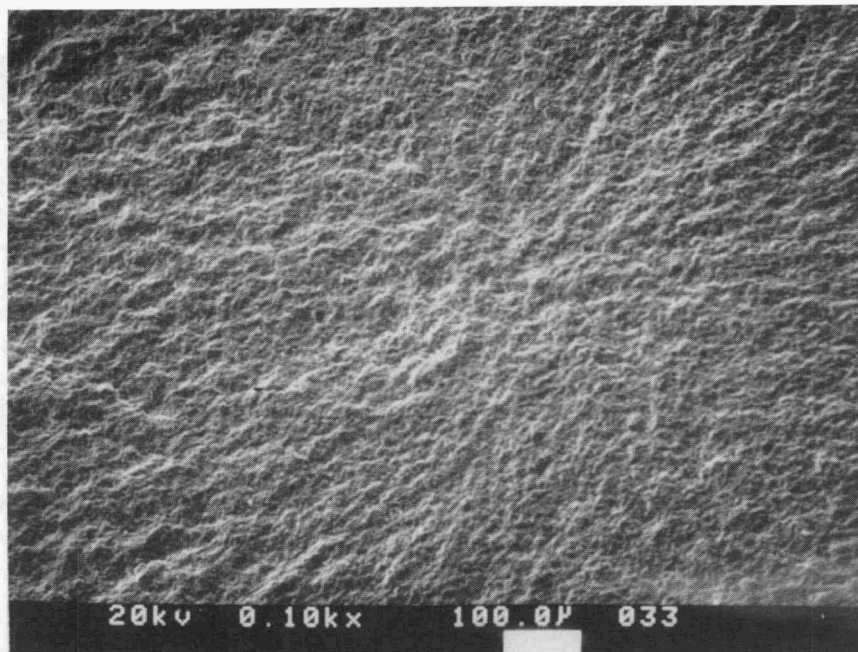


Figure 1a: Fracture origin in a tensile rod of NCX-5100

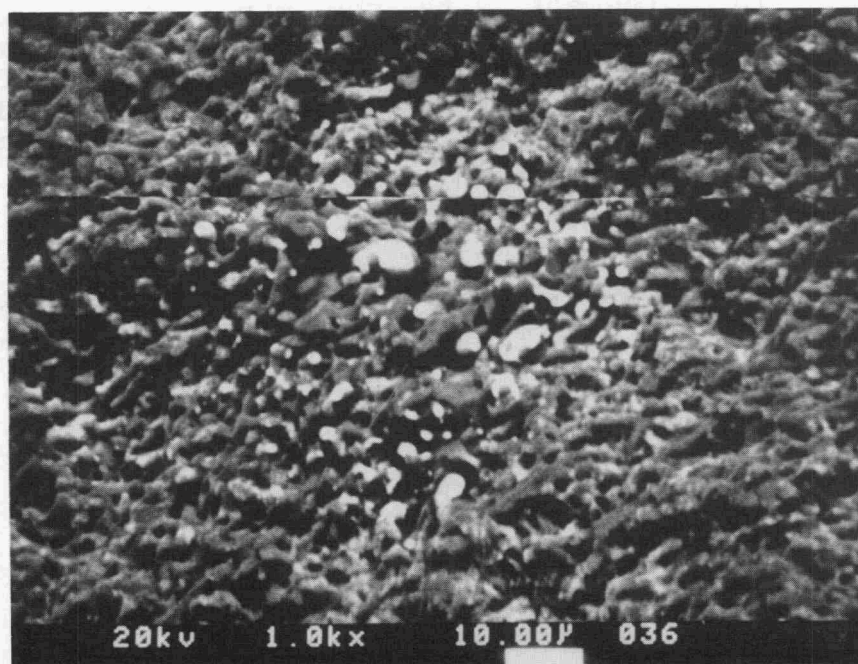


Figure 1b: Higher magnification of Figure 1a, showing metallic impurity.

ROD#26 JOINING

SPECTRUM LABEL

ROD#26

SPECTRUM FILE NAME

000001

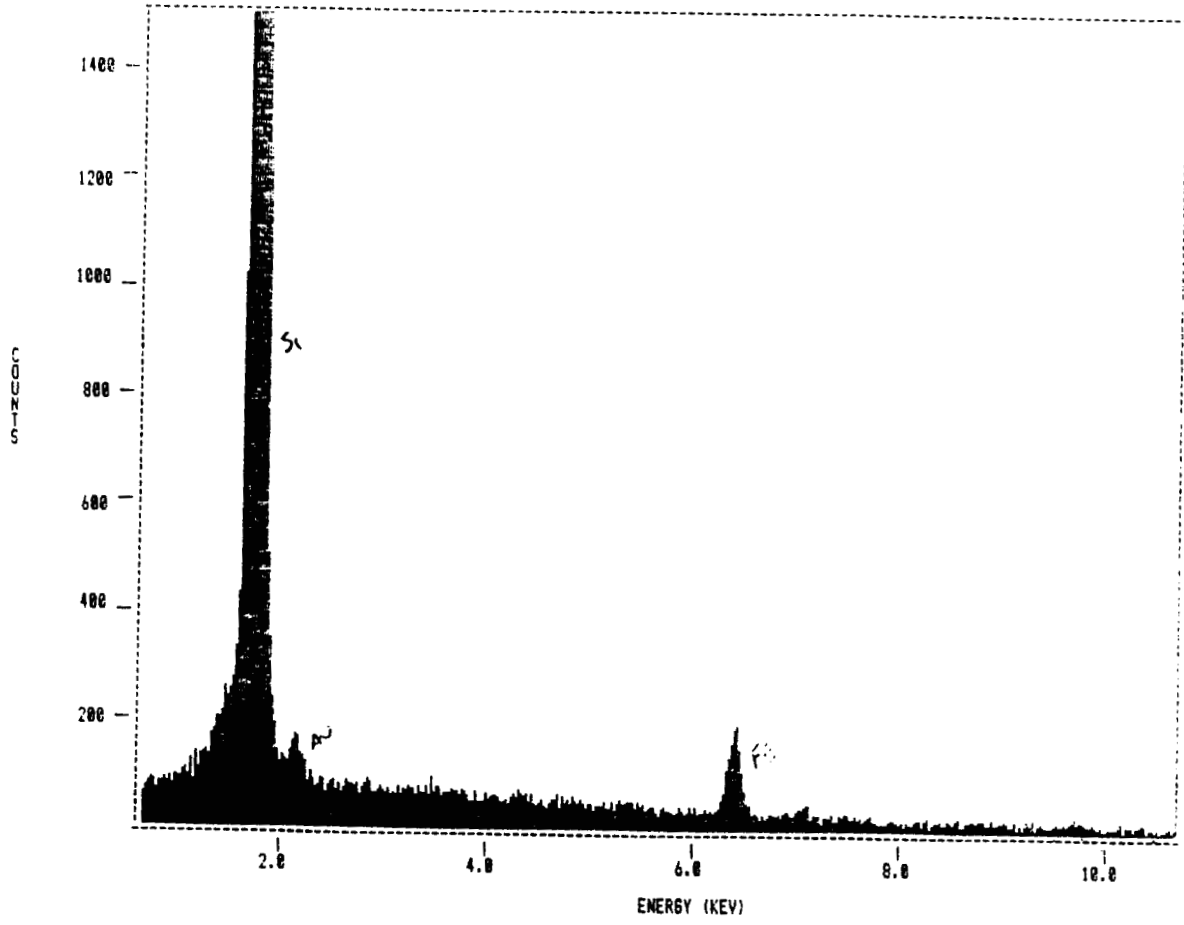


FIGURE 1

Figure 2: SEM/EDS spectrum of region shown in Figure 1.

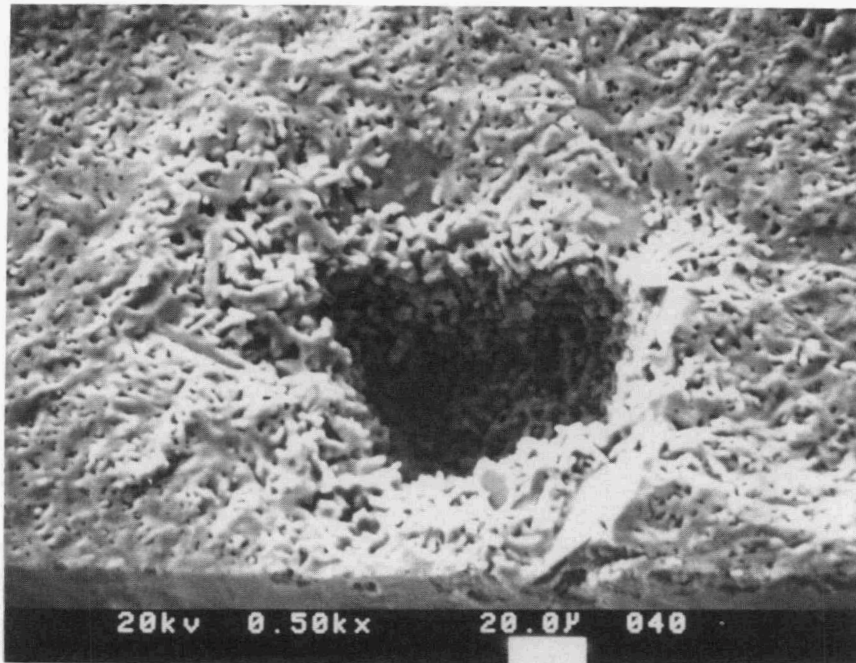


Figure 3: Pore in a joined tensile specimen of NCX-5100

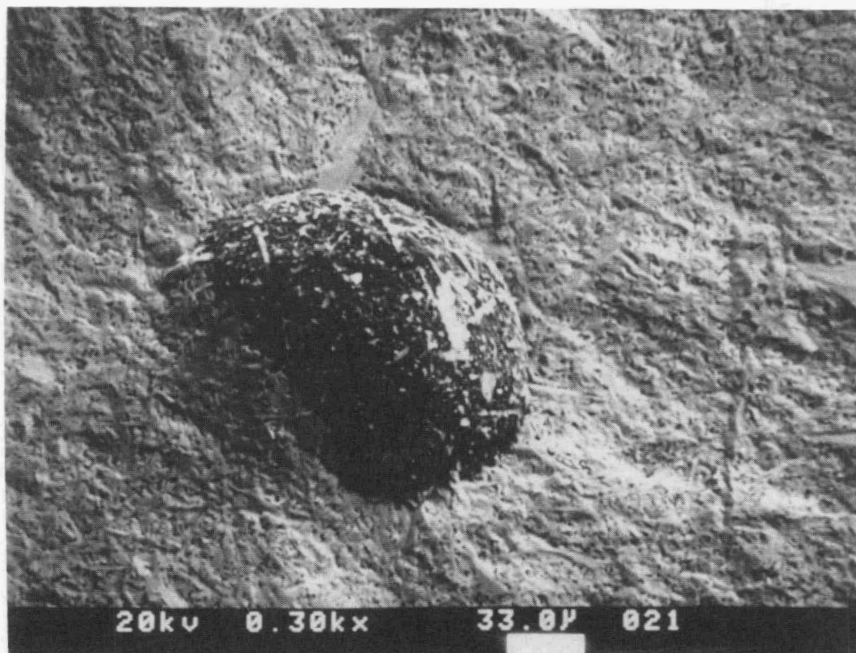


Figure 4: Metallic inclusion in a joined tensile specimen of NCX-4500

ROD# 33-1

SPECTRUM LABEL

SPECTRUM FILE NAME

ROD# 33-1

0420

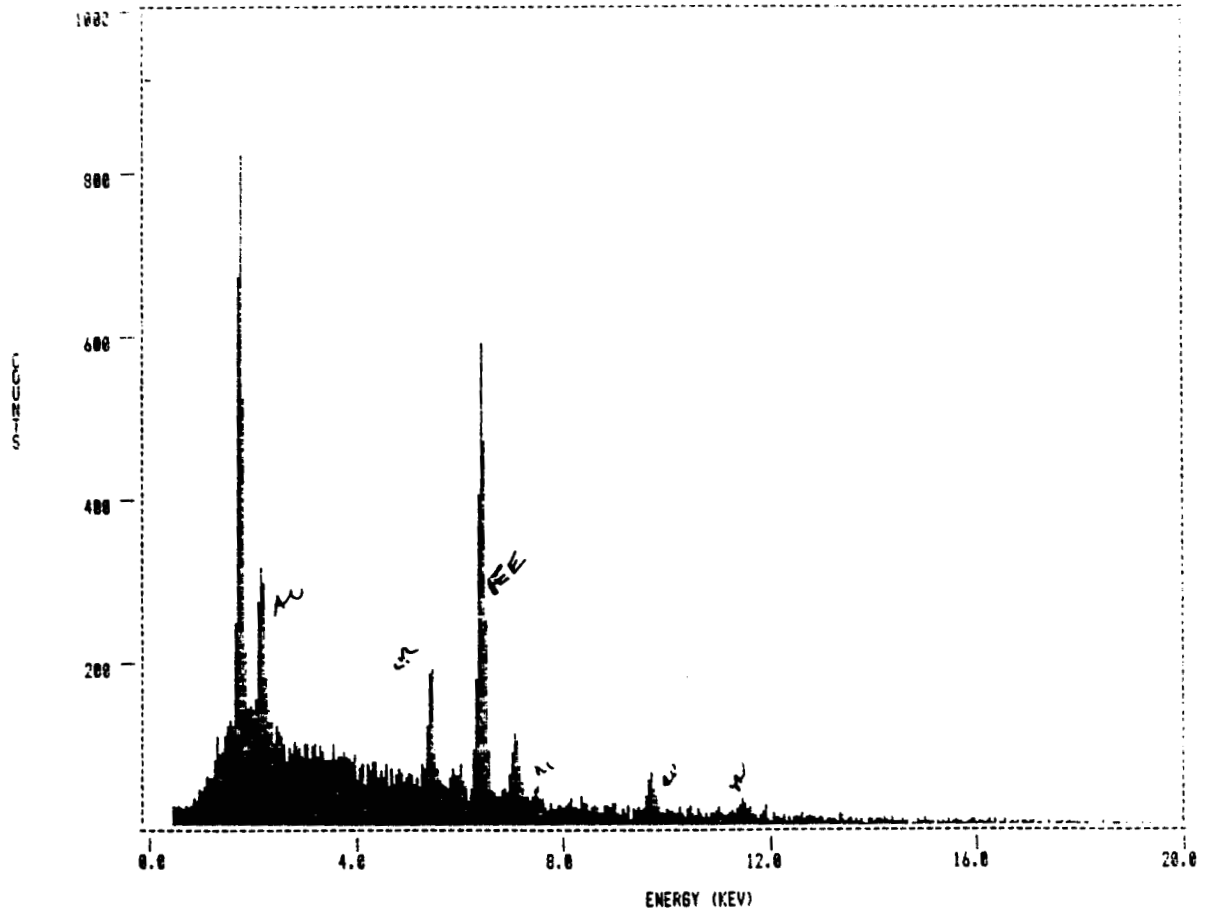


FIGURE 5

Figure 5: SEM/EDS spectrum of foreign inclusion shown in Figure 4

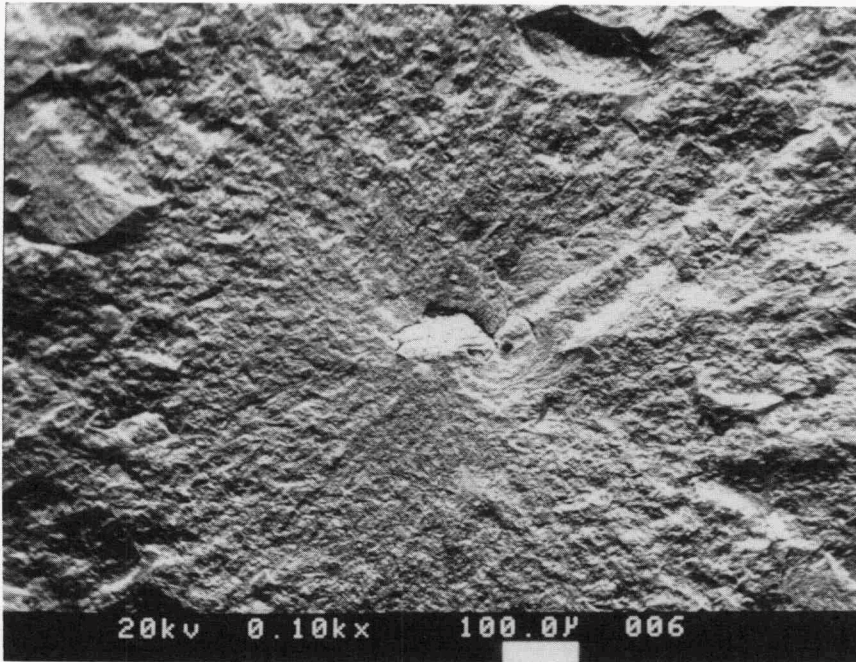


Figure 6a: Agglomerate as fracture origin in tensile rod of NCX-4500

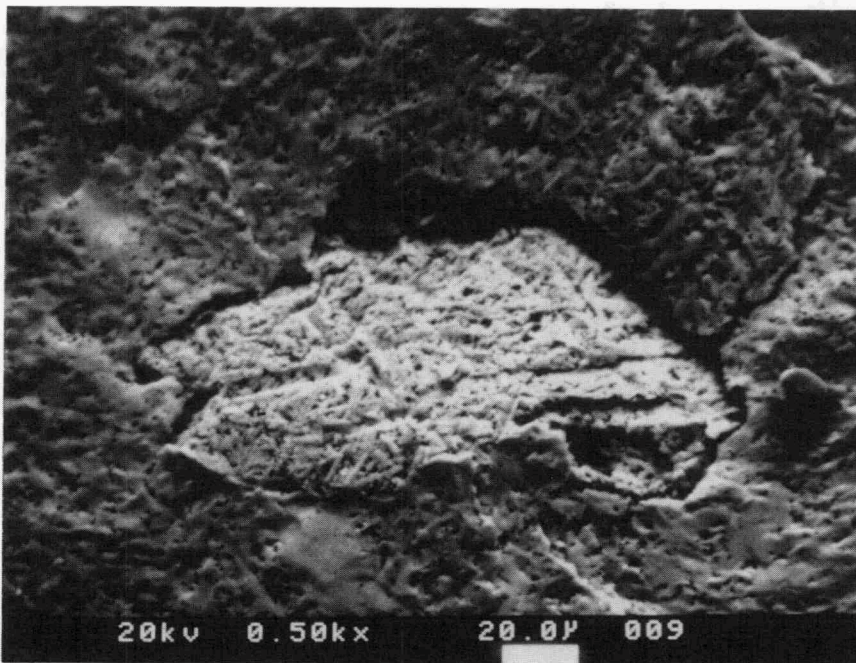


Figure 6b: Higher Magnification of Figure 6a

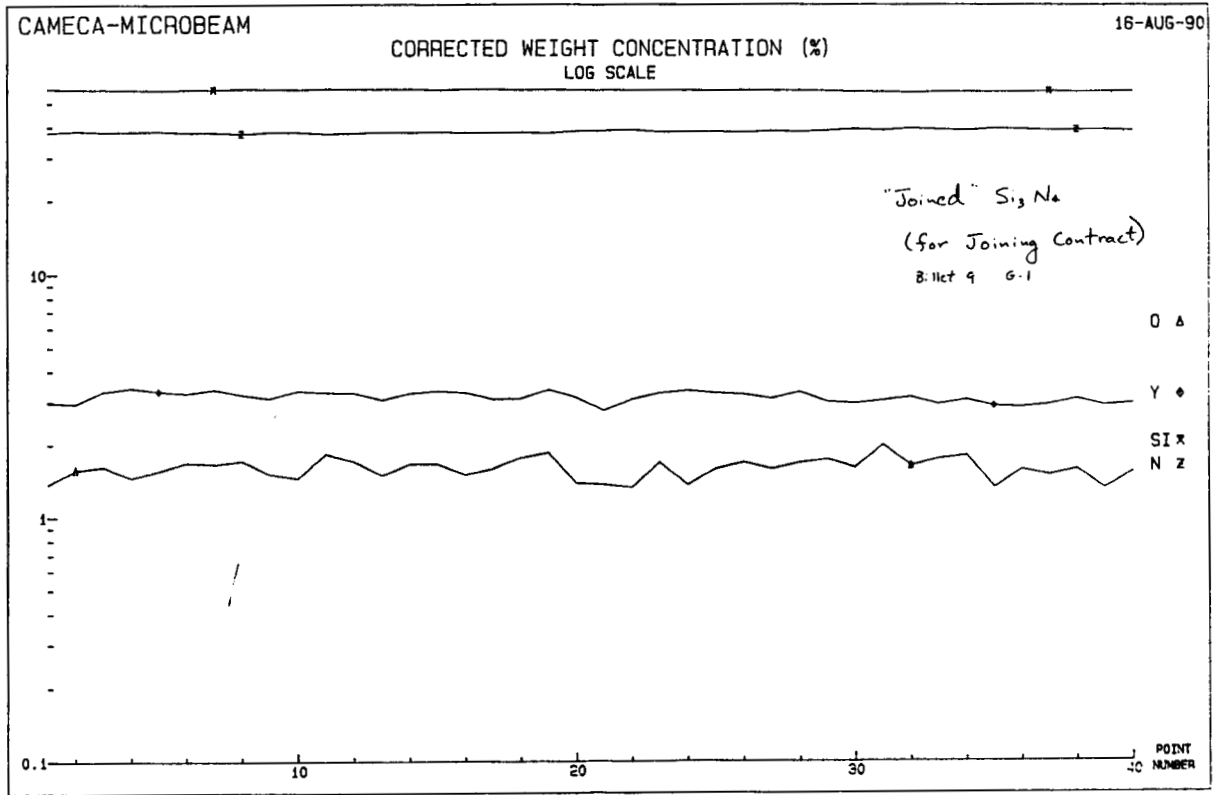


Figure 7a: Microprobe analysis of joined MOR bar of NCX-5100

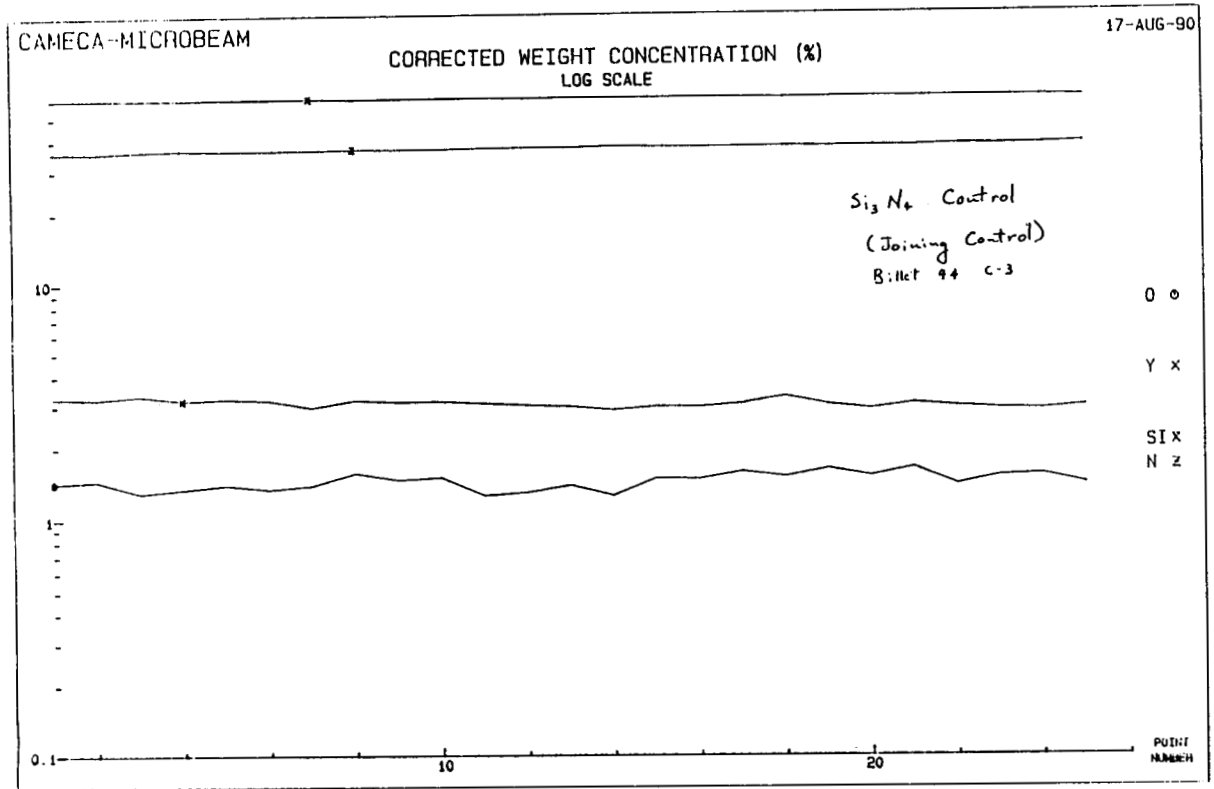


Figure 7b: Microprobe analysis of control MOR bar of NCX-5100

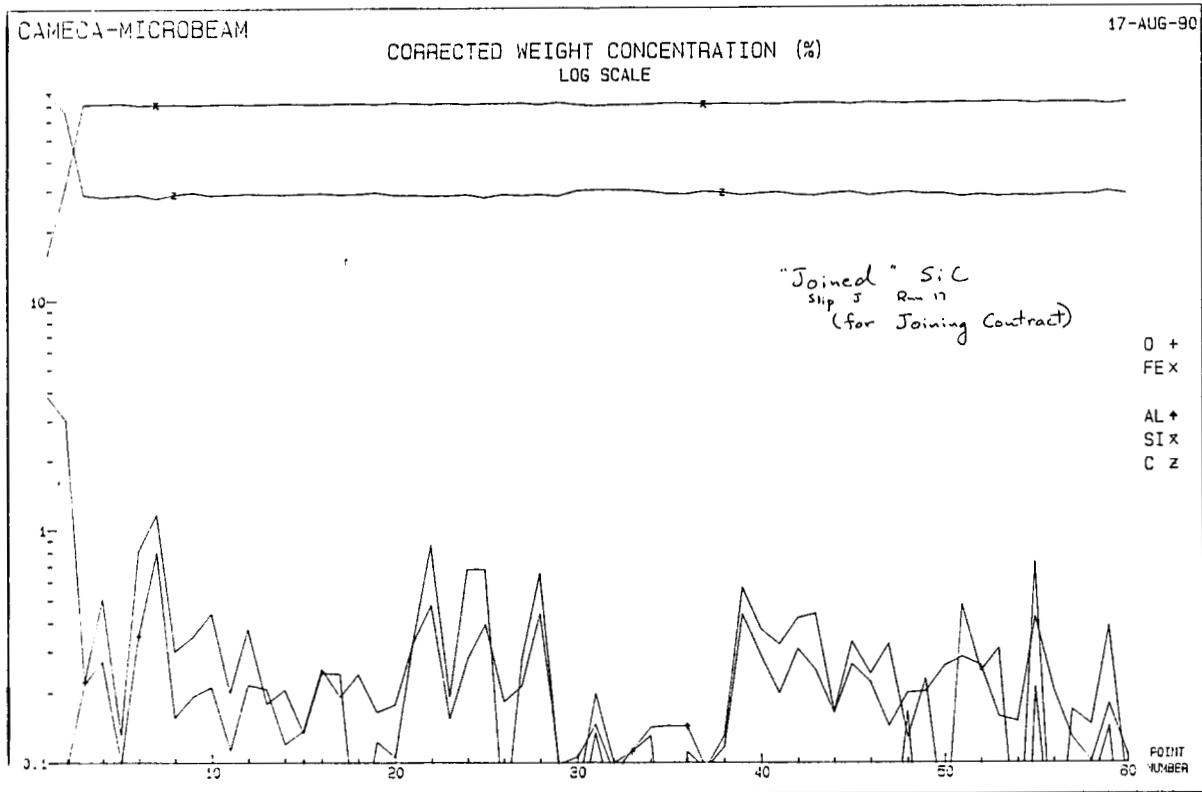


Figure 8a: Microprobe analysis of joined MOR bar of NCX-4500

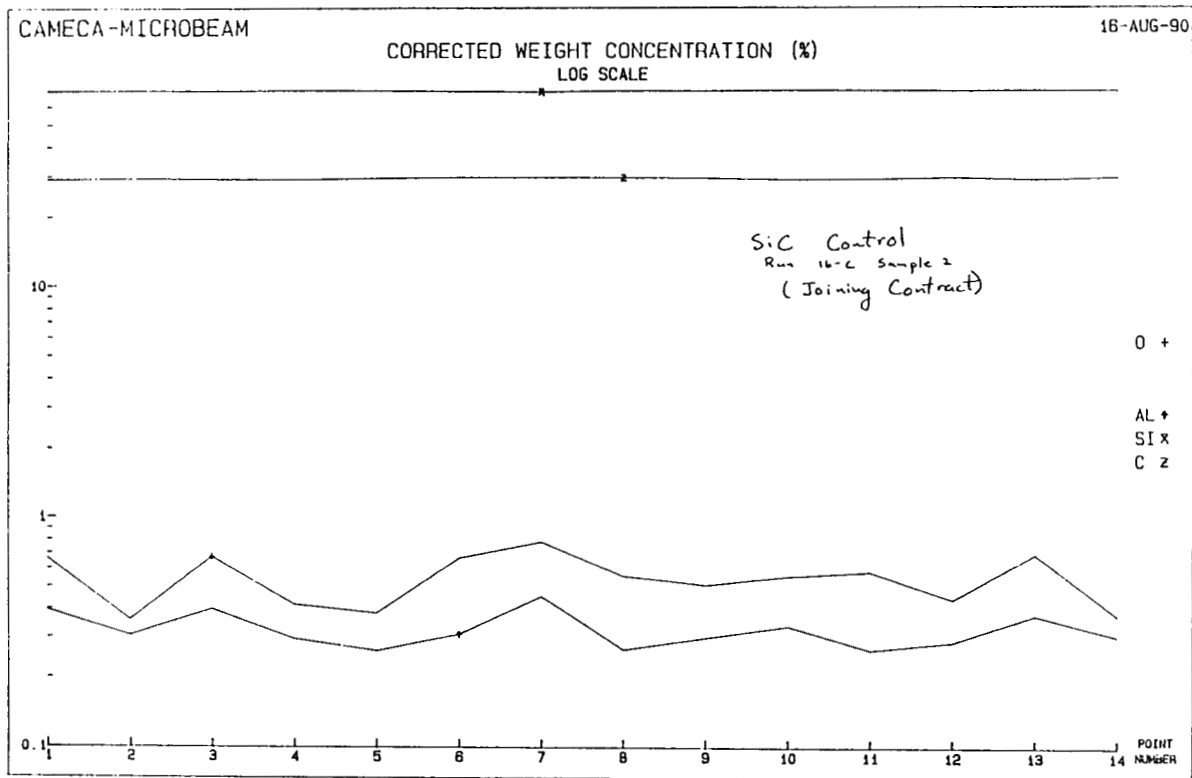


Figure 8b: Microprobe analysis of control MOR bar of NCX-4500

NCX-5100 Jointed Verification Results vs Experimental MOR (5mm x 40mm) Fast Fracture at Room Temperature

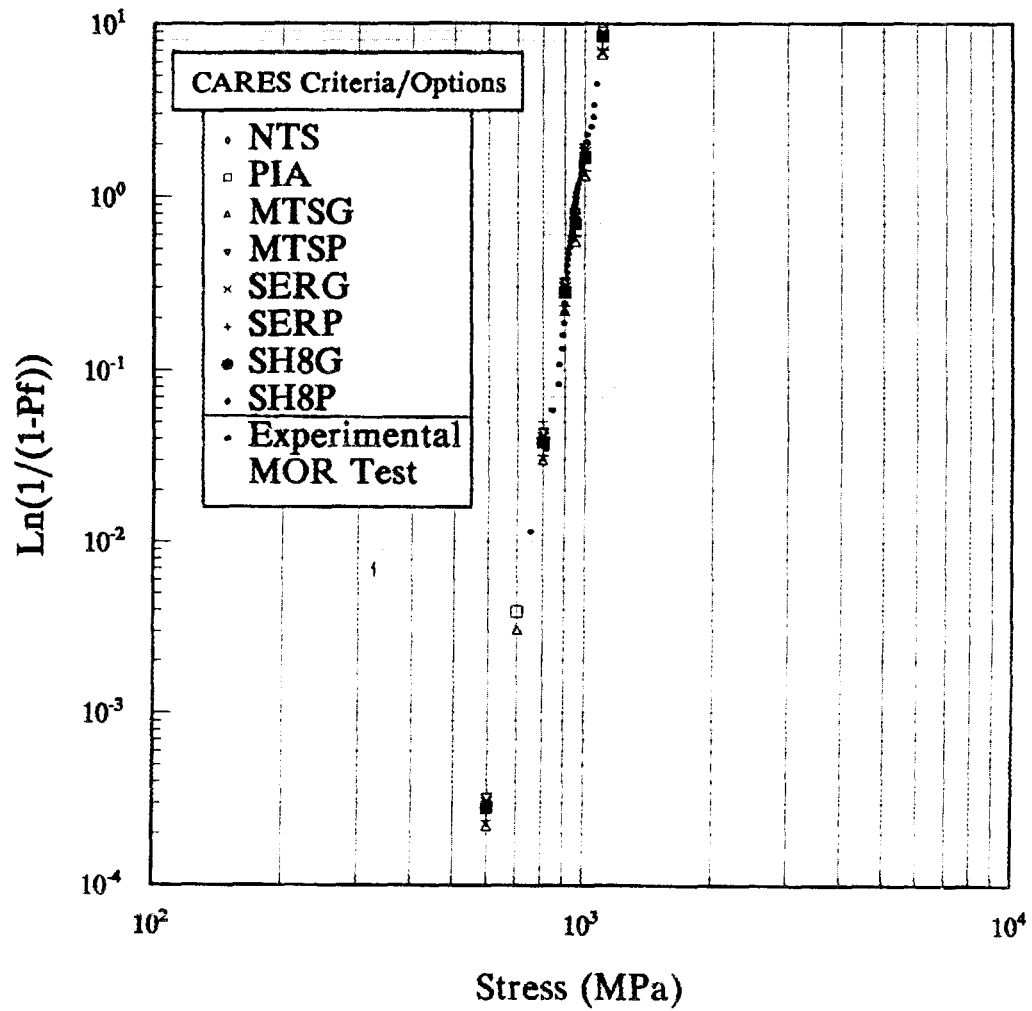


Figure 9

NCX-5100 Jointed Verification Results vs Experimental MOR (5mm x 40mm) Fast Fracture at 1370°C

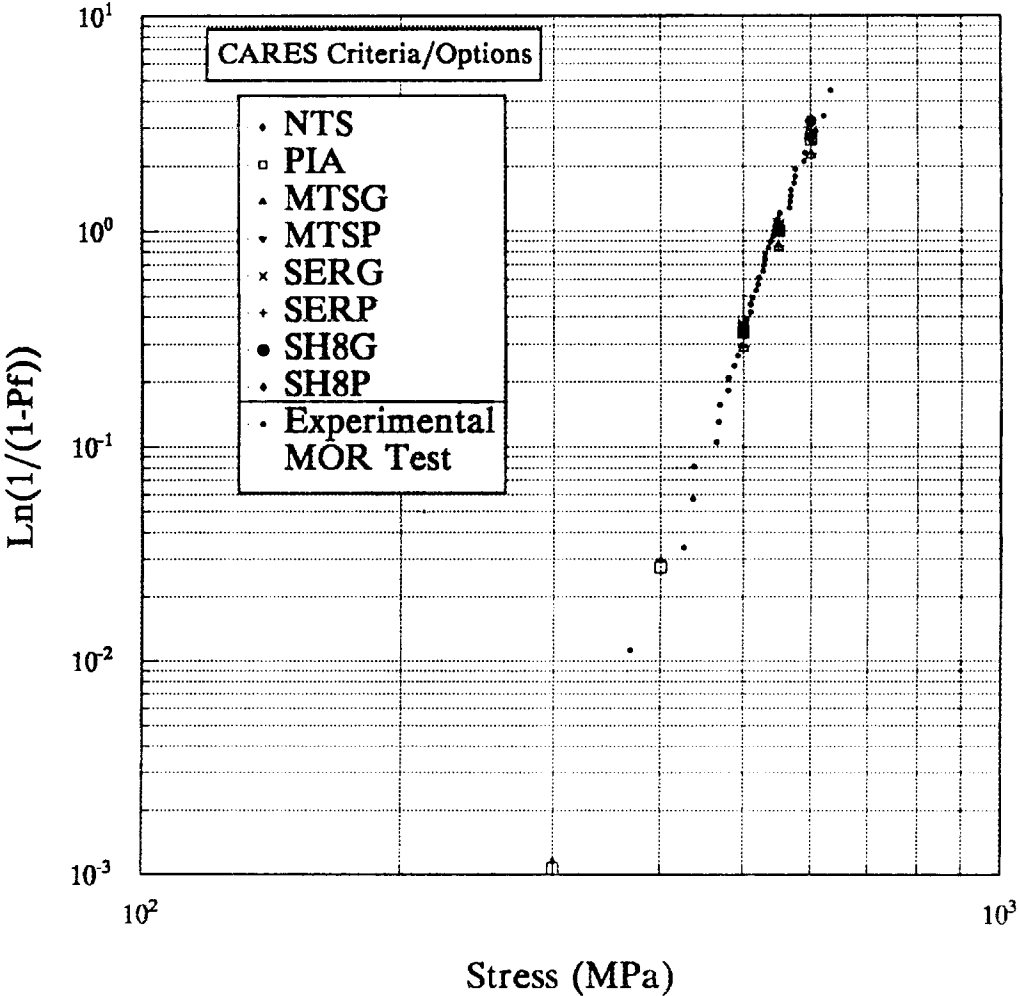


Figure 10

NCX-5100 Joined Prediction Results vs Experimental MOR (5mm x 40mm) Fast Fracture at 1100°C

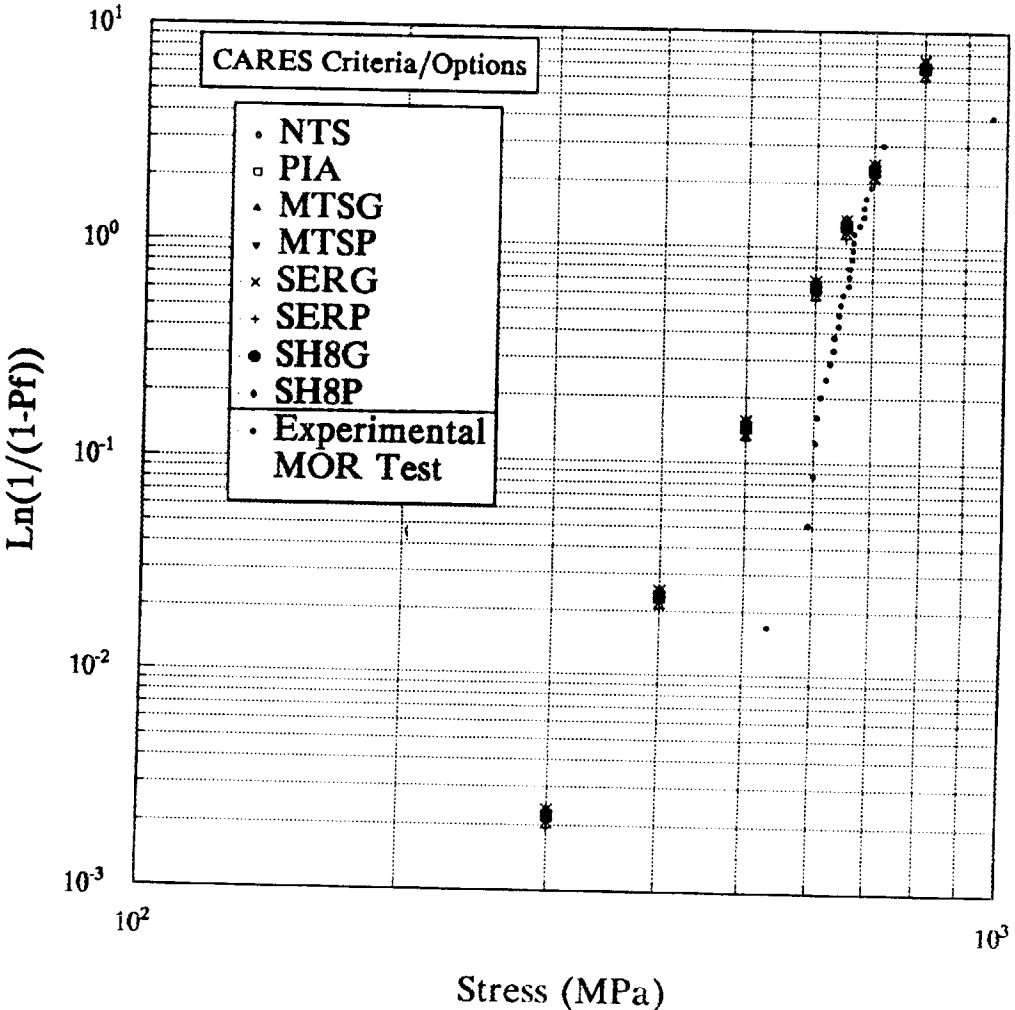
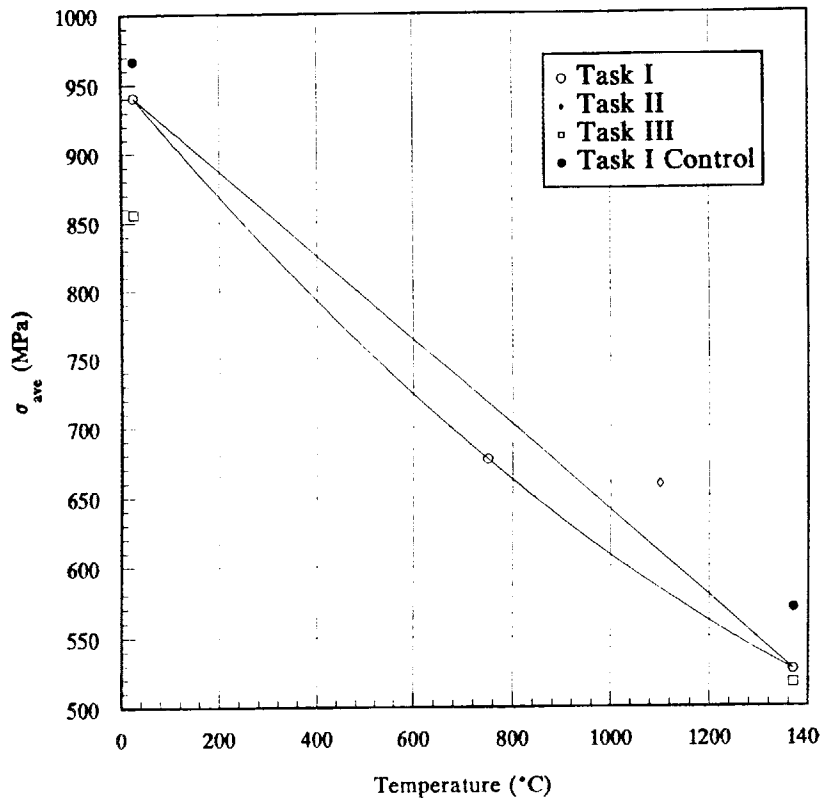


Figure 11

Average MOR Strength for NCX-5100 on 5mm x 40mm Spans



Weibull Modulus for NCX-5100 on 5mm x 40mm Spans

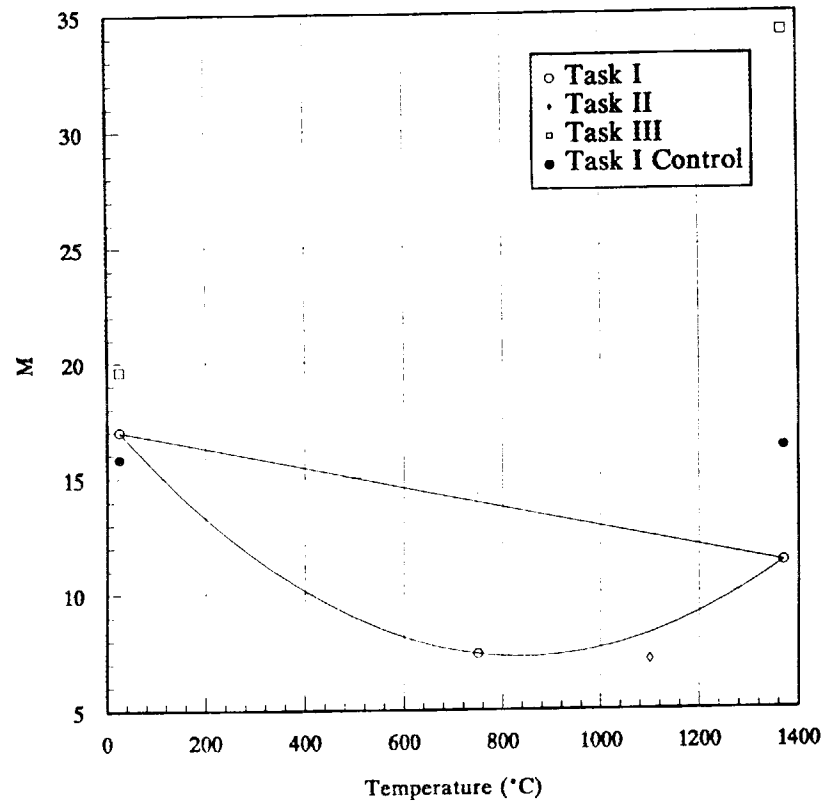


Figure 12

Flexural Strength of NCX-5100 Si₃N₄ Task I, II, and III

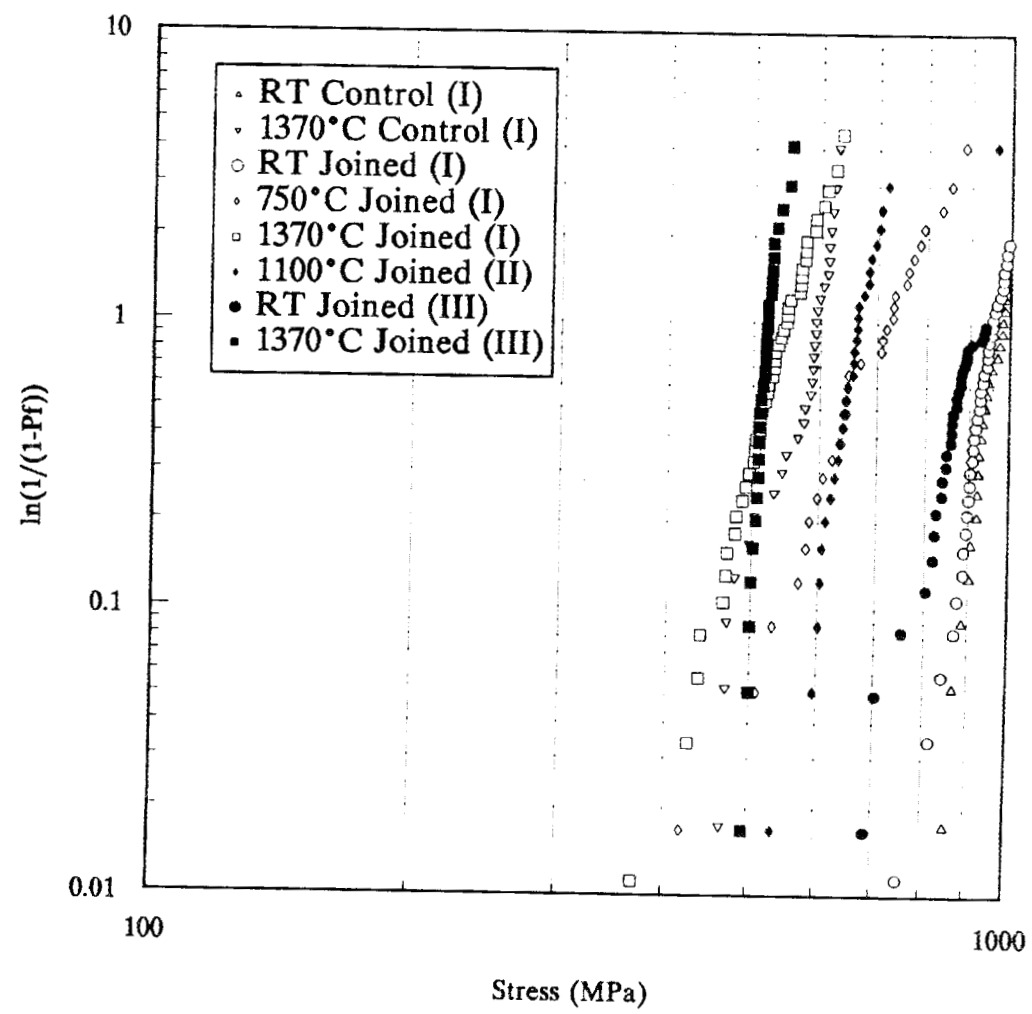


Figure 13

Creep Modeling

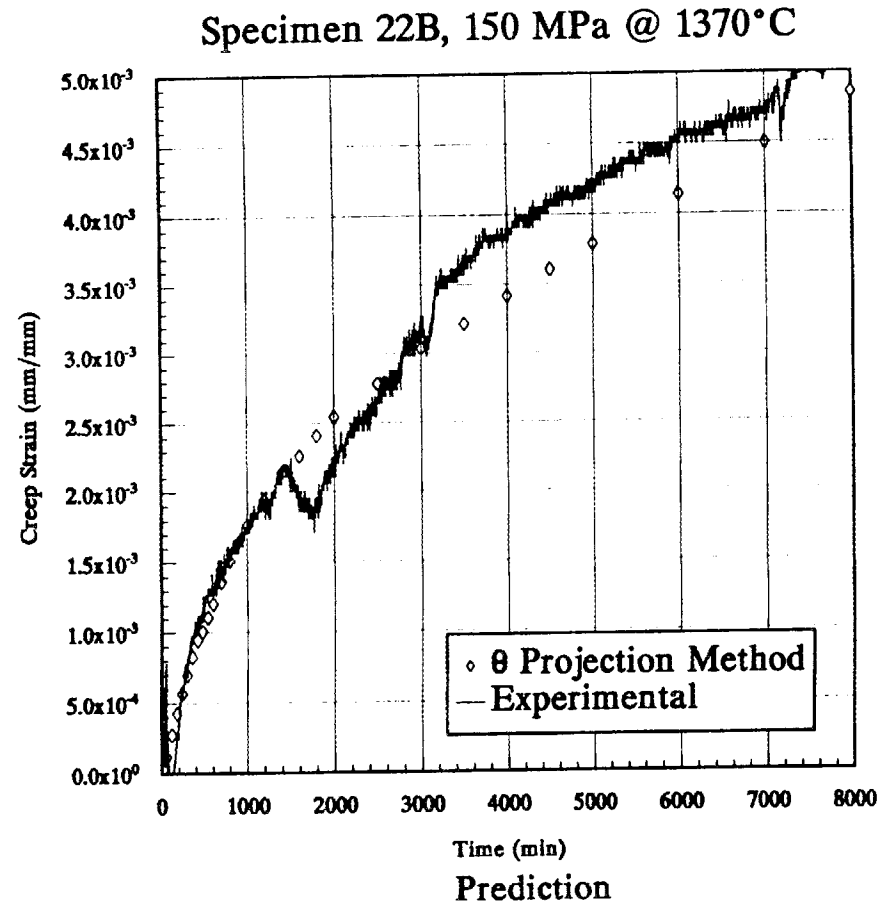
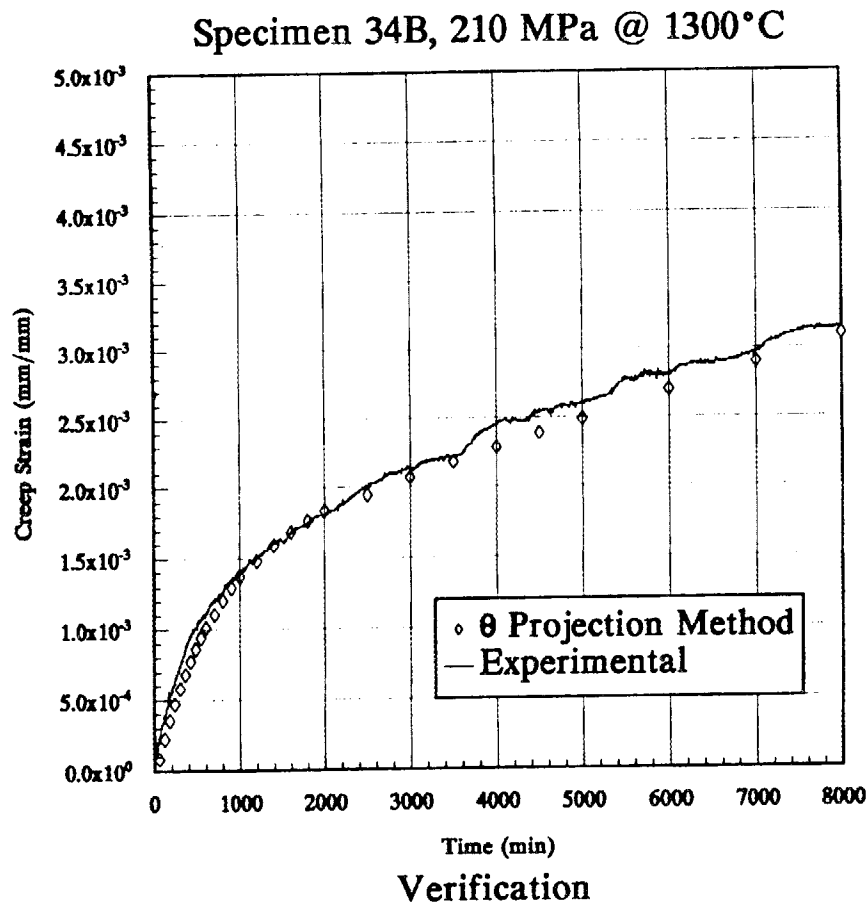


Figure 14

2.0 MATERIALS DESIGN METHODOLOGY

INTRODUCTION

This portion of the project is identified as project element 2 within the work breakdown structure (WBS). It contains three subelements: (1) Modeling, (2) Contact Interfaces, and (3) New Concepts. The subelements include macromodeling and micromodeling of ceramic microstructures, properties of static and dynamic interfaces between ceramics and between ceramics and alloys, and advanced statistical and design approaches for describing mechanical behavior and for employing ceramics in structural design.

The major objectives of research in Materials Design Methodology elements include determining analytical techniques for predicting structural ceramic mechanical behavior from mechanical properties and microstructure, tribological behavior at high temperatures, and improved methods for describing the fracture statistics of structural ceramics. Success in meeting these objectives will provide U.S. companies with methods for optimizing mechanical properties through microstructural control, for predicting and controlling interfacial bonding and minimizing interfacial friction, and for developing a properly descriptive statistical data base for their structural ceramics.

2.1 MODELING

2.1.1 Modeling

Microstructural Modeling of Cracks

J.A.M. Boulet (University of Tennessee, Knoxville)

Objective/scope

The goal of the study is to develop mathematical procedures by which existing design methodology for brittle fracture could accurately account for the influence of protrusion interference on fracture of cracks with realistic geometry under arbitrary stress states. To predict likelihood of fracture in the presence of protrusion interference, a simulation will be developed. The simulation will be based on a three-dimensional model of cracks with realistic geometry under arbitrary stresses.

Technical progress

A survey of existing three-dimensional boundary element methods (BEM) revealed that efficient numerical analysis of arbitrarily shaped, nonplanar cracks can best be achieved using a boundary element method (BEM) based on what is referred to as a traction boundary integral equation (BIE)^{1, 2, 3}. We have acquired a copy of the computer code used in reference 3, which is based on a traction BIE and has been used to analyze three-dimensional elastic deformation of several cracks of differing nonplanar shape. The code was originally used to analyze five crack problems of varying complexity. We have obtained⁴ detailed numerical data produced by the code for these problems. For the first (and simplest) problem, we have tested the code on a mainframe computer at the University of Tennessee Computing Center (UTCC). The results produced on the UTCC computer are identical to those provided in reference 3. The cost for this test run was about \$40. To complete our verification, we plan to run the most complicated of the five problems on the UTCC mainframe. But for reasons discussed below, it is appropriate to find a less expensive platform on which to run the code in the future.

Eventually, each run of the 3-D BEM code we are testing is to become a single step in an iterative process (see below) for computing stresses around a crack experiencing crack-face interference. The 3-D code would be run approximately ten times to solve one such problem. Furthermore, once the iterative process is validated, it will have to be repeated approximately one hundred times to simulate the behavior of a population of real cracks. Even if we do not allow for the computer time required to validate the iteration and simulation processes, nor for the greater complexity of the crack-face interference problem (relative to the simple problem that cost \$40), we expect that simulation of a single population of real cracks on a UTCC mainframe computer would cost about \$40,000. To reduce the simulation cost significantly, we must run on a less expensive machine.

We are in the process of validating the 3-D BEM code on a microcomputer. We have purchased a FORTRAN compiler for the microcomputer (for a few hundred dollars) and have altered the source code so that it compiles on the microcomputer. We expect to have a complete validation of the code for the simplest (\$40) problem in the immediate future. Although the microcomputer takes five to six times as long as the mainframe took

to run the code, there is no charge for use of the microcomputer. Hence, in the long run, the project's computing costs will be considerably reduced by using the microcomputer.

As mentioned above, we plan to use an iterative scheme to account for crack-face interference. For the first problem to be analyzed, the location of the interference (contact) will be prescribed. (In later problems, when the interference locations are not prescribed, algorithms to detect interference will be needed.) The iteration algorithm is as follows.

1. Analyze deformation of the crack subjected only to remote stress.
2. Quantify interpenetration of the crack faces at the interference site.
3. Estimate interference loads required to prevent the interpenetration found in step 2.
4. Analyze deformation of the crack subjected to both remote stress and the interference loads found in step 3.

Steps 2. through 4. are repeated until crack-face interpenetration is zero and the interference loads have stopped changing. This algorithm is being programmed. When completed, the program will be merged with the traction BIE code referred to above.

References

1. T. A. Cruse, "Fracture Mechanics," pp. 333-365 in *Boundary Element Methods in Mechanics*, ed. D. E. Beskos, Elsevier Science Publishers, Amsterdam, 1987.
2. T. A. Cruse, *Boundary Element Analysis in Computational Fracture Mechanics*, Kluwer Academic Publishers, The Netherlands, 1988.
3. T. A. Cruse and G. Novati, "Traction-BIE Solutions for non-planar and surface cracks," pp. ed. proceedings of presented at 22nd National Symposium on Fracture Mechanics, June 26-28, Atlanta, Georgia, 1990.
4. T. A. Cruse, personal communication, August, 1990.

Status of milestones

Work is on schedule.

2.2 CONTACT INTERFACES

2.2.2 Dynamic Interfaces

Studies of Dynamic Contact of Ceramics and Alloys for Advanced Heat Engines

P.A. Gaydos and K.F. Dufrane (Battelle)

Objective/Scope

The objective of the program is to develop an understanding of the friction and wear processes of ceramic interfaces based on experimental data. The supporting experiments are to be conducted at temperatures to 650 C under reciprocating sliding conditions reproducing the loads, speeds, and environment of the ring/cylinder interface of advanced engines. The test specimens are to be carefully characterized before and after testing to provide detailed input to the model. The results are intended to provide the basis for identifying solutions to the tribology problems limiting the development of these engines.

Technical Highlights

Apparatus

The apparatus developed for this program uses specimens of a flat-on-flat geometry, which facilitates specimen procurement, finishing, and testing. The apparatus reproduces the important operating conditions of the piston/ring interface of advanced engines. The specimen configuration and loading is shown in Figure 1. The contact surface of the ring specimen is 3.2 x 19 mm. A crown with a 32 mm radius is ground on the ring specimen to ensure uniform contact. The ring specimen holders are pivoted at their centers to provide self-alignment. A chamber surrounding the specimens is used to control the atmosphere and contains heating elements to control the temperature. The exhaust from a 4500 watt diesel engine is heated to the specimen temperature and passed through the chamber to provide an atmosphere similar to that of actual diesel engine service. A summary of the testing conditions is presented in Table 1.

Materials

Ring and Cylinder Materials

The compositions of the various materials used in the study are presented in Table 2. A variety of monolithic and coating materials were selected to represent various chemical compositions and materials with previously demonstrated successful sliding performance.

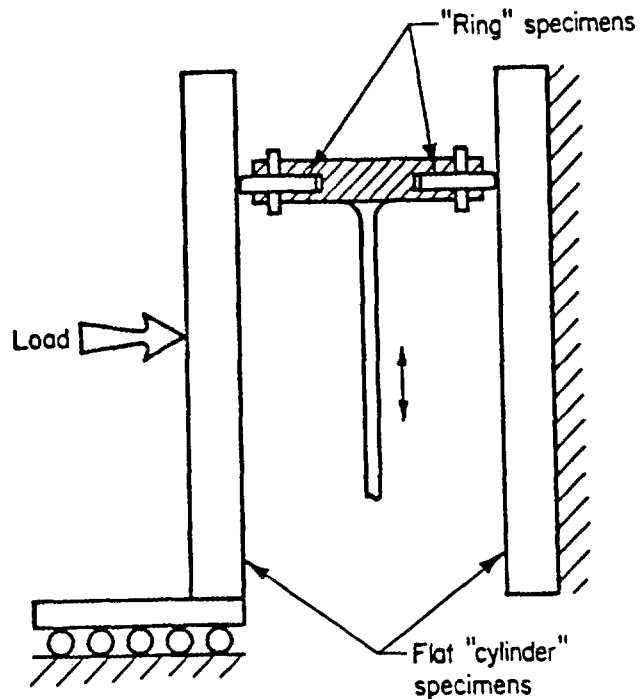


FIGURE 1. TEST SPECIMEN CONFIGURATION AND LOADING

TABLE 1. SUMMARY OF TESTING CONDITIONS

Sliding Contact:	Dual flat-on-flat
"Cylinder" Specimens:	12.7 x 32 x 127 mm
"Ring" Specimens:	3.2 x 19 x 19
"Ring" crown radius:	32 mm
Motion:	Reciprocating, 108 mm stroke
Reciprocating Speed:	500 to 1500 rpm
Average Specimen Speed:	1.8 x 5.4 m/s
Load:	to 950 N
Ring Loading:	to 50 N/mm
Atmosphere:	Diesel exhaust or other gases
Measurements:	Dynamic friction (during test) Specimen wear (after test)

TABLE 2. MATERIALS FOR EVALUATION

Monolithic Ceramics	Coatings
YPSZ	Tribaloy 400
MPSZ	METCO 130 (13 TiO ₂ , 87 Al ₂ O ₃)
ATTZ	METCO 501 (30 Mo, 12 Cr, bal Ni)
αSiC	Plasmalloy 312M (MoSi ₂)
SiC/Al ₂ O ₃	Cr ₂ O ₃ (5 Cr, bal Cr ₂ O ₃)
Sialon	Jet-Kote WC (12 Co, bal WC)
K162B (TiC - Ni/Mo)	Cr (Electroplated)
Si ₃ N ₄	PS212 (Cr ₃ C ₂ + BaF ₂ /CaF ₂ + Ag)
	VR73 (WC/TaC/TiC/Co)
	VA 20 (WC/TaC/TiC/Ni)
	CA 815 (Cr ₃ C ₂ /Ni)
	Mo
	Duplex (WC and Mo)
	Ion Implanted (N in Cr ₂ O ₃)
	Cr ₂ O ₃ + SiO ₂
	High Carbon Fe + Mo

Wear Experiments

Testing began on coatings supplied by Caterpillar, Inc. A chromia-silica ring coating was tested against a cylinder liner coated with a high carbon iron-molybdenum. The tests thus far have produced ring wear rates equal to or better than the best chromia and tungsten carbide coatings tested in the past. The iron-molybdenum coatings on the cylinder liner specimens, however, are not as hard as cylinder specimen materials used in the past such as plasma sprayed chromia and may greatly improve ring wear performance. Ring specimens that performed well against hard cylinder liners will be tested against the softer Caterpillar liner to see if ring wear decreases. These coatings from Caterpillar and the forthcoming wear specimens from Cummins represent optimization of materials that not only possess excellent high temperature wear characteristics, but are also practical from a manufacturing standpoint. No other technical work was performed during this reporting period as time was spent preparing the final report for the second phase of this program and working out the details of the current (third) phase.

Publications

A final report for work completed during the second phase of this contract was submitted to ORNL.

A paper was submitted entitled "Current Progress in Studies of Dynamic Contact of Ceramics for Advanced Heat Engines" to be published in the Proceedings of the Castine Coatings Workshop.

2.3 NEW CONCEPTS

Advanced Statistical Concepts of Fracture in Brittle Materials

C. A. Johnson and W. T. Tucker (General Electric Corporate Research and Development)

Objective/Scope

The design and application of reliable load-bearing structural components from ceramic materials requires a detailed understanding of the statistical nature of fracture in brittle materials. The overall objective of this program is to advance the current understanding of fracture statistics, especially in the following four areas:

- Optimum testing plans and data analysis techniques.
- Consequences of time-dependent crack growth on the evolution of initial flaw distributions.
- Confidence and tolerance bounds on predictions that use the Weibull distribution function.
- Strength distributions in multiaxial stress fields.

The studies are being carried out largely by analytical and computer simulation techniques. Actual fracture data are then used as appropriate to confirm and demonstrate the resulting data analysis techniques.

Technical Highlights

Work performed during this reporting period includes continuing effort in two areas: Bias correction using bootstrap simulation and probabilistic strength analysis in multiaxial stress states. The following sections describe recent progress in each.

1. Bias Correction using Bootstrap Simulation

Bootstrap analyses of confidence and tolerance bounds for Class IV problems (where the fracture data include strengths from multiple specimen sizes and loading geometries, while the component of interest may be of yet a different size and loading configuration) have been described in earlier semi-annual reports. Bootstrap analyses utilize estimators such as maximum likelihood and linear regression to digest a set of fracture strengths and estimate quantities such as the Weibull parameters and/or the probability of failure of a component at any quantile of interest (at any probability of failure of interest). As with most estimators, these Weibull estimators

have the property of yielding offset or "biased" estimates. Strength estimates are particularly prone to large bias errors, especially if the strength is being estimated for a specimen or component with a much larger (or smaller) effective size than the test specimens. This large bias after size extrapolation can generally be traced to bias in the estimate of m . Of course, a small error in m will lead to progressively larger errors in predicted strength as one extrapolates farther and farther from the effective size of the test specimen data.

Although not always utilized, bootstrap simulations for estimation of confidence and tolerance bounds contain information about the magnitude of bias introduced by the estimator. This information is now being used within the bootstrap analysis computer program to yield estimates of distribution parameters, strengths and confidence and tolerance bounds that have been corrected for bias. The remainder of this section demonstrates the magnitude of correction involved, and accordingly, the magnitude of error that would have been incurred without such bias correction.

The fracture data used herein is the same set of 137 bend strengths of sintered beta SiC used in prior reports for various purposes. The specimens were fabricated in the three Mil Std 1942MR specimen sizes: A, B, and C. Specimens of each size were tested in both 3-point and 4-point bending, thus resulting in a total of six different specimen sizes and geometries. Each of the six groups consisted of approximately 18 specimens except for the 4-point B group which consisted of 48 specimens. Fractography indicated that fracture was initiated predominately from surface-related defects, therefore all size scaling is carried out using surface areas.

Figures 1-4 are similar plots of log fracture stress versus log stressed area that result from the full bootstrap analysis of the data. The plots differ in the estimator used and/or the data set analyzed. Linear regression was used in Figures 1 and 3, while maximum likelihood was used in 2 and 4. All 137 strengths were analyzed in Figures 1 and 2, while only the 4-point B strengths were analyzed in Figures 3 and 4. First, Figure 1 will be described in moderate detail; then Figures 2-4 will be compared and contrasted with Figure 1.

In Figure 1, the strengths of all 137 specimens are included as open symbols with the lower left key identifying the associated specimen size and testing geometry. The combined data from the six specimen types were analyzed using the linear regression estimator for Class IV problems described in earlier reports. Bootstrap simulation was then used to determine confidence bounds on Weibull parameters and tolerance bounds on strength estimates. Finally, bias information created during the bootstrap was used to correct bias in parameters and strength estimates.

The dashed lines in Figure 1 represent strength estimates and tolerance bounds that were not corrected for bias. The solid lines, conversely, have been corrected for bias as described above. Predicted relationships for strength versus stressed area are included for two quantiles: The upper straight lines (solid and dashed) are for the median or 0.5 quantile where 50 percent are expected to fail; the lower straight lines are for the 0.05 quantile where 5 percent are expected to fail. The 95 percent

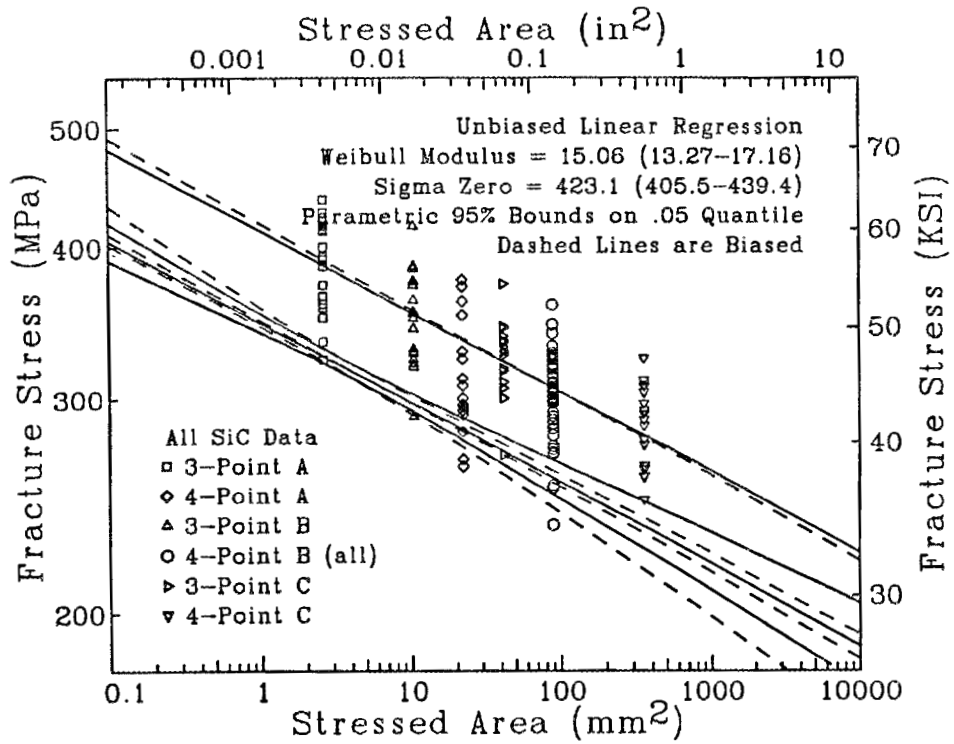


Figure 1

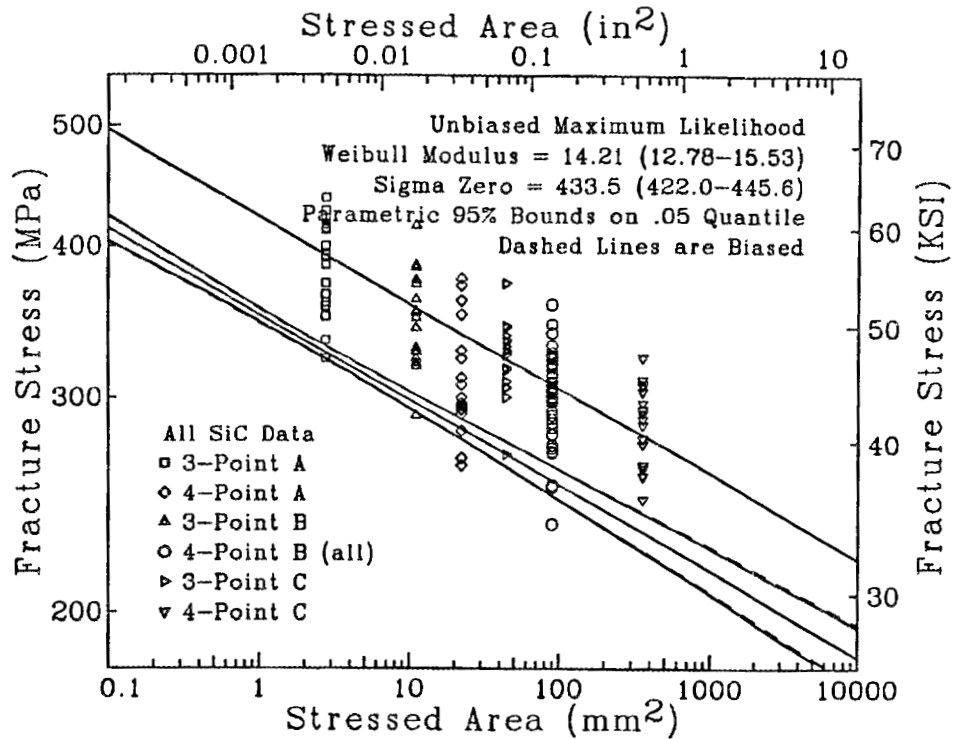


Figure 2

tolerance bounds are included for the 0.05 quantile as the pair of hyperbolic shaped curves bounding each lower straight line. Again, the uncorrected bounds are drawn as dashed lines while the bias corrected bounds are drawn as solid lines.

As shown in Figure 1, the bias using this estimator is significant, even with 137 strengths. The difference in slopes at the 0.5 quantile shows that the linear regression estimator biases the Weibull modulus toward lower numbers (uncorrected $m = 14.38$; bias corrected $m = 15.06$). The error in predicted strengths incurred by ignoring the bias increases with increasing extrapolation from the observed strengths and specimen sizes. Interestingly, the error in tolerance bounds incurred by ignoring the bias increases faster than that for strength. This can be observed on Figure 1. The tolerance bounds are influenced by the bias both in the original analysis of the data and in the subsequent bootstrap simulations, thus contributing to the greater sensitivity of the tolerance bounds to bias.

Figure 2 is identical to Figure 1 except that maximum likelihood was used as the estimator. Again, both the biased (dashed lines) and unbiased (solid lines) are included. The bias is so small in this estimator that the solid and dashed lines are virtually superimposed. The separation is again largest in tolerance bounds but is still very small. The uncorrected $m = 14.22$; the bias corrected $m = 14.21$. It is important to note that the width of the 95% bounds on Figure 2 is smaller than those of Figure 1, therefore suggesting that maximum likelihood can extract more information from this data set than linear regression can. More will be said about this aspect of efficiency below.

Figure 3 uses the linear regression estimator of Figure 1 but analyzes only one of the six data sets, the 48 4-point B specimens. Because there is less information contained in this smaller data set, the width of the confidence bounds on the 0.05 quantile is larger than that of Figure 1. The bias contained in the estimate of m using this estimator is very small (uncorrected $m = 15.31$; bias corrected $m = 15.38$). The tolerance bounds from linear regression, however, are asymmetrical. Therefore, the inversion of the tolerance bounds that occurs on bias correction inverts the asymmetry, and results in a substantial difference between the biased and unbiased tolerance bounds. This difference occurs despite the absence of bias in the strength estimates themselves.

Figure 4 analyzes the 48 4-point B specimens using maximum likelihood. There is a moderate bias in Weibull modulus (uncorrected $m = 14.28$; bias corrected $m = 13.96$). The tolerance bounds in maximum likelihood, however, are very symmetrical and are therefore well behaved upon bias correction. Again, the widths of the tolerance bounds using maximum likelihood are smaller than those from linear regression analysis of the same data.

Two general conclusions can be reached based on comparisons such as Figures 1-4. First, the maximum likelihood estimator for Class IV data yields estimates of strengths and distribution parameters with smaller bias and (more importantly) smaller confidence and tolerance bounds than equivalent estimates using the linear

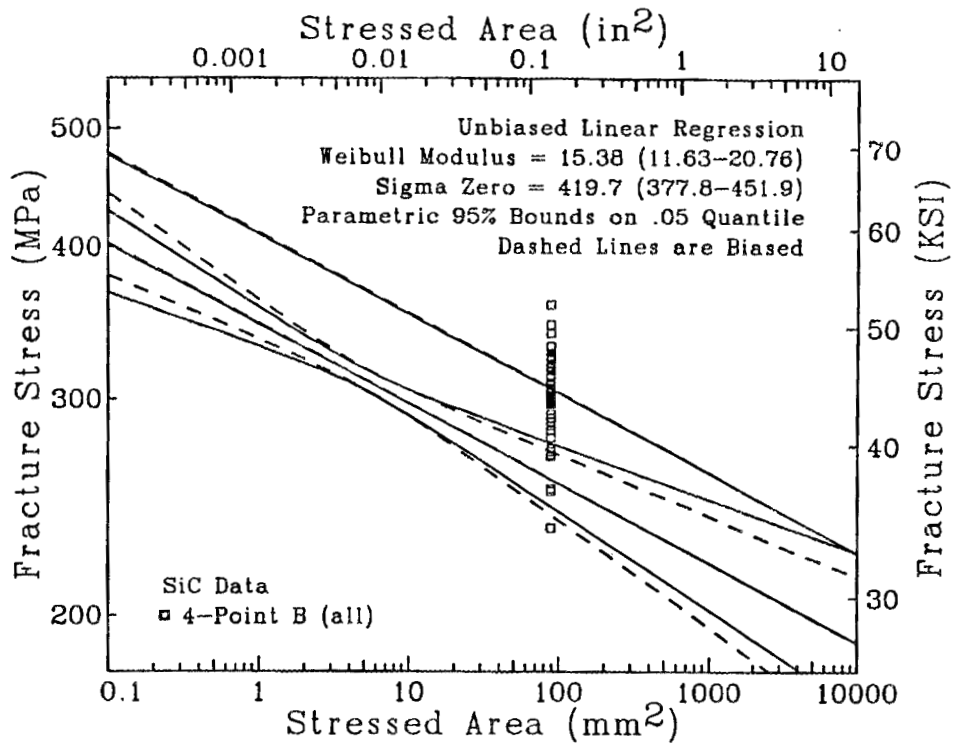


Figure 3

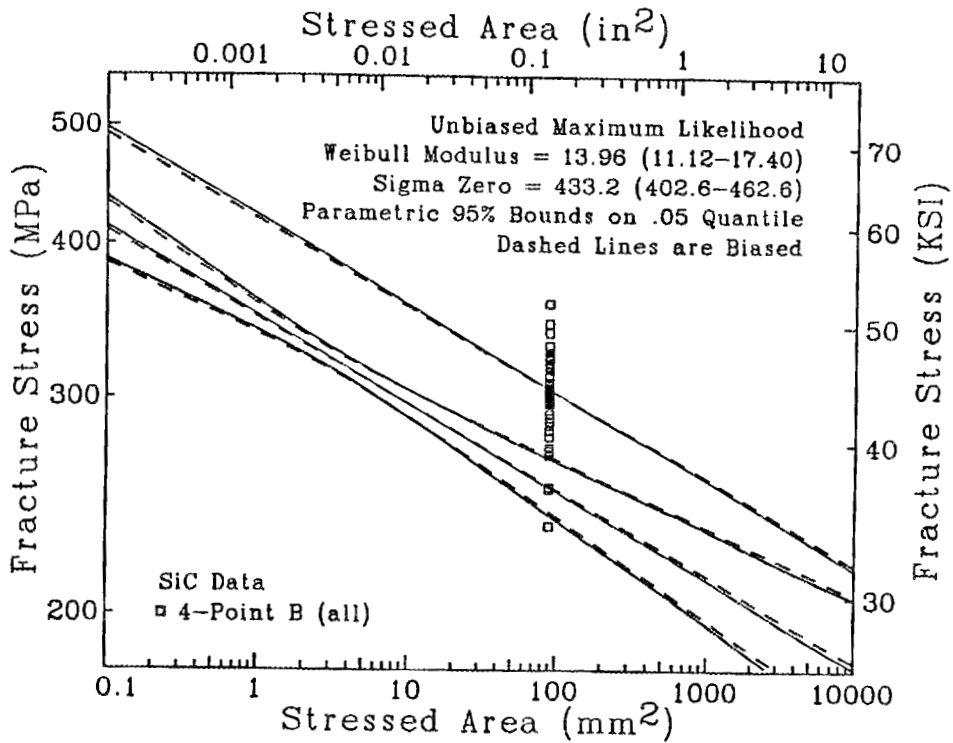


Figure 4

regression estimator for Class IV data. Second, the magnitude of the bias created by an estimator cannot be predicted for an arbitrary combination of specimen sizes, geometries and numbers. Therefore, it is recommended that estimates of distribution parameters, predicted strengths and confidence and tolerance bounds all be corrected for bias.

Recent work that is not completed has expanded on bias correction and efficiency. Because of the importance of the tentative conclusions, a summary of that work is included here. Six variations of linear regression estimator were compared with each other and with the maximum likelihood estimator. The comparisons were made with both a complex Class IV problem that involved specimens of multiple sizes and geometries (such as Figures 1 and 2) and with a simpler Class I problem that involved only one specimen size and geometry (such as Figures 3 and 4). Most conclusions are based on bias corrected estimates of the Weibull parameters and the confidence intervals for those parameters. Similar statements could be made about strength estimates and bounds on those strengths.

The six linear regression estimators were very similar but differed from each other in two respects--ranking scheme and direction of regression. Three different ranking schemes were used:

$$P = (i-.5)/N$$

$$P = (i-.3)/(N+.4)$$

$$P = i/(N+1)$$

where P is the cumulative probability of failure assigned to the i -th specimen of a group of N specimens that are ordered in strength from weakest to strongest. All three have been proposed and used in the statistical and materials literature. The first is typically used in the linear regression estimators within our contract effort (including the WeibEst program).

The second variation in linear regression estimator is the direction of regression. On Weibull probability paper, the regression is normally carried out by regressing the probability on the strengths; that is minimizing the sum of squared errors of predicted versus observed probabilities of failure. This direction of regression is typically used in the literature and in most output of our contract effort (both are available in the WeibEst program). The regression for both Class I and IV problems, however, can be inverted such that the strength is regressed on the probability of failure. (In the case of transformed variables of the type described in earlier reports, this translates to regressing strength on effective volume or area on figures such as Figures 1-4.)

Combinations of three variations of ranking schemes and two variations of regression result in six different linear regression estimators. The following are some qualitative results of our preliminary comparison of estimates from these six regression estimators and the one maximum likelihood estimator.

- After bias correction, there is virtually no difference in estimated parameters from different ranking schemes. The m values of the different ranking schemes agreed within 0.3 percent. The sigma zero values agreed within 0.1 percent. There is no apparent equivalence of estimates from different ranking schemes prior to bias correction. Therefore bias errors are the primary source of differences that, in the past, have been attributed to different ranking schemes.
- After bias correction, there is very little difference in confidence bounds on estimated parameters from different ranking schemes. The width of the bounds differ by approximately 1.0 percent. A corollary of this statement is that the different ranking schemes yield equivalent efficiencies. (For a given data set, the narrower the confidence bounds, the more efficient the estimator is in using the available information.)
- There is much less difference in estimates from the two directions of regression after bias correction than is typical before bias correction. This conclusion is probably more sensitive to the particular data sets considered in this study than for previous conclusions.
- The efficiency of "backwards" regression (regressing strength on size, i.e. probability) appears to be 10-15 percent more efficient than conventional regression.
- Possibly the most important conclusion is: regression methods in general seem to be 40-50 percent less efficient than maximum likelihood. Therefore much more fracture data is necessary when using linear regression in order to yield an equivalent confidence bound on Weibull parameters and strength estimates.

2. Probabilistic Strength Analysis in Multiaxial Stress States

Also during this reporting period, work has continued on assessing the effects of the equivalence of the Batdorf-Heinisch (B-H) and Lamon-Evans (L-E) approaches to multiaxial stress states, as shown in the previous semiannual contract report. It has been further shown that by employing the equivalence of the Batdorf and Heinisch (Ref. 1) and Lamon and Evans (Ref. 2) approaches to multiaxial stress states a size factor, or k factor, can be determined for general loadings and geometry of specimen, and multiaxial failure criteria. Previous investigators have also made some progress in this area. Recently, Chao and Shetty (Ref. 3) have shown by numerical methods the equivalence of the B-H and L-E approaches for two specific failure criteria. But, the equivalence is much more general than that determined by Chao and Shetty.

Both the B-H and L-E methods are analytically involved and numerically complex in their present implementations. In both cases, the distribution of flaw sizes is either assumed or inferred from experimental fracture data. The stress state of the component is generally determined by finite element techniques. After the finite element analysis is completed, the elements are redefined as constant-stress elements (volume or area) at the local stress state. The probability of failure (and survival) of each constant-stress element is estimated using a model of multiaxial fracture combined

with the B-H or L-E approaches. The probability of the component surviving is then estimated from the product of the survival probabilities of each of the elemental elements.

However, use of the general k factor offers another way to determine the component survival probability. When finite element stress analysis is used for components with complex geometries, non-uniformly stressed elements result in more accurate results than a comparable number of constant stress elements. The same should be true in relationship to multiaxial effects. But the equivalence of B-H to L-E shows that effects due to geometry, loading, and multiaxial stress can all be accounted for by a generalized k factor. This k factor can be applied on an elemental basis or to the component structure as a whole.

This follows since it can be shown that another way to determine the probability of failure is from

$$P_f = 1 - \exp\left[-k(m)V\sigma_M^m/\sigma_0^m\right], \quad (1)$$

where

$$k(m) = \frac{1}{2\pi V} \int_0^{\pi/2} \int_0^{2\pi} \left(\int_V (\sigma_e/\sigma_M)^m dv \right) \cos\phi d\phi d\psi. \quad (2)$$

In (1) and (2) V is the component size, m is the Weibull modulus (shape factor), σ_0 is the inherent strength (scale factor), σ_e is the failure criterion, σ_M is the maximum tensile strength in the component. Also σ_e is a function of the local principal stresses (and hence location) and the orientation of the principal plane of a potential failure producing flaw, and this accounts for the limits of integration in (2). The importance of (1) lies in the fact that all methods developed to date for combining data and obtaining confidence bounds (via bootstrapping and likelihood methods) have a direct application in (1). This follows since for a given loading, geometry, and failure criterion, the k factor given by (2) is only a function of m . Thus, at worst, for a particular problem (2) need be determined only once. Evaluation of (2) may be laborious and the best way to proceed is open at this point, but the implications of its use are clear. All in all, the equivalence of the B-H and L-E approaches has very important consequences.

The most straightforward way to derive (1) is to start with

$$P_f = 1 - \exp\left[-\int_V dv \int_0^\infty d\sigma_c \left(\frac{dN(\sigma_c)}{d\sigma_c} \right) \frac{\Omega(\Sigma, \sigma_c)}{4\pi} \right] \quad (3)$$

which is just equation (3) of the B-H approach shown in Ref. 1. Then as shown in the previous semiannual report, the hazard function in (3) with a Weibull "strength" distribution is given by

$$\int_V dv \int_0^\infty d\sigma_c \left[\frac{dN(\sigma_c)}{d\sigma_c} \right] \frac{\Omega(\Sigma, \sigma_c)}{4\pi} = \quad (4)$$

$$\int_V dv \frac{K\sigma_M^m}{2\pi} \int_0^{\pi/2} \int_0^{2\pi} \left[\int_0^\infty mx^{m-1} I(\Sigma, \sigma_M x) dx \right] \cos\phi d\phi d\psi$$

where K is a constant, $x = \sigma_c/\sigma_M$, and

$$1, \quad \sigma_e \geq \sigma_c \text{ for a given } (\phi, \psi) \text{ at a particular location in } V$$

$$I(\Sigma, \sigma_c) = \quad (5)$$

$$0, \quad \text{otherwise}$$

with Σ denoting the local stress state (cf. Ref. 1). Moreover, $I(\Sigma, \sigma_c) = 0$, always, if $\sigma_c > \sigma_M$, since

$$\sigma_M = \max_{V, \phi, \psi} \{\sigma_e\}.$$

Thus the upper limit of integration on the inner integral on the right hand side of (4) is 1. Furthermore, by interchanging the limits of integration we obtain

$$\int_V dv \int_0^\infty d\sigma_c \left[\frac{dN(\sigma_c)}{d\sigma_c} \right] \frac{\Omega(\Sigma, \sigma_c)}{4\pi} = \quad (6)$$

$$\frac{K\sigma_M^m}{2\pi} \int_0^{\pi/2} \int_0^{2\pi} \left\{ \int_V dv \left[\int_0^1 mx^{m-1} I(\Sigma, \sigma_M x) dx \right] \right\} \cos\phi d\phi d\psi.$$

Now fixing V, ϕ, ψ fixes the value of σ_e and picking x , ($0 \leq x \leq 1$), determines σ_c , via $\sigma_c = \sigma_M x$. But since I is one, if and only if, $\sigma_e \geq \sigma_c$ it must be that $\sigma_e/\sigma_M \geq x$ when and only when I is one. This determines the upper limit of integration on the inner integral on the right hand side of (6) so that, finally, the hazard becomes

$$\int_V dv \int_0^\infty d\sigma_c \left[\frac{dN(\sigma_c)}{d\sigma_c} \right] \frac{\Omega(\Sigma, \sigma_c)}{4\pi} = \quad (7)$$

$$\frac{K\sigma_M^m}{2\pi} \int_0^{\pi/2} \int_0^{2\pi} \left\{ \int_V (\sigma_e/\sigma_M)^m dv \right\} \cos\phi d\phi d\psi$$

where σ_e is a function of V, ϕ, ψ . In (7) set $K = \sigma_0^m$, define $k(m)$ by (2), and then (1) follows from (7).

The equivalence of the B-H and L-E approaches has been employed to study the error incurred in employing the PIA (Principle of Independent Action) assumption to the principle stresses. Batdorf (Ref. 4) has shown that the independence assumption can be either conservative or nonconservative when compared to more refined approaches. The PIA method involves the relationship

$$P_s = P_s(\sigma_1)P_s(\sigma_2)P_s(\sigma_3), \quad (8)$$

where P_s gives the total probability of survival, $P_s(\cdot)$ gives the probability of success

when the effects of only one of the principle stresses are considered, and σ_1 , σ_2 , σ_3 , are the principal stresses.

The failure criterion

$$\sigma_e = \frac{1}{2}[\sigma + \sqrt{\sigma^2 + Q^2\tau^2}] \quad (9)$$

where σ is the stress component normal to the crack surface and τ is the shear component, and Q is a "material" constant was employed in (2) to study the conservativeness of the PIA method. In doing this, we have duplicated the results of Batdorf (Ref. 4) shown in his Figure 3 (and given herein in Figure 5) and generalized them to cover failure situations of increasing shear sensitiveness ($Q > 0$) of the failure criterion. Since we only considered elemental volumes, the k factor given by (2) reduces to just that of Lamon and Evans (Ref. 2):

$$k = \frac{1}{2\pi} \int_0^{\pi/2} \int_0^{2\pi} F^m \cos\phi d\phi d\psi \quad (10)$$

where F is such that

$$\sigma_e = \sigma_M F[\Sigma, \phi, \psi] = \sigma_M F[.]$$

A typical set of results are shown in Figures 5-8 which treat, respectively, the cases of $Q = 0, 1, 2, 3$. The results are given on an elemental volume basis shown on the abscissas in terms of the ratio of σ_2 to σ_1 ; in all cases $\sigma_3 = 0$. The ordinates give the ratio of the probability of success determined by use of (1) and (2,10) with (9) with a stress state given by $(\sigma_1, \sigma_2, 0)$ to the probability of success determined by use of (8) and then (1), (2,10), and (9) for a stress state given by $(\sigma_1, 0, 0)$ for $P_s(\sigma_1)$ and a stress state given by $(\sigma_2, 0, 0)$ for $P_s(\sigma_2)$. In producing these Figures, (10) was evaluated numerically. Thus situations of general triaxial loading (and biaxial loading involving compression) can be investigated (we have not yet done so), further generalizing the work of Batdorf (Ref. 4).

In the $Q = 0$ situation as indicated by Batdorf (Ref. 4) for values of m of practical interest, the PIA method consistently underestimates the contribution of the second stress, and the error is largest, in absolute terms, for the equibiaxial case, $s = 1$. This is clearly shown in Figure 5. However, for $Q > 0$, this conclusion no longer holds. Perusal of Figures 6-8 indicates that as the shear sensitivity of the failure criterion increases, the maximum (absolute) error decreases. For Q sufficiently large, PIA is actually conservative. But this requires a value of Q of around 3 or larger. This is probably not realistic since a value of Q of 1 corresponds, in uniaxial compression, to a failure load of eight times that for uniaxial tension while the corresponding factor is three for a Q of 2, and is 16/9 for a Q of three. Thus with the failure criterion given by (9), values for Q are probably less than three and more than likely between 1 and 2. Also as indicated by Batdorf, the results given in Figures 5-8 can be employed to obtain bounds for small values of P_f . However, the upper bound is lower than that obtained by Batdorf when Q is greater than 0. And the the PIA method no longer gives a lower bound. In general terms, the PIA method is prone to less

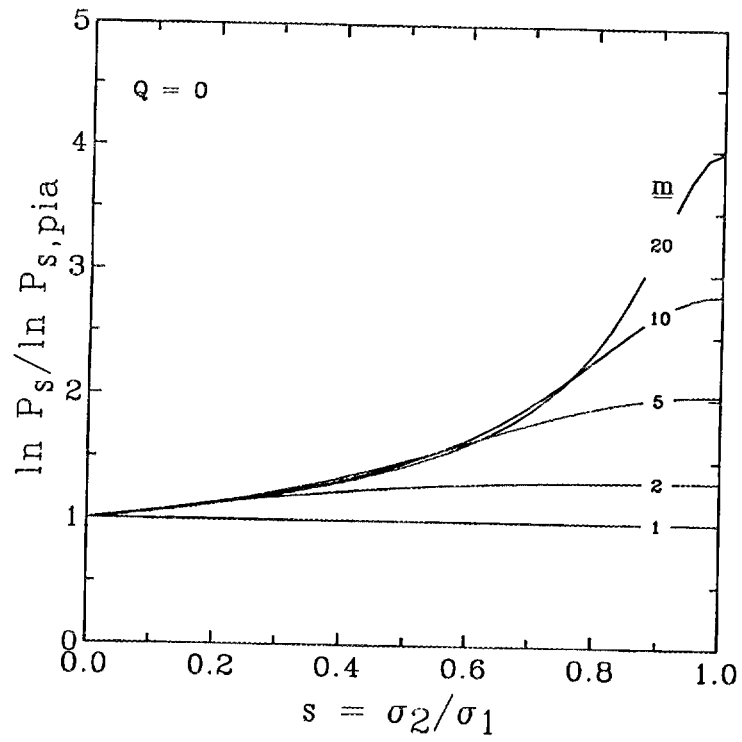


Figure 5

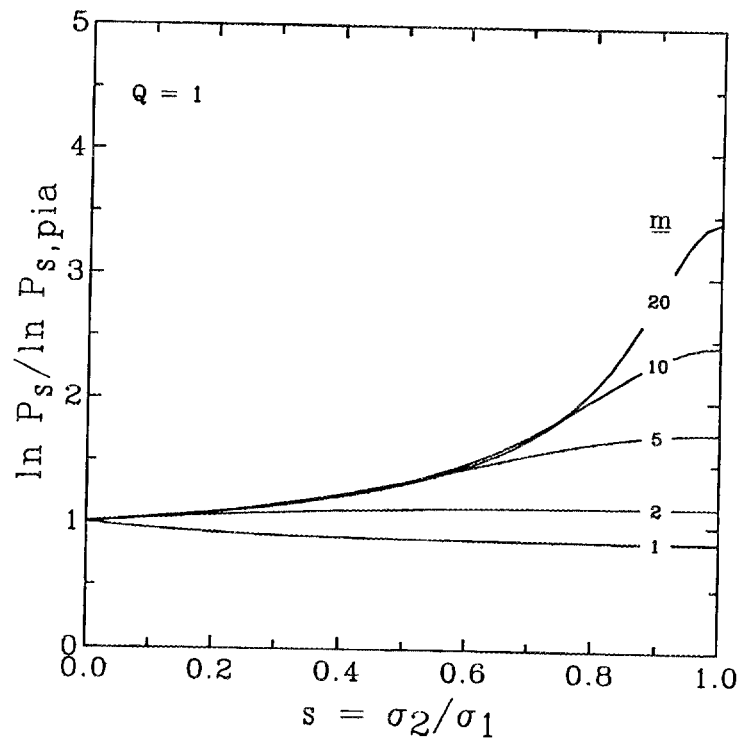


Figure 6

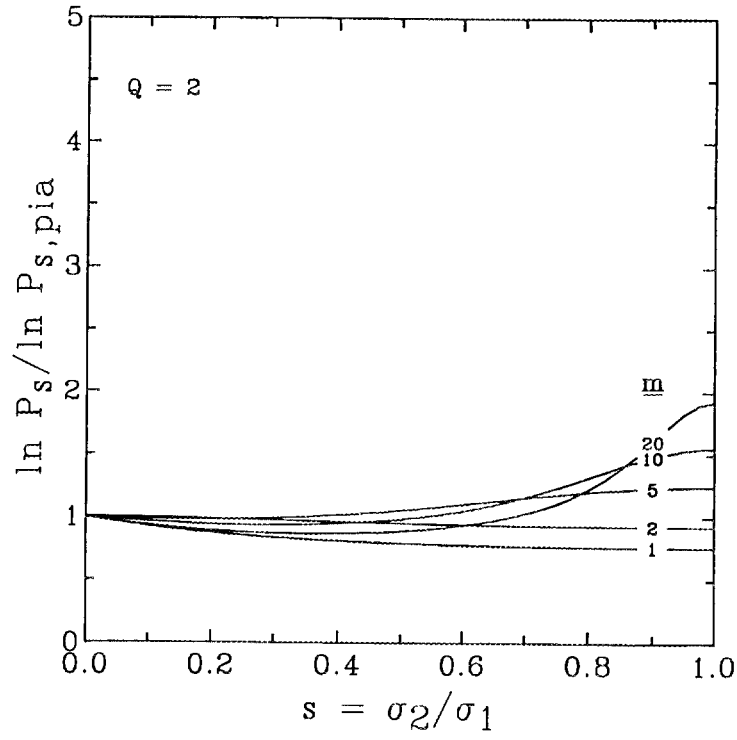


Figure 7

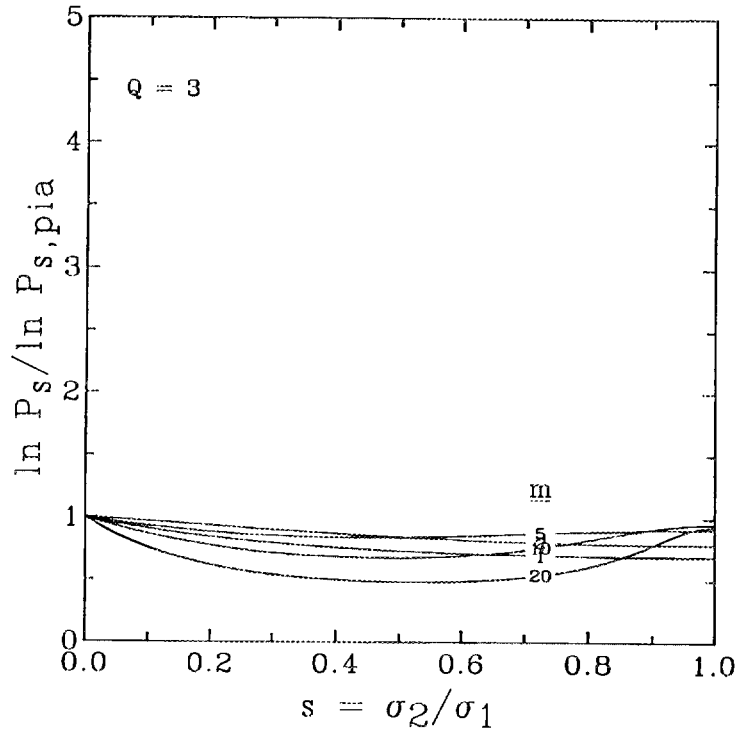


Figure 8

unconservative error as the shear sensitivity increases.

Status of Milestones

All milestones are on schedule.

Publications

None.

References

1. S.B. Batdorf and H.L. Heinisch (1978), "Weakest Link Theory Reformulated for Arbitrary Fracture Criterion," *J. Am. Ceram. Soc.*, **61**, 7-8, 355-58.
2. J. Lamon and A.G. Evans (1983), "Statistical Analysis of Bending Strengths for Brittle Solids: A Multiaxial Fracture Problem," *J. Am. Ceram. Soc.*, **66**, 3, 177-82.
3. L. Chao and D.K. Shetty (1990), "Equivalence of Physically Based Statistical Fracture Theories for Reliability Analysis of Ceramics in Multiaxial Loading," *J. Am. ceram. Soc.*, **73**, 7, 1917-21.
4. S.B. Batdorf (1977), "Some Approximate Treatments of Fracture Statistics for Polyaxial Tension," *Inter. Jour. of Fracture*, **13**, 1, 5-11.

3.0 DATA BASE AND LIFE PREDICTION

INTRODUCTION

This portion of the project is identified as project element 3 within the work breakdown structure (WBS). It contains five subelements, including (1) Structural Qualification, (2) Time-Dependent Behavior, (3) Environmental Effects, (4) Fracture Mechanics, and (5) Nondestructive Evaluation (NDE) Development. Work in the Structural Qualification subelement includes proof testing, correlations with NDE results and microstructure, and application to components. Work in the Time-Dependent Behavior subelement includes studies of fatigue and creep in structural ceramics at high temperatures. Research in the Environmental Effects subelement includes study of the long-term effects of oxidation, corrosion, and erosion on the mechanical properties and microstructures of structural ceramics. Work in the fracture mechanics subelement includes development of techniques for measuring the tensile strength and creep resistance of ceramic materials at high temperatures, and testing ceramic materials at high temperatures under uniaxial tension. Work in the NDE development subelement is directed at identifying approaches for quantitative determination of conditions in ceramics that affect their structural performance.

Major objectives of research in the Data Base and Life Prediction project element are understanding and application of predictive models for structural ceramic mechanical reliability, measurement techniques for long-term mechanical property behavior in structural ceramics, and physical understanding of time-dependent mechanical failure. Success in meeting these objectives will provide U.S. companies with the tools needed for accurately predicting the mechanical reliability of ceramic heat engine components, including the effects of applied stress, time, temperature, and atmosphere on the critical ceramic properties.

3.1 STRUCTURAL QUALIFICATION

Microstructural Analysis of Structural Ceramics

B. J. Hockey and S. M. Wiederhorn (National Institute of Standards and Technology)

Objective/Scope

The objective of this part of the program is to identify mechanisms of failure in structural ceramics subjected to mechanical loads at elevated test temperatures. Of particular interest is the damage that accumulates in structural ceramics as a consequence of high temperature exposure to stresses normally present in heat engines.

Design criteria for the use of ceramics at low temperature differ from those at high temperature. At low temperature ceramics are elastic and brittle; failure is controlled by a distribution of flaws arising from processing or machining operations, and the largest flaw determines the strength or lifetime of a component. By contrast, at high temperature where ceramics are viscoelastic, failure occurs as a consequence of accumulated, or distributed damage in the form of small cavities or cracks that are generated by the creep process. This damage effectively reduces the cross-section of the component and increases the stress that must be supported. Such increases in stress are autocatalytic, since they increase the rate of damage and eventually lead to failure as a consequence of loss in cross section. When this happens, the individual flaw loses its importance as a determinant of component lifetime. Lifetime now depends on the total amount of damage that has occurred as a consequence of the creep process. The total damage is now the important factor controlling lifetime.

Recent studies of high temperature failure of the non-oxide ceramics intended for use for heat engines indicates that for long term usage, damage accumulation will be the primary cause of specimen failure. Mechanical defects, if present in these materials, are healed or removed by high temperature exposure so that they have little influence on long term lifetime at elevated temperature. In this situation, lifetime can be determined by characterizing the damage and the rate of damage accumulation in the material at elevated temperatures. In ceramic materials such as silicon nitride and SiAlON, such characterization required high resolution analyses because of the fine grain size of these materials: hence the need for transmission electron microscopy as an adjunct to the mechanical testing of ceramics for high temperature applications is apparent.

In this project, the creep and creep-rupture behavior of several ceramic materials will be correlated with microstructural damage that occurs as a function of creep strain and rupture time. Materials to be studied include: SiAlON; hot-pressed silicon nitride; sintered silicon carbide. This project will be coordinated with WBS 3.4.1.3, Tensile Creep Testing, with the ultimate goal of developing a test methodology for assuring the reliability of structural ceramics for high temperature applications.

Technical Highlights

During the past six months, microstructural characterization studies were initiated on Norton NT-154, Hip'ed silicon nitride to provide a basis for explaining the tensile creep behavior of this material, as determined under Task 2. To date, the results of this study indicate that the relatively high resistance to creep deformation and the long-term transient behavior exhibited by this material relates to both the interlocked, composite-like β - Si_3N_4 grain structure and to changes in the amount and composition of retained intergranular glass. As a consequence of these microstructural properties, simple interfacial grain boundary sliding is inhibited and grain-to-grain contact occurs so that continued deformation requires diffusional transport or limited dislocation activity within the Si_3N_4 grains. As a further consequence, cavity growth along the interphase interfaces to form full-facet, crack-like cavities is also inhibited. Instead, distributions of isolated, ellipsoidal cavities, having dimensions exceeding the interfacial separations, are preferentially produced on tensile oriented boundaries. As these cavities show little evidence for interactive growth, it appears that rupture is determined by the density of cavities produced.

Experimental Technique

The bulk of the results obtained in this project were obtained by analytical transmission electron microscopy. Observations were made on the NT-154 material in both the as-received and post-crept conditions. Test samples selected for examination covered the range of creep conditions and included samples that failed after times ranging from 4 to 256 hrs., depending on applied stress and temperature. Specimens from interrupted tests that survived for over 1000 hrs were also examined. In all cases, the gage sections of crept specimens were cut parallel to the stress axis to obtain both the near-surface and mid-plane sections. Prior to final TEM specimen preparation, these sections were examined optically for evidence of distributed creep cavitation or crack damage.

Results and Discussion

Examination of NT-154 silicon nitride revealed a matrix grain structure that varied in size and morphology, Figure 1. Typically, β - Si_3N_4 grains were equi-axed with dimensions in the submicron range and in the 2-3 microns range or were whisker-like with lengths of 1-6 microns and an aspect ratio of ≈ 3 . Presumably, this composite-like microstructure results from limited grain growth during processing. In this regard, continued β - Si_3N_4 grain growth during prolonged tensile testing at 1350-1400°C was not apparent. In the as-received state, the intergranular regions exhibit partial devitrification, in that multi-grain junctions contain clusters of small (< 100nm) crystallites, identified as either N-Apatite (a hexagonal yttrium-silicon oxynitride) or α - $\text{Y}_2\text{Si}_2\text{O}_7$ (a triclinic yttrium silicate), Figure 2a. During creep testing, the devitrification process

continues and results in the growth of the secondary crystalline phases, Figure 2b. Regardless of time at temperature, however, a residual yttrium-silicate glassy interface exists, separating the various crystalline phases. Importantly, because of the irregular morphology of the silicon nitride grains, the retained glass interfaces are often not only narrow ($\approx 1\text{nm}$), but are highly irregular (i.e. non-linear). Moreover, because continued devitrification during creep leads to the formation of crystalline phases relatively rich in yttrium, the composition of the retained glass should become more silica-rich and, hence, more viscous.

As a consequence of both the composition and the irregular nature of the narrow glassy interfaces, creep deformation by simple grain boundary sliding appears inhibited. This is evidenced by the presence of localized stress "swirls", indicative of grain-to-grain contact, at distributed points along grain boundaries in samples from interrupted tests, Figure 3. In addition, comparison of crept and uncrept samples appears to reveal a relative increase in dislocation content within the silicon nitride grains after creep, suggesting the possible occurrence of plastic deformation by thermally activated dislocation slip/climb. Further study will be required to fully substantiate this result.

One result clearly brought and by TEM examination is that the cavitation process that occurs in NT-154 is significantly different from that in most other liquid phase sintered materials. As illustrated in Figure 4, cavitation during tensile creep at temperatures of 1350-1400°C results in the formation of isolated, ellipsoidal-shaped cavities, which are preferentially (but not exclusively) distributed on tensile oriented interfaces. Regardless of test conditions, these cavities tend to have major axis dimensions of up to 100-200 nm along the interface and minor axis dimensions of 50 to 100 nm. Since the interphase interface widths are typically 1 to 10 nm at most, cavity growth clearly involves diffusive growth into the silicon nitride grains. This type of behavior can be contrasted with other grades of silicon nitride in which cavities are contained within the residual glass interface and grow rapidly along the interface to form creep crack nuclei. As such, creep rupture in NT-154 appears to be determined by the density of cavities, with failure occurring by rapid crack growth once a critical density of cavities are developed locally. This conclusion is supported by the fact that observable creep crack segments are not found distributed within the test samples regardless of time or strain to failure.

Future studies will be aimed at determining the cavity nucleation process and the effect of strain on cavity density. In addition, the possible role of plastic deformation by dislocations will be explored, with regard to both creep deformation and cavity nucleation.

Status of Milestones

All milestones are on schedule.

Publications

1. B. J. Hockey, S. M. Wiederhorn, W. Liu, J. G. Baldoni and S.-T. Baljan, "Tensile Creep of Whisker Reinforced Silicon Nitride", accepted for publication in *J. Mat. Sci.*
2. S. M. Wiederhorn and B. J. Hockey, "High Temperature Degradation of Structural Composites", to be published in *Proceedings of the Seventh Cimtec World Ceramics Congress, 1990.*
3. S. M. Wiederhorn, B. J. Hockey and T.-J. Chuang, "Crack Growth, Creep, and Creep Rupture at High Temperatures", to be published in *Toughening Mechanisms in Quasi-Brittle Materials, 1990.*

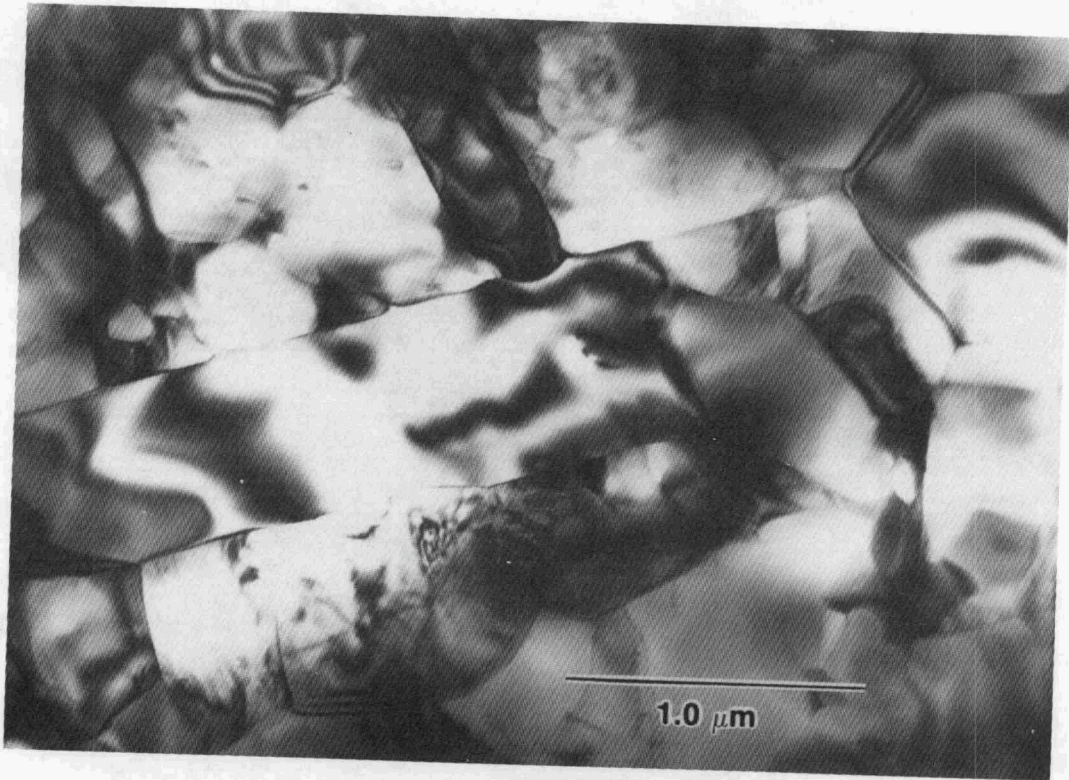


Figure 1. Representative view of NT-154 microstructure, illustrating variable size and morphology of β - Si_3N_4 grains.

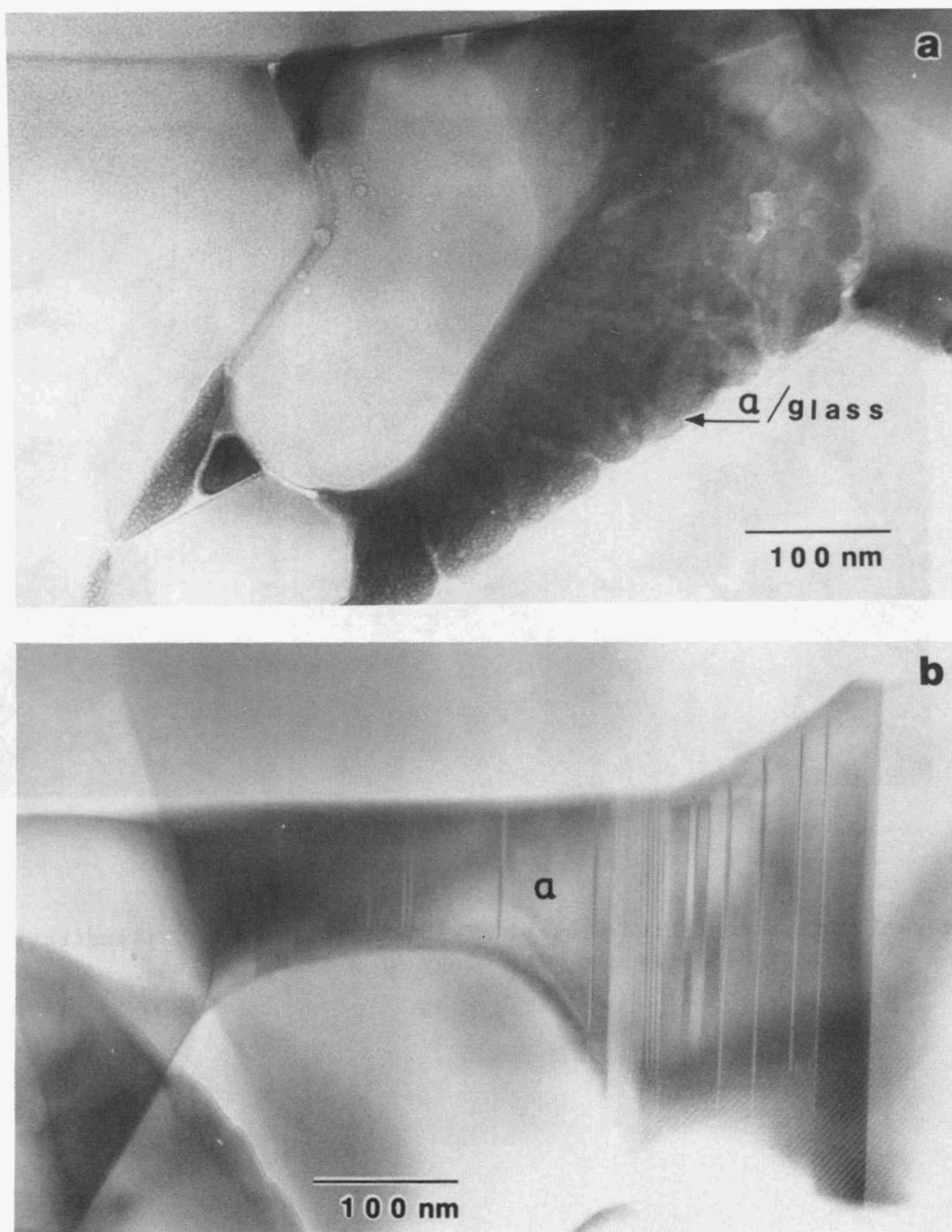


Figure 2. Comparison of intergranular phase distribution in NT-154 before (a) and after (b) tensile creep testing. In as received state, a, multi-grain junctions contain small crystallites dispersed in residual glass. During creep crystal growth occurs, leaving residual glass only at narrow crystalline interfaces. In both a and b, crystalline phase is $\alpha\text{-Y}_2\text{Si}_2\text{O}_7$.

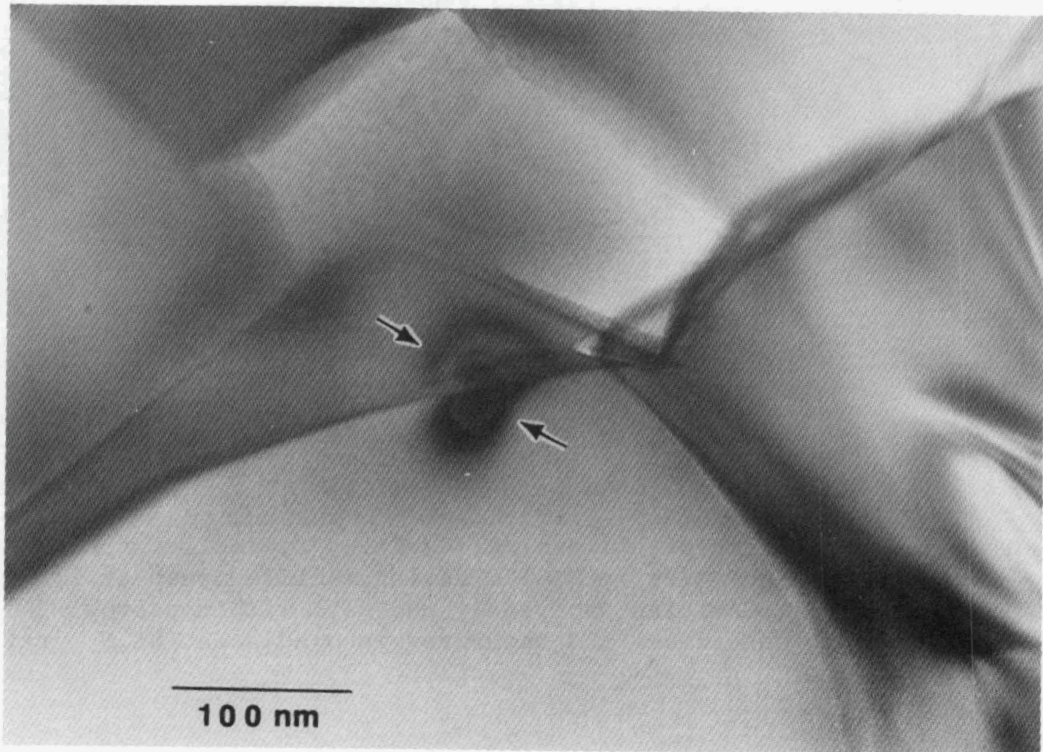


Figure 3. Localized strain contrast contours ("stress swirls") at grain boundary in NT-154 creep sample cooled under load. Presence of such "stress swirls" indicates grain-to-grain contact.

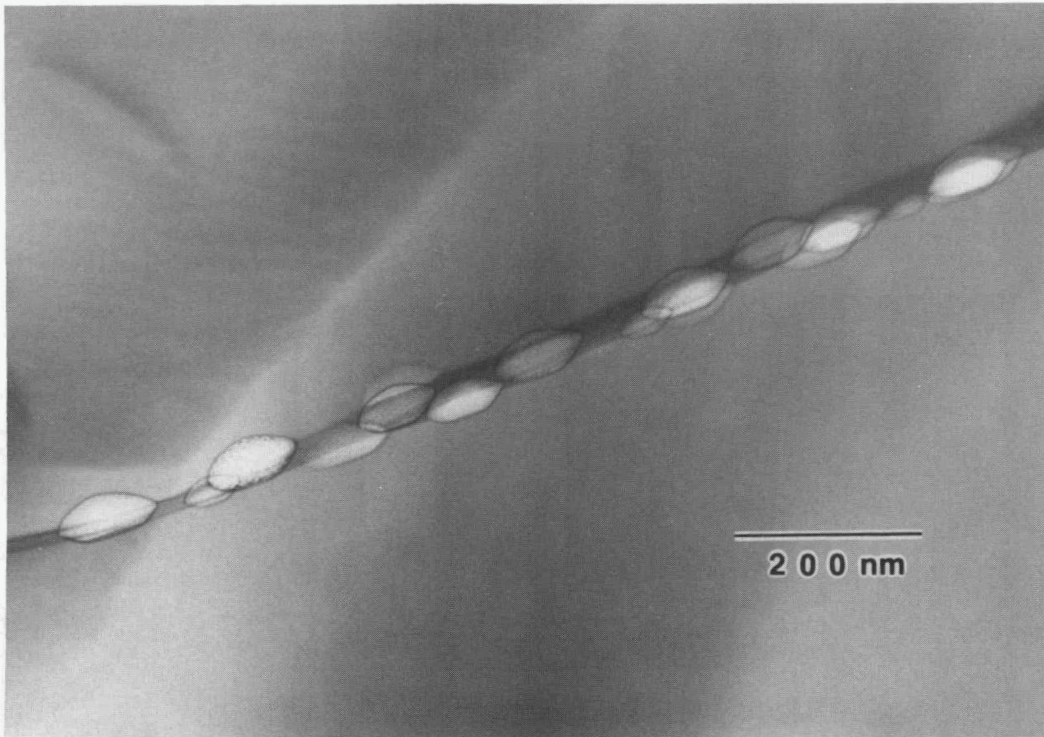


Figure 4. Distribution of ellipsoidal cavities typically produced at grain boundaries in NT-154 during tensile creep at 1350-1400°C. Cavities apparently nucleate within narrow glassy interfaces and then grow into adjacent Si₃N₄ grains.

Microstructural Characterization

Karren L. More (Oak Ridge National Laboratory)

Objective/scope

The objective of the research is to use analytical and high resolution electron microscopy to characterize the microstructure of a SiC whisker reinforced Si_3N_4 ceramic composite before and after creep deformation. This work represents a collaboration with North Carolina State University and GTE Laboratories.

Technical highlights

The material under investigation is a hot-pressed SiC whisker-reinforced Si_3N_4 containing 30 vol% SiC whiskers and 1.5 wt.% Al_2O_3 and 6.0 wt.% Y_2O_3 intentionally added as sintering aids. Constant compressive stress creep experiments were conducted in both a continuously purified 0.11 MPa flowing nitrogen atmosphere and in air in the temperature and stress ranges of 1470-1720 K and 50-350 MPa, respectively. Transmission electron microscopy (TEM), scanning electron microscopy (SEM), and x-ray diffraction (XRD) techniques have been used to characterize the microstructure of the composite prior to and after creep deformation. Results of the creep experiments and subsequent TEM and SEM characterization were reported in the previous report. Work in the second half of 1990 has focussed on finishing the characterization of the composite crept in nitrogen and starting the characterization of the compressive creep behavior of the composite in air as well as the creep deformation of the same material in four-point bending in air.

It has been reported that creep of this composite material occurred by two primary mechanisms. In the low stress regime, creep occurred via the viscous flow of the glassy grain boundary phase (glass was present at virtually all SiC/ Si_3N_4 and Si_3N_4 / Si_3N_4 grain boundaries) whereas in the high stress regime, creep occurred primarily by grain boundary diffusion and/or a solution/precipitation process accompanied by grain boundary sliding. In the high stress regime, little glass was present at the grain boundaries. Evidence for grain boundary sliding was observed at many Si_3N_4 / Si_3N_4 interfaces following a full creep experiment, as shown in Fig. 1. According to Lange et al.,¹ "strain whorls" observed at grain boundaries occur as a result of ledge asperities at the grain edges, as shown in Fig. 2. As the grains slide past each other in the presence of a glassy phase and as the thickness of the glass continually decreases, strain whorls will arise when opposing ledges meet and lock. This phenomenon actually inhibits grain boundary sliding. Strain whorls were not observed in the as-received composite or in samples taken following creep in the low stress regime, thus it is assumed that grain boundary sliding occurred only at higher stresses.

X-ray diffraction results have shown that the amorphous phase in the as hot-pressed composite crystallized upon annealing. During relatively short anneals at 1620 K, the phase crystallized as two structures; $\text{Y}_2\text{Si}_3\text{N}_4\text{O}_7$ and $\text{Y}_{20}\text{Si}_{12}\text{N}_4\text{O}_{48}$. After longer anneals and during creep these phases further transformed to $\gamma\text{-Y}_2\text{Si}_2\text{O}_7$, which is one of the high temperature polytypes in the $\text{Y}_2\text{Si}_2\text{O}_7$ system. According to Ito and Johnson,² $\text{Y}_2\text{Si}_2\text{O}_7$ displays polymorphic transitions as follows:

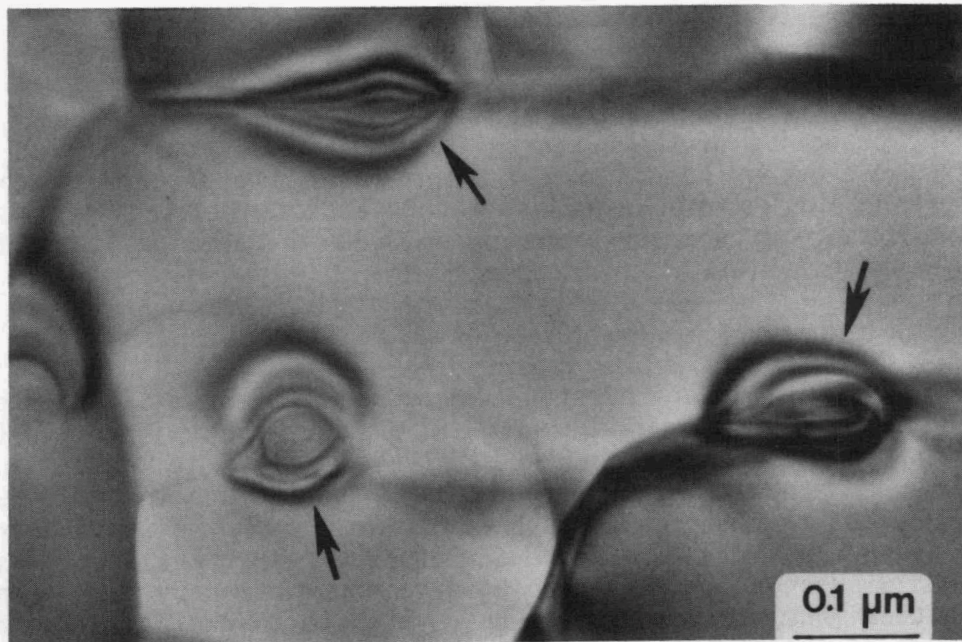


Fig. 1. Centers of localized strain (strain whorls) were observed at many $\text{Si}_3\text{N}_4/\text{Si}_3\text{N}_4$ interfaces following creep.

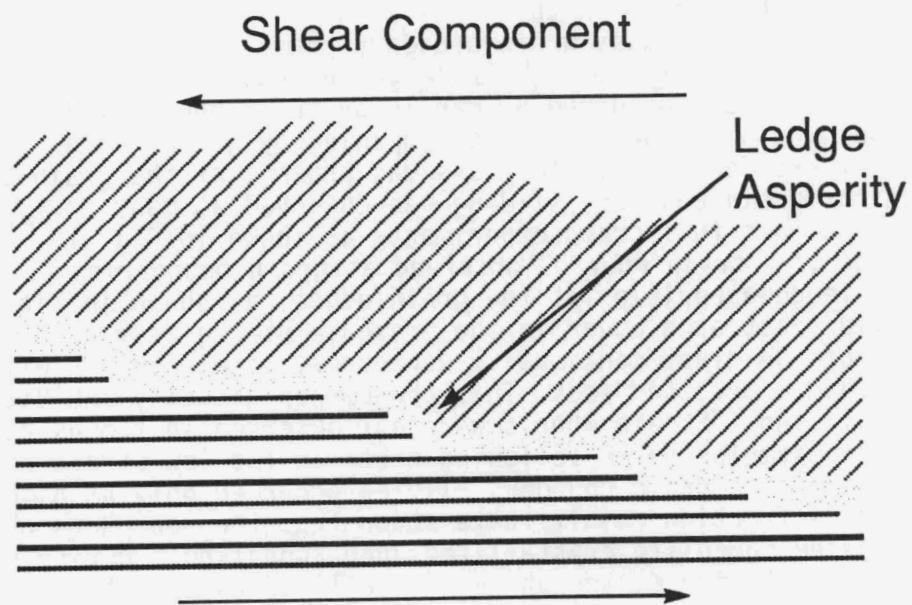


Fig. 2. Schematic showing origin of "strain whorls" which occur as a result of grain boundary sliding.

1500 K 1720 K 1810 K

α " β " γ " δ

There has also been reports of much lower temperature polytypes (γ and z phases). Thus, stable γ - $Y_2Si_2O_7$ should not form at 1620 K. There are actually two sets of x-ray diffraction data given for γ - $Y_2Si_2O_7$ in the card files. The x-ray data provided by Ito and Johnson,² Liddell and Thompson,³ and Batalieva, et al.,⁴ for monoclinic γ - $Y_2Si_2O_7$ do not match the d-spacings determined for the grain boundary phase (JC-PDF #20-1416) in the composite. However, the d-spacings found do match the data given in JC-PDF #32-1448 for γ - $Y_2Si_2O_7$. This phase was found by Nekrasov and Kashitseva⁵ and termed "metastable γ " but only the XRD data was presented. There was no information about the crystal structure given. Work is currently underway to determine the crystal structure and lattice parameters of this phase using convergent beam electron diffraction and high resolution TEM together with XRD.

Constant compressive stress creep experiments were also conducted in air. Preliminary results have shown that the general bilinear behavior observed for the composite crept in a nitrogen atmosphere was also observed for the composite crept in air. Figure 3 shows a comparison of typical

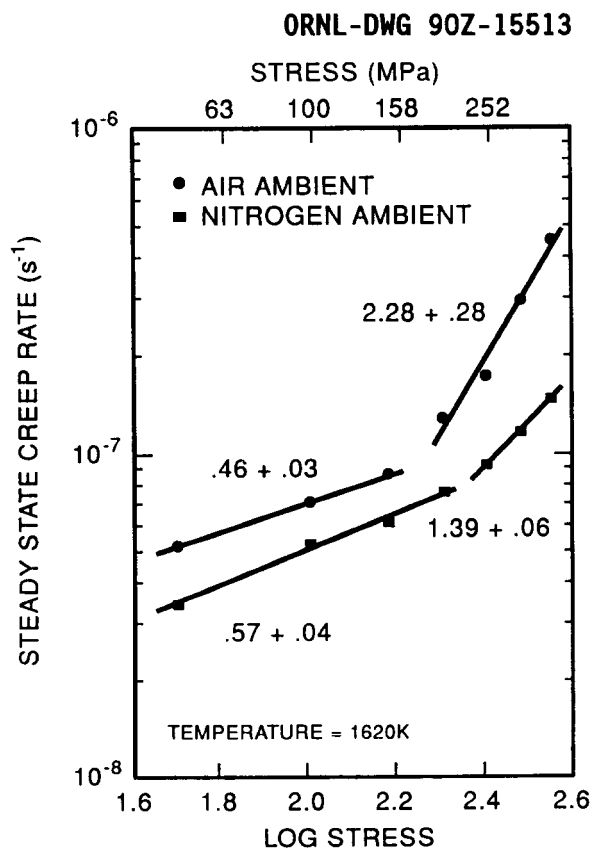


Fig. 3. Constant compressive stress creep curves comparing behavior of composite in air and nitrogen atmospheres.

creep curves for samples crept in both air and nitrogen with the corresponding stress exponents. Higher creep rates were observed for the sample crept in air and the stress exponent was significantly higher in the high stress regime for the sample crept in air, i.e. 2.28 ± 0.28 in air and 1.39 ± 0.06 in nitrogen, perhaps indicating a change in mechanism at the higher stresses. This is currently under investigation. Transmission electron microscopy samples have been prepared to investigate interface phenomenon in these specimens.

Bulk XRD have been performed on samples crept in air to determine the crystalline phases present in the composite. Only δ - $Y_2Si_2O_7$ was found in addition to Si_3N_4 and SiC following creep at 1620 K in air. The δ -polytype is the high temperature polytype (stable at $T > 1800$ K) and it is unclear why it appears to be stable under the creep conditions employed. According to the literature, the γ -polytype found in the samples crept and annealed in nitrogen is also only stable at temperatures greater than the creep temperature of 1620 K.

The major emphasis of future work will be the full characterization of the compressive creep of the composite in air and creep in four-point bending of the composite in air. Transmission electron microscopy samples have been prepared from the compressive and tensile faces of several specimens crept in air in four-point bending.

References

1. F.F. Lange, B.I. Davis, and D.R. Clarke, J. Mat. Sci. 15 (1980) 611.
2. J. Ito and H. Johnson, Amer. Miner. 53 (1968) 1940.
3. K. Liddell and D.P. Thompson, Br. Ceram. Trans. J., 85(1986) 17-22.
4. N.G. Batalieva, I.A. Bondar, G.A. Sidorenko, and N.A. Toropov, Dokl. Chem., 173(1967) 235.
5. I.Ya. Nekrasov and G.A. Kashirtseva, Dokl. Akad. Nauk, 231(1976) 166.

Status of milestones

Program on schedule

Publications

1. K.L. More, D.A. Koester, and R.F. Davis, "Microstructural Characterization of a Creep-Deformed SiC Whisker-Reinforced Si_3N_4 Composite," presented at the Frontiers of Electron Microscopy in Materials Science Meeting, May 20-24, 1990, Oak Brook, Illinois. To be published in *Ultramicroscopy*.

2. K.L. More, D.A. Koester, and R.F. Davis, "The Role of Interfaces in the Creep-Deformation of a SiC Whisker-Reinforced Si₃N₄ Composite," in *Electron Microscopy 1990*, 4, L.D. Peachey and D.B. Williams, eds., San Francisco Press, San Francisco, California (1990) 382.

Project Database

B. L. Keyes (Oak Ridge National Laboratory)

Objective/scope

The objective of this task is to develop a comprehensive computer database containing the experimental data on properties of ceramic materials generated in the total effort. This computer system should provide a convenient and efficient mechanism for the compilation and distribution of the large amounts of data involved. The database will be available in electronic form to all project participants. In addition, periodic hard copy summaries of the data, including graphical representation and tabulation of raw data, will be issued to provide convenient information sources for project participants.

Technical highlights

The database now contains 6093 test results on over 360 different batches of ceramic materials. Approximately 48% of these are on zirconia-based ceramics, 7% are on silicon carbides, 22% are on silicon nitrides, 6% are on whisker-reinforced silicon nitrides, 15% are on alumina-based ceramics (including whisker-reinforced aluminas and mullites), and 2% are on other ceramics. Table 1 gives a detailed breakdown by material class of the data stored in the system. A list of materials within a material class is available on request.

Several new files were added to the database to further enhance the usefulness of the system. Brazed specimen data files now include shear strength, MOR 4-point bend, torsion, fracture toughness and torsion fatigue tests. A special joint description file was added to better explain the details of the brazed joints tested, since the characteristics of these joints are more complex than for non-jointed specimens. Table 2 lists all the files now in the database.

A hard copy of the user's guide was completed during the previous semiannual period, but was pulled from review when it was discovered the computerized user interface would be completed before the final hardcopy user's guide was published. However, funding cuts for FY 91 have decreased the available time required to finish the computerized interface, so the user's guide will be put back into review soon.

Progress on publication of the past two semiannual database summary reports was delayed because of a major error discovered in a data table in the reviewed report and dissatisfaction with the wording in the last semiannual draft. These problems are being corrected now.

We recently began to gather information on the various types of specimens used in mechanical properties tests to help characterize our test results more completely. Many tests use the MIL-STD1942(MR) type "B" 3mm x 4mm x 50mm bar, but numerous variations on this sizing exist. All contributors are requested to provide specimen geometry information with the test data because the morphology of the specimen can influence the test results.

The ASTM E-49 Committee on Computerized Materials Databases has proven to be a very valuable source of ideas for the database. Most of the work done so far has been on metals databases, but many of the same principles apply to ceramics. Factors such as quality indicators, test parameters and

TABLE 1. CTAHE DATABASE SUMMARY AS OF SEPTEMBER 30, 1990

Material Class	Braze Specimens					Creep	Cyclic Fatigue	Density	Dynamic Fatigue	Elasticity
	MOR 4	Shear Str.	Toughness	Torsion	Tor. Fatigue					
Alumina							15		9	28
Alumina + reinforcing fibers								7		
Alumina + Zirconia										
Mullite										2
Mullite + reinforcing fibers										11
Silicon Carbide		12						10	13	15
Silicon Nitride	69	48		15	7	37	19	28	16	24
Silicon Nitride + reinforcing fibers							15	2		16
Zirconia	160	58	2				51	158		119
Zirconia + reinforcing fibers										
Other										
Totals	229	118	2	15	7	37	100	205	38	215

Material Class	Fracture Toughness	Hardness	Interrupted Fatigue	MOR		Oxidation Rate	Poisson's Ratio	Shear Modulus	Tensile	Thermal Conductivity
				3 Pt Bend	4 Pt Bend					
Alumina	39	4			411				28	3
Alumina + reinforcing fibers	39				144				11	34
Alumina + Zirconia					7					
Mullite				1	4					
Mullite + reinforcing fibers	16			9	22					
Silicon Carbide	24	27			235					
Silicon Nitride	94	112		10	647	1	2	1	73	9
Silicon Nitride + reinforcing fibers	53				144	3	17	16	86	9
Zirconia	347	24	239		1554				50	
Zirconia + reinforcing fibers					2				36	
Other	3	25			59					
Totals	615	192	239	20	3229	4	19	17	284	55

(CONTINUED)

TABLE 1. CTAHE DATABASE SUMMARY AS OF SEPTEMBER 30, 1990

Material Class	Thermal Contraction	Thermal Diffusivity	Thermal Expansion	Thermal Shock	Torsion	X-Ray Diffraction	Wear Resist.	Material Char.	Chemistry
Alumina			1	2				13	14
Alumina + reinforcing fibers		18	4	6				94	
Alumina + Zirconia	23		21					8	
Mullite								2	
Mullite + reinforcing fibers								24	
Silicon Carbide			23			17		9	57
Silicon Nitride		10	44		3	49	2	50	6
Silicon Nitride + reinforcing fibers		17	14					52	
Zirconia						72		37	44
Zirconia + reinforcing fibers								5	
Other					4			18	2
Totals	23	45	107	8	7	138	2	312	123
Grand Total (test data only)	5970								

TABLE 2. CTAHE DATABASE FILE LISTING FOR SEPTEMBER 28, 1990

Material Characteristics/Background Information Files	
MATLCHAR	General information on a single batch of a material, including intrinsic values where available
CERSOURC	Bibliography for database
CHEMSTUF	Chemical analyses for individual batches of materials
JOINTEXT	Brazed joint descriptions
PHASES	Phase content quantities of batches of materials
POWDERS	Information on powders used to make ceramics
TEXTUF	General text information on batches of materials, including processing details
WHISKERS	Details on reinforcement whiskers
Test Data Files	
CERPRPTY	Miscellaneous properties not covered in other files. Includes oxidation rate, thermal contraction, thermal conductivity, thermal diffraction, specific heat, shear modulus, and poisson's ratio.
CREEP	Creep test results
CYCFAT	Cyclic fatigue test results
DATATXT	Expanded comments file for individual test results, when needed
DENSITY	Densities of various batch of materials in various conditions
DYNFAT	Dynamic fatigue test results
FRACTUFF	Fracture toughness test results
HARDNESS	Hardness test results
INTFATIG	Interrupted fatigue results
MCE	Modulus of elasticity test results
MOR3PTB	Modulus of rupture, 3-point bend test results
MOR4PTB	Modulus of rupture, 4-point bend test results
STRSRUPT	Stress rupture test results
TENSILE	Tensile test results
TESTBKGD	Information on specimen description and testing methods used
THERMEXP	Thermal expansion test results
TORSION	Torsion test results
TSHOCK	Thermal shock test results
WEARESES	Wear resistance test results
XRAYDIFF	X-ray diffraction results
Brazed Specimen Test Data Files	
BRAZMOR4	Modulus of rupture 4-point bend test results
BRAZSHER	Shear strength test results
BRAZTORQ	Torsion test results
BRAZTUFF	Fracture toughness test results
BRZTORFT	Torsion fatigue test results

traceability are similar for both types of materials, but ceramics require a much more intensive basic material background characterization. We hope to gain more knowledge in this area through exchange of ideas with other materials database people in the future.

Work during this semiannual period included answering requests for information about the database in response to an article that appeared in the January-March 1990 issue of the *Ceramic Technology Newsletter*. So far, full sets of database disks have been sent to ten individuals.

After working with a small user community for several months now, a need has arisen to facilitate specific material searches in the database. One problem with ceramics is that a material may go by several different names (a company-assigned name and a generic name, for example). No standardization in the industry appears to exist. Since information in the database is stored using the material name as a guide, the potential problems are immediately obvious. Another aspect to this problem involves accessing a material by creation process or heat treatment. All processing history data are stored in a text file (sentence-type structure) and accessing such information requires more specialized techniques that are readily available in dBASE IV. Development of a thesaurus-like structure will take place during development of the computerized user interface.

Status of milestones

The sixth semiannual database summary has been completed through the first draft and will go into review soon. Status of future milestones is contingent on the funding level for next year, but plans have been made to start on the computerized user interface as originally scheduled.

Publications

The Ceramic Technology for Advanced Heat Engines Project Database: September 1990 Summary Report is ready for review .

The Ceramic Technology for Advanced Heat Engines Project Database: March 1990 Summary Report and *The CTAHE Database User's Guide* are back in review.

The Ceramic Technology for Advanced Heat Engines Project Database: September 1989 Summary Report is in publication .

The Ceramic Technology for Advanced Heat Engines Project Database: March 1989 Summary Report, ORNL/M-1098, has been published.

3.2 TIME-DEPENDENT BEHAVIOR

Characterization of Transformation-Toughened Ceramics

Jeffrey J. Swab (U.S. Army Materials Technology Laboratory)

Objective/scope

To evaluate and characterize toughened ceramic matrix composite (CMC) materials for potential high temperature structural applications. At the present time four-point flexure testing is being used to determine the high temperature performance of these CMCs. However, a related in-house program to develop a tensile test for CMC materials is underway. Once this test has been developed and refined both techniques will be used to provide a more comprehensive characterization of CMC materials at elevated temperatures.

Technical highlights

None - FY90 funds were not received during the period 1 April - 30 September 1990.

Status of milestones

All milestones will be delayed due to the lack of funds.

Publications

None.

Fracture Behavior of Toughened Ceramics

H. T. Lin, P. F. Becher and W. H. Warwick (Oak Ridge National Laboratory)

Objective/scope

Ceramic composites, such as fiber and whisker-reinforced ceramics, particulate phase composites, and ceramics with elongated grain structures, offer important advantages for heat engine applications. Chief among these is the improved fracture toughness which can be achieved by appropriate design of microstructural and material parameters. Previous studies show that these materials often exhibit substantial improvements in damage, thermal shock and slow crack growth resistances. However, design of such systems must also consider those factors influencing their performance at elevated temperatures.

In response to these needs, studies are conducted to determine the mechanical properties, e.g., creep, delayed failure, strength, and toughness at elevated temperatures for these toughened ceramics. Particular emphasis is placed on understanding how microstructure and composition influence the mechanical performance at elevated temperatures and the stability of these properties for extended periods at these temperatures. The knowledge gained from these studies provide input on how to modify materials to optimize their mechanical properties for the temperature ranges of interest.

Technical highlights

Over the past six months, the research efforts were primarily directed to (1) the understanding of the creep controlling mechanisms of alumina composites reinforced with 30 and 50 vol % SiC whiskers, and (2) the study of the creep behavior of silicon nitride ceramics containing elongated grain structures obtained from Allied Signal. The objective of the creep study of a self-reinforced silicon nitride ceramic is to understand how the elongated grain structures affect the time-dependent deformation processes of silicon nitride ceramics at elevated temperatures.

SiC Whisker-reinforced alumina composites

The creep data shown in the previous report¹ indicated that the creep resistance of alumina composites reinforced with SiC whiskers in air is reduced by one to two orders in magnitude as the whisker content ≥ 30 vol %. These whisker-reinforced alumina composites have been subjected to flexure stresses from 37 to 300 MPa at temperatures of 1200 and 1300°C in air. It was suggested that the enhanced creep of the composites with higher whisker contents (30 and 50 vol %) arose from the more extensive creep cavitation and oxidation. Scanning and transmission electron microscopy (SEM and TEM) studies and an oxidation experiment were, therefore, conducted to confirm the above stated hypothesis.

Figure 1 shows a TEM micrograph of the tensile surface regions for the alumina composites reinforced with 30 vol % whiskers tested at 1300°C. In general, the higher whisker content composites (30 and 50 vol %) exhibit a cavity number density which was twice that of alumina composites reinforced with 20 vol % whiskers. This is due to the fact that the SiC whiskers act

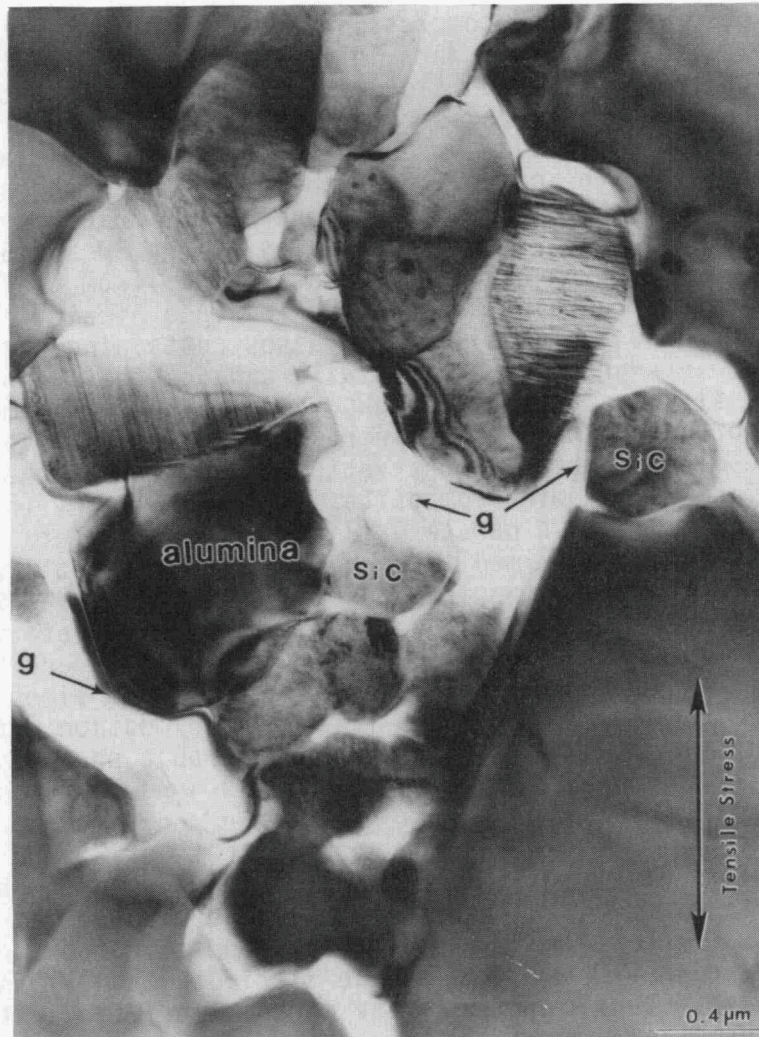


Fig. 1. TEM micrograph of tensile surface regions of 30 vol % SiC-alumina composite tested at 1300°C. Note extensive cavitation occurs at grain boundaries and whisker-matrix interfaces. Alumina grains and whiskers are surrounded by glassy phases.

as additional sites for cavity nucleation. The creep cavities were also occasionally observed in the compressive surface region, but the number density was about one to two orders in magnitude less than those in the tensile surface region. In addition, the alumina grains and SiC whiskers were often found to be surrounded by amorphous phases which were not observed in the as fabricated composites. The amount of glass formed during creep tests of the composites with ≤ 20 vol % whiskers was negligible. In addition, the glassy phases were rarely observed penetrating beneath the compressive surface oxide scales of the 30 and 50 vol % alumina composites. The formation of glassy phases arises from the oxidation of SiC whiskers on the crack surfaces in the presence of air. These glasses were identified to be aluminosilicate glasses containing calcia as well. The presence of intergranular glasses will enhance the creep deformation by grain boundary sliding leading to higher creep rates. The more extensive cavitation also contributes to the increased creep strains and rates.

The above microstructural observations suggest that the creep behavior of whisker-reinforced alumina composites is influenced by the oxidation reaction. Accordingly, a separate oxidation experiment at 1300°C for up to 100 h in air was then performed to correlate the creep data with the oxidation rates for alumina composites containing 20 to 50 vol % SiC whiskers. Optical microscopy and SEM techniques were employed to determine the thickness of oxide scales formed. On the surface of 30 and 50 vol % alumina composites, the oxide scale was at least three times that of the 20 vol % alumina composites after 100 h (Fig. 2). Oxidation data for the higher whisker content composites yielded comparable parabolic reaction rate constant at 1300°C (3×10^{-8} m/ \sqrt{s}) and both were approximately three times that of 20 vol % composites (1×10^{-8} m/ \sqrt{s}). The results support the hypothesis that the higher oxidation reaction rate of 30 and 50 vol % alumina composites is one of the key factors leading to the higher creep rates and stress exponents. Therefore, it is concluded that the higher creep rate, plus higher stress exponent, of alumina composites reinforced with 30 and 50 vol % SiC whiskers can be attributed to (1) the greater creep cavity number density and (2) the more extensive oxidation rates and glassy phase formation.

Self-reinforced silicon nitride

Recent studies show that the fracture resistance of monolithic silicon nitride ceramics can be substantially improved via a microstructural engineering approach. It is achieved by the *in-situ* growth of the elongated grain structures (whisker-like grains).²⁻⁴ The toughening mechanism for Si₃N₄ ceramics with whisker-like grains is attributed to crack bridging, crack deflection, and pullout processes. The reinforcement via the use of SiC whiskers has been shown to significantly increase the creep resistance of polycrystalline alumina.^{5,6} At present, a full understanding of the effect of the elongated grain structure on the creep behavior of Si₃N₄ ceramic systems is not yet available. During this reporting period, the research efforts were to evaluate the creep properties and to elucidate the role that the whisker-like grains play during creep of Si₃N₄ ceramics.

The creep tests in four-point flexure loading with inner and outer spans of 12.7 and 25.4 mm, respectively, were conducted in air at temperatures at 1200 and 1300°C at stress levels ranging from 100 to 360 MPa. The

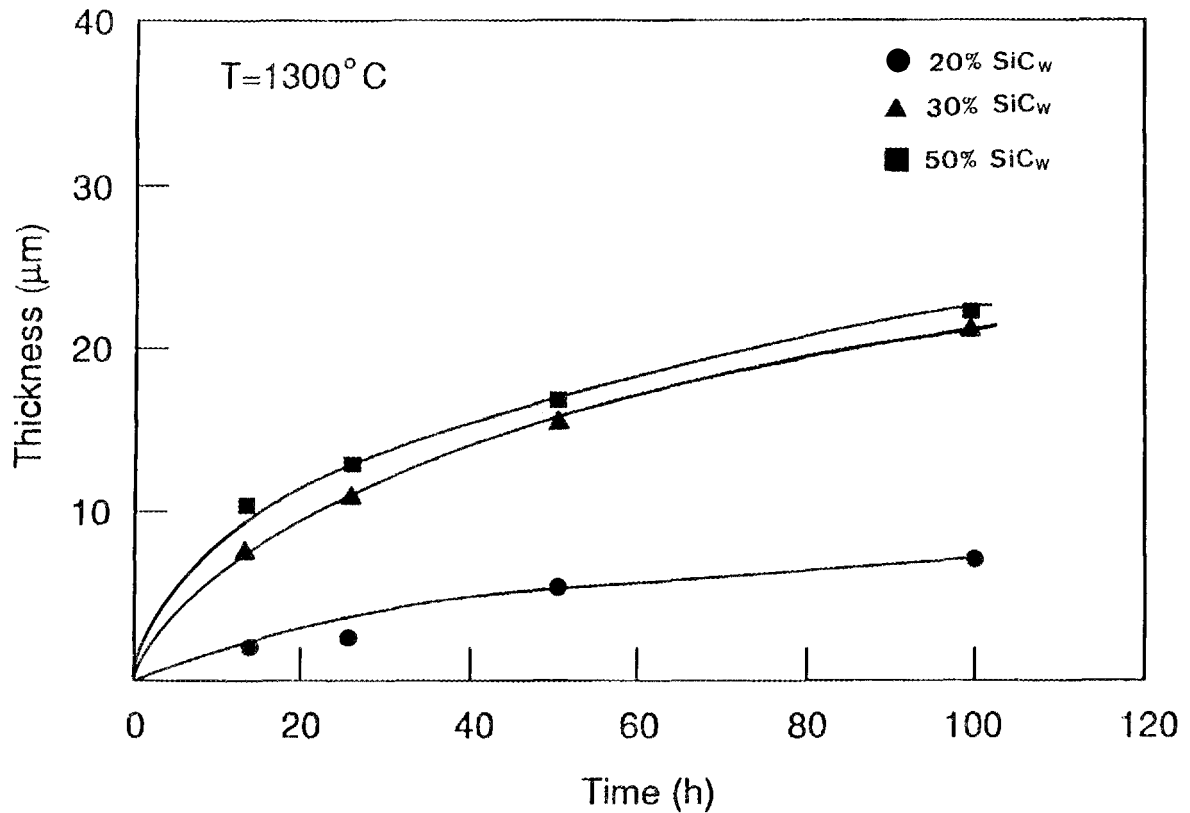


Fig. 2. Oxidation data at 1300°C in air for 20, 30, and 50 vol % whisker-reinforced alumina composites.

gas pressure sintered Si_3N_4 ceramics with elongated grain structure were supplied by Allied Signal (designated as SN0112) which exhibit an extensive R-curve behavior and the values of fracture toughness $\geq 10 \text{ MPa m}^{1/2}$.⁴ The SN0112 has an amorphous phase present at grain boundaries. The creep data for Si_3N_4 ceramics is shown in Fig. 3. The data at 1200°C for SN 251 (Kyocera Corp.)⁷ and AY6 #3 (GTE),⁸ which exhibit similar elongated grain structures and exhibit extensive grain boundary phase also as that of SN0112, are also included for creep property comparison.

The results indicate that the SN0112 has higher creep resistance at 1200 and 1300°C in air. Indeed, the SN0112 exhibits a creep rate that is somewhat lower than the SN 251 and AY6 #3. The difference in creep resistance may be due to the difference in chemical composition, microstructure and degree of crystallization of the intergranular amorphous phases that have been shown to have substantial influence on the creep behavior of sintering adds containing Si_3N_4 ceramics.⁹ In addition, the aspect ratio, volume percent, and diameter of the elongated grains of these materials may be different. The steady state creep rate vs stress curves show that SN0112 exhibits stress exponent of approximately one under the test conditions employed in the present study. For ceramic materials stress exponent of one is generally attributed to viscous or diffusional creep. A detailed

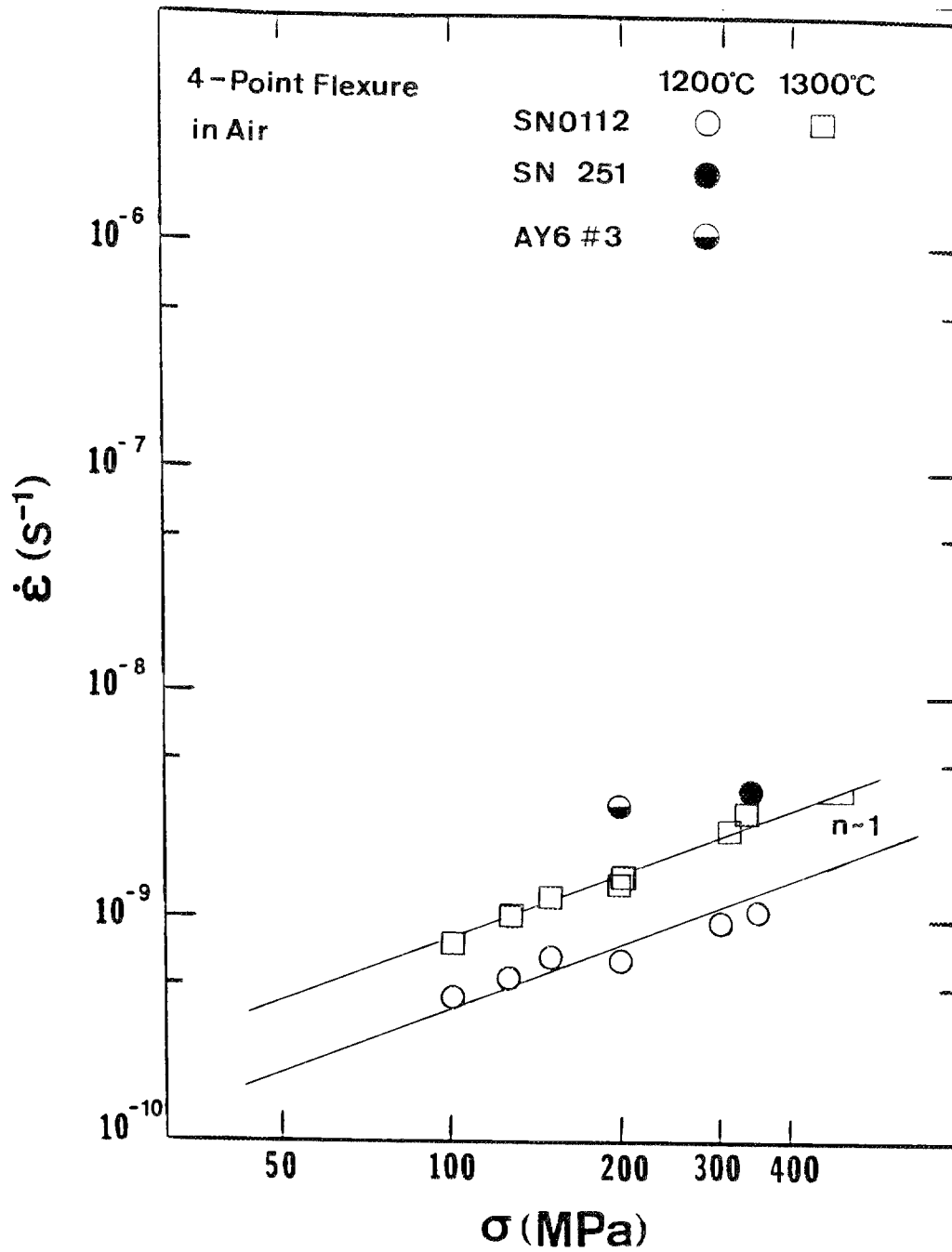


Fig. 3. Steady creep rate vs applied stress curves for a silicon nitride ceramic containing elongated grain structures at temperatures of 1200 and 1300°C.

electron microscopy study will be carried out to understand the creep controlling mechanisms of Si_3N_4 containing whisker-like grains. In addition, the creep tests are currently conducted up to 1400°C to investigate the temperature dependence of the creep response for SN0112. As a consequence, the activation energy for the creep controlling mechanism can then be determined.

Status of milestones

On schedule. Milestone 321308: Creep studies of alumina as a function of SiC whisker content and sintering aids were completed.

Publications

H. T. Lin and P. F. Becher, "Creep Behavior of a SiC-Whisker-Reinforced Alumina," *J. Am. Ceram. Soc.* 73(5), 1378-81 (1990).

A paper entitled "High-Temperature Creep Deformation of Alumina-SiC Whisker Composites" was submitted to *J. Am. Ceram. Soc.*

References

1. H. T. Lin, P. F. Becher, and W. H. Warwick, "Fracture Behavior of Toughened Ceramics," in *Ceramics Technology for Advanced Heat Engines Project Bimonthly Technical Progress Report*, October-November 1989.
2. G. Himsolt, H. Knoch, H. Huebner, and F. W. Kleinlein, "Mechanical Properties of Hot-Pressed Silicon Nitride with Different Grain Structures," *J. Am. Ceram. Soc.* 62(1), 29-32 (1979).
3. M. H. Lewis, "Microstructural Engineering of Ceramics for High-Temperature Application," pp. 713-30 in *Fracture Mechanics of Ceramics*, eds. R. C. Bradt, A. G. Evans, D. P. H. Hasselman, and F. F. Lange, Plenum Press, New York, 1986.
4. C. W. Li and J. Yamanis, "Super-Tough Silicon Nitride with R-Curve Behavior," *Ceram. Eng. Sci. Proc.* 10(7-8), 632-45 (1989).
5. A. H. Chokshi and J. R. Porter, "Creep Deformation of an Alumina Matrix Composite Reinforced with Silicon Carbide Whiskers," *J. Am. Ceram. Soc.* 68(6), C-144-45 (1985).
6. H. T. Lin and P. F. Becher, "Creep Behavior of a SiC-Whisker-Reinforced Alumina," *J. Am. Ceram. Soc.* 73(5), 1378-81 (1990).
7. "Silicon Nitride as Structural Materials," General Research Laboratory, Kyocera America, Inc., Des Plaines, Ill., July 19, 1989.

8. S. T. Buljan, M. L. Huckabee, J. G. Baldoni, and J. T. Neil, "Ceramic Matrix Composites," pp. 115-22 in *Ceramic Technology for Advanced Heat Engines Project Bimonthly Technical Progress Report*, August-September 1989.

9. F. F. Lang, B. I. Davis and D. R. Clarke, "Compressive Creep of $\text{Si}_3\text{N}_4/\text{MgO}$: Part 1, Effect of Composition," *J. Mater. Sci.* 15, 601-10 (1980).

Cyclic Fatigue of Toughened Ceramics

K. C. Liu, J. L. Ding, H. Pih, C. O. Stevens, and C. R. Brinkman
(Oak Ridge National Laboratory)

Objective/scope

The objective of this task is to develop, design, fabricate, and demonstrate the capability to perform tension-tension dynamic fatigue testing on a uniaxially loaded ceramic specimen at elevated temperatures. Three areas of research have been identified as the main thrust of this task: (1) design, fabrication, and demonstration of a load train column which truly aligns with the line of specimen loading; (2) development of a simple specimen grip that can effectively link the load train and test specimen without complicating the specimen geometry and, hence, minimize the cost of the test specimen; and (3) design and analysis of a specimen for tensile cyclic fatigue testing.

Technical progress

Cyclic fatigue behavior of SiC (Hexoloy-SA)

This is a new effort initiated during this reporting period. Tensile and cyclic fatigue tests were performed on SiC at 1300 and 1400°C. The tensile tests were run at a slow stressing rate of 21 MPa/min and the fatigue tests were run in a tension-tension mode at a stressing rate of 21,000 MPa/min. Test parameters and results are given in Table 1. Data are summarized in Figs. 1 and 2. Closed symbols indicate the end of the tests and that fractures occurred within the gage section. Open symbols indicate premature failures, where fractures occurred either in the specimen shank or buttonhead. The arrows attached to the open symbols signify that the strength and lifetime would have been higher if the specimens had not failed outside the gage section. As indicated in Table 1, four specimens failed at the shank and buttonhead simultaneously. It appeared that the buttonheads were broken by the shock waves originated from the shank failures. In all cases, the buttonhead fracture occurred in a fracture plane. In contrast, three specimens failed at the root radius of the buttonhead with multiple fractures in pieces as thin flakes. Since the specimens were made from long plates (75 x 175 mm), the strength of the material may vary inherently due to the manufacturing processes. The buttonhead problem was reported earlier in SiC testing at the University of Dayton Research Institute (UDRI)¹.

Careful examinations of the fracture morphology indicate that this material is apparently sensitive to residual surface flaws resulting from machining. After four unsuccessful tests, five specimens were annealed at 1400°C for 100 h. Subsequently, testing on the annealed specimens showed significant improvement with only one buttonhead failure in specimen 3-2.

Figure 1 shows that coaxing has significantly enhanced the fatigue life of specimen 1-2. Enhanced tensile strength was also reported by UDRI² in several interrupted stress-rupture tests at 1400°C for the same material subjected to a variety of stresses in a range between 169 to 200 MPa for 100 h. It was speculated that the improved tensile strength was due to the synergistic effects of stress and temperature exposure. Surface flaw

Table 1. Summary of tensile and cyclic fatigue tests of Hexoloy-SA SiC tested at elevated temperatures.

Specimen	Tensile strength (MPa)	Cyclic stress to failure (MPa)	Intermediate cyclic stress (MPa)	Number of cycles at intermediate cyclic loading	Number of cycles to failure	Locations of fractures
<i>Temperature = 1300°C</i>						
1-9	220				1	
1-3		199			2	
1-1		204			165	
1-4			189	239,361	(239,361) ^a	BH & SHNK ^b
1-2			187	231,000	(231,000)	
			200	193,800	(424,800)	
			208	394,000	(818,800)	
			222	352,513	(1,171,313)	
		235			1,171,415	
<i>Temperature = 1400°C</i>						
2-2	243				1	
4-1			169	1	(1)	BH
4-2			172	1	(1)	BH
2-4		194			167	
3-4			206	433	(433)	BH & SHNK
2-1			193	185,299	(185,299)	BH & SHNK
3-1			188	1,032,500	(1,032,500)	SHNK
			202		(1,032,618)	

^aNumber of cycles accumulated at the end of intermediate loading.

^bBH = Buttonhead failure; SHNK = Shank failure.

ORNL-DWG 90-13986

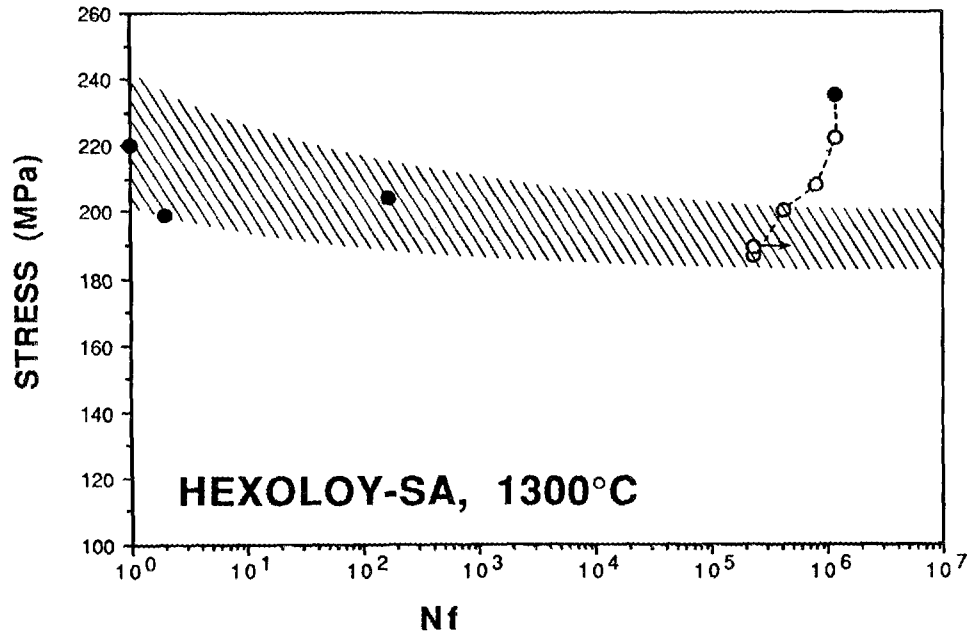


Fig. 1. Cyclic fatigue behavior of Hexoloy-SA silicon carbide tested at 1300°C. Coaxing or step loading from low to higher stresses can enhance the fatigue resistance of the material.

ORNL-DWG 90-13987

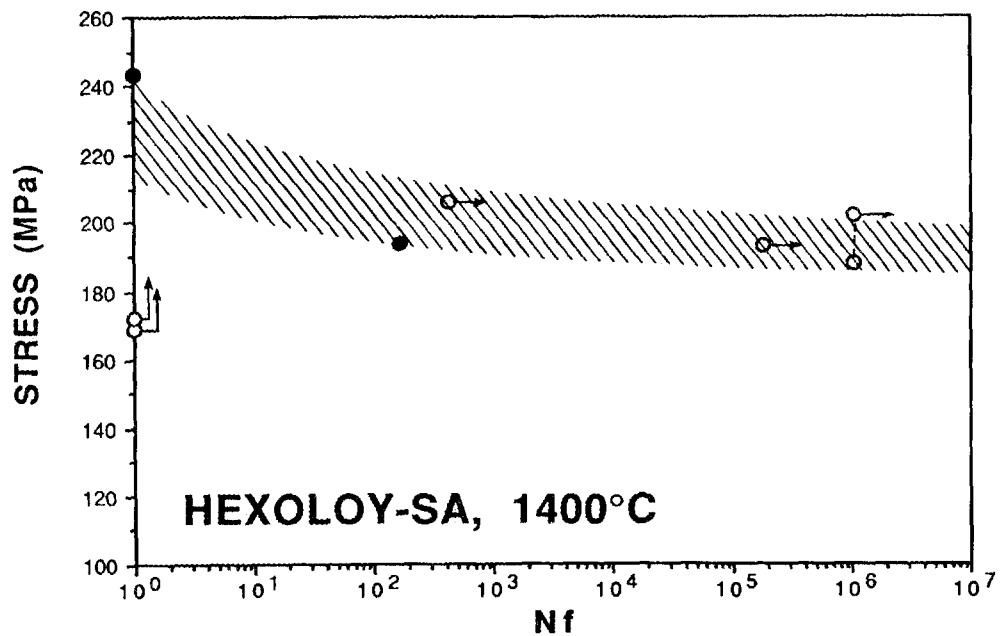


Fig. 2. Cyclic fatigue behavior of Hexoloy-SA silicon carbide tested at 1400°C.

healing was considered as another possibility, since a high percentage of untreated specimens appeared to have failed from surface initiation sites.

Fatigue behavior of this material at 1400°C appears to be about the same compared to that at 1300°C. The UDRI data² suggest that coxing at 1400°C may enhance the fatigue life by about the same amount as that observed in the 1300°C test. The fatigue curves portrayed in Figs. 1 and 2 are rough approximations which were determined based on the limited information. Therefore, the fatigue curves will be revised as more data are generated.

Cyclic fatigue behavior of thermally aged NT-154 Si₃N₄

To investigate the effect of thermal aging on cyclic fatigue behavior, two virgin specimens were randomly selected from lot No. 20 and aged at 1370°C for 150 h. One of the aged specimens (No. 20-14) was then cycled to a peak stress of 234 MPa at 1370°C until fracture occurred at 306,086 cycles, as reported previously. The second specimen (No. 20-11) was tested initially under the same loading and temperature conditions. After cycling for 523,000 cycles with no apparent indication of imminent fatigue failure, the cyclic peak stress was increased to 248 MPa because the specimen outperformed specimen 20-14 by a factor of nearly two. Subsequently, fatigue failure occurred with a total number of cycles to failure in excess of 1,000,000 cycles. Comparisons of test data show that both specimens outperformed precoaxed specimen CP-24 (from lot-CP) by a substantial amount in terms of fatigue strength as well as fatigue lifetime.

To ensure that the test data obtained for specimen CP-24 were not biased by lot-to-lot variations, a virgin specimen 20-19 was randomly selected from lot No. 20 and used to repeat the CP-24 test. By coincidence, test results obtained for both specimens were nearly identical, indicating that lot variations in terms of fatigue resistance within the two lots may be minimal. In summary, we tentatively concluded that fatigue performance of NT-154 can be enhanced merely by appropriate thermal aging, which appears to be as effective as or superior to that of precoxing.

Creep testing of NT-154 Si₃N₄

A total of nine specimens were randomly selected from lot-20 and tested in creep at three temperatures: one at 1200°C, three at 1300°C, and five at 1370°C. Two tests were interrupted by a power outage which resulted in specimen failure at the gripping end. Two tests are currently in progress and test results obtained to date are reported.

Creep behavior at 1200°C

Specimen 20-29 was tested at 1200°C under an applied stress of 150 MPa for 280 h until the specimen was fractured at the specimen shank due to a weather-related power outage. Test data are shown in Fig. 3. To facilitate determination of the first stage creep behavior, data for the first 100 h of testing are enlarged and shown in Fig. 4. It appears that the transient creep might have peaked at 20 h, followed by a mild strain recovery until the second stage creep commenced at 50 h. The creep curve

ORNL-DWG 90-13988

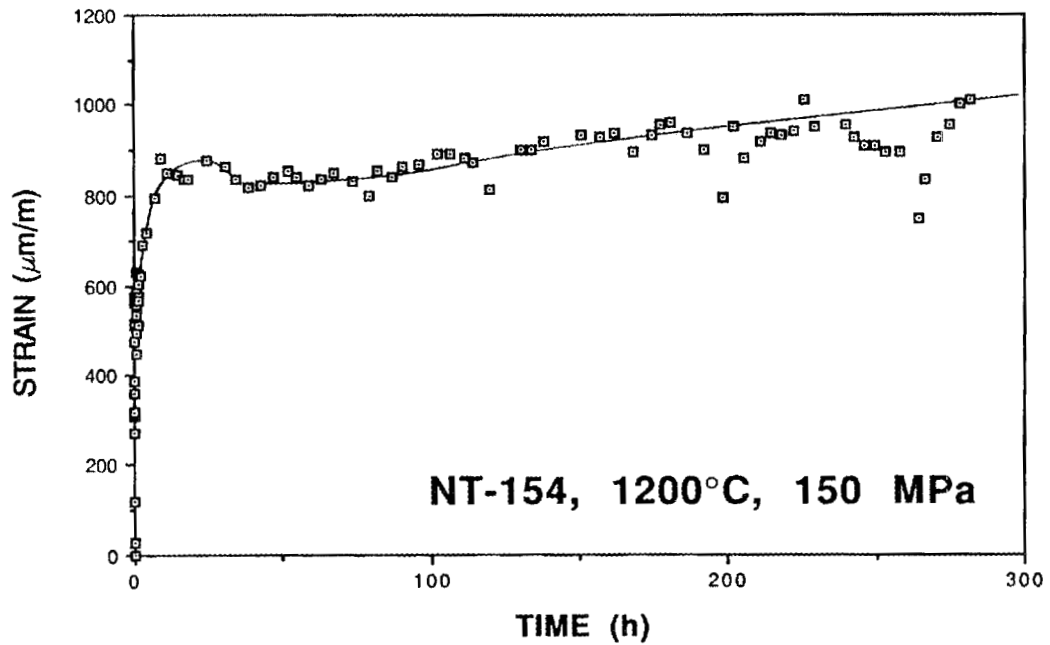


Fig. 3. Creep curve of NT-154 specimen 20-29 tested at 1200°C under an applied stress of 150 MPa.

ORNL-DWG 90-13989

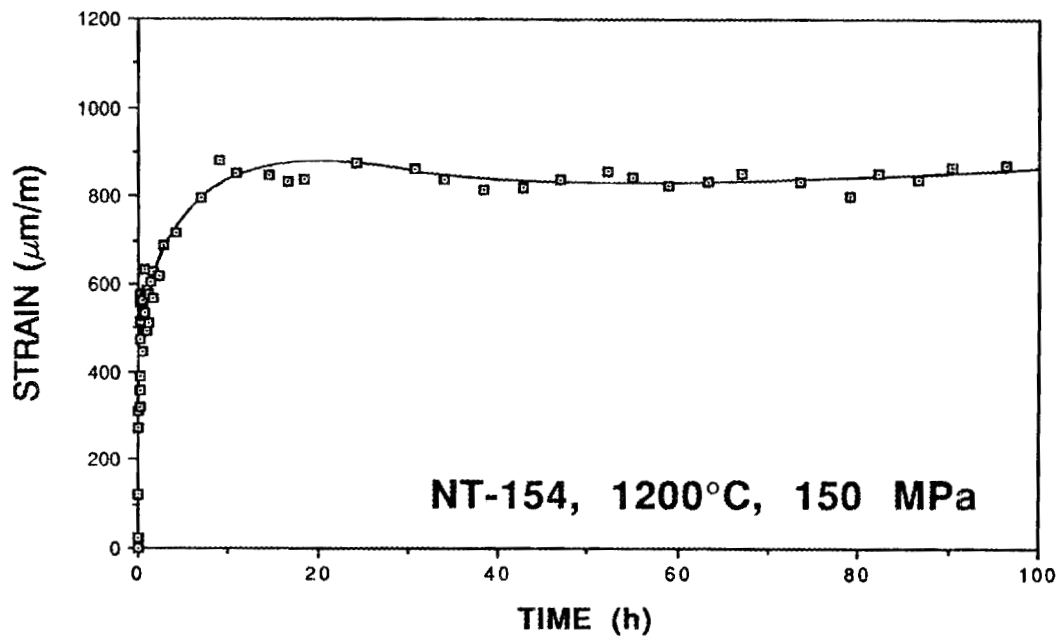


Fig. 4. Transient creep behavior of specimen 20-29 during the first 100 h of testing.

beyond 60 h, as shown in Fig. 3, was determined approximately due to data scatter. The steady-state creep rate was determined to be $2.0 \times 10^{-10} \text{ s}^{-1}$.

Creep behavior at 1300°C

Figure 5 shows the test results of a virgin specimen (20-06) subjected to an applied stress of 120 MPa. The characteristic features of the creep curve are similar to those exhibited in the creep curves obtained previously for CP-lot specimens also tested at 1300°C. The inflection discernable in the creep curve at the transition between the primary and secondary creep regions appears to be a common feature of creep behavior at this temperature. There was no indication of tertiary creep occurring at the end of the test. The slight decrease in strain rate at the end portion of the creep curve was probably due to the slippage of the fiducial marking targets used in conjunction with the laser based extensometry.

Creep behavior of silicon nitride is known to be influenced by the crystalline structure of the grain boundary material. Information gained from previous cyclic fatigue studies suggests that silicon nitride can be devitrified by thermal aging in the high temperature range to promote crystallization of the grain boundary phase or by low-stress cyclic loading in addition to the thermal aging. To investigate the effects of precycling on the creep behavior, two virgin specimens were thermally aged at 1370°C for 150 h in air. Additionally, two more specimens (20-09 and 20-13) were precycled from 158 to 222 MPa in four intermittent steps with a total accumulation of about 500,000 cycles in a period of 150 h.

After precycling, specimen 20-13 was reheated to 1300°C and loaded to a stress of 120 MPa as was done with specimen 20-06. Strain deformation was measured during the first two hours but lost thereafter due to poor bonding of the fiducial marks used in the strain measurement. Therefore, the creep deformation was subsequently measured outside the furnace using a mechanical dial gage. The test was completed in 2415 h of testing. To facilitate comparison, test results are also plotted in Fig. 5. It should be noted that the creep curve of specimen 20-13 was determined outside the gage section. Therefore, the accuracy of the creep curve is less reliable compared to those determined by the optical strain extensometer. However, the relative accuracy is reliable and the behavioral features exhibited by the creep curve are believed to be true. A comparison of the two creep curves shows that the virgin specimen showed more creep deformation compared to the precycled one during the primary creep period. The low primary creep strain and mild strain recovery occurring in specimen 20-13 during the first 200 h of testing were probably due to the devitrification resulting from the precycling. Upon the completion of the first stage creep, both specimens deformed at about the same strain rate. Specimen 20-06 completed the first stage of creep deformation with a total strain of about 0.6% in about 500 h, whereas specimen 20-13 did it in about 250 h with no significant accumulation of creep strain because it was canceled by strain recovery. The initial transient creep curves for specimens 20-06 and 20-13 are expanded and compared in Fig. 6. The reason for an apparent decrease in creep strain immediately following the initial loading of specimen 20-13 was not determined as it could be due to creep strain recovery or data scatters since the fiducial marks on the specimen slipped after 2 h of testing.

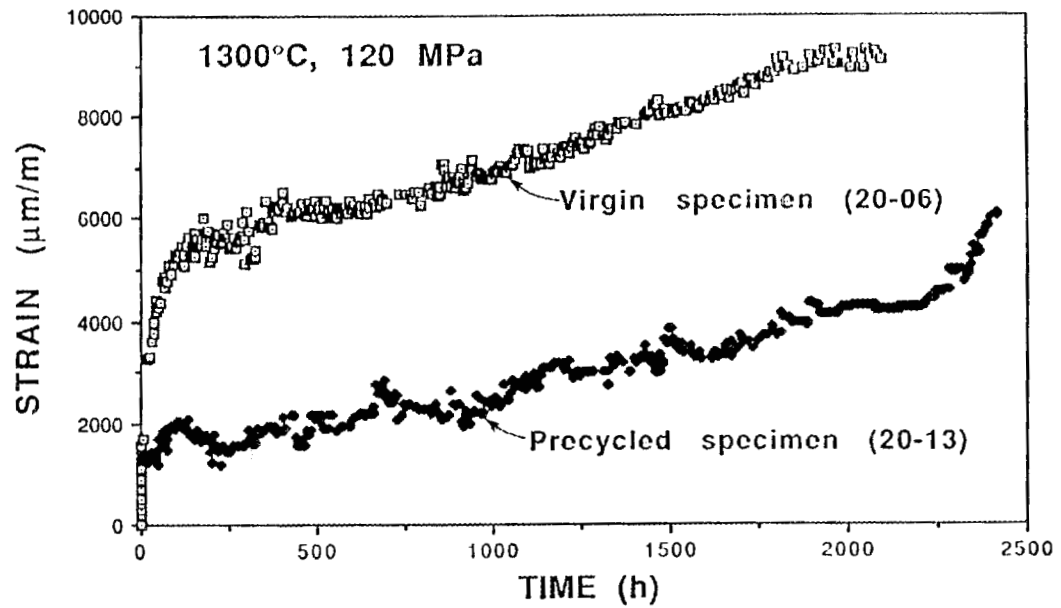


Fig. 5. Comparison of the creep curve of virgin specimen 20-06 and that of precycled specimen 20-13 tested at 1300°C under an applied stress of 120 MPa.

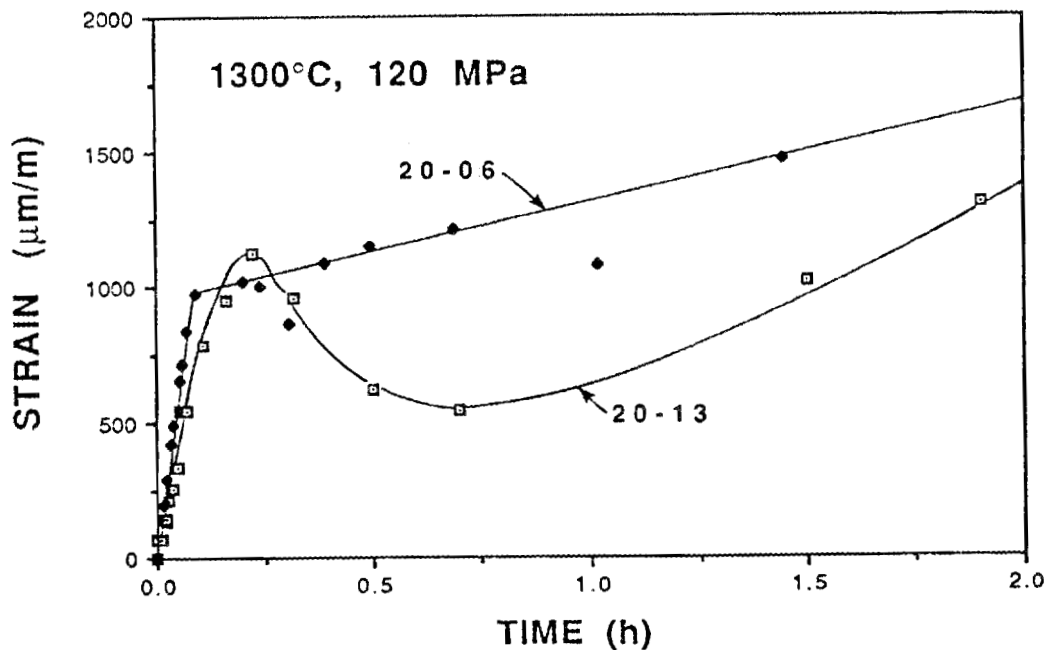


Fig. 6. Comparison of initial creep behavior of virgin specimen 20-06 and that of precycled specimen 20-13.

A creep test is currently in progress on specimen 20-34 under an applied stress of 150 MPa. Test results obtained to date are shown and compared with those of specimen 20-06 in Fig. 7. Specimen 20-34 shows a greater resistance to deformation compared to specimen 20-06 under creep loading. Since both were virgin specimens, the difference in creep behavior may be attributable to the residual crystallinity in the grain boundary material after HIPing.

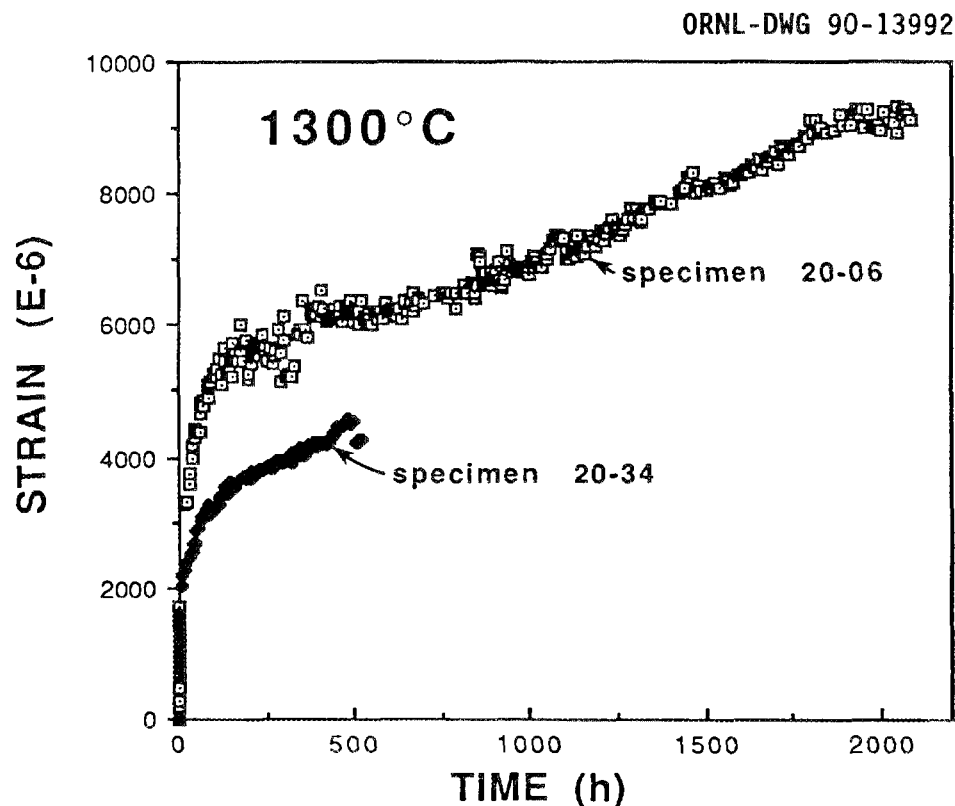


Fig. 7. Tensile creep curves of NT-154 Si_3N_4 tested at 1300°C . Specimen 20-06 was tested at 120 MPa and specimen 20-34 at 150 MPa.

Creep behavior at 1370°C

Creep tests were performed on three specimens having different pre-loading backgrounds. A virgin specimen (20-07) without post-machining heat treatment was used as a control specimen subjected to an applied stress of 100 MPa. The creep curve of specimen 20-07 is shown in Fig. 8 for comparison with those obtained from previous tests on another lot of NT-154 Si_3N_4 . The specimen ruptured after 1300 h of testing with a total strain accumulation of 1.12%. In contrast to a combination of short first stage creep

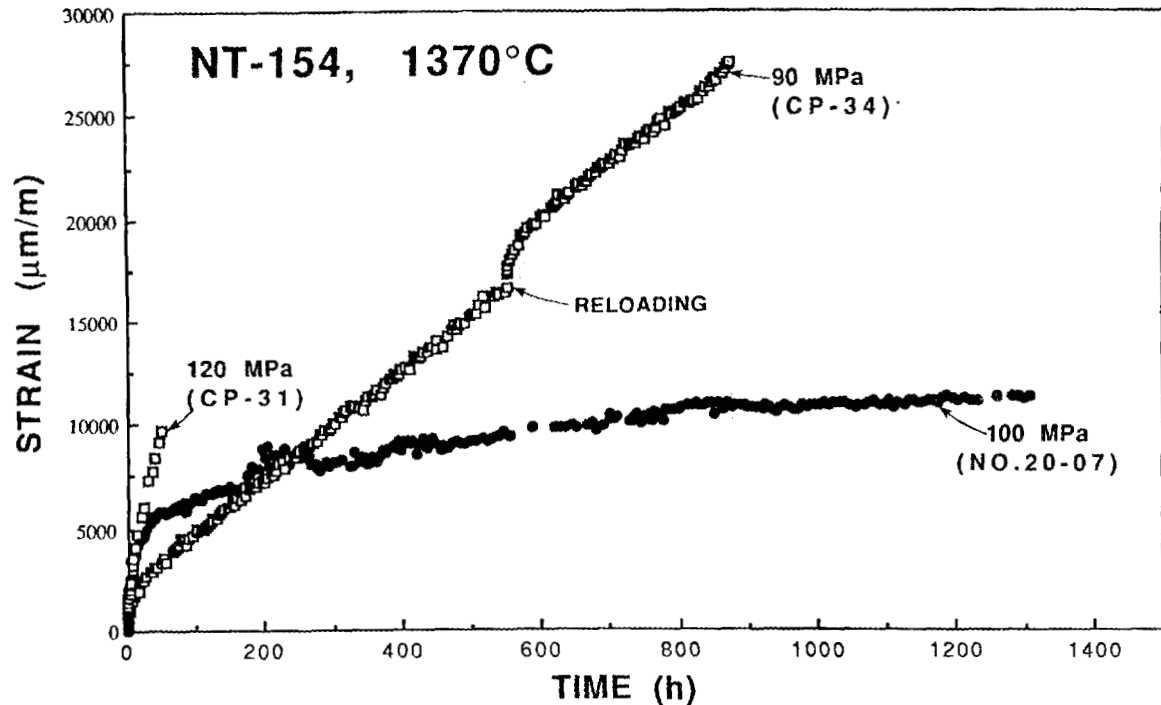


Fig. 8. Creep behavior of NT-154 Si_3N_4 is a function of temperature, stress, and lot number.

and long second stage creep exhibited by specimen CP-34, first stage creep of specimen 20-07 was extensive. A careful examination of the creep curve, however, indicates that second stage creep may be obscured by the data scatter if it exists. Creep behavior appears to be reasonably consistent and predictable within the same lot. However, the diversity of the creep behavior from lot to lot, as demonstrated in Fig. 8, indicates a complete description of the cross-lot variations may be complex.

Substantial information has been acquired concerning the creep behavior of the second precycled specimen (20-09). To make a meaningful comparison with the control test, the specimen was also loaded to 100 MPa. The test was completed in about 3200 h. Test data are presented in Fig 9. It should be noted that the test was interrupted at about $t = 1400$ h due to a power outage. Subsequently, the specimen was reloaded as indicated in Fig. 9. Absence of accelerated primary creep behavior usually seen in a virgin specimen, such as that exhibited by specimen 20-07, is a significant departure in creep behavior for a precycled specimen. However, when the precycled specimen was reloaded, it behaved as if it was somewhat like a virgin specimen exhibiting both first and second stage creep. Perhaps, by coincidence, the second leg of the creep curve of the precycled specimen appeared as an extension of the creep curve of the virgin specimen. This observation suggests that a devitrification process might have been occurring at a much lower rate in the virgin specimen during creep loading compared to that induced by cyclic preloading.

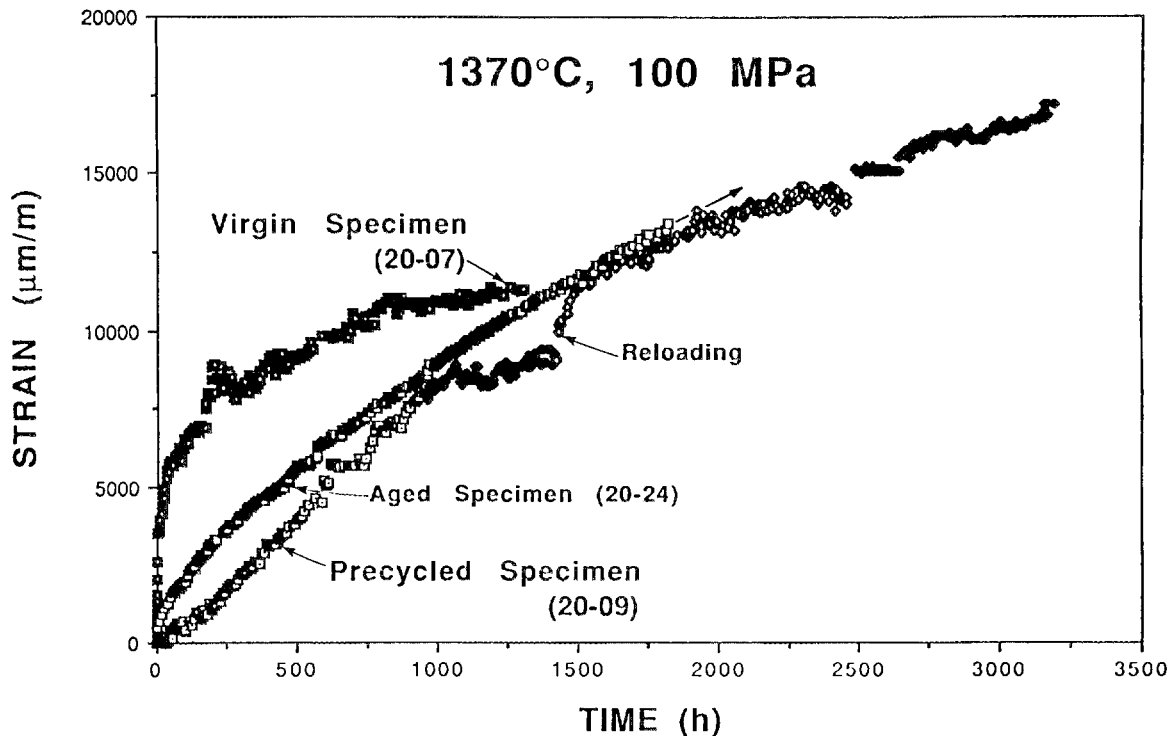


Fig. 9. Prethermal aging of a specimen at 1370°C can dramatically modify the initial transient creep behavior and enhance the creep rupture lifetime.

Figure 10 shows the initial creep behavior of the precycled specimen. The strain recovery immediately following the initial loading was similar to that seen in Fig. 6, and the erratic deformation behavior exhibited in the strain-time curve may be real. However, the reasons for causing such erratic behavior are unknown at this time.

To investigate the effects of prethermal aging on creep behavior, specimen 20-24 (aged at 1370°C for 150 h with no applied stress) was tested also under 100 MPa. The test is currently ongoing with a total test time of about 1800 h accumulated to date. Test data obtained to date are shown in Fig. 9 for comparison with those of specimens 20-07 and 20-09 tested under the same loading condition. As expected that the creep curve of specimen 20-24 fell above and closer to that of the precycled specimen. There is a clear trend indicating that both creep curves may eventually merge together.

Figure 11 shows the creep curve of a virgin specimen (20-25) which was initially tested under an applied stress of 100 MPa for 250 h. The stress was then increased to 110 MPa without changing the specimen temperature. Only a small amount of accelerated creep occurred as a result of the load change. Also discernable is the increase in creep strain rate after the stress was increased. The specimen broke at the shank when the power outage occurred.

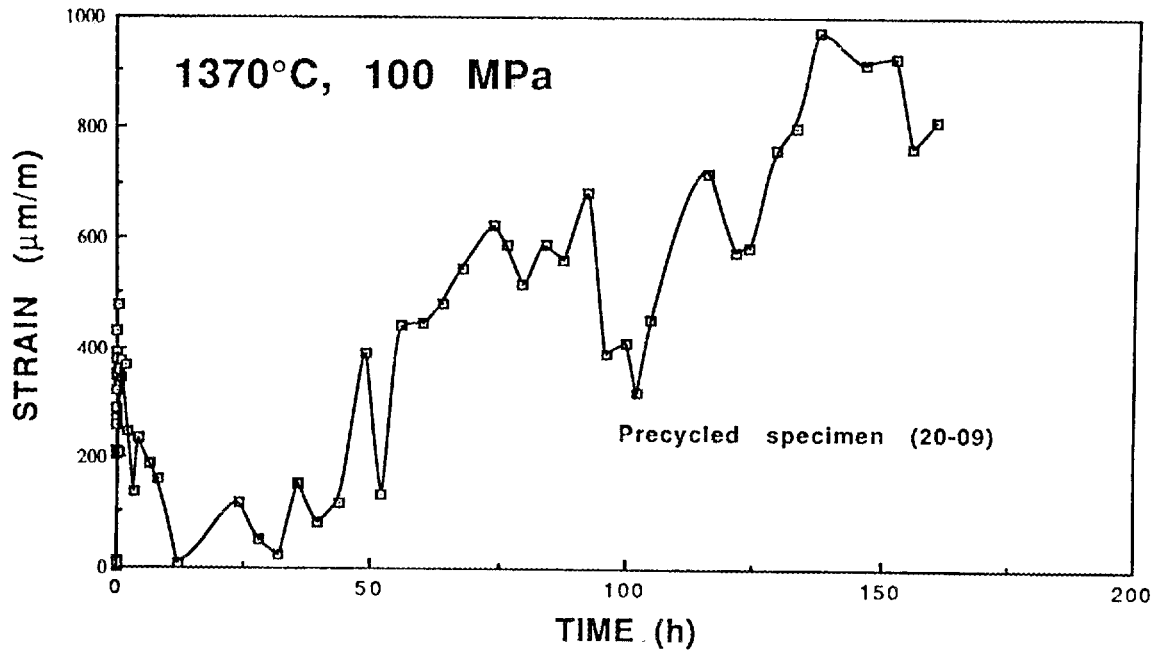


Fig. 10. Enlargement of the initial creep behavior of precycled specimen 20-09.

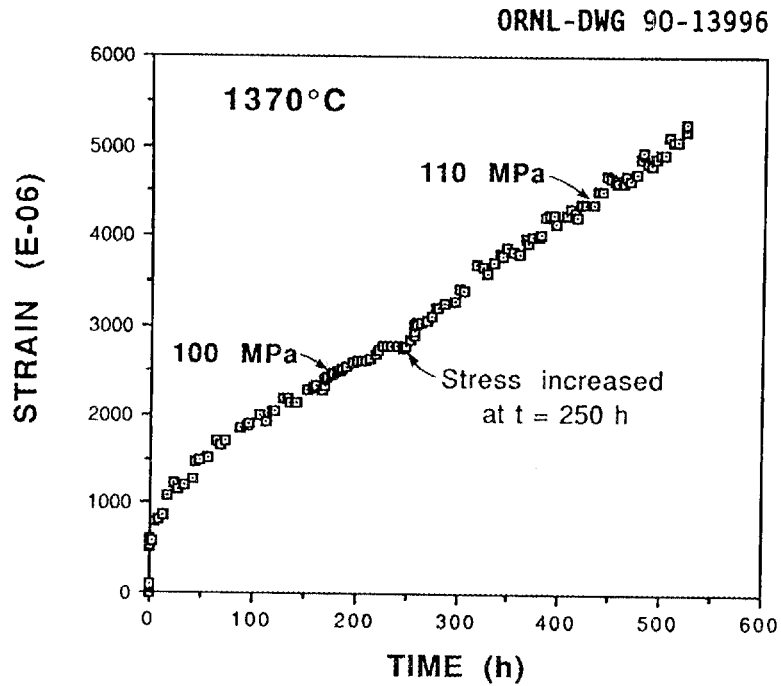


Fig. 11. Tensile creep curve of a virgin specimen (20-25) tested at 1370°C, initially at a stress level of 100 MPa for 250 h followed by a step increase to 110 MPa until fracture by a power outage.

Figure 12 illustrates the dependence of applied stress on the steady-state creep rate. The creep rates were determined directly from the strain-time curves and tabulated in Table 1. Because of the limited number of data, the stress exponent, n , for the Dorn equation was estimated to be in the range of 4 to 6.

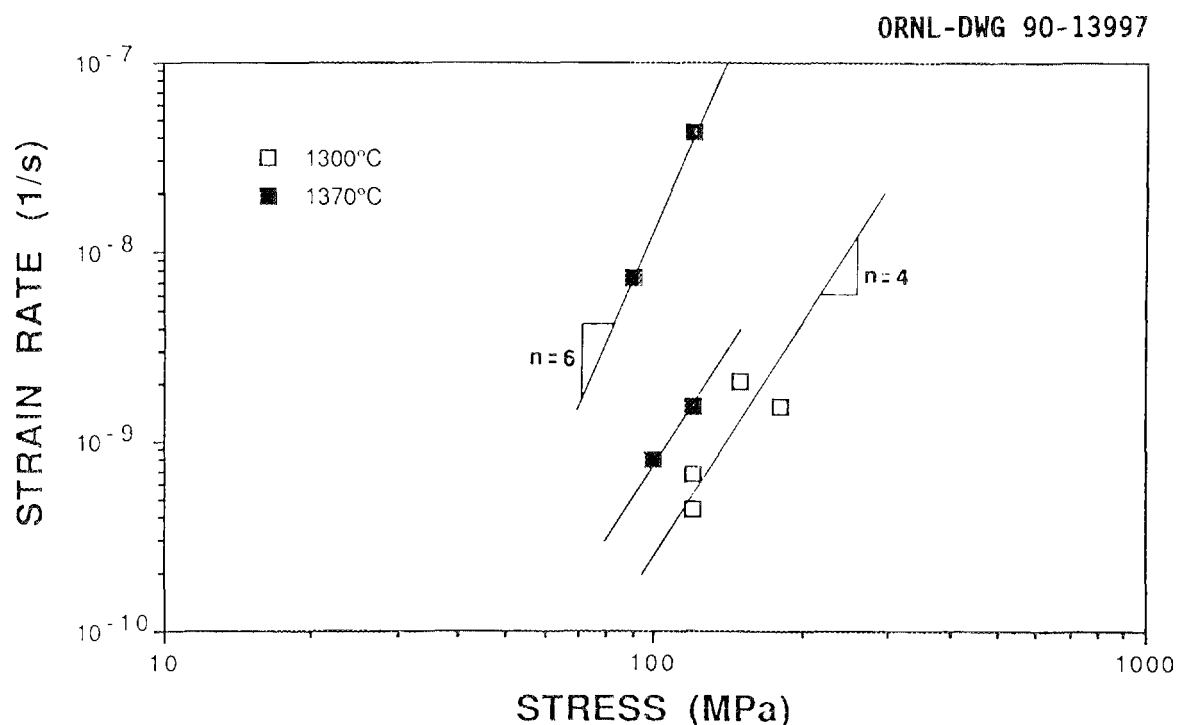


Fig. 12. A log-log plot showing the dependence of strain rate on temperature and applied stress.

The following observations were made based on the limited information obtained to date:

(1) Generally, the creep curves of this material in the as-received condition were similar to those considered characteristic of most metal alloys, consisting of three typical behavioral features defined as transient, steady state, and tertiary stages. Dominance of each stage in the life span varied from lot to lot and the condition of heat treatment. Little or no tertiary creep was usually detected before specimen rupture occurred.

(2) The creep behavior of NT-154 Si_3N_4 is reasonably consistent and predictable within the same lot. However, the complexity of the cross-lot variations complicates a complete description of the creep behavior by a simple mathematical representation.

(3) Steady state creep may be absent under certain conditions of temperature, stress, and heat treatment.

(4) Thermal aging or precycling of specimens at 1370°C can dramatically modify the initial transient creep behavior and enhance creep lifetime. However, no significant advantage was gained in the creep lifetime of a precycled specimen tested at 1300°C.

(5) The initial transient creep behavior of NT-154 Si₃N₄ is governed probably by the level of crystallinity of the grain boundary material and the state of microstructure at the onset of creep loading. However, the biases due to thermal aging and precycling may be obscured by high temperature exposure as time elapses.

(6) Pronounced transient creep reoccurring at each unloading/reloading process may accelerate the creep process and lead to the reduction of creep lifetime.

(7) Strain recovery or negative creep strain behavior occurring immediately following the initial loading was discerned only in the testing of precycled specimens. Accelerated creep following strain recovery however did not lead to tertiary creep.

(8) Steady-state creep rate of this material is a function of applied stress, temperature, and possibly the level of crystallinity of the grain boundary material. The stress exponent, n , for Dorn equation was estimated to be in the range of 4 to 6.

Creep testing of GN-10 Si₃N₄

This is also a new experimental effort initiated during this reporting period. Mechanical strain extensometers were used instead of optical ones for GN-10 testing, because of the space limitation in the testing facility and the stringent laser safety rules enacted by the laboratory management. Some difficulties were encountered initially due to the drifting of the transducer signal when the mechanical strain extensometers were placed in service. These problems were largely associated with the change of the ambient temperature in the proximity of the high temperature furnaces. Most of the problems have been solved but still further improvement is being attempted.

Creep behavior of GN-10 Si₃N₄

Eight creep tests have been performed with GN-10 specimens. Results are summarized in Figs. 13-15 for six specimens tested in the temperature range from 1150 to 1300°C. The negative creep strain readings shown in Figs. 13 and 15 are probably not actual material behavior, but due to the aforementioned extensometer problems. Test results of the remaining specimens are being analyzed. One of the specimens tested at 1300°C under an applied stress of 150 MPa ruptured with a rupture time $t = 13.5$ min and the other at 1320°C and 150 MPa with $t = 58.6$ h.

Creep rupture of GN-10 Si₃N₄

Two empirical equations were developed for predicting the creep rupture time of GN-10 Si₃N₄ based on the limited data obtained to date. The first equation was based on the minimum commitment method and the second based on the Larson-Miller model.

ORNL-DWG 90-13998

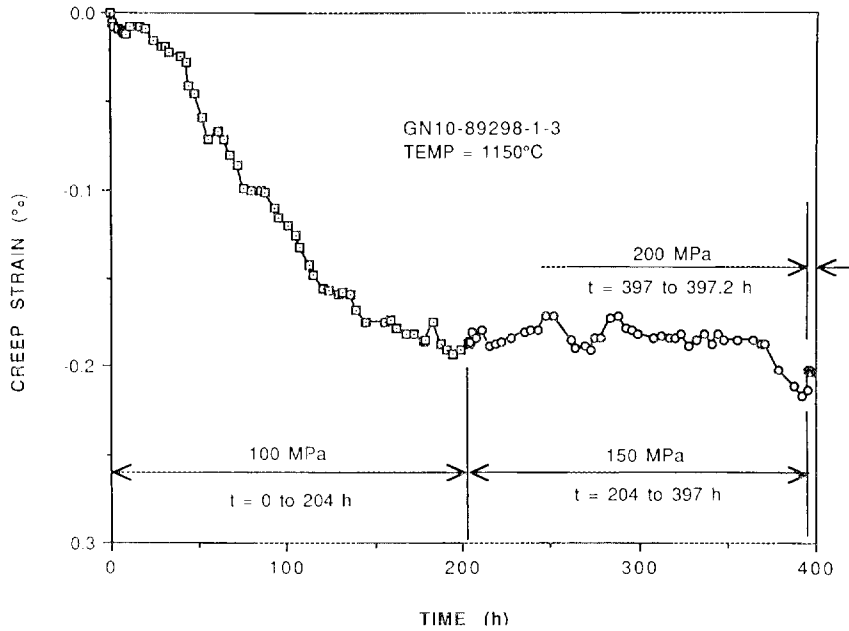


Fig. 13. Creep curve of GN-10 specimen 1-3 tested at 1150°C under three increasing steps of loading. The decrease in measured creep strain is attributed to the downward drifting of the transducer output and is not true creep behavior.

ORNL-DWG 90-13999

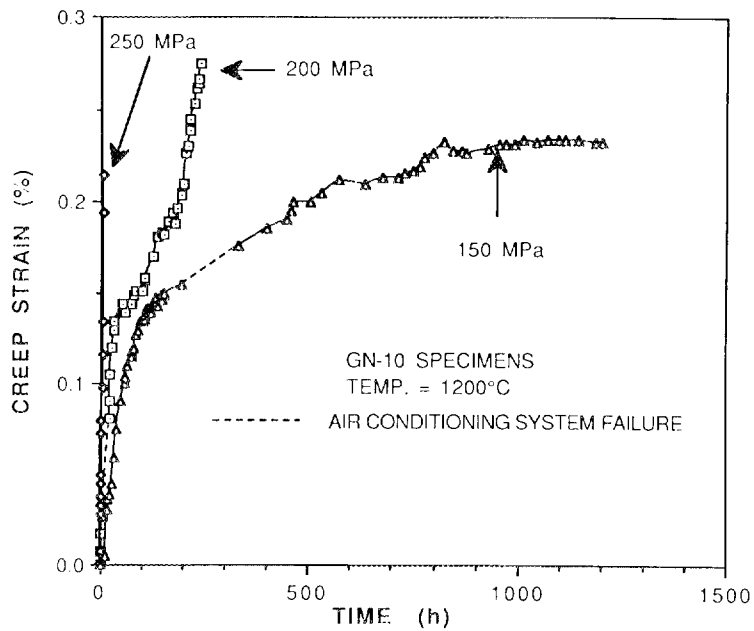


Fig. 14. Creep curves of GN-10 Si_3N_4 tested at 1200°C under a variety of constant stress levels.

ORNL-DWG 90-17092

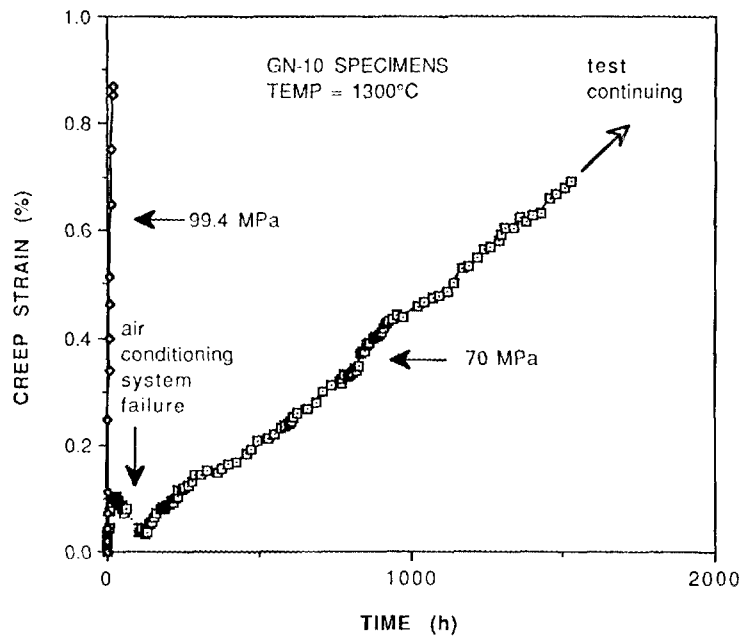


Fig. 15. Creep curves of GN-10 Si_3N_4 tested at 1300°C under two levels of applied stresses. The decrease in creep strain occurred during the air conditioning system shutdown.

The minimum-commitment model is described by the following equation:

$$\log t + [R_1(T - T_m) + R_2(1/T - 1/T_m)] = B + C \log S + DS + ES^2 \quad (1)$$

where t is the rupture time in hours, T the absolute temperature in K, $T_m = 1473^\circ\text{K}$, S the stress in MPa, and R_1 , R_2 , B , C , D , and E material constants. For GN-10 Si_3N_4 , the material constants are given as $R_1 = -0.1011914$, $R_2 = -320829$, $B = 144.8311$, $C = -88.48136$, $D = 0.4372496$, $E = -6.575497\text{E-}4$. Figure 16 shows good agreement between the experimental rupture data and predictions. The rupture time of the 1150°C test was not included in Fig. 16 because the specimen was not tested under a constant stress.

The Larson-Miller model is described by the following equation:

$$\log t = B_0 + B_1/T + B_2 \log S/T \quad (2)$$

where $B_0 = -56.03591$, $B_1 = 119583.5$, and $B_2 = -14845.64$. Again, good agreement between the experimental data and the predictions is demonstrated in Fig. 17. The analysis given above and shown in Figs. 16 and 17 is obviously preliminary due to the limited data.

ORNL-DWG 90-17093

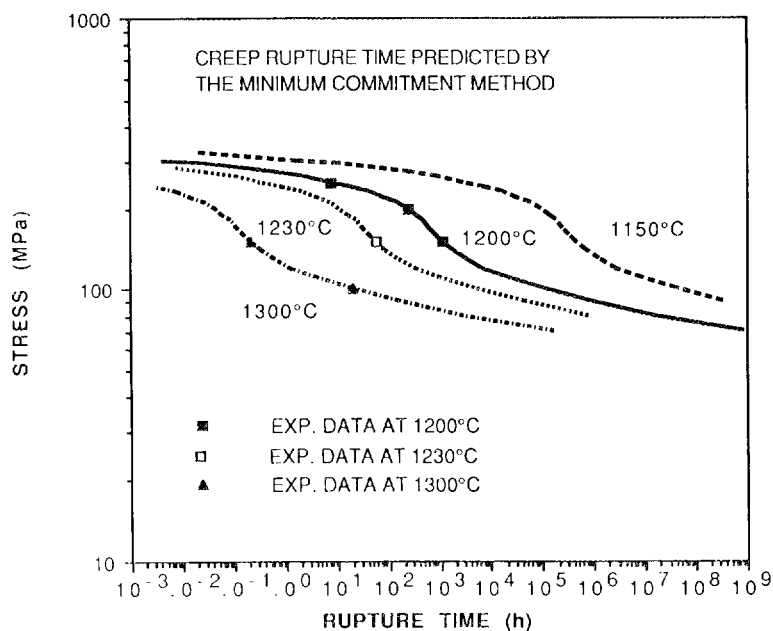


Fig. 16. Creep rupture times predicted by the minimum commitment method show good agreement with the experimental results.

ORNL-DWG 90-17094

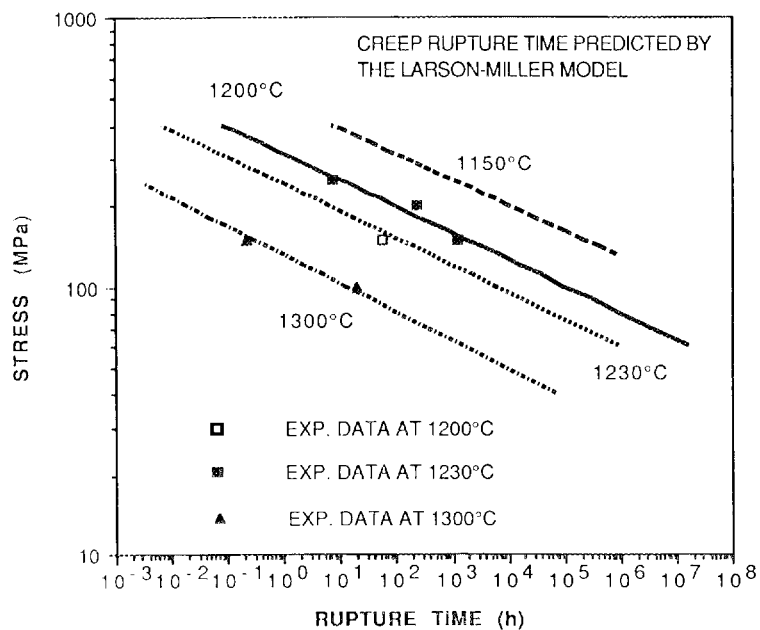


Fig. 17. Creep rupture times predicted by the Larson-Miller model also show agreement with the experimental data within the test range.

Important findings and observations

Information obtained from recent tests in cyclic fatigue suggests that fatigue resistance of Si_3N_4 at high temperature may be enhanced by appropriate thermal aging, which appears to be as effective as or superior to the method by precoaxing. Similarly, the fatigue strength of SiC at 1300°C may also be enhanced by precoaxing at low stresses.

Status of milestone

Completed a draft report covering initial results of tensile creep tests of NT-154 silicon nitride (Milestone 321505).

Publications

H. Pih and K. C. Liu, "Laser diffraction methods for high-temperature strain measurements," *Experimental Mechanics* (in press).

K. C. Liu, H. Pih, C. O. Stevens, and C. R. Brinkman, "Tensile creep behavior and cyclic fatigue/creep interaction of hot-isostatically-pressed Si_3N_4 ," to be published in the Proceedings of the Twenty eighth Automotive Technology Development Contractors' Coordination Meetings to be held in Dearborn, Michigan, October 1990.

References

1. N. L. Hecht, "Environmental Effects in Toughened Ceramics," pp. 379-422 in *Ceramic Technology for Advanced Heat Engines Project Semiannual Progress Report for Period April through September 1989*, ORNL/TM-11489, Oak Ridge National Laboratory, Oak Ridge, Tenn., August 1990.

2. Unpublished results, N. L. Hecht, "Environmental Effects in Toughened Ceramics," WBS Element 3.3.1.4, *Ceramic Technology for Advanced Heat Engines Project Bimonthly Technical Progress Report*, April-May 1990.

Rotor Data Base Generation

M. K. Ferber, M. Jenkins, and R. L. Martin (Oak Ridge National Laboratory)

Objective/scope

The goal of the proposed research program is to systematically study the tensile strength of a silicon nitride ceramic as a function of temperature and time in an air environment. Initial tests will be aimed at measuring the statistical parameters characterizing the strength distribution of three samples types (two tensile specimens and one flexure specimen). The resulting data will be used to examine the applicability of current statistical models as well as sample geometries for determining the strength distribution.

In the second phase of testing, stress rupture data will be generated by measuring fatigue life at a constant stress. The time-dependent deformation will also be monitored during testing so that the extent of high-temperature creep may be ascertained. Tested samples will be thoroughly characterized using established ceramographic, SEM, and TEM techniques. A major goal of this effort will be to better understand the microstructural aspects of high-temperature failure including:

- (1) extent of slow crack growth;
- (2) evolution of cavitation-induced damage and fracture;
- (3) transition between brittle crack extension and cavitation-induced growth; and
- (4) crack blunting.

The resulting stress rupture data will be used to examine the applicability of a generalized fatigue-life (slow crack growth) model. If necessary, model refinements will be implemented to account for both crack blunting and creep damage effects. Insights obtained from the characterization studies will be crucial for this modification process. Once a satisfactory model is developed, separate stress-rupture (confirmatory) experiments will be performed to examine the model's predictive capability. Consequently, the data generated in this program will not only provide a critically needed base for component utilization in automotive gas turbines, but also facilitate the development of a design methodology for high-temperature structural ceramics.

Technical progress

The evaluation of tensile collet systems was continued during this reporting period. The primary objective of this study is to gain a better understanding of the factors responsible for recent button-head failures. Initial efforts focused upon evaluating the button-head strength of gage-less samples fractured using both straight and tapered collets (Fig. 1). As reported previously, the tapered collet arrangement provided the better performance in terms of both the fracture strength and average percent bending at failure. While the use of soft copper collets in the straight-collet grips gave similar values of the button-head fracture strength, the percent bending at failure was slightly higher.

ORNL-DWG 90-17110

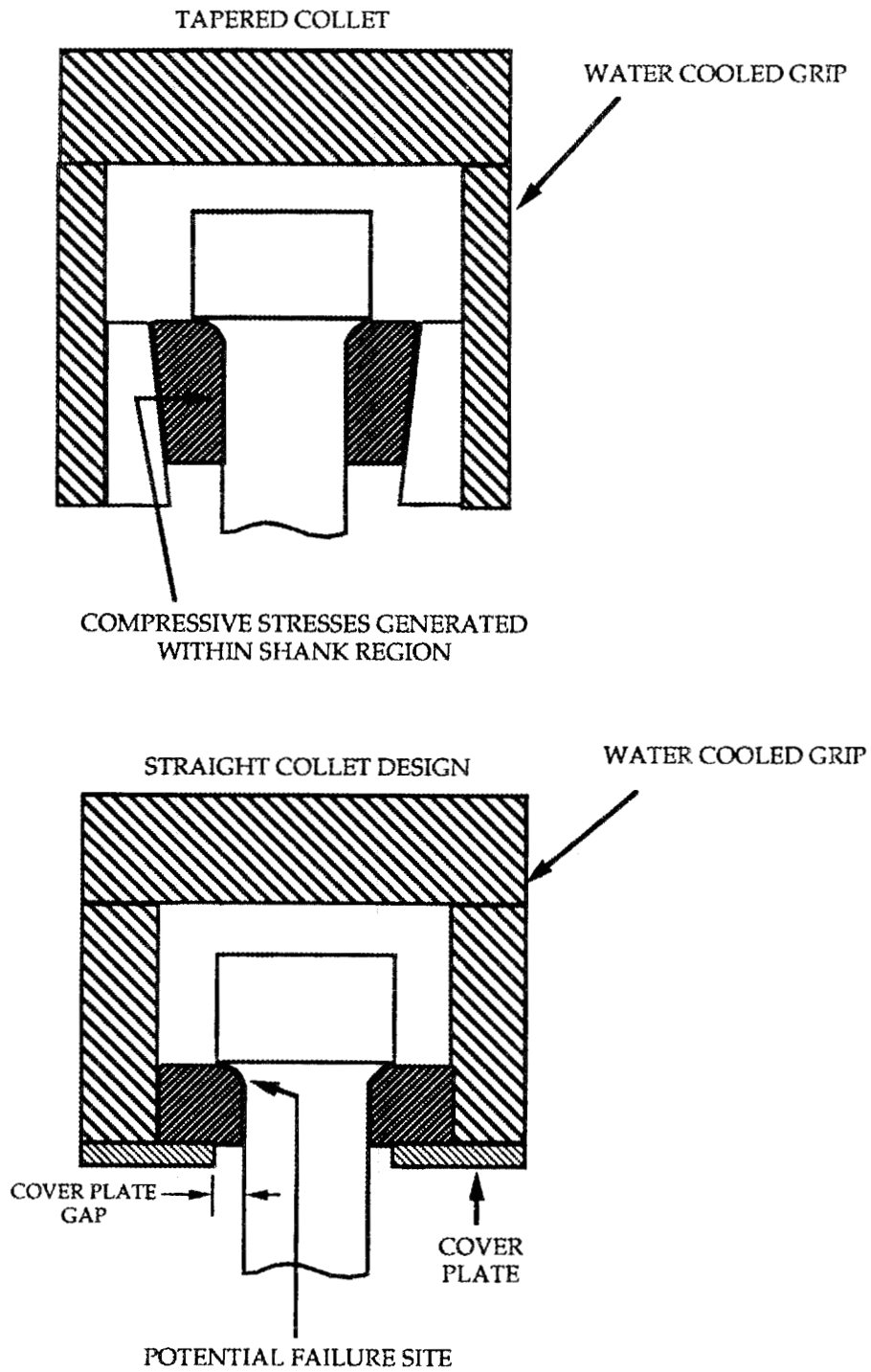


Fig. 1. Schematic illustration of two grip designs used in current tensile test equipment.

The aforementioned tests used gageless specimens so that the fracture behavior in the grip region could be directly evaluated. In order to verify the ability of the tapered collet grips to minimize button-head failures, additional strength tests of a high performance silicon nitride were initiated. Initial fast fracture tensile testing of NT-154 (supplied by Norton/TRW) and PY6 (supplied by GTE Laboratories) specimens with strain-gaged, gage sections was conducted at room temperature using both the tapered and straight-collet gripping systems. The tapered collets and holders were the same as those used with the alumina, straight-shank specimens. Additionally, other factors such as lubrication of the collet/holder interface, stressing rate, (11 MPa/s), and ambient conditions were maintained as consistently as possible with the previous tests.

As reported previously,¹ three problems with the present tapered collet/holder assembly were identified: (1) mismatch of the angle between the collet and holder which leads to non-uniform loading (pinching), (2) hard, super-alloy collets which can cause localized surface damage to the ceramic hence initiating failure, (3) variations in collet dimensions and/or sharp corners which can cause localized damage to the surface of the specimen. An additional concern which has been identified is the non-optimized angle of the taper. The present, arbitrary angle of 10° is "steeper" than the necessary, calculated angle of -30° (for collet/specimen $\mu = 0.6$) thus causing higher than necessary lateral (normal) forces to achieve the needed frictional load transfer.

Following modifications of the tapered collet design to eliminate the three problems noted above, five additional room temperature strength tests were conducted. Of these five, only three fractured in the gage section with multiple failure points located very close to the gage-to-shank transition. This result suggests that the bending was not uniform in the gage section. To examine this possibility, additional strain gages were mounted to the as-fabricated specimens such that the percent bending could be measured at both the gage midspan and the gage-to-shank transitions. Preliminary results have shown that the bending can be 2-3 times larger near the transition regions. Possible reasons for this are currently under investigation.

Initial fracture tests conducted with the straight collet system were generally more successful than with the tapered collet grips. Of the ten specimens tested, six failed in the gage section. Of the four unsuccessful tests, one was attributed to an improper button-head radius and one to improperly annealed collets. The collets must be sufficiently soft to deform during the specimen loading. This deformation along with a close dimensional match between the collet and button-head radius facilitates the transfer of mechanical load into the button-head while minimizing the stress concentration.

Careful examination of the specimens which failed in the button-head/shank region revealed fairly extensive machining damage. In order to eliminate this problem, a two-step machining procedure was used to fabricate the tensile specimens. This procedure consisted of rough grinding the shanks with a 220 grit diamond, resinoid-bonded grinding wheel until the radius was within 0.20-0.25 mm (0.008-0.010 in) of the required value. The remaining material was removed with a 320 grit diamond, resinoid-bonded grinding wheel. The use of the two-step grinding procedure in conjunction with the resinoid-bonded grinding wheels minimize deleterious subsurface

grinding damage which could act as surface flaws and failure initiation sites.

Subsequent room-temperature tensile strength tests with the straight-collet specimens fabricated using the modified machining procedure resulted in 100% gage-section failures. Figure 2 illustrates the Weibull plots for the the two materials. The average strengths for the NT 154 and PY6 were 669 and 667 MPa, respectively. The maximum likelihood estimate of the Weibull modulus was 9.3 for the NT 154 and 8.8 for the PY6. Examination of the fracture surfaces with a low-power optical microscope indicated that most of the critical defects were located near the surface. However, the exact nature of these defects has not been identified.

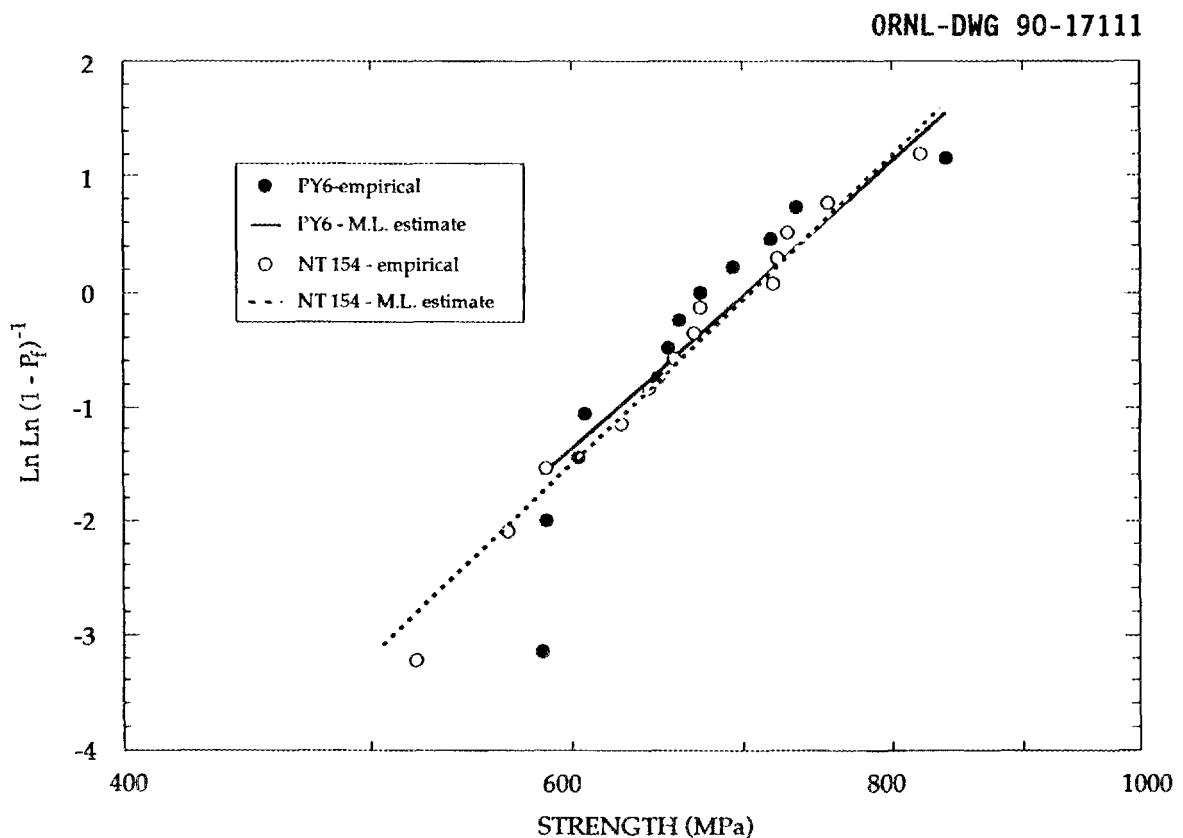


Fig. 2. Weibull plots for PY6 and NT 154 silicon nitride tensile specimens fractured at room temperature.

The creep/fatigue studies involving a high performance silicon nitride were continued this reporting period.* As reported previously,¹ the fatigue resistance (as characterized by the fatigue exponent, n) measured for the button-head tensile samples at 1370°C decreased as the test time increased (Fig. 3). At long times, n fell within the 4 to 6 range.

*Norton NT 154 silicon nitride.

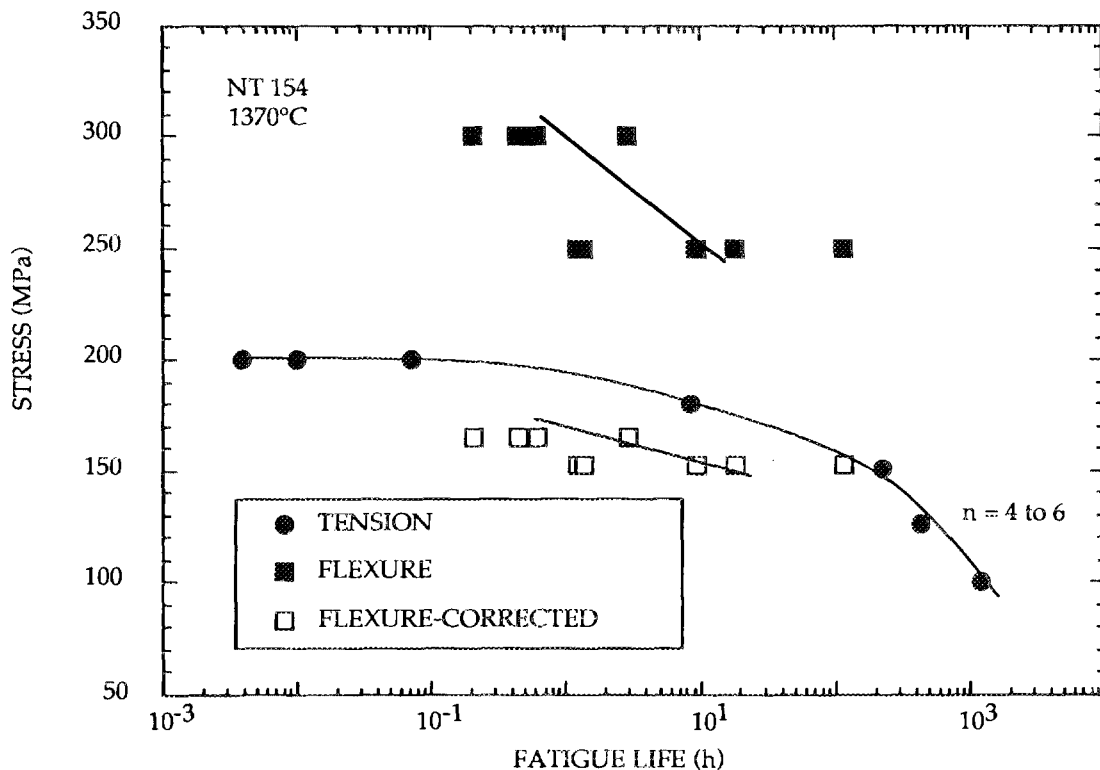


Fig. 3. Creep rupture results for NT154 silicon nitride measured at 1370°C using both flexure and tension specimens.

Examinations of the fracture surfaces of the corresponding test samples indicated that failure was characterized by the accumulation of creep damage. These results are consistent with a creep-constrained cavitation process in which the growth and coalescence of cavities is controlled by the creep rate of the bulk material.²

The creep fatigue life, t , resulting from the evolution of creep-related damage (e.g., cavities and microcracks) can be described by a modified Monkman-Grant relationship,³

$$t = B (d\epsilon_s/dt)^m, \quad (1)$$

where $d\epsilon_s/dt$ is the steady-state creep rate while B and m are constants. The creep rate depends upon the applied stress according to,

$$d\epsilon_s/dt = A (\sigma/\sigma_0)^N, \quad (2)$$

where σ_0 is a normalizing constant; A is the pre-exponential factor, which depends only upon temperature and the material's properties; and N is the stress exponent.⁴ By combining Eqs. 1 and 2, the creep fatigue life is,

$$t = B A^m (\sigma/\sigma_0)^{N*m}. \quad (3)$$

Much of the experimental creep data indicate that the creep response is different in compression than in tension.^{5,6} Therefore, Eq. 2 is often written as $de_{sc}/dt = A_c (\sigma/\sigma_0)^{N_c}$ for $\sigma < 0$ and $de_{st}/dt = A_t (\sigma/\sigma_0)^{N_t}$, for $\sigma > 0$ where de_{st}/dt and de_{sc}/dt are the steady-state creep rates measured under uniform tensile and compressive stresses, respectively. In general, $A_t \neq A_c$ and $N_t \neq N_c$ such that four parameters are required to fully characterize the creep behavior at a given temperature. Equation 2 represents the time-independent creep response. The more general time-dependent formulation, which includes the elastic contribution to the strain, is described in refs. 7 and 8. The differences in creep response between tension and compression loading reflect the effect of stress state upon the dominant creep mechanism. For example, in polycrystalline ceramics, grain boundary cavitation can occur under tensile loading. With time, the cavities will coalesce to form macroscopic cracks, which may grow to a sufficient size to cause failure.

In addition to the fatigue behavior, the creep rates in flexure and tension were measured as a function of applied stress. In the case of the button-head tensile samples, a direct-contact capacitance extensometer was used to monitor the displacement during constant load tests. The deflection of the specimen midspan in the flexure samples was measured with respect to the inner load points using a three-probe displacement extensometer. Additional details of the experimental procedure are given elsewhere.⁹

The stress dependencies of the steady-state creep rates (displacement rates for the flexure specimens) are shown in Fig. 4. The high creep exponent (Table 1) is consistent with a diffusion-assisted cavitation process.

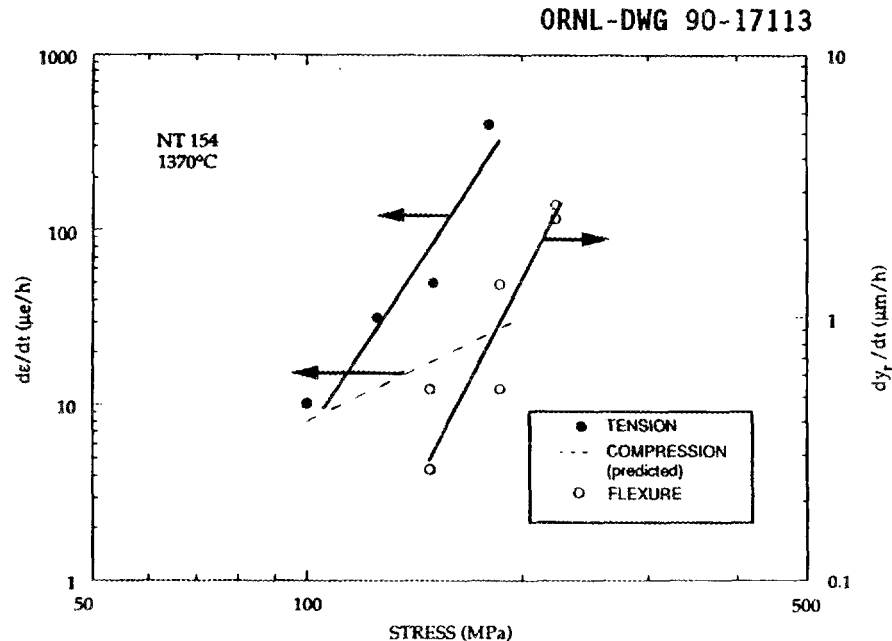


Fig. 4. Stress dependency of steady-state creep rate (and displacement rate in the case of flexure) of silicon nitride at 1370°C. Note the stresses given for the flexure creep tests are based upon the initial elastic values.

Table 1: Summary of Steady-State Creep Parameters for NT 154 Measured at 1370°C.

TEST TYPE	NT 154	
	N	A ($\mu\epsilon/h$)
Tension	5.7	3.73×10^{-11}
Compression (predicted)	2	8.00×10^{-4}
Flexure*	4.7	7.26×10^{-10}

*The estimates for the flexure tests are based upon the assumption that the creep rates in compression and tension are equal (ref. 10).

The presence of these cavities was also confirmed by SEM studies. By utilizing the equations given in ref. 4, it was possible to predict the compression creep parameters from the flexure and tension data (see Table 1). The tension and compression parameters were then used to estimate the extent of creep-induced stress relaxation in the flexure specimens. Table 2 the outer fiber tensile stress normalized by the initial elastic stress, σ_e , as a function of σ_e .

Table 2: Predicted Values of Neutral Axis Location (h_t/h), Steady-State Creep Displacement Rate, and Outer Fiber Tensile Stress [$\sigma(Y = h_t)$] Associated with Flexure Loading of NT 154 at 1370°C. (The σ_e stress values are based upon the elastic solution for bending).

σ_e (MPa)	MOMENT (N•mm)	h_t/h	dy_r/dt ($\mu m/h$)	$\sigma(Y=h_t)$ (MPa)
223	1335	0.567	1.58	135.87
186	1115	0.530	0.85	120.65
148	890	0.488	0.44	103.94

The relaxation of stress in the flexure specimen provides one explanation for the poor agreement between the flexure and tensile fatigue results (Fig. 3). The flexure data represented by the closed squares are based upon the σ_e values which over estimate the actual stresses. Much better agreement results if the relaxed stress values from Table 2 are used to plot the data. The fact that the corrected flexure fatigue plot falls

slightly below the tensile plot may reflect the fact the model used to calculate the stress relaxation assumes steady-state creep conditions only. These conditions were probably not achieved in the present study particularly for the short fatigue lives.

The tensile creep rate and fatigue-life data were used in conjunction with Eq. 1 to estimate the parameter, m . The resulting value of m for the NT 154 was found to increase slightly from -1.3 to -1.0 as the creep rate became smaller (i.e., as the fatigue life became larger). Based upon Eq. 3, one would predict a fatigue exponent of 5.7 ($N^*m = |-1 \times 5.7|$), which is in excellent agreement with the experimental results for $t > 100h$ (see Fig. 3).

Status of milestones

A rough draft of a report describing the results of the button-head grip comparison was completed.

Publications

1. M.G. Jenkins, M.K. Ferber, and J.A. Salem, "Determination of the Stress Distributions in a Ceramic, Tensile Specimen Using Numerical Techniques", to be published in the Proceedings of the 1990 ASME International Computers in Engineering Conference and Exposition.
2. M. K. Ferber, M. G. Jenkins, T. A. Nolan, and R. Yeckley, "Creep-Fatigue of Structural Ceramics: I, Comparison of Flexure, Tension, and Compression Testing," to be published in the proceedings of the Thirty-Seventh Sagamore Conference on Structural Ceramics held in Plymouth, MA during Oct. 1-4, 1990.

References

1. M. K. Ferber and M. G. Jenkins, "Rotor Data Base Generation," pp 373 in Ceramic Technology for Advanced Heat Engines Project Semiannual Progress Report for October 1989 through March 1990, ORNL/TM-11586.
2. Hermann Riedel, pp. 172-197 in Fracture at High Temperatures, Springer-Verlag, Berlin, Heidelberg, 1987.
3. D. C. Cranmer, B. J. Hockey, and S. M. Wiederhorn, "Creep and Creep Rupture of HIPed Silicon Nitride," unpublished data.
4. T. Chuang, "Estimation of Power-Law Creep Parameters from Bend Test Data," J. Mater. Sci., 21, 165-75 (1986).
5. D. F. Carroll, T-J Chuang, and S. M. Wiederhorn, "A Comparison of Creep Rupture Behavior in Tension and Bending," pp. 635-41 in Ceram. Eng. Sci. Proc., 9 [7-8] American Ceramic Society, Westerville, OH, 1988.
6. A. R. Rosenfield, W. H. Duckworth, and D. K. Shetty, "Damage Analysis of Creep in Bending," J. Am. Ceram. Soc., 68, [9] 483-85 (1985).

7. H. Cohrt, G. Grathwohl, and F. Thummler, "Non-Stationary Stress Distribution in a Ceramic Bending Beam during Constant Load Creep," Res. Mechanics, 10 [1] 55-71 (1984).

8. T. Fett, K. Keller, M. Missbach, D. Munz, and L. Pintscovius, "Creep Parameters of Alumina Containing a Glass Phase in Bending Creep Tests," J. Am. Ceram. Soc., 71, [12] 1046-49 (1988).

9. M. K. Ferber, M. G. Jenkins and V. J. Tennery, "Comparison of Tension, Compression, and Flexure Creep for Alumina and Silicon Nitride Ceramics," pp. 1028-37 in Proceedings of the 14th Annual Conference on Composites and Advanced Ceramic Materials, American Ceramic Society, Westerville, OH, July-August, 1990.

10. G. W. Hollenburg, G. R. Terwilliger, and R. S. Gordon, "Calculation of Stresses and Strains in Four-Point Bending Creep Tests." J. Am. Ceram. Soc., 54, [4] 196-99 (1971).

Toughened Ceramics Life Prediction

J. A. Salem and S. R. Choi (NASA Lewis Research Center)

Objective/scope

The purpose of this research is to understand the room temperature and high temperature [1370°C (2500°F)] behavior of in situ and SiC-whisker toughened ceramics as the basis for developing a life prediction methodology. A major objective is to understand the relationship between microstructure and the mechanical behavior within the bounds of a limited number of materials. A second major objective is to determine the behavior as a function of time and temperature. Specifically, the room temperature and elevated temperature strength and reliability, the fracture toughness, slow crack growth and the creep behavior will be determined for the as-manufactured material. The same properties will also be evaluated after long-time exposure to various high temperature isothermal and cyclic environments. These results will provide input for parallel materials development and design methodology programs. Resultant design codes will be verified.

Technical progress

The mechanical characterization of a whisker reinforced silicon nitride and a similar monolithic were completed. Previously reported results on strength, toughness, and oxidation are included along with unreported measurements of dynamic fatigue, creep, crack growth resistance, and fractographic analysis.

Materials and Test Procedures

(A) Materials

The materials used in this study were based on Garrett GN-10* composite and monolithic Si₃N₄'s. The material fabrication has been described elsewhere¹. Briefly, a Si₃N₄ powder composition was slip cast into 50 mm diameter by 75 mm height billets, glass encapsulated by the ASEA[®] method and hot-isostatically pressed to produce monolithic Si₃N₄ material. Part of the same powder batch was blended with 30 vol % SiC whiskers by APMC[®] and processed with the same procedures as the monolithic. Densities of the composite and monolithic materials were 3.27 and 3.31 g/cm³, respectively. Etched microstructures of the materials are shown in Figure 1.

(B) Strength

The billets of both composite and monolithic materials were cut to produce flexure test specimens such that the longitudinal axis of the

* Garrett Ceramic Components Division, Torrance, California.

@ ABB Autoclave Systems, Columbus, Ohio.

& Advanced Composite Materials Corp., Greer, South Carolina.

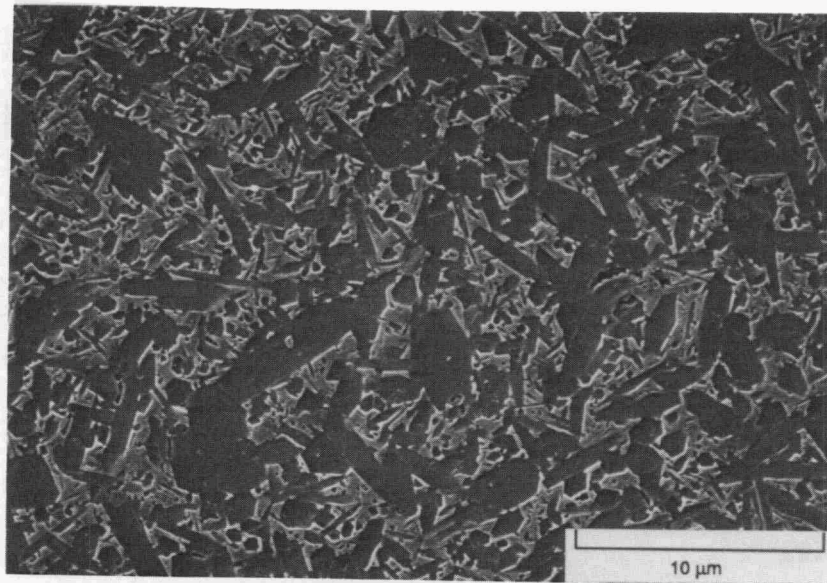
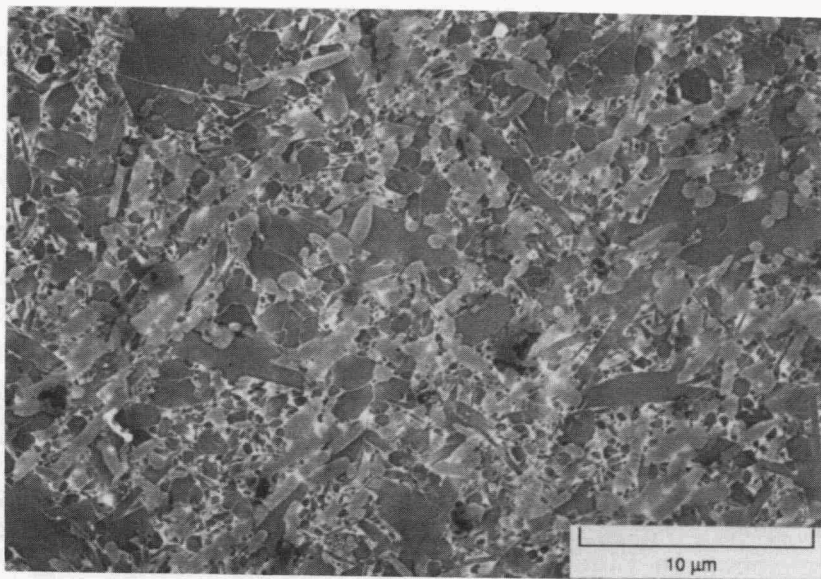
(a) Si₃N₄.(b) SiC_w/Si₃N₄.

Figure 1. Etched microstructures: where darkest regions are Si₃N₄, grey regions are SiC whiskers, and light regions are intergranular phases.

specimens was parallel to the billet height. The flexure strength was determined in four-point bending at temperatures from 25 to 1400 °C. The specimens measured 3 x 4 mm in height and width and the inner and outer spans were 20 and 40 mm, respectively. Flaw type and location were determined with scanning electron microscopy.

(C) Fracture Toughness

Fracture toughness from room temperature to 1400 °C was determined with the chevron-notch² (CN) method in four-point bending. Specimens measured 3 x 6 mm in width and height and the inner and outer spans were 20 and 40 mm, respectively. Chevron-notch specimens were tested at 0.01 mm/min. The slow stroke rate used for chevron-notch testing was required to insure stable crack extension. The fracture toughness was also measured with single-edged-precracked-beam (SEPB)³ and indentation strength⁴ (IS) methods at room temperature.

(D) Crack Growth Resistance

The room temperature crack growth resistance was estimated using the indentation strength method proposed by Krause⁴, and from the results of the SEPB fracture toughness tests. Test specimens for indentation strength were 3 x 6 x 25 mm bars with the center of the polished tensile surface indented with a Vickers indenter at loads ranging from 49 to 294 N. The subsequent strength tests of the indented samples were conducted in four-point bending with spans of 10 and 18 mm, and a stroke rate of 0.2 mm/min. Three to four specimens were tested at each indentation load. Krause et al⁴ have shown that R-curve behavior can be evaluated from indentation strength data, assuming that fracture resistance (K_r) is related to the crack length (c) by a power-law relationship. The fracture resistance and the indentation strength (σ_f) relations are expressed

$$K_r = kc^m \quad (1)$$

$$\sigma_f = [k(3+2m)/(4\beta)][4P\gamma/(k(1-2m))]^{2m-1/2m+3} \quad (2)$$

where k and m are constants, β and γ are the dimensionless quantities associated with the residual contact stress intensity and the crack geometry, respectively, and P is the indentation load. When $m = 0$, Equation (2) reduces to the case of no crack resistance toughening. Also, $K_r = K_{IC}$ for $m = 0$. The parameter m was evaluated from the best-fit slope of the $\text{Log } \sigma_f$ - $\text{Log } P$ data and equation (2). The constant k was evaluated from Eq. (1) with the estimated m and the toughness value obtained from the average macroscopic crack size of $c = 1600 \mu\text{m}$ from the SEPB specimens.

(E) Fatigue Susceptibility

Dynamic fatigue tests were conducted in four point bending with 20/40 mm spans at temperatures of 1100, 1200 and 1300 °C in air. Four loading rates of 2000 N/min to 2 N/min, corresponding to the stressing

rates of 2000 MPa/min to 2.0 MPa/min, were applied at temperatures of 1100 and 1300 °C. At 1200 °C only two loading rates of 2000 and 2 N/min were employed due to the limited number of the specimens. The number of test specimens at each loading rate was three to five. The heating rate of the furnace was 12 °C/min, and each specimen was held at test temperature for 20 min prior to testing.

For comparison, an additional dynamic fatigue test was carried out with indented specimens at 1100 °C in air. Specimens measuring 2.7 x 4 x ≥ 25 mm were indented using an indentation load of 98 N with a Vickers microhardness indenter such that one of the indentation diagonals was aligned normal to the direction of the applied tensile stress. Four loading rates of 4200 to 4.2 N/min, corresponding to the stressing rates of 2000 to 2.0 MPa/min, were utilized. A four point flexure fixture with spans of 19.0/9.5 mm was used. Three specimens were tested per loading rate.

The fatigue susceptibility parameters n and B were obtained, respectively, from the slope and intercept of the dynamic fatigue curve of $\text{Log } \sigma_f$ vs. $\text{Log } \dot{\sigma}$ based on linear regression analysis^{5,6}

$$\sigma_f^{n+1} = B(n+1)S_i^{n-2}\dot{\sigma} \quad (3)$$

where $B = 2/[AY^2(n-2)K_{IC}^{n-2}]$, S_i is the inert strength, and Y is the crack geometry factor. Consequently, the parameter A of the empirical crack velocity equation⁷

$$V = A'[K_I/K_{IC}]^n = AK_I^n \quad (4)$$

was evaluated using Eq. (3) with appropriate constants.

(F) Oxidation

Oxidation tests were conducted by heating bend bars at 1000, 1200, or 1400 °C for 500 hours in 100 ccm flowing oxygen. Four-point bend strength of the materials after the 500 hour exposures was determined at 25 °C. Specimens measured 3 x 4 mm in height and width, and they were tested between spans of 20 and 40 mm at a crosshead speed of 0.05 mm/min. Five specimens were tested for each exposure temperature.

(G) Creep

Creep tests were conducted by dead weight loading of 3 x 4 x 50 mm flexure specimens between spans of 19.05 and 38.1 mm. Stress levels of 200, 250, 300, and 350 MPa were applied at 1250 °C in air. The displacement measurement system included an LVDT transducer with a 3-point extensometer made of Al₂O₃ gaging rods with SiC points. The SiC points contacted the specimen tensile surface at the center and beneath the inner load points. The strain calculation assumed a constant radius of curvature between the inner load points and the simple relation $e_{\max} = 4h \times d/a^2$, where e_{\max} is the maximum strain in the outer fiber, d is the relative deflection of the bar center with respect to the inner load points, and a is the inner span⁸.

Results and Discussion

(A) Strength

Bend strength of the as-received materials as a function of temperature is shown in Figure 2. The room temperature strength was $\sigma_f = 698 \pm 85$ MPa and 732 ± 61 MPa for the composite and monolithic materials, respectively. Weibull modulus in the strength distribution was not available due to the limited number of test specimens (typically less than 10). However, Weibull modulus (τ) can be estimated approximately using the formula of $\tau \approx 1.2/[C.V.]$ as proposed by Ritter et al.⁹, where C.V. is the coefficient of variation of the mean strength. Using this relation together with the obtained values of C.V. for the two materials at room temperature, Weibull moduli of the composite and monolithic are estimated to be $\tau \approx 9.8$ and 14.4, respectively. Despite the insufficient number of test specimens for the reliable evaluation of Weibull parameters, the estimated Weibull modulus, however, is in a good agreement with the typical range of $\tau \approx 7$ to 15 commonly observed from sintered Si_3N_4 materials. It is important to note that a low Weibull modulus suggests nonuniformity and/or inhomogeneity in composition and microstructure for the materials.

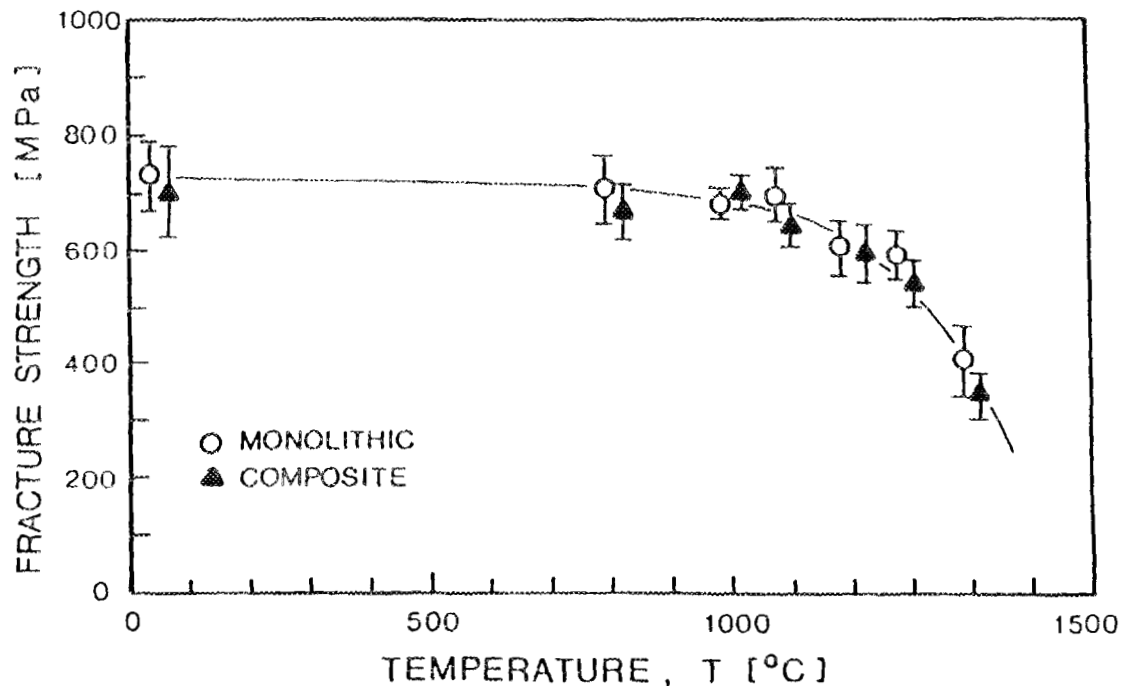


Figure 2. As-received strength of monolithic and SiC whisker-reinforced Si_3N_4 as a function of temperature in air. Error bar indicates ± 1.0 standard deviation.

Examination of the fracture surfaces for both materials showed that most failures originated from surface and subsurface porous regions, coarse grained regions, chunks of silicon nitride, and agglomerates. Typical examples of failures are shown in Figure 3. The chunks of nitride were not associated with processing contaminants such as metallic particles (e.g. iron). For both materials, the room temperature strength was retained with little variation up to 1100 °C; however, appreciable strength degradation occurred at 1200 °C and was much greater at 1400 °C. The large degradation at 1400 °C, relative to the room temperature strength, reached 50 and 45 % for the composite and monolithic materials, respectively. This high temperature strength degradation, particularly at 1400 °C, is believed to be associated with slow crack growth and creep deformation due to the softening of the grain boundaries. A large region of such stable crack growth that occurred at 1400 °C for the composite material is shown in Figure 4.

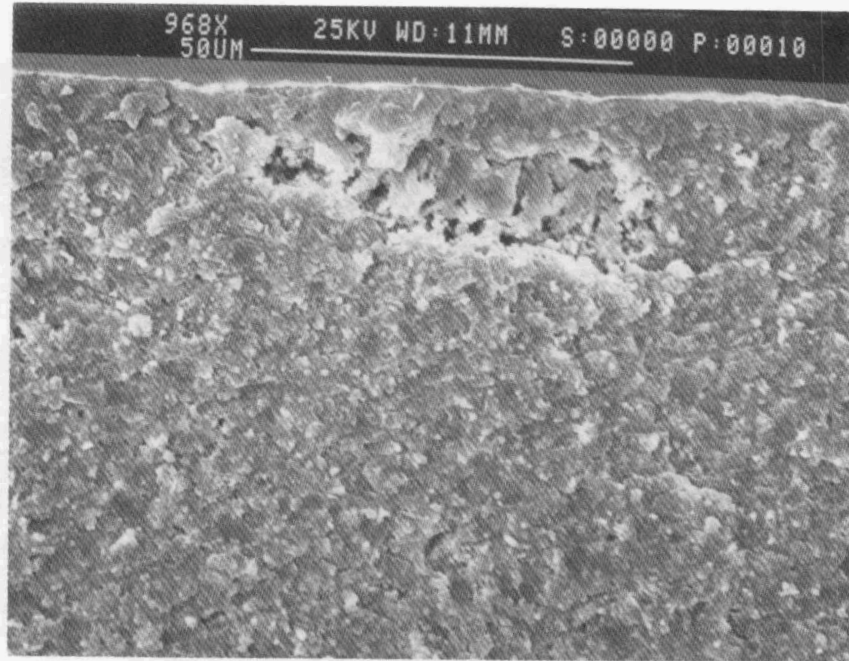
In general, the strength of the monolithic material was about 5 to 15 % higher compared to that of the composite. However, in view of the range of experimental error, it can be concluded that the strengths of both composite and monolithic materials are virtually the same, as seen in Figure 2. This indicates that the whisker addition to the Si_3N_4 matrix did not provide any favorable effect on strength, consistent with earlier work¹.

(B) Fracture Toughness

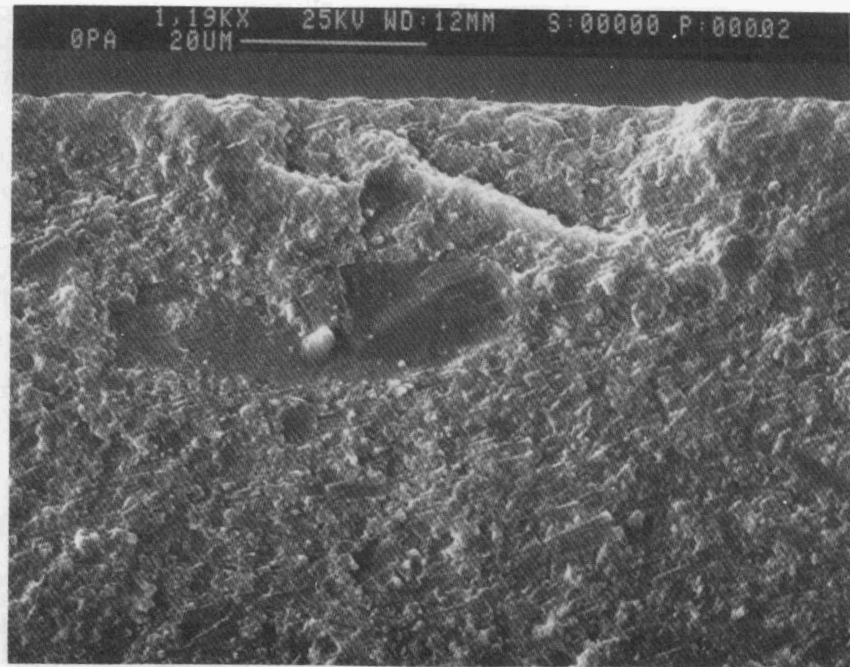
The results of the fracture toughness measurements from the chevron-notch method are presented in Figure 5. The measured fracture toughness for both materials is plotted against test temperature from 25 to 1200 °C. Contrary to the case found for the strength behavior, toughness degradation with increasing temperature was not observed for the two materials. Over the test temperature range, the toughness (room temperature $K_{IC} = 5.46 \pm 0.28$ and 5.32 ± 0.30 MPa/m for the composite and monolithic, respectively) remained almost unchanged (within $\leq 10\%$), indicating that toughness for both materials is independent of test temperature up to 1200 °C. Also, note the negligibly small difference in toughness values between the two materials. The overall fracture toughness was found to be $K_{IC} = 5.66 \pm 0.26$ MPa/m, as indicated by the a horizontal line in Figure 5.

It should be noted that, although not presented in Figure 5, an unusually high fracture toughness of $K_{IC} \geq 10$ MPa/m was obtained for both materials at the temperature of 1400 °C. This was due to increased plasticity and/or creep deformation associated with the combined effects of high temperature and slow testing speed 0.01 mm/min, as reported previously¹. The SEP method in inert environment is thought to be a good alternative to measure fracture toughness at that high temperature.

A summary of the fracture toughness evaluated at room temperature with the chevron notch, SEP, and indentation strength methods is shown in Figure 6. The fracture toughness thus obtained was not dependent on the test method for both materials. Also, note that there was virtually no difference in fracture toughness between the two materials. The overall fracture toughness was found to be $K_{IC} = 5.41 \pm 0.20$ MPa/m, as

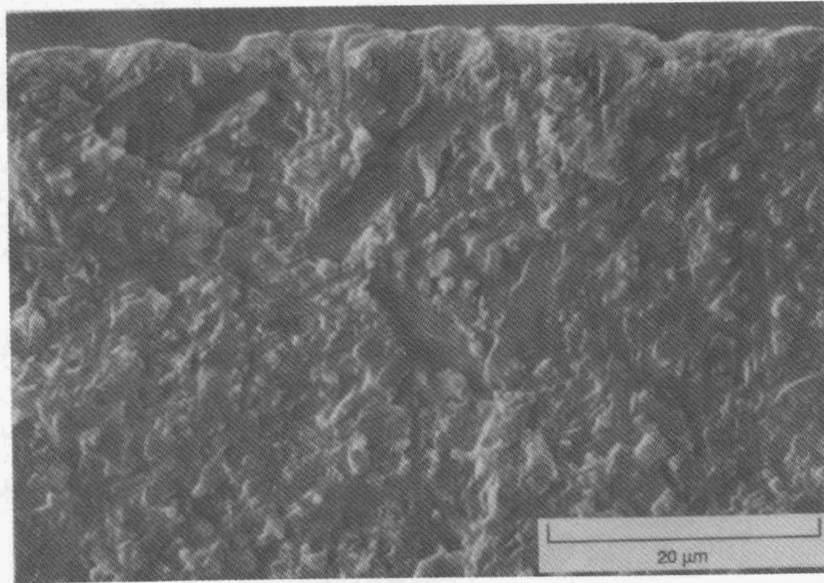


(a)

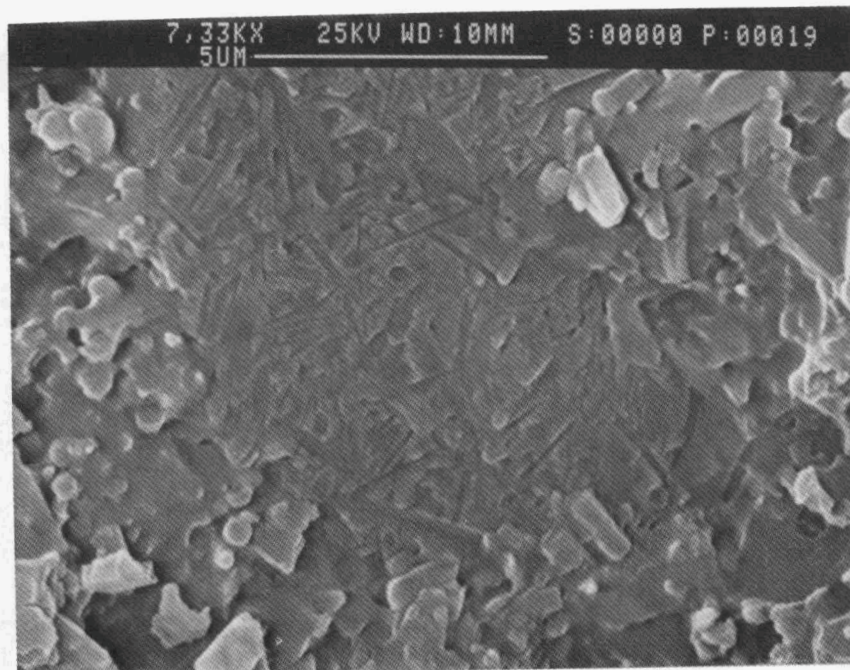


(b)

Figure 3. Fracture origins: (a) Porous region (composite), (b) coarse grain (composite), (c) coarse grains (monolithic), and (d) glassy patch associated with coarse grain (composite).

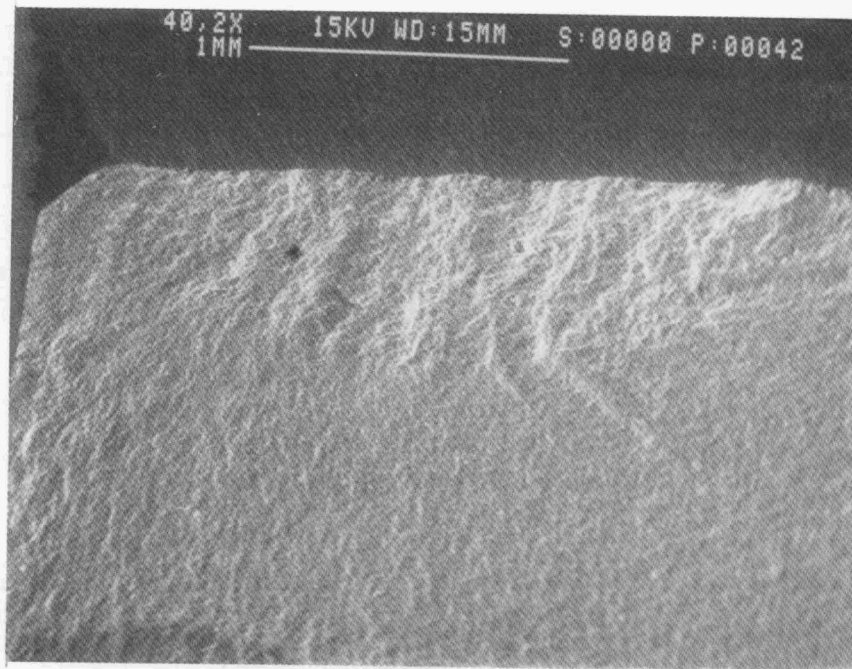


(c)

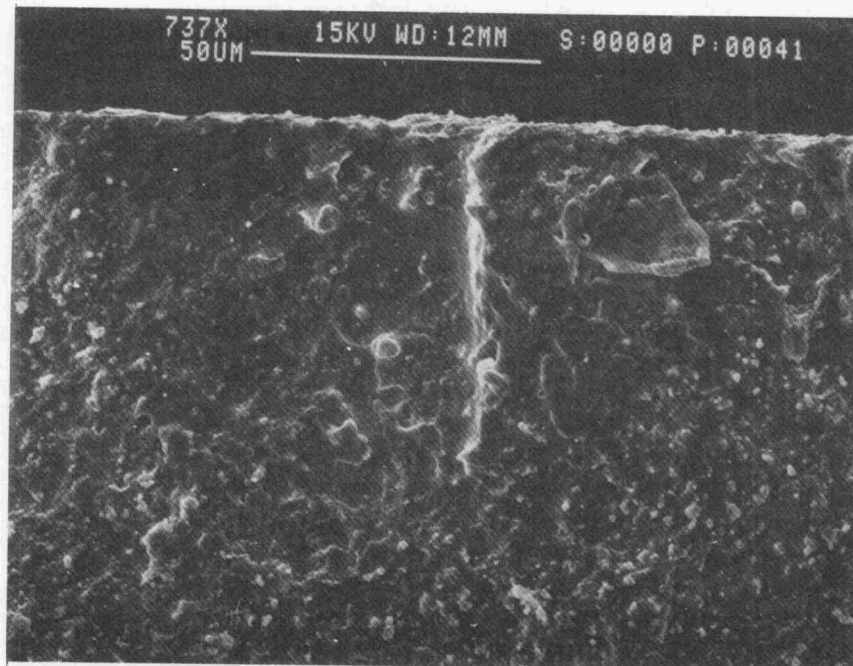


(d)

Figure 3. Continued. Fracture origins: (c) coarse grains (monolithic), and (d) detail of a glassy patch associated with a coarse grain (composite).



(a)



(b)

Figure 4. Fracture surface of a specimen failed at $\sigma_f = 329$ MPa under test conditions of 1300°C with $\dot{\sigma} = 2$ MPa/min: (a) overall view showing the stable crack growth region; (b) extensive glassy phases covering the stable crack growth region.

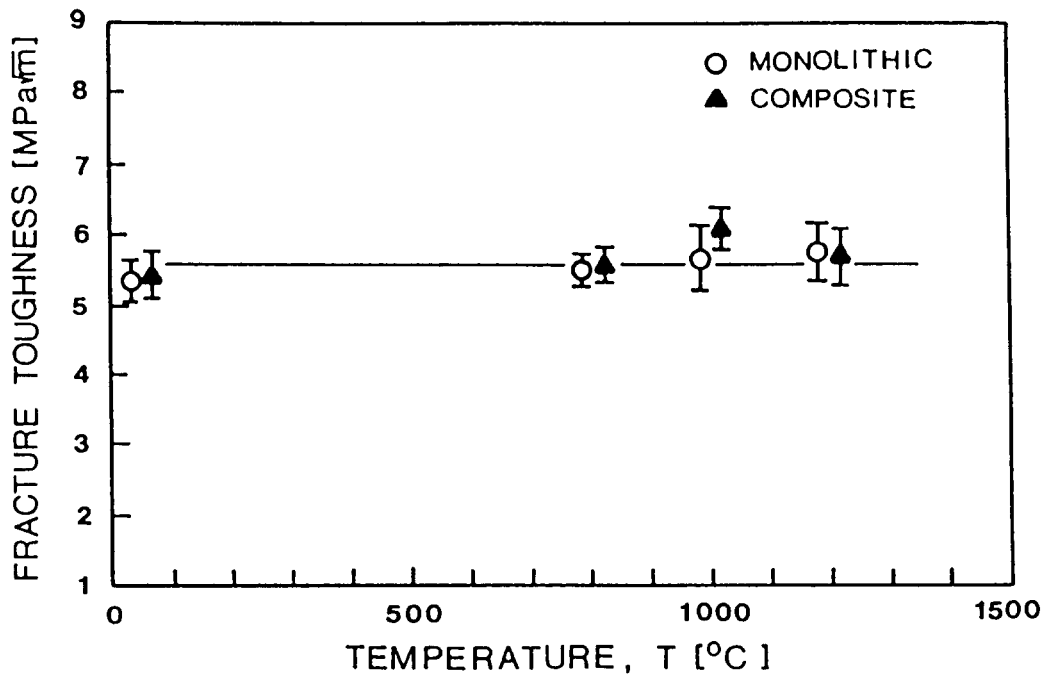


Figure 5. Fracture toughness of composite and monolithic materials as a function of temperature in air. The horizontal line represents an average value of toughness ($= 5.66 \text{ MPa}/\text{m}$) for all data. Error bar indicates ± 1.0 standard deviation.

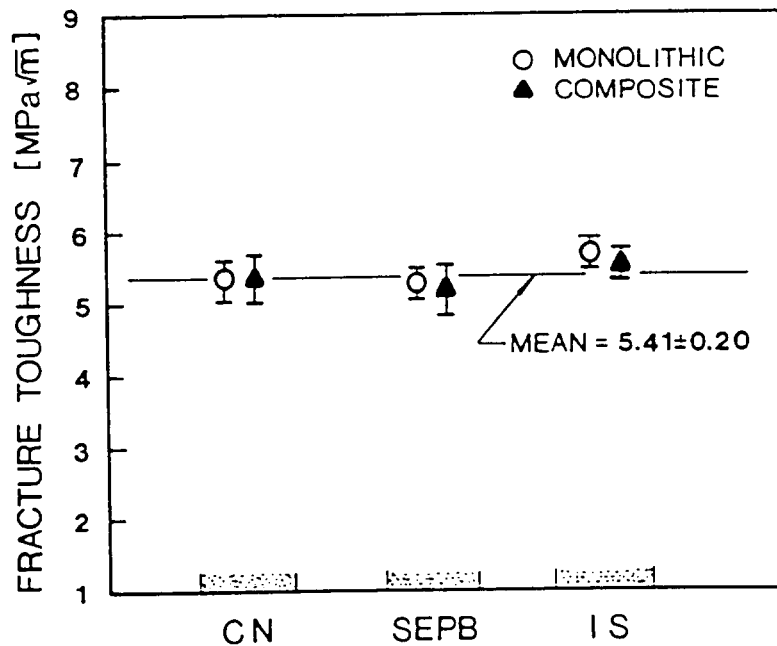


Figure 6. Room temperature fracture toughness of composite and monolithic materials evaluated from the chevron-notch (CN), Single-Edge-Pre-cracked-Beam (SEP) and indentation strength (IS) methods. A mean value of $5.41 \text{ MPa}/\text{m}$ was obtained for all data. Error bar indicates ± 1.0 standard deviation.

shown in Figure 6. This result implies that crack growth resistance of the materials remains constant regardless of the crack size, for either the micro-crack (indented) or the macro-crack (SEPB and CN) regime. Crack growth resistance as a function of crack size, called R-curve behavior, will be discussed in the next section.

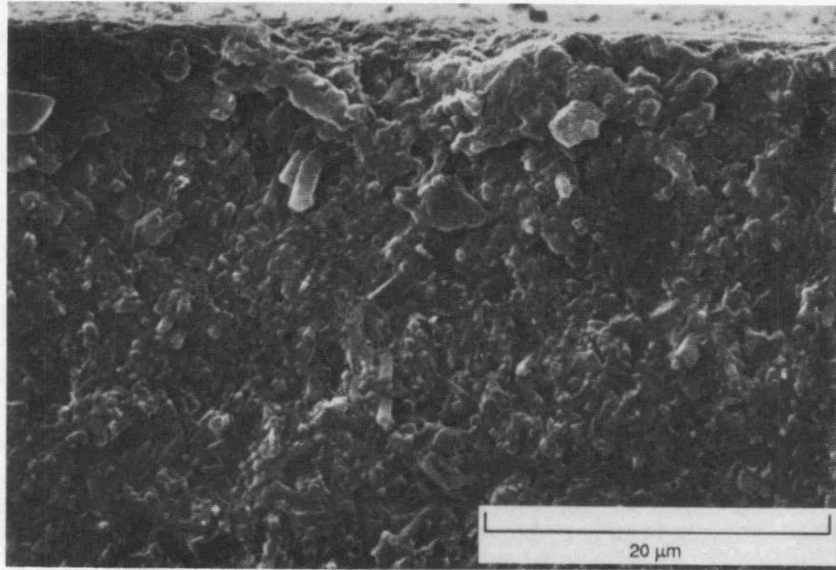
The lack of appreciable difference in fracture toughness between the two materials implies that the whisker addition was ineffective as a toughening mechanism for the current composite material system. Toughening mechanisms such as crack deflection by the whiskers and both whisker bridging and whisker pullout have been suggested and observed to be operative for some reinforced ceramics^{10, 11}. Fracture surfaces of this composite material exhibited whisker pullout and their impressions to some extent (Figure 7). However, the number and extent of fiber pullouts are thought to be insufficient to achieve a noticeable gain in fracture toughness. Also, note that many fibers were aligned to the direction parallel to the fracture plane, as observed from the orientation of the fiber impressions in Fig. 6(b). It should be noted that proper alignment of whiskers relative to crack plane (i.e., whisker axis aligned perpendicular to crack plane) is a prerequisite to enhance fracture toughness of the composite material.

Recently, Becher et al¹² modeled the toughening behavior of whisker reinforced ceramics based on both the stress intensity and the energy change introduced by bridging whiskers with some simplifying assumptions. Their resulting expression of toughening contribution (δK) is

$$\delta K = 1/2 [(K_0^2 + Q)^{1/2} - K_0] \quad (5)$$

$$\text{where } Q = 2(\sigma_f^w)^2 r V_f E^c G^m / 3(1-\nu^2) E^w G^i$$

and where K_0 is the matrix toughness, r is the whisker radius, σ_f^w the whisker strength, V_f the volume fraction of whiskers, ν the Poisson's ratio of the composite, and E and G are the Young's modulus and fracture energy, respectively. The superscripts c , w , m , and i denote composite, whisker, matrix, and interface, respectively. For the given whisker (σ_f^w , E and V_f) and given matrix (toughness) conditions, the toughening is strongly dependent on the interface fracture energy G^i . In other words, the interfacial fracture energy must be small so that partial debonding of the whisker along the whisker/matrix interface occurs to form the whisker bridging. In order to obtain a $\delta K = 10\%$ increase in toughening from the current composite, the fracture energy ratio of matrix to interface given in Eq. (5) needs to be $G^m/G^i \approx 6$ for experimental and literature values of $\sigma_f^w \approx 8 \text{ GPa}$ ¹³, $r \approx 0.21 \mu\text{m}$, $\nu \approx 0.2$, $E^c \approx 300 \text{ GPa}$, $E^w \approx 580 \text{ GPa}$ ¹³, $K_0 = 5.4 \text{ MPa/m}$, and $\delta K = 0.54 \text{ MPa/m}$ together with $V_f = 0.3$. To achieve a 50% increase in toughening, for example, the ratio G^m/G^i should be increased by factor of 10 from the 10% toughened composite system. Controlling the matrix/whisker interface is thus crucial in tailoring toughness property of the composite materials. However, additional complexities involved with interface surface chemistry, whisker morphology and thermal expansion mismatches are also known to strongly influence whisker toughening¹⁴.



(a)



(b)

Figure 7. Fracture surfaces of composite material showing (a) whisker pullout, and (b) orientation of whisker impressions which is parallel to the fracture surface.

(C) R-Curve Behavior

A summary of the fracture parameters m and k is given in Table I. Included in this table is the best-fit slope for each material estimated from the linear regression analysis of $\text{Log } \sigma_f$ vs $\text{Log } P$. The predicted fracture resistance curve based on Eq. (1) is presented in Figure 8. Both composite and monolithic materials did not exhibit any rising R-curve behavior, with a negligibly small toughening exponent of $m \leq 0.04$.

The flat R-curve behavior of the composite material was also observed from the fracture toughness values evaluated using SEPB specimens at room temperature. Figure 9 shows a plot of fracture toughness as a function of normalized crack size a/W , where a is the precrack size and W is the specimen height. Here, the different crack sizes were obtained by varying the applied indentation load, which not only triggers crack pop-in, but determines the precracking load and precrack size³. It can be seen from Figure 9 that the fracture toughness is insensitive to the crack size, which is consistent with the result obtained from the indentation method, since most values are within ± 1.0 standard deviation of the mean ($=5.18 \text{ MPa}/\text{m}$).

This result of a flat R-curve behavior for the composite material indicates that the whisker addition to the Si_3N_4 matrix did not result in any favorable effect on crack growth resistance. This result is consistent with the previous work for another 30 vol % SiC whisker/ Si_3N_4 composite material where the toughening exponent was obtained to be $m = 0.03$ ¹⁵. Rising R-curve behavior has been observed with some varying degree for ceramic materials such as Al_2O_3 ($m=0.13$)⁹, 25 wt % SiC whisker reinforced Al_2O_3 's ($m=0.08$)¹⁶, and in-situ toughened Si_3N_4 's ($m=0.1-0.2$)^{17,18}.

Table I. Summary of fracture resistance parameters for monolithic and 30 vol % SiC whisker-reinforced silicon nitrides

Material	Best-Fit Slope in $\text{Log } \sigma_f$ - $\text{Log } P$ Curve*	Fracture Resistance Parameters	
		m	k
Monolithic	-0.30(0.03)	0.04(0.01)	6.77
Composite	-0.34(0.04)	0	5.18

* The units are in MPa for σ_f , and N for P .

† The units are in MPa/m for K_{Ic} , and meter for c in Eq.(2).

‡ The parenthesis indicates ± 1.0 standard deviation.

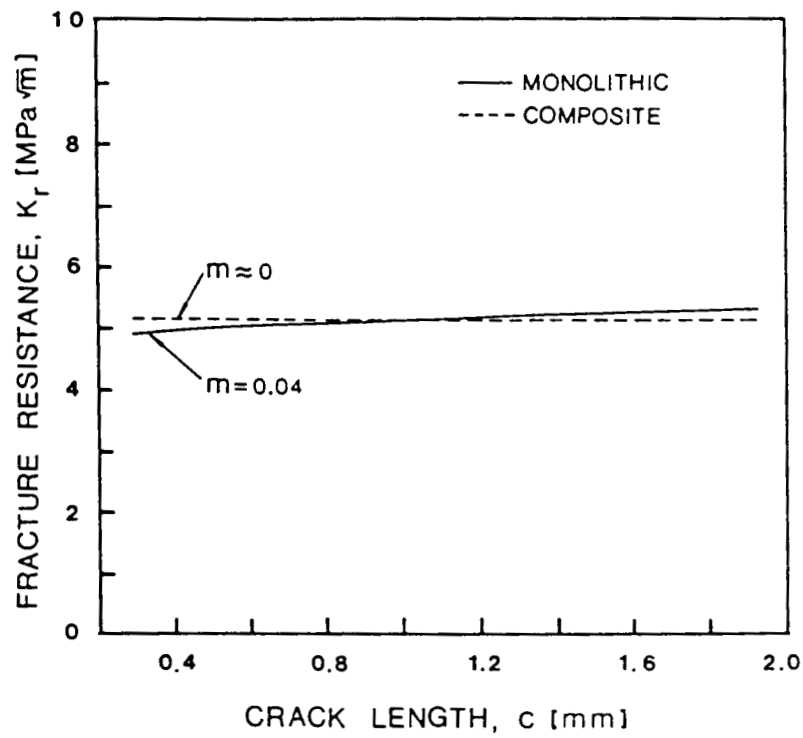


Figure 8. Predicted fracture resistance curves for composite and monolithic materials.

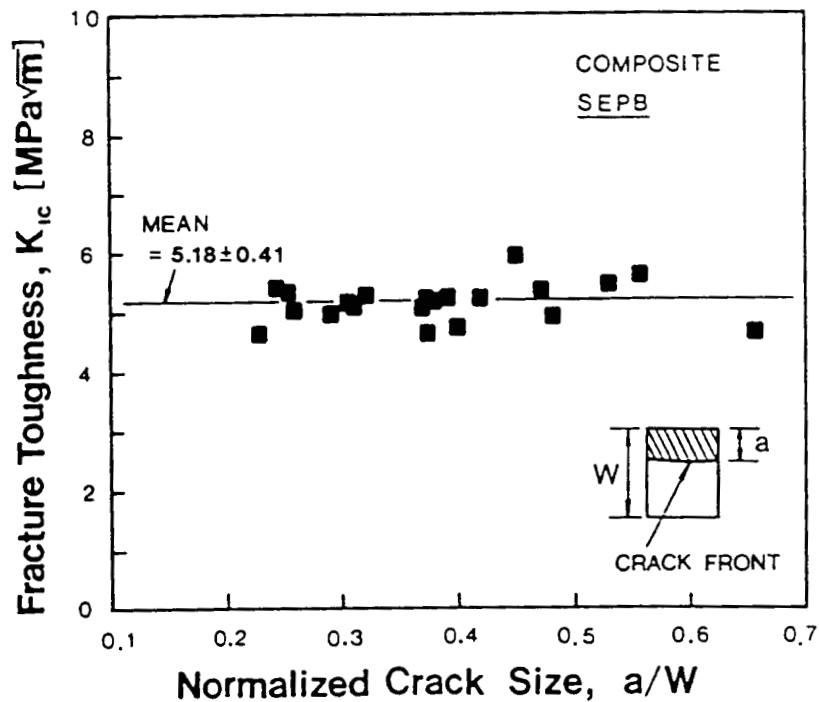


Figure 9. Fracture toughness of composite material as a function of normalized crack size (a/W) measured from the SEPB specimens at 25 °C.

(D) Fatigue Susceptibility

A summary of the dynamic fatigue results is presented in Table II. The stressing rate ($\dot{\sigma}$) was calculated using the relation $\dot{\sigma} = 3(L_o - L_i)P/[2bh^2]$ where L_o and L_i are the outer and inner spans of the test fixture, respectively, P is the loading rate, and b and h are the specimen width and height, respectively. Table III summarizes the parameters n , B and A evaluated from these data based on Eq. (3). The parameters B and A for the indented specimens were not estimated due to the unknown inert strength (S_i) data.

Figure 10 shows the dynamic fatigue results of the as-received composite specimens. The decrease in fatigue strength with decreasing stressing rate indicates that stress corrosion due to fatigue (stable crack growth) occurred at all test temperatures. The fatigue susceptibility parameter n decreased rapidly from 88.1 to 20.1 as the corresponding temperature increased from 1100 to 1300 °C, which indicates that fatigue susceptibility increases very rapidly with increasing temperature. It is also important to note that a transition in the dynamic fatigue curve occurs at the lowest stressing rate of $\dot{\sigma} = 2.0$ MPa/min at 1300 °C, resulting in a very low value of $n = 5.8$. The transition was attributed to creep deformation enhanced by both the high temperature and very slow stressing rate. Appreciable creep strain was also observed for the specimens tested at this condition. It should be emphasized that such transition should be taken into account when reliability and lifetime prediction (design methodology) are made for structural components, as mentioned by Fett and Munz¹⁹. This requires a more in-depth understanding of both stable crack growth and creep behaviors, particularly under a constant loading rate condition.

The results of dynamic fatigue tests of the monolithic material are presented in Figure 11. As seen for the composite material (Fig. 10), the fatigue strength decreases with both increasing stress rate and increasing temperature. However, the fatigue parameter n for the monolithic decreased monotonically from 50.8 to 40.4 with increasing temperature from 1100 to 1300 °C. This behavior contrasted to that of the composite material which exhibited a transition in the fatigue curve at 1300 °C due to creep. Although the monolithic material exhibited creep at the lowest stressing rate of $\dot{\sigma} = 2$ MPa/min, it did so less than the composite material.

Results of dynamic fatigue tests of the indented composite specimens at 1100 °C are presented in Figure 12. For comparison the fatigue strength data of the as-received specimens was included. The parameter ($n=50.8$) for the indented specimens is lower than that ($n=88.1$) obtained from the as-received specimens. In other words, the fatigue resistance of inherent flaws is greater than that of artificial flaws produced by indentation. This indicates that fatigue behavior of the well-defined cracks is somewhat different from that of the inherent flaws, implying that the two flaw systems may not be identical to each other. It is thought that the inherent flaws have a more ill-defined crack configuration as compared to the indent crack, thereby resulting in a more deviated crack propagation behavior.

Table II. Summary of dynamic fatigue results of monolithic and 30 vol % SiC whisker-reinforced silicon nitrides

Temp (°C)	Specimen Condition	Stressing Rate, $\dot{\sigma}$ (MPa/min)	# of specimens	Composite	Monolithic
				Fracture Strength σ_f (MPa)	Fracture Strength σ_f (MPa)
1100	As-received	2	5	598.9(63.1)*	3 609.2(35.1)
1100	AS-received	20	5	584.5(82.0)	4 649.0(45.3)
1100	As-received	200	5	615.9(54.8)	3 675.3(41.8)
1100	As-received	2000	5	641.5(33.8)	4 697.4(5.1)
1200	As-received	2	4	463.0(106.4)	3 537.2(48.4)
1200	As received	2000	4	558.9(19.5)	4 621.5(63.4)
1300	As-received	2	4	318.0(14.1)	4 513.3(49.3)
1300	As-received	20	3	445.2(44.2)	4 523.3(47.3)
1300	As-received	200	3	487.6(48.5)	4 596.4(75.1)
1300	As-received	2000	4	553.9(38.0)	4 591.4(21.0)
1100	Indented ^{&}	2	3	351.5(4.8)	
1100		20	3	353.1(11.3)	
1100	Indented	200	3	372.4(11.1)	
1100	Indented	2000	3	400.5(26.9)	

* The numbers in parenthesis indicate ± 1.0 standard deviation.

& Indent load applied for the indented specimens = 98 N.

· Test environment was ambient air.

Table III. Summary of fatigue parameters of monolithic and 30 vol % SiC whisker-reinforced silicon nitrides

Fatigue parameter	Temperature (°C)					
	1100		1200		1300	
	comp	mono	comp	mono	comp	mono
n	88.1	50.8	35.7	46.4	20.1*/5.8#	40.43
Ln B (MPa ² min)	-1.0219	6.0924	0.2809	0.5762	3.9784/11.6921	0.4346
Ln A (m/min)	-151.3	-93.51	-61.4	-86.1	-39.6/-19.1	-75.6

* Evaluated based on the stressing rates of 2000, 200 and 20 MPa/min.

Evaluated based on the stressing rates of 20 and 2 MPa/min.

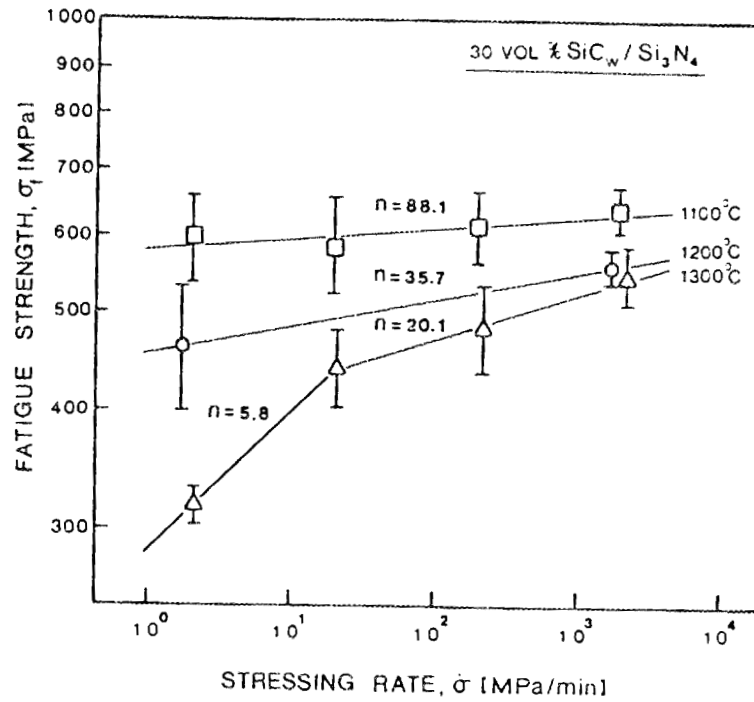


Figure 10. Dynamic fatigue data for 30 vol % SiC whisker-reinforced silicon nitride material (as-received condition) in ambient air.

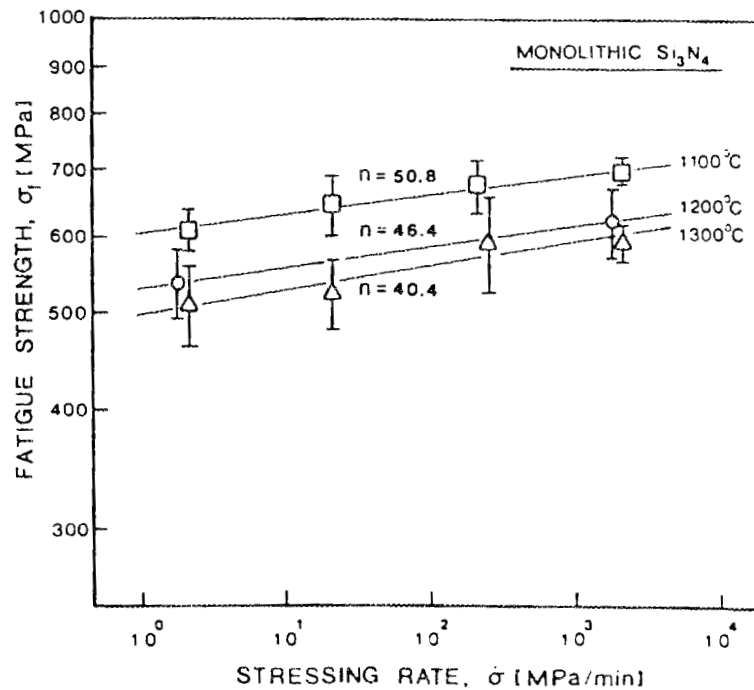


Figure 11. Dynamic fatigue data for monolithic silicon nitride material (as-received condition) in ambient air.

A typical example of the fracture surface for the specimen tested at 1300 °C with a stressing rate of 2.0 MPa/min is shown in Figure 4. Note the extensive glassy phases in the stable crack growth region that probably occurred by oxidation.

Based on these dynamic fatigue results, it can be concluded that whisker addition to monolithic Si₃N₄ deteriorates the inherent fatigue resistance. This contrasts with results of strength, fracture toughness, and crack growth resistances described earlier, for which no appreciable differences were found between the two materials.

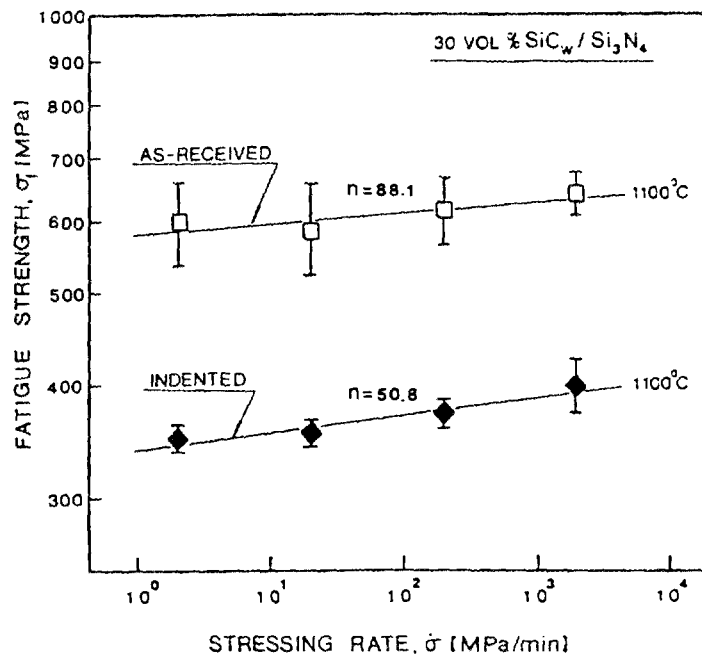


Figure 12. Dynamic fatigue data for indented composite specimens in ambient air. The fatigue data for as-received specimens is included for comparison.

(E) Oxidation

Results from X-ray diffraction of the oxidized surfaces are given in Table IV. Silica was present on the surfaces in the form of α -cristobalite after the 1000 and 1200 °C exposures. The higher temperature form of tridymite was present on the 1400 °C samples. Silicon carbide was not detected on the surface of SiC whisker toughened Si₃N₄ after 1400 °C exposure.

Bend strength results of oxidized specimens are shown in Figure 13. The room temperature bend strengths of the 1200 and 1400 °C toughened Si₃N₄ samples were statistically different (447±28 MPa vs 555±73 MPa). Fractography was conducted with scanning electron microscopy. A summary of the nature of the origins is found in Table V.

Table IV. X-Ray Diffraction Results

Sample	Exposure Temperature	Phases Present
Toughened Si_3N_4	1000°C	$\beta\text{-Si}_3\text{N}_4$, $\alpha\text{-Si}_3\text{N}_4^*$, SiC, $\alpha\text{-Cristobalite}$
Monolithic Si_3N_4	1000°C	$\beta\text{-Si}_3\text{N}_4$, $\alpha\text{-Cristobalite}$
Toughened Si_3N_4	1200°C	$\beta\text{-Si}_3\text{N}_4$, $\alpha\text{-Si}_3\text{N}_4^*$, SiC, $\alpha\text{-Cristobalite}^*$
Monolithic Si_3N_4	1200°C	$\beta\text{-Si}_3\text{N}_4$, $\alpha\text{-Cristobalite}^*$
Toughened Si_3N_4	1400°C	$\beta\text{-Si}_3\text{N}_4$, $\alpha\text{-Cristobalite}$, Tridymite
Monolithic Si_3N_4	1400°C	$\beta\text{-Si}_3\text{N}_4$, $\alpha\text{-Cristobalite}$, Tridymite

* Denotes minor phase.

Table V. Nature of Failure Origins (Room Temperature 4-Pt Bend)

Sample	Exposure Temperature	Flaw Type*	Number of Occurrences
Toughened Si_3N_4	1000°C	VP	4
		SP	1
Monolithic Si_3N_4	1000°C	SP	4
		ND	1
Toughened Si_3N_4	1200°C	SP	4
		VP	1
Monolithic Si_3N_4	1200°C	VP	1
		VG	1
		SG	1
		ND	2
Toughened Si_3N_4	1400°C	SP	5
Monolithic Si_3N_4	1400°C	SP	3
		VP	2

* Surface grain (SG); Surface pore (SP); Volume Grain (VG); Volume Pore (VP); Nature not determined (ND).

In the composite specimens oxidized at 1000 °C, areas of volume porosity 20-40 μm in diameter acted as fracture origins. These processing flaws were much larger than the surface pores (5-10 μm) that acted as origins in the 1000 °C monolithic samples. Fractography did not explain the apparent increase in strength of toughened Si_3N_4 after exposure to 1400 °C versus 1200 °C. Surface flaw size was approximately 30-50 μm for all samples after exposure at both of these temperatures.

In summary, the monolithic Si_3N_4 material retained its original room temperature strength after 500 hours of oxidation up to 1200 °C, but lost 41 % of that value after exposure at 1400 °C. By comparison, the toughened material retained its original room temperature strength after 500 hours at 1000 °C, but lost 37 % of that strength after exposure at 1200 °C. Fracture originated primarily at surface pores or surface oxidation pits. Volume pores dominated only in the toughened Si_3N_4 after 1000 °C exposure.

It is concluded that the toughened Si_3N_4 exhibited no performance gain over monolithic Si_3N_4 in this series of tests.

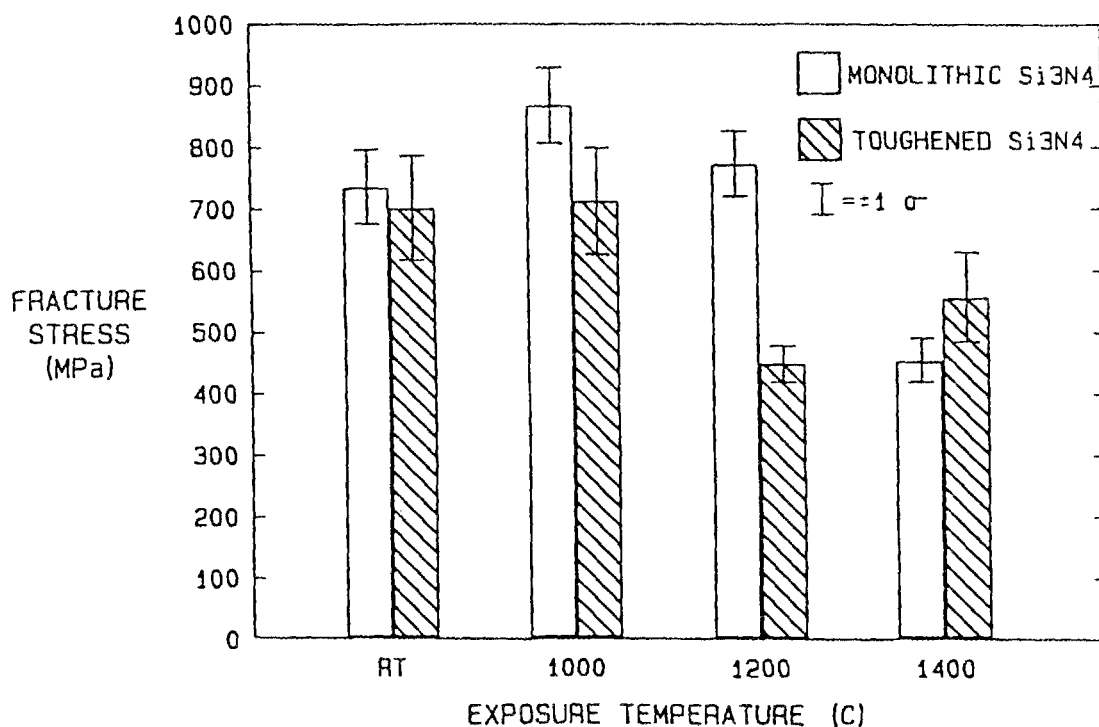


Figure 13. Room temperature four-point bend strength of monolithic and 30 vol % SiC whisker-reinforced silicon nitride after 500 hours exposure in flowing oxygen at 1000, 1200, and 1400 °C. Error bar indicates ± 1.0 standard deviation.

(F) Creep

Creep strain as a function of time at 350 MPa is shown in Figure 14. It should be noted that the neutral axis was not assumed to shift toward the compression side during the creep deformation. The resulting steady state creep rate, based on the equation

$$\dot{\epsilon} = \alpha \sigma^N \quad (6)$$

is illustrated as a function of applied stress in Figure 15. The apparent strain and creep rates were substantially higher for the composite material. The monolithic material exhibited a creep parameter, $N = 0.99$, typical of values given in the literature for silicon nitrides. The composite material, however, exhibited a much higher parameter, $N = 5.61$, indicating a poor resistance to creep at 1250 °C. It has been reported by Nixon et al.²⁰ that SiC whiskers in a Si_3N_4 matrix did not directly contribute to the kinetics of compressive creep. However, the addition of whiskers did enhance compressive creep because of the additional SiO_2 contributed by the whiskers. The amorphous grain boundary phase ultimately controlled creep by grain boundary sliding.

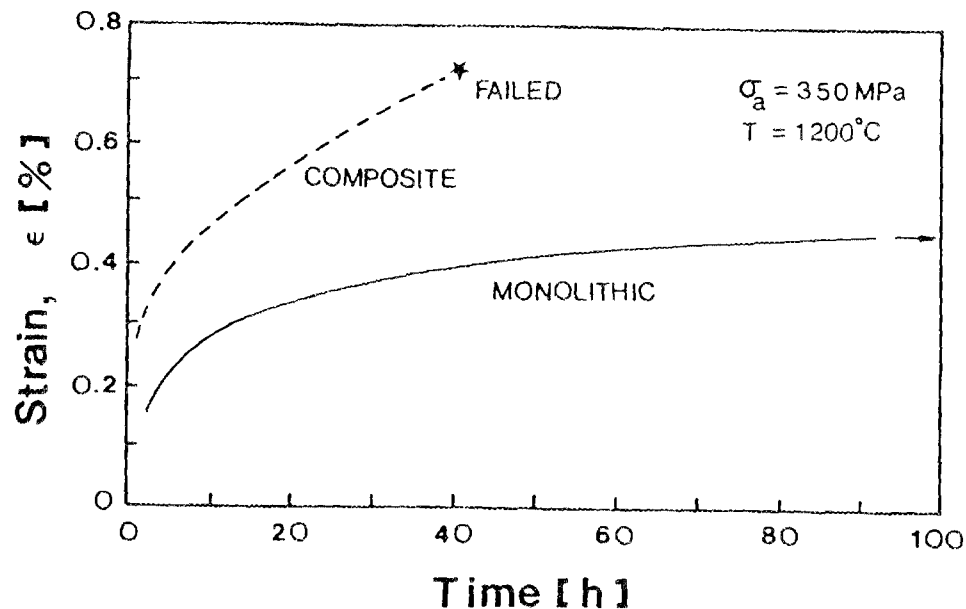


Figure 14. Creep strain as a function of time at 1250 °C and 350 MPa.

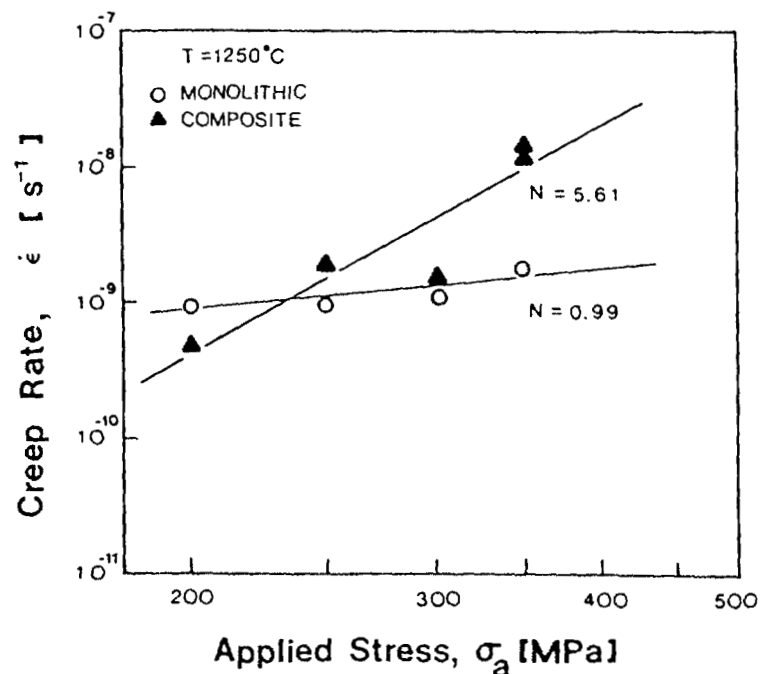


Figure 15. Creep rate as a function of applied stress at 1250 °C.

Conclusions

The monolithic material used in this study exhibited very good fatigue resistance and reasonable strength, toughness, and creep as compared to available monolithic Si_3N_4 's. The addition of 30 vol % SiC whiskers to the monolithic Si_3N_4 did not substantially improve the strength, fracture toughness, or crack growth resistance. However, the whisker addition did deteriorate the fatigue, creep, and oxidation resistance inherent to the monolithic material.

References

1. J. A. Salem, "Strength and Toughness of Monolithic and Composite Silicon Nitrides," NASA T.M. 102423 (1990).
2. D. Munz, R. T. Bubsey and J. L. Shannon, Jr., "Fracture Toughness Determination of Al_2O_3 Using Four-Point-Bend Specimens with Straight Through and Chevron-Notches," *J. Am. Ceram. Soc.* 63(5-6), 300 5 (1980).
3. T. Nose and T. Fujii, "Evaluation of Fracture Toughness for Ceramic Materials by a Single-Edge-Pre-cracked-Beam Method," *J. Am. Ceram. Soc.* 71(5), 328 33 (1988).
4. K. F. Krause, "Rising Fracture Toughness for the Bending Strength of Indented Alumina Beams," *ibid.* 71(5), 338 43 (1988).

5. A. G. Evans, "Slow Crack Growth in Brittle Materials Under Dynamic Loading Conditions," *Int. J. Fract.* 10, 251 9 (1974).
6. J. E. Ritter, in *Fracture Mechanics of Ceramics*, Plenum Press, NY, Vol. 4, 667 86 (1978).
7. A. G. Evans and S. M. Wiederhorn, "Proof Testing of Ceramic Materials-An Analytical Basis for Failure Prediction," *Int. J. Fract.*, 10, 379 92 (1974).
8. G.W. Hollenburg, G.R. Terwilliger, and R.S. Gordon, "Calculation of Stresses and Strains in Four-Point Bending Creep Tests," *J. Am. Ceram. Soc.*, 54(4), 196 9 (1971)
9. J. E. Ritter, N. Bandyopadhyay, and K. Jakus, *Am. Ceram. Soc. Bull.* 60, 798 (1981).
10. P. F. Becher and G. C. Wei, *J. Am. Ceram. Soc.* 67c-267 (1984)
11. T. N. Tieggs and P. F. Becher, in *Tailoring Multiphase and Composite Ceramics*, Materials Science Research, 20, 639, Plenum Press, New York 1986.
12. P. F. Becher, C. H. Hsueh, P. Angelini, and T. N. Tieggs, *J. Am. Ceram. Soc.* 71, 1050 (1988).
13. J. J. Petrovic, J. V. Milewski, D. L. Rohr, and F. D. Gac, *J. Mater. Sci.* 20, 1167 (1985).
14. J. Homeny, W. L. Vaughn, and M. K. Ferber, *J. Am. Ceram. Soc.* 73, 394 (1990).
15. S. R. Choi and J. Salem, to be presented in the Symposium on Composites sponsored by Am. Ceram. Soc., Orlando, Fla., Nov 12-15, 1990.
16. R. F. Krause, E. R. Fuller, and J. F. Rhodes, *J. Am. Ceram. Soc.* 73, 559 (1990).
17. J. E. Ritter, S. R. Choi, K. Jakus, P. J. Whalen, and R. G. Rateick, to be published in *J. Mater. Sci.* (1991).
18. C. W. Li and Y. Yamanis, *Ceram. Eng. Sci. Proc.* 10, 632 (1989).
19. T. Fett and D. Munz, in *Methods for Assessing the Structural Reliability of Brittle Materials*, ASTM STP 844, American Society for Testing and Materials, Philadelphia, 1984.
20. R.D. Nixon, D.A. Koester, S. Chevacharoenkul, and R.F. Davis, in *Composites Science and Technology* 37, 313 28 (1990).

Status of Milestones

Milestones are on time.

Publications

J. A. Salem, J. M. Manderscheid, M. R. Freedman, and J. P. Gyekenyesi, "Reliability Analysis of a Structural Ceramic Combustion Chamber," NASA T.M. 103264 (1990).

Life Prediction Methodology

D. L. Vaccari & P. K. Khandelwal (Allison Gas Turbine Division of General Motors Corporation)

Objective/scope

The objective of this project is to develop and demonstrate the necessary nondestructive examination (NDE) technology, materials data base, and design methodology for predicting useful life of structural ceramic components of advanced heat engines. The analytical methodology will be demonstrated through confirmatory testing of ceramic components subject to thermal-mechanical loading conditions similar to those anticipated to occur in actual vehicular service. The project addresses fast fracture, slow crack growth, creep, and oxidation failure modes.

Technical progress

MOR bars

During this reporting period, all the PY6 MOR bars needed for this program were received from GTE. The bars are nominally 3 x 4 x 50 mm in size and represent Specimen 'B' of MIL-STD-1942(MR). A total of 850 bars have been fabricated. In addition to the bars intended for flexural testing, five MOR bars with random laser-drilled hole patterns were produced. They are being used as reference standards for calibrating and fine tuning the NDE equipment. The bars contain a variety of hole sizes and depths. The bars have been examined using Allison microfocus radiography. Initial results indicate that a 50 to 100 micron surface hole can be found. Attempts to further refine the inspection technique are continuing in hopes of finding a 25 micron flaw or smaller.

The reference standard bars were also sent to Sonoscan along with the first batch of MOR test bars for inspection using the C-SAM ultrasonic imaging system. The surface of the specimens was characterized by a 100 MHz focused transducer. The reference specimens were inspected along with the other specimens to ascertain the repeatability of the inspection techniques. Figures 1 and 2 show C-scans of reference standard bars containing holes 100 microns and 50 microns in diameter, respectively. Holes of 25 micron diameter were also detected with this inspection method. The technique has proven the ability to find these small holes.

A total of 20 PY6 MOR bars have now been tested at room temperature as shown in Table 1. The specimens were tested with an inner load span of 20 mm and an outer support span of 40 mm. The average failure strength was 771.4 MPa (111.9 ksi) with a standard deviation of 118.9 MPa (17.2 ksi). Preliminary fractographic analysis indicates most failures originated on the surface. Prior to testing, these bars had been inspected with both ultrasonic and radiographic techniques.

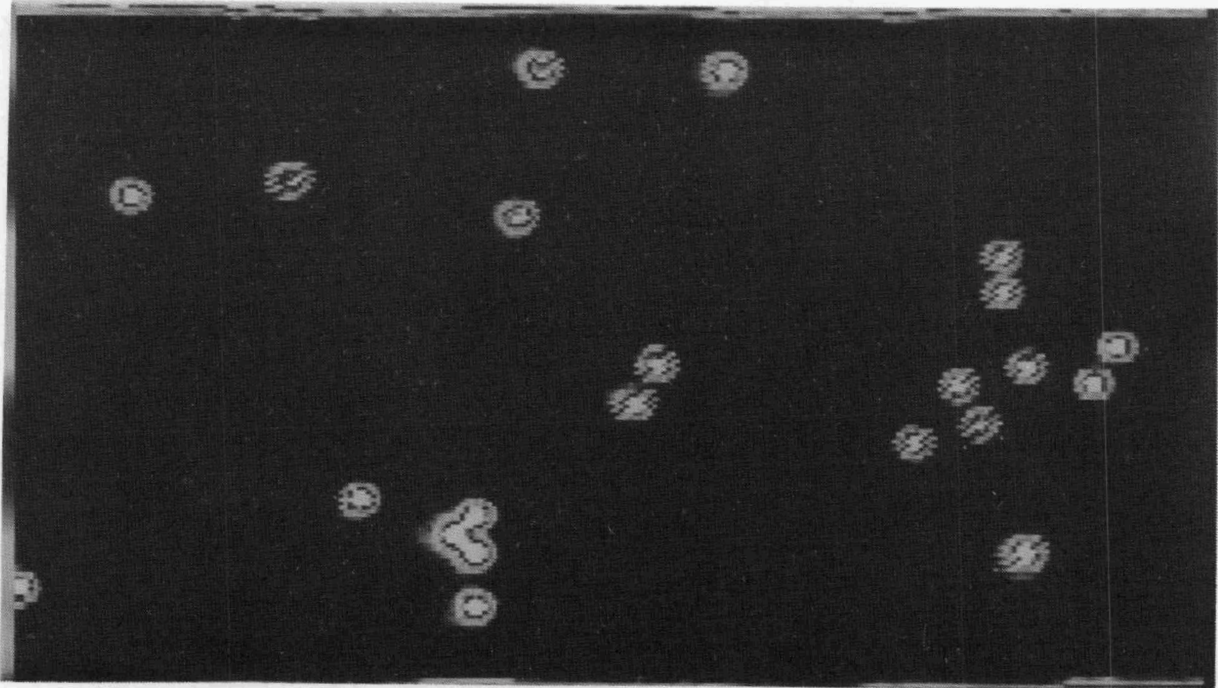


Figure 1. C-scan of reference specimen with 100 micron diameter surface holes.

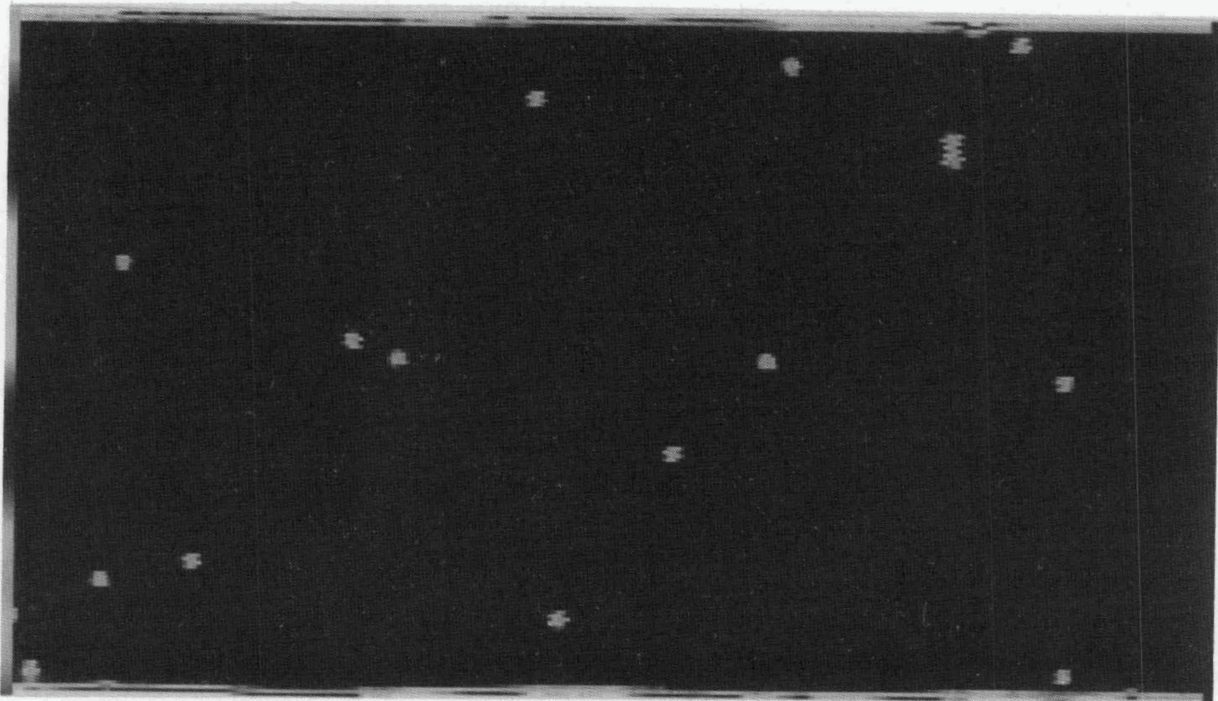


Figure 2. C-scan of reference specimen with 50 micron diameter surface holes.

Effort is underway attempting to correlate the fracture origin with observed NDE results.

Tensile bars

Tensile testing of the PY6 material has commenced this reporting period. The specimen is an injection-molded, cylindrical button-head bar having a 55.9 mm (2.20 in.) long gage section with a 4.762 mm (0.1875 in.) diameter. Testing is being performed by Southern Research Institute. Initial results, performed at room temperature, are shown in Table 2. A previous set of five isopressed bars had been tested to verify that the specimen design would give good test results (i.e. failures would occur in the gage section and not the button head). One of the five isopressed bars, and as shown in Table 2, one of the six injection molded bars failed in the button head. Figure 3 shows the post-test results of four of the injection molded bars. Only the injection molded bars are formally being studied in this program, and these initial results suggest that the specimen design will indeed provide good test data.

Figure 4 shows the scanning electron micrographs of the failure surface for specimen 103B. The fracture origin was an internal flaw. Figure 5 is the energy dispersive x-ray analysis of the failure site. It shows that the internal flaw was an iron inclusion. The Au and Pd spikes on the plot are artifacts of a thin gold coating applied to the surface of the fracture face.

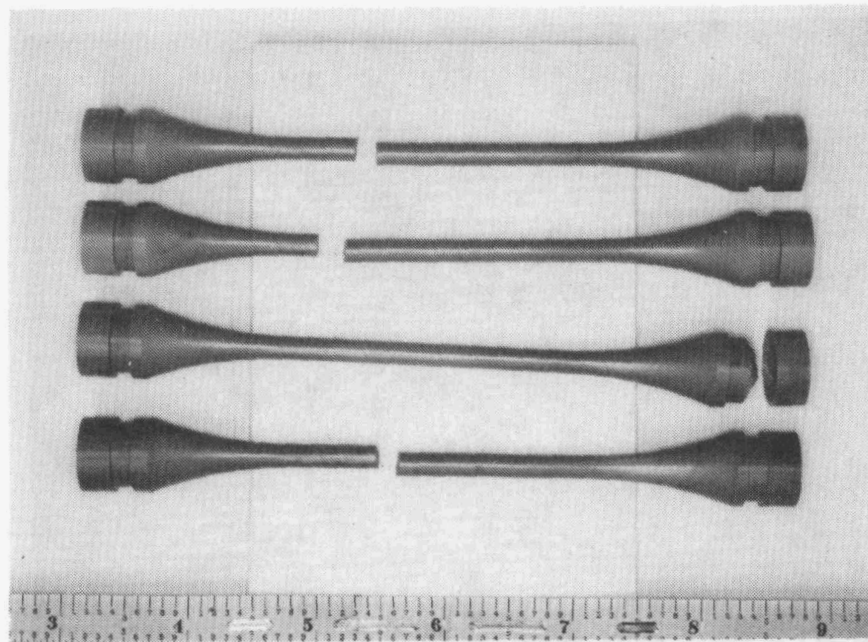


Figure 3. Post-test condition of tensile bars.

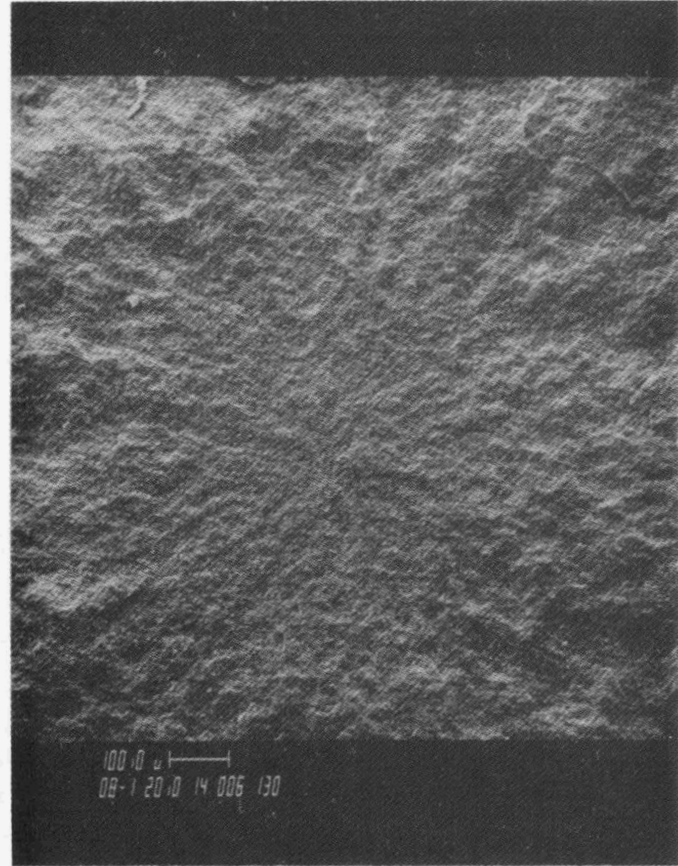
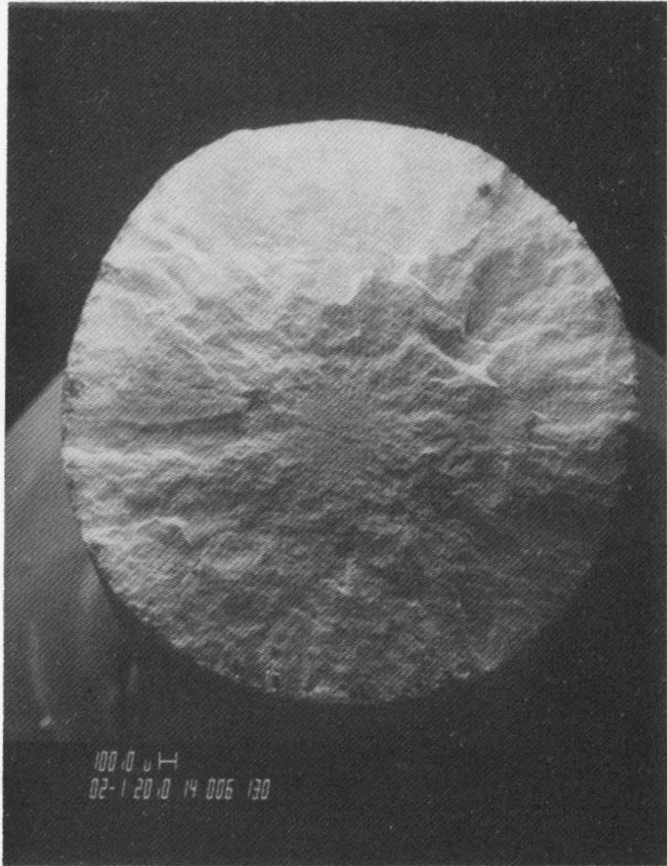


Figure 4. Tensile gage section fracture surface of specimen 103B at 20X and 80X.

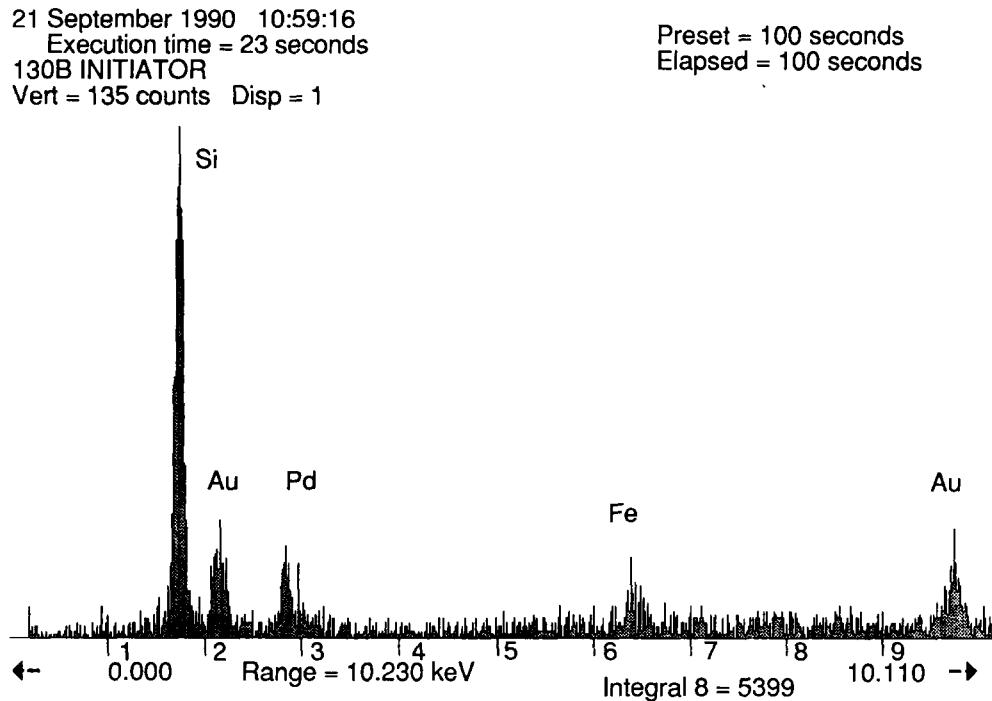


Figure 5. Energy dispersive x-ray analysis of specimen 103B failure site.

Figure 6 shows the scanning electron micrographs of the failure surface for specimen 93A. The fracture originated from a surface flaw on this specimen. Figure 7 shows the energy dispersive x-ray analysis of the failure site. No iron was detected. Again, note that the Au and Pd spikes are the result of a thin gold coating applied to the fracture face.

Another 35 tensile bars are available for testing with an additional 120 bars in final machining at GTE that will be shipped to Allison soon. Another 200 bars are currently being molded.

Dog-bone specimens

Twenty-one PY6 billets of 60 x 50 x 15 mm (2.362 x 1.968 x 0.590 in.) nominal size were received from GTE to fabricate dog-bone specimens to measure creep behavior at the National Institute of Standards and Technology (NIST). The billets were examined with radiography, and then shipped to NIST for the fabrication of the specimens. After fabrication, they will be inspected by ultrasonics and then tested.

Circular disks

The first 70 circular disks, to be used by Battelle in biaxial testing, are in final machining and will be delivered to Allison within a week. The final 70 disks are in process and should be received by Allison by the end of October. Five

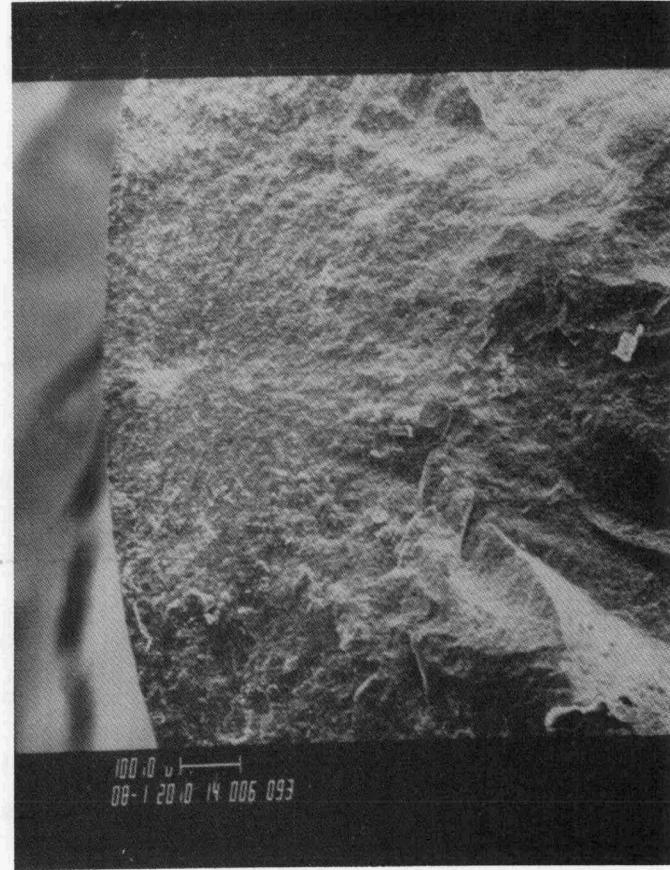
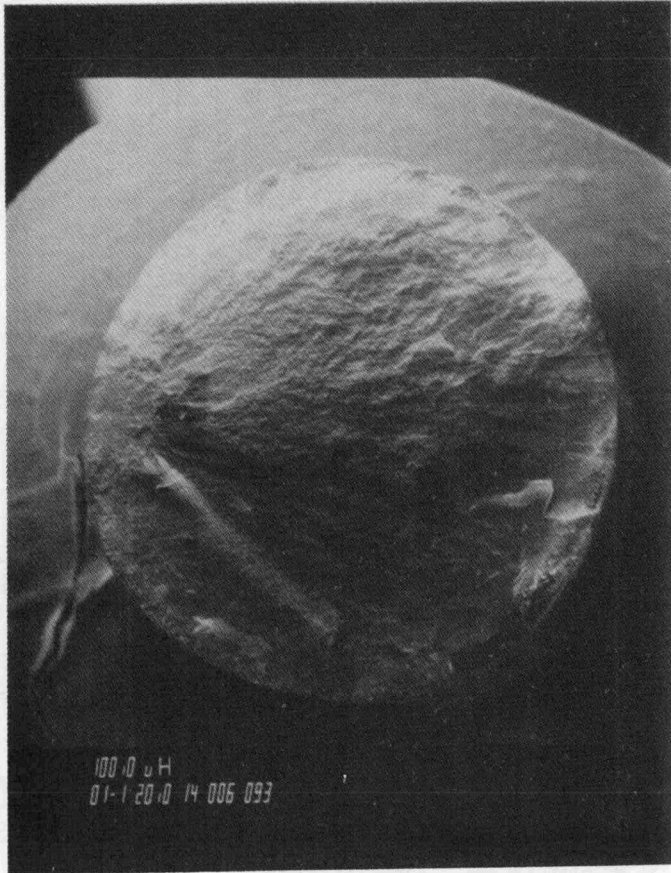


Figure 6. Tensile gage section fracture surface of specimen 93A at 10X and 80X.

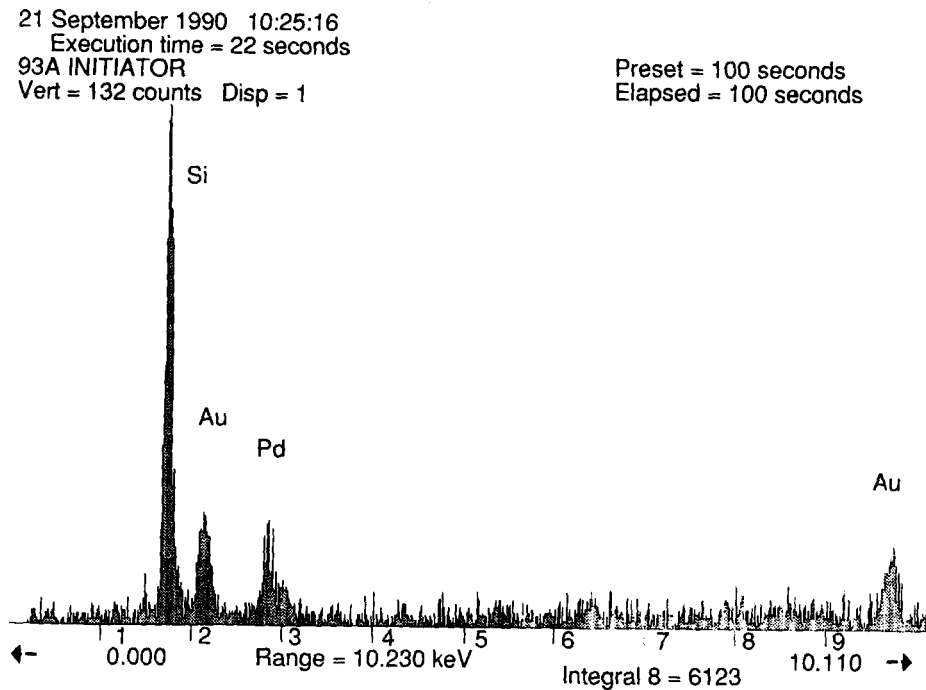


Figure 7. Energy dispersive x-ray analysis of specimen 93A failure site.

MOR bars have been sent to Battelle. They will be used for some preliminary studies aimed at providing an initial idea of how the PY6 material behaves.

NDE laboratory enhancement

A 100 MHz computer-controlled ultrasonic imaging system for Allison is currently being developed at Automated Systems Div. Panametrics, Ithaca, New York. This system will consist of a 100 MHz pulser/receiver and a single shot peak detector, a 50 MHz 0.5 in. focal length surface wave transducer (F # = 0.8), AST 386/20 MHz based data acquisition and imaging system, and a Seiko Model 5504 color printer. This printer will be multiplexed with the microfocus x-ray signal processing system which is currently being developed at Allison.

Status of Milestones

- 322201: Computer Implementation of Initial Failure Models - complete.
- 322202: Initiation of MOR Testing - accomplished this reporting period.
- 322203: Initiation of Tensile Testing - accomplished this reporting period.
- 322204: Initiation of Biaxial Testing - on schedule.
- 322205: Initiation of Confirmatory Testing - on schedule.
- 322206: Completion of All Specimen Testing - on schedule.
- 322207: Finalization/Verification of Computer Code - on schedule.
- 322208: Draft Final Report - on schedule.
- 322209: Final Report - on schedule.

Table 1. MOR test results.

<u>specimen number</u>	<u>Width --mm</u>	<u>Thick --mm</u>	<u>Load --N</u>	<u>Strength --MPa</u>	<u>Strength --ksi</u>
34.1396	4.028	3.007	747.3	615.4	89.3
34.1397	4.026	3.012	849.6	697.7	101.2
34.1398	4.028	3.007	849.6	699.5	101.5
34.1399	4.031	3.002	1005.3	830.1	120.4
34.1400	4.034	3.007	987.5	812.1	117.8
34.1401	4.031	3.000	947.5	783.7	113.7
34.1402	4.034	3.007	1112.1	914.5	132.6
34.1403	4.031	3.007	1045.3	860.2	124.8
34.1404	4.028	3.015	987.5	809.0	117.3
34.1405	4.028	3.010	1058.7	870.3	126.2
34.1406	4.028	3.010	1063.1	873.9	126.8
34.1407	4.028	3.012	943.0	773.9	112.2
34.1408	4.026	3.012	822.9	675.8	98.0
34.1409	4.026	3.010	885.2	728.1	105.6
34.1410	4.031	3.005	511.5	421.7	61.2
34.1411	4.031	3.007	822.9	677.2	98.2
34.1412	4.034	3.007	920.8	757.3	109.8
34.1413	4.031	3.007	934.1	768.7	111.5
34.1414	4.031	3.005	1138.7	938.7	136.1
34.1415	4.031	3.005	1116.5	920.3	133.5

Table 2. Tensile test results.

<u>Specimen number</u>	<u>Strength --MPa</u>	<u>Strength --ksi</u>	<u>Failure mode</u>	<u>Remarks</u>
76A	418.1	60.7	internal flaw	in gage
64A	483.1	70.2	internal/surface	in gage
93A	357.7	51.9	surface flaw	in gage
103B	505.8	73.4	internal flaw	in gage
83B	368.7	53.5	internal flaw	in gage
53B	>434.4	>60.0	head failure	-

Publications

None

Life Prediction Methodology

A. Comfort, J. Cuccio, and H. Fang (Garrett Auxiliary Power Division, Allied-Signal Aerospace Company)

Objective/Scope

The feasibility of using ceramic components and the application of probabilistic design methods were first demonstrated by Garrett in the DARPA/Navy Ceramic Engine and DOE/NASA AGT101 programs. These programs highlighted the need for improved material properties and advanced design methods to assure adequate ceramic component life in engine use. Ceramic manufacturers are improving material properties through their own R&D efforts as well as Government-funded programs in processing ceramics (e.g., DOE/ORNL Ceramic NDE/Processing program). Garrett Auxiliary Power Division (GAPD) has defined a program to develop the methodology required to adequately predict the useful life of ceramic components used in advanced heat engines.

GAPD's approach to ceramic life prediction consists of comprehensive testing of various specimen geometries under both uniaxial and multiaxial loads at different environmental conditions to determine the strength-controlling flaw distributions and to identify various failure mechanisms. This information will be used to develop the flaw distribution statistical models and material behavior models for fast fracture, slow crack growth, creep deformation, and oxidation. As sub-routines, these models will be integrated with stress and thermal analyses into a failure risk integration analytical tool to predict the life of ceramic components. The methodology developed will be verified (for completeness and accuracy) by analytically predicting the life of several ceramic components and testing these components under stress and temperature conditions encountered in ceramic turbine engines.

Technical Highlights

Material Testing and Analysis

H. Fang

Material Testing

Test specimen deliveries from Norton/TRW Ceramics (NTC) are on schedule. All specimens are NT154 silicon nitride, processed under identical conditions and finish machined and heat treated by NTC. Selected specimens will be notched and precracked for testing. All specimens will be subjected to visual inspection, laser marking, and NDE (which may include fluorescent penetrant, radiography, and ultrasonic inspection) before testing.

The square fracture toughness bars have been chevron notched and are awaiting testing. To monitor process consistency, the large 4-point bend and tensile fast fracture specimen orders have been split into three batches. The first batch of these specimens has been received and is being inspected.

Visual inspection of the tensile specimens revealed that most have chips at the top and underside of the buttonhead. The chips at the underside of the buttonhead are of concern, because they may contact the split collet in the grip during testing and may cause buttonhead failures. The chips occurred during machining; corrective action has been taken.

Development of a pre-cracking technique for diametral compression disks is in progress at the University of Utah, under subcontract with Professor Dinesh Shetty. Chevron-notched diametral compression disks are being used to generate the mixed-mode fracture toughness parameters K_{IC} and K_{IIC} , as shown in Figure 1. To date, Professor Shetty has polished and chevron notched six NT154 disks. He has also deposited metallic grids across the chevron notches to monitor crack growth by the potential drop method, in order to stop the pre-cracking after the crack has propagated beyond the chevron notch. This technique has previously been verified with alumina ceramics, but has not been applied to silicon nitride.

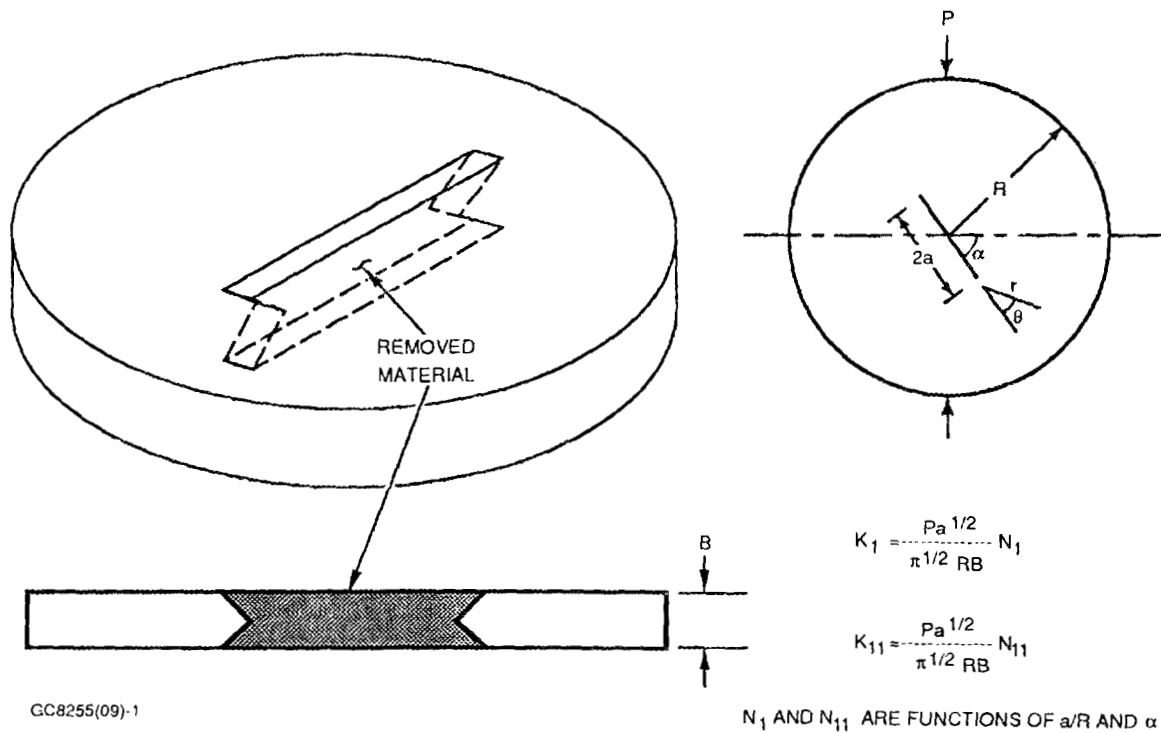


Figure 1. Chevron Notched Compression Disk Specimens Are Being Used to Generate Mixed-Mode Fracture Toughness Parameters, K_{IC} And K_{IIC} .

Data Analysis and Methodology Development
J. Cuccio, D. Wu, A. Peralta, and N. Menon

Ceramic structural reliability has traditionally focused on predicting the probability of failure of a component from the calculated Weibull parameters describing the material strength. However, these parameters are only estimates, due to the sample and specimen sizes typically used in material testing. In addition, the large scatter in material properties also contributes to uncertainty in the Weibull parameters. Consequently, only estimates of the probability of failure are possible. Thus, there is a need to assign confidence limits to the predicted probability of failure.

Confidence limits on component reliability prediction is a function not only of the sample size, but of other variables as well. Figure 2 summarizes the variables considered to have a significant effect in the prediction of confidence limits. Three methods are being considered to predict these limits:

- a) Root-Strap Approach
- b) Maximum Likelihood Ratio Approach
- c) Fast Probability Integration Approaches

	A	A B	A B C	A B C E	A B C E F	A B C E F G
ANALYTICAL APPROACH						
MULTIAXIAL RISK INTEGRATION - STRESS BASED (EVANS) - FLAW BASED (BATDORF)	■	■	■	○	○	○
CONFIDENCE CALCULATIONS - BOOT-STRAP - LIKELIHOOD RATIO - FAST PROB. INTEGRATION	■	○	○			

■ IMPLEMENTED	A - SIZE EFFECTS
○ APPROACH DEFINED	B - MULTIAXIAL STRESSES
	C - MULTIPLE FLAW DISTRIBUTIONS
	D - CONFIDENCE INTERVALS
	E - FLAW ANISOTROPY
	F - TEMPERATURE GRADIENTS
	G - TIME DEPENDENT MECHANISMS

GC8491(03)-2A

Figure 2. Development Status of Probabilistic Methods, Listed in Order of Development.

Multiaxial fast fracture reliability methods are also being evaluated. The Batdorf^{(1)*} and the Evans⁽²⁾ approaches are being considered. It has been shown [Johnson and Tucker⁽³⁾, Chao and Shetty⁽⁴⁾] that these approaches provide equal predictions of multiaxial fracture probabilities. Since they provide equivalent predictions, both methods are being compared for computational efficiency and applicability to anisotropic flaw distributions.

Life Prediction Verification Testing

As part of the effort to verify life prediction methods, spin disk tests are planned. Environmental exposure experiments are being performed under the GAPD Advanced Turbine Technology Applications Project (ATTAP) on NT154 flexure bars to identify acceptable atmosphere conditions (oxygen/nitrogen partial pressure window) for the inert crack growth and spin disk tests. These tests revealed significant weight loss and strength degradation, probably due to 1) Si_3N_4 dissociation at low nitrogen partial pressures, and 2) grain boundary phase dissociation and active oxidation at low oxygen partial pressures. These tests are being repeated at lower temperatures (2100F and 2200F) for the crack growth tests. It is desirable to observe crack growth without the effects of oxidation or dissociation. Design changes to the spin test facility are needed, to support spin disk test requirements for testing in air at elevated temperatures.

NDE Methods Development and Application

J. Minter

Calibration Standards

The first samples from the laser-drilled hole study have been received and evaluation of the samples has begun. The purpose of the laser-drilled hole study was to identify a laser drilling source that could provide holes from 0.0005 to 0.0100 inch diameter to depths between 0.005 to 0.050 inch. Only one source, Resonetics Inc., has been identified that is capable of drilling holes to these specifications. The laser drilling study concentrated on small holes with large aspect ratios, as Resonetics already had experience drilling larger holes with small aspect ratios. Dimensional evaluation of through-thickness holes in 0.020- and 0.050-inch thickness samples indicated the feasibility of producing round holes down to 0.001-inch diameter with less than 1 degree taper through 0.050 inch of material. The 0.0005-inch diameter holes can be fabricated to depths of 0.010 inch and possibly 0.020 inch. Both through-thickness holes and holes drilled to 0.050-inch depth are currently being evaluated with acoustic microscopy and radiographic methods. Based on the success of this machining study, the designs for both acoustic microscopy and radiography calibration standards have been finalized.

The acoustic microscopy calibration standards will consist of a series of 0.0005- to 0.002-inch diameter holes at various depths for ultrasonic beam profiling, calibration, and evaluation of sensitivity. Volumetrically seeded standards have been designed to evaluate the detectability of "real" defects and to compare the ultrasonic responses from these defects with the response from a small hole. The seeded defect samples will contain high-, low-, and near-density defects for evaluation of both ultrasonic and radiographic methods.

*References in parentheses () are given at the end of this report.

The radiographic/computed tomography (CT) calibration standards include both standard penetrameters as well as detection and resolution gages for computed tomography. The penetrameters will contain 0.1T, 0.5T, 1T, and 2T holes (where T is the penetrameter thickness) to assess and compare film, enhanced film, computed tomography, digital radiography, and ultrasonic methods. The minimum penetrameter thickness will be limited to 0.0050 inch and the smallest hole diameter will be limited to 0.0005 inch, due to fabrication and handling limitations.

Acoustic Microscopy

General Electric NDE Systems and Services has been subcontracted to provide acoustic microscopy and computed tomography inspection services, including necessary development in these two areas, for the program. A kick-off meeting for their work was held April 3, 1990.

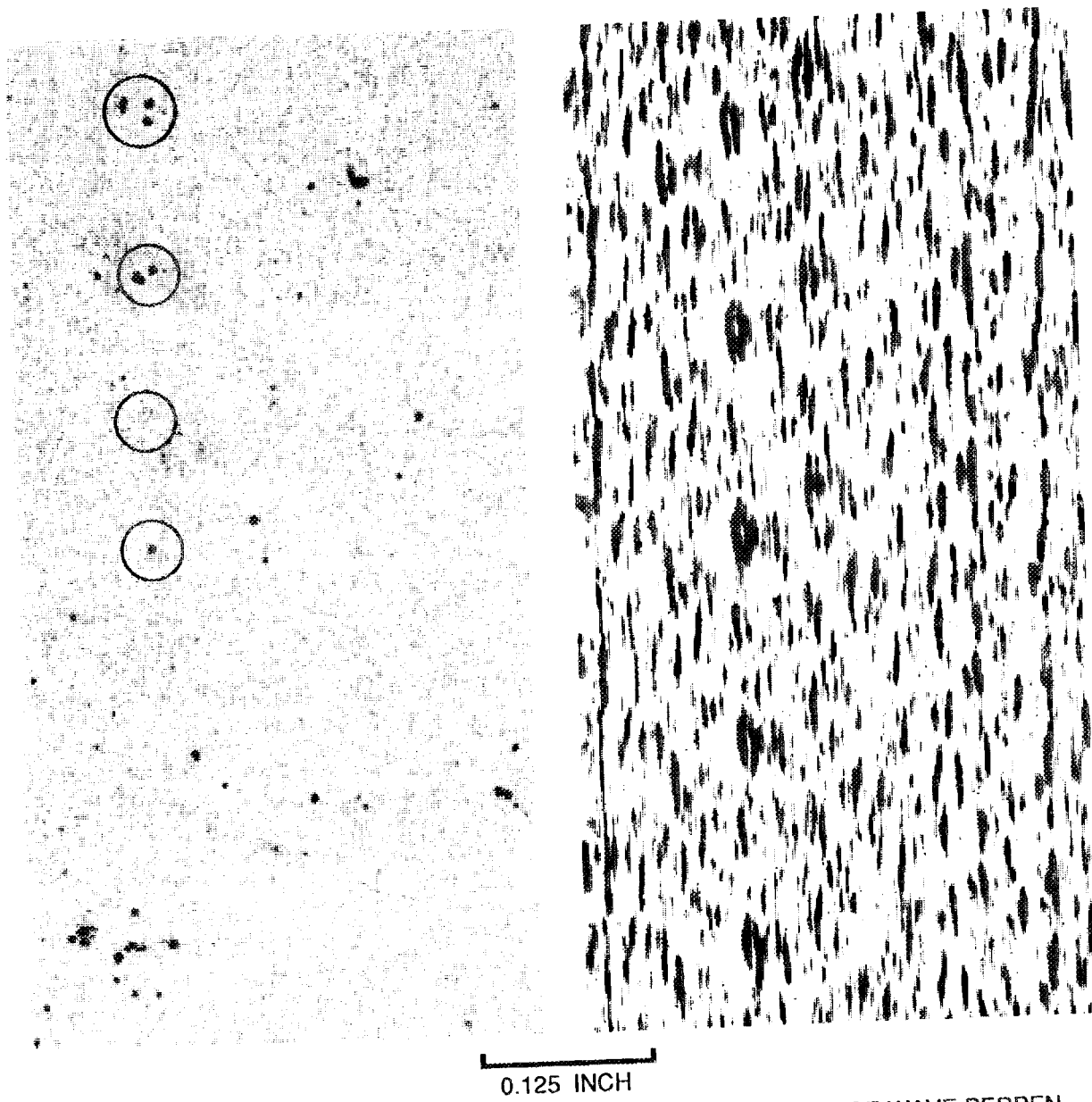
Preliminary transducer selection and design are nearing completion, and several transducers have been received for evaluation of surface and bulk detection capabilities. The transducers identified for use in the program are primarily 50 MHz transducers with a variety of focal depths, which cover the thickness range of test specimens in this program but limit the water path to 1.0 inch. This will retain as much of the high frequency component as possible when the ultrasonic pulse enters the ceramic material. Two remaining tasks are selection of transducers for the tensile rod specimens and transducer design/selection for inspection of the shaft/disk transition radius on the spin disk. Two approaches have been identified for inspection of the tensile rods and the spin disk:

- o Evaluate conventional cylindrically-focused transducers, which may result in reduced inspection sensitivity compared to flat-focus inspection
- o Evaluate special transducer designs with improved inspection capability for this geometry but limited application, because the focus is specialized for the geometry.

Task 1 of the acoustic microscopy study, to evaluate the effects of different surface finish conditions on the ability of acoustic microscopy to detect surface and near-surface defects, has begun. Visual documentation of the specimens was completed and all specimens have been forwarded to GE NDE Systems and Services for inspection.

Preliminary evaluation of the samples indicates that both machining severity and direction can cause difficulties in surface defect detection. Use of both omnidirectional and unidirectional surface waves is being evaluated.

Evaluation of unidirectional surface wave data perpendicular to the direction of machining and omnidirectional surface wave data is compounded by noise introduced from the machining, as illustrated in Figure 3. Figure 3 (a) shows indications corresponding to known defects in the bar as well as other indications, using a unidirectional surface wave parallel to the machining direction. In Figure 3 (b) the same bar was scanned perpendicular to the machining direction; the defect indications are lost in the noise from machining. General Electric NDE Systems and Services is continuing work to select the best scanning parameters and post-analysis techniques to identify harmful surface conditions.



(a) 50 MHz SURFACE WAVE PARALLEL TO MACHINING DIRECTION. (KNOWN DEFECTS CIRCLED.)

(b) 50 MHz SURFACE WAVE PERPENDICULAR TO MACHINING DIRECTION. (ONLY MACHINING INDICATIONS ARE VISIBLE.)

GB8491(03)-3

Figure 3. Acoustic Microscopy Surface Inspection Data Shows Machining Indications Can Obscure Defects.

Surface and near-surface inspection evaluations have been extended to include shear and refracted longitudinal inspections at both 25 and 50 MHz. Evaluations at higher frequencies have not resulted in noticeable improvement in detection sensitivity but increased the apparent noise in the images. Figure 4 shows an early 50 MHz scan of one of the 0.005-inch thick penetrameters with small diameter holes. This is a rough scan taken at 0.001-inch data point spacing of a normally-incident longitudinal wave inspection. The 0.0005-inch diameter hole is easily detectable on the normally-machined surface when all the data points are displayed [Figure 4(b)].

Computed Tomography and Radiography

Both computed tomographic (CT) and digital radiographic (DR) evaluations have begun, using the 0.020-inch thick laser-drilled hole evaluation sample. Initial CT and DR images have been used to evaluate digital filtering techniques, to reduce image noise that reduces contrast sensitivity. Digital filtering removes or reduces the amplitude of certain data frequencies and then converts the resulting data into a new image profile. The net effect on the image is to reduce the low and high frequency noise in the image; however, some of the useful data are also lost with these techniques. Multiple filtering trials on samples with known defects must be evaluated to select the optimum filtering parameters. The best filtering may also depend on the defect type. Digital filtering techniques have been used to successfully image a 0.002-inch diameter hole using a non-ideal detector arrangement.

In addition to digital filtering, various scanning techniques are also being evaluated. These include varying the detector collimator width, the exposure time, and the number of images averaged. The initial images show that averaging is one of the most promising techniques for improving image quality. Once beam-hardening corrections for NT154 have been made and an optimized detector is installed, additional image improvements are expected.

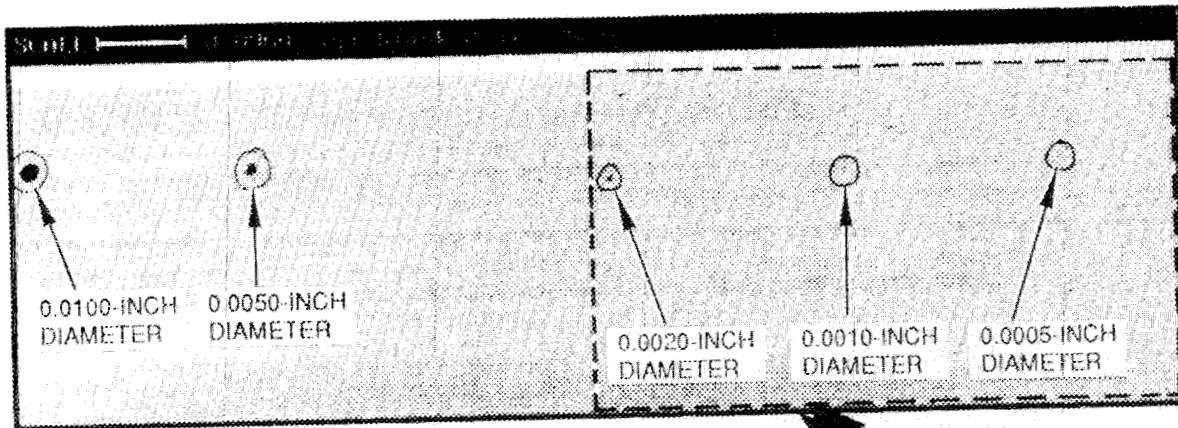
Radiographic images using a third film type and image projection have been completed for the film enhancement work. The images obtained were of porosities, iron inclusions, and agglomerate-seeded samples from the ATTAP program. In addition, the images included one of the laser-drilled test samples with 0.002-inch diameter minimum hole size.

Status of Milestones

On schedule.

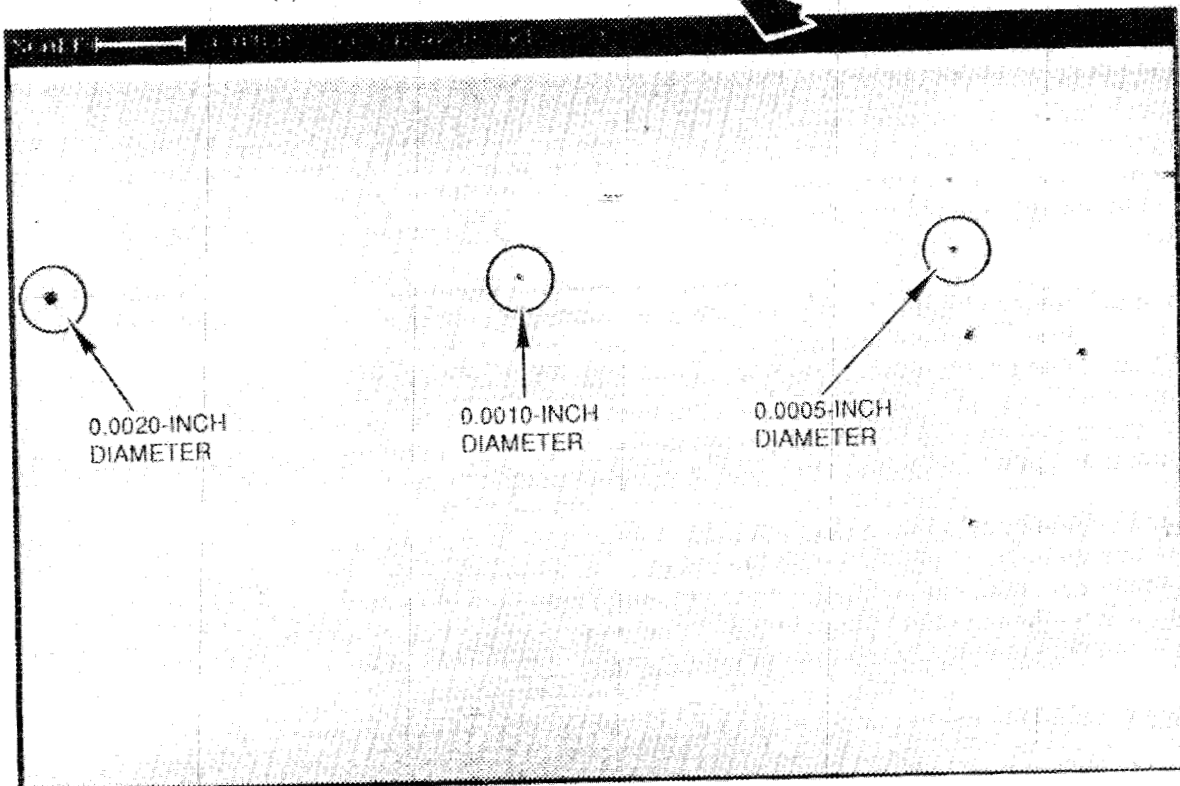
Communications/Visits/Travel

The second semiannual program review was held at GAPD, Phoenix, Arizona on May 22, 1990. Attending from ORNL were C. Brinkman, A.F. Johnson, B. Moses, S. Winslow, and B. McClung. J. Salem and P. Kerwin, from NASA-Lewis, also attended the review meeting.



(a) Compressed Full Image (Above)

(b) Area In Dashes Expanded 2X (Below)



GB8255(09)-4A

Figure 4. Acoustic Microscopy Surface Scan of Laser-Drilled Test Sample Detects Small Holes. (a) Compressed Image. (b) Expanded Area Showing Smallest Holes (50 MHz Scan at 0.001-inch Data Point Spacing).

Ms. Janet (Minter) Wade attended the ASNT/ACerS Conference on Structural NDE in Columbus, Ohio July 9-12, 1990 and then visited General Electric NDE Systems and Services in Cincinnati, Ohio to review progress on the subcontract work for this program.

John Cuccio and Alonso Peralta of GAPD travelled to General Electric Corporate Research and Development on August 22, 1990 to review statistical methods development with Curtis Johnson and William Tucker.

Publications

None.

References

1. S.B. Batdorf and H.L. Heinisch, "Weakest Link Theory Reformulated for Arbitrary Failure Criterion," J. Am. Ceram. Soc., 61, 7-8, pp. 355-358 (1978).
2. A.G. Evans, "A General Approach for the Statistical Analysis of Multiaxial Fracture," J. Am. Ceram. Soc., 61, 7-8, pp. 302-308 (1978).
3. C.A. Johnson and W.T. Tucker, "Investigation of Advanced Statistical Concepts of Fracture in Brittle Materials," Ceramic Technology for Advanced Heat Engines Project Bimonthly Technical Progress Report to DOE Office of Transportation Systems, December 1989-January 1990, ORNL/CF-90/38.
4. L.Y. Chao and D.K. Shetty, "Equivalence of Physically-Based Statistical Fracture Theories for Reliability Analysis of Ceramics in Multiaxial Loading," J. Am. Ceram. Soc., 73, Vol. 7, pp. 1917-1921 (1990).

3.3 ENVIRONMENTAL EFFECTS

Environmental Effects in Toughened Ceramics

Norman L. Hecht (University of Dayton)

Objective/scope

Since December 1984, the University of Dayton has been involved in a three-phase project to investigate the effects of environment on the mechanical behavior of commercially available ceramics being considered for heat engine applications. In the first phase of this project, the effects of environment on the mechanical behavior of transformation-toughened ZrO_2 ceramics were investigated. In the second phase, two Si_3N_4 ceramics (GTE PY6 and Norton/TRW XL144) and one SiC ceramic (Hexoloy SA) were evaluated. In the third phase, the tensile, flexural, and fatigue strength of 10 SiC and Si_3N_4 ceramics were evaluated at temperatures ranging from 20°C to 1400°C. Microstructure, chemistry, and physical properties were also investigated.

During the past six months (April 1990 through September 1990), evaluations of one SiC and two Si_3N_4 ceramics were conducted. The tensile and flexural dynamic fatigue was evaluated at 20°C and 1300°C for Norton/TRW NT-154 Si_3N_4 . In addition, the effects of oxidation at 1300°C on the flexural strength were investigated. Tensile cyclic fatigue of Carborum Hexoloy SA SiC and NT-154 Si_3N_4 at 1300°C was also measured using loads of 200-400 MPa. During this reporting period evaluation of Garrett's GN-10 Si_3N_4 was also initiated.

Experimental procedures

The tensile strength measurements were made using buttonhead cylindrical specimens on an Instron Electro-Mechanical Test System (Model 1361) equipped with Instron "Super-Grip" universal coupling and water-cooled holders for high-temperature tensile testing. For high-temperature measurements an Instron high-temperature short

*Research sponsored by the U.S. Department of Energy, Assistant Secretary for Conservation and Renewable Energy, Office of Transportation Systems, as part of the Ceramic Technology for Advanced Heat Engines Project of the Advanced Materials Development Program under Contract DE-AC05-84OR21400 with Martin Marietta Energy Systems, Inc., Work Breakdown Structure Subelement 3.3.1.4.

furnace was used. Measurements were made using both fast and slow loading rates (actuator speeds of 0.004 and 0.00004 cm/s) to determine strength and calculate dynamic fatigue.

The flexural strength measurements were made using an Instron Universal Testing Machine (Model 1123) following MIL-STD-1942(A). Test specimens were 3 x 4 x 50 mm with the tensile surface ground and polished to a 16-microinch finish. The test specimens were loaded at both fast and slow loading rates (machine crosshead speeds of 0.004 and 0.00004 cm/s). For the measurements made at elevated temperatures an ATS #3320 high-temperature furnace and four-point bend fixture of SiC was used.

During this reporting period cyclic tensile-testing at 1300°C was initiated using buttonhead tensile specimens of NT-154 and Hexoloy SA. The cyclic tensile testing procedures used are outlined in Table 1. Sixteen NT-154 specimens were evaluated at maximum tensile loads of 200 to 400 MPa for a maximum 450,000 cycles (~100 hours). Nine Hexoloy-SA specimens were also evaluated at maximum tensile loads of 200 to 300 MPa for a maximum 450,000 cycles. Test specimens withstanding 450,000 cycles were fast loaded to failure.

Tensile strength measurements were used to determine strength and dynamic fatigue of NT-154. Flexural strength measurements were used to determine strength and dynamic fatigue and to study the effects of oxidation at 1300°C on NT-154. Flexural strength measurements were also used to characterize GN-10.

During this reporting period dynamic fatigue analysis of NT-154 at 20°C continued. In the last reporting period, flexural strength measurements at 20°C using rapid and slow loading rates (crosshead speeds of 0.004 and 0.00004 cm/s) verified the susceptibility of NT-154 to slow crack growth. To further evaluate the slow crack growth behavior of NT-154 at 20°C the flexural strength of five flexure specimens coated with oil was measured at the slow loading rate.

The NT-154 flexure test specimens were placed in a glass container which was evacuated by a roughing pump to approximately 1 Torr. The specimens were then heated to 200°C and held at this temperature for 48 hours while maintaining the vacuum in the container. Upon cooling to room temperature, the container was back-filled with a methyl polysiloxane diffusion pump oil (Dow Corning DC-

Table 1. Cyclic Tensile Testing Procedures

1. Seating of tensile specimens in copper collets (slow loaded to 1000 lbs for 5 min.)

2. Specimen heating and cyclic tensile loading

- a) heat to 1300°C
- b) hold at temperature for 15 min
- c) initiate tensile loading

- starting load formula

$$[(\text{load @ } \sigma_{\max}) - (\text{load @ } \sigma_{\min})]/2 + [\text{load @ } \sigma_{\min}]^*$$

Note: $\sigma_{\min} \approx 0.1 \sigma_{\max}$ (i.e., $\sigma_{\max} = 200 \therefore \sigma_{\min} = 20$)

- load values for σ_{\max} levels investigated are

σ_{\max} (MPa)	Load in lbs
200	784
250	980
300	1176
350	1372
400	1568

- d) loading sequence

- reset function generator
- set sawtooth amplitude on load controller
- set function generator on sawtooth with a ramp time of 0.2 sec
- set load controller limits slightly higher than function amplitude
- reset cycle counter
- start function generator
- set load controller to interlock

3. Fast fracture procedure specimens which survive 450,000 cycles are fast fractured (crosshead speed 0.1 in/min)

704) to cover the flexure test specimens before removing the vacuum. Specimens were removed from the oil bath individually and immediately tested in four-point flexure (slow fracture) according to procedures described in MIL-STD-1942A. Residual oil on the specimen surface was not removed prior to testing.

Technical progress

Dynamic Fatigue Studies of NT-154

The tensile dynamic fatigue of NT-154 was analyzed at 20°C and 1300°C. Ten specimens were slow loaded (0.00004 cm/sec crosshead speed) at both 20°C and 1300°C. In addition, 10 specimens were fast loaded (0.004 cm/sec) at 1300°C. The tensile strengths measured at these three different conditions are tabulated in Table 2. For purposes of comparison, the average tensile strength measured (based on 15 specimens) at 20°C at fast loading conditions is included. In addition, the results of the flexural strength measurements of NT-154 at 20°C and 1300°C using the fast and slow loading rates are also included in Table 2, as are the results of the flexural strength measurements made on the oil-coated specimens at 20°C. These results strongly reinforce earlier findings about the susceptibility of NT-154 to low-temperature stress corrosion. The dynamic fatigue results (both flexural and tensile) for NT-154 are shown graphically in Figure 1. These results demonstrate the susceptibility of NT-154 to fatigue at both 20°C and 1300°C. The fatigue at 20°C appears to be moisture corrosion and at 1300° it appears to be creep related.

Table 2. Results of the Dynamic Fatigue Analysis of NT-154

Temperature (°C)	Loading Rate Crosshead Speed (cm/s)	Tensile Strength (MPa)	Std. Dev. (MPa)	Flexural Strength (MPa)	Std. Dev. (MPa)
20	0.004	726	117	907	79
20	0.00004	647	89	769	95
20*	0.00004	-	-	879	99
1300	0.004	399	54	650**	-
1300	0.00004	322	27	475**	-

*Oil coated; **Estimated average strength

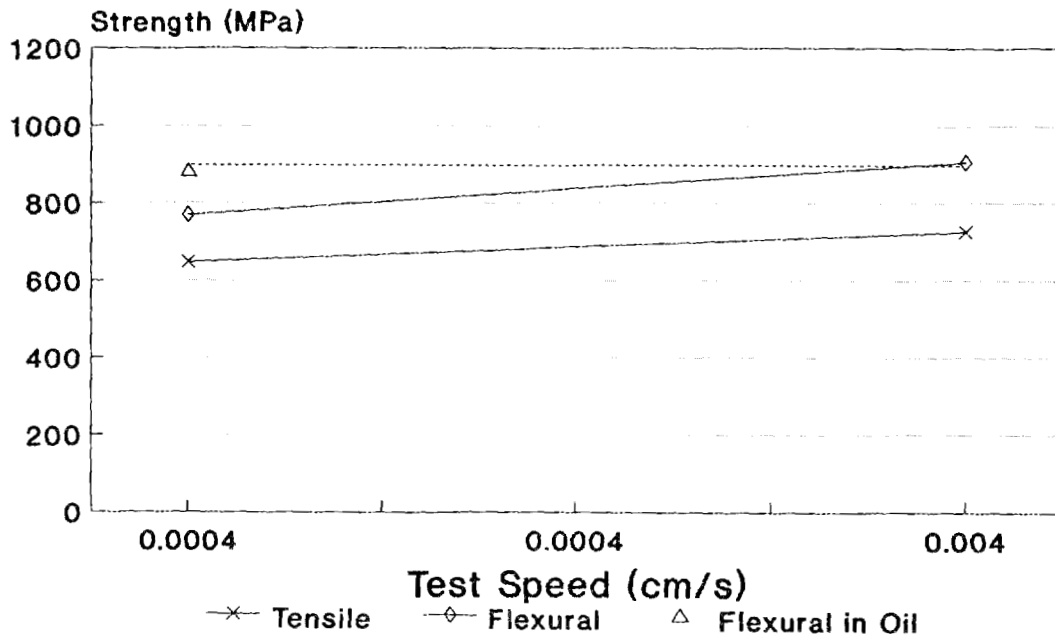


Figure 1. Dynamic fatigue analysis of NT-154 tested at 20°C.

Oxidation Studies of NT-154

The effects of extended exposure at 1300°C in air on the room-temperature flexural strength of NT-154 were investigated. Sets of five flexural test specimens were exposed for 100, 500, and 1000 hours at 1300°C. The flexural strength of all the exposed specimens was measured at 20°. In addition the flexural strength of five test specimens exposed for 500 hours was measured at 1300°C. The results of these flexural strength measurements are presented in Table 3. For purposes of comparison the as-received flexural strength in included in Table 3.

Table 3. Effects of Oxidation on the Flexural Strength of NT-154

Testing Temperature (°C)	Exposure Time (hours)	Average Flexural Strength (MPa)	Standard Deviation (MPa)
20	100	802	118
20	500	735	22
1300	500	747	43
20	1000	784	32
20	0 (as-received)	907	79

After 100 hours exposure at 1300°, the room-temperature flexural strength drops to 802 MPa (12% drop). After 500 hours exposure, the room-temperature strength drops further to 735 MPa (19% drop). The five specimens exposed for 500 hours and tested at 1300°C had slightly higher flexural strengths (747 MPa) than the values measured at room temperature (735 MPa). This higher strength may be due to the effects of crack healing. Similar behavior was observed for the GTE PY6 specimens tested during the previous reporting period. After 100 hours of exposure at 1300°C, the average room-temperature flexural strength was 784 MPa which is slightly higher (~5%) than the flexural strength measured after 500 hours of exposure. Considering the limits of variation, it would seem that the room-temperature flexural strength after 500 hours of exposure in air at 1300°C is not much different from the room-temperature strength after 1000 hours of exposure. This behavior is similar to the behavior observed for PY6. The major difference between the PY6 and NT-154 Si₃N₄ ceramics was the magnitude of flexural strength decrease measured at 20°C after 100, 500, and 1000 hours of exposure in air at 1300°C. The NT-154 flexural strength decreased from 12 to 19 to 14%, respectively, as compared to the PY6 flexural strength which decreased from 34 to 43 to 43.5%, respectively.

Cyclic tensile/tensile fatigue studies of NT-154

The results of the cyclic tensile tests for NT-154 are presented graphically in Figure 2. Fracture failures were observed to have initiated at both surface and volume flaws. A more detailed fracture analysis is in progress; however, preliminary results indicate that the failure mechanism is by the nucleation and coalescence of voids generated during cyclic fatigue. As shown in Figure 2, one of five specimens loaded to 300 MPa survived the 450,000 cycles. All three of the specimens loaded to 200 MPa survived the 450,000 cycles. These results would suggest that NT-154 may not be effective when subjected to cyclic tensile loading at 1300°C at and above loads of 300 MPa.

The results of the cyclic tensile tests for Hexoloy SA are presented graphically in Figure 3. All the Hexoloy SA tensile specimens failed by the growth of surface-initiated flaws. As shown in Figure 3, three of the four tensile specimens loaded to 200 MPa survived the 450,000 cycles, and only one of the four tensile specimens loaded to 250 MPa survived 450,000 cycles. The results of

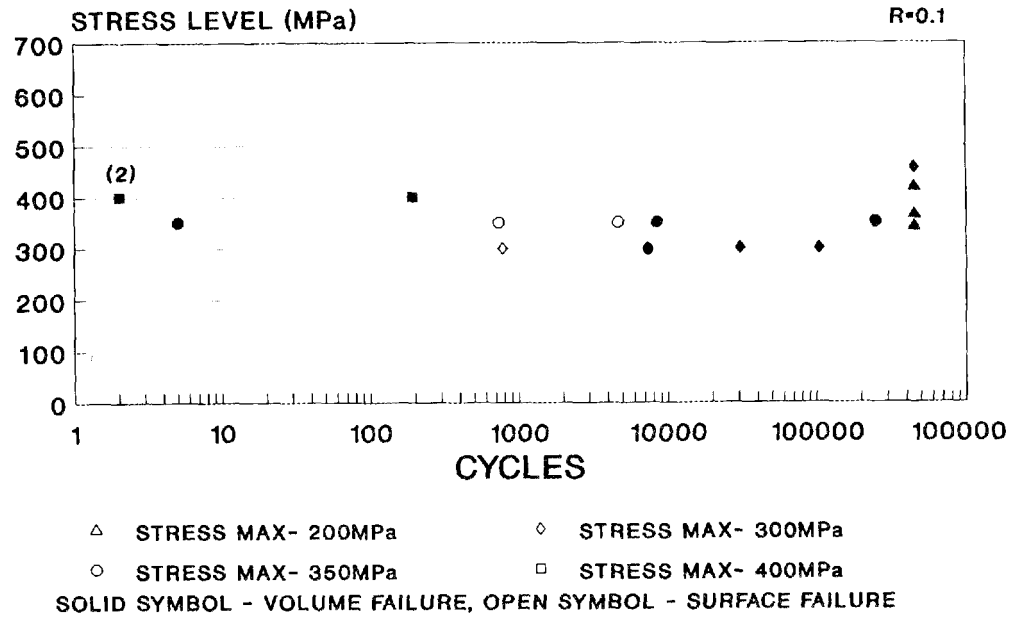


Figure 2. Cyclic tensile test results for NT-154 at 1300°C.

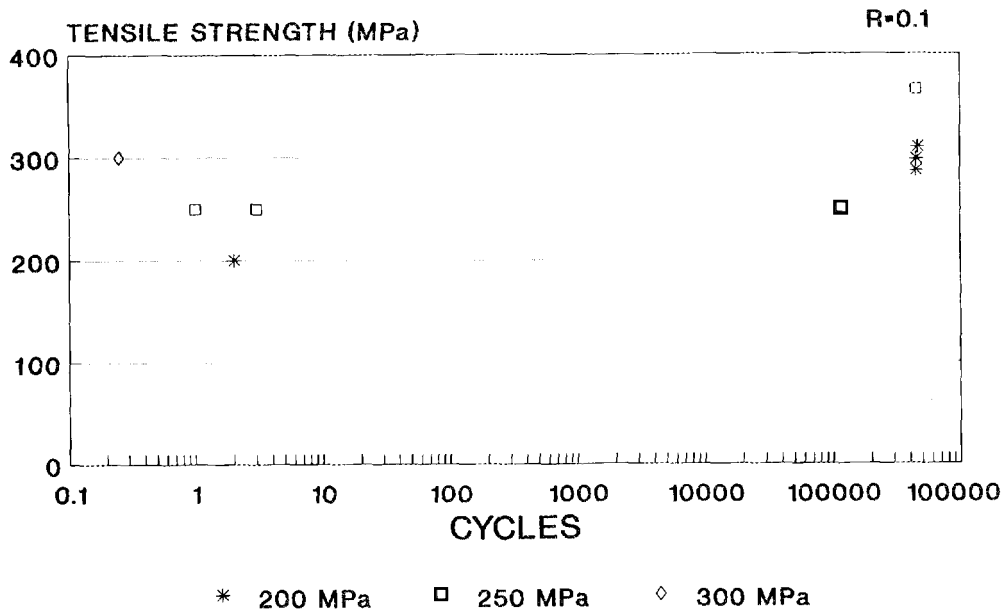


Figure 3. Tensile cyclic fatigue test results for Hexoloy SA.

cyclic loading tests would suggest that Hexoloy SA would not be suitable in applications requiring loads above 200 MPa at 1300°C.

Characterization of Garrett's GN-10

An evaluation of GN-10 was initiated using flexural strength measurements to characterize GN-10 at 20°C and 1300°C. Flexural strength of 20 test specimens was measured at 20°C using a machine crosshead speed of 0.004 cm/s, and 10 specimens were tested at a crosshead speed of 0.004 cm/s. Ten specimens were tested at 1300°C at a machine crosshead speed of 0.00004 cm/s. In addition, the density of five test specimens was measured by immersion methods. The average density obtained from these measurements was 3.33 g/cc. The results of the flexural strength measurements for GN-10 are compiled in Table 4.

Table 4. Results of Flexural Strength Measurements of Garrett's GN-10

Temperature (°C)	Machine Crosshead Speed (cm/s)	Flexural Strength (MPa)	Standard Deviation (MPa)	Fracture Origin
20	0.004	779	83	12 surface flaws (7 at inclusion) 8 edge chips
1300	0.004	563	40	10 surface flaws
1300	0.00004	444	63	Difficult to identify due to large amount of slow crack growth

All the specimens prepared had a mottled appearance which extended through the volume. A typical mottled surface is shown in Figure 4. The mottled surface was examined by EDXA and XRD; however, no change in chemistry or crystal phase could be detected.

As shown in Table 4, the average fast fracture flexural strength dropped 28% from 20°C to 1300°C. This decrease is similar to the strength decrease measured for NT-154 and is not as severe as the strength decrease measured for PY6. At 1300°C the fast fracture flexural strength was 21% higher than the slow fracture flexural

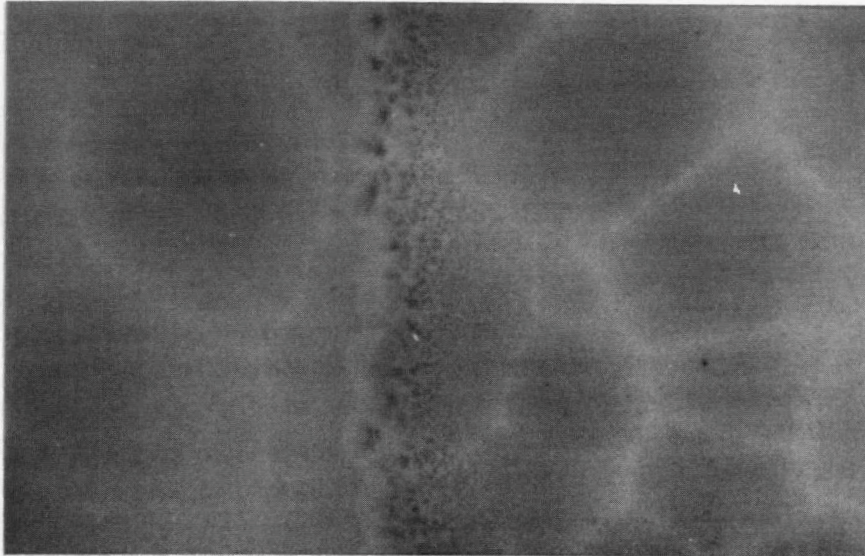


Figure 4. A typical mottled surface found for GN-10.

strength. The lower strength at the slower loading condition reinforced the observation of the fracture surface which showed slow crack growth at 1300°C.

Status of milestones

Milestone 331409 is completed.

Low Heat Rejection Diesel Coupon Tests

C. R. Brinkman, R. L. Graves, B. H. West, and K. C. Liu (Oak Ridge National Laboratory)

Objective/scope

The objective of this task is to expose various structural ceramics to conditions found in small diesel engines. Commercially available ceramics, as well as new candidate monolithic and whisker-toughened ceramics, will be fabricated into small MOR bars, nondestructively examined, and exposed to a variety of operating conditions within small diesel engines. Subsequent to exposure, the bars will be nondestructively and destructively examined and the results compared to an unexposed data base.

Technical progress

1. Engine Combustion Chamber Temperature Measurements

Additional in situ thermocouple measurements have been made in both the single and two cylinder engines in an effort to define an appropriate post engine exposure rupture test temperature for the MOR bar tests. A thermocouple (3.2 mm dia., type K) was inserted in the diesel combustion environment and quickly reached a steady state temperature of 782°C in the single cylinder engine. This was in good agreement with earlier estimates of average temperature in either engine. This temperature was at a setting of 14.5-15.0 ft-lb (20 N-m), and 1800-1900 RPM. Moving the load around from 10.0 to 17.5 ft-lb only made the temperature vary from 741 to 816°C.

Tests at the typical load and speed in either cylinder of the two cylinder engine showed a somewhat cooler steady-state temperature of 593 to 616°C. Increasing the load far above the normal operating point still only produced temperatures in the 700°C range. Reasons for this cooler temperature in the two cylinder engine are unclear. Plots of cylinder temperature as a function of fuel flow rate (per cylinder) showed a near linear increase in temperature with flow rate for both engines but the curves did not overlap. The fuel flow rate (per cylinder) used for all bar exposure conducted to date was 0.3-0.32 cc/s.

In an attempt to quantify the differences in the two engines, cylinder pressure measurements were made. On "motoring" the engine (cranking with no fuel flow so the engine did not start), the cylinder pressures were essentially the same, indicating that the compression ratios were the same. Several pressure traces (at least 10 cycles) were then recorded for each engine at several different loads in order to evaluate the relation between fuel flow and cylinder pressure. As expected from the temperature data, the two cylinder engine ran at lower peak pressures. Plots of average cylinder pressure as a function of fuel flow rate (per cylinder) showed a linear relationship. During the past year the single cylinder engine experienced a fouled injector problem, it was suspected that perhaps the new injector on that engine could be responsible for higher cylinder temperatures and pressures (due perhaps to better mixing). Therefore, one of the "old" injectors was taken from the two cylinder engine and installed in the single cylinder engine, no change in temperature was recorded. At

present, we have no explanation for the differences in the engines. Based on the above, it was decided to use 700°C as the post engine exposure test temperature for bars exposed in either engine.

2. Silicon Nitride (Norton NT-154)

Results of post engine exposure MOR tests conducted at room temperature along with control bar strengths are given in Table 1. Similarly, Weibull statistics for these four-point bend tests are also given in Table 2. The data given in Table 2 show that the average strength of the engine exposed bars is about the same regardless of which engine was used for the 100 h exposure. A comparison of the combined data for the engine exposed bars indicates that the strength of the exposed bars was not adversely influenced by engine exposure and in fact may have increased slightly as shown in the Weibull plot given in Fig. 1.

Results are given in Table 3 for four-point bend rupture tests conducted at 700°C on both engine exposed and unexposed material. The tests were conducted at several strain rates ranging from 1.1×10^{-7} to $1.1 \times 10^{-4} \text{ s}^{-1}$. Average values for a given strain rate and exposure condition are plotted in Fig. 2 as rupture strength as a function of strain rate. The plot shows little or no influence of strain rate or exposure condition on the rupture strength of the bars tested.

Table 1. Results of four-point bend rupture tests conducted on Norton NT-154 silicon nitride tested at room temperature

Unexposed control		Engine exposed ^a			
		Two cylinder		Single cylinder	
Specimen no.	Strength (MPa)	Specimen no.	Strength (MPa)	Specimen no.	Strength (MPa)
81.0	769.8	24	934.3	10	959.9
82.0	748.1	15	919.5	22	889.7
83.0	785.1	12	897.0	9	885.0
84.0	714.9	30	884.7	38	841.9
85.0	676.4	21	872.6	16	829.7
86.0	621.9	18	870.2	17	816.2
87.0	730.1	20	862.7	37	799.4
88.0	738.1	27	852.2	23	776.3
89.0	767.0	8	852.0	36	732.0
90.0	761.0	31	848.6	39	720.6
91.0	871.7	6	834.9		
92.0	748.9	13	831.6		
93.0	755.6	25	821.3		
94.0	764.2	5	817.3		
95.0	870.8	28	785.1		
96.0	869.0	14	765.1		
97.0	890.8	19	753.2		
98.0	815.5	29	743.7		
99.0	839.5	26	707.4		
100.0	836.8	7	696.9		
101.0	830.2				
102.0	846.6				
103.0	890.1				
104.0	874.9				
105.0	729.3				
106.0	792.4				
107.0	877.1				
108.0	735.2				
109.0	755.8				
110.0	850.2				
111.0	673.9				
112.0	639.2				
113.0	647.5				
114.0	762.9				
115.0	809.7				
116.0	712.8				
117.0	780.4				
118.0	805.5				
119.0	657.8				
120.0	569.9				

^aExposed for 100 h in the combustion chambers of the indicated diesel engine prior to rupture testing.

Table 2. Room temperature four-point bend rupture strengths for engine exposed and unexposed Norton NT-154 silicon nitride

No.	Exposure condition ^a	Number of specimens	Average rupture strength	Standard deviation (MPa)	Weibull summary linear regression		Weibull summary maximum likelihood	
					Weibull modulus	Intercept	Weibull modulus	Intercept
1	None	40	771	80	11.6	-77.9	11.8	-78.7
2	Single	10	825	74	13.3	-89.5	12.3	-83.2
3	Two cylinder engine	20	828	67	14.9	-100.3	15.4	-103.8
4	Combine (single & two cylinder)	30	827	68	14.8	-99.8	14.0	-94.3

^aEngine exposure consisted of 100 h in the combustion chamber of the indicated engine. The engines were run for approximately 8 h per day.

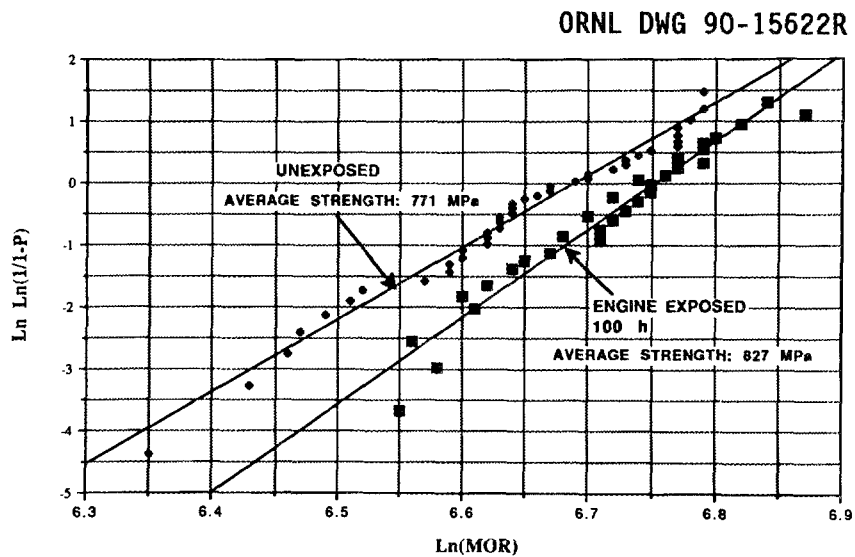


Fig. 1. Comparison of engine exposed and unexposed four-point bend room temperature rupture strengths of Norton NT-154 silicon nitride.

Table 3. Rupture Strengths of(MOR) of exposed and unexposed Norton NT-154 silicon nitride subsequently tested at 700°C at several strain rates.

Unexposed controls		Exposed 100 h single cylinder engine		Exposed 100 h two cylinder engine	
Strength (MPa)	Strain rate (1/s)	Strength (MPa)	Strain rate (1/s)	Strength (MPa)	Strain rate (1/s)
627.5	1.1×10^{-7}	627.0	1.1×10^{-4}	596.2	1.1×10^{-7}
507.5	1.1×10^{-7}	788.6	1.1×10^{-4}	704.0	1.1×10^{-7}
609.4	1.1×10^{-7}	702.3	1.1×10^{-7}	675.7	1.1×10^{-7}
640.0	1.1×10^{-7}	792.3	1.1×10^{-6}	674.9	1.1×10^{-6}
731.7	1.1×10^{-6}	471.8	1.1×10^{-6}	538.4	1.1×10^{-6}
636.2	1.1×10^{-6}	732.3	1.1×10^{-5}	717.4	1.1×10^{-6}
580.8	1.1×10^{-6}	778.5	1.1×10^{-5}	600.2	1.1×10^{-4}
817.8	1.1×10^{-6}			608.8	1.1×10^{-4}
458.3	1.1×10^{-5}			685.8	1.1×10^{-4}
596.4	1.1×10^{-5}			677.2	1.1×10^{-5}
693.9	1.1×10^{-5}			687.0	1.1×10^{-5}
710.9	1.1×10^{-5}			625.0	1.1×10^{-5}
696.5	1.1×10^{-4}				
748.0	1.1×10^{-4}				
845.2	1.1×10^{-4}				
697.9	1.1×10^{-4}				

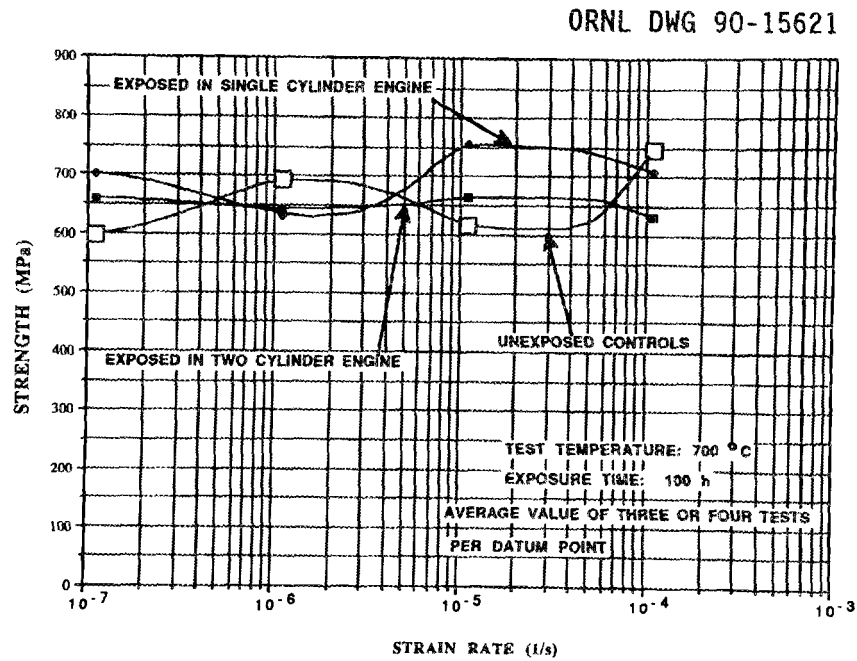


Fig. 2. Fracture strengths of engine exposed and unexposed Norton NT-154 silicon nitride obtained at several strain rates and at 700°C.

3.4 FRACTURE MECHANICS

Testing and Evaluation of Advanced Ceramics at High Temperature in Uniaxial Tension

J. Sankar, A. D. Kelkar, V. S. Avva, and Jun Gao (Department of Mechanical Engineering, North Carolina A & T State University, Greensboro, North Carolina 27411)

Objective/Scope

The purpose of this effort will be test and evaluate advanced ceramic materials at temperatures up to 1500 °C in uniaxial tension. Testing may include fast fracture strengths, stepped static fatigue strength along with analysis of fracture surfaces by scanning electron microscope. This effort will comprise of the following tasks:

- Task 1. Specifications for Testing Machine and controls + (procurement)
- Task 2. Identification of Test Material (s) + (procurement of specimens)
- Task 3. Identification of Test specimen configuration
- Task 4. Specifications for Testing grips and Extensometer + (Procurement)
- Task 5. Specifications for Testing Furnace (Procurement) and controls
- Task 6. Development of Test Plan
- Task 7. High Temperature Tensile Testing
- Task 8. Reporting (Periodic)
- Task 9. Final Report

It is anticipated that this program will help in understanding the behavior of Ceramic materials at very high temperatures in uniaxial tension.

Technical Progress

During the reporting period, creep tests were completed on GTE SNW-1000 (Si_3N_4) specimens at temperatures of 1200 deg. C and 1100 deg.C. For tests at 1200 deg. C, applied loads were 1625 N (57 MPa), 2600 N (92 MPa), 3223 N (115 MPa), 3858 N (138 MPa), and 4492 N (161 MPa), which are 0.25σ , 0.4σ , 0.5σ , 0.6σ , and 0.7σ respectively of the tensile strength (σ) of this material at 1200 deg. C. For the tests at 1100 deg. C, applied loads were 6132 N (224 MPa), 8585 N (314 MPa), and 10624 N (381 MPa), which are 0.5σ , 0.7σ , and 0.85σ respectively of the tensile strength (σ) of this material at 1100 deg. C. A set of platinum flags attached to the sample along with Zygo laser system were used to measure the deflection between the flags. Figure 1 shows the strain versus time for all the five specimens tested at 1200 deg. C. The results are compiled and given in Table 1. Figure 2 shows strain versus

time for all the three specimens tested at 1100 deg. C. The results are compiled and given in Table 2. The creep rates at 1200 deg. are higher than those at 1100 deg. C even at lower applied stresses. This indicates that the creep behavior of the silicon nitride is dependent on temperature. The influence of temperature on creep behavior is somewhat similar to the tensile behavior, because the creep strength is determined in parallel to the magnitude of the tensile strength.

The steady creep rate as function of applied stress is shown in Figure 3 and plotted logarithmically in Figure 4. The stress exponent n are ≈ 4.0 and ≈ 3.1 for 1200 deg. C and 1100 deg. C respectively for this material. Figure 5 shows the plot of log steady state creep rate versus log rupture time. As shown in Figure 5, the creep rupture behavior of this material can be approximated by a straight line on logarithmic plot of steady state creep rate versus creep rupture time, regardless of test temperature or applied load. The magnitude of the slope of the line is about 0.2. The data points with arrow in Figure 5 represent the creep tests in which the specimen did not break.

Figures 6(A) and 6(B) show the polished and unetched microstructure of the creep tested specimen. The microstructure surface is 2 mm away from the fracture surface. Initial observation indicates that the pores are larger in size than the average pore sizes in specimens untested and tested in tension at various temperatures previously. It may be further observed that the edges of the pores are softening and the fissures are advancing beyond the pores into the specimen (Figure 6(B)). Figure 6(C) is the fracture surface under high magnification showing evidence of intergranular fracture mode.

Status of Milestone

Tasks 1-7 are complete.

Publications & Presentations

None

Research sponsored by the U. S. Department of Energy under prime contract DE-AC05-84OR21400 with the Martin Marietta Energy Systems, Inc., subcontract 19X-89867C.

Table 1. The results of the creep test, SNW-1000, 1200 deg. C

Specimen	1	2	3	4	5
load (N)	1625	2600	3223	3858	4492
stress (σ) MPa	57 (0.25 σ_f)	92 (0.4 σ_f)	115 (0.5 σ_f)	138 (0.6 σ_f)	161 (0.7 σ_f)
$\log(\sigma)$	7.756	7.964	8.061	8.140	8.207
duration of test (t) (hour)	175 did not break	560 did not break	331 broke at gage section	306 broke at gage section	58.5 broke at gage section
$\log(t)$	/	/	6.076	6.042	5.323
strain rate (2nd stage) 1/s ($\dot{\epsilon}$)	5.5 E-10	2.4 E-9	8.8 E-9	1.7 E-8	5.4 E-8
$\log(\dot{\epsilon})$	-9.260	-8.620	-8.056	-7.770	-7.268

(note: σ_f is the tensile fracture stress at 1200 deg. C)

Table 2. The results of the creep test, SNW-1000, 1100 deg. C

Specimen	6	7	8
load (N)	6132	8585	10624
stress(σ) MPa	224 ($0.5\sigma_f$)	314 ($0.7\sigma_f$)	381 ($0.85\sigma_f$)
$\log(\sigma)$	8.35	8.50	8.58
duration of test (t) (hour)	470 did not break	89 did not break	42 broke at gage section
$\log(t_r)$	/	/	5.174
strain rate (2nd stage) 1/s ($\dot{\epsilon}$)	1.04 E-9	1.52 E-9	6.08 E-9
$\log(\dot{\epsilon})$	-8.981	-8.818	-8.216

(note: σ_f is the tensile fracture stress at 1100 deg. C)

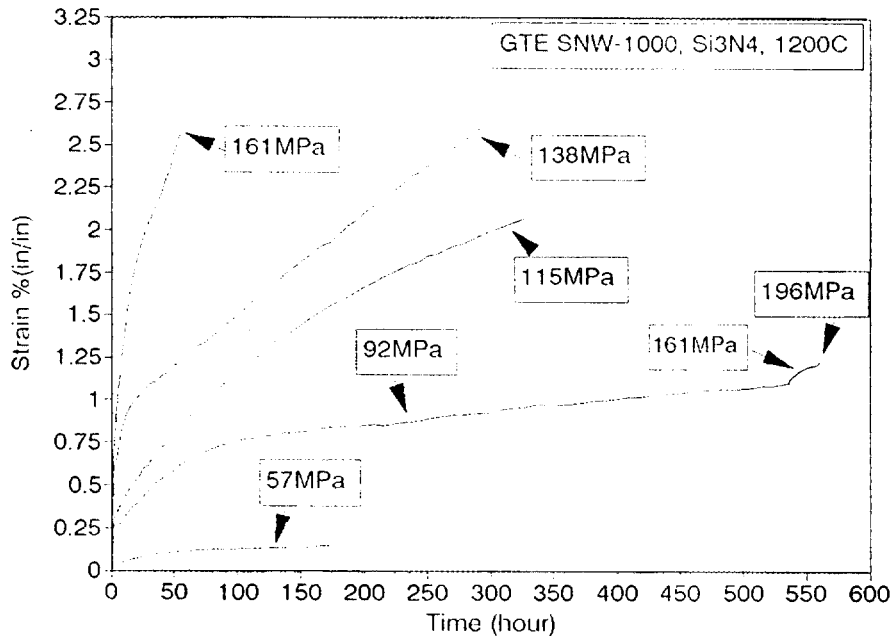


Figure 1 Strain vs time for five specimens tested at 1200C

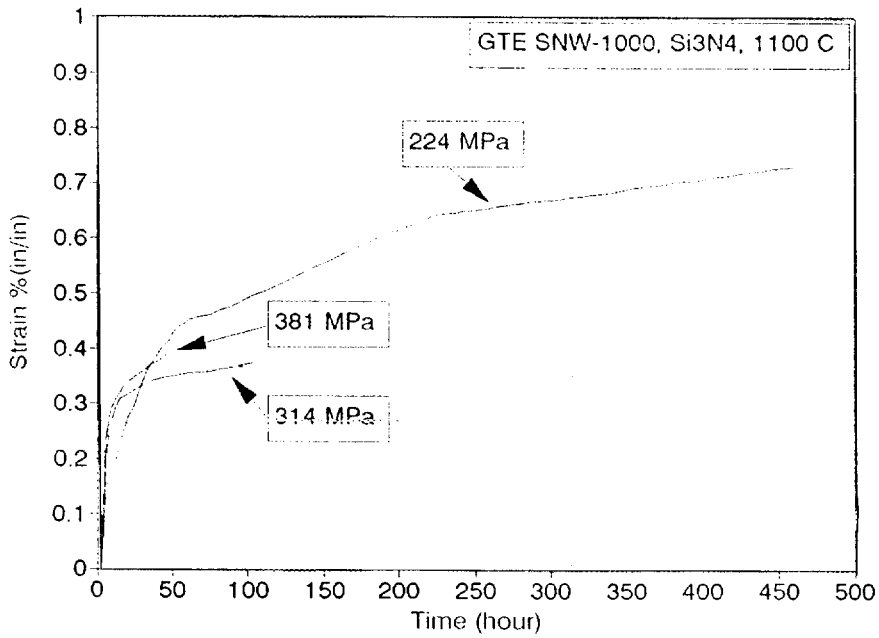


Figure 2 Strain vs time for three specimens tested at 1100C

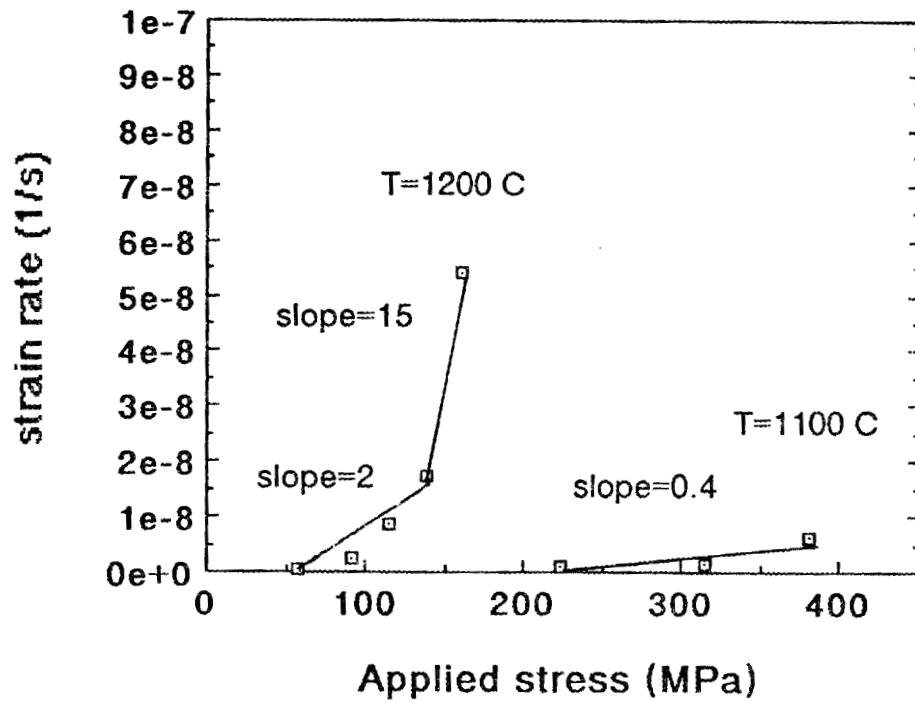


Figure 3. Steady state creep rate vs applied stress

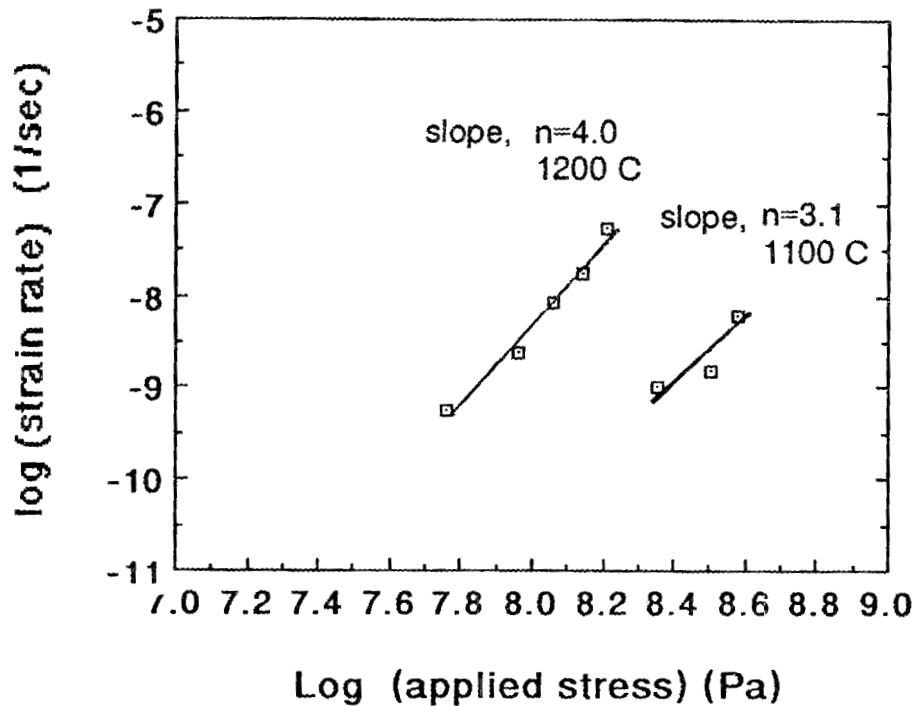


Figure 4. Log creep rate vs log applied stress

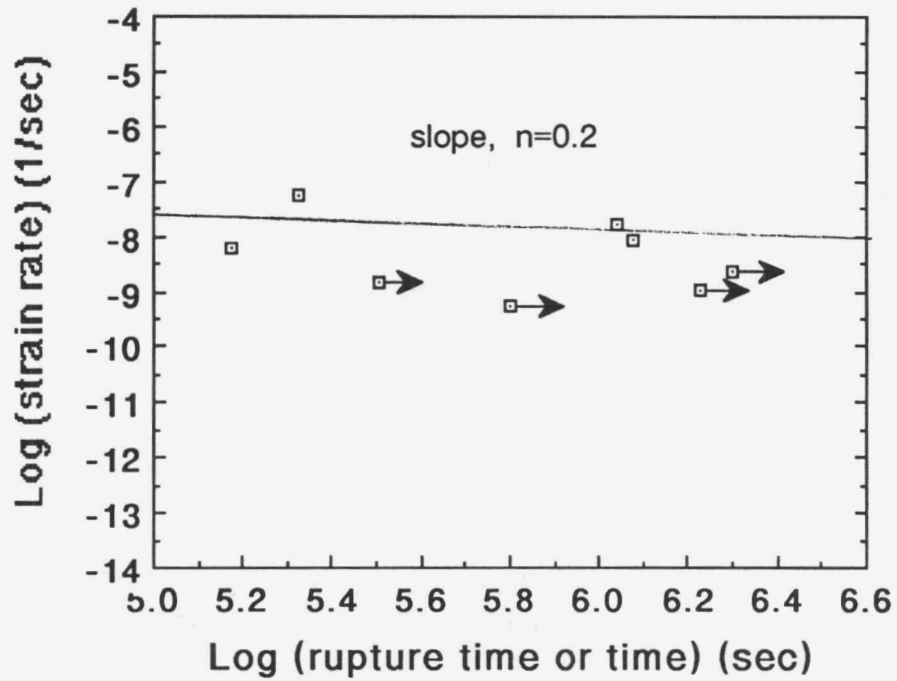


Figure 5. Log creep rate vs log rupture time

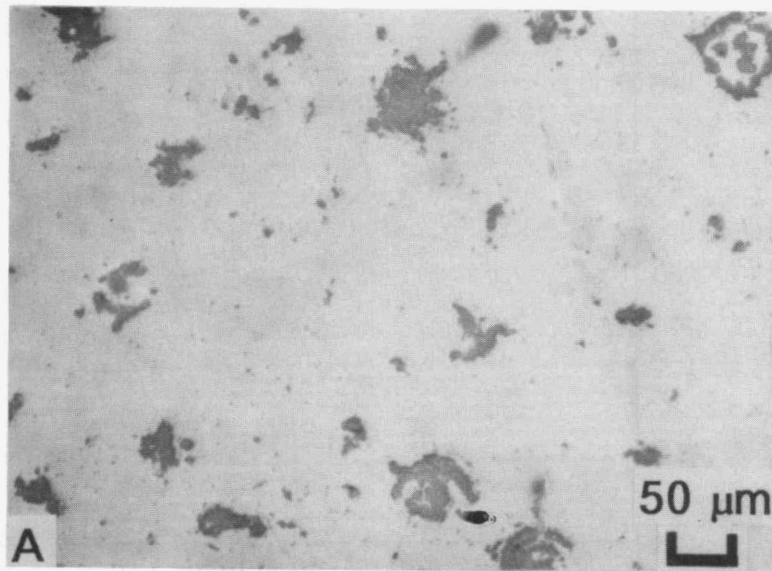
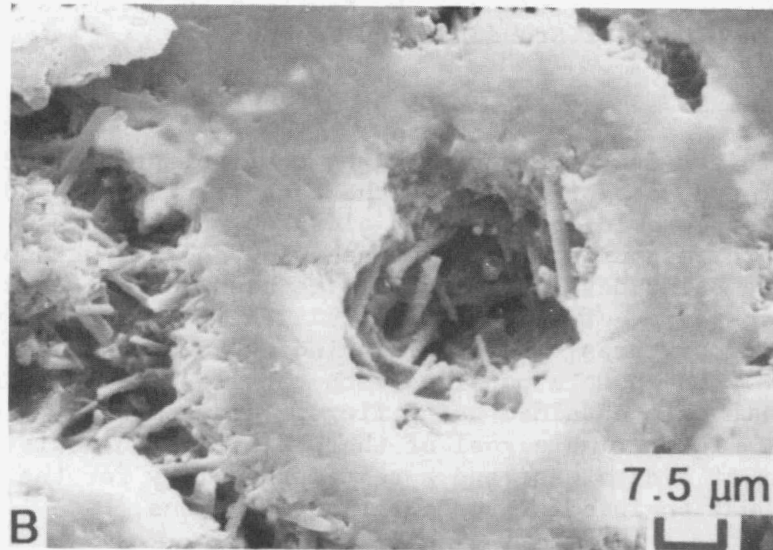


Figure 6. GTE SNW-1000, creep tested specimen, 1200 C, 138 MPa

(A) Polished surface



- (B) Pore showing softening
(C) Fracture surface close to fracture initiation area

Standard Tensile Test Development

S. M. Wiederhorn, D. C. Cranmer, D. Kauffman and D. E. Roberts
(National Institute of Standards and Technology)

Objective/Scope

This project is concerned with the development of test equipment and test procedures for measuring the tensile strength and creep resistance of ceramic materials at elevated temperatures. Inexpensive techniques for measuring the creep behavior and strength of structural ceramics are being developed and will be used to characterize the mechanical behavior of these materials. The test methods will use self-aligning fixtures, and simple grinding techniques for specimen preparation. Creep data obtained with tensile test techniques will be compared with data obtained using flexure and compressive creep techniques. The ultimate goal of the project is to assist in the development of a data base and a test methodology for the structural design of heat engines for vehicular applications.

Technical Highlights

During the past six months, the creep and creep rupture behavior of silicon nitride was studied as a function of applied tensile stress and temperature. Two commercial grades of material are being investigated: Norton/TRW NT-154, and Allied-Signal GN-10. The creep and creep rupture behavior of these materials are being characterized in tension and compression and a data base is being obtained to compare materials manufactured by different companies. This report presents data collected on both materials.

Experimental Technique

Dog-bone specimens, Figure 1, developed as part of our tensile creep program were used in this study. To assure that failure of the test specimens occurred within the gauge section, the central section of the specimen was reduced by surface grinding with a 38 mm diameter grinding wheel. After grinding, the total thickness of the gauge section was ≈ 2 mm. The width and length of the gauge sections were approximately 2.5 mm and 10 mm respectively.

Creep tests were conducted using the tensile equipment developed in an earlier phase of the project. The gauge length of the test specimen was monitored by placing small α -SiC flags on the central portion of the test specimen. The position of the flags were monitored as a function of time with a laser extensometer, which was capable of an accuracy of better than $\pm 1 \mu\text{m}$ in the measurement of distance between the two flags. This level of accuracy resulted in a precision of $\pm 2 \mu\text{m}$ in the displacement measurements during the evaluation of creep curves for each specimen. Details of the experimental apparatus were published previously [1].

In the studies on NT-154, the test temperature ranged from 1300°C to 1400°C. Tests were conducted in air, with a short ≈ 24 hour anneal to assure thermal equilibrium within the test furnace prior to

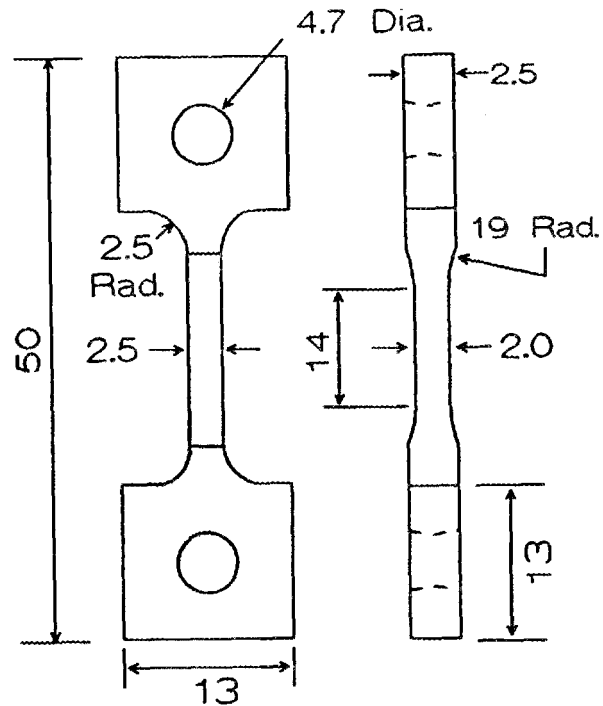


Figure 1. Specimen configuration. All dimensions are in mm. Note the double reduction in specimen gauge section. Also, the holes are tapered at an angle of $\approx 15^\circ$.

application of the stress. Applied stresses ranged from 75 to 175 MPa. Most studies to date were conducted on the NT-154, which is a HIP-ed grade of Si_3N_4 using Y_2O_3 as a sintering aid. The billets used were made specifically for this study, and do not relate to billets used on other parts of the DOE heat engine program. As transient effects were observed in the creep of the NT-154 during the previous six-month period, long-term creep measurements were initiated and are continuing on two specimens to clarify the effect of time at temperature on the creep rate. Other specimens were loaded to a level that rupture occurred within a relatively short time, < 250 hr. Data were then expressed in terms of a Monkman-Grant curve in which the creep rate was plotted as a function of the time to failure.

Similar experiments have been conducted on the GN-10 with temperatures ranging from 1200 to 1350°C and applied stresses ranging from 75 to 125 MPa. Several specimens have been loaded to levels such that failure has occurred at times less than 1000 hrs.

Results and Discussion

Initial tests on the NT-154 indicated long term transient creep behavior for this material. This has been confirmed on other long term creep specimens, and as illustrated in Figure 2, transient creep is observed for the full test period (>3500 hr). One specimen has now

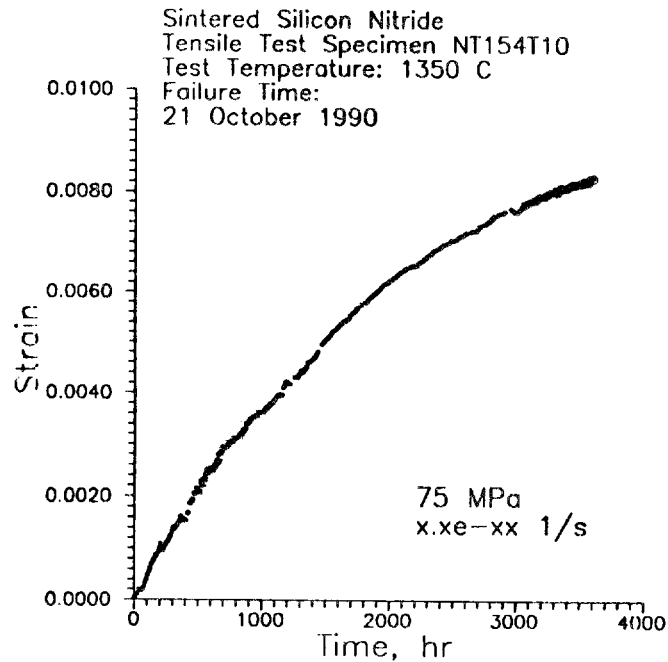


Figure 2. Extended creep curve for NT154. Note that transient creep occurs over the entire creep period. The minimum creep rate was determined by a least squares fit over the last 200 hr. of the creep curve.

been creeping for over 3500 hrs, the second for over 2000 hrs. Both specimens exhibit creep rates of less than $2 \times 10^{-9} \text{ s}^{-1}$, are exhibiting decreasing creep rates with increasing time, and are still showing non-steady state behavior.

The long transient behavior suggests that the microstructure of the material is slowly modified by exposure to elevated temperatures. Similar observations were made earlier on AY6 (made by GTE), in which case the increase in creep resistance of the material was attributed to devitrification of the glass phase at Si_3N_4 grain interfaces. The devitrification process was slow, and only affected the creep rate when the narrowest boundaries between the grains became devitrified. TEM studies on the material will be completed during the next 6 months to determine if the NT-154 is behaving in a similar fashion.

Because the apparent activation energy for creep, 1,183 kJ/mol, is greater than the heat of formation of Si_3N_4 , 744.8 kJ/mol [2], creep in this material is probably not controlled by any of the normal creep mechanisms (diffusion, climb of dislocations, etc.) used to explain the creep of ceramic materials. This high apparent activation energy may be a consequence of cavity formation in the silicon nitride, which has been reported by a number of investigators for NT-154 [3,4]. TEM studies presently underway at NIST have confirmed the formation of cavities in NT-154. Cavities in Si_3N_4 usually form in the glass that

surrounds the Si_3N_4 grains, so the estimation of the activation energy for cavitation given here is specific for cavity formation in glass. From the work of Raj and Ashby, the activation energy for cavity formation is $16 \cdot \pi \cdot \Gamma^3 / 3 \cdot \sigma^2$, where Γ is the surface tension of the cavity, and σ is the local stress. By assuming $\Gamma=0.3 \text{ J/m}^2$ (a normal value for glass at high temperature) and $\sigma=1$ to 2 GPa (i.e. the cohesive stress of glass) an activation energy ranging from 600 to 2400 J/mol can be calculated. This range of activation energies is consistent with those measured in the present experiment, tending to support our assumption that creep is a cavitation controlled process.

From a practical point of view, the high apparent activation energy for creep indicates a sharp transition in the performance of this material at elevated temperatures. Based on other creep studies conducted at NIST on structural ceramics, the only material that has better creep behavior is $\alpha\text{-SiC}$. However, this material has a lower fracture toughness ($\approx 2 \text{ MPa}\cdot\text{m}^{1/2}$ for the SiC compared to $\approx 6 \text{ MPa}\cdot\text{m}^{1/2}$ for the Si_3N_4), which reduces its susceptibility to thermal shock and to foreign particle damage.

To determine the susceptibility of the NT-154 to stress rupture, seven specimens were crept to failure. Both the time to failure and the creep rate were measured during these experiments. A tensile creep stress exponent (n) of 4.7 has been determined from the data obtained at 1350°C over the range of applied stresses from 75 to 150 MPa. As can be seen in Figure 3, all of the creep rupture data fall on a single curve when the creep rate is plotted as a function of the time to failure. This curve, in combination with creep curves, can be used to establish stress allowables for high temperature applications. This is shown in Figure 4, where preliminary lifetime predictions for this material are shown. The predictions indicate that the material can withstand a combined stress and temperature of 50 MPa and 1370°C for a period of about 1 year.

Six tensile creep tests on Garrett's GN-10 have also been conducted at temperatures from 1250 to 1300°C , and applied stresses from 75 to 150 MPa. The creep rates range from approximately 5×10^{-9} to 10^{-7} s^{-1} over these conditions. Times to failure taken from five of these specimens range from 25 to 850 hrs, and, when plotted in a Monkman-Grant fashion, exhibit a slope of 0.91. This value is very close to that obtained previously on the NT-154 material, although the amount of data is limited. Additional experiments on the GN-10 will be conducted during the next reporting period.

HIP-ED SILICON NITRIDE
TENSILE TEST SPECIMENS

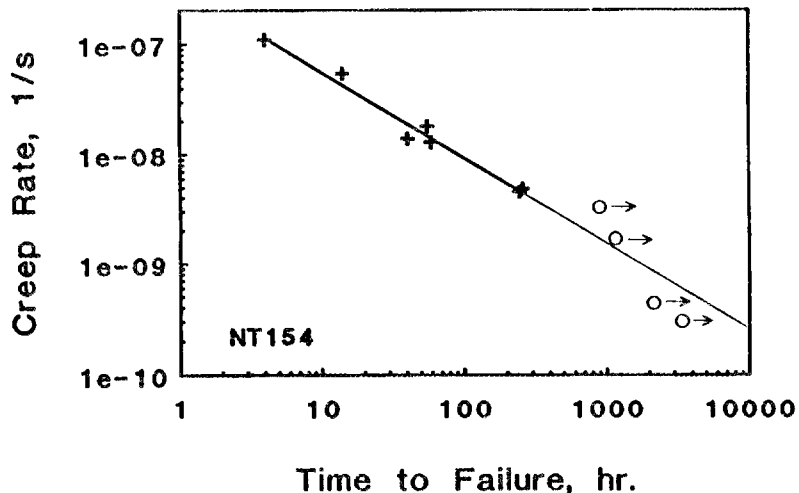


Figure 3. Creep rupture data: minimum creep rate as a function of the time to failure. Time-to-failure seems to be determined uniquely by the rate of creep.

Lifetime Predictions
HIP'ed Silicon Nitride (NT154)

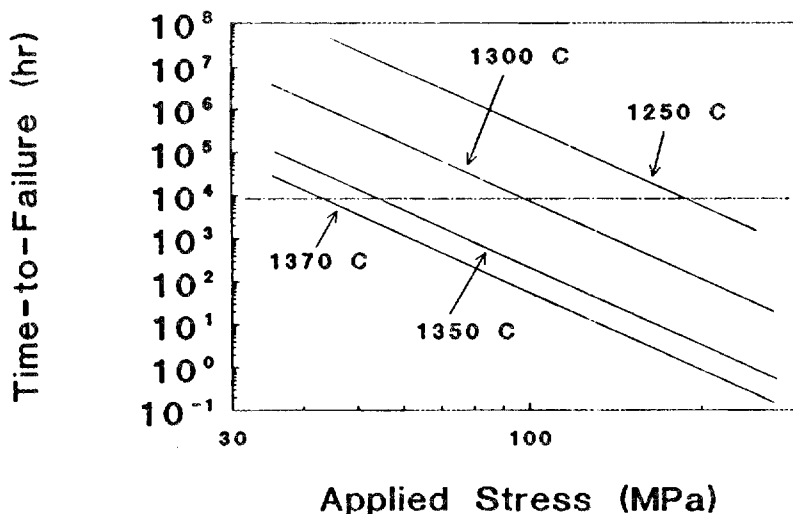


Figure 4. Preliminary lifetime predictions for NT-154 silicon nitride. Material is expected to survive combined stress and temperature of 50 MPa and 1370°C for 1 year.

Status of Milestones

All milestones are on schedule.

Publications

1. B. J. Hockey, S. M. Wiederhorn, W. Liu, J. G. Baldoni and S.-T. Baljan, "Tensile Creep of Whisker Reinforced Silicon Nitride", accepted for publication in *J. Mat. Sci.*
2. S. M. Wiederhorn and B. J. Hockey, "High Temperature Degradation of Structural Composites", to be published in *Proceedings of the Seventh Cimtec World Ceramics Congress, 1990.*
3. S. M. Wiederhorn, B. J. Hockey and T.-J. Chuang, "Crack Growth, Creep, and Creep Rupture at High Temperatures", to be published in *Toughening Mechanisms in Quasi-Brittle Materials, 1990.*

References

1. D. F. Carroll, S. M. Wiederhorn and D. E. Roberts, *J. Am. Ceram. Soc.*, 72 [9] 1610-1614 (1989).
2. JANAF Thermochemical Tables, 2nd ed., U.S. Govt. Printing Office, Washington, DC, 1971.
3. R. Yeckley, private communication.
4. L. Chuck, private communication.
5. R. Raj and M.F. Ashby, *Acta Metall.*, 23 653 (1975).
6. R. Raj, *Acta Metall.*, 26 995 (1978).

Development of a Fracture Toughness Microprobe

G. M. Pharr and D.S. Harding (Rice University)

Objective/scope

The objective of this study is to develop a technique for measuring fracture toughness in thin films and small volumes on a spatially resolved basis using the Mechanical Properties Microprobe at ORNL (MPM or Nanoindenter). The MPM is currently used to measure both hardness and elastic modulus with a spatial resolution of better than 1 μm . Once developed, the technique will be useful in probing toughness at the scale of the microstructure and thus in establishing important relations between microstructure and fracture behavior.

Technical progress

The method we are pursuing is based on the cracking which occurs when brittle materials are indented by a sharp indenter, such as a Vickers diamond. The indentation cracking method has been developed by several investigators over the last 15 years¹⁻¹². A critical review of its predictive capabilities has been presented by Anstis et al.⁷, who have applied the method to a wide variety of ceramics and glasses and found its accuracy to be better than 40%.

The basis of the method is to compute the fracture toughness, K_{IC} , from the length of the cracks, c , through the semi-theoretical relation⁷

$$K_{IC} = \alpha \left(\frac{E}{H} \right)^{1/2} \left(\frac{P}{c^{3/2}} \right) \quad (1)$$

Here, α is an empirically determined geometric constant (for a Vickers indenter, its value is about 0.016⁷), P is the indentation load, and E and H are the elastic modulus and hardness of the material, respectively. One attractive feature of applying this method with the MPM is that, in addition to being able to produce very small indents with very precise positioning, the load-displacement data provided by the instrument can be used to establish the local modulus and hardness. Since a knowledge of both these quantities is needed for the computation of toughness, the MPM provides a simple and convenient means for obtaining *all* the data needed to measure toughness on a spatially resolved basis.

To date, the indentation cracking method has been applied to indents which, by MPM standards, are fairly large. The indents typically used in the indentation cracking method are produced at loads of 1000 grams or greater, and the cracks are of the order of 100 μm or so in length. Since the size of the cracks sets a limit on the spatial resolution of the technique, much of the work in the early stages of the program will be concerned with how the indent size can be reduced without having the method break down or become impractical.

The main issue we have addressed during this period concerns the fact there are often well defined loads below which indentation cracking does not

occur. For example, for a Vickers indenter, cracking thresholds in most ceramics are about 25 gms or more^{13,14}. Since the indents associated with these loads are relatively large (several microns wide), cracking thresholds place severe restrictions on the spatial resolution which can potentially be achieved.

Our approach to reducing cracking thresholds has been to use indenter geometries different from the Berkovich geometry used standardly in the Nanoindenter. The Berkovich indenter is a three sided pyramid with a depth to area ratio the same as a Vickers indenter (4-sided pyramid). To study how indenter shape influences cracking, a testing device was assembled which allows for in situ optical observation of cracking during indentation in transparent materials. The device includes a video system which can be used to image fracture events while concurrently recording the displacement of the indenter and the load applied to the specimen. An investigation of the cracking behavior of soda-lime glass, fused silica, and sapphire was undertaken which showed that thresholds can be substantially reduced by changing the indenter geometry. The study also indicated that for certain geometries, the predominant cracks are radial cracks which consistently form during loading. This is in contrast to the behavior of the Berkovich or Vickers indenters, for which other cracks predominate (such as cone cracks), thereby limiting the materials to which the method can be applied.

To establish the extent to which the cracking threshold can be reduced, a study was undertaken in which indents were made in the Nanoindenter over a wide load range using one specific indenter geometry which appears to be quite promising. Indents were made in four brittle materials - soda-lime glass, fused silica, sapphire, and silicon. Scanning electron micrographs of the indents showed that radial cracks form consistently in all of the materials at loads as low as 0.5 grams. For lower loads, it is difficult to image the indents, so what the true threshold loads are is yet to be established. Nevertheless, the thresholds are substantially reduced, and this paves the way for implementation of the method in the Nanoindenter. It is worth noting that of the four materials studied, the only one which cracks with the Berkovich indenter at loads which can be achieved in the Nanoindenter (12 grams) is silicon.

Status of milestones

All milestones are proceeding on schedule.

Publications

A short paper entitled "New Evidence for a Pressure-Induced Phase Transformation During the Indentation of Silicon" was prepared for publication as a rapid communication in the *Journal of Materials Research*. This paper results from SEM observations of cracked indents in silicon.

References

1. A.G. Evans and E.A. Charles, "Fracture Toughness Determinations by Indentation", *J. Am. Ceram. Soc.* **59**, 371 (1976).

2. B.R. Lawn, T. Jensen, and A. Arora, "Brittleness as an Indentation Size Effect", *J. Mater. Sci. Let.* **11**, 573 (1976).
3. B.R. Lawn and A.G. Evans, "A Model for Crack Initiation in Elastic/Plastic Indentation Fields", *J. Mater. Sci.* **12**, 2195 (1977).
4. B.R. Lawn and D.B. Marshall, "Hardness, Toughness, and Brittleness: An Indentation Analysis", *J. Am. Ceram. Soc.* **62**, 347 (1979).
5. T.P. Dabbs, D.B. Marshall, and B.R. Lawn, "Flaw Generation by Indentation in Glass Fibers", *J. Am. Ceram. Soc.* **63**, 224 (1980).
6. B.R. Lawn, D.B. Marshall, and P. Chantikul, "Mechanics of Strength-Degrading Contact Flaws in Silicon", *J. Mater. Sci.* **16**, 1769 (1981).
7. G.R. Anstis, P. Chantikul, B.R. Lawn, and D.B. Marshall, "A Critical Evaluation of Indentation Techniques for Measuring Fracture Toughness: I, Direct Crack Measurements", *J. Am. Ceram. Soc.* **64**, 533 (1981).
8. P. Chantikul, G.R. Anstis, B.R. Lawn, and D.B. Marshall, "A Critical Evaluation of Indentation Techniques for Measuring Fracture Toughness: II, Strength Method", *J. Am. Ceram. Soc.* **64**, 539 (1981).
9. J. Lankford, "Indentation Fracture in the Palmqvist Regime: Implications for Fracture Toughness by the Indentation Method", *J. Mater. Sci. Let.* **1**, 493 (1982).
10. K. Niihara, "A Fracture Mechanics Analysis of Indentation Induced Palmqvist Crack in Ceramics", *J. Mater. Sci. Let.* **2**, 221 (1983).
11. M.T. Laugier, "Palmqvist Cracking in WC-Co Composites", *J. Mater. Sci. Let.* **4**, 207 (1984).
12. M.T. Laugier, "Palmqvist Indentation Toughness in WC-Co Composites", *J. Mater. Sci. Let.* **6**, 897 (1987).
13. J. Lankford and D.L. Davidson, "The Crack-Initiation Threshold in Ceramic Materials Subject to Elastic/Plastic Indentation", *J. Mater. Sci.* **14**, 1662 (1979).
14. J. Lankford, "Threshold-Microfracture During Elastic/Plastic Indentation of Ceramics", *J. Mater. Sci.* **16**, 1177 (1981).

3.5 NONDESTRUCTIVE EVALUATION DEVELOPMENT

Nondestructive Characterization

D. J. McGuire (Oak Ridge National Laboratory)

Objective/Scope

The purpose of this program is to conduct nondestructive evaluation (NDE) development directed at identifying approaches for quantitative determination of conditions (including both properties and flaws) in ceramics that affect the structural performance. Those materials that have been seriously considered for application in advanced heat engines are all brittle materials whose fracture is affected by structural features whose dimensions are on the order of the dimensions of their microstructure. This work seeks to characterize those features using high-frequency ultrasonics and radiography to detect, size, and locate critical flaws and to measure nondestructively the elastic properties of the host material.

Technical Progress

Ultrasonics - W. A. Simpson, Jr. and K. V. Cook

We have determined nondestructively the elastic properties of a number of ceramic samples ranging from aluminum titanate to zirconia containing a range of additives. Since all of these samples were fine grained and exhibited no measurable degree of velocity dispersion over the bandwidth employed, digital pulse-echo velocity measurements were deemed sufficiently accurate for the purpose. The quantities determined were the shear modulus, bulk modulus, Poisson's ratio and the Young's modulus for each of the samples. Of particular interest for the zirconia samples was the effect of various amounts of such additives as yttrium on the Young's modulus. The velocity measurements were found to be sufficiently accurate to characterize the change in modulus with the amount of each additive. For the aluminum titanate samples, destructive measurements were also performed and yielded results in excellent agreement with the values obtained ultrasonically.

One of our concerns has been the minimum flaw size detectable using 50-MHz radially propagating surface waves. In typical structural ceramics (silicon nitride, silicon carbide, alumina), the wavelength of such a wave is approximately 120 μm . Although one would not expect to resolve two flaws whose separation was much less than this amount, it is possible to detect single flaws whose size is considerably less than a wavelength. The smallest intentional flaws which we have previously been able to produce were about 50 μm in diameter. In order to investigate the ultimate sensitivity of our surface wave inspection system, we have obtained four silicon nitride modulus of rupture (MOR) bars containing laser-drilled holes of controlled diameters and depths. Three of the bars contained a single hole whose depth was equal to the diameter. The diameters were 100 μm , 20 μm , and 10 μm . The fourth bar contained three zones having several 10- μm diameter holes in each zone. The depths of these holes in the three zones were 20 μm , 10 μm , and 5 μm , respectively. None of the holes were flat

bottomed but had tapered ends terminating in a point. The reported depths were measured from the surface of the sample to the terminal point.

The specimens were examined using a 50-MHz, $f/0.2$ surface wave transducer. This unit produces a radially propagating surface wave which is capable of detecting cracks in any orientation and is maximally efficient for detection of holes of circular cross section. Each bar was scanned using a 25- μm index along both the x and y axes, which is the finest index available with our current hardware. The acquired data were displayed on a gray-scale recorder, which has rather poor discrimination for adjacent-level amplitude data. A color system having excellent adjacent-level discrimination was available but was not used for reasons which will become evident shortly.

Because the holes to be examined were so small (except for the 100- μm standard), it was advantageous to focus the transducer as near the surface as possible, thereby minimizing the surface wave damping, commensurate with maintaining adequate separation between the direct (front surface) signal and the delayed surface wave signal. As this is difficult to achieve for separations of less than 50 ns because of the ring-down time of the front surface signal, the procedure was facilitated by introducing a small (~ 1 mm) air bubble onto the surface of the transducer lens. This bubble will settle at the exact center of the lens, thereby blocking the direct front surface signal. The only signal present will then be the surface wave, which may be gated in the usual manner. If the transducer is first focused so as to produce ample separation (say, 100 ns or so) between the direct and surface wave signals before introduction of the bubble, the surface wave response can be definitively identified. After introduction of the bubble, the transducer focus can be raised to provide minimal surface wave damping with confidence that it is the surface wave rather than the direct wave which is being monitored. For scan speeds of up to 12 cm/s, which is the highest available with our current gray-scale hardware, the air bubble will remain firmly in place.

As expected, the 100- μm diameter hole was readily detected and easily discerned on the gray-scale display. We have often imaged holes as small as 50 μm in diameter with this display, however, and thus this sample provided no challenges to our hardware. For the 20- μm diameter hole, on the other hand, the display showed only one digitizer unit change for a single pixel. It was recordable, but one could not identify it as a flaw without a *priori* knowledge. On the analog A-scan display, however, the presence of the hole was easily seen as an abrupt drop in the surface wave amplitude. This result suggests that the 50-MHz surface wave has adequate sensitivity to detect the 20- μm hole, but the resolution of our digitizer, which is a four-bit unit, is not adequate to record reliably the amplitude change produced by the hole. For a four-bit digitizer, the maximum resolution between the two highest levels is 0.6 dB, which means that the signal must change by at least this amount to be recordable.

The response from the 10- μm flaw could not, of course, be recorded. To our surprise, however, it was discernable in the A-scan display, where the amplitude change varied from 0.3-0.5 dB, depending on how near the exact center of the hole an acquired data point could be located. (Since the scan index was 25 μm , which is larger than the hole, in both the x and y directions, the acquired data point could be as much as one hole diameter removed from the center of the hole.) Since the change produced by such

small flaws was not sufficient to produce a one-unit change in our digitizer, there would be no advantage in using a color display.

For the MOR bar which contained numerous 10- μ m holes, no indications were recorded. Those holes which were 10- or 20- μ m deep, however, were discernable in the A-scan display. We could not definitively locate any of the 5- μ m deep holes although some form of hard copy record would probably be necessary to achieve this result.

It is evident from our results on these samples that an 8-bit, high-speed digitizer is necessary to record flaws smaller than about 20 μ m. Such a unit would have an amplitude resolution of 0.03 dB and should be able to record the 10- μ m holes easily. We are currently examining two such systems and preparing a specification.

Our studies on the use of synthetic aperture techniques for ceramic evaluation were also continued. We have previously reported both plane-wave and focused beam implementations of the technology as well as the development of software to perform the necessary computations. Currently, our greatest need is to acquire a scan system which can be programmed to move to the required aperture sample points, pausing between adjacent points while the backscattered signal from the sample is digitized and processed. Again, two such systems have been identified and are being evaluated. One of these systems appears to be readily adaptable to our current hardware, but a trip to at least one of the vendors will probably be necessary to select the proper system.

We have rewritten much of the software to perform synthetic aperture calculations on scattering data acquired from two-dimensional scans on ceramic specimens. This software was originally written for illustrative purposes only to perform the appropriate calculations on one-dimensional scans and is part of our effort to develop techniques capable of detecting critical flaws in ceramics at depths greater than can be obtained currently with real-time focused transducer technology. We have previously reported examining two approaches to achieve this goal, one based on plane-wave insonification of the ceramic with attendant spatial and temporal averaging and the other using synthetic aperture techniques. It now appears that the latter approach will be the more useful of the two because of the ease of adapting it to automated evaluation and because it appears to be inherently more sensitive. Figure 1 shows the result obtained using our one-dimensional implementation of an ultrasonic synthetic aperture. The target consisted of two small diameter parallel wires which were separated by one half of the Rayleigh criterion for the transducer frequency used in the study. The wires could therefore not be resolved by the transducer. A scan was then made in the plane of the wires and along a line perpendicular to the axes of the wires. When the acquired data were 'focused' by applying the appropriate quadratic phase shift for the transducer-to-target distance, the result of figure 1 was obtained, where the wires are clearly resolved. In effect, the transducer has been replaced by one whose diameter is equal to the length of the scan; i.e., a much larger effective transducer aperture has been synthesized. The small amplitude ripples evident in the figure are believed to originate from signals bouncing between the two wires.

In order to take full advantage of synthetic aperture technology for ceramic inspection, it is necessary to have low-level computer control of the hardware used to scan the sample. This requirement is engendered by

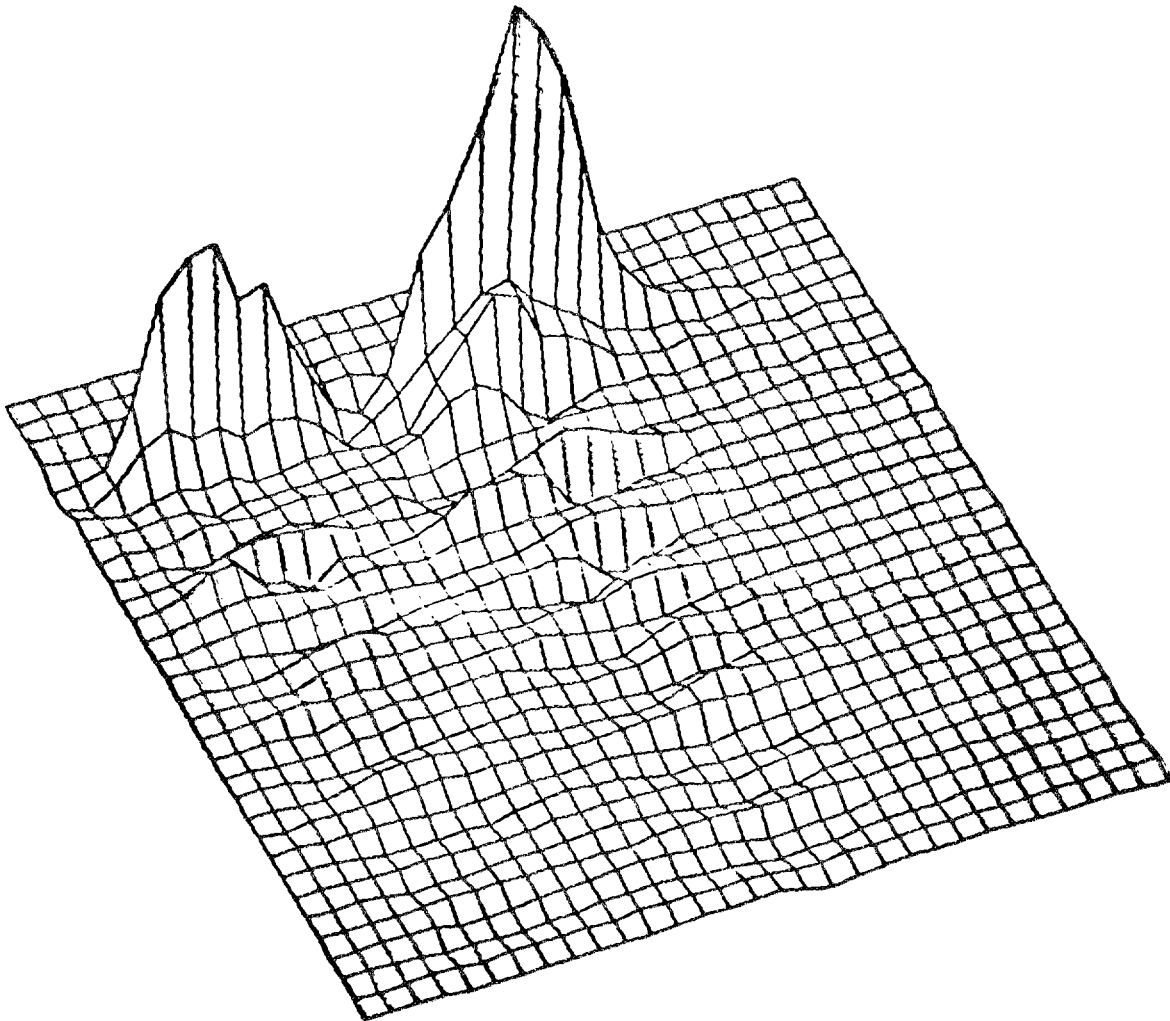


Fig. 1. One-dimensional synthetic aperture superresolution of two close ultrasonic targets.

the need to perform temporal averaging at each point of the synthetic aperture; hence, the scan controller must be capable of moving to the requisite point and then pausing until ordered to move to the next location. Our present high-resolution commercial scanning system does not have this capability. A second system for which we designed and built the controller and wrote the software can perform this function, but the spatial resolution and stepping accuracy and repeatability are not adequate for ceramic inspection. However, we have identified several commercial firms who provide stepping motor controllers designed to plug into an expansion slot in a standard PC-compatible computer. One such controller was designed for the specific motors used in our high-resolution scan system. In addition, the same vendor provides a card-level, 100-MHz, 8-bit digitizing peak detector and a software package designed to implement scanning with resolution down to 25 μm . This package should allow us to convert our existing high-resolution scanner into a two-dimensional synthetic aperture system as well as upgrade our current 16-level amplitude resolution hardware to 256-level. An optional modification to the scan controller card is available which will allow scan resolutions of less than 1 μm , but this level of performance is not justifiable with our present frequency limitation of 150 MHz. A specification for this system is being written.

We have begun transferring our ceramic evaluation programming from a mainframe minicomputer to PC-based systems. The former system is outdated and actually slower than our current 80386-based computers, which have been used primarily for computationally intensive applications such as our transducer beam distribution modelling. The minicomputer has been retained thus far because of superior graphics hardcopy capabilities and because it is already interfaced to a large ultrasonic scan tank. The first applications programming to be transported is our software for determining ceramic transfer curves, i.e., attenuation vs. frequency characteristics, which are very useful for characterization of the ceramic microstructure. A PC-based GPIB card was obtained for extracting data from our high-frequency waveform digitizer. Software was then written to convert the acquired data into a form acceptable to any of the several plot packages residing on our PC. Software has also been completed for plotting the rf waveform of the ultrasonic data and for computing the Fast Fourier Transform of acquired signals. The source code for performing the required deconvolution and computing the diffraction and water coupling corrections is currently being modified to run on the PC.

A PC-based general purpose parallel I/O board has been purchased for interfacing our large scan tank, which is the system in which we generate color renditions of the ultrasonic response of the sample under evaluation. Unfortunately, the tank hardware does not conform to any standard interface definition, and thus we are forced to write software in assembly language. We have succeeded thus far in generating the required interface signals, but we have not yet been able to get the system to run in full interrupt mode, which is necessary to operate the scanner correctly. We are working to correct this problem.

Computerized Tomography -- B. E. Foster

Twenty-nine cylindrical silicon nitride tensile specimens (noted as buttonhead) were received for inspection with the CT system. Initial inspection was done utilizing digital radiography. Any sample that showed any type of discontinuity was further evaluated with one or more CT slices through the longitudinal center of the sample.

In thirteen of the specimens, we noted voids (0.5- to 1-mm diameter) or very short (less than 1-mm) linear indications. The indications were also noted in four of the samples with subsequent CT slices. Specimen 357-2 contained a void 0.7-mm diameter, specimen 340-2-1 contained a void 1.0-mm diameter, specimens 367-1-4 and 340-1-2 each contained a small linear indication. It should be noted that the beam hardening corrections that were used in the image reconstructions were inadequate for ceramic materials.

The high resolution beam hardening software has been installed and is working quite well. However, in order to obtain optimum beam hardening corrections for the ceramic samples, a beam hardening correction wedge (triangle) fabricated of silicon nitride was needed. The wedge was ordered and has now been received. The triangle is approximately 12-mm thick with sides of 150 X 250 X 350-mm.

Additional operator training for the CT system was received at Scientific Measurement Systems, Austin, TX from July 9-20. Colorization, filtering, enlarging, and command language programming were some of the advanced areas covered during the training period. It was very beneficial.

The defective power supply (5 volt) has been replaced and the inoperative terminal repaired. All systems are operating properly.

The Exebyte (8-mm) tape drive developed an internal short circuit and has been returned to the vendor for repair. The auxiliary TK-50 tape drive is being used for backing up data.

Three ceramic (one silicon carbide and two silicon nitride) rotors have been received for detailed evaluation with the CT system and is in progress.

References

1. W. A. Simpson, Jr., "Nondestructive Evaluation Development," in *Ceramics Technology for Advanced Heat Engines Project Bimonthly Technical Progress Report*, February-March 1990.

Milestones

Milestone 351104 was completed on schedule.

Publications

W. A. Simpson, Jr. presented a paper entitled "Spherical Wave Decomposition Modeling of Transducer Beam Distributions for Ceramics Evaluation" at the joint ACerS/ASNT Conference on Nondestructive Evaluation of Modern Ceramics, which was held July 9-12 in Columbus, Ohio. An extended abstract of this paper was published in the conference proceedings. W. A. Simpson, Jr., R. W. McClung, and D. R. Johnson were

also invited contributors to an chapter entitled "Ultrasonic Testing Applications in Advanced Materials and Processes" of the ASNT Nondestructive Testing Handbook (in press).

NDE Standards for Advanced Ceramics

R. W. McClung (Oak Ridge National Laboratory)

The development of standards is important for the establishment of reliability and acceptance of advanced structural materials. A new committee, C-28, on Advanced Ceramics, has been organized in the American Society for Testing and Materials (ASTM) to address this issue. One of the activities of the C-28 committee is nondestructive examination (NDE). The Task Group on NDE is reviewing existing standards on NDE (primarily developed for metals) to determine potential applicability for ceramics. Use of existing or modified standards is more efficient than generation of new documents and will assure the input of a large body of NDE expertise. Close liaison has been established with ASTM Committee E-7 on Nondestructive Testing and documents are in various stages of review, recommendations for change, modification, and balloting. R. W. McClung is a member of both committees and the official liaison.

Liaison and technical support have been continued between ASTM Committees C-28 and E-7. To date, twenty-six E-7 NDE standards have been reviewed in detail with recommendations made to E-7 for modifications. Successful action is complete on thirteen documents; E-7 balloting action is in progress on eight items; the others require action by C-28. Another advisory C-28 (Task Group on NDE) ballot is in progress for detailed review on five additional E-7 standards. An NDE advisory ballot approved a table of ultrasonic velocities in typical ceramic materials. After minor corrections, this will be submitted to E-7 for incorporation in an existing NDE standard. A document on fabrication of seeded voids in pressureless sintered ceramics is being balloted in C-28 at the subcommittee level. A guideline document that describes available approved standards and their applicability for examination of ceramics is being balloted at both subcommittee and committee levels of C-28.

X-ray Computed Tomographic Imaging – W. A. Ellingson,
N. Gopalsami (Argonne National Laboratory) and T. Luethi,
(Visiting Scientist, EMPA Laboratory, Zurich, Switzerland)

Objective/scope

The objective of this program is to develop X-ray computed tomographic (CT) imaging technology for application to structural ceramic materials. This technique has the potential for mapping short-range (<5 mm) and long-range (>5 mm) density variations (to perhaps 0.5–1%), detecting and sizing high- and low-density inclusions, and detecting and sizing (within limits) cracks in green-state and densified ceramics. CT imaging is capable of interrogating the full volume of a component and is noncontacting. It is also relatively insensitive to part shape and thus can be used to inspect components with complex shapes, such as turbocharger rotors, rotor shrouds, and large individual turbine blades.

Technical progress

During the current reporting period, we continued to assess the accuracy of X-ray CT to measure density variations in complex shaped ceramic parts. Two of the new Si₃N₄ injection-molded phantoms (turbocharger rotors) received last period were used as the test specimens.

Density measurements

To better obtain an idea of X-ray CT sensitivity to density variations within the critical hub-blade region of a turbocharger rotor, a set of rotors was produced by Garrett Ceramic Components (GCC) of Allied-Signal Aerospace Corporation. Figure 1 shows the drawing from which the rotors were made. These T-25 turbocharger rotors were produced by injection-molding of Garrett's GN-10 Si₃N₄. Three insert slugs at the critical hub-blade region have from 9.0 to 15.5 wt.% binder difference (see table 1) which resulted in an approximate 0.08 g/cm³ mass density difference per 2 wt.% binder from a nominal 2.28 g/cm³ base material. The slugs were inserted into the hub region so that part of the region has these known variations and part does not.

We noted in our earlier report that the new T-25 turborotors were to be received from Cape Canaveral, Florida, following CT tests using a ⁶⁰Co source. A change was made from the earlier set of samples in that the nominal concentration of organic binder of the main body was dropped from 15.5 wt.% to 12.5 wt.%. Thus the inserts were also changed. Table 1 below gives insert code and wt.% of organic for these rotors. Photographs of the rotors with the inserts are shown in Fig. 2.

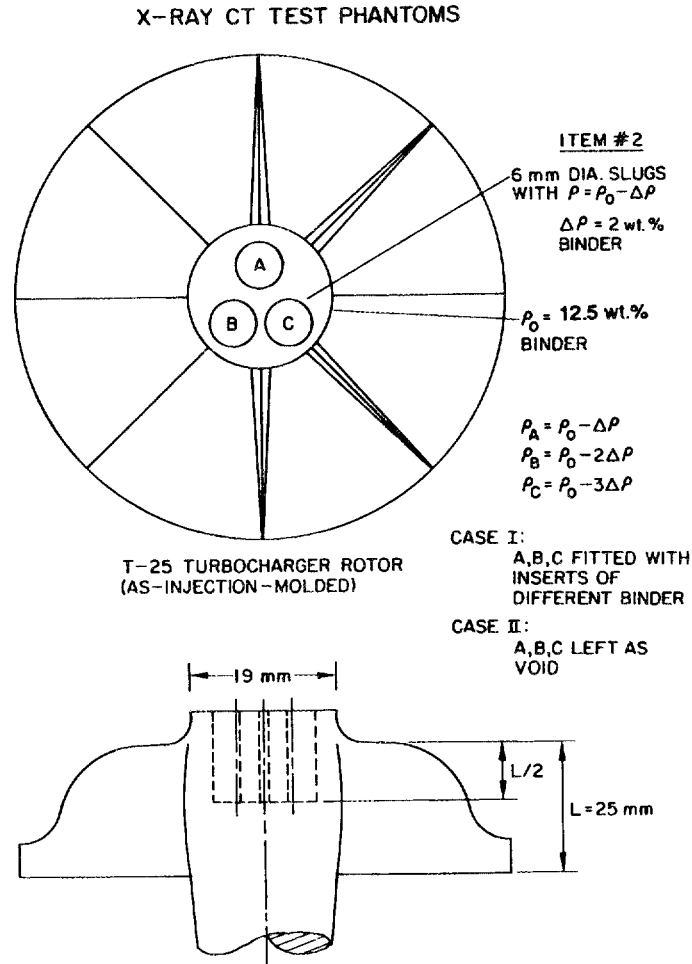


Fig. 1. Schematic diagram of the T-25 injection molded turbo rotors showing the general arrangement of the inserts with various concentrations of organic binder.

TABLE 1

Organic binder insert code for inserts in turborotors.

<u>Insert identification</u>	<u>Wt. % organic</u>	<u>Density</u>
A	9.0	
B	10.0	
C	11.5	
D	13.5	
E	14.5	
F	15.5	
Rotor I	12.5	
Rotor II	12.5	

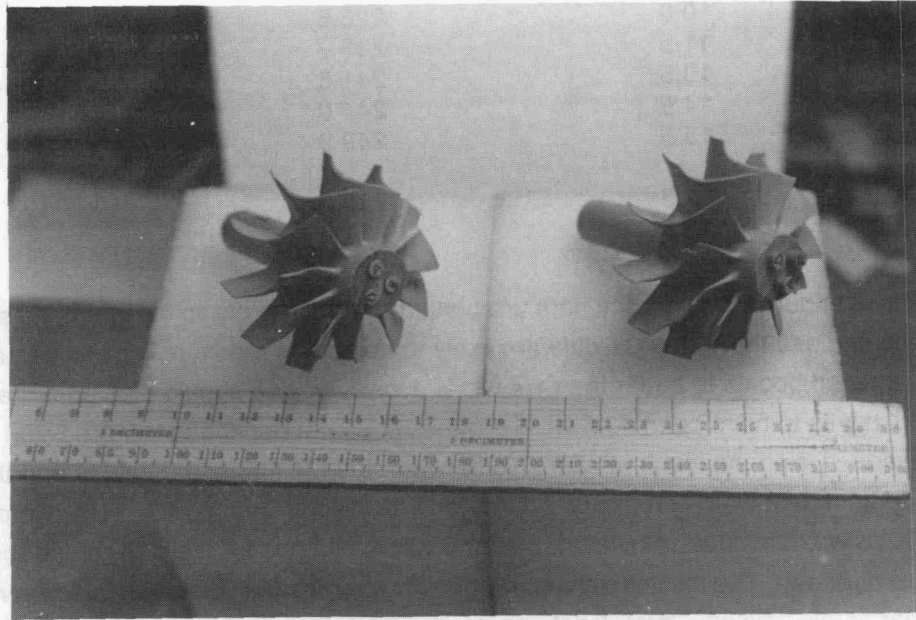


Fig. 2. Photograph of the T-25 injection molded Si_3N_4 turborotors with various density inserts.

We conducted a set of 3D microfocus X-ray CT scans of the rotors using the ANL designed and built 3D microfocus X-ray CT scanner. All data were acquired using a significant amount (.070 in 1.78 mm) of copper filtration at the X-ray source and we used extensive collimation at the image intensifier detector. The image intensifier was set at 9" field of view. We obtained 1 mm thick cross-sectional images of the rotor starting upstream of the bladed section such that we obtained at least one cross-section without interference caused by blades. The purpose of this is to establish the extent to which blades degrade density values as determined by X-ray CT measurements. All data were obtained using 359 projections and used 256 x 256 reconstruction. The convolution filter selected was the Feldkamp filter. We used normalized image reconstructions (that is we used equal max-min gray scale values for the main rotor bodies), for the data presentation. Table 2 shows the approximate gray scale values obtained for each insert in the rotor at the upstream position of the blades.

TABLE 2

X-ray computed tomography measurement of organic content.

<u>Insert</u>	<u>Organic content wt.%</u>	<u>Gray scale values</u>	<u>Measured density g/cm³</u>
A	9.0	228.1	
B	10.0	228.8	
C	11.5	233.7	
D	13.5	241.8	
E	14.5	244.0	
F	15.5	249.9	
Rotor I (ABC)	12.5	230.2	
Rotor II (DEF)	12.5	231.2	

If the X-ray computed tomography data are plotted against the organic content, as shown in Fig. 3, one can see that X-ray CT data are likely to be able to measure organic content of complex shaped bodies to better than 1/4 wt.%. However, one should also note that the main body, which was to have been 12.5 wt.% organic, does not behave in the predicted manner of the inserts. Using the linear relationship between the CT measured values and the known organic content, one would predict that the rotor was injected with a 10.5 wt.% content, not 12.5 wt.% as was provided. However, the fabrication methods for the inserts and the turbo rotor were different. The inserts were cold pressed whereas the rotor was injection molded. It is not clear at this time why the CT data so drastically detects the difference in fabrication methods.

Figure 4 shows 1 mm thick X-ray CT cross sections obtained through the rotors with inserts in the section upstream of the blades. Figure 5 shows a typical X-ray CT image taken through rotor I with inserts A, B, C, and Fig. 6 shows the CT image of the rotor II with inserts DEF. Next period we will compare data from the ⁶⁰Co NASA data to the polychromatic X-ray CT data obtained at ANL. In addition, a more thorough analysis of the ceramic inserts will be undertaken so that porosity, powder content, and other variables can be studied relative to the X-ray attenuation values.

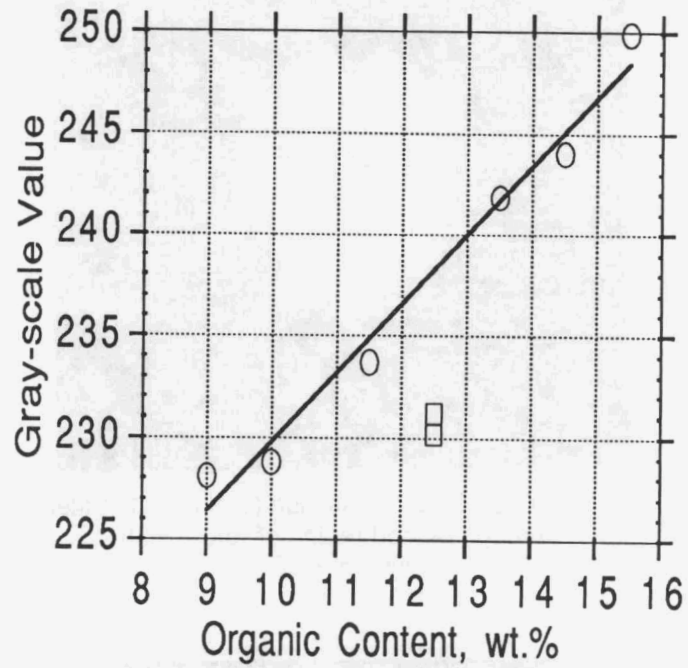


Fig. 3. Plot of X-ray computed tomography gray scale as a function of wt.% organic in injection molded turborotors.

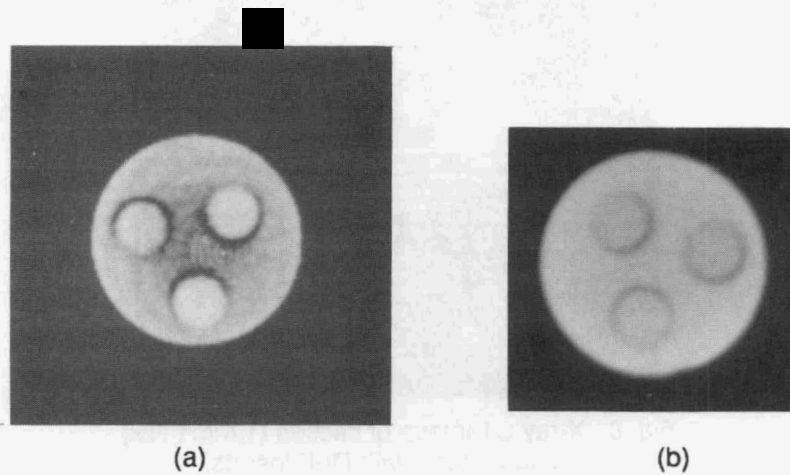


Fig. 4. X-ray CT cross section images taken upstream of the bladed region on both rotors (a) ABC, (b) DEF.

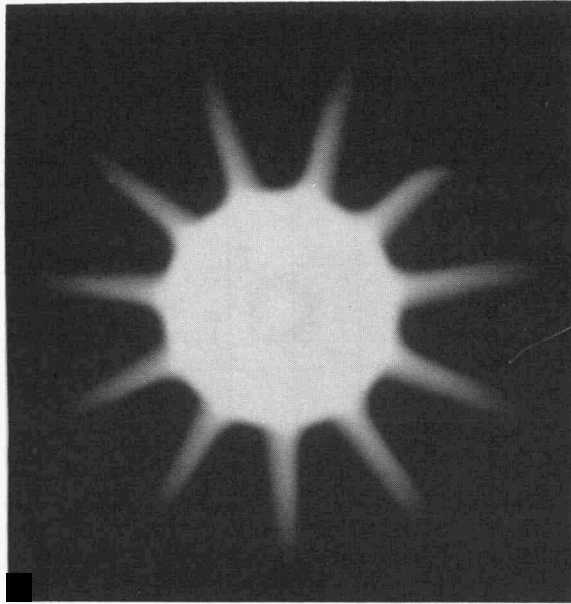


Fig. 5. X-ray CT cross section (1 mm thick) taken through bladed region of rotor I with inserts ABC.

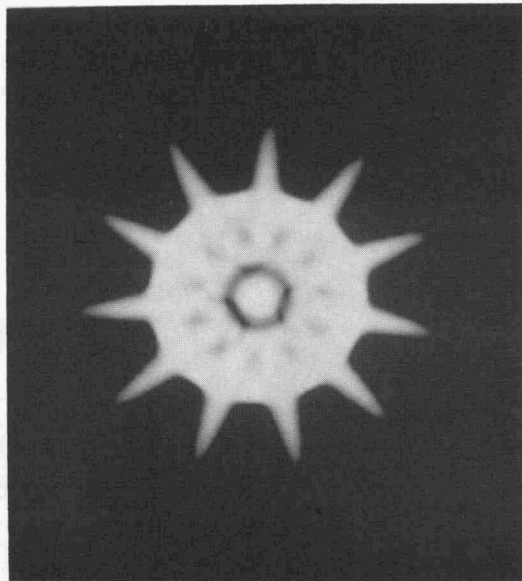


Fig. 6. X-ray CT image of section (1 mm thick) through rotor II with DEF inserts.

Nuclear Magnetic Resonance Imaging – N. Gopalsami, S. L. Dieckman, W. A. Ellingson, and R. E. Botto (Argonne National Laboratory), and H. Yeh and J. P. Pollinger (Garrett Ceramic Components Division of Allied-Signal Aerospace Corporation)

Objectives/scope

The objectives of this program are to: utilize NMR imaging techniques developed at ANL to study the distribution of whiskers and other possible variations in composite green-state (as cast) billets; perform 3-D X-ray (in a related activity (3.5.1.5)) and optical microscopic analysis (to be performed by Garrett Ceramic Components a Division of Allied Signal Corp.) of the composite billets; correlate the results obtained from the NMR imaging techniques with those obtained from both the 3-D X-ray and the optical microscopy.

Technical Highlights: Part A - NMR Studies

The previous work has established the utility of two-dimensional (2-D) back-projection NMR imaging techniques for NDE of the semi-solid organic distributions in injection-molded green-state ceramics. In this work, two-dimensional back-projection techniques were employed because these techniques offer advantages over conventional slice-selection techniques for application to semi-rigid materials (such as the semi-solid organic binders.) However, for systems where there exists a great deal of molecular mobility, such as water in slip-cast composites, echo recalled techniques can be more conveniently and perhaps more accurately applied. In this reporting period, three-dimensional slice-selected echo-recalled (also termed spin-echo) techniques were developed for MRI imaging of the residual water in green as-cast slip-cast billets.

The slice selection techniques have been well developed and have become the method of choice for medical diagnostic applications of magnetic resonance imaging. The principal of slice selection is based upon the selection of a narrow spatial region (a slice) in one direction, then encoding the remaining two dimensions in the slice. For example, in the slice-selected spin-echo pulse sequence shown in Fig. 1, the shaped RF pulse occurring in concert with the Z gradient pulse selects a narrow frequency slice in the X-Y plane. The X and Y gradients then phase and frequency encode the signal along the X and Y directions, respectively. The experiment is repeated, varying the amplitude of the X gradient, to enable correct phase encoding of the two dimensional slice along the X axis. The data is then reconstructed using a variety of filtering techniques and multidimensional Fast Fourier Transforms (FFTs).

Initial attempts at slice selection were made of a water filled spherical glass phantom on our custom solid NMR imaging accessory. Implementing the pulse sequence in Fig. 1, initial images were obtained of slices from various locations throughout the spherical sample (Fig. 2). Further work is in progress to improve the image signal-to-noise ratio,

resolution and aspect ratio. Additionally, experiments using specialized calibration phantoms will be performed to determine slice selectivity (thickness and position), as well as the spatial resolution, and sensitivity of the slice-selection technique. The slice-selection technique will then be evaluated for application to slip-cast composites.

Status of Milestones

We were delayed on some milestones because the subcontract to Garrett Ceramic Components Division of Allied-Signal Aerospace Corporation was not finalized on schedule.

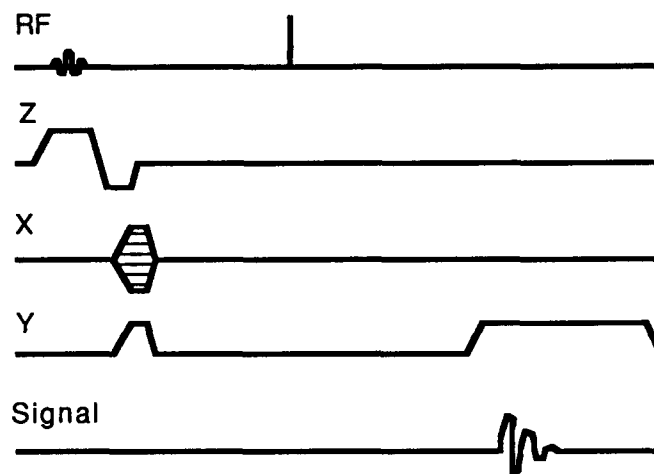


Fig. 1. Diagram of the three-dimensional slice-selected echo-recalled imaging technique implemented for characterization of "fluids" contained in green-state as-cast composites.

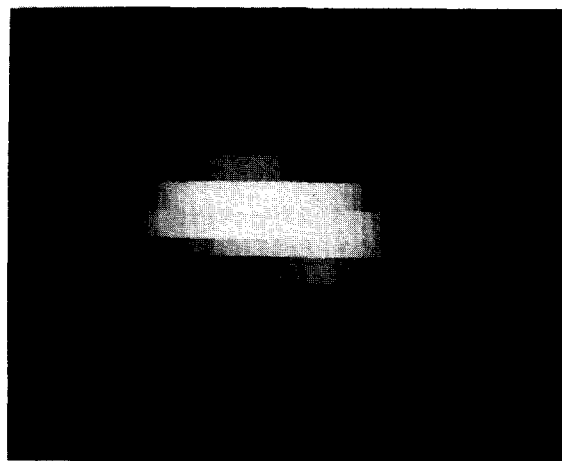


Fig. 2. Three-dimensional slice-selected image acquired from a narrow region of a glass sphere containing water. The data was acquired using the pulse sequence were shown in Fig.. 1.

PHYSICOCHEMICAL CHARACTERIZATION AND SURFACE MODIFICATION OF SILICON NITRIDE CERAMIC POWDERS - Prof. Marc A. Anderson (University of Wisconsin - Madison)

Objective/scope

This project is designed to fulfill two primary objectives:

1. characterization of the aqueous surface chemistry of silicon nitride, which also requires the development of a standard for mobility measurements and participation in a round-robin characterization of this standard; and
2. spectroscopic characterization of aqueous suspensions of silicon nitride.

Technical progress

Our work in the past six months has focused on two primary areas:

1. analyze the results of the second round robin using phosphated goethite and incorporate the conclusions reached therefrom into the design of a third round robin using phosphated goethite; and
2. investigate the hydrolysis reactions and kinetics of silicon nitride powder (Ube E-10) exposed to solutions of different pH by using electrophoretic mobility studies coupled with determinations of dissolved silica and ammonia.

Round Robin Analysis of Mobility Measurements: In the last six month report, the protocols used to prepare samples of phosphated goethite for study in the round robin were described. Analysis of the second round robin using phosphated goethite suspensions [Goethite Electrophoretic Mobility Study (GEMS) 2] has now been completed with the following conclusions being reached.

1. Variations in measured pH values at pH 5.1 or higher are likely due to CO₂ dissolution within the suspensions. Such dissolution can occur during shipment of the samples as well as during the actual measurement of sample pH. One method of minimizing CO₂ uptake while performing pH measurements is to perform these measurements under a blanket of CO₂-free gas, with stirring, until a constant pH is obtained. This approach to pH measurement is being tested. CO₂ dissolution in samples during shipping will be accepted but will be studied by comparing the pH of samples kept at the University of Wisconsin - Madison (UW) to the pH of samples shipped from UW to Oak Ridge and then back to UW.
2. Variations in measured mobility values at higher pH can be attributed, in part, to the pH variations noticed under these conditions. Since the mobility of goethite is pH dependent, variations in measured pH would lead to variations in measured mobility. Given this problem, the agreement in measured mobility

values is quite promising, especially considering that these values were obtained using four separate instruments. However, near the isoelectric point, mobility measurements on the PenKem System 3000 appeared to be consistently more negative than mobility measurements on the Malvern Zetasizer.

3. Isoelectric points for the phosphated goethite lie between pH 4.9 and 5.4. Thus, even though differences in measurements were noted, the isoelectric point is a reasonable indicator of system behavior. However, the differences between the two instruments in measuring mobilities near the isoelectric point resulted in the observation that isoelectric points obtained using the PenKem System 3000 were between pH 4.9 and 5.2 while isoelectric points from the Malvern Zetasizer were between pH 5.2 and 5.4. These differences should be studied further.

4. Other than for one or two isolated incidents, sample aging was not observed.

5. Sonication of samples did cause significant effects on occasion, but no obvious trends were apparent. Since both probe and bath sonicators were employed, a consistent sonication procedure should be utilized in future round robin measurements. It was decided that samples should be placed in a bath sonicator for 15 minutes before use. The effect of using this procedure will be tested.

6. Enough questions remain to justify a GEMS 3 round robin. Measurement protocols will be controlled more closely than in GEMS 2, so that statistical evaluation of the results will be easier to perform. The effect of ionic strength on the measurements will be evaluated by preparing samples at three ionic strengths - 0.001 M, 0.01 M and 0.05 M KNO_3 . For each ionic strength, samples will be prepared at five pH values - 3.5, 4.4, 5.2, 6.1 and 7.0. Thus, 15 different samples will be measured on each measurement date. Either four or five sets of measurements will be performed.

Another question is the ability of these different instruments to measure samples which consist of two different particles with different mobilities. An attempt was made to answer this question by preparing a sample of silicon nitride particles (Ube E-10) mixed with polystyrene latex particles (0.5 micron diameter) in a 1:1 volume ratio. Both the Malvern Zetasizer and the PenKem System 3000 measured only one mobility in this sample, but this result was shown to be due to heterocoagulation of the particles, not an inherent deficiency in the instruments. A valid test of this concern requires very careful preparation of the samples being used for the evaluation.

Aging of Aqueous Suspensions of Silicon Nitride: Complex changes in electrophoretic mobility values as a function of pH are observed for aqueous suspensions of Si_3N_4 which have equilibrated with air. These changes suggest that another surface reaction is occurring at the surface sites of hydrated Si_3N_4 particles besides the expected protonation-deprotonation reactions. Curves of mobility vs. pH for these systems give clear pH_{IEP} values (between pH 6.5-7.2), after 2 h of equilibration at different pH values between 4 and 9.5. Little change in pH is noted in the suspensions over this time period. After 20 h of aging under the same conditions, the pH values of the basic

suspensions drop considerably, to below pH 7.5. Under these conditions, all particles display positive mobilities, with a minimum mobility at or slightly below pH 7 and higher positive mobilities at slightly higher pH values. (These findings are similar in several respects to observations reported by Rutgers Univ.) Further aging gives even more complex behavior. These observations indicate that these other types of surface reactions are slower than the protonation-deprotonation process.

Although the profiles of the mobility vs. pH curves for Si_3N_4 suspensions aged for 2.5 h and the pH_{IEP} values for these systems (between pH 6.5-7.2) are practically independent of solid concentration (between 0.5 g/l and 60 g/l), this is not true for suspensions aged at least 20 h. In addition, pH is the most important variable affecting the kinetics of surface aging, as the differences in mobility values with time are larger at higher pH. Mobility values as a function of pH for Si_3N_4 suspensions, which have been aged while the pH has been held near 9.5 for 20 h to a few days previous to titration, are very reproducible. No charge reversal is observed in these systems and the particles develop a highly positive charge, as indicated by the pH_{IEP} of 8.5 (compare this value to the 2.5 h aged suspensions mentioned above where $\text{pH}_{\text{IEP}} \approx 7$).

These observations suggest that the Si_3N_4 surface (Ube powder which has been kept in a closed container under air for over one year) is probably covered with patches of silica. Note that the entire surface is not covered with silica because the measured pH_{IEP} is too high. Dissolution of silica from this surface by aging in a high pH solution would expose more N-H groups (the exact form of these groups must still be determined), shifting the pH_{IEP} to more basic values.

Support for this suggestion comes from several observations.

- 1.) Protonation-deprotonation reactions of organic amines in water typically display pK values of 10 to 11.
- 2.) Addition of fine silica particles (surface area of 90 m^2/g) to washed suspensions shifts the pH_{IEP} to more acidic values, presumably due to heterocoagulation (adsorption of the fine silica particles onto the Si_3N_4 surface).
- 3.) The concentration of dissolved silica in the supernate of Si_3N_4 suspensions which have been aged for more than 150 h near pH 9.5 is a function of solid concentration (2E-3 M at 5 g/L and 4E-3 M at 10 g/L).
- 4.) After discarding the supernatant solution from the 5g/L suspension analyzed in #3 above, the remaining solid was reexposed to a pH 9.3 solution. After 24 h exposure, the dissolved silica concentration was 4E-4 M, compared to 1.4E-3 M in the comparable system in #3.
- 5.) The concentration of dissolved ammonia in the same systems is only 5% to 10% of the concentration of dissolved silica. Based on the stoichiometry of dissolution of pure silicon nitride, we would expect to observe a dissolved ammonia:silica ratio of 4:3.

The complex mobility changes observed in these suspensions after long-term aging, without base washing of the suspensions, can also be explained by this hypothesis. Aging under acidic conditions causes little dissolution of silica from the surface and little change in

suspension properties over time. Aging under basic conditions, though, causes considerable silica dissolution and a net release of protons. Silica dissolution, as discussed above, shifts the isoelectric point to more basic values (at a given pH, the mobility becomes more positive). The net release of protons causes a fairly rapid drop in pH (from pH 9.5 to pH 7.2 after 20 h aging) with a concomitant increase in mobility. Although CO₂ absorption also occurs in these systems, the kinetics involved in this reaction (which also acidifies the system) are much slower because the reacting suspensions are kept capped.

Thus, it appears that a more pristine Si₃N₄ surface can be obtained by washing the powder in a basic solution for some time (pH 9.5 for 24 hours worked well), then discarding the supernate and using the cleaned powder to prepare further suspensions under the desired conditions. It is clear that the as received powder is not completely covered with silica, as the p*H*_{IEP} of the as received powder is still much too basic to be attributed to a pure silica surface. A reasonable description of the silicon nitride surface after 1 year aging in air would be that it is covered with patches of silica in places but that silicon nitride is exposed elsewhere. Whether this silica is amorphous silica or a silicate polymer on the surface is not yet known, although we favor the idea of amorphous silica because this form is the most stable.

Further studies have been undertaken of SiO₂ dissolution kinetics from silicon nitride surfaces as a function of solid concentration. All systems are aqueous suspensions held at pH 9.5. The molybdenum blue colorimetric method was used to measure concentrations of dissolved SiO₂ in filtrates prepared by filtration of suspensions through 0.05 micron Nuclepore filters. The maximum SiO₂ concentrations measured and the time required to reach those concentrations are reported in Table 1.

Table 1. Silicon Nitride Dissolution Kinetics

Solid Conc. (in g/L)	Max. Dissolved SiO ₂ (in M)	Time Needed to Reach Max. (in days)
5	2.0 x 10 ⁻³	4 to 5
10	4.0 x 10 ⁻³	between 2 and 7
20	6.2 x 10 ⁻³	3
40	7.2 x 10 ⁻³	2
60	7.2 x 10 ⁻³	2

Since the solubility limit for dissolved SiO₂ in water at pH 9.5 is about 6 x 10⁻³ M, the measured values at low solid concentrations show the system approaching this solubility limit, which has been reached when 20 g/L of solid is present. However, if this solubility limit is the only factor operating in these systems, then the maximum values at 40 and 60 g/L would also be about 6.2 x 10⁻³ M. Two other explanations for these higher than expected values were investigated.

1. Very fine colloidal SiO_2 particles are being formed in systems with high solid concentrations and are being measured along with dissolved SiO_2 during the analysis. Light scattering measurements were made of filtrates which have been passed through filters with different pore sizes. Fine particles are present in filtrates passed through 0.4 micron filters but not in filtrates passed through 0.05 micron filters. However, both filtrates give identical concentrations of dissolved SiO_2 . It appears that the presence of colloidal SiO_2 particles does not affect the analysis for dissolved SiO_2 .

2. Another soluble silicate species, besides dissolved SiO_2 , forms in systems with high solid concentrations and is measured along with dissolved SiO_2 by our analytical technique. Since we suspect that such a compound would contain both Si and N, possibly some form of silicon oxynitride, we performed several types of nitrogen analysis to obtain further information.

First, a specific electrode was used to measure dissolved ammonia (NH_3) gas in the same systems used for dissolution kinetics studies. The dissolved NH_3 concentrations are always at least an order of magnitude less than the corresponding dissolved SiO_2 concentrations. These concentrations should be similar, with $[\text{N}] > [\text{Si}]$, if the dissolved SiO_2 comes primarily from the pristine silicon nitride surface interacting with water. Thus, this observation shows that dissolved SiO_2 in these systems arises primarily from islands of SiO_2 which are already present on the silicon nitride surface before the silicon nitride is placed in water. Also, values for dissolved NH_3 are very similar in both closed systems and in systems open to the atmosphere, showing that movement of dissolved NH_3 gas to the atmosphere is very slow.

Second, nitrogen concentrations of selected samples were determined by the Kjeldahl method, which measures both ammonia and organic nitrogen but not nitrite or nitrate nitrogen, and by a method for nitrate nitrogen. All systems were aged for 6 days at pH 9.5 in closed containers. Table 2 shows the results of replicate measurements.

Table 2. Nitrogen Analyses of Aqueous Suspensions of Si_3N_4

Solid Conc. (in g/L)	Total Kjeldahl-N (in M)	Ammonia-N (in M)	Nitrate-N (in M)
10	8.5×10^{-4}	3.5×10^{-4}	1.8×10^{-4}
10	8.5×10^{-4}	4.2×10^{-4}	1.4×10^{-4}
20	10.6×10^{-4}	6.0×10^{-4}	3.2×10^{-4}
20	12.4×10^{-4}	5.3×10^{-4}	3.9×10^{-4}
60	15.2×10^{-4}	7.1×10^{-4}	2.1×10^{-4}
60	16.3×10^{-4}	7.4×10^{-4}	3.2×10^{-4}

There is clear evidence for the presence of some nitrogen species in these systems which is being measured as organic nitrogen. Although the exact compound is not known at present, the concentration of this compound does increase with the solid concentration. If this species contains both Si and N, it could well be responsible for the anomalous dissolved SiO_2 concentrations which were observed at high concentrations of silicon nitride.

CIR-FTIR Spectroscopy of Silicon Nitride Suspensions: CIR-FTIR spectra of positively and negatively charged silicon nitride suspensions show some differences in the region from 3600 to 3000 cm^{-1} . This spectral region is associated with N-H and/or O-H stretching modes of the Si_3N_4 surface groups. Since the Ube Si_3N_4 has very low surface area (10 m^2/g), the intensity of absorption bands coming from the surface is very weak in comparison with bands from the bulk solid. Thus, a higher surface area Si_3N_4 should be used to obtain more useful information from in situ infrared spectroscopy. However, attempts to obtain higher surface area Ube silicon nitride powders have been unsuccessful. Other powders with higher surface area than the Ube may be available, but these powders would have somewhat different surfaces if they are prepared by different processes. Note that, because the energies of N-H and O-H stretching modes are very similar, we expect to have some difficulty in making peak assignments for the infrared spectra we do obtain, even if we can locate the perfect powder for our studies.

Status of Milestones

1. Complete round robin characterization of "benchmark" colloid. Expected completion: Dec. 31, 1990. Delayed because of need for a third round robin study using phosphated goethite (Goethite Electrophoretic Mobility Study 3 -- GEMS 3).
2. Complete initial round robin mobility testing of silicon nitride. Expected completion: Apr. 30, 1991. Delayed while GEMS 3 is performed.
3. Complete round robin mobility testing of silicon nitride. Expected completion: July 31, 1991. Delayed while GEMS 3 is performed.
4. Complete peak assignments for CIR-FTIR spectra of aqueous suspensions of silicon nitride. Expected completion: Nov. 30, 1991. On schedule.

Publications

None.

Surface Thermodynamics

J.-F. Wang, R. E. Riman, and D. J. Shanefield
(Rutgers University)

Objective/scope

The purpose of this effort is to (1) identify and characterize those aspects of the chemistry and physics of the ceramic powder and powder/solvent interface that control processing, (2) develop standard methods of analysis for item (1), and (3) develop procedures for writing specifications for ceramic powders to include any methods of analysis developed in this project.

Technical progress

The work that has been done in the past six months is summarized as follows: (1) the electrophoretic properties of silicon nitride powder, UBE E-10, were studied as a function of pH, electrolyte concentration, aging condition, and dispersant adsorption; (2) the distribution of electrophoretic mobilities of UBE E-10 and a reference colloid, polystyrene latex, was studied and the size effect of polystyrene latex was investigated using the Malvern 4700c Size analyzer and Zetasizer II; (3) good dispersants for silicon nitride powder were investigated using sedimentation, ball milling, microelectrophoresis, and thermal analysis; (4) round robin silicon nitride powder was divided into equivalent samples by a chute splitter and spinning riffler and sent to the other contractors; and (5) goethite, a benchmark colloid, was prepared using the University of Wisconsin's procedure and characterized utilizing XRD, BET, TGA, DTA, and microelectrophoresis.

Electrophoretic properties of silicon nitride powder (UBE E-10):

The electrophoretic mobility of silicon nitride powder, UBE E-10, in aqueous solution as a function of pH, aging time, indifferent electrolyte concentration, and dispersant adsorption was measured.

The electrophoretic mobility of one day aged UBE E-10 (0.01 vol%) as a function of pH is shown in Figure 1 for KNO_3 concentrations of 10^{-2} and 10^{-3} M. The isoelectric point (IEP) measured is about pH 7.4 and the mobility curves obey the DLVO theory -- at higher electrolyte concentrations, a more depressed mobility is expected. The IEP obtained agreed well with the value reported at the last contractor meeting.

The electrophoretic mobility of a series of aged UBE E-10 samples in 0.01M KNO_3 solution was measured on a finer pH scale than for previous studies. A discontinuity inside the pH range 6 to 8 was observed for aged samples, which was smoothed out after 30 days of aging (Figure 2). This was also noticed by the coworkers at the University of Wisconsin-Madison and reported in the last contractor meeting held in ORNL. Based on their studies, this discontinuity was due to the different silica dissolution and re-adsorption rates from the surface of silicon nitride powder in different solution pH ranges.

The dispersant-adsorbed UBE E-10 powder was prepared by adding 0.5 wt% Darvan C (R. T. Vanderbilt Company Inc., Norwalk, CT) or KD-2 (ICI Americas Inc., Wilmington, DE) in a UBE E-10 powder suspension. The suspension was then well mixed by shaking and sonication and equilibrated for a certain period of time. A dilute dispersion, 0.01 vol% UBE E-10, for electrophoretic mobility measurement was prepared by using the centrifuged sediment obtained from the above equilibrated suspension.

The IEP of the received UBE E-10 powder in 0.01M KNO_3 aqueous solution for one day aging was 7.4. Since the Figure 3 shows that the measurements of the electrophoretic mobilities of UBE E-10 powder with 1- or 45-day adsorption of the dispersant gave no significant difference, the sufficient equilibration for the adsorption of Darvan C or KD-2 on silicon nitride powder surfaces in aqueous solution could be obtained within a day.

Figure 3 also shows that the Darvan C, a highly negatively-charged ammonium acrylate polyelectrolyte, adsorbed strongly on the slightly positively-charged UBE E-10 powder surface and shifted the IEP from 7.4 to 3.8. The zeta potential measured for the Darvan C adsorbed UBE E-10 powder in the pH range 6 to 10 was greater than -50 mV. The slightly cationic KD-2, polymer imide, moved the IEP towards the other direction from 7.4 to 8.1 and showed relatively less charging capability on UBE E-10 powder than Darvan C. The stability of the UBE E-10 suspension offered by KD-2 is believed to be contributed by steric hindrance effects rather than electrostatic effects. This will be discussed in the section of determination of dispersant effectiveness.

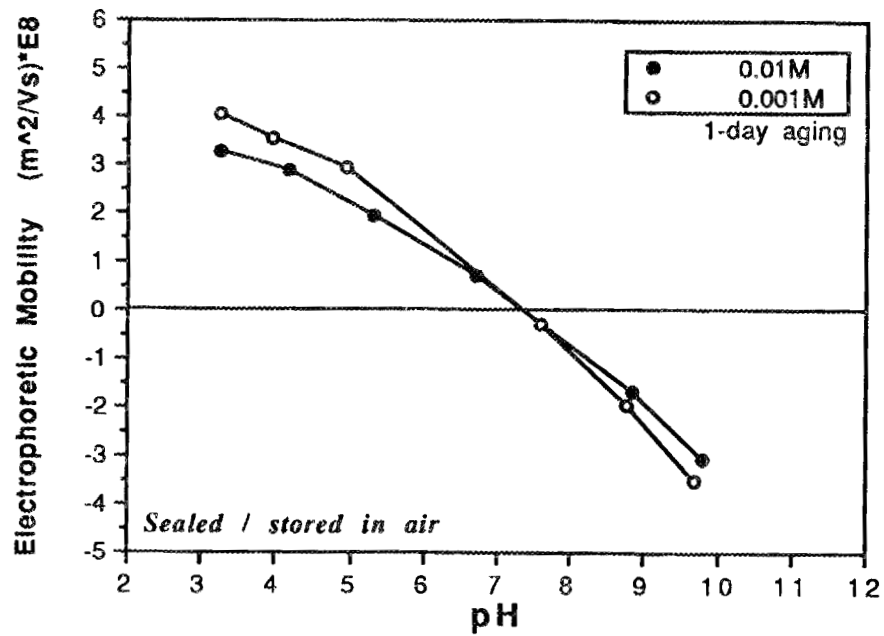


Figure 1. The electrophoretic mobility of 0.01 vol% UBE E-10 powder as a function of electrolyte, KNO₃, concentration.

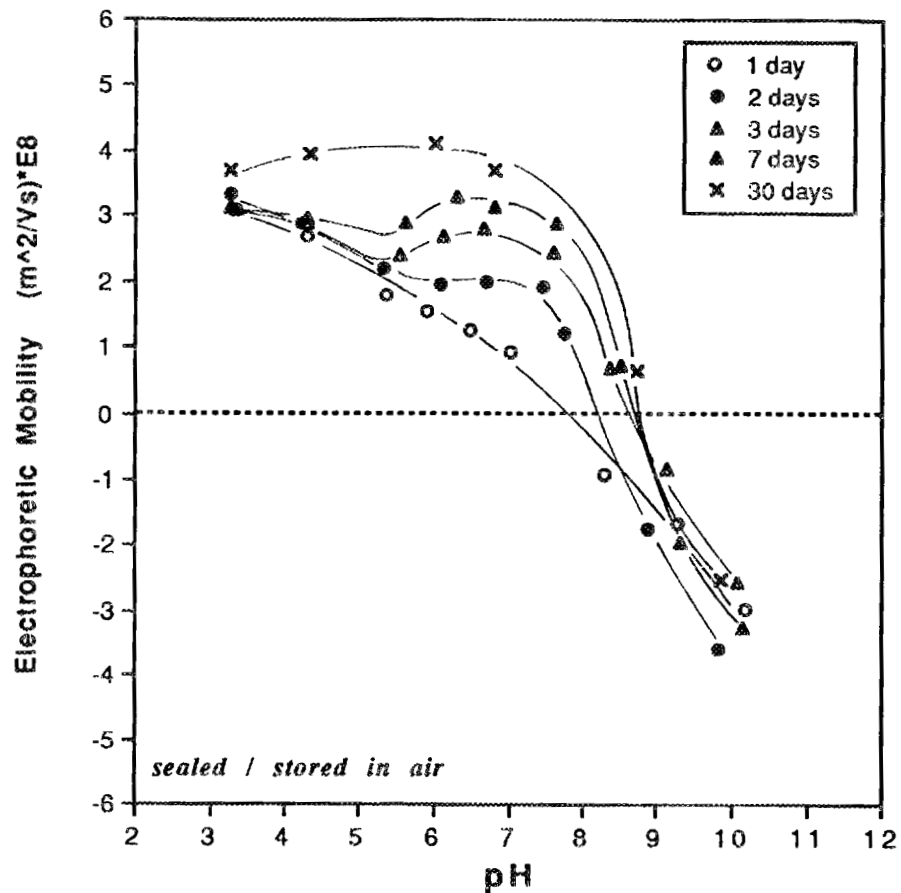


Figure 2. The electrophoretic mobility of 0.01 vol% UBE E-10 powder in 0.01M KNO₃ as a function of aging time.

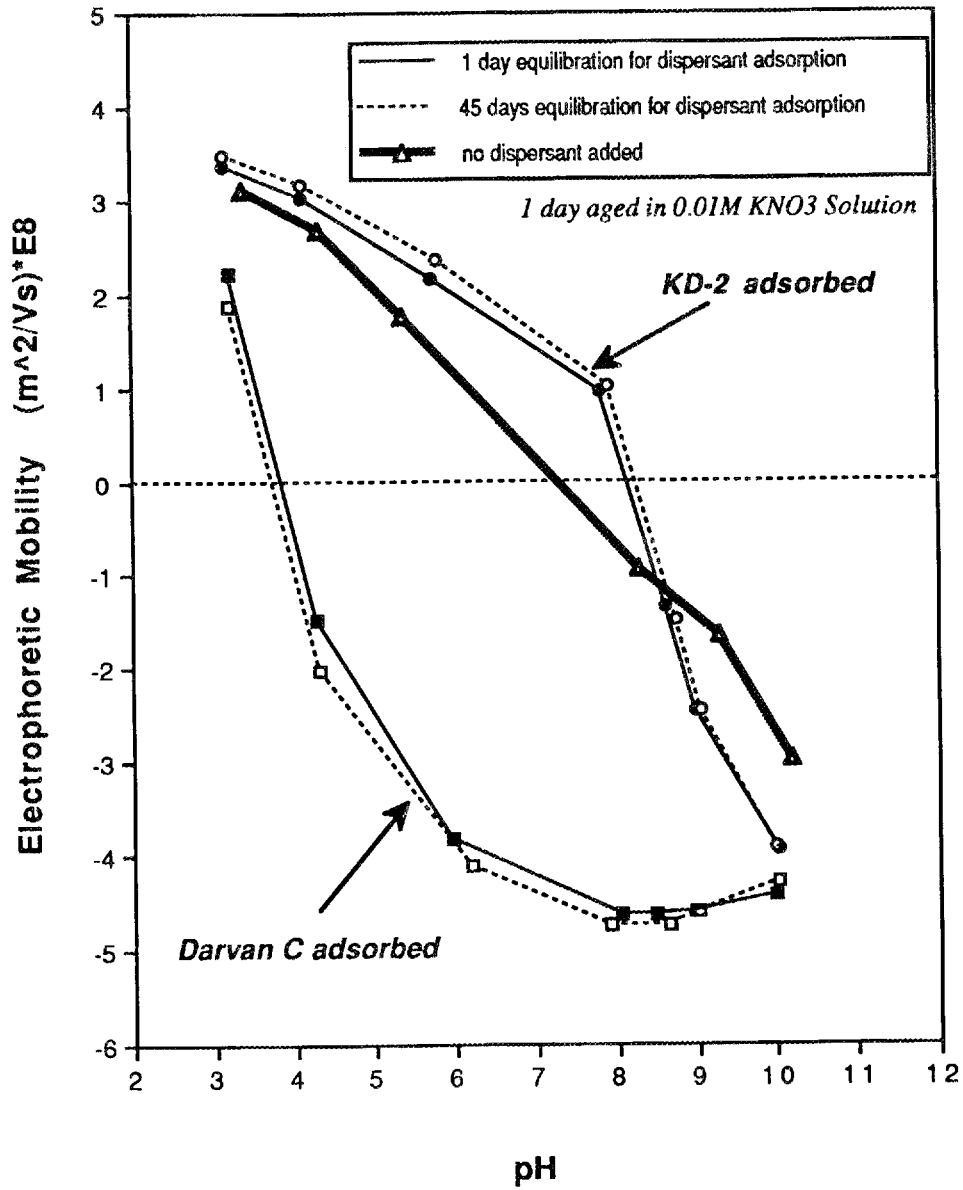


Figure 3. The electrophoretic mobility of 0.01 vol% UBE E-10 as a function of dispersant addition.

The adsorption mechanism of polyelectrolytes on silicon nitride powder surfaces in aqueous solution could be explained by the electrophoretic mobility curves. When the solution pH is higher than the IEP, the surfaces of ceramic powder will become more negatively charged. Since the Darvan C is an anionic polyelectrolyte and highly charged in high pH, the adsorption of it on UBE E-10 surfaces should be limited as the solution pH increases. However, the curve shows that the mobility of the Darvan C adsorbed UBE E-10 at $\text{pH} > \text{IEP}$ is even more negative than that without any Darvan C adsorption.

The adsorption of Darvan C shifts the whole mobility curve towards more negative side and its slope changes little in the pH range from 4 to 8. At $\text{pH} > 8$, the adsorption of Darvan C becomes saturated -- the adsorbed Darvan C molecules expel the ones in solution preventing further adsorption. At $\text{pH} < 4$, the Darvan C was only slightly charged with more carboxylic acid groups than charged carboxylate groups. The adsorption of the Darvan C, therefore, gives not much negative charges to the surface of the powder.

Another example, the adsorption of KD-2, a slightly cationic polyelectrolyte, did not increase as the solution pH increased, e.g., $\text{pH} > 9$. The electrophoretic mobility measured was more negative than that without any KD-2 adsorption.

All of the above phenomena observed made us believe that the adsorption of the polyelectrolytes used was not mainly contributed by the electrostatic effect. The van der Waals attraction force between the powder surfaces and the macromolecules of the polyelectrolyte was the dominated factor for the adsorption. Therefore, the surface property of the particle, e.g., electrophoretic mobility or surface potential, could be a way to depict the characteristic of the dispersant adsorption.

Distribution of electrophoretic mobility and size effect: In order to monitor the change in surface properties of doped ceramic powder or to differentiate the mobility of an individual particle component from a mixture of different particles of various chemical compositions, mobility distribution studies were initiated.

A preliminary study on the effect of aging of the reference colloid, polystyrene latex, and the received UBE E-10 powder on the mobility distribution was carried out using the Malvern Zetasizer II. Sulfated 0.5 μm polystyrene latex (Polysciences, Inc., Warrington, PA) was aged in 0.01 M KNO_3 aqueous solution (0.01 vol%) for three different time periods, 1, 4, and 7 days. Figure 4 presents the mobility change of polystyrene latex after aging 7 days in electrolyte solution.

Significant differences were noted at high pH. However, if polystyrene latex was aged in the original dispersion as received from the company instead of in an electrolyte solution and stored in the refrigerator, the electrophoretic mobility of the latex would deviate very little over a six months period ($\pm 3.4 \times 10^{-9}$ m²/Vs) as reported in the last semi-annual report.

The distribution of electrophoretic mobility of polystyrene latex became narrower regardless of solution pH after aging in 0.01M KNO₃ solution for more than seven days (Figure 5a). In contrast, the UBE E-10 powder showed wider mobility distributions for samples with longer aging time (Figure 5b).

The distribution of electrophoretic mobility was also found to be broader at two ends of solution pH than in between, regardless of sample aging time (Figure 5b). All the percentage widths reported in Figure 5 were relative to the %width of a sample with one day aging at lowest pH. Unfortunately, no correlations between the distribution of electrophoretic mobility and the aging factor can be made in a conclusive manner.

Two 0.01 vol% suspensions (i.e. polystyrene latex and UBE E-10 powder), both with the pH value at about 10, were used separately or mixed to test the mobility resolution sensitivity of the Malvern Zetasizer II.

The electrophoretic mobility measurements of 7-day aged polystyrene latex and 2-day aged UBE E-10 powder were given as -7.88 and -3.38×10^{-8} m²/Vs, respectively. The 1:1 mixture of these two suspensions with or without one day equilibration all gave only a single and broad electrophoretic mobility distribution with a mean value at -5.25×10^{-8} m²/Vs.

The results suggested that the instrument either might fail to separate the electrophoretic mobility distributions of a mixture or that the specific adsorption of polystyrene latices on the surfaces of UBE E-10 powder occurred. The adsorption could occur either via a strong van der Waals forces between the "fuzzy hairs" of the latex and the surface of the UBE E-10 powder or the formation of chemical bonds.

Two suspensions prepared by identical procedures were sent to one of the contractors (the University of Wisconsin at Madison) to investigate this phenomena using Pen Kem 3000 system. According to their study, the adsorption of the latices on the UBE E-10 surface has been observed through the microscope which is associated with the Pen Kem 3000. They also obtained the separated mobility distributions of the latex adsorbed UBE E-10 and the latex itself. However, the

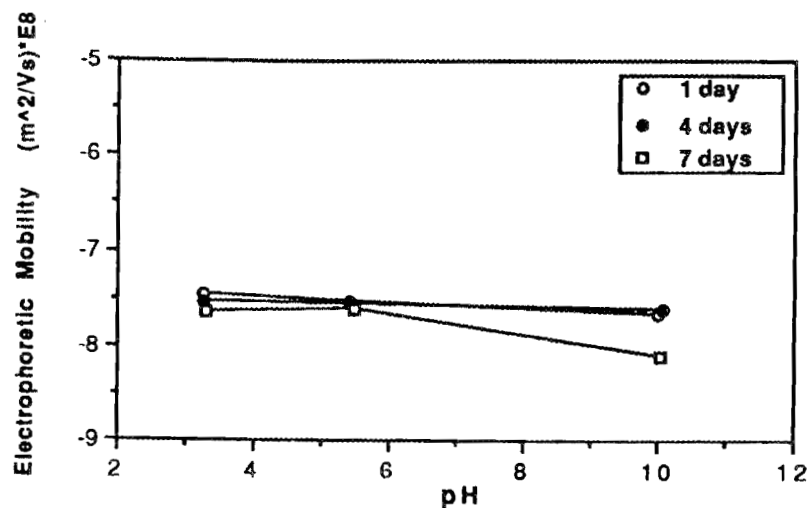


Figure 4. The electrophoretic mobility of 0.01vol% Polystyrene latex in 0.01M KNO₃ as a function of aging time.

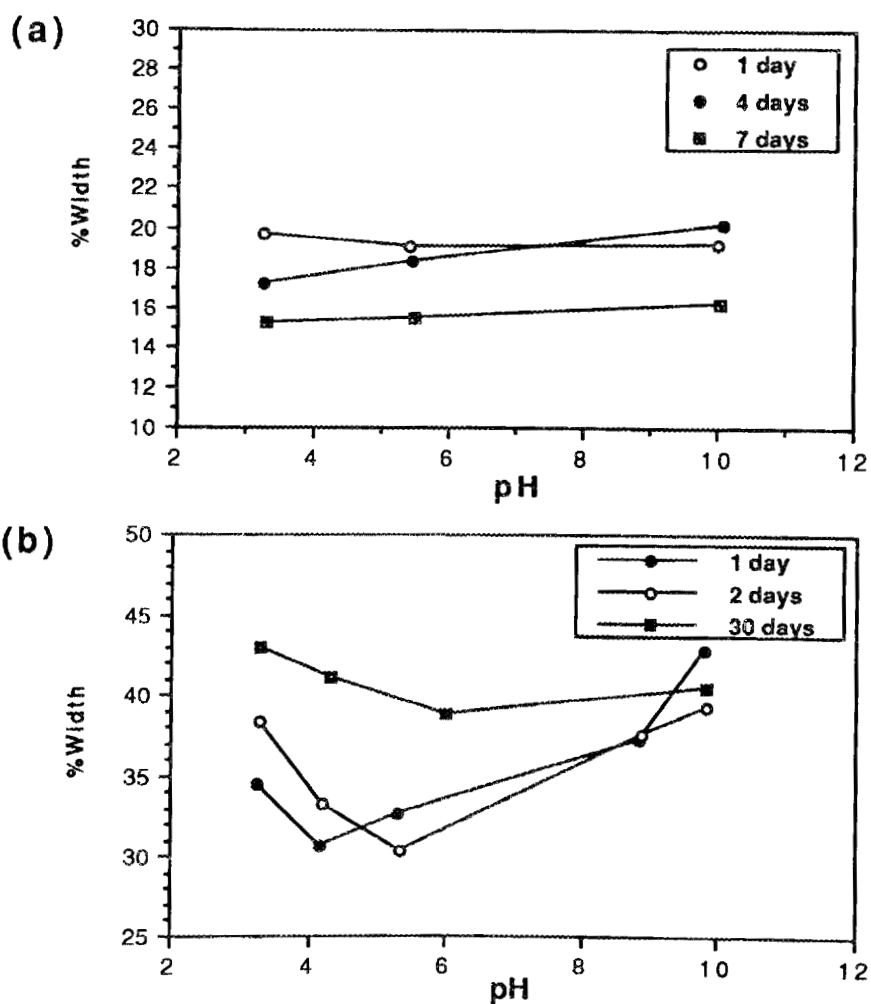


Figure 5. The %width of electrophoretic mobility distribution in 0.01M KNO₃ as a function of aging time and pH: (a) 0.01vol% polystyrene latex (b) 0.01vol% UBE E-10 powder.

measurement is strongly dependent on the sample preparation and the reproducibility is not high.

To avoid the problem of specific adsorption, mixtures of polystyrene latices were prepared, which has the same sulfated surface groups but with different sizes (i.e. nominal 0.1, 0.5, and 1.0 μm). The latices were characterized in terms of their electrophoretic mobility, particle size, and particle size distribution to investigate how particle size affects the mobility measurement.

Particle size analysis from the Malvern 4700c Size Analyzer reveals that the nominal 0.5 μm latex has a mono-modal distribution with weight average at 0.48 μm (Figure 6a). However, the 1.0 μm powder was found to be poly-modal with a weight average at 1.18 μm (Figure 6b).

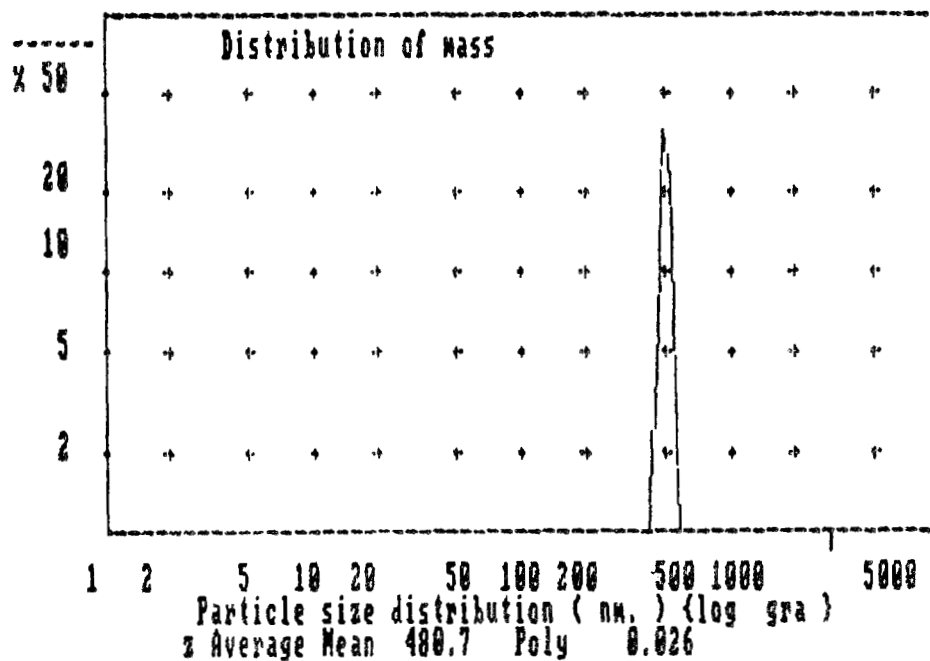
It was found that the average of the absolute mobility differences for the 0.5 and 1.0 μm powders for five pH values was $(0.44 \pm 0.08) \times 10^{-8} \text{ m}^2/\text{Vs}$ (Figure 7). The 1.0 μm sulfated polystyrene latex consistently has a higher surface charge than the 0.5 μm powder.

Unfortunately, our Malvern Zetasizer II was not successful in resolving the mobility distribution of the 0.1 μm latex, while the mobility distributions for the 0.5 and 1.0 μm powders could be reliably determined. This thwarted our efforts in getting a clear picture of the size effect on mobility and mobility distribution measurements.

The distribution of electrophoretic mobility for the 1:1 mixture of 0.5 and 1.0 μm latices at solution pH 5.5 also gave only a single and broad electrophoretic mobility distribution with a mean value at $-8.22 \times 10^{-8} \text{ m}^2/\text{Vs}$. This strongly indicates that the indistinct mobility distribution of a mixture is due to the insufficient resolution of the instrument.

We expect to have difficulty in revolving the component mobility distributions from a system having multiple distributions, unless we could perform the work with a machine offering much better resolution. Besides the instrumental resolution there are still many factors which would complex the measurement of the mobility distribution. For example, they can be the particle size distribution of the sample, the homogeneity of the mixture, the inherent chemical property of powder surface, the property of the supporting electrolyte solution, etc. It needs much more research to understand the source of this not well understood field.

(a) sample : 0.5 μm PS; pH=9.14
Data from accumulation file sum of 7 blocks



(b) sample : 1.0 μm PS; pH=9.31
Data from accumulation file sum of 6 blocks

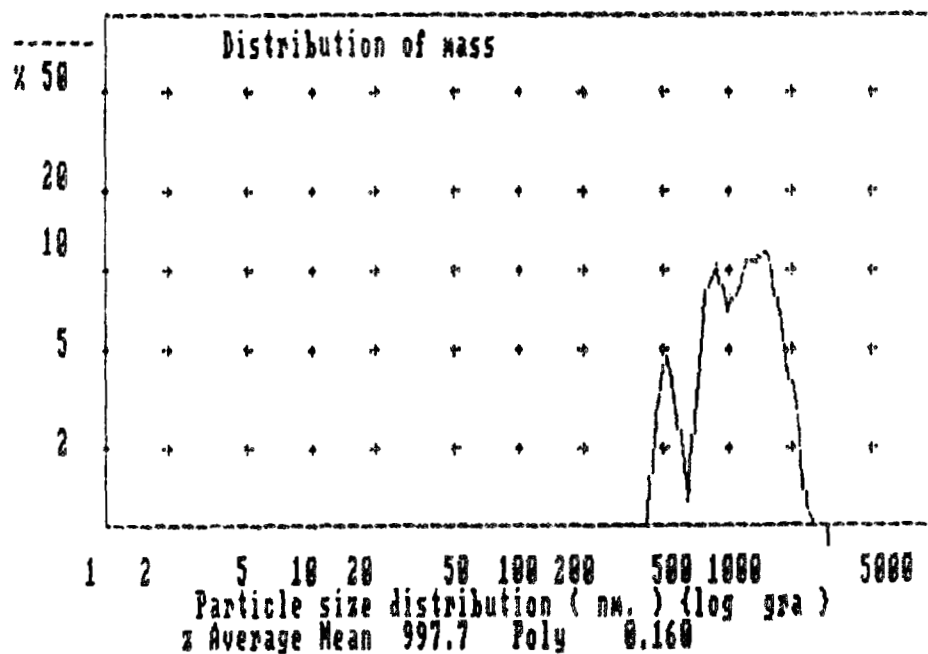


Figure 6. The particle size analysis of received polystyrene latices: (a) 0.5 μm (b) 1.0 μm .

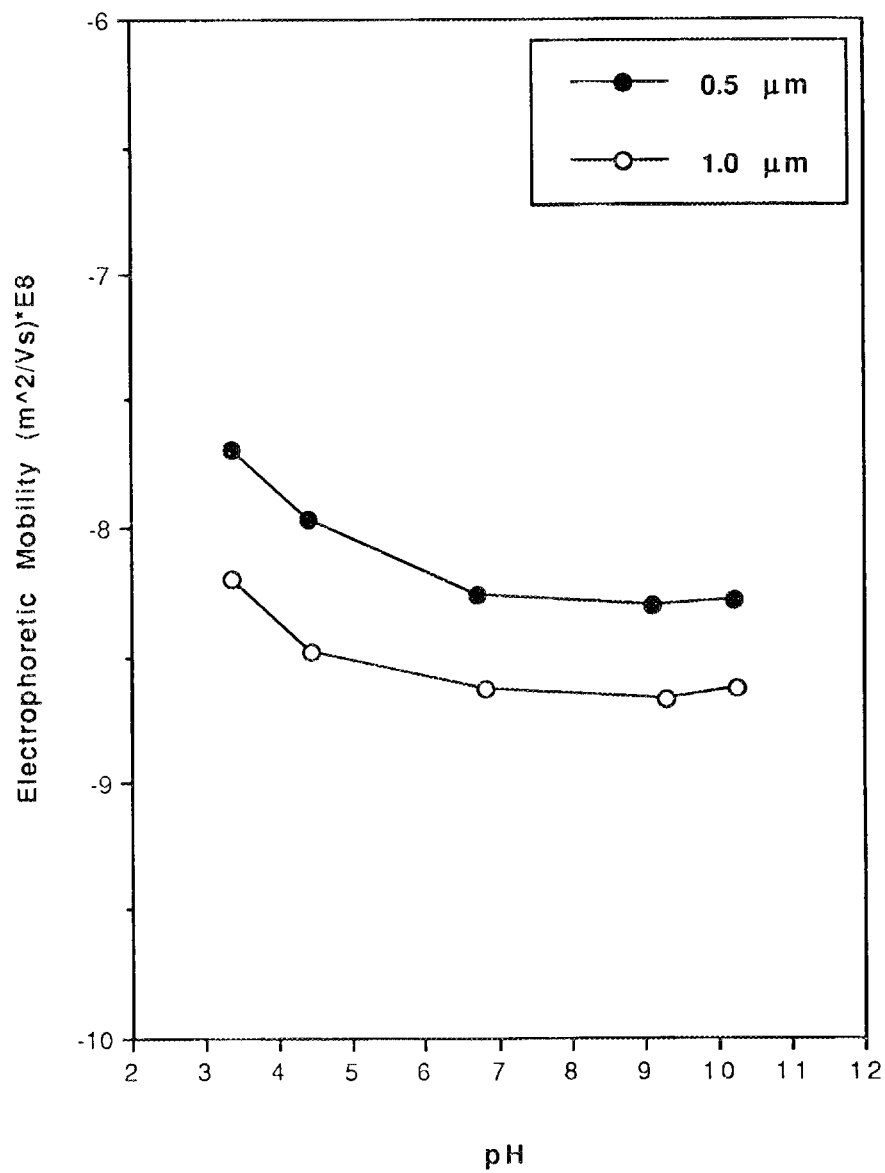


Figure 7. The electrophoretic mobility of 0.01 vol% polystyrene latex in 0.01M KNO₃ as a function of particle size.

Determination of dispersant effectiveness: The effectiveness of dispersants for processing the UBE E-10 powder both in water and in i-propanol was studied by sedimentation. A series of 10 vol% UBE E-10 suspensions was prepared both in water and in i-propanol. Three different solution pH values, 3.05, 4.82, and 9.40, were used. Four dispersants, Menhaden fish oil and three polyelectrolytes, Darvan C, Darvan 821A, and KD-2 were utilized. The weight of dispersant used relative to the weight of solvent for all suspensions was kept at 0.5%.

Sedimentation measurements were conducted by allowing the equilibrated well-dispersed suspension to settle in a Falcon plastic tube (with screw-cap) and measuring the height of the sharp interface between the sedimenting suspension and the supernatant as a function of time.

Figure 8 shows the fast sedimentation of suspensions in i-propanol with or without the addition of dispersant in the first 24 hours. However, the highest densities (~28% theoretical density) obtained were the suspensions in aqueous media using KD-2 or Darvan C. These suspensions were stable and showed no clear interfaces for almost 200 hours. Darvan C performed well for a wide range of solution pH, while KD-2 was found to be not so good as the pH decreased to 3.

In addition, the packing density of the UBE E-10 powder sediment in aqueous solution was found to be a function of the amount of dispersant added (Figure 9). For 10 vol% UBE E-10 aqueous suspension, a 0.5 wt% Darvan C or Darvan 821A addition gave the highest sediment packing density at 28.0% or 21.6%T.D., respectively. However, the addition of KD-2 gave the highest packing density at 28.1%T.D. throughout the range from 0.5 to 4.8 wt%.

In order to obtain and understand the stability of concentrated UBE E-10 suspensions, the characterization of ball milled UBE E-10 suspension in water and in i-propanol with the addition of dispersant, acid, or base was conducted. The maximum solids loading of the ball milled UBE E-10 powder by investigating the suspension viscosity was found to be much higher in the aqueous solution than in i-propanol with the addition of the dispersant, KD-2 (Figure 10).

A solids loading of 45 vol% UBE E-10 powder in water with 3 wt% KD-2 was achieved. Interestingly, in i-propanol, an aqueous dispersant, KD-2, was found to be better than KD-3, which was designed for nonaqueous systems. In i-propanol, the maximum solids loading obtained was ~30 vol% with an addition of 5 wt% KD-2.

According to the results obtained from the electrophoretic mobility and from the solids loading data, we believed the suspension stability offered by KD-2 was mainly attributed by the steric hindrance effect rather than the electrostatic effect. Most likely, the KD-2 is

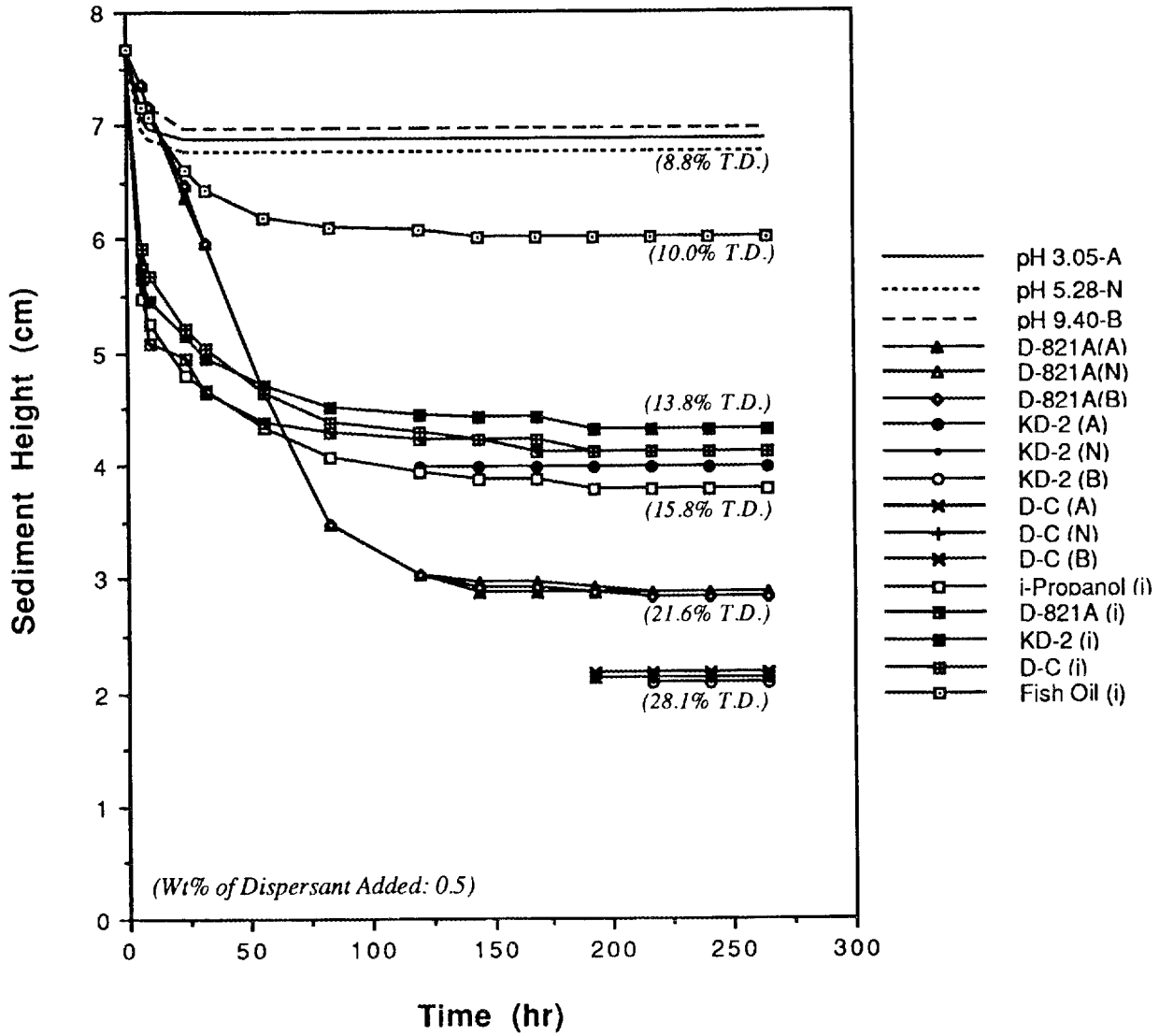


Figure 8. Sedimentation height of 25wt% UBE E-10 as a function of time, solvent, pH, and dispersant.

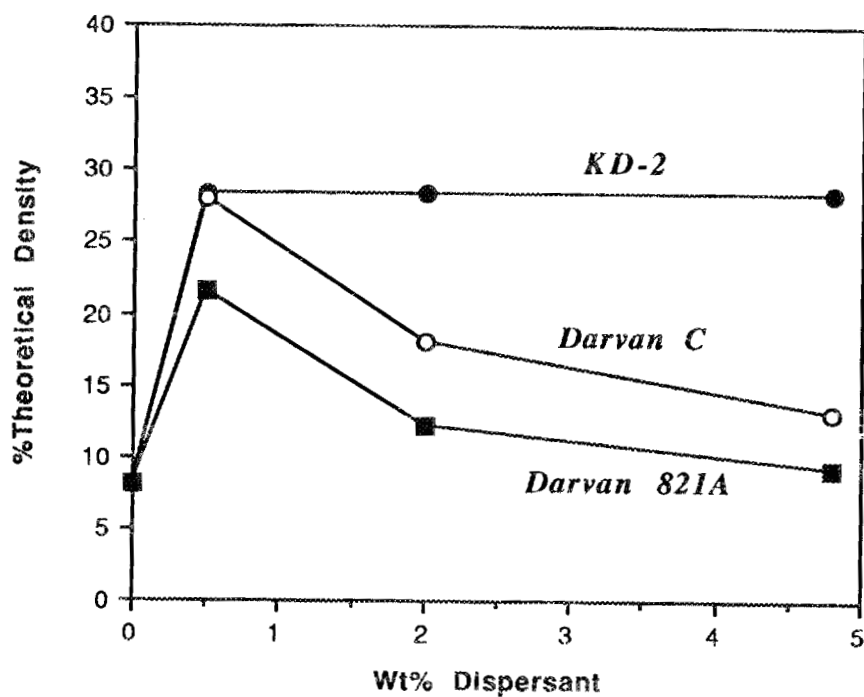


Figure 9. Sediment density of 25wt% UBE E-10 powder as a function of wt% dispersant.

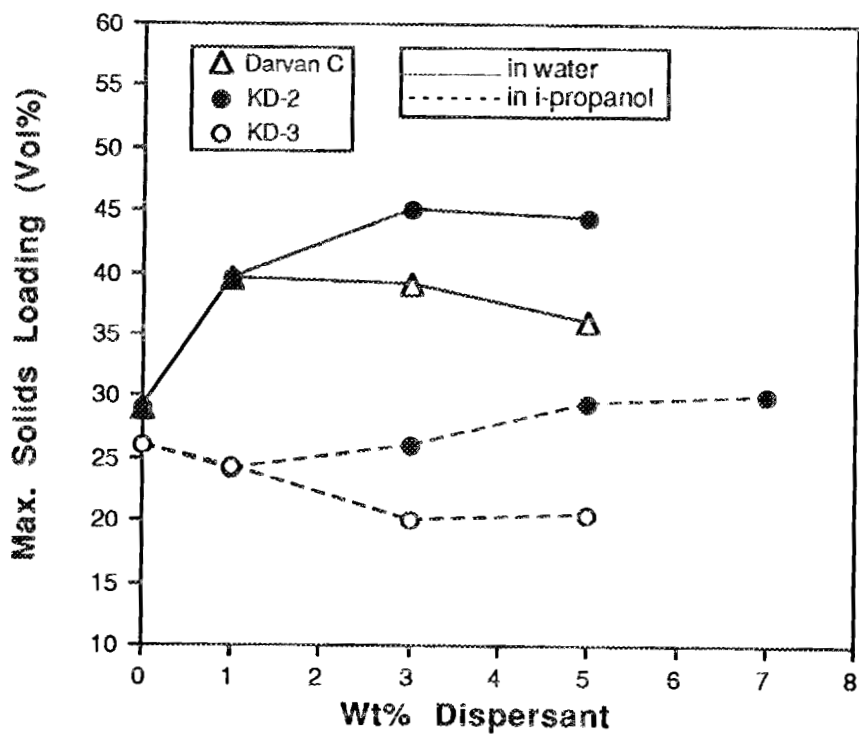


Figure 10. The maximum solids loading of ball milled UBE E-10 powder as a function of solvent and wt% dispersant.

physically adsorbed on the UBE E-10 powder surface and behaves both as a dispersant and a lubricant.

The physical adsorption of the Darvan C also can be evident by simultaneous DTA/TGA analysis (Differential thermal Analysis / Thermogravimetric Analysis). Figure 11 shows a narrow range of burn-out temperature of KD-2 and a wider one of Darvan C from the UBE E-10 powder surface. The burn-out temperature of KD-2 starts from ~250 °C which is same as its boiling point.

The ball milled concentrated UBE E-10 suspensions containing acids or bases either in water and in i-propanol were also investigated. In aqueous solution using either without dispersant, with KD-2 or with Darvan C, the maximum solids loading observed was 29, 45, and 40 vol%, respectively. All systems appeared to behave best at pH 5.7 using the deionized water only without acid (HNO₃) or base (KOH) addition (Figure 12).

In i-propanol, the maximum solids loading was strongly reduced with the utilization of base (NaOH) with or without dispersant (Figure 13). However, the use of trichloroacetic acid up to 0.5 N in i-propanol did not change the maximum solids loading of UBE E-10.

The amount of dispersant added here was chosen from the optimized value obtained in Figure 10. The charging of UBE E-10 powder surface both in aqueous and in nonaqueous systems using either low or high solution pH did not improve the stability of the concentrated suspension regardless of the dispersant addition. The best result was obtained using aqueous dispersant-added solution only without any acid or base treatment (Figure 12). The utilization of different nonaqueous solvent (e.g. cyclohexane) will be conducted in the future.

Round robin UBE E-10 powder separation: A 50 Kg UBE E-10 powder received from the Oak Ridge National Laboratories has been divided and riffled using a chute splitter and a spinning riffler. The equivalent and packaged samples (e.g. nominal 1, 3, 6, 20, 200 and 1,000 g) are being sent to each of the contractors for future round robin work.

Goethite (benchmark colloid) preparation and characterization: A batch of the electrophoretic mobility referencing material, goethite, was synthesized. The physical properties and the electrophoretic mobility of goethite were studied and compared to the round robin results obtained previously.

Goethite was prepared according to a procedure obtained from the University of Wisconsin at Madison with the exception of hydrolyzing and aging the suspension at pH 13.0 instead of 12.5. The solid was

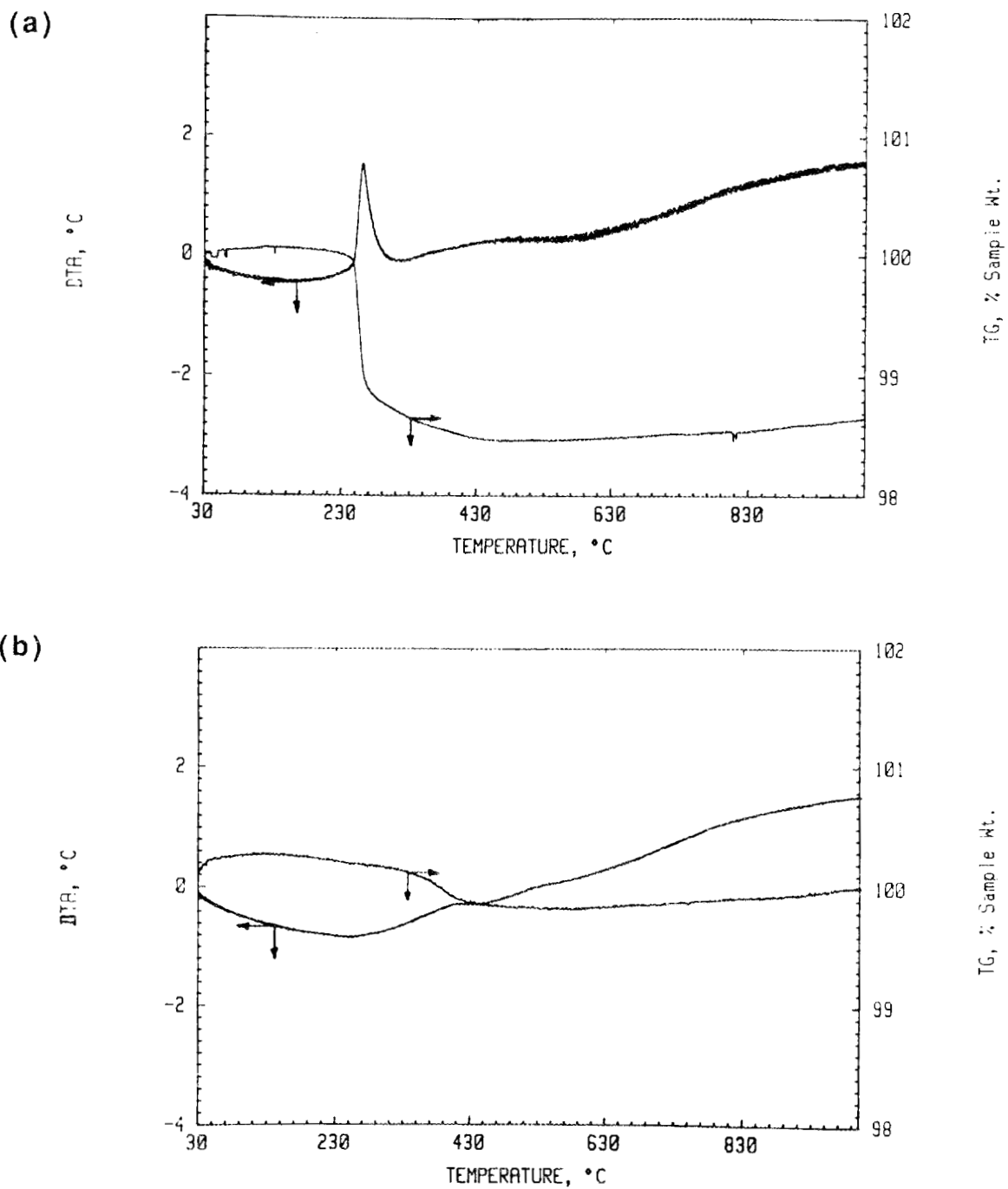


Figure 11. Simultaneous DTA/TGA thermal analyses of dispersant adsorbed UBE E-10 powder: (a) KD-2 (b) Darvan C.

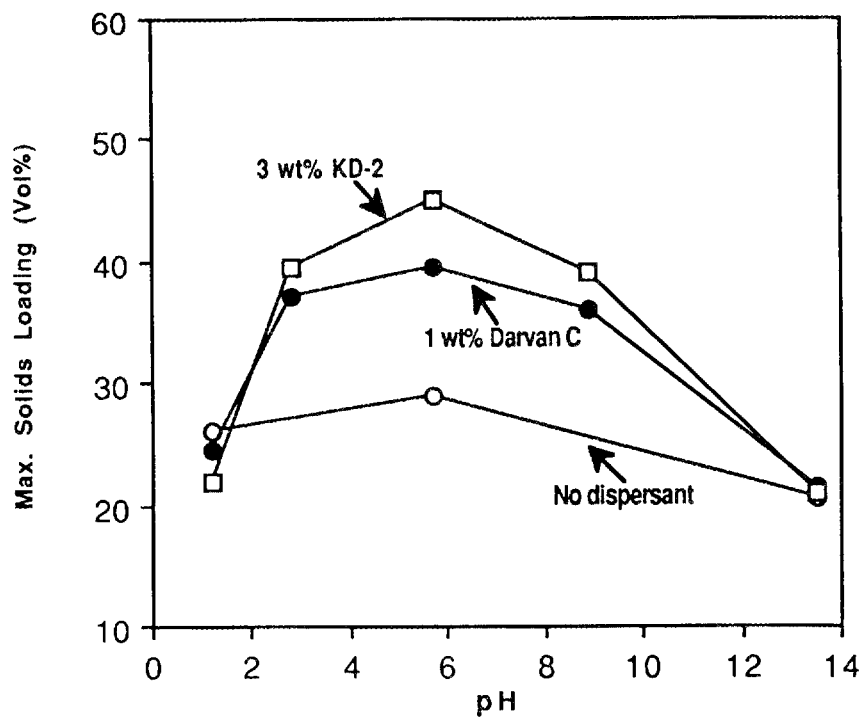


Figure 12. The maximum solids loading of UBE E-10 powder in water as a function of solution pH.

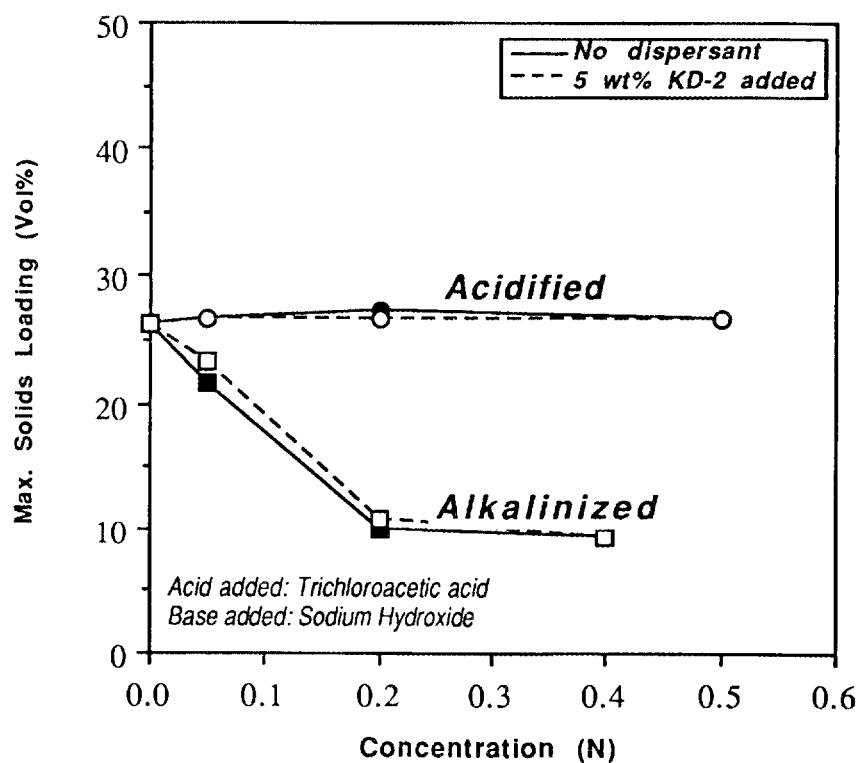


Figure 13. The maximum solids loading of UBE E-10 powder in i-propanol as a function of acid/base addition.

washed by settling and decantation until no further decrease in supernatant conductivity was observed ($\sim 6 \mu\text{S}$).

The N_2 , single point BET surface area was $64 \text{ m}^2/\text{g}$ and transmission electron microscopy revealed acicular, rod-like particles with approximate dimensions of $80 \times 20 \text{ nm}$ (Figure 14). X-ray diffraction confirmed the solid as goethite (Figure 15). The surface area and particle dimensions of the goethite prepared by the University of Wisconsin earlier were somewhat different; they were $80 \text{ m}^2/\text{g}$ and $60 \times 20 \text{ nm}$, respectively.

A portion of the goethite was phosphated using KH_2PO_4 instead of NaH_2PO_4 at the concentration of $100 \mu\text{mol}$ phosphate per gram of goethite. The solids content of goethite in the suspension was determined by freeze-drying technique. The electrophoretic mobilities of the phosphated and original goethite were determined using 0.01M KNO_3 solution as the buffer.

The original goethite has an IEP near pH 9.0, and the phosphated one has an IEP at about pH 5.1 (Figure 16). The later one is almost identical to the previously reported value that was obtained from the round robin study on the phosphated goethite prepared by the University of Wisconsin. It should be noticed that even they did not have the same specific surface area.

A new batch of goethite will be synthesized to understand the surface area effect on the mobility measurement. The surface area measurement will be conducted simultaneously at Rutgers University and at University of Wisconsin at Madison to take into account instrumental factors.

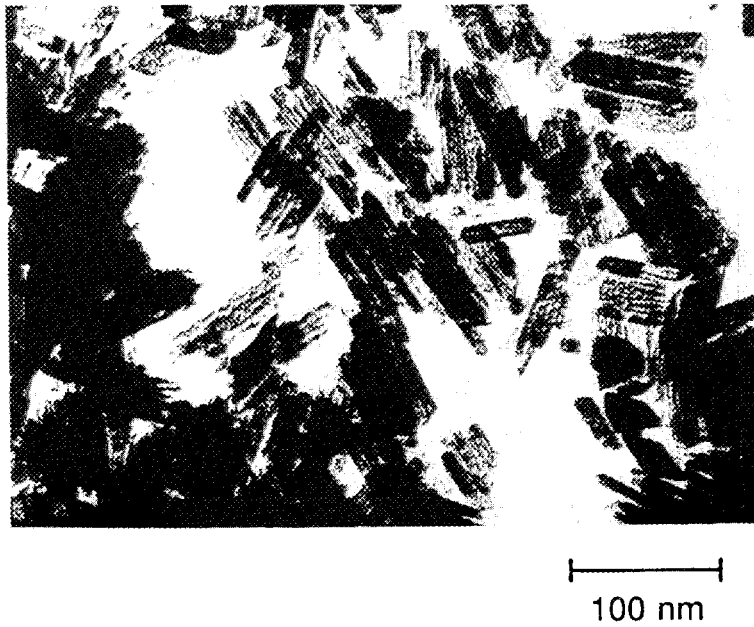


Figure 14. The micrograph of synthesized goethite particle (x190,000).

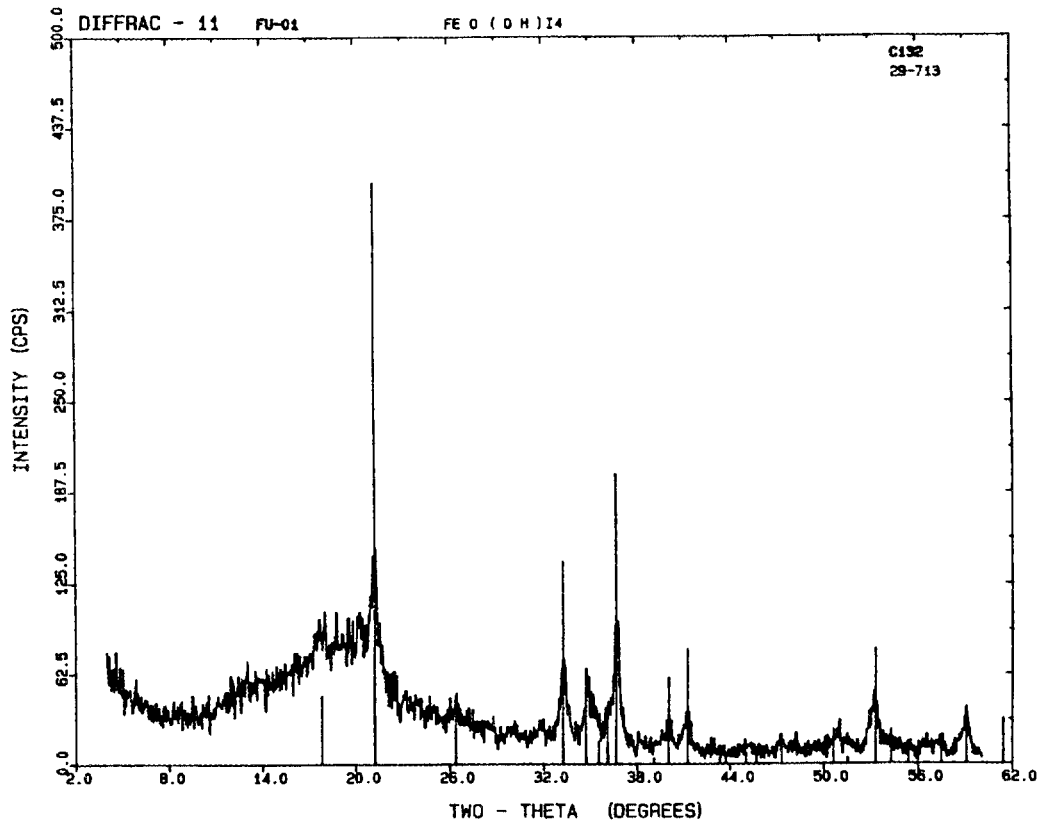


Figure 15. The x-ray powder diffraction pattern of synthesized goethite particle.

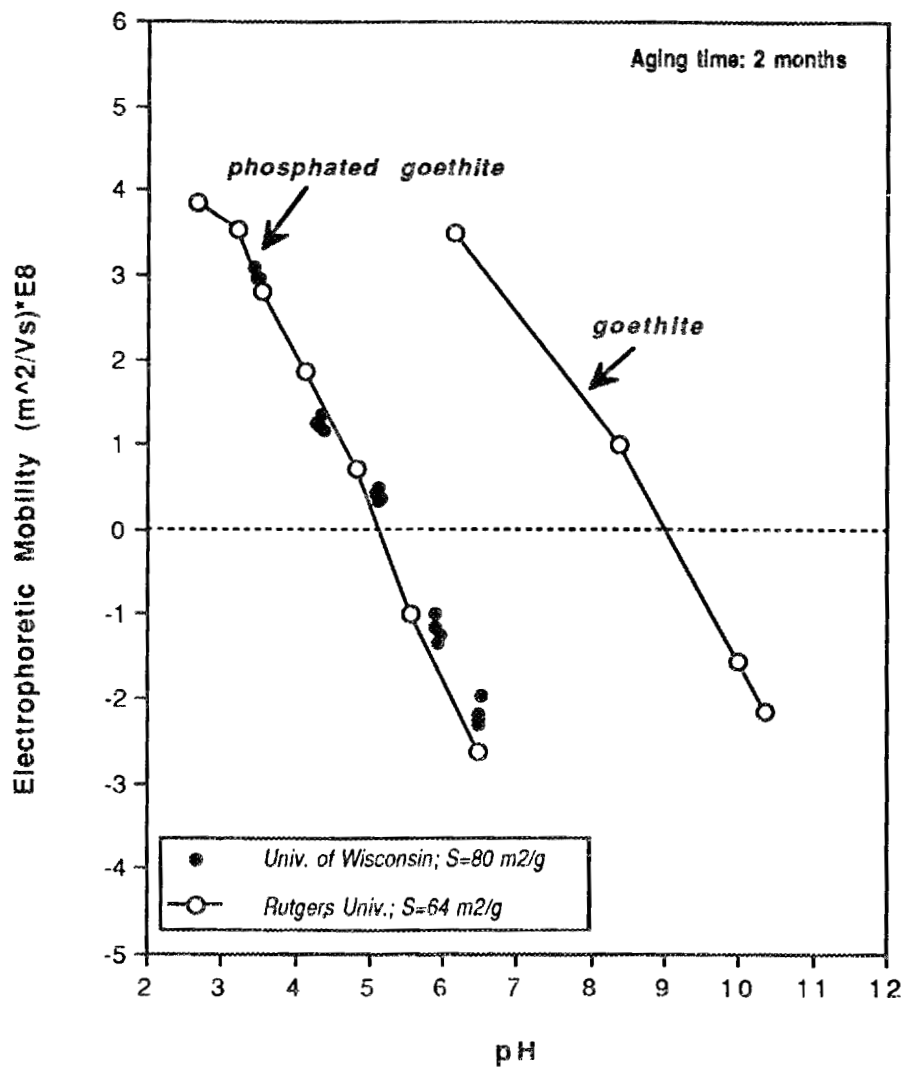


Figure 16. The electrophoretic mobility of 0.01vol% phosphated or non-phosphated goethite in 0.01M KNO₃ as a function of pH.

Status of milestones

Milestone 352004---Complete initial mobility testing of silicon nitride
---is completed.

Milestone 352005---Present mobility measurement of silicon nitride in
program semi-annual report---is completed.

Milestone 352006---Divide silicon nitride into equivalent samples and
sent to other contractors---is completed.

Milestone 352007---complete round robin mobility testing of silicon
nitride---is expected to be completed before the
next contractor meeting held in May1991.

Publication

J.-F. Wang, R. E. Riman, and D. J. Shanefield, "Reliable Electrokinetic
Characterization Procedures for Ceramic Powders," to appear in the
Proceedings of Symposium A, Better Ceramics Through Chemistry IV,
Spring Materials Research Society Meeting, April 16, 1990, San
Francisco, CA.

4.0 TECHNOLOGY TRANSFER

4.1 TECHNOLOGY TRANSFER

4.1.1 Technology TransferTechnology Transfer

D. R. Johnson (Oak Ridge National Laboratory)

Technology transfer in the Ceramic Technology Project is accomplished by a number of mechanisms including the following:

Trade Shows - A portable display describing the program has been built and has been used at numerous national and international trade shows and technical meetings.

Newsletter - A Ceramic Technology Newsletter is published regularly and sent to a large distribution.

Reports - Semiannual technical reports, which include contributions by all participants in the program, are published and sent to a large distribution. Informal bimonthly management and technical reports are distributed to the participants in the program. Open-literature reports are required of all research and development participants.

Direct Assistance - Direct assistance is provided to subcontractors in the program via access to unique characterization and testing facilities at the Oak Ridge National Laboratory.

Workshops - Topical workshops are held on subjects of vital concern to the ceramics community.

International Cooperation - This program is actively involved in and supportive of the cooperative work being done by researchers in West Germany, Sweden, the United States, and, most recently, Japan under an agreement with the International Energy Agency. This effort is ultimately aimed at development of international standards and includes physical, morphological, and micro-structural characterization of ceramic powders and dense ceramic bodies, and mechanical characterization of dense ceramics.

IEA Annex II Management

V. J. Tenney (Oak Ridge National Laboratory)

Objective/scope

The purpose of this task is to organize, assist, and facilitate international research cooperation on the characterization of advanced structural ceramic materials. A major objective of this research is the evolution of measurement standards. This task, which is managed in the United States by ORNL, now includes a formal IEA Annex agreement identified as Annex II between the United States, the Federal Republic of Germany, Sweden, and Japan. The original annex included four subtasks, including: (1) information exchange, (2) ceramic powder characterization, (3) ceramic chemical and physical characterization, and (4) ceramic mechanical property measurements. The research in Subtasks 2, 3, and 4 is now completed. For the new Subtasks 5 and 6, there are 35 and 45 laboratories participating, respectively. During CY 1990, agreements have been reached for Japan to join the Annex, and for research in two new subtasks to be initiated. These include, Subtask 5, Tensile and Flexural Properties of Ceramics; and Subtask 6, Advanced Ceramic Powder Characterization. The next IEA Annex II Executive Committee meeting will be held at Cocoa Beach, Florida, during the American Ceramic Society's Engineering Ceramics Division 15th Annual Conference on Composites and Advanced Ceramics meeting (January 17, 1991). Further work has been done in this period toward finalizing the draft of the new amendment to this annex for final formal signature by representatives of the participating countries. The final version of the Amendment to Annex II (dated August 30, 1990) was received on September 6 from Dr. L. Boesch.

Technical progress

Subtask 2 - Ceramic Powder Characterization

The final report on ceramic powder characterization and analysis has been published and copies distributed on April 30. This step completes Subtask 2.

The report "Characterization of Ceramic Powders: Data and Analyses (Final Report)" was sent to the following Subtask 6 participants: one German participant and five United States participants on August 9 and to eight Japanese participants on September 7, 1990.

Subtask 5 - Flexural and Tensile Properties of Ceramics

United States - M. K. Ferber attended the IEA Annex II Executive Committee Meeting held on June 28, 1990, in Montecatini Terme, Italy, and presented an update to the committee of the status of Subtask 5. During this reporting period, 405 flexure specimens (30 for ambient-temperature and 15 for high-temperature tests) were sent to 9 outside participating laboratories (4/18/90). An additional 45 specimens are being fractured at ORNL. Visits to all participating laboratories were completed for ambient- and high-temperature flexure specimen strength measurements. The laboratories visited were NASA-Lewis (June 12-13), Ford Research Laboratory

(June 14-15), Allison Gas Turbine Operations (June 18-19), Garrett Turbine Engine (June 26-27), General Electric Research Center (July 30-31), Corning (July 31-August 1-2), Carborundum (August 2-3), GTE Laboratories (August 6-7), and Norton High Performance Ceramics (August 8-9). The ambient temperature strength measurements have also been completed at ORNL. After fracturing 30 specimens of GN-10 silicon nitride at ambient temperature, the gaged specimen measurements were completed. This completes the strain gage specimen measurements to the ten participating laboratories (including ORNL). To date, four of the participating laboratories (Allison, GE, Garrett, NASA Lewis) have returned the flexure fixture which was loaned to them for the ambient flexure measurements. Analyses of the gage outputs are in progress. Weibull and other statistical analyses on some of the strength data sets have been started at ORNL. The high-temperature flexural strength measurements on sets of 15 flexure bars each have been completed (except Corning, Inc.) in the participating laboratories and all of the data sets have been provided to ORNL. In addition we have asked each participant to provide us with a summary of the load cell calibration procedure (e.g., electronic or mechanical) for the high-temperature flexure fixture and a picture of the high-temperature fixture used. Fractography analyses have also been started at most of the participating laboratories.

We have now received our full complement of the originally ordered 160 rods of GN-10 silicon nitride (June 7). We returned seven rod blanks (tensile) to Garrett Ceramic Components Division for replacement due to damage during machining. We received the seven replacement rods on June 13. In addition, we received partial shipment (27) of our additional GN-10 tensile specimen blanks (June 13) for use in the tapered collet studies. The balance of this order was received September 5.

A request has been received from a member of ASTM Committee C-28 regarding consideration for additional strain gaging of the U.S. tensile specimens to be fractured in Subtask 5. The additional gaging will provide a more complete indication of bending stresses in the specimens than the originally planned three gages. Funds for this purpose have been requested. The proposal includes use of 9 gages on each of 175 specimens. A total of 210 tensile specimen blanks of GN-10 silicon nitride have been randomized, preparatory to machining into tensile specimens. A total of 175 tensile specimens will be prepared, including those to be exchanged with Germany, Sweden, and Japan. The remaining blanks will be held as spares. Justification for a sole source of this order was completed September 25.

Letters were sent to the Federal Republic of Germany, Sweden, and Japan on July 25 indicating that we are proposing exchange of both tensile and flexure specimens within Subtask 5 research. Specifically, we plan to exchange 5 tensile specimens prepared for the straight collet grips and 30 flexure specimens of our silicon nitride for 30 specimens of the Kyocera silicon nitride which will be studied in Japan, 30 specimens of the ESK silicon nitride which will be studied in Germany, and 30 specimens of the ASEA silicon nitride which will be studied in Sweden as part of Subtask 5.

Germany - Letters were exchanged in August with a representative of Germany agreeing to exchange 30 flexure and 5 tensile specimens of the ESK silicon nitride.

Sweden - We received an updated list on May 11 listing the Swedish participants in Subtask 5 (flexure testing): ABB Cerama, Swedish Ceramic

Institute, United Turbine, Linköping University and (tensile testing) Volvo Aerospace Division.

Japan – On September 14, a letter was received from Mr. Nagamatsu in Japan indicating that the length of the flexure specimens to be received in the United States from Japan will be 48 mm. Flexure strength measurements at ambient temperature using a common fixture design are now underway in Japan.

Subtask 6 – Advanced Ceramic Powder Characterization

Major responsibility for this subtask in the United States is at NIST, and a detailed report of progress on this subtask is provided in the section of this report submitted by NIST. Only a brief summary is provided here.

A meeting was held in Dallas on April 22 including all national representatives to finalize the commitments of each participating laboratory to characterize ceramic powders. Equality of the contributions of participating laboratories is still being resolved.

A meeting of United States participants was held on June 7 and 8 at the Coors Ceramic Company, Golden, Colorado. Improvement suggestions for procedures to be used were presented by participants and resulted in essentially a finalization of the U.S. position on the various procedures to be used for the analysis of ceramic powders as part of this annex.

Technical leaders of Subtask 6 met in Montecatini Terme, Italy, on June 26, and reviewed progress in each country on the procedure tightening studies.

The "procedures tightening" activity is in the final stages and measurements are planned to start in the near future. Ruggedness testing of the agreed to powder characterization procedures is also nearly completed. These final procedures are being compiled and will be distributed to all participants with a set of powder samples.

Samples of all powders have been packaged and sealed in glass vials. In addition, approximately 3500 new samples were prepared and are now being flame sealed. It is planned to ship all of the powder samples by the first week of September.

Status of milestones

A letter report on initiation of the distribution of flexure specimens was completed April 19 (ORO Milestone 90CR-25).

Publications

V. J. Tennery made a presentation in Tokyo, Japan, on May 23, reviewing some of the statistical analysis used in Subtask 4 of IEA Annex II on fracture strength values obtained in Subtask 4.

Characterization of Ceramic Powders

S. G. Malghan, L.-S. Lum, J. F. Kelly, and S. M. Hsu
(National Institute of Standards and Technology)

Objective/Scope

Ceramics have been successfully employed in engines on a demonstration basis. The successful manufacture and use of ceramics in advanced engines depends on the development of reliable materials that will withstand high, rapidly varying thermal stress loads. Improvement in the characterization of ceramic starting powders is a critical factor in achieving reliable ceramic materials for engine applications. The production and utilization of such powders require characterization methods and property standards for quality assurance.

The objectives of the NIST program are (1) to assist with the division and distribution of five ceramic starting powders for an international round-robin on powder characterization; (2) to provide reliable data on physical (dimensional), chemical and phase characteristics of powders; and (3) to conduct statistical assessment, analysis and modeling of round-robin data. This program is directed toward a critical assessment of powder characterization methodology and toward establishment of a basis for the evaluation of fine powder precursors for ceramic processing. This work will examine and compare by a variety of statistical means the various measurement methodologies employed in the round-robin and the correlations among the various parameters and characteristics evaluated. The results of the round-robin are expected to provide the basis for identifying measurements for which Standard Reference Materials are needed and to provide property and statistical data which will serve the development of internationally accepted standards.

Technical Progress

The technical progress covered in this report includes description of work on finalization of powder properties for evaluation, development of tightened procedures, distribution of powders samples and procedures, and data collection.

Finalization of Powder Properties in Subtask 6. The properties to be included in the Subtask 6 were finalized in collaboration with participants in the FRG, Japan, Sweden and the U.S. Shown in Table 1 are 28 properties of powders included in this study. Each participant has selected a set of properties from these three groups.

Development of Tightened Procedures. Procedures were collected from the participants for each of the properties shown in Table 1. Through a series of consensus building discussions and meetings, one procedure for each property of the powder was developed. These procedures were reviewed at various stages by the participants. Finally, several of these procedures were subjected to ruggedness testing to determine the effects of major parameters of the

procedures. The technical descriptions of these procedures in Group I and II contained extensive details.

Table 1. List of properties included in Group I, II and III of Subtask 6.

Group I - Physical Properties

Particle Size Distribution by
Gravity sedimentation (Sedigraph)
Centrifugal sedimentation
Light diffraction
Scanning electron microscopy

Specific Surface Area by
Single point BET
Multipoint BET

X-Ray Diffraction by
Intensity ratio
Height ratio
Modified ratio
Rietveld analysis

Group II - Bulk Chemical Properties

Major Impurities by
Inductively coupled plasma
Direct coupled plasma
Atomic absorption spectroscopy
X-Ray fluorescence

Halides by
Ion selective electrode
Titration

Free Carbon by
Partial Combustion

Nitrogen by
Kjeldahl
Combustion

Total Carbon and Oxygen by
Combustion

Group III - Surface Chemistry

Spectroscopy by

FTIR
Raman
ESCA
NMR

Electrokinetics by

Z-Meter
Electrokinetic sonic amplitude
Ultrasonic vibration potential

Distribution of Powder Samples and Procedures. Samples of five powders were prepared by riffling and packaging in glass sealed vials. Three of the five powders were involved in the preparation of new samples; whereas, the remaining two powder samples were prepared in 1988. Approximately 3500 samples of 4.0 g each of silicon nitride, silicon carbide and aluminum nitride were prepared during June-August period. Each participant received a set of finalized procedures and powder samples in September. The samples analysis phase is in full swing.

Data Collection. The Subtask 6 is a large program involving 45 participants, 5 powders and 28 properties. As a result, the data collection will be an enormously large activity. Hence, computer programs are being developed to allow data input in a systematic manner.

Status of Milestones

On target

Publication

Compilation of Powder Characterization Procedures. Distributed to current participants.

INTERNAL DISTRIBUTION

- | | | | |
|--------|-------------------------------|-----|--------------------|
| 1-2. | Central Research Library | 41. | M. A. Karnitz |
| 3. | Document Reference Section | 42. | B. L. Keyes |
| 4-5. | Laboratory Records Department | 43. | H. D. Kimrey, Jr. |
| 6. | Laboratory Records, ORNL RC | 44. | T. G. Kollie |
| 7. | ORNL Patent Section | 45. | T. B. Lindemer |
| 8-10. | M&C Records Office | 46. | K. C. Liu |
| 11. | L. F. Allard, Jr. | 47. | E. L. Long, Jr. |
| 12. | B. R. Appleton | 48. | W. D. Manly |
| 13. | R. L. Beatty | 49. | R. W. McClung |
| 14. | P. F. Becher | 50. | D. L. McElroy |
| 15. | T. M. Besmann | 51. | J. R. Merriman |
| 16. | P. J. Blau | 52. | A. J. Moorhead |
| 17. | A. Bleier | 53. | T. A. Nolan |
| 18. | E. E. Bloom | 54. | J. L. Rich |
| 19. | K. W. Boling | 55. | C. R. Richmond |
| 20. | R. A. Bradley | 56. | J. M. Robbins |
| 21. | C. R. Brinkman | 57. | M. Rohr |
| 22. | V. R. Bullington | 58. | M. W. Rosenthal |
| 23. | R. S. Carlsmith | 59. | M. L. Santella |
| 24. | P. T. Carlson | 60. | A. C. Schaffhauser |
| 25. | G. M. Caton | 61. | G. M. Slaughter |
| 26. | R. H. Cooper, Jr. | 62. | W. B. Snyder, Jr. |
| 27. | S. A. David | 63. | E. J. Soderstrom |
| 28. | J. H. DeVan | 64. | D. P. Stinton |
| 29. | J. I. Federer | 65. | R. W. Swindeman |
| 30. | M. K. Ferber | 66. | V. J. Tennery |
| 31. | W. Fulkerson | 67. | T. N. Tiegs |
| 32. | R. L. Graves | 68. | J. R. Weir, Jr. |
| 33. | D. L. Greene | 69. | F. W. Wiffen |
| 34. | M. A. Janney | 70. | R. K. Williams |
| 35-39. | D. R. Johnson | 71. | S. G. Winslow |
| 40. | R. R. Judkins | 72. | C. S. Yust |

EXTERNAL DISTRIBUTION

73. Donald F. Adams
University of Wyoming
Mechanical Engineering
Department
Laramie, WY 82071
74. Jane W. Adams
Corning Glass Works
SP-DV-21
Corning, NY 14831
75. J. Ahmad
Battelle Columbus Laboratories
Engineering Mechanics Department
505 King Avenue
Columbus, OH 43201-2693
76. Richard L. Allor
Ford Motor Company
Material Systems
Reliability Division
20000 Rotunda Drive
Post Office Box 2053
Dearborn, MI 48121-2053
77. Richard T. Alpaugh
U.S. Department of Energy
Office of Transportation
Technologies
1000 Independence Avenue, S.W.
Forrestal Building CE-322
Washington, DC 20585
78. Norman C. Anderson
Ceradyne, Inc.
Ceramic-to-Metal Division
3169 Redhill Avenue
Costa Mesa, CA 92626
79. H. Arbabi
Brunel University
Department of Materials
Technology
Uxbridge Middlesex UB8 3PH
UNITED KINGDOM
80. V. S. Avva
NC A&T State University
Department of Mechanical
Engineering
Greensboro, NC 27411
81. Michel Badia
Embassy of France
4101 Reservoir Road, S.W.
Washington, DC 20007-2176
82. Kirit J. Bahnsali
U.S. Army Materials
Technology Laboratory
SLCMT-EMM
405 Arsenal Street
Watertown, MA 02172
83. John M. Bailey
Caterpillar Inc.
Research Department
Technical Center
Building L
Post Office Box 1875
Peoria, IL 61656-1875
84. Murray Bailey
NASA Lewis Research Center
21000 Brookpark Road
MS:77-6
Cleveland, OH 44135
85. R. R. Baker
Ceradyne, Inc.
3169 Red Hill Avenue
Costa Mesa, CA 92626
86. J. Gary Baldoni
GTE Laboratories Inc.
40 Sylvan Road
Waltham, MA 02254
87. P. M. Barnard
Ruston Gas Turbines Limited
New Products Division
Firth Road
Lincoln LN6 7AA
ENGLAND

88. A. L. Bement, Jr.
TRW, Inc.
23555 Euclid Avenue
Cleveland, OH 44117
89. M. Bentele
Xamag, Inc.
259 Melville Avenue
Fairfield, CT 06430
90. Clifton G. Bergeron
University of Illinois
Department of Ceramic
Engineering
105 South Goodwin Avenue
204 Ceramic Building
Urbana, IL 61801
91. Deane I. Biehler
Caterpillar Inc.
Engineering and Research Materials
Technical Center, Building E
Post Office Box 1875
Peoria, IL 61656-1875
92. William D. Bjorndahl
TRW, Inc.
Materials Characterization and
Chemical Analysis Department
One Space Park
Building 01, Room 2060
Redondo Beach, CA 90278
93. Dan Blake
Solar Energy Research Institute
1617 Cole Boulevard
Golden, CO 80401
94. Keith Blandford
Boride Products, Inc.
2879 Aero Park Drive
Traverse City, MI 49684
95. Paul N. Blumberg
Ricardo-ITI
415 East Plaza Drive
Westmont, IL 60559
96. Larry P. Boesch
Engineering and Economics
Research Systems
1593 Spring Hill Road
Vienna, VA 22182-2239
97. Tibor Bornemisza
Sundstrand Turbomach
Division of Sundstrand
Corporation
4400 Ruffin Road
Post Office Box 85757
San Diego, CA 92138-5757
98. Han Juergen Bossmeyer
BMW Technologies, Inc.
Watermill Center
800 South Street
Waltham, MA 02154
99. J. A. M. Boulet
University of Tennessee
310 Perkins Hall
Knoxville, TN 37996
100. Les J. Bowen
GTE Laboratories, Inc.
40 Sylvan Road
Waltham, MA 02254
101. Steve Bradley
Signal UOP Research Center
50 UOP Plaza
Des Plaines, IL 60016-6187
102. Raymond J. Bratton
Westinghouse Electric
Corporation
R&D Center
1310 Beulah Road
Pittsburgh, PA 15235
103. Catherine E. Brown
E. I. DuPont de
Nemours & Company, Inc.
Experimental Station
Information Center
E302/301
Wilmington, DE 19898

104. J. J. Brown
Virginia Polytechnic Institute
and State University
Department of Materials
Engineering
Blacksburg, VA 24061
105. S. L. Bruner
Ceramatec, Inc.
2425 South 900 West
Salt Lake City, UT 84119
106. W. Bryzik
U.S. Army Tank Automotive
Command
R&D Center
Propulsion Systems Division
Warren, MI 48090
107. S. T. Buljan
GTE Laboratories Inc.
40 Sylvan Road
Waltham, MA 02254
108. John M. Byrne, Jr.
PPG Industries, Inc.
Corporate Development
Department
One PPG Place
Pittsburgh, PA 15272
109. Donald J. Campbell
Air Force Wright
Aeronautical Laboratory
AFWAL/POX
Wright-Patterson AFB,
OH 45433
110. Roger Cannon
Rutgers University
Department of Ceramics
Bowser Road
Post Office Box 909
Piscataway, NJ 08855-0909
111. Harry W. Carpenter
19945 Acre Street
Northridge, CA 91324
112. David Carruthers
Allied-Signal Aerospace
Company
Garrett Auxiliary Power
Division
2739 East Washington Street
Post Office Box 5227
Phoenix, AZ 85010
113. Jere G. Castor
J. C. Enterprise
5078 North 83rd Street
Scottsdale, AZ 85253
114. En-sheng Chen
B&C Engineering Research
13906 Dentwood Drive
Houston, TX 77014
115. Albert A. Chesnes
U.S. Department of Energy
Office of Transportation
Technologies
1000 Independence Avenue, S.W.
Forrestal Building CE-30,
5G-048
Washington, DC 20585
116. Gilbert Y. Chin
Bell Telephone Laboratories
R&D
Murray Hill, NJ 07974
117. Melvin H. Chiogioji
U.S. Department of Energy
Office of Transportation
Technologies
1000 Independence Avenue, S.W.
Forrestal Building CE-22
Washington, DC 20585
118. William J. Chmura
Torrington Company
Corporate Research
59 Field Street
Torrington, CT 06790
119. Eugene V. Clark
Turbine Metal Technology, Inc.
7327 Elmo Street
Tujunga, CA 91042-2204

120. William L. Cleary
ORI, Inc.
1375 Piccard Drive
Rockville, MD 20850
121. W. J. Clegg
ICI Advanced Materials
Post Office Box 11
The Heath, Runcorn Chesire
WA7 4QE
ENGLAND
122. Jack L. Clem
J. M. Huber Corporation
Carbon Black Division
Post Office Box 2831
Borger, TX 79008-2831
123. Stephen Copley
University of Southern California
Materials Science Department
Los Angeles, CA 90089-0241
124. John A. Coppola
Carborundum Company
Post Office Box 1054
Niagara Falls, NY 14302
125. Normand D. Corbin
Norton Company
Advanced Ceramics
Goddard Road
Northboro, MA 01532-1545
126. Charles H. Craig
Defense Technology Security
400 Army-Navy Drive, Suite 300
Arlington, VA 22202
127. William J. Croft
U.S. Army Materials
Technology Laboratory
405 Arsenal Street
Watertown, MA 02172
128. Gary M. Crosbie
1430 Culver Avenue
Dearborn, MI 48121
129. Floyd W. Crouse, Jr.
U.S. Department of Energy
Morgantown Energy
Technology Center
Collins Ferry Road
Post Office Box 880
Morgantown, WV 26505
130. Raymond Cutler
Ceramatec, Inc.
2425 South 900 West
Salt Lake City, UT 84119
131. David A. Dalman
Dow Chemical Company
Central Research, Organic
Specialties
1776 Building
Midland, MI 48674
132. James I. Dalton
Reynolds Metals Company
Metallurgy Laboratory
Fourth and Canal Streets
Post Office Box 27003
Richmond, VA 23219
133. Stephen C. Danforth
Rutgers University
Bowser Road
Post Office Box 909
Piscataway, NJ 08854
134. Robert F. Davis
North Carolina State
University
Materials Engineering
Department
232 Riddick Laboratory
Post Office Box 7907
Raleigh, NC 27695
135. Evelyn M. DeLiso
Corning Glass Works
Corning, NY 14831
136. J. Franklyn DeRidder
Omni Electro Motive, Inc.
12 Seely Hill Road
Newfield, NY 14867

137. Keith F. Dufrane
Battelle Columbus Laboratories
505 King Avenue
Columbus, OH 43201
138. Edmund M. Dunn
Texel Company
21 Eire Street
Cambridge, MA 02139
139. Jeremy D. Dunning
Indiana University
Industrial Research
Liaison Program
Bloomington, IN 47405
140. Sunil Dutta
NASA Lewis Research Center
21000 Brookpark Road
MS:49-3
Cleveland, OH 44135
141. Paul N. Dyer
Air Products and Chemicals, Inc.
Post Office Box 538
Allentown, PA 18105
142. Robert J. Eagan
Sandia National Laboratories
Department 1840
Post Office Box 5800
Albuquerque, NM 87185
143. Christopher A. Ebel
Business Development Manager
Carborundum Company
Technology Division
P.O. Box 337
Niagara Falls, NY 14302
144. J. J. Eberhardt
U.S. Department of Energy
Office of Advanced Transportation
Materials
1000 Independence Avenue, S.W.
Forrestal Building CE-34
Washington, DC 20585
145. William A. Ellingson
Argonne National Laboratory
9700 South Cass Avenue
Argonne, IL 60439
146. Charles D. Estes
U.S. Senate
Committee on Appropriations
SD-152 Dirksen Senate
Office Building
Washington, DC 20510
147. John N. Eustis
U.S. Department of Energy
Office of Industrial
Technologies
1000 Independence Avenue, S.W.
Forrestal Building CE-221
Washington, DC 20585
148. Peggy Evanich
National Aeronautics
and Space Administration
Energy Systems Office
Washington, DC 20546
149. Anthony G. Evans
University of California
College of Engineering
Santa Barbara, CA 93106
150. Robert C. Evans
NASA Lewis Research Center
Vehicular Gas Turbine and
Diesel Project Office
21000 Brookpark Road
MS:77-6
Cleveland, OH 44135
151. Katherine T. Faber
Ohio State University
Ceramic Engineering
Department
2041 College Road
Columbus, OH 43210

152. John W. Fairbanks
U.S. Department of Energy
Office of Transportation
Technologies
1000 Independence Avenue, S.W.
Forrestal Building CE-151, 5G-042
Washington, DC 20585
153. Larry Farrell
Babcock and Wilcox
Old Forrest Road
Lynchburg, VA 24505
154. Rolf Fasth
Chem Systems, Inc.
303 South Broadway
Tarrytown, NY 10591
155. H. W. Foglesong
Dow Corning Corporation
3901 South Saginaw Road
Midland, MI 48686
156. Thomas F. Foltz
Avco Corporation
Special Materials Division
Two Industrial Avenue
Lowell, MA 01851
157. Robert G. Frank
Technology Assessment Group
10793 Bentley Pass Lane
Cincinnati, OH 45140
158. Douglas W. Freitag
LVT Missiles and Electronics Group
Post Office Box 650003
Dallas, TX 75265-0003
159. P. A. Gaydos
Battelle Columbus Laboratories
505 King Avenue
Columbus, OH 43201
160. George E. Gazza
U.S. Army Materials
Technology Laboratory
Ceramics Research Division
405 Arsenal Street
Watertown, MA 02172-0001
161. Bruce W. Gerhold
Phillips Petroleum Company
Engineering Materials, R&D
91-G, PRC
Bartlesville, OK 74004
162. Charles M. Gilmore
George Washington University
Civil, Mechanical, and
Environmental Engineering
Washington, DC 20052
163. Paul Glance
Concept Analysis
R&D
950 Stephenson Highway
Dupont Automotive Development
Building
Troy, MI 48007-7013
164. Fred M. Glaser
U.S. Department of Energy
Office of Fossil Energy
FE-14 GTN
Germantown, MD 20545
165. Joseph W. Glatz
Naval Air Propulsion Test
Center
Systems Technology Division
Post Office Box 7176, PE 34
Trenton, NJ 08628
166. W. M. Goldberger
Superior Graphite Company
R&D
2175 East Broad Street
Columbus, OH 43209

167. Stephen T. Gonczy
Signal UOP Research Center
Materials Science Department
50 UOP Plaza
Des Plaines, IL 60016-6187
168. Robert J. Gottschall
U.S. Department of Energy
Office of Material Sciences
ER-131 GTN, MS:G-256
Germantown, MD 20545
169. Earl Graham
Cleveland State University
Department of Chemical
Engineering
Euclid Avenue at East 24th Street
Cleveland, OH 44115
170. Kenneth Green
Coors Ceramics Company
17750 West 32nd Street
Golden, CO 80401
171. Robert E. Green, Jr.
Johns Hopkins University
Center for Nondestructive
Evaluation
Maryland Hall 107
Baltimore, MD 21218
172. Lance E. Groseclose
General Motors Corporation
Allison Gas Turbine Division
Post Office Box 420
Indianapolis, IN 46206-0420
173. P. Ulf Gummeson
Hoeganaes
R&D
River Road and Taylors Lane
Riverton, NJ 08077
174. Bimleshwar P. Gupta
Solar Energy Research Institute
Solar Heat Research Division
1617 Cole Boulevard
Golden, CO 80401
175. M. D. Gurney
NIPER
Post Office Box 2128
Bartlesville, OK 74005
176. John P. Gyekenyesi
NASA Lewis Research Center
21000 Brookpark Road
MS:49-7
Cleveland, OH 44135
177. J. J. Habeeb
Esso Petroleum Canada
Research Division
Post Office Box 3022
Sarina Ontario N7T 7M1
CANADA
178. H. T. Hahn
Pennsylvania State University
ESM Department
227 Hammond Building
University Park, PA 16802
179. Nabil S. Hakim
Detroit Diesel Corporation
13400 West Outer Drive West
Detroit, MI 48239
180. Friedrich Harbach
Asea Brown Boveri AG
Department of Functional
Ceramics
Eppelheimer Strasse 82
D-6900 Heidelberg 1
WEST GERMANY
181. Kay Hardman-Rhyne
DARPA
1400 Wilson Boulevard
Arlington, VA 22209
182. R. A. Harmon
25 Schalren Drive
Latham, NY 12110

183. Stephen D. Hartline
Norton Company
Advanced Ceramics
Goddard Road
Northboro, MA 01532-1545
184. Michael H. Haselkorn
Caterpillar Inc.
Engineering Research Materials
Technical Center, Building E
Post Office Box 1875
Peoria, IL 61656-1875
185. Willard E. Hauth
Dow Corning Corporation
Composite Development Ceramics
Program
3901 South Saginaw Road
Midland, MI 48640
186. Norman L. Hecht
University of Dayton Research
Institute
300 College Park
Dayton, OH 45469-0001
187. S. S. Hecker
Los Alamos National Laboratory
Material Science and
Technology Division, G-756
Post Office Box 1663
Los Alamos, NM 87545
188. Peter W. Heitman
General Motors Corporation
Allison Gas Turbine Division
Post Office Box 420, W-5
Indianapolis, IN 46206-0420
189. Richard L. Helferich
The Duriron Company, Inc.
Post Office Box 1145
Dayton, OH 45401
190. H. E. Helms
General Motors Corporation
Allison Gas Turbine Division
Post Office Box 420
Indianapolis, IN 46206-0420
191. Thomas L. Henson
GTE Products Corporation
Chemical & Metallurgical Division
Hawes Street
Towanda, PA 18848-0504
192. Thomas P. Herbell
NASA Lewis Research Center
21000 Brookpark Road
MS:49-3
Cleveland, OH 44135
193. Hendrik Heystek
Bureau of Mines
Tuscaloosa Research Center
Post Office Box L
University, AL 35486
194. Robert V. Hillery
General Electric Company
One Neumann Way
Post Office Box 156301
Cincinnati, OH 45215
195. Jonathan W. Hinton
Carborundum Company
Structural Ceramics Division
Post Office Box 1054
Niagara Falls, NY 14302
196. Joe Homeny
University of Illinois
Department of Materials Science
and Engineering
105 South Goodwin Avenue
Ceramics Building
Urbana, IL 61801
197. A. T. Hopper
Battelle Columbus Laboratories
Engineering Mechanics Department
505 King Avenue
Columbus, OH 43201-2693
198. George Hsu
Jet Propulsion Laboratory
4800 Oak Grove Drive
MS:512-103
Pasadena, CA 91109

199. Shih Hsu
Digital Equipment Corporation
77 Reed Road
MS:HL02-1/L8
Hudson, MA 01749-2895
200. Stephen M. Hsu
National Institute of Standards
and Technology
Institute for Materials Science
and Engineering
Gaithersburg, MD 20899
201. Harold A. Huckins
Princeton Advanced
Technology, Inc.
56 Finley Road
Princeton, NJ 08540
202. Fred Huettig
Advanced Ceramic Technology, Inc.
17 Deerfield Road
East Brunswick, NJ 08816
203. O. Richard Hughes
Celanese Research Company
86 Morris Avenue
Summit, NJ 07901
204. Joseph E. Hunter, Jr.
General Motors Corporation
Research Labs
Metallurgy Department
12 Mile and Mound Roads
Warren, MI 48090-9055
205. Louis C. Ianniello
U.S. Department of Energy
Office of Material Sciences
ER-13 GTN
Germantown, MD 20545
206. Robert H. Insley
Champion Spark Plug Company
Ceramic Division
20000 Conner Avenue
Detroit, MI 48234
207. Curtis A. Johnson
General Electric Company
Ceramics Branch, Physical
Chemistry
Post Office Box 8, K1/3C7
Schenectady, NY 12301
208. Larry Johnson
Argonne National Laboratory
Center for Transportation
Research
9700 South Cass Avenue
Bldg. 362
Argonne, IL 60439
209. L. A. Joo
Great Lakes Research
Corporation
Post Office Box 1031
Elizabethton, TN 37643
210. A. David Joseph
Sealed Power Corporation
R&D
100 Terrace Plaza
Muskegon, MI 49443
211. Debra Joslin
University of Tennessee
Metallurgical Engineering
Department
Knoxville, TN 37996
212. Adam Jostsons
Australian Nuclear Science &
Technology Organisation
Lucas Heights Research
Laboratories
New Illawarra Road
Lucas Heights, New South Wales
AUSTRALIA
213. Tom Kalamasz
Norton/TRW
7A-4 Raymond Avenue
Salem, NH 03079
214. Roy Kamo
Adiabatics, Inc.
630 South Mapleton
Columbus, IN 47201

215. Allan Katz
Air Force Wright Aeronautical
Laboratory
Metals and Ceramics Division
Materials Laboratory
AFWAL/MLLM
Wright-Patterson AFB, OH 45433
216. R. N. Katz
U.S. Army Materials Technology
Laboratory
405 Arsenal Street
Watertown, MA 02172
217. Ted Kawaguchi
Tokai Carbon
375 Park Avenue, Suite 3802
New York, NY 10152
218. Frederick L. Kennard, III
General Motors Corporation
AC Spark Plug Division
Department 32-24
1300 North Dort Highway
Flint, MI 48556
219. J. R. Kidwell
Allied-Signal Aerospace Company
Garrett Auxiliary Power Division
2739 East Washington Street
Post Office Box 5227
Phoenix, AZ 85010
220. H. J. Kim
GTE Laboratories, Inc.
40 Sylvan Road
Waltham, MA 02254
221. Max Klein
Gas Research Institute
8600 West Bryn Mawr Avenue
Chicago, IL 60631
222. C. E. Knapp
Norton Research Corporation
8001 Daly Street
Niagara Falls, Ontario L2G 6S2
CANADA
223. A. S. Kobayashi
University of Washington
Department of Mechanical
Engineering
MS:FU10
Seattle, WA 98195
224. Wolfgang Kollenberg
Projektleitung Material-
Rohstofforschung - PLR
Kernforschungsanlage
Juelich GmbH
Postfach 1913
D-5170 Juelich
WEST GERMANY
225. David M. Kotchick
Allied-Signal Aerospace Company
AiResearch Los Angeles Division
2525 West 190th Street
Torrance, CA 90509
226. Joseph A. Kovach
Eaton Corporation
Manufacturing Technologies
Center
32500 Charvon Road
Willoughby Hills, OH 44094
227. Bruce Kramer
George Washington University
Aerodynamic Center
Room T715
Washington, DC 20052
228. Saunders B. Kramer
U.S. Department of Energy
Office of Transportation
Systems
1000 Independence Avenue, S.W.
Forrestal Building CE-151
Washington, DC 20585
229. Dan M. Kreiner
Allied-Signal Aerospace Company
Garrett Auxillary Power
Division
Post Office Box 5227
Phoenix, AZ 85010

230. A. S. Krieger
Radiation Science, Inc.
Post Office Box 293
Belmont, MA 02178
231. Pieter Krijgsman
Ceramic Design Int. Hold., Ltd.
Post Office Box 68
8050 AB Hattem
THE NETHERLANDS
232. Jack H. L'Amoreux
11346 Gates Mill Drive
Knoxville, TN 37922
233. W. J. Lackey
Georgia Tech Research Institute
Energy and Materials Sciences
Georgia Institute of Technology
Atlanta, GA 30332
234. Everett A. Lake
Air Force Wright Aeronautical
Laboratory
AFWAL/POSL
Wright-Patterson AFB,
OH 45433-6563
235. Hari S. Lamba
General Motors Corporation
Electro-Motive Division
LaGrange, IL 60525
236. Manfred Langer
Volkswagen AG
Forschung-Neue Technologien
Werkstofftechnologie
D-3180 Wolfsburg 1
WEST GERMANY
237. James Lankford
Southwest Research Institute
Department of Materials Sciences
6220 Culebra Road
Post Office Drawer 28510
San Antonio, TX 78284
238. David C. Larsen
Corning Glass Works
Materials Research Department
Sullivan Park, FR-51
Corning, NY 14831
239. S. K. Lau
Carborundum Company
Technology Division
Post Office Box 832
Niagara Falls, NY 14302
240. Harry A. Lawler
Carborundum Company
Niagara Falls R&D Center
Post Office Box 832
Niagara Falls, NY 14302
241. Alan Lawley
Drexel University
Materials Engineering
Philadelphia, PA 19104
242. Daniel Lee
Temescon
2850 7th Street
Berkeley, CA 94710
243. June-Gunn Lee
Korea Advanced Institute of
Science and Technology
Post Office Box 131
Dong Dac Mun Seoul
KOREA
244. E. M. Lenoë
Air Force Office of Scientific
Research
Office of Naval Research
Liaison Office, Far East
APO San Francisco,
CA 96503-0110
245. Stanley R. Levine
NASA Lewis Research Center
21000 Brookpark Road
Cleveland, OH 44135
246. David Lewis
Naval Research Laboratory
Materials Science and Technology
4555 Overlook Avenue, S.W.
Code 63-70
Washington, DC 20375

247. Laura J. Lindberg
Allied-Signal Aerospace
Company
Garrett Fluid Systems
Division
Post Office Box 22200
Tempe, AZ 85285-2200
248. Bill Long
Babcock and Wilcox
Post Office Box 1260
Lynchburg, VA 24505
249. L. A. Lott
EG&G, Inc.
Idaho National Engineering
Laboratory
Post Office Box 1625
Idaho Falls, ID 83415
250. Raouf O. Loutfy
Materials and Electrochemical
Research Corporation
7960 South Kolb Road
Tucson, AZ 85706
251. Bryan K. Luftglass
Chem Systems, Inc.
303 South Broadway
Tarrytown, NY 10591
252. Robert Lundberg
Swedish Institute for Silicate
Research
Box 5403
S-402 29 Gothenburg
SWEDEN
253. Michael J. Lynch
General Electric Company
Medical Systems Group
Post Office Box 414, 7B-36
Milwaukee, WI 53201
254. Vincent L. Magnotta
Air Products and Chemicals, Inc.
Technical Diversification R&D
Post Office Box 538
Allentown, PA 18105
255. Tai-il Mah
Universal Energy Systems
Ceramics and Composites Research
4401 Dayton-Xenia Road
Dayton, OH 45432
256. L. Manes
Commission of the European
Communities
Joint Research Centre
Ispra Establishment
1-21020 Ispra (Varese)
ITALY
257. Giel Marijnissen
Interturbine R&D
R&D
Post Office Box 4339
5944 ZG Arcen
THE NETHERLANDS
258. Gerald R. Martin
Fleetguard, Inc.
Cookeville, TN 38501
259. J. W. McCauley
U.S. Army Materials Technology
Laboratory
SLCMT-OMM
405 Arsenal Street
Watertown, MA 02172-0001
260. Bryan J. McEntire
Norton Company, TRW Ceramics
Goddard Road
Northboro, MA 01532-1545
261. Thomas D. McGee
Iowa State University
Department of Materials Science
and Engineering
Ames, IA 50011
262. H. Christopher McGowan
Advanced Ceramic Technology, Inc.
17 Deerfield Road
East Brunswick, NJ 08816

263. Malcolm G. McLaren
Rutgers University
Department of Ceramics
Bowser Road
Busch Campus
Post Office Box 909
Piscataway, NJ 08854
264. Arthur F. McLean
6225 North Camino Almonte
Tucson, AZ 85718
265. Brian L. Mehosky
British Petroleum
440 Warrensville, Center Rd.
Cleveland, OH 44128
266. Joseph J. Meindl
Reynolds International, Inc.
6603 West Broad Street
Post Office Box 27002
Richmond, VA 23230
267. D. Messier
U.S. Army Materials Technology
Laboratory
DRXMR-MC
405 Arsenal Street
Watertown, MA 02172
268. Brad Miller
Norton Company
Advanced Ceramics
Goddard Road
Northboro, MA 01532-1545
269. Bill Moehle
Ethyl Corporation
R&D Laboratories
Post Office Box 341
Baton Rouge, LA 70821
270. Helen Moeller
Babcock and Wilcox
Post Office Box 11165
Lynchburg, VA 24506-1165
271. Peter E. D. Morgan
Rockwell International
Science Center
1049 Camino Dos Rios
Post Office Box 1085
Thousand Oaks, CA 91360
272. Lawrence M. Murphy
Manager
Solar Energy Research Institute
Thermal Systems Research Branch
1617 Cole Boulevard
Golden, CO 80401
273. Solomon Musikant
General Electric Company
Space Systems Division
Post Office Box 8555, MS:U-1219
Philadelphia, PA 19101
274. Pero Nannelli
Pennwalt Corporation
900 First Avenue
Post Office Box C
King of Prussia, PA 19406-0018
275. William D. Nix
Stanford University
Department of Materials Science
and Engineering
Stanford, CA 94305
276. Richard D. Nixdorf
ReMaxCo Technologies, Inc.
231 Sherway Rd
Knoxville, TN 37922
277. S. D. Nunn
University of Michigan
Materials Science and
Engineering
Ann Arbor, MI 48109-2136
278. Brian M. O'Connor
Lubrizol Corporation
Tribology Section
29400 Lakeland Boulevard
Wickliffe, OH 44092

279. W. Richard Ott
Alfred University
Center for Advanced Ceramic
Technology
Alfred, NY 14802
280. William C. Owen
Sundstrand Turbomach
Division of Sundstrand
Corporation
4400 Ruffin Road
Post Office Box 85757
San Diego, CA 92138-5757
281. Muktesh Paliwal
GTE Products Corporation
Hawes Street
Towanda, PA 18848-0504
282. Joseph E. Palko
General Electric Company
Gas Turbine Division
TTD Building, 55-113
Schenectady, NY 12345
283. Hayne Palmour, III
North Carolina State University
Engineering Research Services
Division
2158 Burlington Engineering
Labs
Post Office Box 5995
Raleigh, NC 27607
284. Joseph N. Panzarino
Norton Company
Advanced Ceramics
Goddard Road
Northboro, MA 01532-1545
285. Pellegrino Papa
Corning Glass Works
Corning Technical Products
Division
Corning, NY 14831
286. James G. Paschal
Reynolds Metals Company
Post Office Box 76154
Atlanta, GA 30358
287. Arvid E. Pasto
GTE Laboratories Inc.
40 Sylvan Road
Waltham, MA 02254
288. James W. Patten
Cummins Engine Company, Inc.
Box 3005, Mail Code 50183
Columbus, IN 47202-3005
289. Robert A. Penty
Eastman Kodak Company
Manufacturing Technology
Department
Apparatus Division
901 Elmgrove Road
Rochester, NY 14650
290. Robert W. Pepper
Textron Inc.
Specialty Materials
2 Industrial Avenue
Lowell, MA 01851
291. Gary R. Peterson
U.S. Department of Energy
Idaho Operations Office
785 D.O.E. Place
Idaho Falls, ID 83402
292. R. Byron Pipes
University of Delaware
Center for Composite Materials
2001 Spencer Laboratory
Newark, DE 19716
293. Bruce J. Pletka
Michigan Technological
University
Department of Metallurgical
Engineering
Houghton, MI 49931
294. Robert C. Pohanka
Office of Naval Research
800 North Quincy Street
Code 431
Arlington, VA 22217

295. J. P. Pollinger
Allied-Signal Aerospace Company
Garrett Ceramic Components
Division
19800 South Van Ness Avenue
Torrance, CA 90509
296. Bob Powell
General Motors Corporation
Metallurgy Department
30200 Mound Road
Warren, MI 48090-9055
297. Stephen C. Pred
ICD Group, Inc.
1100 Valley Brook Avenue
Lyndhurst, NJ 07071
298. Karl M. Prewo
United Technologies Corporation
Research Center
Silver Lane , MS:24
East Hartford, CT 06108
299. Joseph M. Proud
GTE Laboratories Inc.
Materials Science Laboratory
40 Sylvan Road
Waltham, MA 02254
300. D. W. Prouse
Ceramatec, Inc.
2425 South 900 West
Salt Lake City, UT 84119
301. Carr Lane Quackenbush
Norton Company
Advanced Ceramics
Goddard Road
Northboro, MA 01532-1545
302. Brian Quigy
National Aeronautics and Space
Administration
Energy Systems Office
Washington, DC 20546
303. George Quinn
U.S. Army Materials Technology
Laboratory
405 Arsenal Street
Watertown, MA 02172
304. Dennis T. Quinto
Kennametal, Inc.
Phillip M. McKenna Laboratory
Post Office Box 639
Greensburg, PA 15601
305. Dennis W. Readey
Ohio State University
2041 College Road
Columbus, OH 43210
306. Michael J. Readey
Coors Ceramics Company
R&D
17750 West 32nd Street
Golden, CO 80401
307. Robert R. Reeber
U.S. Army Research Office
Post Office Box 12211
Research Triangle Park, NC 27709
308. K. L. Reifsnider
Virginia Polytechnic Institute
and State University
Department of Engineering
Science and Mechanics
Blacksburg, VA 24061
309. Paul E. Rempes
McDonald Douglass Missile Systems
Company
Department E-467
Building 107, Level 1
Post Office Box 516
Mail Code 1066086
St. Louis, MO 63166-0516
310. Theresa M. Resetar
U.S. Army Materials Technology
Laboratory
Materials Characterization Center
405 Arsenal Street
SLCMT-OMM
Watertown, MA 02172
311. K. T. Rhee
Rutgers University
College of Engineering
Bowser Road
Post Office Box 909
Piscataway, NJ 08854

312. Roy W. Rice
W. R. Grace and Company
7379 Route 32
Columbus, MD 21044
313. David W. Richerson
Ceramatec, Inc.
2425 South 900 West
Salt Lake City, UT 84119
314. Scott L. Richlen
U.S. Department of Energy
Office of Industrial Programs
1000 Independence Avenue, S.W.
Forrestal Building CE-141
Washington, DC 20585
315. Paul Rieth
Ferro Corporation
661 Willet Road
Buffalo, NY 14218-9990
316. Michael A. Rigdon
Institute for Defense Analyses
1801 Beauregard Street
Alexandria, VA 22311
317. John E. Ritter, Jr.
University of Massachusetts
Mechanical Engineering
Department
Amherst, MA 01003
318. Giulio A. Rossi
Norton Company
Advanced Ceramics
Goddard Road
Northboro, MA 01532-1545
319. Barry R. Rossing
Lanxide Corporation
Tralee Industrial Park
Newark, DE 19711
320. Bruce Rubinger
Goba1
50 Milk Street, 15th Floor
Boston, MA 02109
321. Robert Ruh
Air Force Wright Aeronautical
Laboratory
Metals and Ceramics Division
AFWAL/MLLM
Wright-Patterson AFB, OH 45433
322. Robert J. Russell, Sr.
Norton Company
Advanced Ceramics
Goddard Road
Northboro, MA 015332-1545
323. George P. Safol
Westinghouse Electric Corporation
R&D Center
1310 Beulah Road
Pittsburgh, PA 15235
324. J. A. Salem
NASA Lewis Research Center
21000 Brookpark Center
Cleveland, OH 44135
325. J. Sankar
North Carolina A&T State
University
Mechanical Engineering Department
Greensboro, NC 27411
326. Vin K. Sarin
Boston University
Department of Manufacturing
Engineering
44 Cummington Street
Boston, MA 02215
327. Maxine L. Savitz
Allied-Signal Aerospace Company
Garrett Ceramic Components
Division
19800 South Van Ness Avenue
Torrance, CA 90509
328. Ashok Saxena
Georgia Institute of Technology
Materials Engineering
Atlanta, GA 30332-0245

329. Richard Schapery
Texas A&M University
Civil Engineering Department
College Station, TX 77843
330. Jim Schienle
Allied-Signal Aerospace Company
Garrett Auxiliary Power Division
2739 East Washington Street
Post Office Box 5227, MS:1302-2P
Phoenix, AZ 85010
331. Liselotte J. Schioler
Air Force Office of Scientific
Research
Bolling AFB
Washington, DC 20332-6448
332. Richard A. Schmidt
Battelle Columbus Laboratories
Mechanics Section
505 King Avenue
Columbus, OH 43201-2693
333. Arnie Schneck
Deere & Company Technical
Center
Post Office Box 128
Wood-Ridge, NJ 07075
334. Matthew Schreiner
ALANX Products L.P.
101 Lake Drive
Newark, DE 19702
335. John Schuldies
Industrial Ceramic Technology, Inc.
37 Enterprise Drive
Ann Arbor, MI 48103
336. R. B. Schulz
U.S. Department of Energy
Office of Transportation Systems
1000 Independence Avenue, S.W.
Forrestal Building CE-34, 5G-046
Washington, DC 20585
337. Wesley J. C. Schuster
Thermo Electron Corporation
Metals Division
115 Eames Street
Post Office Box 340
Wilmington, MA 01887
338. Murray A. Schwartz
Bureau of Mines
30 Orchard Way, North
Potomac, MD 20854
339. Douglas B. Schwarz
Dow Chemical Company
52 Building
Midland, MI 48674
340. Thomas M. Sebestyen
U.S. Army Tank Automotive
Command
AMSTA-RGRT
Warren, MI 48397-5000
341. Brian Seegmiller
Coors Ceramics Company
17750 West 32nd Street
Golden, CO 80401
342. Peter T. B. Shaffer
Advanced Refractory
Technologies, Inc.
699 Hertel Avenue
Buffalo, NY 14207
343. Laurel M. Sheppard
Advanced Materials and
Processes
Route 87
Metals Park, OH 44073
344. Dinesh K. Shetty
University of Utah
Department of Materials Science
and Engineering
Salt Lake City, UT 84112
345. Jack D. Sibold
Coors Ceramics Company
17750 West 32nd Street
Golden, CO 80401

346. Neal Sigmon
U.S. House of Representatives
Subcommittee on Interior and
Related Events
Rayburn Building, Room B308
Washington, DC 20515
347. Richard Silbergitt
Quest Research Corporation
7600 Leesburg Pike #A
Falls Church, VA 22043
348. A. Sinha
North Carolina A&T State
University
Department of Mechanical
Engineering
Greensboro, NC 27411
349. Maurice J. Sinnott
University of Michigan
Chemical and Metallurgical
Engineering
438 West Engineering Building
Ann Arbor, MI 48109-2136
350. S. R. Skaggs
Los Alamos National Laboratory
Program Office
Post Office Box 1663, MS:F-682
Los Alamos, NM 87545
351. Jay R. Smyth
Allied-Signal Aerospace Company
Garrett Auxillary Power Division
Post Office Box 5227
MS:93-172/1302-2K
Phoenix, AZ 85010
352. Rafal Sobotowski
British Petroleum
R&D
3092 Broadway Avenue
Cleveland, OH 44115
353. E. Solidum
Allied-Signal Aerospace Company
Garrett Ceramic Components
Division
19800 South Van Ness Avenue
Torrance, CA 90509
354. Thomas M. Sopko
Lubrizol Enterprises, Inc.
29400 Lakeland Boulevard
Wickliffe, OH 44092
355. Richard M. Spriggs
Alfred University
Center for Advanced Ceramic
Technology
Alfred, NY 14802
356. Charles Spuckler
NASA Lewis Research Center
2100 Brookpark Road
Cleveland, OH 44135
357. M. Srinivasan
Materials Solutions
Post Office Box 663
Grand Island, NY 14702-0663
358. L. Brian Starling
ICI Advanced Ceramics
2055 East Technology Circle
Tempe, AZ 85284
359. Gordon L. Starr
Cummins Engine Company, Inc.
Metallic/Ceramic Materials
Department
Post Office Box 3005
Mail Code 50183
Columbus, IN 47202-3005
360. Harold L. Stocker
General Motors Corporation
Allison Gas Turbine Division
2001 South Tibbs Avenue
Post Office Box 420, T-23
Indianapolis, IN 46206-0420
361. Paul D. Stone
Dow Chemical Company
1801 Building
Midland, MI 48674
362. Roger Storm
Carborundum Company
Niagara Falls R&D Center
Post Office Box 337
Niagara Falls, NY 14302

363. E. E. Strain
Allied-Signal Aerospace Company
Garrett Auxiliary Power Division
Department 76-50
2739 East Washington Street
Building 1302-1N
Post Office Box 5227, MS:301-2N
Phoenix, AZ 85010
364. Thomas N. Strom
NASA Lewis Research Center
21000 Brookpark Road, 77-6
Cleveland, OH 44135
365. Jerry Strong
Albright & Wilson
Post Office Box 26229
Richmond, VA 23260
366. Richard Suddeth
Boeing Motor Airplane Company
Post Office Box 7730, MS:K-76-67
Wichita, KS 67277
367. Paul Sutor
Midwest Research Institute
425 Volker Boulevard
Kansas City, MO 64116
368. P. L. Sutton
U.S. Department of Energy
Office of Transportation Systems
1000 Independence Avenue, S.W.
Forrestal Building CE-322
Washington, DC 20585
369. J. J. Swab
U.S. Army Materials Technology
Laboratory
Ceramics Research Division
SLCMT-EMC
405 Arsenal Street
Watertown, MA 02172
370. John W. Swain, Jr.
Kollmorgen Corporation
PCK Technology Division
15424 Garrison Lane
Southgate, MI 48195
371. Lewis Swank
Ford Motor Company
Material Systems Reliability
Department
20000 Rotunda Drive
Building SRL, Room S-2023
Post Office Box 2053
Dearborn, MI 48121-2053
372. Chris Tarry
GTE Products Corporation
Hawes Street
Towanda, PA 18848
373. Anthony C. Taylor
U.S. House of Representatives
Committee on Science and
Technology
Rayburn Building, Room 2321
Washington, DC 20515
374. Monika O. Ten Eyck
Carborundum Company
Technology Division
Post Office Box 337
Niagara Falls, NY 14302
375. John K. Tien
Columbia University
Center for Strategic Materials
1137 S.W. Mudd Building
New York, NY 10027
376. T. Y. Tien
University of Michigan
Materials and Metallurgical
Engineering
Dow Building
Ann Arbor, MI 48109-2136
377. Julian M. Tishkoff
Air Force Office of Scientific
Research
(AFOSR/WC) Bolling AFB
Washington, DC 20332
378. Louis E. Toth
National Science Foundation
Division of Materials Research
1800 "G" Street, N.W.
Washington, DC 20550

379. Richard E. Tressler
 Pennsylvania State University
 Ceramic Science and Engineering
 201 Steidle Building
 University Park, PA 16802
380. W. T. Tucker
 General Electric Company
 Research Laboratory
 Post Office Box 8
 Schenectady, NY 12301
381. Donald L. Vaccari
 General Motors Corporation
 Allison Gas Turbine Division
 2001 South Tibbs Avenue
 Post Office Box 420
 Speed Code T10B
 Indianapolis, IN 46241
382. O. Van Der Biest
 Katholieke Universiteit Leuven
 Departement Metaalkunde en
 Toegepaste
 de Croylaan 2
 B-3030 Leuven
 BELGIUM
383. Edward C. Van Reuth
 Technology Strategies, Inc.
 10722 Shingle Oak Court
 Burke, VA 22015
384. Mark Van Roode
 Solar Turbines, Inc.
 2200 Pacific Highway
 Mail Zone R-1
 San Diego, CA 92138
385. V. Venkateswaran
 Carborundum Company
 Niagara Falls R&D Center
 Post Office Box 832
 Niagara Falls, NY 14302
386. Ted Vojnovich
 U.S. Department of Energy
 Office of Transportation Systems
 1000 Independence Avenue, S.W.
 Forrestal Building CE-151
 Washington, DC 20585
387. K. E. Voss
 Engelhard Corporation
 Research Department
 Menlo Park, CN-28
 Edison, NJ 08818
388. John B. Wachtman, Jr.
 Rutgers University
 College of Engineering
 Bowser Road
 Post Office Box 909
 Piscataway, NJ 08855-0909
389. Harlan L. Watson
 U.S. House of Representatives
 Committee on Science and
 Technology
 Rayburn Building, Suite 2321
 Washington, DC 20515
390. John D. Watson
 Broken Hill Proprietary Co., Ltd.
 Melbourne Research Laboratories
 245 Wellington Road
 Mulgrave 3170 Victoria
 AUSTRALIA
391. Karen E. Weber
 Detroit Diesel Corporation
 13400 West Outer Drive
 Detroit, MI 48239
392. C. David Weiss
 Caterpillar Inc.
 Technical Center, Building E
 Post Office Box 1875
 Peoria, IL 61656-1875
393. Albert R. C. Westwood
 Martin Marietta Laboratories
 R&D
 1450 South Rolling Road
 Baltimore, MD 21227
394. Thomas J. Whalen
 Ford Motor Company
 Material Systems Reliability
 Department
 20000 Rotunda Drive
 Building SRL, Room S-2023
 Post Office Box 2053
 Dearborn, MI 48121-2053

395. Sheldon M. Wiederhorn
National Institute of Standards
and Technology
Inorganic Materials Division
Gaithersburg, MD 20899
396. James C. Williams
General Electric Company
Engineering Materials
Technology Labs
One Neumann Way
Cincinnati, OH 45215-6301
397. Janette R. Williams
Kollmorgen Corporation
PCK Technology Division
322 L.I.E. South Service Road
Melville, NY 11747
398. Craig A. Willkens
Norton Company
Advanced Ceramics
Goddard Road
Northboro, MA 01532-1545
399. Roger R. Wills
TRW, Inc.
Valve Division
1455 East 185th Street
Cleveland, OH 44110
400. J. M. Wimmer
Allied-Signal Aerospace Company
Garrett Auxiliary Power Division
2739 East Washington Street
Post Office Box 5227, MS:1302-2P
Phoenix, AZ 85010
401. David Wirth
Coors Ceramics Company
Technical Operations and
Engineering
17750 West 32nd Street
Golden, CO 80401
402. Thomas J. Wissing
Eaton Corporation
Engineering & Research Center
26201 Northwestern Highway
Post Office Box 766
Southfield, MI 48037
403. Dale Wittmer
Southern Illinois University
at Carbondale
Department of Mechanical
Engineering
Carbondale, IL 62901
404. Stanley M. Wolf
U.S. Department of Energy
Office of Industrial Technologies
1000 Independence Avenue, S.W.
Forrestal Building CE-232
Washington, DC 20585
405. George W. Wolter
Howmet Turbine Components
Corporation
Technical Center
699 Benston Road
Whitehall, MI 49461
406. James C. Wood
NASA Lewis Research Center
21000 Brookpark Road
MS:500-210
Cleveland, OH 44135
407. Roger P. Worthen
Eaton Corporation
Engineering and Research Center
26201 Northwestern Highway
Post Office Box 766
Southfield, MI 48076
408. J. C. Wurm
Commission of the European
Communities
Advanced Materials Research
Programme
Rue de la Loi 200
B-1049 Brussels
BELGIUM
409. John Yamanias
Allied-Signal, Inc.
Metals and Ceramics Lab
Post Office Box 1021R
Morristown, NJ 07960-1021

410. Harry C. Yeh
Allied-Signal Aerospace Company
Garrett Ceramic Components Division
19800 South Van Ness Avenue
Torrance, CA 90509
411. Thomas M. Yonushonis
Cummins Engine Company, Inc.
Post Office Box 3005
Mail Code 50183
Columbus, IN 47202-3005
412. Jong Yung
Sundstrand Aviation Operations
Department 789-6
4747 Harrison Avenue
Rockford, IL 61125
413. Don Zabierek
Air Force Wright Aeronautical
Laboratory
AFWAL/POTC
Wright-Patterson AFB, OH 45433
414. Charles Zeh
U.S. Department of Energy
Morgantown Energy Technology
Center
Post Office Box 880
Morgantown, WV 26505
415. Anne Marie Zerega
U.S. Department of Energy
Office of Transportation Systems
1000 Independence Avenue, S.W.
Forrestal Building CE-30
Washington, DC 20585
416. Martin Zlotnick
Nichols Research Corporation
8618 Westwood Center Drive
Suite 200
Vienna, VA 22180-2222
417. Klaus M. Zwilsky
National Research Council
National Materials Advisory Board
2101 Constitution Avenue
Washington, DC 20418
418. Department of Energy
Oak Ridge Operations Office
Assistant Manager for Energy
Research and Development
Post Office Box 2001
Oak Ridge, TN 37831-8600
- 419-428. Department of Energy
Office of Scientific and
Technical Information
Office of Information Services
Post Office 62
Oak Ridge, TN 37831
- For distribution by microfiche
as shown in DOE/OSTI-4500,
Distribution Category UC-332
(Ceramics/Advanced Materials).

